INL/EXT-15-36520
Revision 3 Part 1

Metallic Fuels Handbook, Part 1:

Alloys Based on U-Zr, Pu-Zr, U-Pu, or U-Pu-Zr, Including Those with Minor Actinides (Np, Am, Cm), Rare-earth Elements (La, Ce, Pr, Nd, Gd), and Y

Dawn E. Janney

With special assistance from Cynthia A. Adkins and contributions from Douglas E. Burkes, James I. Cole, Randall S. Fielding, Steven M. Frank, Thomas Hartmann, Timothy A. Hyde, Dennis D. Keiser, Jr., J. Rory Kennedy, Andrew Maddison, Robert D. Mariani, Scott C. Middlemas, Thomas P. O'Holleran, Bulent H. Sencer, and Leah N. Squires

August 2018

NTRD-FUEL-2018-000085 / Part 1

The INL is a U.S. Department of Energy National Laboratory
operated by Battelle Energy Alliance

DISCLAIMER

This information was prepared as an account of work sponsored by an agency of the U.S. Government. Neither the U.S. Government nor any agency thereof, nor any of their employees, makes any warranty, expressed or implied, or assumes any legal liability or responsibility for the accuracy, completeness, or usefulness, of any information, apparatus, product, or process disclosed, or represents that its use would not infringe privately owned rights. References herein to any specific commercial product, process, or service by trade name, trade mark, manufacturer, or otherwise, does not necessarily constitute or imply its endorsement, recommendation, or favoring by the U.S. Government or any agency thereof. The views and opinions of authors expressed herein do not necessarily state or reflect those of the U.S. Government or any agency thereof.

INL/EXT-15-36520
Revision 3 Part 1

Metallic Fuels Handbook, Part 1: Alloys Based on U-Zr, Pu-Zr, U-Pu, or U-Pu-Zr, Including Those with Minor Actinides (Np, Am, Cm), Rare-earth Elements (La, Ce, Pr, Nd, Gd), and Y

Dawn E. Janney

With special assistance from Cynthia A. Adkins and contributions from Douglas E. Burkes, James I. Cole, Randall S. Fielding, Steven M. Frank, Thomas Hartmann, Timothy A. Hyde, Dennis D. Keiser, Jr., J. Rory Kennedy, Andrew Maddison, Robert D. Mariani, Scott C. Middlemas, Thomas P. O'Holleran, Bulent H. Sencer, and Leah N. Squires

August 2018

Idaho National Laboratory
Idaho Falls, Idaho 83415

http://www.inl.gov

Prepared for the
U.S. Department of Energy
Office of Nuclear Energy
Under DOE Idaho Operations Office
Contract DE-AC07-05ID14517

INTENTIONALLY BLANK

SUMMARY

Transmutation of minor actinides such as Np, Am, and Cm in spent nuclear fuel is of international interest because of its potential for reducing the long-term health and safety hazards caused by the radioactivity of the spent fuel. One important approach to transmutation (currently being pursued by the DOE Fuel Cycle Research & Development Advanced Fuels Campaign) involves incorporating the minor actinides into U-Pu-Zr alloys, which can be used as fuel in fast reactors. U-Pu-Zr alloys are well suited for electrolytic refining, which leads to incorporation rare-earth fission products such as La, Ce, Pr, and Nd. It is, therefore, important to understand not only the properties of U-Pu-Zr alloys but also those of U-Pu-Zr alloys with concentrations of minor actinides (particularly Np and Am) and rare-earth elements (particularly La, Ce, Pr, and Nd) similar to those in reprocessed fuel.

In addition to requiring extensive safety precautions, alloys containing U, Pu, and minor actinides are difficult to study for numerous reasons, including their complex phase transformations, characteristically sluggish phase-transformation kinetics, tendency to produce experimental results that vary depending on the histories of individual samples, rapid oxidation, and sensitivity to contaminants such as oxygen in concentrations below a hundred parts per million. Although less toxic, rare-earth elements such as La, Ce, Pr, and Nd are also difficult to study for similar reasons. Many of the experimental measurements were made before 1980, and many of the references for data on the rare-earth elements were originally published in Soviet journals. The level of documentation for experimental methods and results varies widely. It is therefore not surprising that little is known with certainty about U-Pu-Zr alloys, particularly those that also contain minor actinides and rare-earth elements. General acceptance of results commonly indicates that there is only a single measurement for a particular property rather than multiple measurements with similar results.

The Metallic Fuels Handbook summarizes currently available information about phases and phase diagrams, heat capacity, thermal expansion, and thermal conductivity of elements and alloys in the U-Pu-Zr-Np-Am-La-Ce-Pr-Nd system. Many sections in this revision are updates of material in previous versions of the Handbook [1-4]. New material in this revision involves primarily additional details about U-Zr and U-Pu-Zr alloys, including some information about properties not included in earlier revisions of the Handbook. In addition to presenting information about materials properties, this handbook emphasizes data assessments and provides information about how well each property is known and how much variation exists between measurements. Although the Handbook includes some results from models, its primary focus is experimental data.

Because of its size, the Handbook has been split into two parts, which are presented as separate documents. Part 1 (this document) contains introductory material and information about the U-Pu-Zr system (U-Zr, Pu-Zr, U-Pu, and U-Pu-Zr alloys, including those with minor actinides, rare-earth elements, and Y). Part 2 (reference [5]) contains information about elements and the remaining alloys in the U-Np-Pu-Am-La-Ce-Pr-Nd-Zr system.

INTENTIONALLY BLANK

ACKNOWLEDGEMENTS

This Handbook would not have been possible without the dedication, enthusiastic help, and expertise of the staff of the INL Research Library. Their ability to find even the most obscure documents is truly outstanding.

I would like to thank Dr. Steven L. Hayes for his support and insightful comments, Dr. Pavel Medvedev for Russian translation, and Dr. Steven M. Frank for helpful discussions. Ms. Cynthia A. Adkins not only provided project management support and thorough proofreading, but contributed some data and provided invaluable assistance in assessing the quality of the thermochemical data.

Funding for researching and writing the handbook was provided by the U.S. Department of Energy, Office of Nuclear Energy, under DOE Idaho Operations Office Contract DE-AC07-05ID14517.

INTENTIONALLY BLANK

CONTENTS

SUMMARY iii

ACKNOWLEDGEMENTS v

ACRONYMS xxi

1. INTRODUCTION 1
   - 1.1 Basic Constants, Units, and Conversion Factors 7
   - 1.2 Relationships between Masses, Volumes and Densities 8
   - 1.3 Relationships between Densities, Volumes and Thermal Expansion 9
   - 1.4 Calculating Volumes and Densities from High-Pressure Data: the Clausius-Clapeyron Relation 10
   - 1.5 Calculating Thermal Conductivity from Thermal Diffusivity, Density, and Heat Capacity 10
   - 1.6 Common Approximations 10
     - 1.6.1 Approximate Heat Capacities: The Kopp-Neumann Law 10
     - 1.6.2 Approximate Thermal Conductivities: The Wiedemann-Franz Law 11

2. U-Pu-Zr SYSTEM, INCLUDING U-Pu, U-Zr, Pu-Zr, AND U-Pu-Zr ALLOYS WITH AND WITHOUT MINOR ACTINIDES (Np, Am, Cm), RARE-EARTH ELEMENTS (La, Ce, Pr, Nd, Gd), AND Y 12
   - 2.1 Alloys Based on U-Zr, Including U-Zr and U-Zr Alloys with Minor Actinides (Np, Am), Rare-Earth Elements (La, Ce, Pr, Nd), and Y 12
     - 2.1.1 U-Zr 12
     - 2.1.2 U-Zr-Np 62
     - 2.1.3 U-Zr-Ce 64
     - 2.1.4 U-Zr-La-Ce-Pr-Nd 65
     - 2.1.5 U-Zr-Ce-Nd-Y 66
   - 2.2 Alloys Based on Pu-Zr, Including Pu-Zr and Pu-Zr Alloys with Minor Actinides (Np, Am) 66
     - 2.2.1 Pu-Zr 66
     - 2.2.2 Pu-Zr-Np (Alloy AFC1-MB) 78
     - 2.2.3 Pu-Zr-Am (Alloys AFC1-MC and DOE2) 79
     - 2.2.4 Pu-Zr-Np-Am (Alloy AFC1-MD) 80
   - 2.3 Alloys Based on U-Pu, Including U-Pu and U-Pu Alloys with Minor Actinides (Np, Am) 81
     - 2.3.1 U-Pu 81
     - 2.3.2 U-Pu-Np 93
     - 2.3.3 U-Pu-Am 94
   - 2.4 Alloys Based On U-Pu-Zr, including U-Pu-Zr and U-Pu-Zr Alloys with Minor Actinides (Np, Am, Cm), Rare-Earth Elements (La, Ce, Pr, Nd, Gd), and Y 97
     - 2.4.1 U-Pu-Zr 97
     - 2.4.2 U-Pu-Zr Alloys with Minor Actinides (Np, Am, Cm), Sorted by Increasing Weight Percentage of Zr 150
     - 2.4.3 U-Pu-Zr alloys with rare-earth elements (La, Ce, Pr, Nd) 172

2.4.4 U-Pu-Zr Alloys with Minor Actinides (Np, Am) and Rare-Earth Elements (La, Ce, Pr, Nd), Sorted by Increasing Weight Percentage of Zr 174
2.4.5 U-Pu-Zr Alloys with Minor Actinides (Np, Am, Cm), Rare-Earth Elements (La, Ce, Pr, Nd, and Y 194

3. REFERENCES 196

FIGURES

Figure 1. Comparison between the experimentally measured temperature dependence of the Lorenz number for Nd (red curve) and the theoretical value (dashed black line) (re-drawn with selected data from reference [14]). 11

Figure 2. Room-temperature lattice parameters of γ-U. Upward pointing triangle: [28] sample 635q and [27] sample 635q, left-pointing triangle: [28] sample 720q, right-pointing triangle: [28] sample 875q, squares: [84], circles: [86], star: [58], pentagon: [87] sample 4. 17

Figure 3. Room temperature lattice parameters, δ-UZr_2. Different symbols indicate data from different references, and numbers indicate point numbers in Table 5. 20

Figure 4. Solid-state phase-transition temperatures in Table 7. Symbols indicate references: Solid squares: [29], solid circles: [95], solid upward pointing triangles: [96], solid downward pointing triangles: [76], solid diamonds: [80], solid left-pointing triangles: [71], solid right-pointing triangles: [63], solid stars: [64], open squares: [87], open circles: [109], open upward-pointing triangles: [110], open downward-pointing triangles: [75], open left-pointing triangles: [111], open right-pointing triangles: [112], open stars: [25]. Colors indicate reported concentrations of oxygen: green: < 350 ppm, yellow: 351-650 ppm, red: 651-1000 ppm, black: not reported. 24

Figure 5. Phase-transition enthalpies (ΔH) reported in J/g from Table 8. Colors indicate ranges of values. 32

Figure 6. Comparison between Sheldon and Peterson (top) and Rough and Bauer (bottom) phase diagrams (Figure 2 of reference [20]). Colored symbols represent phase-transition temperatures from references [110] (green "+" symbols), [75] (red "+" symbols), [74] (black "+" symbols), and [29] (red, blue, and green triangles indicating measurements from samples annealed for 72, 168, and 672 hours, respectively.) Some symbols were moved horizontally for readability. All phase-transition temperatures in this figure are in Table 7. 36

Figure 7. U-Zr phase diagram according to Sheldon and Peterson [21], with changes in the liquidus and solidus as a result of the work of Balakrishnan et al. in red and changes to phase relationships at the high-Zr end of the composition range of δ-UZr_2 as a result of the work of Akabori et al. 1992 [88] near the large arrow. 37

Figure 8. Experimentally determined heat capacities of U-Zr alloys at temperatures from 300-850 K. Equation 13 through Equation 25 are plotted as solid lines. Colored symbols indicate tabulated data from references [63, 110-112], with colors corresponding to lines representing polynomial fits to the same data. Different symbols indicate data from different references. 40

Figure 9. Heat capacities of U-Zr alloys reported by Takahashi et al. (Equation 19 through Equation 22 and tabulated data in reference [112]). 41

Figure 10. Heat capacities of U-Zr alloys reported by Fedorov and Smirnov [114] (Equation 13 through Equation 17) 42

Figure 11. Variations in lattice parameters of δ-UZr_2 in U-70.7 at% Zr as a function of temperature (Equation 26 and Equation 27), with data points from Table 10. 44

Figure 12. Thermal expansion of U-Zr alloys according to Saller et al. and Touloukian et al. [60, 61], with thermal expansion of U and Zr [61, 119] for comparison. Values for 10 wt% and 20 wt% Zr are polynomial fits to tabulated data from Touloukian et al. [61] (Equation 28 and Equation 29) 45

Figure 13. Thermal expansion of U and U-Zr alloys according to Basak et al. [62] (Equation 30 through Equation 37) and Kaity et al. [63, 64] 47

Figure 14. Room-temperature density of δ-UZr_2 calculated from lattice parameters in references [26, 28, 88, 89, 95] 49

Figure 15. Room-temperature densities of (α-U) solid solutions in U-Zr alloys, calculated from data in references [26, 75] using Equation 5. Dotted line connects densities of α-U and α-Zr. 50

Figure 16. Room-temperature lattice parameters and densities of γ-(U,Zr) solid solutions calculated from lattice parameters in references [27, 28, 58, 84]. Dotted line connects the density of γ-U at 1060 K and the room-temperature density of α-Zr. 51

Figure 17. Room-temperature densities of as-cast U-Zr alloys. Blue circles and dotted line: Data from reference [103]. Red "+" symbols: Data from Figure 6d of reference [62]. Green vertical bar: Range of densities of U-10Zr (wt%) alloys produced using different casting methods [121-123]. Solid black line: Theoretical density. 52

Figure 18. Thermal conductivity of U-Zr alloys [63, 66, 124, 125]. Data from [115] at temperatures between 650 and 1000°C are not included because individual measurements were not presented and because of significant differences between the polynomial fit to the data and the graphical presentation of the same data. Thermal conductivities of U [126] and Zr [127] are included for comparison. 54

Figure 19. Measured and predicted thermal conductivity for U-Zr alloys with 6-17 wt% Zr. Ogata's predicted value is from Equation 39 55

Figure 20. Elastic modulus for U-Zr alloys at 295 K (redrawn from refrence [133]) 58

Figure 21. Tensile properties of U-Zr alloys at room temperature (black) and 375°C (red), after Figure 11 and Figure 12 from reference [132]. Different measurements use different symbols, which are the same for room-temperature and high-temperature data. Asterisks: Yield strength (0.2% offset), psi × 1000. "X" symbols: ultimate tensile strength, psi × 1000. "+" symbols: reduction in area, %. Dots: elongation in 2 inches, %. 59

Figure 22. a: Tentative partial isothermal section of the U-Np-Zr system at 700°C suggested by Rodríguez et al. [140]. b: Isothermal section of the U-Np-Zr system at 700°C calculated by Xie and Morgan [141]. Phase identifications in black are from reference [141]; identifications in red were added for this Handbook to assist in interpretation. 63

Figure 23. a: Tentative partial isothermal section of the U-Np-Zr system at 595°C suggested by Rodríguez et al. [140]. b: Isothermal section of the U-Np-Zr system at 595°C calculated

by Xie and Morgan [141]. Phase identifications in black are from reference [141], except that the phase identified as "ζ"in the reference is called δ-(U, Np) for consistency with earlier research and the rest of this Handbook. Identifications in red were added for this Handbook to assist in interpretation. 64

Figure 24. a: Tentative partial isothermal section of the U-Np-Zr system at 520°C suggested by Rodríguez et al. [140]. b: Isothermal section of the U-Np-Zr system at 520°C calculated by Xie and Morgan [141]. Phase designations in black are from reference [141], except that the phase identified as "ζ" in the reference is called δ-(U, Np) for consistency with earlier research and the rest of this Handbook. Identifications in red were added for this Handbook to assist in interpretation. 64

Figure 25. Variations in the room-temperature value of the lattice parameter, δ-(Pu,Zr). Data are from Marples [154] and Ellinger and Land [156]. 68

Figure 26. Variations in the room-temperature value of the *c* lattice parameter, (α-Zr) solid solutions with Pu. Data are from Marples [154] and Ellinger and Land [156]. Multiple data points with the same composition in data from Marples are from samples with different thermal histories. 69

Figure 27. Variations in the room-temperature value of the *a* lattice parameter, (α-Zr) solid solutions with Pu. Data are from Marples [154] and Ellinger and Land [156]. Multiple data points with the same composition in data from Marples are from samples with different thermal histories. 69

Figure 28. Pu-Zr phase diagram simplified from Okamoto 1995 [151]. See Figure 29 and Figure 30 for details of high-Pu phases. 72

Figure 29. Identities and boundaries of high-Pu phases according to the 1995 Okamoto phase diagram [151]. α, β, γ, δ, δ', ε, and θ refer to (α-Pu), (β-Pu), (γ-Pu), (δ-Pu), (δ'-Pu), (ε-Pu), and θ-(Pu,Zr) respectively. ζ-$Pu_{28}Zr$ is not shown. 72

Figure 30. Identities and boundaries of high-Pu phases according to Taylor [153]. α, β, γ, δ, δ', ε, θ, and ζ refer to (α-Pu), (β-Pu), (γ-Pu), (δ-Pu), (δ'-Pu), (ε-Pu), θ-(Pu,Zr), and ζ-$Pu_{28}Zr$, respectively. Maximum concentrations of Zr in (α-Pu), (β-Pu), and (γ-Pu) are smaller than in Figure 29, and there are additional two-phase fields involving ζ-$Pu_{28}Zr$. 73

Figure 31. Thermal expansion of δ-Pu-Zr alloys, calculated from data in Table 18 [171] using a reference temperature of 400°C. 74

Figure 32. Densities of (α-Zr) solid solutions with Pu [154, 156]. Dotted line shows values that would be predicted by linear interpolation from the room-temperature densities of α-Pu and α-Zr. 76

Figure 33. Densities of δ-(Pu,Zr) solid solutions [154, 156]. 76

Figure 34. Thermal diffusivity of Pu-10 wt% Zr and Pu-30 wt% Zr alloys (INL preliminary data from reference [3], also available in reference). Data for Pu-10 wt% alloy are the average of two measurements. 78

Figure 35. Variations in the room-temperature lattice parameter of ζ-(U,Pu) as a function of composition [192 (Figure 7), 203]. Although Ellinger et al. indexed their data based on a cubic unit cell and Lawson et al. used a rhombohedral unit cell, lattice parameters from these references are comparable because the rhombohedral lattice angle α is approximately 90 degrees. 83

Figure 36. 1989 U-Pu phase diagram of Peterson and Foltyn [186], with more recent measurements from Y. Okamoto et al. [190] (red dots) and Kaity et al. [191] (green dots). α, β, γ, δ, and δ' refer to solid solutions of the corresponding Pu phases, ζ is ζ-(U,Pu), and η is η-(U,Pu). 84

Figure 37. Incremental enthalpy (H(T) – H(298)) of U-10Pu, calculated from Equation 40 through Equation 43. 85

Figure 38. Heat capacity of U-10Pu (calculated from Equation 44 through Equation 47), with the heat capacity of U [210] for comparison. 87

Figure 39. Thermal expansion of U-15 wt% (15 at%) Pu, calculated using Equation 48, Equation 49, and Equation 50. 88

Figure 40. Calculated densities of ζ-(U,Pu) alloys assuming isotopes present are U-238 and Pu-239 based on structure data from references [192, 203]. 91

Figure 41. As-cast densities of U-Pu alloys. Red symbols and dotted line are from Ellinger et al. [192], blue "+" symbol is from Boucher and colleagues [211, 212], and green "+" symbol is from Kelman et al. [193]. 92

Figure 42. Calculated U-Np-Pu phase diagram [38], with phase identifications suggested by comparison to binary phase diagrams. β refers to β-U solid solutions, δ refers to δ-(U,Np) solid solutions, and γ refers to γ-(U,Np) or γ-(U,Pu) depending on composition. 94

Figure 43. Calculated isothermal sections at 1200 K based on the models of Ogawa [195], Kurata [216] (as calculated by Perron et al. [199 (Figure 7)]), and the preferred model of Perron et al. [199 (Figure 8)]. 95

Figure 44. Calculated isothermal sections at 900 K based on the model of Kurata [216] (as calculated by Perron et al. [199 (Figure 7)]) and the preferred model of Perron et al. [199 (Figure 8)]. 96

Figure 45. Calculated isothermal sections at 600 K based on the model of Kurata [216] (as calculated by Perron et al. [199 (Figure 7)]) and the preferred model of Perron et al. [199 (Figure 8)]. 96

Figure 46. Calculated isothermal sections at 300 K based on the model of Kurata [216] (as calculated by Perron et al. [199 (Figure 7)]) and the preferred model of Perron et al. [199 (Figure 8)]. 97

Figure 47. Measured liquidus temperatures for U-Pu-Zr alloys with at least 40 at% U (Table 23). Shapes indicate sources of data: circles are from references [193, 209, 213], right-pointing triangles are from reference [217], left-pointing triangle is from reference [149], and downward-pointing triangles are from reference [42]. Colors indicate temperature ranges: blue is 1050-1100°C, light green is 1200-1250, yellow is 1250-1290, orange is 1300-1350, and brown is 1400-1450. Numbers next to data points are temperatures. 101

Figure 48. Measured solidus temperatures for U-Pu-Zr alloys with at least 40 at% U (Table 23). Shapes indicate sources of data: circles are from references [193, 209, 213], right-pointing triangles are from reference [217], and downward-pointing triangles are from reference [42]. Colors indicate temperature ranges: purple is < 1000°C, blue is 1050-1100, turquoise is 1100-1150, and green is 1150-1200. Numbers next to data points are temperatures. 102

Figure 49. Liquidus temperatures (°C) from models of Leibowitz et al. [42] (solid lines), Kurata [38] (dotted lines), and Ogata [48] (colored symbols showing examples of calculated

points, with each color indicating a different temperature). Reference [38] also includes a curve corresponding to a temperature of 1321°C, which is not shown here for clarity. Melting temperatures of U, Pu, and Zr are shown for comparison. 103

Figure 50. Solidus temperatures (°C) from models of Leibowitz et al. [42] (solid lines), Kurata [38] (dotted lines), and Ogata [48] (colored symbols showing examples of calculated points). 104

Figure 51. Compositions of U-Pu-Zr alloys with measurements of sub-solidus phase-transition temperatures, with point numbers from Table 25. Data are from Mound Laboratory [166], Argonne National Laboratory [219], Los Alamos National Laboratory [217], CEA [211], Idaho National Laboratory, and the METAPHIX programme [149]. Colors and symbols indicate data from different laboratories. 106

Figure 52. Compositions of alloys whose phase-transition temperatures and enthalpies were measured at INL. Colors and symbols indicate sources of data (dark gray squares: Harbur et al., red circle: Savage, blue triangles: INL). Numbers indicate point numbers from Table 26. 110

Figure 53. The gamma solvus in the U-Pu-Zr ternary system. Contours indicate solvus temperatures in °C. Colors indicate corresponding temperatures in both parts of the figure. a. As interpreted by researchers at Mound Laboratory [166, 220]. α indicates α-U, δ indicates δ-UZr_2, η indicates η-(U,Pu), ζ indicates ζ-(U,Pu), and all phases are ternary solid solutions. Capital letters indicate four-phase reactions identified in Section 2.4.1.2.3.2. b. Composite phase diagram from O'Boyle and Dwight [81]. The truncated 605-degree contour line is an artifact of the way the figure was constructed. 120

Figure 54. Isothermal sections of O'Boyle and Dwight , based on figures 4-6 of reference [81]. δ refers to δ-UZr_2, ζ refers to ζ-(U,Pu), η refers to η-(U,Pu), and Pu-L is liquid Pu. Dotted lines indicate four-phase reactions. Large numbers adjacent to each section indicate its temperature in °C. 123

Figure 55. Comparison of measured phase-transition temperatures (Table 25) with transition temperatures from the isothermal sections of O'Boyle and Dwight (Figure 54). Large numbers adjacent to each isothermal section identify the temperature of the section. Smaller numbers in parentheses indicate a range of measured temperatures. Colored symbols represent compositions that have reported phase transitions in the specified temperature ranges. Numbers adjacent to the symbols correspond to point numbers in Table 25. 128

Figure 56. Incremental enthalpy (H(T) – H(25)) of U-15Pu-10Zr [204]. Triangles are measured data points, and the polynomial fit is calculated from Equation 53 and Equation 54. 129

Figure 57 (corrects Figure 61 of reference [3]). Heat capacities of U-Pu-Zr alloys, calculated from Equation 55 through Equation 60, and converted to J/mol-K. Compositions in legend are in wt%. The heat capacity of pure U [210] is provided for comparison. 131

Figure 58 (corrects and updates Figure 62 of reference [3]). Room-temperature densities of U-Pu-Zr alloys (blue line and "+" symbols are from Figure 5 of reference [213], blue "x" symbols are from Table 1 of reference [213], purple "#" symbol is from [149], orange "*" symbols are INL data, dotted and dashed red lines are from [217], green line indicates range of values in data from references [211, 212], black line is theoretical density). 135

Figure 59. Thermal conductivity of U-Pu-Zr alloys (data from Table 33). Compositions are in wt%. Symbols indicate sources of data: squares are from [245], circles are from [217], triangles are from [213], and asterisk is from [211]. 137

Figure 60. Comparison of measured and predicted thermal conductivity of U-Pu-Zr alloys (compositions in wt%) 138

Figure 61. Ultimate tensile strength of U-Pu-Zr alloys. Data values are in Table 34. Different shapes indicate different data sources (circle: reference [209], squares: as-extruded data from reference [217], triangle: as-cast data from reference [217]. Numbers and colors indicate individual samples 141

Figure 62. Yield strength of U-Pu-Zr alloys (0.2% deformation). Data values are in Table 34. Shapes, colors, and sample numbers are like those in Figure 61 142

Figure 63. Elastic modulus of U-Pu-Zr alloys. Data values are in Table 34. Shapes, colors, and sample numbers are like those in Figure 61. 143

Figure 64. Hot hardness of U-15Pu-6.8Zr (wt%) (data from Table IV of reference [217].) 149

Figure 65. Incremental enthalpies of U-20Pu-10Zr-2Am alloys (Equation 61 and Equation 62). 151

Figure 66. Heat capacities of U-20Pu-10Zr-2Am alloys from Equation 63 and Equation 64. 151

Figure 67. Thermal conductivity of U-20Pu-10Zr-2Am alloys with varying concentrations of oxygen (Equation 65, Equation 66, and Equation 67). Dotted lines indicate upper and lower boundaries for each equation based on errors of ±11% for Equation 65, ±12% for Equation 66, and ±17% for Equation 67 [250]. Thermal conductivities at temperatures above 923K are based on heat capacities extrapolated from lower temperatures. Thermal conductivities between 773 and 973 K were not determined 153

Figure 68. SEM BSE images of U-20Pu-2Np-3Am-10Zr (FCRD alloy AFC2-E3). Black areas are high-Zr inclusions. Arrows indicate examples of polygonal boundaries. 154

Figure 69. Heat capacity of Alloy AFC2-E3 (Equation 68). 155

Figure 70. BSE SEM images of Alloy AFC2-A1. Black spots are high-Zr inclusions, light areas are relatively high in U and low in Zr, and dark areas are relatively high in Zr and low in U. Concentrations of other actinides show little variation in the matrix. Image b was also published by Janney and Kennedy [254], and image c was also published in references [10, 230, 231]. 156

Figure 71. Specific heat of Alloy AFC2-A1 (Equation 69). 159

Figure 72. BSE (left) and SE (right) SEM images of U-30Pu-5Am-3Np-20Zr (FCRD alloy AFC2-A6). Black arrows show clusters of high-Zr inclusions; white arrows indicate pores that have been mistakenly identified as inclusions in other publications 160

Figure 73. SEM images of as-cast U-2Np-34Pu-4Am-20Zr (Alloy AFC1-MG). Arrows indicate linear features that may have originated as grain boundaries in higher-temperature phases 163

Figure 74. Experimental X-ray diffraction patterns from U-2Np-34Pu-4Am-20Zr (Alloy AFC1-MG) with simulated pattern from δ-UZr_2 for comparison. a: Experimental pattern. b: Experimental pattern [230 (Figure 4, Pattern C)]. c. Simulated pattern from d-UZr_2. Dashed red lines indicate positions of peaks from δ-UZr_2; blue arrows indicate positions of peaks from the aluminum sample holder, which was used as an internal standard. Patterns were measured with Cu K_α X-rays. 164

Figure 75. BSE images of U-29Pu-4Am-2Np-30Zr. a: Alloy AFC1-MI [230] b: Alloy AFC1-MJ (DOE1) [185] c: Alloy AFC1-MJ (DOE1). Large black areas in Part C are pores. 167

Figure 76. Experimental X-ray diffraction patterns from U-29Pu-4Am-2Np-30Zr with simulated pattern from δ-UZr_2 for comparison. a: Experimental pattern. b: Experimental pattern [230 (Figure 4, Pattern D)]. c. Simulated pattern from δ-UZr_2. Dashed red lines indicate positions of peaks from δ-UZr_2; blue arrows indicate positions of peaks from the Al used as an internal standard. Patterns were measured with Cu K_α X-rays. 168

Figure 77. Experimental X-ray diffraction patterns from Alloy AFC1-MH with simulated pattern from δ-UZr_2 for comparison. a: Experimental pattern. b: Experimental pattern [230 (Figure 4, Pattern F)]. c: Simulated pattern from δ-UZr_2. Dashed red lines indicate positions of peaks from δ-UZr_2; blue arrows indicate positions of peaks from the Al used as an internal standard. Patterns were measured with Cu K_α X-rays. 171

Figure 78. SEM images of as-cast alloy AFC2-B4. a: SE image. Black arrows show examples of high-Zr inclusions; white arrows show examples of high-RE inclusions. Note that small high-RE inclusions are commonly adjacent to high-Zr inclusions. b: BSE image with contrast adjusted to emphasize features in matrix. Black arrows show examples of polygonal boundaries; white arrows show examples of areas with fine parallel microstructures. 173

Figure 79. X-ray maps from the area of Figure 78 Part a, showing Nd as a representative rare-earth element. Contrast was adjusted independently for individual maps. Brighter areas indicate higher concentrations of the indicated elements. 173

Figure 80. SEM SE images of annealed alloy AFC2-B4. Large black arrows show examples of polygonal boundaries. Small black arrows show examples of high-Zr inclusions. Small white arrows show examples of high-RE inclusions. 174

Figure 81. SEM BSE image and X-ray maps showing distributions of selected elements from Alloy AFC2-A2. Concentrations of U and Zr vary inversely and are correlated to contrast in BSE image. Concentration of Pu is homogeneous at the spatial scale of the data except in high-Zr inclusions. The Np map is similar to the Pu map, but has a very low number of total counts. Distributions of La, Ce, and Pr are similar to that of Np. The Am map resembles those of the rare-earth elements more closely than those of other actinides. 176

Figure 82. Experimental X-ray diffraction patterns from Alloy AFC2-A2 [231 (Figure 2, Pattern B)]. Arrows indicate peaks from the LaB_6 internal standard. The pattern was collected using Cu K_α radiation. 177

Figure 83. SEM images and X-ray maps from as-cast Alloy AFC2-A3. Black arrows indicate the same high-Zr inclusion; white arrows indicate the same small high-RE inclusion and adjacent high-Am inclusion. 180

Figure 84. SEM images from Alloy AFC2-A3 after DSC experiment [265]. Black arrows indicate high-U polygonal boundaries. 181

Figure 85. X-ray maps showing distributions of elements in as-cast AFC2-A5. 186

Figure 86. Experimental X-ray diffraction patterns from Alloy AFC2-A5 (re-drawn from [236 (Figure 2, Pattern E)]). Arrows indicate peaks from the LaB_6 internal standard. The pattern was collected with Cu K_α radiation. 187

Figure 87. SEM images and X-ray maps from Alloy AFC2-A4. Distributions of La, Ce, and Pr are similar to that of Nd. 190

Figure 88. Experimental X-ray diffraction patterns from Alloy AFC2-A4 (re-drawn from [236 (Figure 2, Pattern D)]). Arrows indicate peaks from the LaB_6 internal standard. Two-theta angles correspond to Cu K_a radiation. 190

Figure 89. SEM images of Alloy AFC2-A8. Large white arrows indicate examples of high-Am RE inclusions, small white arrows indicate examples of low-Am RE inclusions, and black arrows indicate high-Zr inclusions. Note variations in high-Zr inclusion indicated by black arrows in parts b and c. Also note small bright spots in matrix and polygonal boundaries in upper right and center left of Part d. 193

TABLES

Table 1. Contents of both volumes of the Handbook organized by material group. References are to sections in this document unless otherwise noted. Reference [5] is Part 2 of this Handbook. 2

Table 2. Contents organized by composition. References are to sections in this document unless otherwise noted. Reference [5] is Part 2 of this Handbook.. 3

Table 3. Contents organized by alloy name. All references are to sections in this document. 6

Table 4. Room-temperature lattice parameters of γ in U-Zr alloys. 15

Table 5. Room-temperature lattice parameters of δ-UZr_2 with known compositions. 18

Table 6. Solidus and liquidus measurements of U-Zr alloys (references [63, 64, 75 (Table V), 106 (Table 6)]). Data from Balakrishnan et al. (reference [106], in bold type) is preferred, and has an estimated maximum composition error of ±1.3%. 22

Table 7. Solid-state phase transition temperatures in U-Zr alloys. α refers to α-U, β refers to β-U, γ refers to (γ-U, β-Zr) solid solutions, and δ refers to δ-UZr_2. Temperatures for each sample are listed in increasing order, with no attempt to ensure that temperatures in each column represent the same reactions. 26

Table 8. Enthalpies (ΔH) and entropies (ΔS) of phase transitions in U-Zr alloys from calorimetry. 32

Table 9. Heat capacities of γ-(U,Zr) solid solutions at 1000 K. 43

Table 10. Lattice parameters of δ-UZr_2 in alloys with ~70.5 at% Zr. [95] 43

Table 11. Room-temperature lattice parameters and densities of δ-UZr_2. 48

Table 12. Room-temperature lattice parameters and densities of (α-U) solid solutions in U-Zr alloys, calculated from lattice parameters in specified references using Equation 5. 50

Table 13. Room-temperature molar masses, lattice parameters, unit cell volumes, and densities of γ-(U,Zr) solid solutions. 51

Table 14. Room-temperature tensile properties of uranium-zirconium alloys. 56

Table 15. Hot-hardness values for injection-cast alloys made with uranium from Fernald (I-F) and arc-cast alloys made with uranium from Derby (A-D) [130, 131]. Refer to data from references [130, 131] in Table 14 for more information about these alloys. 59

Table 16. Indentation creep of U-6Zr, U-7Zr, and U-50Zr (reference [73] Table 2, reference [134] Table 1 and Table 2, and reference [135] Table 2.). 61

Table 17. As-cast and theoretical densities of U-Zr-La-Ce-Pr-Nd alloys with 0-7 wt% of a rare-earth alloy consisting of 53% Nd, 25% Ce, 16% Pr, and 6% La by weight. 66

Table 18. Coefficients for equations expressing lengths of U-Pu alloys, $L = a + b \times T + c \times T^2$, where L is a length (for dilatometer data) or lattice parameter in Å(for X-ray data) and T is a temperature in °C [171]. The authors emphasize that these coefficients should only be used within the stated temperature ranges. 74

Table 19. Coefficients of thermal expansion for δ-(Pu, Zr). Data for Pu are from reference [173]; other data are from reference [171]. Coefficients should not be used outside the listed temperature ranges. 75

Table 20. Lattice parameters and unit-cell volumes for ζ-(U,Pu) as a function of temperature, based on data read from [203 Figure 8]. 89

Table 21. Room-temperature densities of U-Pu liquids at the liquidus based on extrapolation of higher-temperature data from the specified temperature downwards to the liquidus. 91

Table 22. Thermal conductivity of U-10Pu [193]. 93

Table 23. Comparison of experimental and calculated liquidus temperatures (°C) for U-Pu-Zr alloys. 104

Table 24. Comparison of experimental and calculated solidus temperatures (°C) for U-Pu-Zr alloys. 105

Table 25. Measured sub-solidus transition temperatures in U-Pu-Zr alloys, sorted by increasing at% Zr. 107

Table 26. Combined enthalpies of transitions between 400 and 800°C. 110

Table 27. Coexisting phases from room-temperature analyses of annealed samples[a]. 112

Table 28. Phases and volume percentages of coexisting phases from high-temperature neutron-diffraction data [77, 78]. α and β refer to α-U and β-U, δ refers to δ-UZr_2, ζ refers to ζ-(U,Pu), γ refers to the bcc solid solution between γ-U, ε-Pu, and β-Zr, and ? indicates unidentified peaks. Numbers in parentheses are volume percentages of phases. 117

Table 29. Thermal expansion coefficients for U-Pu-Zr alloys between room temperature and ~600°C. 132

Table 30. Thermal expansion coefficients for U-Pu-Zr alloys at higher temperatures. 132

Table 31. Length changes (in %) from phase transformations in U-Pu-Zr alloys. 133

Table 32. Room-temperature densities of U-Pu-Zr alloys, listed in order of increasing atomic fraction of Zr. 133

Table 33. Thermal conductivities of U-Pu-Zr alloys (W/cm-K). 136

Table 34. Tensile properties of U-Pu-Zr alloys. 139

Table 35. Ultimate compressive strengths of U-Pu-Zr alloys. 144

Table 36. Time (in minutes) to attain 2% strain in U-Pu-Zr alloys. 146

Table 37. Time (in minutes) to attain 1% strain in U-18.5Pu-14Zr (wt%) (Table 22-VIII of reference [193]) 147

Table 38. Hardness measurements (Vickers) of U-Pu-Zr alloys. 148

Table 39. Hot hardness of U-15Pu-6.8Zr (wt%) (data from Table IV of reference [217]) 148

Table 40. Phase-transformation temperatures in Alloy AFC2-E3 (U-20Pu-10Zr-2Np-3Am). 155

Table 41. Phase-transformation temperatures in U-20Pu-3Am-2Np-15Zr (Alloy AFC2-A1). 158

Table 42. Phase-transformation enthalpies in U-20Pu-3Am-2Np-15Zr (Alloy AFC2-A1). 158

Table 43. Phase-transformation temperatures in U-3Np-30Pu-5Am-20Zr (Alloy AFC2-A6). 161

Table 44 Phase-transformation enthalpies in U-3Np-30Pu-5Am-20Zr (Alloy AFC2-A6). 161

Table 45. Phase-transformation temperatures and enthalpies in Alloy AFC1-MG (U-2Np-34Pu-4Am-20Zr) [230 (Table 7)]. 165

Table 46. Phase transition temperatures from Alloys AFC1-MI and AFC1-MJ [230 (Table 8)]. 169

Table 47. Phase-transition temperatures in 30U-2Np-25Pu-3Am-40Zr (Alloy AFC1-MH) [230 (Table 9)] 172

Table 48. Phase-transformation temperatures in 59U-20Pu-3Am-2Np-1.0RE-15Zr (Alloy AFC2-A2) [10, 231 (Tables 4 and 5, Alloy B)]. 178

Table 49. Phase-transformation enthalpies in 59U-20Pu-3Am-2Np-1.0RE-15Zr [10 (Table 10, Alloy A2), 231 (Tables 4 and 5, Alloy B)] determined by DTA. 178

Table 50. Reported Phase-transformation temperatures in 58.5U-20Pu-3Am-2Np-1.**5**RE-15Zr [10, 231 (Tables 4 and 5, Alloy C), 256 (Table 3)]. 182

Table 51. Phase-transformation enthalpies in 58.5U-20Pu-3Am-2Np-1.**5**RE-15Zr [10 (Table 10), 231 (Tables 4 and 5, Alloy C), 256 (Table 3)] determined by DTA. 183

Table 52. Phase-transformation temperatures in 41U-30Pu-5Am-3Np-1.0RE-20Zr (Alloy AFC2-A5) [10, 236 (Tables 4 and 5, Alloy E)]. 188

Table 53. Phase-transformation enthalpies in 41U-30Pu-5Am-3Np-1.0RE-20Zr (Alloy AFC2-A5) [236 (Tables 4 and 5, Alloy E)] determined by DTA. 188

Table 54. Phase-transformation temperatures in 40.5U-3Np-30Pu-5Am-1.5RE-20Zr (Alloy AFC2-A4) [10, 236 (Tables 4 and 5, Alloy D)]. 191

Table 55. Phase-transformation enthalpies in 40.5U-3Np-30Pu-5Am-1.5RE-20Zr [236 (Tables 4 and 5, Alloy D)]. 191

EQUATIONS

Equation 1. Conversion of weight fractions to mole fractions 8

Equation 2. Conversion of mole fractions to weight fractions 8

Equation 3. Basic relationship between density (ρ), mass (M), and volume (V) 8

Equation 4. Converting densities from kg/m^3 to g/cm^3 8

Equation 5. Calculating the density in g/cm^3 from crystallographic data (based on equation 1 of reference [8]) 8

Equation 6: Relative volume as a function of linear thermal expansion [10 Equation 4] 9

Equation 7: Density as a function of relative volume 9

Equation 8: Theoretical density of an alloy from Law of Additivity 9

Equation 9. The Clausius-Clapeyron relation 10

Equation 10. Calculating thermal conductivity from thermal diffusivity, density, and heat capacity 10

Equation 11. Kopp-Neumann Law [11] 10

Equation 12. Wiedemann-Franz Law 11

Equation 13. Heat capacity of U-13 at% Zr (Zr-87 at% U) from 20-600°C measured by Fedorov and Smirnov [114, 118] 37

Equation 14. Heat capacity of U-41 at% Zr (Zr-59 at% U) measured by Fedorov and Smirnov [114, 118] 38

Equation 15. Heat capacity of U-61 at% Zr (Zr 39 at% U) measured by Fedorov and Smirnov [114, 118] 38

Equation 16. Heat capacity of U-73 at% Zr (Zr-27 at% U) measured by Fedorov and Smirnov [114, 118] 38

Equation 17. Heat capacity of U-89 at% Zr (Zr-11 at% U) measured by Fedorov and Smirnov [114, 118] 38

Equation 18. Heat capacity of U-20 at % Zr (U-9 wt% Zr) alloy from 289 to 852 K (Polynomial fit by Kaity et al. [63] to data from Matsui et al. [110]). 38

Equation 19. Heat capacity of U-14at% Zr from 300 to 850 K (Polynomial fit by Kaity et al. [63] to data from Takahashi et al. [112]) 38

Equation 20. Heat capacity of U-35at% Zr from 300 to 850 K (Polynomial fit by Kaity et al. [63] to data from Takahashi et al. [112]) 39

Equation 21. Heat capacity of U-72at% Zr from 300 to 850 K (Polynomial fit by Kaity et al. [63] to data from Takahashi et al. [112]) 39

Equation 22. Heat capacity of U-91at% Zr from 300 to 850 K (Polynomial fit by Kaity et al. [63] to data from Takahashi et al. [112]) 39

Equation 23. Heat capacity of U-6Zr from 304-495 K [63] 39

Equation 24. Heat capacity of U-6Zr from 495-802 K [63] 39

Equation 25. Heat capacity of U-7Zr [111] 39

Equation 26. *a* lattice parameter of δ-UZr_2 in U-70.7 at% Zr, in Å (from [95 (Equation 1)]) 43

Equation 27. *c* lattice parameter of δ-UZr_2 in U-70.7 at% Zr, in Å (from [95 (Equation 2)]) 43

Equation 28. Thermal expansion of U-10 wt%-Zr from 293 to 900 K according to Touloukian et al. [61] 45

Equation 29. Thermal expansion of U-20 wt%-Zr from 293 to 900 K according to Touloukian et al. [61] 45

Equation 30. Thermal expansion of (α-U) in U-2 wt%-Zr from 323 to 923 K according to Basak et al. [62] 46

Equation 31. Thermal expansion of (γ-U) in U-2 wt%-Zr from 998 to 1173 K according to Basak et al [62] 46

Equation 32. Thermal expansion of (α-U) in U-5 wt%-Zr from 323 to 923 K according to Basak et al. [62] 46

Equation 33. Thermal expansion of (γ-U) in U-5 wt%-Zr from 998 to 1173 K according to Basak et al. [62] 46

Equation 34. Thermal expansion of (α-U) in U-7 wt%-Zr from 323 to 923 K according to Basak et al. [62] 46

Equation 35. Thermal expansion of (γ-U) in U-7 wt%-Zr from 998 to 1173 K according to Basak et al. [62] 46

Equation 36. Thermal expansion of (α-U) in U-10 wt%-Zr from 323 to 923 K according to Basak et al. [62] 46

Equation 37. Thermal expansion of (γ-U) in U-10 wt%-Zr from 998 to 1173 K according to Basak et al. [62] 46

Equation 38. Thermal conductivity of a U-Zr alloy with 11.4 wt% Zr (equation 8 of reference [125]). λ is thermal conductivity in W/m-K and T is temperature in K. 53

Equation 39. Estimated thermal conductivity of U-Zr alloys according to Ogata [49] 55

Equation 40. Incremental enthalpy of (α-U) phase in U-10Pu between 298 and 865 K [186] 85

Equation 41. Incremental enthalpy of (β-U) phase in U-10Pu between 875 and 1000 K [186] 85

Equation 42. Incremental enthalpy of (γ-U) phase in U-10Pu between 1020 and 1310 K [186] 85

Equation 43. Incremental enthalpy of U-10Pu liquid between 1365 and 1500 K [186] 85

Equation 44. Heat capacity of (α-U) phase in U-10Pu between 298 and 865 K [186] 87

Equation 45. Heat capacity of (β-U) phase in U-10Pu between 875 and 1000 K [186] 87

Equation 46. Heat capacity of (γ-U) phase in U-10Pu between 1020 and 1310 K [186] 87

Equation 47. Heat capacity of U-10Pu liquid between 1365 and 1500 K [186] 87

Equation 48. Thermal expansion of (α-U) in U-15 wt%-Pu from 393 to 823 K according to Kaity et al. [191] 88

Equation 49. Thermal expansion of (β-U) in U-15 wt%-Pu from 863 to 973 K according to Kaity et al. [191] 89

Equation 50. Thermal expansion of (γ-U) in U-15 wt%-Pu from 1023 to 1163 K according to Kaity et al. [191] 89

Equation 51. Incremental enthalpy of U-15Pu-10Zr between 25 and 600°C [204] 129

Equation 52. Incremental enthalpy of U-15Pu-10Zr between 650 and 1150°C [204] 129

Equation 53. Heat capacity of U-15Pu-10Zr between 25 and 600°C [204] 130

Equation 54. Heat capacity of U-15Pu-10Zr between 650 and 1150°C [204] 130

Equation 55. Heat capacity (in J/g-K) of INL Alloy AFC2-E1 (U-20Pu-10Zr in wt%, U-17Zr-23Zr in at%) for temperatures between room temperature and 550°C 130

Equation 56. Heat capacity (in J/g-K) of INL Alloy AFC2-B7 (U-24Pu-15Zr in wt%, U-19Pu-32Zr in at%) for temperatures between 100 and 540°C 130

Equation 57. Heat capacity (in J/g-K) of INL Alloy AFC2-B1 (U-30Pu-20Zr in wt%, U-22Pu-40Zr in at%) for temperatures between 100 and 540°C 130

Equation 58. Heat capacity (in J/g-K) of INL Alloy AFC2-B8 (U-36.5Pu-20Zr in wt%, U-27Pu-40Zr in at%) for temperatures between 100 and 540°C 130

Equation 59. Heat capacity (in J/g-K) of INL Alloy AFC2-B2 (U-55Pu-20Zr in wt%, U-41Pu-40Zr in at%) for temperatures between 100 and 460°C 130

Equation 60. Heat capacity (in J/g-K) of INL Alloy AFC2-B3 (U-20Pu-45Zr in wt%, U-12Pu-68Zr in at%) for temperatures between 100 and 575°C. 130

Equation 61. Incremental enthalpy of U-20Pu-2Am-10Zr Alloy 1 from 335 to 827 K [250]..... 150

Equation 62. Incremental enthalpy of U-20Pu-2Am-10Zr Alloy 2 from 335 to 827 K [250]..... 150

Equation 63. Heat capacity of U-20Pu-2Am-10Zr Alloy 1 [250] 151

Equation 64. Heat capacity of U-20Pu-2Am-10Zr Alloy 2 [250] 151

Equation 65. Thermal conductivity of 68U-20Pu-2Am-10Zr Alloy 1 [250 Equation 8] 152

Equation 66. Thermal conductivity of 68U-20Pu-2Am-10Zr Alloy 2 [250 Equation 9] 152

Equation 67. Speculative thermal conductivity of oxygen-free 68U-20Pu-2Am-10Zr [250 Equation 10] 152

Equation 68. Heat capacity of Alloy AFC2-E3 155

Equation 69. Heat capacity of Alloy AFC2-A1 [256] 158

Equation 70. Linear thermal expansion of Alloys AFC2-A1, AFC2-A2, AFC2-A3, AFC2-A4, AFC2-A5, and AFC2-A6 between 20 and 550°C in percent [10 (Equation 3)]..... 159

ACRONYMS

AFC	Advanced Fuels Campaign
ANL	Argonne National Laboratory
bcc	Body-centered cubic (a crystal structure)
BSE	Back-scattered electron
CALPHAD	CALculation of PHAse Diagrams
CEA	Commissariat a l'Energie Atomique (French Atomic Energy Commission)
CRIEPI	Central Research Institute of Atomic Power (Japan)
dhcp	Double hexagonally close packed (a crystal structure)
DOE	U.S. Department of Energy
DSC	Differential scanning calorimetry
DTA	Differential thermal analysis
EDX	Energy-dispersive X-ray
fcc	Face-centered cubic (a crystal structure)
FCRD	Fuel Cycle Research and Development
hcp	Hexagonally close packed (a crystal structure)
IAEA	International Atomic Energy Agency
INL	Idaho National Laboratory
JRC-ITU	Joint Research Centre – Institute for Transuranium Elements (European Commission)
NIST-JANAF	National Institute of Standards and Technology – Joint Army, Navy, Air Force
OECD/NEA	Organisation for Economic Co-Operation and Development/Nuclear Energy Agency
RE	Rare-earth element
SE	Secondary electron
SEM	Scanning electron microscope
SI	Systeme International d'Unites (French) (International System of Units)
TEM	Transmission electron microscope
TMA	Thermomechanical analysis
XRD	X-ray diffraction

INTENTIONALLY BLANK

Metallic Fuels Handbook, Part 1:
Alloys Based on U-Zr, Pu-Zr, U-Pu, or U-Pu-Zr, Including Those with Minor Actinides (Np, Am, Cm), Rare-earth Elements (La, Ce, Pr, Nd, Gd), and Y

1. INTRODUCTION

Transmutation of minor actinides such as Np, Am, and Cm in spent nuclear fuel is of international interest because of its potential for reducing the long-term health and safety hazards caused by the radioactivity of the spent fuel. For this reason, the DOE Fuel Cycle Research & Development (FCRD) Advanced Fuels Campaign (AFC) has been performing research on nuclear fuel technologies that could be used in conjunction with a future actinide transmutation mission. One important approach to transmutation involves incorporating the minor actinides into U-Pu-Zr alloys, which can be used as fuel in fast reactors. U-Pu-Zr alloys are well suited for electrolytic refining, which leads to retention of rare-earth fission products such as La, Ce, Pr, and Nd. It is, therefore, important to understand not only the properties of U-Pu-Zr alloys but also those of U-Pu-Zr alloys with concentrations of minor actinides (Np, Am) and rare-earth elements (La, Ce, Pr, and Nd) similar to those in reprocessed fuel.

The Metallic Fuels Handbook reviews and summarizes the available data on phases, heat capacities, thermal expansion, and thermal conductivity of elements and alloys in the U-Pu-Zr-Np-Am-La-Ce-Pr-Nd system. Many sections are revisions and updates of material in previous versions of the Handbook [1-4]. New material in this revision involves primarily additional details about U-Zr and U-Pu-Zr alloys, including some information about mechanical properties, vapor pressures, and thermodynamic properties. In addition to presenting information about materials properties, this handbook emphasizes data assessments and provides information about how well each property is known and how much variation exists between measurements. Although the Handbook includes some results from models, its primary focus is experimental data.

Because of its size, the Handbook has been split into two parts. This part contains introductory material and information about alloys in the U-Pu-Zr system, including those with rare-earth elements and minor actinides. Part 2 (reference [5]) contains information about elements and about alloys that are part of the U-Pu-Zr-Np-Am-La-Ce-Pr-Nd system but not the U-Pu-Zr system. Three tables have been provided at the beginning of this document to help readers find the information they are looking for in the Handbook.

As in past years, the focus of the Handbook is the U-Pu-Zr system, which is defined for purposes of this Handbook as consisting of U-Zr, Pu-Zr, and U-Pu-Zr alloys, including those with minor actinides (Np, Am, and Cm), rare-earth elements (La, Ce, Pr, Nd, and Gd), and Y. To emphasize this focus, the first elements to be listed for alloys that are part of this system are U, Pu, and Zr, followed by the minor actinides, rare-earth elements, and Y. This scheme is generally consistent with that used by the METAPHIX Programme.

The Handbook is intended to serve three audiences. One audience is researchers, who may find it useful to know what has been measured, where it has been published, and what kinds of information are needed. A second audience is modelers, who need a concise summary of information about specific properties and the accuracy with which they are known. The third audience is project managers, who need information to help them identify gaps in knowledge. These audiences have different needs and interests, and the Handbook is a compromise intended to be useful to all of them. It includes extensive references and summaries of research results and needs, but is not intended to be a complete presentation of the original data. The Handbook also includes numerous graphs and, where available, equations that provide convenient approximations to materials properties for modelers. It is important to understand that many of the equations provided in the Handbook were developed by fitting polynomials to data and have no physical basis; while they can be used with caution for design studies, fuel modelers should refer to the original experimental data in the references cited by the handbook to develop or validate their own

equations and/or models. Although the Handbook includes some citations to research involving development of models, its primary focus is experimental data. All users of the Handbook are expected to consult the original references for details not presented here.

The Handbook includes information about properties of elements and alloys of interest for FCRD fuels. It does not include fuel types not specifically intended for transmutation in a fast neutron spectrum (e.g., fuels for light-water and high-conversion water reactors), properties not relevant to fuels (e.g., measurements at high pressures), issues involved in materials supplies and fuel fabrication, alloys that include elements other than U, Np, Pu, Am, La, Ce, Pr, Nd and Zr (with the exception of low concentrations of Y, Cm, and Gd in alloys investigated by the METAPHIX Programme) and (to the extent that they can be avoided) sample-specific properties such as microstructures whose values depend on fabrication parameters, characteristics, or histories of specific samples.

The metals and alloys in this edition of the Handbook are uniquely difficult to study for a number of reasons. Experimental designs may be constrained by radioactive and other hazards of some of the materials. Kinetics of phase transformations are commonly sluggish, and it is highly unlikely that all of the samples in previous research had equilibrium phases and microstructures. Thermal cycling effects (changes in sample characteristics during heating that are not fully reversed during cooling) are commonly reported and may be significant. Careful control of impurities (particularly oxygen) during sample fabrication and data collection is both crucial and difficult, and oxygen contents below 100 ppm by weight in samples may significantly affect thermophysical properties. Many of the measurements presented in this Handbook were made before 1980, and documentation of sample compositions and experimental methods may be incomplete. For all of these reasons, differences between measured values for similar alloys are commonly far larger than the estimated errors for individual measurements.

Further research on well-characterized materials with careful control of impurities is needed for almost all of the alloys and properties presented here.

Table 1. Contents of both volumes of the Handbook organized by material group. References are to sections in this document unless otherwise noted. Reference [5] is Part 2 of this Handbook.

Material	Handbook Section
U-Pu-Zr system, including U-Pu, U-Zr, Pu, Zr, and U-Pu-Zr alloys with and without minor actinides (Np, Am, Cm), rare-earth elements (La, Ce, Pr, Nd, Gd) and Y	2
Alloys based on U-Zr, including U-Zr and U-Zr alloys with minor actinides (Np, Am), rare-earth elements (La, Ce, Pr, Nd), and Y	2.1
Alloys based on Pu-Zr, including Pu-Zr and Pu-Zr alloys with minor actinides (Np, Am)	2.2
Alloys based on U-Pu, including U-Pu and U-Pu alloys with minor actinides (Np, Am)	2.3
Alloys based on U-Pu-Zr, including those with minor actinides (Np, Am, Cm), rare-earth elements (La, Ce, Pr, Nd, Gd), and Y	2.4
U-Pu-Zr	2.4.1
U-Pu-Zr alloys with minor actinides (Np, Am, Cm), sorted by increasing weight percentage of Zr	2.4.2
U-Pu-Zr alloys with rare-earth elements (La, Ce, Pr, Nd)	2.4.3
U-Pu-Zr alloys with minor actinides (Np, Am) and rare-earth elements (La, Ce, Pr, Nd), sorted by increasing weight percentage of Zr	2.4.4

Table 1 (continued).

Material	Handbook Section
U-Pu-Zr alloys with minor actinides (Np, Am, Cm), rare-earth elements (La, Ce, Pr, Nd, Gd), and Y	2.4.5
Elements (U, Np, Pu, Am, La, Ce, Pr, Nd, and Zr)	Reference [5] Section 2
Alloys containing only actinides (U, Np, Pu, Am), except those based on U-Pu	Reference [5] Section 3
Alloys containing only rare-earth elements (La, Ce, Pr, Nd) and mischmetals	Reference [5] Section 4
Binary alloys of an actinide (U, Np, Pu, Am) and a rare-earth element (La, Ce, Pr, Nd)	Reference [5] Section 5
Binary alloys of a minor actinide (Np, Am) and Zr	Reference [5] Section 6
Binary alloys of a rare-earth element (La, Ce, Pr, Nd) and Zr	Reference [5] Section 7

Table 2. Contents organized by composition. References are to sections in this document unless otherwise noted. Reference [5] is Part 2 of this Handbook..

Element(s)	Handbook Section
U	Reference [5] Section 2.1
Np	Reference [5] Section 2.2
Pu	Reference [5] Section 2.3
Am	Reference [5] Section 2.4
La	Reference [5] Section 2.5
Ce	Reference [5] Section 2.6
Pr	Reference [5] Section 2.7
Nd	Reference [5] Section 2.8
Zr	Reference [5] Section 2.9
U-La	Reference [5] Section 5.1
U-Ce	Reference [5] Section 5.2
U-Pr	Reference [5] Section 5.3
U-Nd	Reference [5] Section 5.4
U-Np	Reference [5] Section 3.1
U-Pu	2.3.1
U-Am	Reference [5] Section 3.2
U-Zr	2.1.1
Np-La	Reference [5] Section 5.5
Np-Ce	Reference [5] Section 5.6

Table 2. (continued).

Element(s)	Handbook Section
Np-Pr	Reference [5] Section 5.7
Np-Nd	Reference [5] Section 5.8
Np-Pu	Reference [5] Section 3.3
Np-Am	Reference [5] Section 3.4
Np-Zr	Reference [5] Section 6.1
Pu-La	Reference [5] Section 5.9
Pu-Ce	Reference [5] Section 5.10
Pu-Pr	Reference [5] Section 5.11
Pu-Nd	Reference [5] Section 5.12
Pu-Am	Reference [5] Section 3.5
Pu-Zr	2.2.1
Am-La	Reference [5] Section 5.13
Am-Ce	Reference [5] Section 5.14
Am-Zr	Reference [5] Section 6.2
La-Ce	Reference [5] Section 4.1
La-Pr	Reference [5] Section 4.2
La-Nd	Reference [5] Section 4.3
La-Zr	Reference [5] Section 7.1
Ce-Pr	Reference [5] Section 4.4
Ce-Nd	Reference [5] Section 4.5
Ce-Zr	Reference [5] Section 7.2
Pr-Nd	Reference [5] Section 4.6
Pr-Zr	Reference [5] Section 7.3
Nd-Zr	Reference [5] Section 7.4
U-Pu-Np	2.3.2
U-Pu-Am	2.3.3
U-Pu-Zr	2.4.1
U-Zr-Ce	2.1.3
U-Zr-Np	2.1.2
Np-Pu-Am	Reference [5] Section 3.6
Pu-Zr-Np	2.2.2
Pu-Zr-Am	2.2.3
U-Pu-Zr-Am	2.4.2.1 and 2.4.2.6
Pu-Zr-Np-Am	2.2.4
U-Pu-Zr-Np-Am	2.4.2.2 through 2.4.2.5, 2.4.2.7, and 2.4.2.8

Table 2. (continued).

Element(s)	Handbook Section
U-Zr-Ce-Nd-Y	2.1.5
U-Pu-Zr-Np-Ce-Nd	2.4.4.3
U-Zr-La-Ce-Pr-Nd	2.1.4
U-Pu-Zr-La-Ce-Pr-Nd	2.4.3.1
U-Pu-Zr-Np-Am-Ce-Nd	2.4.4.1 and 2.4.4.2
U-Pu-Zr-Np-Am-Ce-Nd-Y	2.4.5.1
U-Pu-Zr-Np-Am-La-Ce-Pr-Nd	2.4.4.4 through 2.4.4.9
U-Pu-Zr-Np-Am-Cm-Ce-Nd-Gd-Y	2.4.5.2 and 2.4.5.3
Mischmetals (rare-earth alloys that include La, Ce, Pr, and Nd)	Reference [5] Section 4.7

Table 3. Contents organized by alloy name. All references are to sections in this document.

Name	Nominal Composition (wt%)	Handbook Section
FCRD DOE1	U-29Pu-30Zr-2Np-4Am	2.4.2.7
FCRD DOE2	Pu-40Zr-12Am	2.2.3
FCRD AFC1-MB	Pu-40Zr-10Np	2.2.2
FCRD AFC1-MC	Pu-40Zr-12Am	2.2.3
FCRD AFC1-MD	Pu-40Zr-10Np-10Am	2.2.4
FCRD AFC1-MF	U-28Pu-30Zr-7Am	2.4.2.6
FCRD AFC1-MG	U-34Pu-20Zr-2Np-4Am	2.4.2.5
FCRD-AFC1-MH	U-25Pu-40Zr-2Np-3Am	2.4.2.8
FCRD AFC1-MI and MJ	U-29Pu-30Zr-2Np-4Am	2.4.2.7
FCRD AFC2-A1	U-20Pu-15Zr-2Np-3Am	2.4.2.3
FCRD AFC2-A2	U-20Pu-15Zr-2Np-3Am-1RE[a]	2.4.4.4
FCRD AFC2-A3	U-20Pu-15Zr-2Np-3Am-1.5RE[a]	2.4.4.5
FCRD AFC2-A4	U-30Pu-20Zr-3Np-5Am-1.5RE[a]	2.4.4.8
FCRD AFC2-A5	U-30Pu-20Zr-3Np-5Am-1RE[a]	2.4.4.7
FCRD AFC2-A6	U-30Pu-20Zr-3Np-5Am	2.4.2.4
FCRD AFC2-A7	U-20Pu-15Zr-2Np-3Am-8RE[a]	2.4.4.6
FCRD AFC2-A8	U-30Pu-20Zr-3Np-5Am-8RE[a]	2.4.4.9
FCRD AFC2-B1	U-30Pu-20Zr	2.4.1
FCRD AFC2-B2	U-55Pu-20Zr	2.4.1
FCRD AFC2-B3	U-20Pu-45Zr	2.4.1
FCRD AFC2-B4	U-20Pu-15Zr-1.5RE[a]	2.4.3.1
FCRD AFC2-B7	U-24Pu-15Zr	2.4.1

Table 3. (continued).

Name	Nominal Composition (wt%)	Handbook Section
FCRD AFC2-B8	U-36.5Pu-20Zr	2.4.1
FCRD AFC2-E3 and E5	U-20Pu-10Zr-2Np-3Am	2.4.2.2
METAPHIX CR1	U-5.2Ce-16.1Nd-15.0Zr-1.0Y	2.1.5
METAPHIX CR6	U-19.3Pu-10.7Zr-9.7Np-3.7Ce-11.6Nd	2.4.4.3
METAPHIX CR10	U-18.3Pu-10.2Zr-9.3Np-4.7Am-3.2Ce-10.2Nd	2.4.4.2
METAPHIX CR11	U-18Pu-10Zr-1.2Np-0.8Am-0.5Ce-1.4Nd	2.4.4.1
METAPHIX CR12	U-19Pu-10Zr-3Np-2Am-1.2Ce-3.6Nd-0.2Y	2.4.5.1
METAPHIX CR13	U-19.0Pu-10.0Zr	2.4.1
METAPHIX U-19Pu-10Zr-5MA	U-19Pu-10Zr-3.0Np-1.6Am-0.4Cm	2.4.2.9
METAPHIX U-19Pu-10Zr-2MA-2RE	U-19Pu-10Zr-1.2Np-0.6Am-0.2Cm-1.4Nd-0.2Ce-0.2Gd-0.2Y	2.4.5.2
METAPHIX U-19Pu-10Zr-5MA-5RE	U-19Pu-10Zr-3Np-1.6Am-0.4Cm-0.5Ce-3.5Nd-0.5Gd-0.5Y	2.4.5.3
a. RE is a rare-earth alloy whose nominal composition (by weight) is 6La-16Pr-25Ce-53Nd		

1.1 Basic Constants, Units, and Conversion Factors

Much of the experimental data on the U-Pu-Zr system was reported in the 1940s through 1970s, before SI units and the Kelvin temperature scale were generally adopted. Therefore, it is sometimes necessary to convert between units.

Useful unit conversions include [6]:

- Temperature in Kelvin (K) = Temperature in Celsius (°C) + 273.15
- 1 calorie (cal) = 4.1868 Joules (J)
- 1 calorie/second (cal/sec) = 4.184 Watts (W)
- 1 Ångstrom (Å) = 1 x 10^{-8} cm = 10 nm
- 1 Ångstrom (Å) = 1.00202 kX [7]

Numerical values of properties that vary with temperature (e.g., heat capacities and thermal expansion coefficients) generally do not change when temperatures are converted between °C and K. The Lorenz number (Section 1.6.2) is an exception and requires a temperature in K.

As used in this Handbook, the term “mole” is equivalent to “gram-atom.” It refers to a quantity of material that contains Avogadro’s number of atoms, even if those atoms are of different elements. This convention is followed by most of the references cited in the Handbook. Readers are cautioned that a small number of the original references consider a mole to be a quantity containing Avogadro’s number of formula units, so that a mole of UZr_2 has three times as many atoms as a mole of U.

Solid solutions may be indicated by parentheses. For example, (α -Zr) has the same structure as pure α-Zr, but contains other elements such as U and Pu.

Compositions of alloys are commonly expressed in one of four units: Weight fractions, weight percentages, atomic fractions, and atomic percentages. Weight fractions can be converted to atomic fractions and vice versa using Equation 1 and Equation 2.

Weight fractions can be converted to weight percent, and atomic fractions to atomic percent, by multiplying by 100.

Equation 1. Conversion of weight fractions to mole fractions

$$x_i = \frac{\frac{w_i}{M_i}}{\sum_i \left(\frac{w_i}{M_i}\right)}$$

where w_i and x_i are the weight and atomic fractions of element i and M_i is the atomic weight of the element

Equation 2. Conversion of mole fractions to weight fractions

$$w_i = \frac{x_i \times M_i}{\sum_i (x_i \times M_i)}$$

where w_i and x_i are the weight and atomic fractions of element i and M_i is the atomic weight of the element

These equations assume accurate knowledge of masses, and results of conversions may therefore vary for materials with the same elemental compositions and different isotopes. In most cases, these variations are negligible relative to other sources of error. However, if high-precision conversions are required, calculations should be repeated with isotope-dependent masses as appropriate for specific materials.

1.2 Relationships between Masses, Volumes and Densities

Equation 3 defines the basic relationship between density, mass, and volume. Although each of these quantities can be expressed in a variety of units, it is convenient to convert densities to a single unit (e.g., g/cm^3) to make comparisons easier. Equation 4 is particularly useful for comparisons involving the original units in many publications by Soviet researchers, and Equation 5 is useful for calculating densities from crystal structures determined by X-ray or neutron diffraction.

Densities calculated from lattice parameters or molar volumes depend on accurate knowledge of masses and may therefore vary for materials with different isotopes. In most cases, variations in density due to differences in isotopic masses are negligible relative to other sources of error. However, if high-precision calculated densities are required, calculations should be repeated with isotope-dependent masses as appropriate for specific materials.

Equation 3. Basic relationship between density (ρ), mass (M), and volume (V)

$$\rho = m/V$$

where ρ is density, m is mass, and V is volume

Equation 4. Converting densities from kg/m^3 to g/cm^3

$$\rho_1 = \rho_2 \times 10^{-3}$$

where ρ_1 is the density in g/cm^3 and ρ_2 is the same density in kg/m^3

Equation 5. Calculating the density in g/cm^3 from crystallographic data (based on equation 1 of reference [8])

$$\rho = \frac{M_{uc}}{V_{uc}} = \frac{M_{Mol} \times Z}{N \times V} \approx \frac{1.66 \times M_{Mol} \times Z}{V}$$

where ρ is the density of a unit cell in g/cm^3, M_{uc} and V_{uc} are the mass and volume of the unit cell, M_{mol} is the molar weight of the material in grams, Z is the number of atoms per unit cell (4 for fcc materials, 2 for bcc and hcp materials, and other values provided in structure descriptions), N is Avogadro's number (6.022 x 10^{23}), and V is the unit cell volume in Å^3

The unit cell volume can be calculated from the lattice parameters:

- For cubic unit cells (including fcc and bcc), V = a^3, where *a* is the lattice parameter
- For tetragonal unit cells, V = $a^2 \times c$, where *a* and *c* are the lattice parameters
- For hexagonal unit cells (including hcp and dhcp), V = $\frac{\sqrt{3}}{2} \times a^2 \times c \approx 0.866 \times a^2 \times c$, where *a* and *c* are the lattice parameters
- For orthorhombic unit cells, V = *a* x *b* x *c*, where *a*, *b*, and *c* are lattice parameters
- For monoclinic unit cells, V = *a* x *b* x *c* x sinβ, where *a*, *b*, and *c*, and β are lattice parameters

Formulas for calculating volumes of other unit cells can be found in standard crystallographic references, e.g., [9 Appendix 9].

1.3 Relationships between Densities, Volumes and Thermal Expansion

Although relationships between densities, volumes, and thermal expansion can be derived from the definitions of these quantities, Equation 6 and Equation 7 are convenient for calculating relationships between volume changes and linear thermal expansion or density.

Equation 6: Relative volume as a function of linear thermal expansion [10 Equation 4]

$V/V_0 = (1+ \Delta L/L_0)^3$

Where V is the volume at temperature T, V_0 is the volume at temperature T_0, and $\Delta L/L_0$ is the linear thermal expansion. Note that this equation involves V rather than ΔV and that linear thermal expansion is expressed as a fraction rather than a percent

Equation 7: Density as a function of relative volume

$\rho = \rho_0/(V/V_0)$

Where ρ is the density at temperature T, ρ_0 is the density at temperature T_0, and V/V_0 is the relative volume (Equation 6)

The theoretical density of an alloy can be calculated using Equation 8, which assumes that the volume of an alloy is the same as the combined volumes of all of the individual elements in the alloy if they are considered separately.

Equation 8: Theoretical density of an alloy from Law of Additivity

$$TD = \frac{M}{\sum_i \frac{m_i}{\rho_i}}$$

Where *TD* is the theoretical density, *M* is the total mass, m_i is the mass of the *i*'th element, ρ_i is the density of the *i*'th element, (m_i/ρ_i) is the volume of the *i*'th element, and the summation yields the volume of the alloy if all of the elements are considered separately. It is convenient to assume a total mass *M* of 100 g, so that each m_i is the mass percent of an element in the alloy composition.

1.4 Calculating Volumes and Densities from High-Pressure Data: the Clausius-Clapeyron Relation

Although high-pressure experiments are outside the scope of this Handbook, some researchers have used the Clausius-Clapeyron relation from classical thermodynamics (Equation 9) to determine volume changes associated with atmospheric-pressure phase transitions from high-pressure experimental data and atmospheric-pressure phase-transition enthalpies. If the volume of one of the phases is known, the volume of the other can be calculated from the volume change determined using the Clausius-Clapeyron relation.

Equation 9. The Clausius-Clapeyron relation

$$\frac{dP}{dT} = \frac{\Delta S}{\Delta V}$$

where P is pressure, T is temperature, dP/dT is the slope of the tangent to a phase boundary on a pressure-temperature diagram, ΔS is the change in enthalpy due to the phase transition, and ΔV is the change in volume due to the phase transition

1.5 Calculating Thermal Conductivity from Thermal Diffusivity, Density, and Heat Capacity

Thermal conductivity can be calculated from thermal diffusivity, heat capacity, and density using Equation 10. It is important to note that all of the terms in this equation are functions of temperature, and that room-temperature values may not be appropriate for calculating thermal conductivity at other temperatures.

Equation 10. Calculating thermal conductivity from thermal diffusivity, density, and heat capacity

$$k(T) = \alpha(T) \times \rho(T) \times C_p(T)$$

where k is thermal conductivity, α is thermal diffusivity, ρ is density, and C_p is constant-pressure heat capacity

1.6 Common Approximations

Heat capacities and thermal conductivities or diffusivities for a number of alloys in this Handbook are not available. In some cases, it is possible to estimate the values of these properties in terms of available measurements by use of well-established relationships such as the Kopp-Neumann Law and the Wiedemann-Franz (sometimes called Wiedemann-Franz-Lorenz) Law. Although the estimates provided by these laws may be useful if no other information is available, neither should be considered a substitute for experimental measurements. The use of either of these laws in this Handbook always indicates a need for further research.

1.6.1 Approximate Heat Capacities: The Kopp-Neumann Law

The Kopp-Neumann Law (Equation 11) approximates the heat capacity of an alloy from its composition and the heat capacities of its constituent elements. As noted by Tsuji [11], this law "should be applied with caution for alloys especially near magnetic and phase transitions."

Equation 11. Kopp-Neumann Law [11]

$$C_p = \sum_{i=1}^{n} X_i C_{p_i}$$

where C_p is the heat capacity of the alloy and X_i and C_{p_i} refer to the atomic fractions and atomic heat capacities of each of the *n* elements in the alloy.

Comparison to measured heat capacities suggests that the Kopp-Neumann Law may be a reasonable approximation for heat capacities of alloys where all of the materials have similar structures and heat capacities, but is less reliable where phases in the alloys are significantly different from those in the elements.

1.6.2 Approximate Thermal Conductivities: The Wiedemann-Franz Law

The Wiedemann-Franz (also called Wiedemann-Franz-Lorenz) Law states that the ratio of thermal conductivity to electrical conductivity in metals is proportional to absolute temperature. The proportionality constant is commonly called the "Lorenz number" or "Lorenz value" and is designated by L. In practice, the Wiedemann-Franz law is commonly applied using electrical resistivity rather than electrical conductivity (Equation 12).

Equation 12. Wiedemann-Franz Law

$$k \times \rho_R = L \times T$$

where k is thermal conductivity, ρ_R is electrical resistivity, L is the Lorenz number, and T is the temperature in K

The theoretical (also called "Sommerfeld") value of the Lorenz number calculated from quantum statistics is 2.44×10^{-8} $W\Omega K^{-2}$. In practice, however, experimentally determined values of the Lorenz number vary between different materials and temperatures. The reasons why the actual and theoretical values differ are beyond the scope of this handbook, but are summarized in references [12] and [13].

Binkele measured the temperature dependence of the Lorenz number for several rare-earth elements and found that it decreased with temperature, reaching the theoretical value of the Lorenz number at ~1000 K [14] (Figure 1). Although Binkele did not measure the temperature dependence of the Lorenz number for La, Ce, or Pr, a decrease in Lorenz number with increasing temperature is consistent with the difference in Lorenz numbers calculated from thermal conductivity and electrical resistivity data at room temperature and melting temperature for La, Ce, Pr, and Nd in the CRC Handbook of Chemistry and Physics [15 Tables 9 and 12].

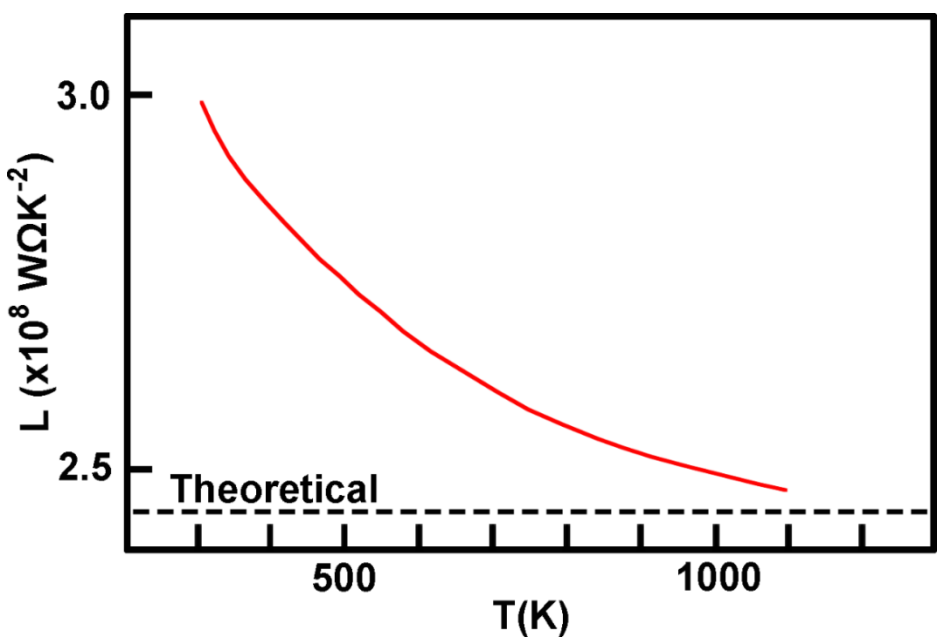

Figure 1. Comparison between the experimentally measured temperature dependence of the Lorenz number for Nd (red curve) and the theoretical value (dashed black line) (re-drawn with selected data from reference [14]).

2. U-Pu-Zr SYSTEM, INCLUDING U-Pu, U-Zr, Pu-Zr, AND U-Pu-Zr ALLOYS WITH AND WITHOUT MINOR ACTINIDES (Np, Am, Cm), RARE-EARTH ELEMENTS (La, Ce, Pr, Nd, Gd), AND Y

2.1 Alloys Based on U-Zr, Including U-Zr and U-Zr Alloys with Minor Actinides (Np, Am), Rare-Earth Elements (La, Ce, Pr, Nd), and Y

2.1.1 U-Zr

2.1.1.1 Introduction

U-Zr alloys have been prepared using a variety of methods including powder metallurgy (e.g., [16-18]) and growth of epitaxial thin films [19]. However, the vast majority of the available information about properties and irradiation behavior of U-Zr alloys involves materials that have been cast from molten liquids. This Handbook emphasizes properties of cast alloys, with data from alloys produced by other methods used only when data on cast alloys are unavailable.

Experimental measurements of alloys with compositions close to U-10Zr (wt%) were critically reviewed by Janney and Hayes in 2018 [20]. Because of the importance of U-10Zr as a nuclear fuel, key information from the review will be summarized in this Handbook. Interested readers are encouraged to consult the Janney and Hayes review for detailed information.

Many features of the U-Zr phase diagram have been known since the 1950s, and a widely accepted phase diagram was developed by Sheldon and Peterson in the late 1980s [21, 22]. Key features of U-Zr phase diagrams include a high-temperature body-centered cubic solid solution that crystallizes at the solidus for all proportions of U and Zr and separates into two body-centered cubic phases with different compositions at lower temperatures, limited solubility of U in Zr and of Zr in U in lower-temperature phases, and the existence of a single intermediate phase that is stable at room temperature. However, more recent work suggests that a number of areas may require further investigation or modification of the phase diagram. Recent research into phase-transition mechanisms has emphasized the importance of metastable phases.

Experimental work on U-Zr alloys is complicated by slow formation of phases on a spatial scale large enough for characterization by optical or microprobe techniques (but perhaps not on a scale of nanometers [23, 24]), a high degree of sensitivity to impurities such as O and N in concentrations of a few hundred ppm (e.g., [21, 25]), and a tendency to form significant quantities of a high-Zr phase not expected from phase diagrams. Phases, microstructures, and measured reaction enthalpies may differ between samples with the same nominal composition and different thermal histories [26-29]. U-Zr alloys experience element segregation in thermal gradients and migration of Zr to sample surfaces during annealing [30-33].

Models of U-Zr phases, phase segregation mechanisms and microstructure development, and the U-Zr phase diagram have been developed using a variety of approaches (e.g., [27, 34-57]).

Although a number of researchers have measured heat capacities of U-Zr alloys at temperatures between ~300 and 850 K, measured heat capacities of alloys with similar compositions made by different research groups may differ by 20-30%. When measurements of different compositions made by a single research group are compared, heat capacities decrease with increasing concentration of Zr. Heat capacities between ~850 and 1000 K (~850 and 900 K for high-Zr compositions) are highly dependent on composition because of phase transformations and cannot be represented by smoothed values. Heat capacities of (γ-U, β-Zr) solid solutions are only slightly dependent on temperature. Experimental measurements of the low-temperature heat capacity of splat-cooled U-Zr alloys with 30 at% Zr have recently become available [58, 59].

Data on the thermal expansion of polycrystalline U-Zr alloys with up to ~20 wt% Zr are originally from one of four publications (Saller et al. [60], which was the source of all of the data from this composition range in the review of Touloukian et al. [61], Basak et al. [62], and two measurements of the thermal expansion of polycrystalline U-Zr alloys with up to ~20 wt% Zr were originally reported in four publications (Saller et al. 1956 [60], which was the source of all of the data from this composition range in the review of Touloukian et al. [61]), Basak et al. 2009 [62], and two publications by Kaity et al. [63, 64]). All of these publications show similar thermal expansion behavior for all alloys in this composition range at temperatures up to ~800 K. However, there is an important qualitative difference: data reported by Saller et al. indicate that the thermal expansion of U-Zr alloys decreases with increasing concentration of Zr; in contrast, data reported by Basak et al. indicate that, at least for alloys with up to 10 wt% Zr, the thermal expansion increases with increasing concentration of Zr. Data reported by Kaity et al. involves only one composition. The qualitative difference between the data of Saller et al. and of Basak et al. becomes quantitatively important at higher temperatures, leading to differences in thermal expansion of up to ~0.5% for alloys with similar compositions.

Data on the thermal expansion of U-Zr alloys with at least 50 wt% Zr is available in references [61] and [65] but is not summarized here because of its limited relevance for FCRD fuels.

Experimental determinations of the thermal conductivity of U-Zr alloys with Zr concentrations between 1 and 79 wt% Zr (~2.5 and 91 at% Zr) have been reported at temperatures up to 1200 K. Thermal conductivities for U-Zr alloys increase with temperature. Conductivities for alloys with different compositions decrease with increasing concentration of Zr to a minimum value at ~72.4 at% (possibly reflecting the very low conductivity of δ-UZr_2) [66] and may increase again in high-Zr compositions.

Three research groups have developed equations to predict the thermal conductivity of U-Zr alloys as functions of composition and temperature. One of these equations is not considered because it was developed before much of the data was available. The other two produce similar results for compositions of interest for nuclear fuels (~10-15 wt% Zr).

Recent experimental research on U-Zr alloys includes investigation of diffusion couples [67], studies of texture evolution [68], and research on formation of surface layers as a result of annealing and exposure to oxygen [32].

2.1.1.2 Phases and Phase Transformations

2.1.1.2.1 Phases

It is generally agreed that the U-Zr system has five solid phases that are stable at atmospheric pressures. All five of these phases are solid solutions. Four of the five are isostructural with phases in pure U or Zr and one is an intermediate phase. At least three additional phases are believed to be common in U-Zr alloys. Two of these phases are generally considered to be metastable. Formation of the third apparently involves impurities.

All of the generally accepted U-Zr phases may occur at appropriate temperatures in alloys with approximately 10 wt% Zr [20].

Boundaries of U-Zr phases are strongly influenced by impurities such as O and N in concentrations as low as a few tens or hundreds of ppm by weight. Compositions and identities of phases in individual samples may also be influenced by other factors including the thermal and processing histories of the samples. Information in this section represents the best available estimates for equilibrium phase boundaries in pure U-Zr alloys.

Lattice parameters in this section were measured at room temperature, but may not represent room-temperature equilibrium. Lattice parameters at other temperatures are presented with measurements of thermal expansion (Section 2.1.1.5).

U-Zr liquids are miscible in all proportions.

2.1.1.2.1.1 Stable Phases

2.1.1.2.1.1.1 (α-U)

(α-U) is a solid solution of the orthorhombic phase α-U (Section 2.1.2.1 of reference [5]). Metallographic observations of annealed and quenched samples with nitrogen concentrations below 65 ppm and low concentrations of zirconium established that the maximum concentration of Zr in α-U solid solutions is ~0.1 wt% at 500°C, increasing to ~0.2 wt% (~0.5 at%) at 662°C [21, 25]. The oxygen contents in the samples were not analyzed. The samples were hot-rolled twice in air, with a thickness reduction of ~70% [25], suggesting the possible introduction of a significant concentration of oxygen. However, the solubility of O in α-U is very low [69], and experimental studies confirm that the boundaries of (α-U) solid solutions in U-Zr alloys are insensitive to the concentration of O [70].

Although peaks in some X-ray diffraction patterns from alloys with 2-14 wt% Zr have been interpreted as indicating single phase (α-U) (e.g., [24, 25, 62, 71-73]), peaks from both (α-U) and δ-UZr_2 have been identified in X-ray diffraction patterns from more slowly cooled samples (e.g., [26]). Using X-ray diffraction data to determine phase boundaries is problematic because of difficulties in determining whether the orthorhombic phase is equilibrium (α-U) or the metastable phase α', systematic difficulties in recognizing peaks from of δ-UZr_2 and ω in X-ray diffraction patterns (e.g., [74]), and TEM observations indicating that some samples whose X-ray patterns can be interpreted as indicating a single phase with a structure similar to that of α-U consist of fine lamellae of two phases (e.g., [23, 24, 75]).

In the absence of further experimental data from high-purity samples that are known to have low concentrations of dissolved oxygen and nitrogen, it seems reasonable to assume that the maximum concentration of ~0.5 at% Zr in equilibrium (α-U) solid solutions in U-Zr alloys is approximately correct, although further experimental data from annealed or slowly cooled alloys with low concentrations of Zr are needed to confirm this assumption.

Lattice parameters for high-U phases with structures similar to that of α-U in U-Zr alloys have been reported by a number of researchers (e.g., [26, 62, 64, 75-79]). However, it is not clear that any of these samples represent equilibrium (α-U) solid solutions and some lattice parameters may be from α'. Because of the low maximum concentration of Zr in equilibrium (α-U), it seems reasonable to assume that its lattice parameters are similar to those of pure α-U (Section 2.1.2.1 of reference [5]).

2.1.1.2.1.1.2 (α-Zr)

(α-Zr) is a solid solution of the hexagonal phase α-Zr (Section 2.9.2.1 of reference [5]). Proportions of (α-Zr) solid solutions in U-Zr alloys are sensitive to oxygen in concentrations below 1000 ppm, and are more strongly influenced by N at similar concentrations (page 9 of reference [70]). The maximum concentration of U in (α-U) solid solutions in compositions with low oxygen and nitrogen is ~1 wt% (~0.4 at%) [21, 70]. α-Zr is called "ε" in some older references (e.g., [80]).

Measurements of lattice parameters of (α-Zr) solid solutions in U-Zr alloys are rare. Xie et al. determined that the lattice parameters of (α-Zr) solid solutions in an alloy with 10 wt% Zr were similar to those of pure α-Zr [79]. Concentrations of O and N in their sample were not reported, and the high-Zr phase in their samples may have been an impurity-stabilized high-Zr inclusion phase similar to that in other actinide-Zr alloys (e.g., [81]) rather than equilibrium (α-Zr). It seems reasonable to assume that lattice parameters of (α-Zr) solid solutions are essentially identical to those of pure α-Zr (Section 2.9.2.1 of reference [5]).

High-Zr inclusions of a phase commonly referred to as "oxygen-stabilized" or "impurity stabilized" α-Zr are commonly reported in U-Zr alloys in compositions in which phase diagrams suggest that α-Zr should not form. Little is known about these inclusions, although their formation appears to involve impurities.

2.1.1.2.1.1.3 (β-U)

(β-U) is a solid solution of the tetragonal phase β-U (Section 2.1.2.1 of reference [5]). Metallographic observations of annealed and quenched samples with nitrogen concentrations below 65 ppm and low concentrations of zirconium established that the maximum concentration of Zr in β-U solid solutions is ~0.4 wt% [21, 25]. The oxygen contents in the samples were not analyzed. The samples were hot-rolled twice in air, with a thickness reduction of ~70% [25], suggesting the possible introduction of a significant concentration of oxygen. However, the solubility of O in β-U is very low [69], and it seems reasonable to assume that any oxygen in the alloy does not have a significant effect on the maximum concentration of Zr in (β–U).

Pure β-U cannot be quenched to room temperature (e.g., [82, 83]). Because of the low maximum concentration of Zr, it seems likely that the lattice parameters of (β-U) solid solutions are similar to those of pure β-U (Section 2.1.2.1 of reference [5]).

2.1.1.2.1.1.4 γ-(U,Zr), γ_1, and γ_2

At high temperatures, there is a continuous solid solution between the bcc phases γ-U and β-Zr. This solid solution is also bcc. It is commonly referred to as "gamma" or "γ," or as "beta" or "β" in high-Zr alloys. At lower temperatures, γ divides into γ_1 (U-rich) and γ_2 (Zr-rich) solid solution phases, both of which have bcc structures. Phase relationships between γ_1 and γ_2 are significantly influenced by oxygen concentrations as low as 160 ppm [25], and also by low concentrations of nitrogen [70]. Metallographic examination of annealed and quenched alloys with less than 150 ppm O and 65 ppm N indicated that the $\gamma_1 + \gamma_2$ phase region extends from ~4.5 to 22 wt% Zr at 693°C, and that the maximum temperature of the two-phase region occurs at ~722°C and 14 wt% Zr [21, 25]. γ_1 is sometimes referred to as γ''.

γ is not stable at room temperature, although it can be retained in samples with more than ~30 at% Zr that have been splat-cooled from liquids [58, 84]. It is also commonly reported in more slowly cooled samples that have been annealed at lower temperatures (e.g., [27, 28, 70, 85]). Retained bcc phases are commonly referred to as "γ," without distinguishing between γ, γ_1 and γ_2.

Table 4 and Figure 2 show the available measurements of room-temperature lattice parameters of γ as a function of the atomic percentage of Zr in the nominal bulk composition of each alloy. Data from references [84] and [58] (squares and star in Figure 2) are from single-phase samples formed by very rapid cooling from a liquid. These data suggest that lattice parameters increase linearly with the proportion of Zr; however, the scatter in reported values is large enough that no high-quality linear fit is possible.

Table 4. Room-temperature lattice parameters of γ in U-Zr alloys.

Composition (wt%)	Composition (at%)	Lattice parameter (Å)	Reference	Notes
U-11.3Zr	U-25Zr	3.550±0.005	[84]	a
U-14.1Zr	U-30Zr	3.543±0.005	[84]	a
U-14.1Zr	U-30Zr	3.543	[58]	b
U-20.4Zr	U-40Zr	3.533±0.005	[84]	a
U-27.7Zr	U-50Zr	3.546±0.002	[84]	a
U-30Zr	U-52.8Zr	3.553	[86]	c
U-33.2Zr	U-56.5Zr	3.568	[87]	d
U-36.5Zr	U-60Zr	3.558±0.002	[84]	a

Table 4. (continued).

Composition (wt%)	Composition (at%)	Lattice parameter (Å)	Reference	Notes
U-47.2Zr	U-70Zr	3.563±0.002	[84]	a
U-50Zr	U-72.3Zr	3.5765	[27]	e
U-50Zr	U-72.3Zr	3.5817	[28]	f
U-50Zr	U-72.3Zr	3.5784	[28]	g
U-50Zr	U-72.3Zr	3.5765	[28]	h
U-50Zr	U-72.3Zr	3.558	[86]	c
U-53.4Zr	U-74.9Zr	3.570±0.002	[84]	a
U-60.5Zr	U-80Zr	3.572±0.003	[84]	a
U-78Zr	U-90.2Zr	3.580	[86]	c

NOTE a: Alloys were homogenized, re-melted, and blown by a blast of helium gas against a curved copper shield. Samples were thin flakes. Lattice parameters were determined from X-ray data. No information about sample purity or actual compositions was provided. Samples were prepared and measured at two universities (Tufts University and University of California at San Diego). Because results from the two universities were identical for the composition they have in common (U-50 at% Zr), they are not distinguished here. Reference: [84]

NOTE b: Sample was prepared by arc-melting high-purity U and Zr in an argon atmosphere and producing a rapidly cooled disk with a diameter of ~20 µm and thickness of 100-200 µm using a commercial splat-cooing instrument. The estimated cooling rate was > 10^6 K/sec. The lattice parameter was determined from X-ray diffraction data. Although no quantitative measurements of impurities were provided, SEM analyses showed surface contamination from Cu, O, and C, and the X-ray diffraction patterns had peaks from ZrC in addition to those from γ Reference: [58]

NOTE c: Lattice parameters of the β-Zr phase in alloys with 22, 50, and 70 wt% U (78, 50, and 30 wt% Zr, respectively) were determined using X-ray diffraction. No information about how the samples were produced, their thermal histories, their actual compositions, or their impurities was provided. Reference: [86], page 16

NOTE d: Sample was arc-melted under argon in a copper crucible, sealed in a quartz tube under argon, held at 850°C for 24 hours, and quenched. Starting materials were U with principal impurities Fe (27 ppm), Mg (60 ppm), and Si (24 ppm) and Zr with principal impurities O_2 (42 ppm) and Fe (<200 ppm). Reference: [87] sample 4

NOTE e: Nuclear-grade uranium and zirconium were arc-melted in a high-purity Ar atmosphere, then turned and re-melted an additional five times. The alloy was wrapped in Ta foil and encapsulated in quartz under a low partial pressure of He, then inserted into a graphite crucible and heated to 1300°C, and held for 4 hours. It was cooled in the furnace, copper-jacketed, and hot-rolled at 750°C for three passes to achieve a total thickness reduction of ~50%. The alloy was soaked for 5 minutes at 750°C between passes, and at 875°C for ten minutes after the final pass, then water quenched. Several slices were removed from the alloy, encapsulated in a quartz tube, heated to 635°C, held at 635°C for 4 hours, and water quenched. The X-ray diffraction showed only peaks from γ, although electron-diffraction patterns showed faint, diffuse, streaked reflections from ω or δ-UZr_2. The lattice parameter for γ was determined by Rietveld refinement of the X-ray diffraction data. No information about the actual composition or the impurities in the starting materials or final alloy were provided. Reference: [27], sample 635q

NOTE f: Early stages of sample preparation (through slicing the alloy) were like those in note e. After slicing, each slice was individually encapsulated in quartz and annealed at 875°C for 4 hours. One of the slices was then water quenched. Analysis of the X-ray diffraction data from the quenched sample indicated that it consisted of ~40% γ and 60% δ-UZr_2. No information about compositions of individual phases, the actual composition of the sample, or impurities in the starting materials or final alloy was provided. Reference: [28], sample 875q

NOTE g: Early stages of sample preparation were like those in note f. After the annealing at 875°C, the furnace temperature was lowered. The sample was held at 720°C for 4 hours, then water quenched. Analysis of the X-ray diffraction data indicated that the sample consisted of ~70% γ and 30% δ-UZr_2. No information about compositions of individual phases, the actual composition of the sample, or impurities in the starting materials or final alloy was provided. Reference: [28], sample 720q

NOTE h: Early stages of sample preparation were like those in note g. After the annealing at 720°C, the furnace temperature was lowered. The sample was held at 635°C and water quenched. Analysis of the X-ray diffraction data indicated that the sample contained only γ. No information about compositions of individual phases, the actual composition of the sample, or impurities in the starting materials or final alloy was provided. Reference: [28], sample 635q

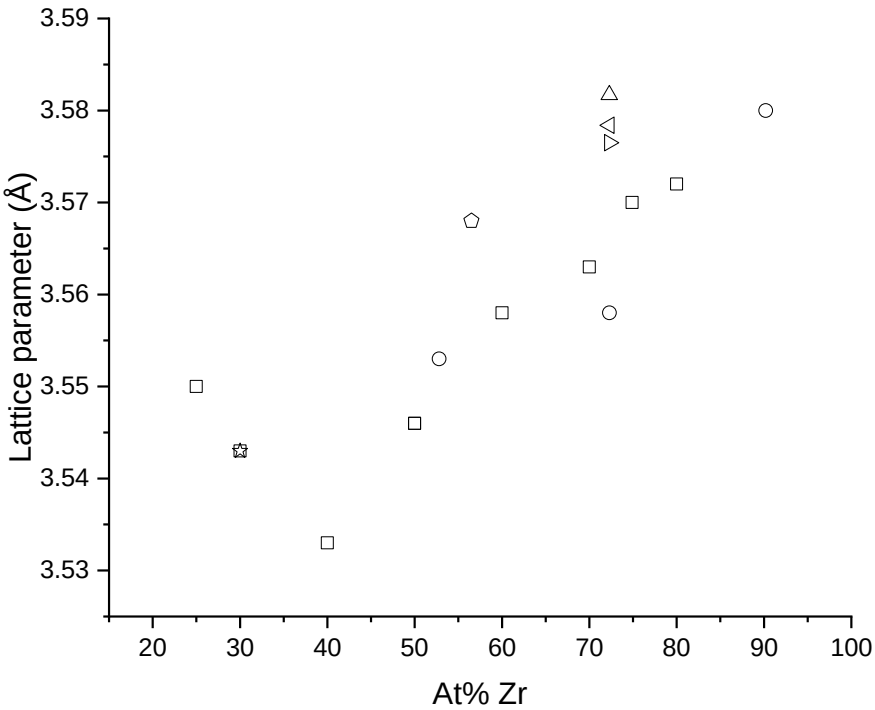

Figure 2. Room-temperature lattice parameters of γ-U. Upward pointing triangle: [28] sample 635q and [27] sample 635q, left-pointing triangle: [28] sample 720q, right-pointing triangle: [28] sample 875q, squares: [84], circles: [86], star: [58], pentagon: [87] sample 4.

2.1.1.2.1.1.5 δ-UZr$_2$

δ-UZr$_2$ is the only stable intermediate phase in binary U-Zr alloys. It is a solid solution whose compositional range is strongly influenced by impurities such as oxygen and nitrogen. In samples with low concentrations of N and O, the minimum concentration of Zr in δ-UZr$_2$ is ~43 wt% at ~500-550°C, decreasing to ~40.5-40.7 wt% at 600°C [80, 88], and the maximum concentration is 59 wt% Zr [88]. Formation of δ-UZr$_2$ may be completely suppressed in alloys with sufficiently high concentrations of oxygen impurities [21, 25] and in powder samples with oxidized surfaces [89], and it does not appear in some early U-Zr phase diagrams (e.g., [90]). δ-UZr$_2$ is known as "epsilon" or "ε" in some older references.

Early researchers proposed several possible crystal structures for δ-Zr$_2$, which are summarized in reference [91]. In 1955, Mueller suggested that δ-UZr$_2$ has a bcc structure with a lattice parameter approximately three times that of γ [92]. This structure was supported by the observation that "superlattice" reflections consistent with the larger bcc cell appeared during the transition from γ to δ-Zr$_2$ (e.g., [85]). However, a cubic structure is not consistent with data showing that δ-UZr$_2$ is optically anisotropic [89, 93]. In 1957, Silcock suggested in a brief communication that the structure of δ-Zr$_2$ might be similar to that of U$_2$Ti, which is hexagonal, and that the apparent cubic symmetry of δ-UZr$_2$ is caused by twinning that forms during the transition from γ [93]. Silcock also noted that X-ray diffraction patterns from δ-UZr$_2$ are inconsistent with a U$_2$Ti-type structure in which the U in δ–Zr$_2$ occupies the same site as the Ti in U$_2$Ti. The same year, Boyko published a more extensive study that largely repeated the results of

Silcock [94]. Later work by Akabori et al. [88, 95] largely confirmed the structure proposed by Silcock, despite differences between observed and predicted intensities of some X-rays and an inability to distinguish positions of U and Zr atoms because of their similar scattering factors in neutron-diffraction data [95].

The structure proposed by Silcock and Boyko is generally accepted. It is hexagonal (space group *P*6/*mmm*, *a* = 5.03Å, *c* =3.09 for a sample with ~70.7 at% Zr [95]). The crystal structure is an unusual modification of a C32 (AlB_2)-type structure, with three atoms per unit cell. It is generally believed to have a partially ordered structure in which the (0,0,0) position is preferentially occupied by Zr and the (1/3, 2/3, ½) and (2/3, 1/3, ½) positions have a random distribution of U and Zr [88, 93-95]. No structure refinements including individual site occupancies are available, although positron annihilation spectroscopy suggests variations in Zr concentration on a scale of a few nanometers [72].

Table 5 and Figure 3 show reported room-temperature lattice parameters for δ-UZr_2 samples with known compositions. Lattice parameters reported by Mueller and by Boyko [92, 94] are not included because neither researcher reported the composition of their sample, although both probably used samples with concentrations of Zr close to 50 wt% to obtain single-phase samples for determination of the crystal structure. Lattice parameters reported by Kaity et al. [64] from a sample of U-6Zr (wt%) that contained only 8 volume percent of δ-UZr_2 are not included because only the composition of bulk sample was reported, and it is likely to be significantly different from the composition of the δ-UZr_2.

Data reported by Akabori et al. (point numbers 3, 4, 5, and 13) show a linear trend in which *a* and *c* lattice parameters increase with increasing concentrations of Zr. The *a* lattice parameter in the data of Holden and Seymour (point 6) is also consistent with this trend, although the *c* lattice parameter is not. Data reported by Basak and colleagues (points 1, 2, and 7-12) show wide variations in lattice parameters that cannot be explained by variations in composition. Further experiments using samples with simpler thermal and processing histories may be useful to understand the variations in these data.

Table 5. Room-temperature lattice parameters of δ-UZr_2 with known compositions.

Point Number	Composition (wt%)	Composition (at%)	*a* (Å)	*c* (Å)	Notes	Reference
1	U-35Zr	U-58.4Zr	5.0369	3.0851	a	[26]
2	U-35Zr	U-58.4Zr	5.0342	3.0913	b	[26]
3	U-43.7Zr	U-66.9Zr	5.025	3.086	c	[88]
4	U-47.5Zr	U-70.2Zr	5.028	3.09	c	[88]
5	U-48.1Zr	U-70.7Zr	5.0317±0.0001	3.0888±0.0001	d	[95]
6	U-50Zr	U-72.3Zr	5.03	3.08	e	[89, 93]
7	U-50Zr	U-72.3Zr	5.0429	3.1052	f	[28]
8	U-50Zr	U-72.3Zr	5.0429	3.1043	g	[28]
9	U-50Zr	U-72.3Zr	5.0419	3.0938	h	[28]
10	U-50Zr	U-72.3Zr	5.0343	3.0938	i	[28]
11	U-50Zr	U-72.3Zr	5.0419	3.0938	j	[28]
12	U-50Zr	U-72.3Zr	5.0343	3.0948	k	[28]
13	U-53.6Zr	U-75.1Zr	5.03	3.097	c	[88]

NOTE a: Data are from an alloy with nominal composition U-35Zr, which was made by arc-melting uranium slugs and crystal bar zirconium in a high-purity Ar atmosphere, then turned and re-melted an additional five times. The alloy was wrapped in Ta foil and encapsulated in quartz under a low partial pressure of He. The sample was heated at 900°C for 4 hours, water quenched, copper-jacketed, and hot-rolled at 900°C for three passes to achieve a total thickness reduction of ~50%. The

Table 5. (continued).

Point Number	Composition (wt%)	Composition (at%)	*a* (Å)	*c* (Å)	Notes	Reference
alloy was soaked for 5 minutes at 900°C between passes, and for ten minutes at 900°C after the final pass, then water quenched. Impurities in the quenched sample included 240 ppm C, 60 ppm N, and 150 ppm O. The final thermal treatment of the sample consisted of soaking at 630°C for 500 hours, furnace cooling to 600°C, and holding at that temperature for 240 hours. X-ray diffraction analysis showed that the sample consisted of ~89 volume percent of δ-UZr_2 and 11 vol% of a phase with a structure similar to that of α-U. SEM analyses indicated the sample had two phases with different Zr contents and that the high-Zr phase in the sample contained ~40 wt%Zr. Data in Table 5 combine lattice parameters from the X-ray diffraction and the composition of the high-Zr phase from the SEM data. Phases in this sample were not believed to represent room-temperature equilibrium. Reference [26], sample 35Zr240h **NOTE b:** Data are from an alloy with nominal composition U-7Zr. Early stages of sample preparation (through the water quench after the hot rolling and the chemical analysis) are described in note a. The sample was then cut, and a piece was encapsulated in a quartz tube. This sample was heated to 900°C, furnace-cooled to 680°C, soaked for 480 hours, furnace-cooled to 650°C, held there for 1520 hours, furnace cooled to 600°C, held there for 2880 hours, and water-quenched. X-ray diffraction analysis showed that the sample consisted of ~25 volume percent of δ-UZr_2 and 75 vol% of a phase with a structure similar to that of α-U. SEM analyses indicated that the high-Zr phase in the sample contained ~40 wt%Zr. Data in Table 5 combine lattice parameters from the X-ray diffraction and the composition of the high-Zr phase from the SEM data. Reference [26], sample 7Zr2880h **NOTE c:** Alloys were prepared by arc-melting pure U and Zr six times to ensure homogeneity, wrapping in Ta foils, sealing in quartz ampoules that had been evacuated and filled with high-purity Ar, homogenized at 800°C for 24 hours, and water-quenched. Samples for X-ray diffraction were prepared by filing the heat-treated alloys, removing iron filings with a magnet, sealing the powder in quartz ampoules, and annealing at 580°C for 24 hours to relieve strain. The total of the metallic impurities in the U feedstock was less than 100 ppm, and consisted primarily of Al, Fe, and Si. This feedstock had 50 ppm O and 40 ppm N. The total of the metallic impurities in the crystal bar Zr feedstock was less than 840 ppm, and consisted primarily of Fe, Hf, Ti, and Al. This feedstock had 140 ppm O and 40 ppm N. After heat treatment, an alloy with 70.7 at% Zr had 60 ppm O and 30 ppm N. Reference: [88] **NOTE d:** Sample preparation and impurities are like those in note c, except that the sample was homogenized at 1123 K (850°C) for 72 hours before being quenched. Lattice parameters were determined by Rietveld refinement of high-resolution neutron-diffraction data. Reference: [95] **NOTE e:** Holden and Seymour prepared samples of U-50Zr (wt%) for X-ray diffraction by arc-melting U and Zr, then hot-working the material to produce wires ~50 mil (1.25 mm) in diameter. The material was heated in a vacuum for up to 48 hours at some temperature below ~595°C and quenched. The U and Zr feedstocks were the purest commercially available materials. No analyses of impurities were performed. X-ray diffraction data were collected from powder samples, and also from a coarse-grained sample using a Weissenberg camera. Data from both sources were indexed using a cubic cell with lattice parameter *a* = 10.68 Å [89]. Silcock re-indexed X-ray diffraction data published by Holden and Seymour using a hexagonal unit cell [93]. Data in Table 5 combine sample-preparation information published by Holden and Seymour with the lattice parameters determined by Silcock. References: [89, 93] **NOTE f:** This sample was described in note f for Table 4. Reference: [28] sample 875q **NOTE g:** This sample was described in note g for Table 4. Reference: [28] sample 720q **NOTE h:** Initial steps in preparing this sample were described in note e for Table 4. Following the water quench from 635°C, the sample was aged at 550°C for 10 hours and water quenched. X-ray diffraction showed that this sample consisted of δ-UZr_2. Reference: [28] sample 550aq **NOTE i:** Initial steps in preparing this sample were described in note e for Table 4. Following the water quench from 635°C, the sample was aged at 300°C for 10 hours and water quenched. X-ray diffraction showed that this sample consisted of δ-UZr_2. Reference: [28] sample 300aq **NOTE j:** Initial steps in preparing this sample were described in note e for Table 4. Following the water quench from 635°C, the sample was aged at 550°C for 24 hours and water quenched. X-ray diffraction showed that this sample consisted of δ-UZr_2. Reference: [28] sample 550/24h **NOTE k:** Initial steps in preparing this sample were described in note e for Table 4. Following the water quench from 635°C, the sample was aged at 300°C for 24 hours and water quenched. X-ray diffraction showed that this sample consisted of δ-UZr_2. Reference: [28] sample 300/24h						

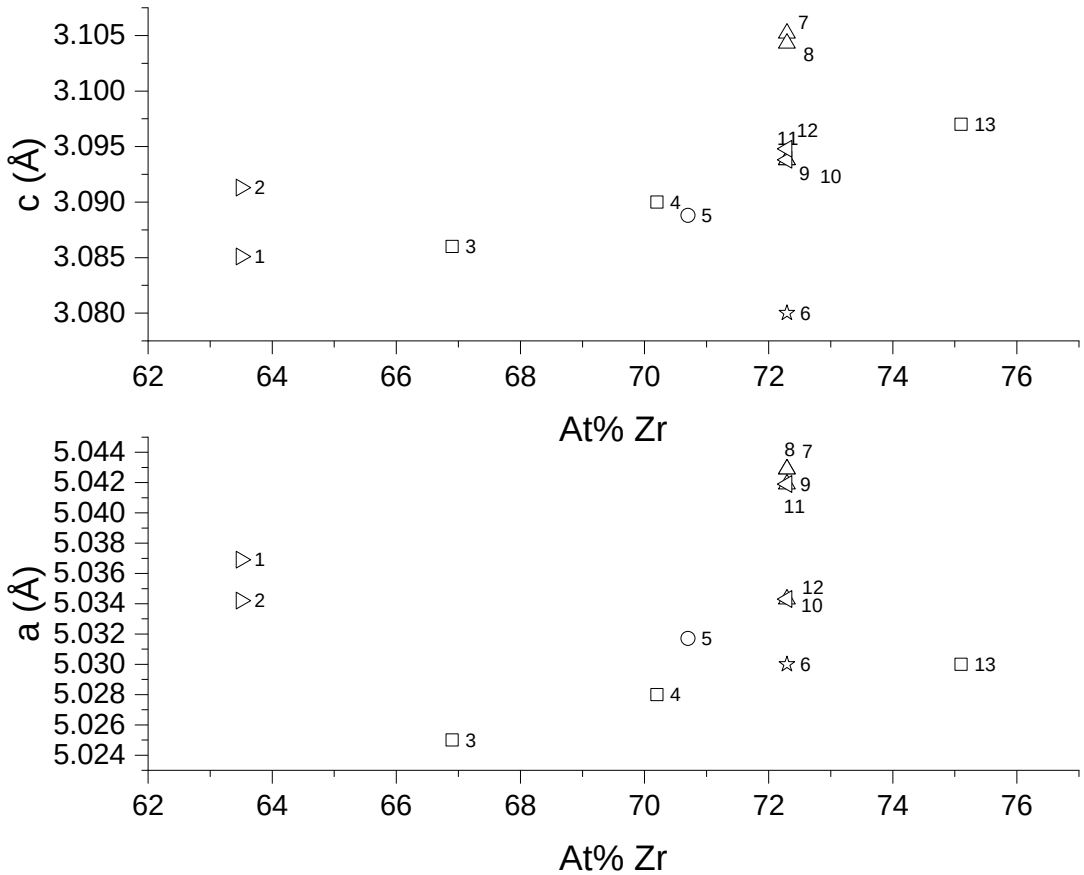

Figure 3. Room temperature lattice parameters, δ-UZr_2. Different symbols indicate data from different references, and numbers indicate point numbers in Table 5.

2.1.1.2.1.2 Metastable Phases

The metastable phases α' and ω are commonly believed to occur in U-Zr alloys. It has also been suggested that the metastable phase α'' also occurs as an intermediate phase in the transition from γ to α'in U-Zr alloys [96]. This phase, which has a monoclinic structure that can be seen as a distortion of α-U, occurs in U-Mo and U-Nb alloys [64, 71]. However, there is no direct evidence for its existence in U-Zr alloys (e.g.,[64, 75, 97],

γ'' is an alternate name for γ_1, not a designation for a metastable phase.

2.1.1.2.1.2.1 α' (supersaturated α)

α' (also known as "supersaturated α") is an orthorhombic phase with a structure similar to that of α-U and a higher concentration of Zr than is present in equilibrium α-U solid solutions. α'_a, α'_b, and α'_n are forms of α' that are distinguished by their appearance in metallographic analyses: α'_a has an acicular structure, α'_b has a banded structure, and α'_n has an appearance that suggests formation by nucleation and growth [98]. α'_a is sometimes referred to as martensitic α' because it is believed to form from γ by a martensitic (diffusionless) transformation. Although some researchers attempt to distinguish between equilibrium α-U solid solutions and α' based on morphology, no systematic studies relating crystal structures, compositions, and morphologies of single crystals are available.

Because of the structural similarities between α-U and α', it is difficult to tell whether lattice parameters of orthorhombic phases in papers reporting observations of low-Zr alloys represent an equilibrium α-U solid solution, α', or a combination of both. Although it has been stated that the *a* and *c* lattice parameters of α' are slightly larger than those of α-U and the *b* lattice parameter is slightly smaller (e.g., [64, 96]), this pattern does not appear consistently in lattice parameters from phases identified as α' [24, 62, 64, 75-78, 96]. The maximum variation in measured values of each lattice parameter in orthorhombic phases in alloys with up to ~15 wt% U is ~0.03 Å.

α' has been identified in U-Zr alloys with up to at least 10 wt% Zr on the basis of metallographic, X-ray diffraction and neutron diffraction analyses (e.g., [71, 75-78, 97, 99, 100]. However, SEM images from these alloys commonly show fine-scale microstructures related to differences in composition (e.g., [62, 64, 101]), as do some optical images (e.g., Figure 4 of reference [76] and Figure 3 of reference [75]). TEM images show intergrowths of lamellae with two distinct compositions on a scale of a few tens or hundreds of nanometers [23, 24, 74, 75, 102]. Further investigation is needed to understand the extent to which the phases identified in a given sample may be a consequence of the spatial resolution of the analytical techniques used to examine it.

2.1.1.2.1.2.2 ω

ω is a hexagonal phase that is believed to occur as an intermediate stage in the transformation from γ to δ-UZr_2. Its role in phase transitions has been defined largely by analogy to ω transformations in high-pressure Zr and in alloys of metals such as Ti and Hf [27, 28, 101]. The structure of ω is similar to that of δ-UZr_2, but fully disordered (i.e., U and Zr are distributed randomly between all three of the crystallographic sites, in proportions dictated by the composition of the phase.)

Direct evidence for the existence of ω in U-Zr alloys is lacking, in large part because the X-ray diffraction peaks from ω are a subset of the peaks from δ-UZr_2 (Figure 11 of reference [74] and Figure 3 of reference [88]) and the transformation from ω to δ-UZr_2 involves a change in ordering rather than a change in crystal structure. Early identifications of ω in papers by Hatt [97] and by Hills and colleagues [99] should be treated with caution because Hatt did not address the distinction between diffraction patterns from ω and δ-UZr_2, and Hills et al. assumed that ω was present without providing evidence for its presence in their samples.

2.1.1.2.2 Phase Transitions

2.1.1.2.2.1 Solidus and Liquidus

Solidus and liquidus temperatures in phase diagrams until about 1989 (e.g., [21, 91, 103]) were based on experimental data published in 1959 by Summers-Smith [90]. More recent measurements involving a small number of compositions [42, 63, 64, 104, 105] suggested that these solidus and liquidus temperatures were approximately correct, but might be too high by a few tens of °C for intermediate compositions. In 2016, Balakrishnan et al. [106] reported new experimental measurements of solidus and liquidus temperatures spanning the entire U-Zr composition range.

Table 6 summarizes measured temperatures for the solidus and liquidus. Measurements from reference [106] were obtained from Zr and eighteen U-Zr alloys using a technique that involved melting a small spot of each alloy using RF induction in a Knudsen cell and measuring the liquidus and solidus temperatures by changes in optical reflectivity. The alloys were cast in yttria crucibles with strenuous attempts to minimize oxidation. The Zr feedstock contained ~0.48 wt% Hf, with a few tens of ppm of other metallic impurities, and the U feedstock was 99.9% wt% U. Errors in alloy compositions were estimated to be at most ±1.3%. The melting temperature of Zr in the data from Balakrishnan et al. is the same as the ITS-90 value [107] to within the stated errors.

The remaining liquidus and solidus temperatures in Table 6 were obtained using DSC or DTA. Reported impurity concentrations in the as-cast alloys ranged from ~70 to ~1650 ppm. The actual concentrations of impurities may be significantly higher than reported in some cases, as some of the analyses did not include common impurities such as C, O, and Si. Hf is a common impurity in Zr, but only Balakrishnan et al. [106] reported it.

The solidus temperatures measured by Rai et al. are consistent with the results of Balakrishnan et al. for alloys with 5 and 12 at% Zr. However, the solidus temperature measured by Rai et al. for the alloy with 22.5 at% Zr seems anomalously high, possibly because of reported difficulties in obtaining an accurate baseline at high temperatures [75]. The solidus temperature reported by Kaity et al. in 2012 [63] is consistent with the solidus measurements of Balakrishnan et al.; however, the corresponding liquidus measurement is significantly below the measurements of Balakrishnan et al. Solidus and liquidus temperatures reported by Kaity et al. in 2018 [64] are both higher than the 2012 values by ~20-50 degrees, even though both sets of measurements are from alloys with the same nominal composition. Balakrishnan et al. suggested that the values reported by Kaity et al. in 2012 might have been influenced by a high-temperature reaction between liquid U and alumina crucibles [106].

The data of Balakrishnan et al. appear to provide an accurate representation of the liquidus and solidus for all proportions of U and Zr and should be used in preference to earlier measurements. These values are generally consistent with those of Summers-Smith but have estimated errors of a few degrees rather than a few tens of degrees.

Measured phase-transition temperatures and enthalpies for U-10Zr (wt%) alloys were presented in Table 1 of reference [20]. These measurements indicate that the solidus and liquidus temperatures of U-10Zr are approximately 1248 and 1355-1360°C, respectively. Although identifications of reactions responsible for peaks in DSC data are unclear, a number of measurements show that U-10Zr has phase transitions at ~595-617, 685, and 700°C, as well as a transition with a small enthalpy that has been reported at 723 and 738°C.

Table 6. Solidus and liquidus measurements of U-Zr alloys (references [63, 64, 75 (Table V), 106 (Table 6)]). Data from Balakrishnan et al. (reference [106], in bold type) is preferred, and has an estimated maximum composition error of ±1.3%.

At% Zr	Solidus T (K)	Enthalpy of melting (J/g)	Liquidus T (K)	Reference
1.9	**1411±4**	**—**	**1429±5**	**[106]**
2.1	**1413±5**	**—**	**—**	**[106]**
4.9	**1418±4**	**—**	**1465±5**	**[106]**
5	1426	97.4	—	[75]
10	1433-1473	—	—	[90]
10.1	**1452±1**	**—**	**1525±2**	**[106]**
11.8	**1441±6**	**—**	**—**	**[106]**
12	1446	112.9	—	[75]
14	1465		1540	[64]
14	1448	—	1488	[63]
14.2	**1468±3**	**—**	**1550±7**	**[106]**
16.4	1488	—	—	[71]
—	1489±7	—	1631±10	[42]
22.5	**1521±7**	**—**	**1628±7**	**[106]**
22.5	1644	128.8	—	[75]

Table 6. (continued).

At% Zr	Solidus T (K)	Enthalpy of melting (J/g)	Liquidus T (K)	Reference
29.9	**1576±3**	**—**	**1690±9**	**[106]**
30	1523-1573	—	—	[90]
39.9	**1659±6**	**—**	**1776±7**	**[106]**
40	—	—	1693-1783	[90]
50	1673-1723	—	1733-1833	[90]
50	**1744±7**	**—**	**1843±5**	**[106]**
59.9	**1832±1**	**—**	**1914±5**	**[106]**
60	—	—	1803-1913	[90]
69	**1900±2**	**—**	**1975±2**	**[106]**
70	—	—	1873-1998	[90]
74.5	**1937±10**	**—**	**—**	**[106]**
75	**1956±6**	**—**	**2003±4**	**[106]**
80	—	—	1943-2083	[90]
82.9	**2002±1**	**—**	**—**	**[106]**
84.9	**2031±1**	**—**	**2060±2**	**[106]**
89.9	**2067±2**	**—**	**2088±1**	**[106]**
94.9	**2084±4**	**—**	**2109±4**	**[106]**
100	—	—	1973-2113	[90]
100	**2128±3**	**—**	**2128±3**	**[106]**

The enthalpies of melting from Rai et al. in Table 6 are the only available values for U-Zr alloys; however, it seems likely that they are significantly too high because the enthalpy of melting for pure U from the same source (88.2 J/g ≈ 23.18 kJ/mol) is well above the highest previously reported value of 12.1 kJ/mol (Section 2.1.2.2 of reference [5]). Rai et al. noted difficulties in obtaining accurate measurements at high temperatures, in part because of problems in maintaining a reproducible baseline. Further investigation of the enthalpy of melting is clearly required.

2.1.1.2.2.2 Temperatures of Solid-state Phase-transitions

More than 150 measurements of solid-state phase-transition temperatures in U-Zr alloys have been published, and more than 120 of them are included in Figure 4 and Table 7. Early data from Summers-Smith [90] and Saller et al. [108] are not included because of evidence that their samples had high concentrations of impurities such as O.

Unless otherwise specified in the notes to Table 7, all of the reported temperatures are onset temperatures measured during heating. All of the compositions in the table are nominal, and some were rounded to the closest percent during conversions between atomic and weight percentages. Reactions corresponding to some of the measured temperatures are from the original references, and were determined by phase-diagram analysis rather than experimental high-temperature measurements. The phase referred to as γ_1 in the table is called γ'' in some references.

Figure 4 shows the data in Table 7, using different symbols to indicate sources of data and colors to indicate reported oxygen contents. It is important to note that actual oxygen contents may be higher than

reported contents because the reported contents do not include oxygen that may have been incorporated in the specimens during analysis or processing after the measurements were made.

Although one can question the accuracy and precision of some of the individual measurements, Figure 4 shows a generally consistent pattern that does not appear to be significantly influenced by the reported oxygen contents. All compositions have a reported phase transition between ~525 and 625°C. Compositions with less than ~22 at% (~10 wt%) Zr have at least two higher-temperature transitions (at ~675 and 685-715°C for alloys with ~5 at% Zr), which occur at more closely spaced temperatures with increasing Zr contents. Alloys with ~40-65 at% Zr have two reported transitions, at approximately 600 and 675°C, and alloys with more than ~60% Zr have only one reported transition, at ~600-625°C.

Alloys with more than ~80 at% Zr have only one reported transition, which appears to increase in temperature with increasing Zr content. It is important to recognize that phase-transition temperatures for alloys with more than ~60 at% Zr were measured to identify the maximum temperature of stability for δ-UZr_2 and the possibility of higher-temperature transitions was not investigated. No phase-transition temperatures that can be used to define the higher-temperature boundary of the (α-Zr+γ) two-phase field have been reported.

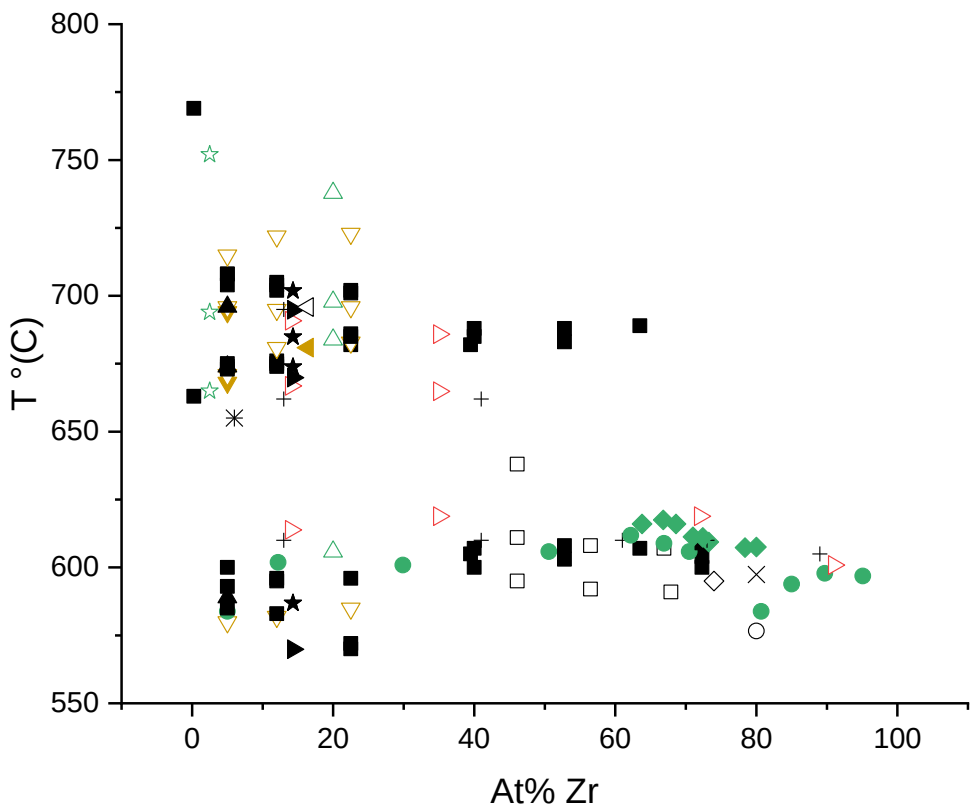

Figure 4. Solid-state phase-transition temperatures in Table 7. Symbols indicate references: Solid squares: [29], solid circles: [95], solid upward pointing triangles: [96], solid downward pointing triangles: [76], solid diamonds: [80], solid left-pointing triangles: [71], solid right-pointing triangles: [63], solid stars: [64], open squares: [87], open circles: [109], open upward-pointing triangles: [110], open downward-pointing triangles: [75], open left-pointing triangles: [111], open right-pointing

triangles: [112], open stars: [25]. Colors indicate reported concentrations of oxygen: green: < 350 ppm, yellow: 351-650 ppm, red: 651-1000 ppm, black: not reported.

Table 7. Solid-state phase transition temperatures in U-Zr alloys. α refers to α-U, β refers to β-U, γ refers to (γ-U, β-Zr) solid solutions, and δ refers to δ-UZr_2. Temperatures for each sample are listed in increasing order, with no attempt to ensure that temperatures in each column represent the same reactions.

Composition (at%)	Composition (wt%)	T1 (°C)	T2 (°C)	T3 (°C)	T4 (°C)	Reference	Notes
U-0.26Zr	U-0.1Zr	663	769	—	—	[29]	a
U-2.5Zr	U-1Zr	665 $\alpha+\gamma_2 \rightarrow \beta$ (eutectoid)	694 $\gamma_2+\beta \rightarrow \gamma_1$ (monotectoid)	752 $\beta+\gamma_1 \rightarrow \gamma_1$	—	[25]	b
U-5Zr	U-2Zr	580 $\alpha'+\delta \rightarrow \alpha+\gamma_2$	671 $\alpha+\gamma_2 \rightarrow \beta+\gamma_2$	696 $\beta+\gamma_2 \rightarrow \beta+\gamma_1$	715 $\beta+\gamma 1 \rightarrow \gamma$	[75]	c
U-5Zr	U-2Zr	584 $\alpha+\delta \rightarrow \gamma$	—	—	—	[95]	d
U-5Zr	U-2Zr	585	675	708	—	[29]	e
U-5Zr	U-2Zr	593	674	704	—	[29]	a
U-5Zr	U-2Zr	589 $\alpha' \rightarrow \alpha$	674 $\alpha+\gamma_1 \rightarrow \gamma$	696 $\beta+\gamma 1 \rightarrow \gamma$	—	[96]	f
U-5Zr	U-2Zr	600	673	708	—	[29]	g
U-5Zr	U-2Zr	668 $\beta \rightarrow \alpha+\gamma_1$	694 $\gamma \rightarrow \beta+\gamma_1$	—	—	[76]	h
U-6Zr	U-2Zr	655	—	—	—	[113]	i
U-12Zr	U-5Zr	582 $\alpha'+\delta \rightarrow \alpha+\gamma_2$	681 $\alpha+\gamma_2 \rightarrow \beta+\gamma_2$	695 $\beta+\gamma_2 \rightarrow \beta+\gamma_1$	722 $\gamma_1+\gamma_2 \rightarrow \gamma$	[75]	c
U-12Zr	U-5Zr	583	676	704	—	[29]	e
U-12Zr	U-5Zr	595	674	705	—	[29]	g
U-12Zr	U-5Zr	596	675	702	—	[29]	a
U-12.2Zr	U-5Zr	602 $\alpha+\delta \rightarrow \gamma$	—	—	—	[95]	d
U-13Zr	U-5Zr	610	662	695 $b+g \rightarrow g$	—	[114]	j
U-14Zr	U-6Zr	614 $\delta \rightarrow \gamma$	667 $\alpha \rightarrow \beta$	691 $\beta \rightarrow \gamma$	—	[112]	k
U-14.3Zr	U-6Zr	570	670	695	—	[63]	l

Table 7. (continued).

Composition (at%)	Composition (wt%)	T1 (°C)	T2 (°C)	T3 (°C)	T4 (°C)	Reference	Notes
U-14.3Zr	U-6Zr	587 $\alpha+\delta \rightarrow \alpha+\gamma_2$?	674 $\alpha+\gamma_2 \rightarrow \beta+\gamma_2$	685 $\beta+\gamma_2 \rightarrow \gamma_1+\gamma_2$	702 $\gamma_1+\gamma_2 \rightarrow \gamma$	[64]	m
U-16.4Zr	U-7Zr	681 $\alpha \rightarrow \gamma$	—	—	—	[71]	n
U-16.4Zr	U-7Zr	696 $\alpha \rightarrow \gamma$	—	—	—	[111]	o
U-20Zr	U-9Zr	606 $\alpha+\delta \rightarrow \alpha+\gamma$	684 $\alpha+\gamma \rightarrow \beta+\gamma$	698 $\beta+\gamma \rightarrow \gamma_1+\gamma_2$	738 $\gamma_1+\gamma_2 \rightarrow \gamma$	[110]	p
U-225.Zr	U-10Zr	570	686	701	—	[29]	g
U-225.Zr	U-10Zr	572	685	—	—	[29]	a
U-225.Zr	U-10Zr	585 $\alpha'+\delta \rightarrow \alpha+\gamma_2$	683 $\alpha+\gamma_2 \rightarrow \beta+\gamma_2$	696 $\beta+\gamma_2 \rightarrow \beta+\gamma_1$	723 $\gamma_1+\gamma_2 \rightarrow \gamma$	[75]	c
U-225.Zr	U-10Zr	596	682	702		[29]	e
U-30Zr	U-14Zr	601 $\alpha+\delta \rightarrow \gamma$	—	—	—	[95]	d
U-35Zr	U-17Zr	619 $\delta \rightarrow \gamma$	665 $\alpha \rightarrow \beta$	686 $\beta \rightarrow \gamma$	—	[112]	k
U-40Zr	U-20Zr	600	688	—	—	[29]	g
U-40Zr	U-20Zr	605	682	—	—	[29]	e
U-40Zr	U-20Zr	607	685	—	—	[29]	a
U-41Zr	U-21Zr	610	662	—	—	[114]	j
U-46Zr	U-25Zr	595	611	638	—	[87]	q
U-51Zr	U-28Zr	606 $\alpha+\delta \rightarrow \gamma$	—	—	—	[95]	d
U-53Zr	U-30Zr	603	683	—	—	[29]	a
U-53Zr	U-30Zr	608	688	—	—	[29]	e
U-57Zr	U-33Zr	592	608	—	—	[87]	q
U-61Zr	U-37Zr	610 $\alpha+\delta \rightarrow \alpha+\gamma$	—	—	—	[114]	j

Table 7. (continued).

Composition (at%)	Composition (wt%)	T1 (°C)	T2 (°C)	T3 (°C)	T4 (°C)	Reference	Notes
U-62Zr	U-39Zr	612 $\alpha+\delta\rightarrow\gamma$	—	—	—	[95]	d
U-63.5Zr	U-40Zr	607	689	—	—	[29]	a
U-63.5Zr	U-40Zr	616	—	—	—	[80]	r
U-67Zr	U-44Zr	618	—	—	—	[80]	r
U-67Zr	U-44Zr	607	—	—	—	[87]	q
U-67Zr	U-44Zr	609 $\delta\rightarrow\gamma$	—	—	—	[95]	d
U-68Zr	U-45Zr	591	—	—	—	[87]	q
U-69Zr	U-46Zr	616	—	—	—	[80]	r
U-71Zr	U-48Zr	606 $\delta\rightarrow\gamma$	—	—	—	[95]	d
U-71Zr	U-48Zr	611	—	—	—	[80]	r
U-72Zr	U-50Zr	619 $\delta\rightarrow\gamma$	—	—	—	[112]	k
U-72Zr	U-50Zr	600	—	—	—	[29]	g
U-72Zr	U-50Zr	604	—	—	—	[29]	e
U-72Zr	U-50Zr	609	—	—	—	[29]	a
U-72Zr	U-50Zr	611	—	—	—	[80]	r
U-73Zr	U-51Zr	609	—	—	—	[80]	r
U-73Zr	U-51Zr	610 $\delta\rightarrow\gamma$	—	—	—	[114]	j
U-78Zr	U-58Zr	607	—	—	—	[80]	r
U-80Zr	U-60Zr	577	—	—	—	[109]	s
U-80Zr	U-60Zr	608	—	—	—	[80]	r
U-80Zr	U-60Zr	597.4	—	—	—	[115]	t
U-81Zr	U-62Zr	584 $\delta\rightarrow\gamma$	—	—	—	[95]	d

Table 7. (continued).

Composition (at%)	Composition (wt%)	T1 (°C)	T2 (°C)	T3 (°C)	T4 (°C)	Reference	Notes
U-85Zr	U-69Zr	594 α-Zr+δ→γ	—	—	—	[95]	d
U-89Zr	U-76Zr	605 α-Zr+δ→α-Zr+γ	—	—	—	[114]	j
U-90Zr	U-77Zr	598 α-Zr+δ→γ	—	—	—	[95]	d
U-91Zr	U-80Zr	601 δ→γ	—	—	—	[112]	k
U-95Zr	U-88Zr	597 α-Zr+δ→γ	—	—	—	[95]	d

NOTE a: Alloys were prepared by melt-casting high-purity Zr crystal bars and nitric-acid washed uranium in yttria crucibles at ~1900°C for 1 hour, then cooling to room temperature at 30°C/minute. The alloys were inverted, and the heating and cooling process was repeated to ensure homogeneity. Cast cylinders were sectioned, annealed for 168 hours at 600°C, and cooled at an unspecified rate.

Temperatures in the table are transition onset temperatures measured with a DSC/TGA instrument and a heating rate of 5°C/min. The sample increased in weight and developed an oxide layer during data collection. Reference: [29] Table 2

NOTE b: Alloys were prepared by induction-heating uranium and zirconium feedstocks in magnesia crucibles and casting into water-cooled copper molds. The alloys were hot-rolled twice in air at temperatures of 800 and 600°C, then heat treated for 2 hours at 1000°C. Chemical analyses showed that the actual composition of the sample had 1.07 wt% Zr, 24 ppm N, 15 ppm C, 70 ppm Fe, 20 ppm Mo, and 40 ppm Si. The oxygen content for the alloy in Table 7 was not reported; however, other alloys in the same series had reported oxygen concentrations of 20-150 ppm.

Thermal arrests were observed during heating and cooling between 625 and 825°C at rates of 0.5 to 1.5°C/minute. Temperatures were measured with a calibrated thermocouple in a small hole drilled into the specimen which was ~3/8 inches in diameter and 1.5 inches long. Reference: [25]

NOTE c: Alloys were induction-melted, homogenized at 1000°C for 10 hours, then cooled at an unspecified rate. Actual concentrations of Zr for the three samples in Table 7 (U-2Zr, U-5Zr, and U-10Zr by weight) differed from nominal concentrations by at most 0.03 wt%. Maximum concentrations of impurities in the three samples were Al (410 ppm by weight), Cr (12.7 ppm), Fe (89.1 ppm), Mg (16.3 ppm), Mn (21.3 ppm), Ni (225 ppm), Co (0.7 ppm), Cd (0.06 ppm), Ce (8.7 ppm), Sm (0.6 ppm), Gd (0.07 ppm), N (76 ppm), O (552 ppm), and Si (615 ppm). Concentrations of C and Hf were not reported. Phase-transition temperatures were collected using a high-resolution heat-flux DSC with a heating rate of 3 K/minute. Temperatures in Table 7 indicate the beginnings of the transformations during heating. Reference: [75].

NOTE d: Alloy was prepared by arc-melting crystal-bar zirconium and uranium feedstocks. The Zr had a total of less than 840 ppm of metallic impurities (primarily Fe, Hf, Ti, and Al), 140 ppm O, and less than 40 ppm N. The U had 16 ppm Al, 16 ppm Fe, 12 ppm Si, 50 ppm O, and less than 40 ppm N. The alloys were melted six times, homogenized at 850°C for 72 hours, and water quenched. The oxygen and nitrogen concentrations in a quenched alloy with ~71 at% Zr alloy were both less than 60 ppm, and the nitrogen concentration was less than 30 ppm.

Phase-transition temperatures were measured with a high-temperature DSC/DTA using a heating rate of 5°C/minute and were calibrated by comparison to phase transition temperatures in pure U. Reference: [95]

Table 7. (continued).

Composition (at%)	Composition (wt%)	T1 (°C)	T2 (°C)	T3 (°C)	T4 (°C)	Reference	Notes

NOTE e: High-purity Zr crystal bars and nitric-acid washed uranium were melt-cast in yttria crucibles at ~1900°C for 1 hour, then cooled to room temperature at 30°C/minute. The alloys were inverted, and the heating and cooling process was repeated to ensure homogeneity. Cast cylinders were sectioned, annealed for 72 hours at 600°C, and cooled at an unspecified rate. Temperatures in the table are transition onset temperatures measured with a DSC/TGA instrument and a heating rate of 5°C/min. The sample increased in weight and developed an oxide layer during data collection. Reference: [29] Table 1

NOTE f: Alloy was prepared by vacuum induction melting U and Zr in an alumina-coated graphite crucible and cast in a quartz glass mold. The total of all impurities, including C, N, and O, was ~1600 ppm. The sample was then hot-rolled at 850°C to a thickness reduction of ~50%, soaked at 900°C for 120 hours, and water quenched.

The phase transition temperatures in Table 7 were measured using a DSC with a heating rate of 1°C/minute. These temperatures are consistent with dilatometer measurements reported in the same reference. Reference: [96]

NOTE g: High-purity Zr crystal bars and nitric-acid washed uranium were melt-cast in yttria crucibles at ~1900°C for 1 hour, then cooled to room temperature at 30°C/minute. The alloys were inverted and the heating and cooling process was repeated to ensure homogeneity. Cast cylinders were sectioned, annealed for 672 hours at 600°C, and cooled at an unspecified rate. Temperatures in the table are transition onset temperatures measured with a DSC/TGA instrument and a heating rate of 5°C/min. The sample increased in weight and developed an oxide layer during data collection. Reference: [29] Table 3

NOTE h: Alloy was prepared by vacuum induction melting U and Zr in an alumina-coated graphite crucible and cast in a quartz glass mold. The alloy had 1.98 wt% Zr, 316 ppm C, 241 ppm N, 552 ppm O, 349 ppm Al, 77.5 ppm Fe, 33 ppm Ni, 16 ppm Cr, 14 ppm Mn, 9.8 ppm Mn, and 4.1 ppm Ce. The sample was hot-rolled at 850°C to a thickness reduction of ~50%, soaked at 900°C for 2 hours, water quenched, and machined.

The phase-transition temperatures in Table 7 were measured with a dilatometer and a heating rate of 1°C/min. These temperatures are consistent with measurements using a quenching dilatometer with a cooling rate of 175°C/second. Reference [76]

NOTE i: Samples of U-6Zr (wt%) were prepared by arc melting, inverting four times, and casting. They were then annealed at 950°C for 500 hours and quenched in oil. Actual sample compositions had 5.3 to 6.1% Zr. The uranium feedstock had a carbon content of 160-260 ppm. Reference: [113]

NOTE j: Samples were prepared from 99.78% pure U and zirconium iodide by arc melting, then were heated to 800°C in a salt bath, forged, turned on a lathe, and annealed at "temperatures corresponding to the upper a-phase region." Transition temperatures were determined from discontinuities in heat capacities measured using a pulsed heating mode in which a sample was heated by 1-3°C by passing a current of 20-30 A through it for several seconds. No information about actual compositions or identities of impurities was provided. Reference: [114]

NOTE k: Four U-Zr alloys were prepared from high-purity U and Zr. Details of sample preparation were not provided in reference [112] or in the publications it cited for this information (references [104, 116]). Chemical analyses of the alloys showed differing levels of impurities, with maximum contents of 367 ppm C, .132 ppm Cu, 119 ppm Fe, 920 ppm Mg, 255 ppm Si, and 776 ppm O between the four alloys. Phase-transition temperatures were determined from peaks in heat-capacity measurements. Samples were annealed at 1100 K for 30 minutes before the heat capacity measurements. Reference: [112]

NOTE l: Alloy was prepared by vacuum induction melting feedstocks to a temperature of 1700 K in an yttria-coated graphite crucible and cast into quartz tubes. The alloy had 5.95 wt% Zr. Metallic impurities were Fe (20 ppm), Cr (2 ppm), Ni (9 ppm), Mn (3 ppm), Ca (6 ppm), Al (26 ppm), Cu (3 ppm), and Zn (2 ppm). No information about C, N, and O impurities was provided.

The phase transition temperatures in Table 7 were measured using a heat-flux TG/DTA/DSC with a heating rate of 5 K/minute and are consistent with dilatometry measurements from the same alloy. The sample was electropolished before the DSC measurements to remove any oxide layer. Reference: [63]

NOTE m: Sample was prepared by arc melting nuclear-grade U and 99.95% pure Zr feedstocks and were inverted and re-melted at least six times to ensure homogeneity. As-cast samples were held at 1173 K for 50 hours, water quenched, and cut into pieces. One of the pieces was again heated to 1173 K, and slowly cooled in the furnace. A second piece was heated to 1173 K, furnace-cooled to 1953 K, soaked for 100 hours, cooled to 923 K and held for 250 hours, cooled to 823 K and held for 500 hours, then air-cooled. The water-quenched material had 5.93 wt% Zr.

Table 7. (continued).

Composition (at%)	Composition (wt%)	T1 (°C)	T2 (°C)	T3 (°C)	T4 (°C)	Reference	Notes

The phase transition temperatures in Table 7 were measured using a heat-flux TG/DTA/DSC with a heating rate of 5 K/minute. All three samples had the same phase transition temperatures, which are consistent with phase-transition temperatures measured using dilatometry The sample was electropolished before the DSC measurements to remove any oxide layer. Reference: [64]

NOTE n: Sample was prepared by arc-melting U and crystal-bar Zr in a water-cooled Cu crucible. The material was inverted and re-melted at least 6 times. The sample was held at 800°C for 24 hours, water quenched, hot rolled at 850°C to a thickness reduction of ~50%, annealed at 850°C for 2 hours and water quenched. X-ray diffraction showed only an orthorhombic phase similar to □-U. The as-cast alloy contained 7.01 wt% Zr, 49 ppm W, 619 ppm O, 97 ppm N, 469 ppm C, 79 ppm Fe, 39 ppm Ni, 21.5 ppm Cr, 7 ppm Ca, and 4 ppm Si.

Transition temperatures were measured by DTA using alumina crucibles and a heating rate of 10°C/min. Reference: [71]

NOTE o: Sample was prepared by arc-melting high-purity U and Zr in a water-cooled Cu crucible. The material was inverted and re-melted at least 6 times. The sample was hot rolled at 850°C to a thickness reduction of ~75%, annealed at 827°C for 50 hours and water quenched. No information about the actual composition or impurities was provided. X-ray diffraction showed only an orthorhombic phase similar to α-U. Transition temperatures were measured by DSC using a heating rate of 5°C/min. Reference: [111]

NOTE p: Sample was prepared by melting uranium and zirconium in an argon plasma jet furnace, annealed for three days at 823 K, and cooled to room temperature over a period of one day. The U feedstock was > 99.98% pure, with a total of less than 159 ppm of major metallic impurities (Fe, Zn, Ni, and Si) and less than 200 ppm O. The zirconium feedstock was 99.8% pure, with major metallic impurities Hf, Ti, and Fe, and had less than 800 ppm O. X-ray diffraction of the cooled alloy showed that the alloy was a two-phase mixture of α-U and δ-UZr_2. Phase-transition temperatures were determined by anomalies in heat capacities measured using a direct heating pulse calorimeter. Reference: [110]

NOTE q: Samples were fabricated by arc-melting U and Zr feedstocks in a copper crucible, annealed at 850°C for 1 or 24 hours, and quenched. The U feedstock had 27 ppm Fe, 60 ppm, Mg, and 24 ppm Si, and the Zr feedstock had < 170 ppm Fe. The oxygen concentration in the U feedstock was not reported, and the Zr feedstock had 50 ppm of O_2. Phase-transition temperatures were identified by changes in the slopes of plots of electrical resistivity vs temperature during cooling. Reference: [87]

NOTE r: Alloys were prepared by arc-melting U and Zr feedstocks in a water-cooled crucible, re-melted six times, hot-rolled at 775°C, and machined. Chemical analyses showed that actual compositions of all of the alloys were within 1 wt% of nominal compositions, that all of the alloys were at least ~99.95% pure, and that oxygen contents were between 130 and 320 ppm (0.013 and 0.032 wt%), carbon contents were between 13 and 110 ppm (0.0013 and 0.011 wt%), and nitrogen contents were between 14 and 140 ppm (0.0014 and 0.014 wt%). Reference: [80] Table 1.

NOTE s: No information about preparation or composition of this alloy was provided. The phase-transition temperature was determined from a peak in heat-capacity data collected using a differential scanning calorimeter with a heating rate of 15°C/minute. Reference [109]

NOTE t: The sample was a pellet ~3 mm in diameter and 1 mm in thickness, with a weight of ~50 mg. No information about sample preparation or the actual composition and impurity content of the sample was provided. The phase transition temperature was determined from heat capacity measurements using DTA. The value in Table 7 represents the start of the transition during heating. Reference: [115]

2.1.1.2.2.3 Enthalpies and entropies of solid-state phase-transitions

Figure 5 summarizes measurements of enthalpies of solid-state phase transitions in U-Zr alloys that were reported in J/g. Table 8 includes the same data, as well as enthalpies reported in kJ/mol. Enthalpies of reactions between ~525 and 625°C are generally consistent for each composition and increase with increasing Zr content. Enthalpies of reactions in alloys with less than ~20 at% Zr are less consistent, as shown by the variations in colors for data from similar compositions and temperatures. Although some of the variations may be explained by two or more transitions with similar temperatures, consideration of the reported enthalpies for U-2.5Zr (at%) at temperatures between 682 and 686°C in Table 8 suggests that much of the variation may be due to differences between research groups and samples.

Table 8 also includes measurements of transition entropies (ΔS) from two research groups [95, 110]. As their measurements do not represent the same compositions and temperatures, no direct comparisons between the values from the two groups are possible.

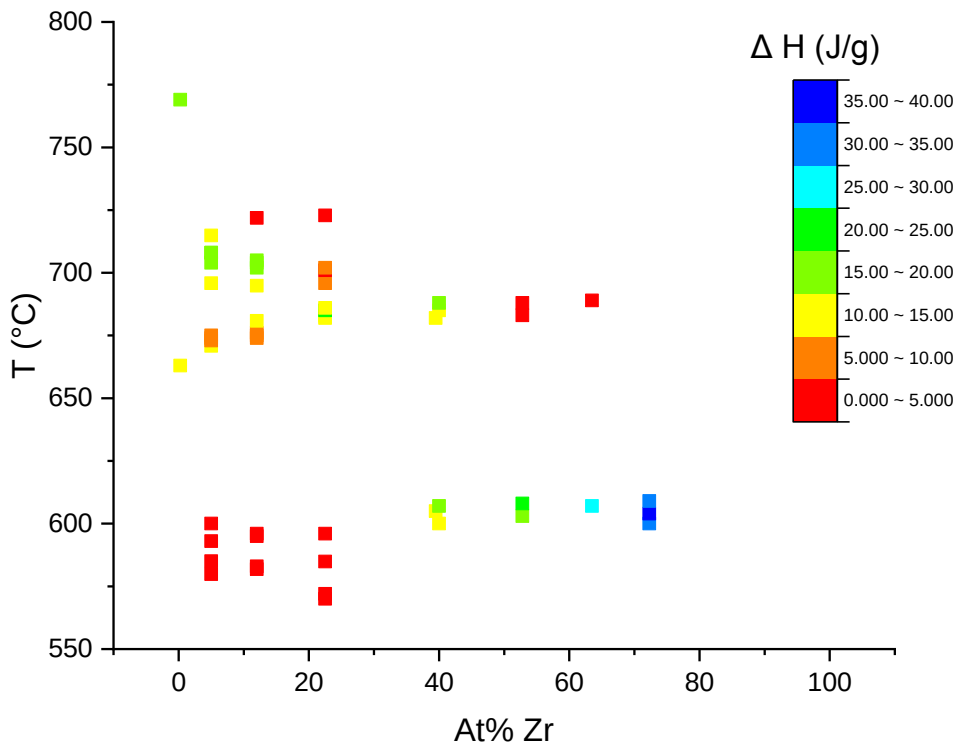

Figure 5. Phase-transition enthalpies (ΔH) reported in J/g from Table 8. Colors indicate ranges of values.

Table 8. Enthalpies (ΔH) and entropies (ΔS) of phase transitions in U-Zr alloys from calorimetry.

T (°C)	Composition (at%)	Composition (wt%)	ΔH (J/g)	ΔH (kJ/mol)	ΔS (J/mol-K)	Reference	Notes
663	U-0.26Zr	U-0.1Zr	10.94 (11.06)	—	—	[29]	a
769	U-0.26Zr	U-0.1Zr	17.74 (18.11)	—	—	[29]	a
580	U-5Zr	U-2Zr	1.21	—	—	[75]	e
584	U-5.0Zr	U-2Zr	—	0.32	0.37	[95]	d
585	U-5Zr	U-2Zr	0.58 (0.61)	—	—	[29]	b

Table 8. (continued).

T (°C)	Composition (at%)	Composition (wt%)	ΔH (J/g)	ΔH (kJ/mol)	ΔS (J/mol-K)	Reference	Notes
593	U-5Zr	U-2Zr	0.18 (0.18)	—	—	[29]	a
600	U-5Zr	U-2Zr	0.26 (0.26)	—	—	[29]	c
671	U-5Zr	U-2Zr	11.2	—	—	[75]	e
673	U-5Zr	U-2Zr	9.36 (9.47)	—	—	[29]	c
674	U-5Zr	U-2Zr	9.00 (9.17)	—	—	[29]	a
696	U-5Zr	U-2Zr	14.9	—	—	[75]	e
704	U-5Zr	U-2Zr	17.63 (18.02)	—	—	[29]	a
708	U-5Zr	U-2Zr	17.43 (18.49)	—	—	[29]	b
708	U-5Zr	U-2Zr	15.50 (15.76)	—	—	[29]	c
715	U-5Zr	U-2Zr	11.1	—	—	[75]	e
582	U-12Zr	U-5Zr	1.85	—	—	[75]	e
583	U-12Zr	U-5Zr	2.50 (2.67)	—	—	[29]	b
595	U-12Zr	U-5Zr	2.80 (2.84)	—	—	[29]	c
596	U-12Zr	U-5Zr	1.64 (1.66)	—	—	[29]	a
602	U-12.2Zr	U-5Zr	—	0.94	1.07	[95]	d
674	U-12Zr	U-5Zr	8.66 (8.85)	—	—	[29]	c
675	U-12Zr	U-5Zr	8.51 (8.70)	—	—	[29]	a
676	U-12Zr	U-5Zr	8.05 (8.78)	—	—	[29]	b
681	U-12Zr	U-5Zr	10.7	—	—	[75]	e
695	U-12Zr	U-5Zr	12.3	—	—	[75]	e
702	U-12Zr	U-5Zr	17.91 (18.35)	—	—	[29]	a
704	U-12Zr	U-5Zr	15.31 (16.81)	—	—	[29]	b
705	U-12Zr	U-5Zr	16.50 (16.96)	—	—	[29]	c
722	U-12Zr	U-5Zr	2.51	—	—	[75]	e
606	U-20Zr	U-9Zr	—	1.57	1.79	[110]	f
684	U-20Zr	U-9Zr	—	1.43	1.49	[110]	f
698	U-20Zr	U-9Zr	—	0.19	0.20	[110]	f
738	U-20Zr	U-9Zr	—	0.1	0.10	[110]	f
570	U-22.5Zr	U-10Zr	1.65 (1.67)	—	—	[29]	c
572	U-22.5Zr	U-10Zr	2.32 (2.33)	—	—	[29]	a
585	U-22.5Zr	U-10Zr	3.71	—	—	[75]	e
596	U-22.5Zr	U-10Zr	3.78 (3.84)	—	—	[29]	b
682	U-22.5Zr	U-10Zr	12.63 (12.94)	—	—	[29]	b
683	U-22.5Zr	U-10Zr	10.26	—	—	[75]	e
685	U-22.5Zr	U-10Zr	20.82 (21.00)	—	—	[29]	a
686	U-22.5Zr	U-10Zr	11.63 (11.93)	—	—	[29]	c
696	U-22.5Zr	U-10Zr	8.01	—	—	[75]	e
701	U-22.5Zr	U-10Zr	4.28 (4.39)	—	—	[29]	c
702	U-22.5Zr	U-10Zr	5.16 (5.30)	—	—	[29]	b
723	U-22.5Zr	U-10Zr	1.51	—	—	[75]	e
601	U-29.9Zr	U-14Zr	—	2.63	3.01	[95]	d

Table 8. (continued).

T (°C)	Composition (at%)	Composition (wt%)	ΔH (J/g)	ΔH (kJ/mol)	ΔS (J/mol-K)	Reference	Notes
600	U-40Zr	U-20Zr	12.61 (13.08)	—	—	[29]	c
605	U-40Zr	U-20Zr	11.53 (11.78)	—	—	[29]	b
607	U-40Zr	U-20Zr	13.04 (13.11)	—	—	[29]	a
682	U-40Zr	U-20Zr	13.19 (13.55)	—	—	[29]	b
685	U-40Zr	U-20Zr	13.19 (13.30)	—	—	[29]	a
688	U-40Zr	U-20Zr	14.32 (15.04)	—	—	[29]	c
606	U-50.6Zr	U-28Zr	—	3.95	4.49	[95]	d
603	U-53Zr	U-30Zr	17.50 (17.53)	—	—	[29]	a
608	U-53Zr	U-30Zr	21.09 (21.09)	—	—	[29]	b
683	U-53Zr	U-30Zr	3.55 (3.56)	—	—	[29]	a
688	U-53Zr	U-30Zr	2.15 (2.15)	—	—	[29]	b
612	U-62.2Zr	U-39Zr	—	5.35	6.05	[95]	d
607	U-63.5Zr	U-40Zr	27.44 (28.22)	—	—	[29]	a
689	U-63.5Zr	U-40Zr	0.54 (0.57)	—	—	[29]	a
609	U-66.9Zr	U-44Zr	—	5.56	6.31	[95]	d
606	U-70.5Zr	U-48Zr	—	5.17	5.89	[95]	d
600	U-72Zr	U-50Zr	34.03 (34.37)	—	—	[29]	c
604	U-72Zr	U-50Zr	30.18 (35.52)	—	—	[29]	b
609	U-72Zr	U-50Zr	29.64 (30.12)	—	—	[29]	a
584	U-80.7Zr	U-62Zr	—	4.41	5.15	[95]	d
594	U-85.0Zr	U-68.5Zr	—	3.98	4.58	[95]	d
598	U-89.7Zr	U-77Zr	—	2.51	2.89	[95]	d
597	U-95.1Zr	U-88Zr	—	1.04	1.2	[95]	d

NOTE a: See note a for Table 7. The number in parentheses is the reaction enthalpy after compensation for formation of oxides during DSC measurement from TGA data. Reference: [29] Table 2

NOTE b: See note e for Table 7. The number in parentheses is the reaction enthalpy after compensation for formation of oxides during DSC measurement from TGA data. Reference: [29] Table 1

NOTE c: See note g for Table 7. The number in parentheses is the reaction enthalpy after compensation for formation of oxides during DSC measurement from TGA data. Reference: [29] Table 3

NOTE d: See note d for Table 7. Enthalpies were determined from DSC/DTA data collected during the first heating run and were calibrated by comparison to data from pure U. Entropies are "apparent entropies," calculated as $\Delta H_t/T_t$, where T is a temperature in K and the subscript t indicates properties of a transition. Reference: [95] Table 2

NOTE e: See note c for Table 7. Reference: [75] Table V

NOTE f: See note p for Table 7. The reference does not provide information about how entropies were determined. Reference: [110] Table 2.

2.1.1.3 Phase Diagrams

Generally accepted features of U-Zr phase diagrams include a continuous bcc solid solution (γ) that forms the solidus in all compositions and separates into two bcc solid solutions (γ_1 and γ_2) at lower temperatures, very limited miscibility between U and Zr at temperatures below ~600-620°C, and the existence of a single intermediate phase (δ-UZr_2). These features have been known since the 1950s (e.g., [25, 103]). In 1989, Sheldon and Peterson [21] suggested a widely accepted phase diagram based on a thorough review of the experimental data available to them. Okamoto modified this phase diagram by substituting the calculated liquidus and solidus from Leibowitz et al. [43] for the original experimentally determined curves to produce the 1990 "Sheldon and Peterson" phase diagram [22]. The 1989 and 1990

versions of the Sheldon and Peterson phase diagrams are sufficiently similar that they are rarely distinguished.

Despite this general agreement, phase relationships in very high-U compositions remain poorly understood. Ahn and colleagues have recently suggested that the Sheldon and Peterson phase diagram does not represent phase transitions in these compositions correctly [29, 117], and that an earlier phase diagram proposed by Rough and Bauer [91, 103] may be more accurate. The two phase diagrams represent the relationship between α-U, β-U and γ-(U,Zr) differently: in the Rough and Bauer phase diagram, this relationship is the peritectoid reaction (β-U) + γ_1 ↔ (α-U); in the Sheldon and Peterson phase diagram, it is the eutectoid reaction (β-U) ↔ (α-U)+ γ_2 (Figure 6). Although the transformation occurs only in alloys with less than ~1 at% Zr, it has implications for phase relationships in all alloys with less than ~60 at% Zr. If the Sheldon and Peterson phase diagram is correct, there is a broad (β-U) + γ_2 field, and the transformation at 684°C corresponds to the (α + γ_2 ↔ β + γ_2) reaction; if the Rough and Bauer phase diagram is correct, there is no (β-U) + γ_2 field and the transformation at 684°C corresponds to the (α + γ_2 ↔ α + γ_1) reaction.

Another consequence of the difference between the phase diagrams is that alloys with 10-20 wt% (~22-40 at%) Zr will undergo three phase transformations at temperatures below ~700°C if the Sheldon and Peterson phase diagram is correct, but only two if the Rough and Bauer phase diagram is correct [29, 117]. The experimental data are inconclusive. DSC traces from two of the three samples whose nominal compositions have 10 wt% Zr measured by Ahn et al. [29] show two peaks, and one shows three. Measurements by Ahn et al. of an alloy with 20 wt% Zr show only two peaks, but a measurement of an alloy with the same nominal composition by Matsui et al. [110] shows three. Takahashi et al. [112] found only two peaks at temperatures below 700°C in their work on an alloy with 35 at% (~17 wt%) Zr. Kaity et al. [63] found three peaks below 700°C in a sample with 6 wt% Zr, but attributed one of them (at 570°C) to a martensitic transformation in (α-U). Rai et al. observed four transitions in DSC data from alloys with 2, 5, and 10 wt% Zr in DSC data collected with a heating rate of 3 K/minute, but not in alloys with 5 and 10 wt% Zr in data collected with a heating rate of 10 K/minute [75].

Janney and Hayes recently demonstrated that neither of the two phase diagrams is a good fit to the available phase-transition data for U-10 wt% Zr (Figure 6), possibly because some of the transitions involve metastable phases. A comparison between Figure 4 and transitions in either of the proposed U-Zr phase diagrams in Figure 6 does not provide clear guidance about which of the proposed phase diagrams is more accurate, even when considering only data with relatively low reported oxygen contents. Temperatures near ~600°C in Figure 4 are probably related to the transition between γ_2 and δ-UZr_2, and temperatures between ~660 and 715°C may be related to transitions between α-U, β-U, and γ_1. The two transitions above 750°C are both in compositions with low Zr contents, and probably represent the transition between β-U and γ. The pattern of reported transitions for alloys with more than ~60 at% Zr is somewhat misleading because these data was collected to identify the maximum temperature of stability for δ-UZr_2 and the possibility of higher-temperature transitions was not investigated. No phase-transition temperatures that can be used to define the higher-temperature boundary of the (α-Zr+γ) two-phase field have been reported.

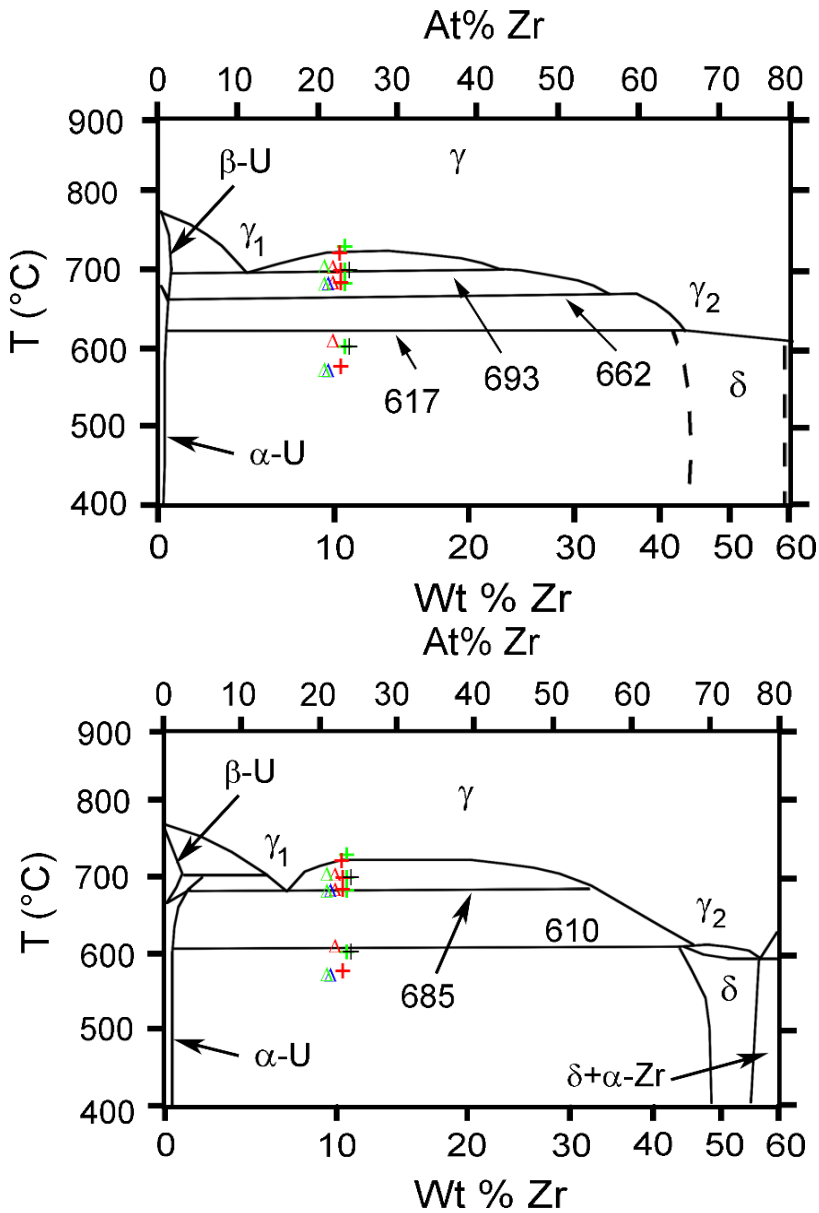

Figure 6. Comparison between Sheldon and Peterson (top) and Rough and Bauer (bottom) phase diagrams (Figure 2 of reference [20]). Colored symbols represent phase-transition temperatures from references [110] (green "+" symbols), [75] (red "+" symbols), [74] (black "+" symbols), and [29] (red, blue, and green triangles indicating measurements from samples annealed for 72, 168, and 672 hours, respectively.) Some symbols were moved horizontally for readability. All phase-transition temperatures in this figure are in Table 7.

Further work is clearly needed to understand solid-state phase transitions in U-Zr alloys, particularly those with low Zr contents. Recent research emphasizing the importance of thermal history and metastable phases suggests that simply counting phase transitions may not be enough to determine which phase diagram best represents the U-Zr system.

Regardless of whether further research favors the phase diagram of Sheldon and Peterson or that of Rough and Bauer, updates to reflect more recent measurements of the liquidus and solidus temperatures (Section 2.1.1.2.2.1) and the composition range of δ-UZr_2 (Section 2.1.1.2.1.1.5) are needed. Figure 7 shows how these updates affect the 1989 Sheldon and Peterson phase diagram.

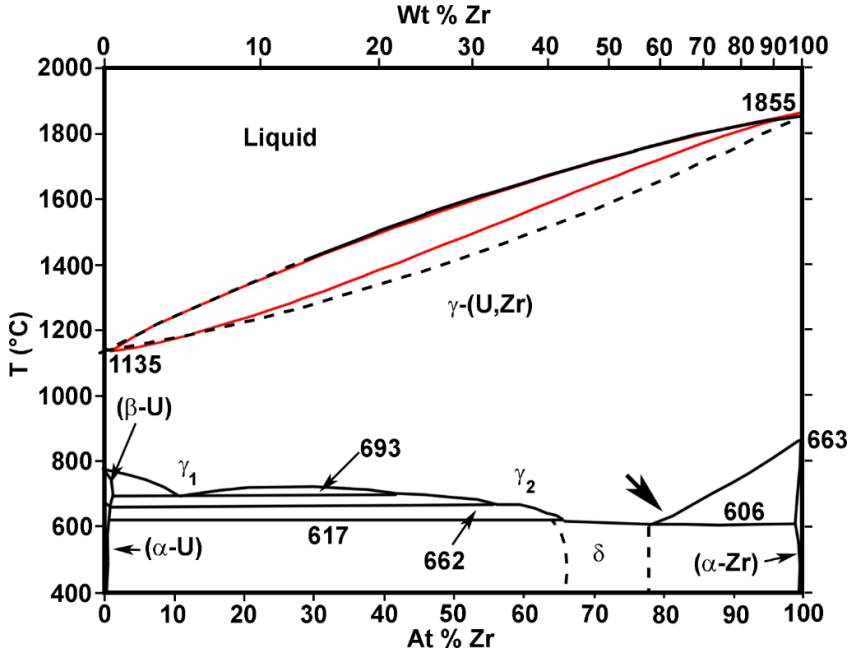

Figure 7. U-Zr phase diagram according to Sheldon and Peterson [21], with changes in the liquidus and solidus as a result of the work of Balakrishnan et al. in red and changes to phase relationships at the high-Zr end of the composition range of δ-UZr_2 as a result of the work of Akabori et al. 1992 [88] near the large arrow.

2.1.1.4 Heat Capacity and Related Properties

2.1.1.4.1 Heat Capacities between 300 and 850 K

Heat capacities of U-Zr alloys were reported by Fedorov and Smirnov in 1968 [114], by Matsui et al. and by Takahashi et al. in 1989 [110, 112], by Lee et al. in 2007 [109], by Kaity et al. in 2012 [63], and by Dash et al. in 2013 [111].

The only available measurement of the heat capacity of a U-Zr alloy with ~ 10 wt% Zr is from an alloy with 8.74 wt% Zr studied by Matsui et al. The heat capacity of this alloy is similar to that of U for temperatures between ~300 and 880 K (i.e., from room temperature to the onset of the lowest-temperature phase transition observed in this sample [20, 110].)

Data from Fedorov and Smirnov [114] are from five alloys that were made from 99.78% pure uranium and zirconium iodide by arc-melting, annealing at 800°C for an unspecified time, turned on a lathe, and annealed at temperatures "corresponding to the upper α-phase region" for an unspecified time. Measurements were made using a pulsed method in which heating was produced by passing a current through the sample. Heat capacities were presented as polynomials (Equation 13 through Equation 17). Fedorov and Smirnov also reported their measurements of the heat capacity of Zr, which is higher than those in Section 2.9.3 of reference [5] by a few J/mol-K.

Equation 13. Heat capacity of U-13 at% Zr (Zr-87 at% U) from 20-600°C measured by Fedorov and Smirnov [114, 118]

$$C_p = 0.356 + 1.425 \times 10^{-2} \times T + 2.59 \times 10^5/T^2$$

where C_p is constant-pressure heat capacity in cal/mol·K, T is temperature in K, and T is between 293 and 873 K

Equation 14. Heat capacity of U-41 at% Zr (Zr-59 at% U) measured by Fedorov and Smirnov [114, 118]

$$C_p = 0.265 + 1.32 \times 10^{-2} \times T + 2.62 \times 10^5/T^2$$

where C_p is constant-pressure heat capacity in cal/mol·K, T is temperature in K, and T is between 293 and 873 K

Equation 15. Heat capacity of U-61 at% Zr (Zr 39 at% U) measured by Fedorov and Smirnov [114, 118]

$$C_p = 3.47 + 9.32 \times 10^{-3} \times T + 7.01 \times 10^4/T^2$$

where C_p is constant-pressure heat capacity in cal/mol·K, T is temperature in K, and T is between 293 and 873 K

Equation 16. Heat capacity of U-73 at% Zr (Zr-27 at% U) measured by Fedorov and Smirnov [114, 118]

$$C_p = 3.08 + 8.43 \times 10^{-3} \times T + 9.83 \times 10^4/T^2$$

where C_p is constant-pressure heat capacity in cal/mol·K, T is temperature in K, and T is between 293 and 873 K

Equation 17. Heat capacity of U-89 at% Zr (Zr-11 at% U) measured by Fedorov and Smirnov [114, 118]

$$C_p = 3.89 + 6.48 \times 10^{-3} \times T + 7.71 \times 10^4/T^2$$

where C_p is constant-pressure heat capacity in cal/mol·K, T is temperature in K, and T is between 293 and 873 K.

Data from Matsui et al. [110] are from alloys that were made from 99.98% pure U with less than 159 ppm of metallic impurities (primarily Fe, Zn, Ni, and Si) and 99.8% pure Zr with major impurities Hf, Ti, and Fe. The U feedstock had less than 200 ppm O, and the Zr feedstock had less than 800 ppm O. Samples were melted together in an arc plasma jet furnace, annealed for three days at 823 K, and cooled over a period of a day. X-ray diffraction analyses indicated that the sample consisted of a-U and δ-UZr_2. Data from Matsui et al. can be represented by Equation 18.

Equation 18. Heat capacity of U-20 at % Zr (U-9 wt% Zr) alloy from 289 to 852 K (Polynomial fit by Kaity et al. [63] to data from Matsui et al. [110]).

$$C_p = 37.99 + 0.2 \times T + 2.73 \times 10^6/T^2$$

where C_p is constant-pressure heat capacity in J/kg·K, T is temperature in K, and T is between 289 and 852 K

Data from Takahashi et al. [112] are from four alloys that were fabricated using high-purity U and Zr. Actual compositions of alloys were within 0.5% Zr of nominal compositions in all cases. Maximum levels of O and C in all four alloys were 776 ppm and 367 ppm, respectively. Heat capacities were measured using a laser calorimeter. Individual measurements were published graphically, and smoothed heat-capacity values were published at 50-degree intervals. These data can be represented by Equation 19 through Equation 22.

Equation 19. Heat capacity of U-14at% Zr from 300 to 850 K (Polynomial fit by Kaity et al. [63] to data from Takahashi et al. [112]).

$$C_p = 55.10 + 0.14 \times T + 2.21 \times 10^6/T^2$$

where C_p is constant-pressure heat capacity in J/kg·K, T is temperature in K, and T is between 300 and 850 K

Equation 20. Heat capacity of U-35at% Zr from 300 to 850 K (Polynomial fit by Kaity et al. [63] to data from Takahashi et al. [112]).

$C_p = 59.18 + 0.16 \times T + 2.74 \times 10^6/T^2$

where C_p is constant-pressure heat capacity in J/kg·K, T is temperature in K, and T is between 300 and 850 K

Equation 21. Heat capacity of U-72at% Zr from 300 to 850 K (Polynomial fit by Kaity et al. [63] to data from Takahashi et al. [112]).

$C_p = 85.12 + 0.22 \times T + 3.98 \times 10^6/T^2$

where C_p is constant-pressure heat capacity in J/kg·K, T is temperature in K, and T is between 300 and 850 K

Equation 22. Heat capacity of U-91at% Zr from 300 to 850 K (Polynomial fit by Kaity et al. [63] to data from Takahashi et al. [112]).

$C_p = 153.07 + 0.20 \times T + 2.73 \times 10^6/T^2$

where C_p is constant-pressure heat capacity in J/kg·K, T is temperature in K, and T is between 300 and 850 K.

Data from Lee et al. [109] are from un-irradiated nuclear fuel. Heat capacities were measured using DSC. The results were only presented graphically. They showed that heat capacities calculated using the Kopp-Neumann method (Section 1.6.1) were lower than the measured values by a few hundredths of a J/g-K.

Data from Kaity et al. [63] are from an alloy that nominally contained 6 wt% Zr that was prepared by melting U and Zr feedstocks (99.9% and 99.95% pure, respectively) in an yttria-lined graphite crucible and injection casting into quartz molds. The total content of the metallic impurities in the as-cast alloys was ~70 ppm. Heat capacities were measured using DSC. These data can be represented by Equation 23 and Equation 24.

Equation 23. Heat capacity of U-6Zr from 304-495 K [63]

$C_p = 119.66 + 0.095 \times T - 1.23 \times 10^6/T^2$

where C_p is constant-pressure heat capacity in J/kg·K, T is temperature in K, and T is between 304 and 495 K

Equation 24. Heat capacity of U-6Zr from 495-802 K [63]

$C_p = -8{,}61 + 0.258 \times T + 10.71 \times 10^6/T^2$

where C_p is constant-pressure heat capacity in J/kg·K, T is temperature in K, and T is between 495 and 802 K

Data from Dash et al. [111] are from an alloy that nominally contained 7 wt% Zr. It was prepared by arc-melting U and Zr feedstocks together, inverting and re-melting at least six times to ensure homogeneity. The alloys were then hot-rolled to 75% reduction in thickness, homogenized again by holding at 1100 K for 50 hours, and water quenched. Heat capacities were measured using DSC. These data can be represented by Equation 25.

Equation 25. Heat capacity of U-7Zr [111]

$C_p = 0.14369 + 9.0 \times 10^5 \times T - 2211.2/T^2$

where C_p is constant-pressure heat capacity in J/g·K, T is temperature in K, and T is between 303 and 802 K

Heat capacities reported by Fedorov and Smirnov [114] were generally accepted until the late 1980s (e.g., [21, 118]). Later experimental work by Matsui et al. [110] and Takahashi et al. [112] suggested that these heat capacities were too high. More recent heat-capacity measurements of alloys with 6 and 7 wt% Zr (~14 and 16.4 at% Zr) [63, 111] are higher than those from Matsui et al. and Takahashi et al. [110, 112], and are higher than those of Federov and Smirnov [114] for alloys with similar compositions at some temperatures.

Figure 8 shows reported heat-capacity data for temperatures between 300 and 850 K. Recent measurements reported by Lee et al. [109] from an alloy with 60 at% Zr are not included because they were only presented graphically. Although almost all of the data indicate that heat capacities increase monotonically with temperature, the heat-capacity values show wide variation with no clear relationship to composition. Comparisons of heat capacity values from different compositions measured by the same research groups (Figure 9 and Figure 10) suggest that heat capacities of U-Zr alloys decrease with increasing Zr content. However, heat capacities for alloys with similar compositions measured by different research groups (e.g., alloys with 14-16.4 at% Zr) may differ by 20 - 30%. Further data are clearly needed to obtain reliable heat-capacity values.

A recent review by Ogata [48] reported that the data of Matsui et al. [110] are in good agreement with a thermodynamic analysis by Kurata et al. [37] for temperatures below 850 K. In the absence of further high-quality measurements, it seems appropriate to use the data of Matsui et al. to approximate the heat capacities of U-Zr alloys with less than ~40 at% (~20 wt%) Zr.

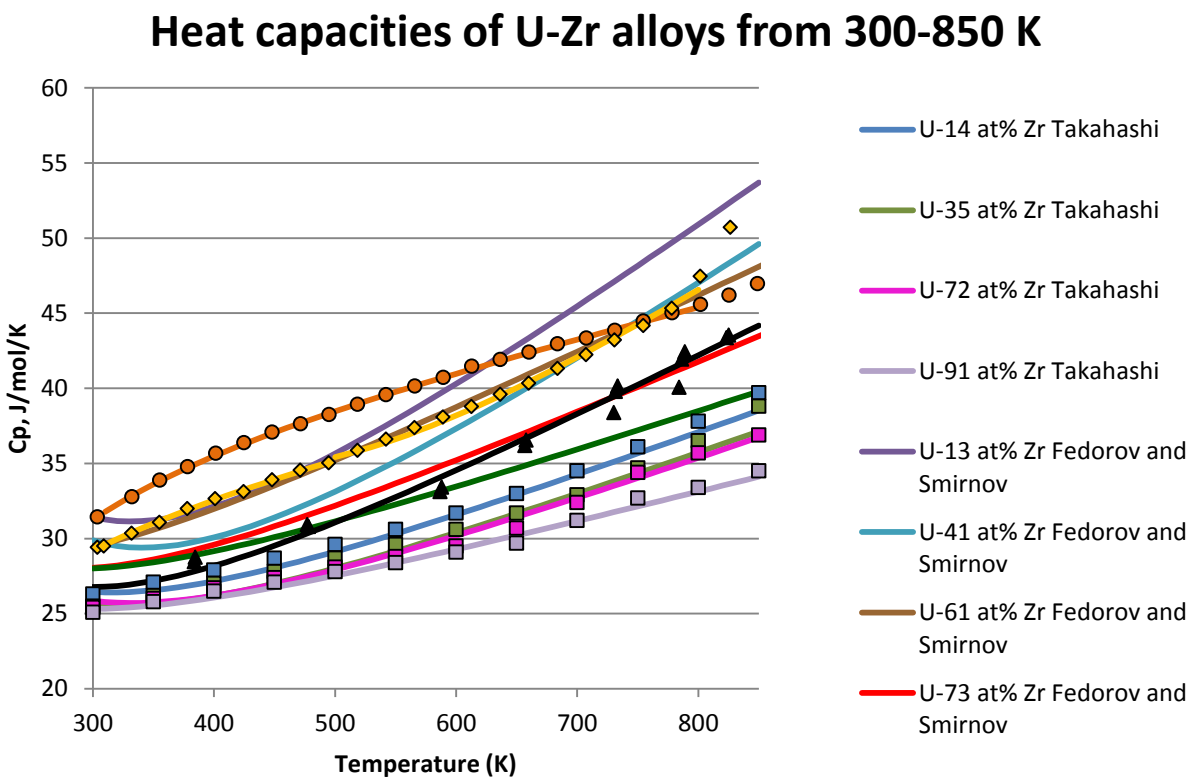

Figure 8. Experimentally determined heat capacities of U-Zr alloys at temperatures from 300-850 K. Equation 13 through Equation 25 are plotted as solid lines. Colored symbols indicate tabulated data from references [63, 110-112], with colors corresponding to lines representing polynomial fits to the same data. Different symbols indicate data from different references.

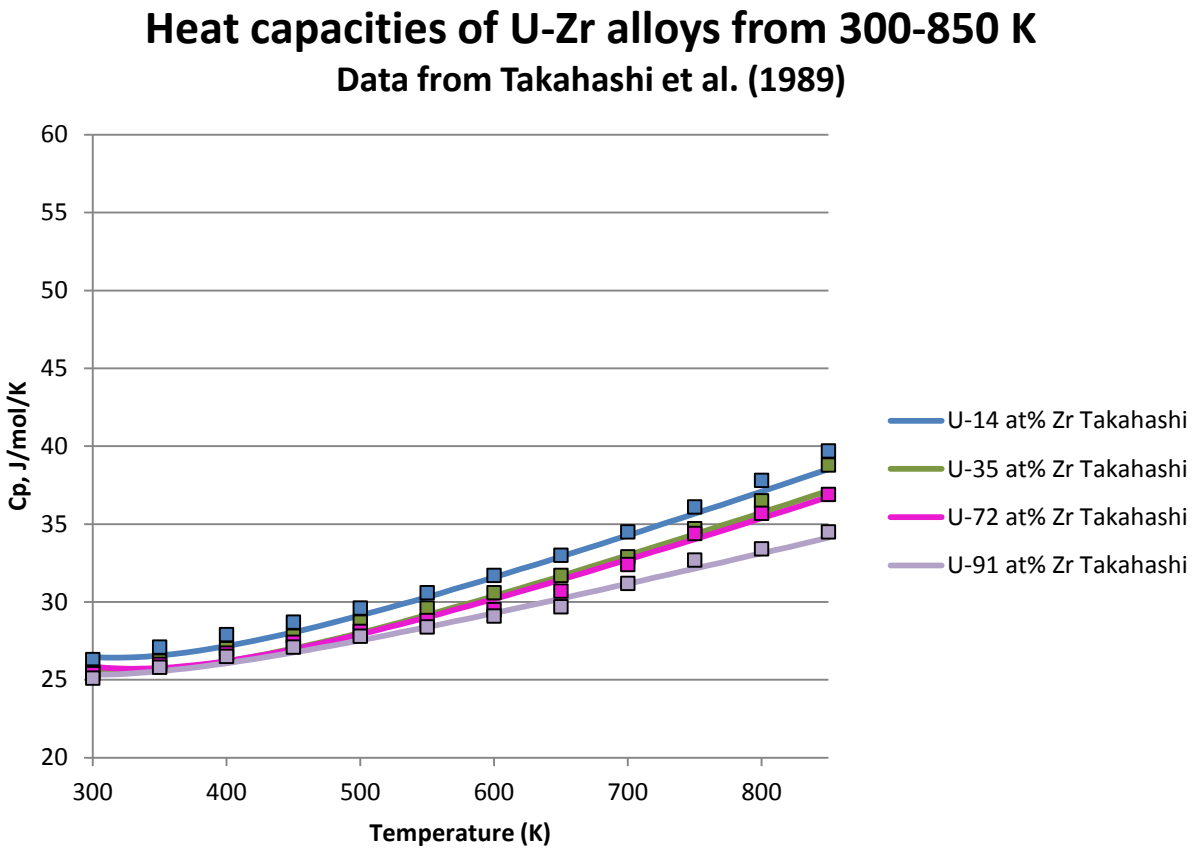

Figure 9. Heat capacities of U-Zr alloys reported by Takahashi et al. (Equation 19 through Equation 22 and tabulated data in reference [112]).

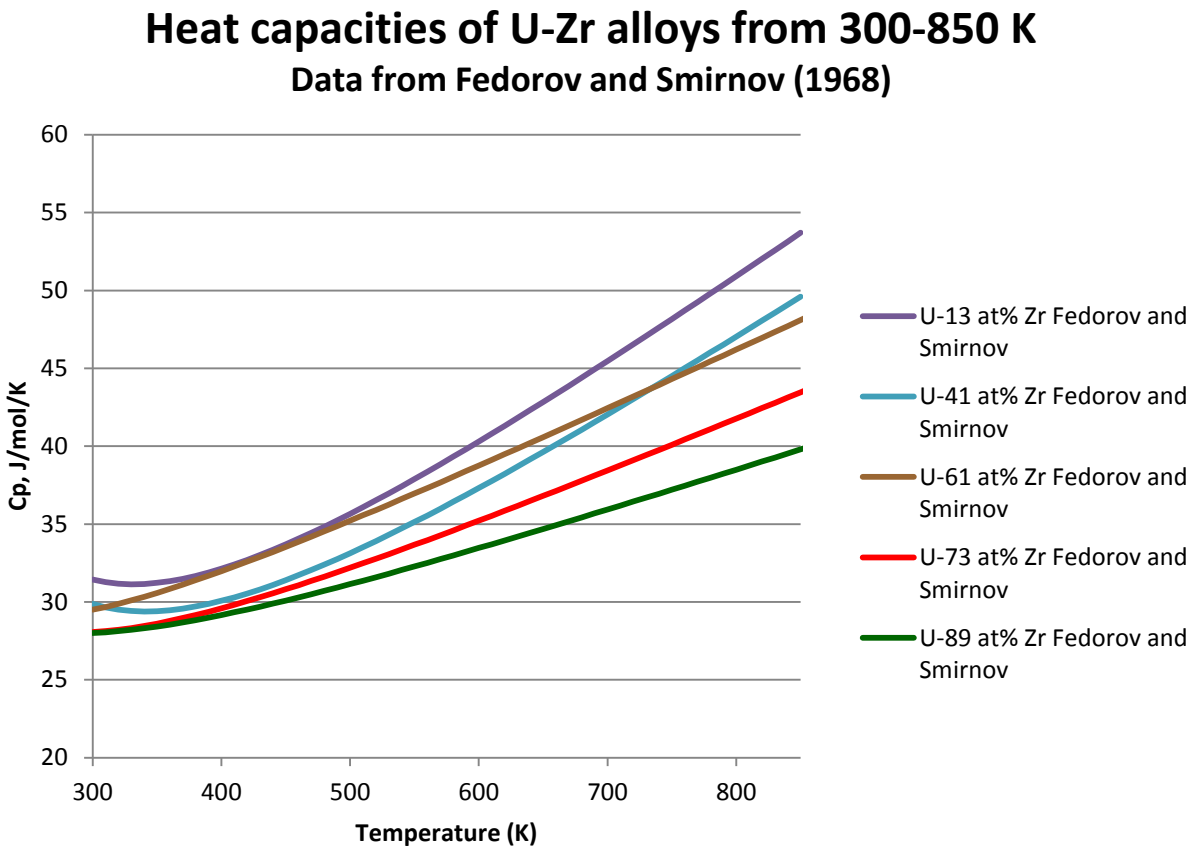

Figure 10. Heat capacities of U-Zr alloys reported by Fedorov and Smirnov [114] (Equation 13 through Equation 17)

2.1.1.4.2 Heat Capacities between 850 and 1000 K

Heat capacities are highly dependent on composition and temperature between ~850 and 1000 K for samples with high concentrations of U (~850 and 900 K for samples with high concentrations of Zr) because of phase transitions involved in reactions involved in the decomposition of γ-(U,Zr). Heat-capacity measurements for specific samples and temperatures can be found in references [63, 109, 110, 112].

2.1.1.4.3 Heat Capacities of γ-(U,Zr) Solid Solutions

Heat capacities of γ-(U,Zr) solid solutions at 1000 K are summarized in Table 9. Measurements by Matsui et al. [110] appear anomalously high relative to those by Takahashi et al. [112]. Ogata [48] notes that the data of Takahashi et al. [112] are in good agreement with the thermodynamic analysis of Kurata et al. [37] for temperatures above 900K.

Although further investigation is required, it seems reasonable to use the data of Takahashi et al. [112] to represent the heat capacities of γ solid solutions. Experimental measurements [109, 110, 112, 114] and thermodynamic models [48] show that the temperature dependence of the heat capacity of γ is limited.

Table 9. Heat capacities of γ-(U,Zr) solid solutions at 1000 K.

At% Zr	Wt% Zr	C_p (J/mol·K)	Reference
14	6	35.8	[112]
20	9	44.45	[110]
35	17	34.3	[112]
72	50	31.1	[112]
91	80	31.0	[112]

2.1.1.5 Thermal Expansion and Density

2.1.1.5.1 Thermal Expansion of δ-UZr_2

The only available measurements of the temperature dependence of lattice parameters of δ-UZr_2 are from a sample with 70.7 at% Zr. Akabori et al. [95] determined the lattice parameters of this alloy from room temperature to 880 K using Rietveld refinement of high-temperature neutron-diffraction data and fitted their results with polynomials (Equation 26 and Equation 27). Their results are shown in Table 10 and Figure 11.

Thermal expansion measurements of three U-10Zr alloys show significant differences, particularly above ~700 K. Differences in thermal expansion between samples with different thermal and processing histories are likely because of the anisotropic thermal expansion of individual phases and possibly because of different proportions of phases as a result of impurities. New measurements of samples with compositions and processing histories of interest for fuels are appropriate [20].

Table 10. Lattice parameters of δ-UZr_2 in alloys with ~70.5 at% Zr. [95]

T (K)	a (Å)	c (Å)	At% Zr	Comments
Room	5.028	3.090	70.2	X-ray diffraction
Room	4.0317 ±0.0001	3.0888 ±0.0001	70.7	Neutron diffraction
665	5.051	3.095	70.7	Neutron diffraction
765	5.060	3.096	70.7	Neutron diffraction
815	5.065	3.097	70.7	Neutron diffraction
865	5.070	3.097	70.7	Neutron diffraction
875	5.071	3.097	70.7	Neutron diffraction
880	5.071	3.097	70.7	Neutron diffraction

Equation 26. *a* lattice parameter of δ-UZr_2 in U-70.7 at% Zr, in Å (from [95 (Equation 1)])

$$a = (0.530 - 1.67\times10^{-6}\times T + 7.22\times10^{-9}\times T^2) \times 10$$

Equation 27. *c* lattice parameter of δ-UZr_2 in U-70.7 at% Zr, in Å (from [95 (Equation 2)])

$$c = (0.3081 + 2.95\times10^{-6}\times T - 1.31\times10^{-9}\times T^2) \times 10$$

where *a* and *c* are lattice parameters in Å, T is a temperature in Kelvin, and T is between room temperature and 880 K

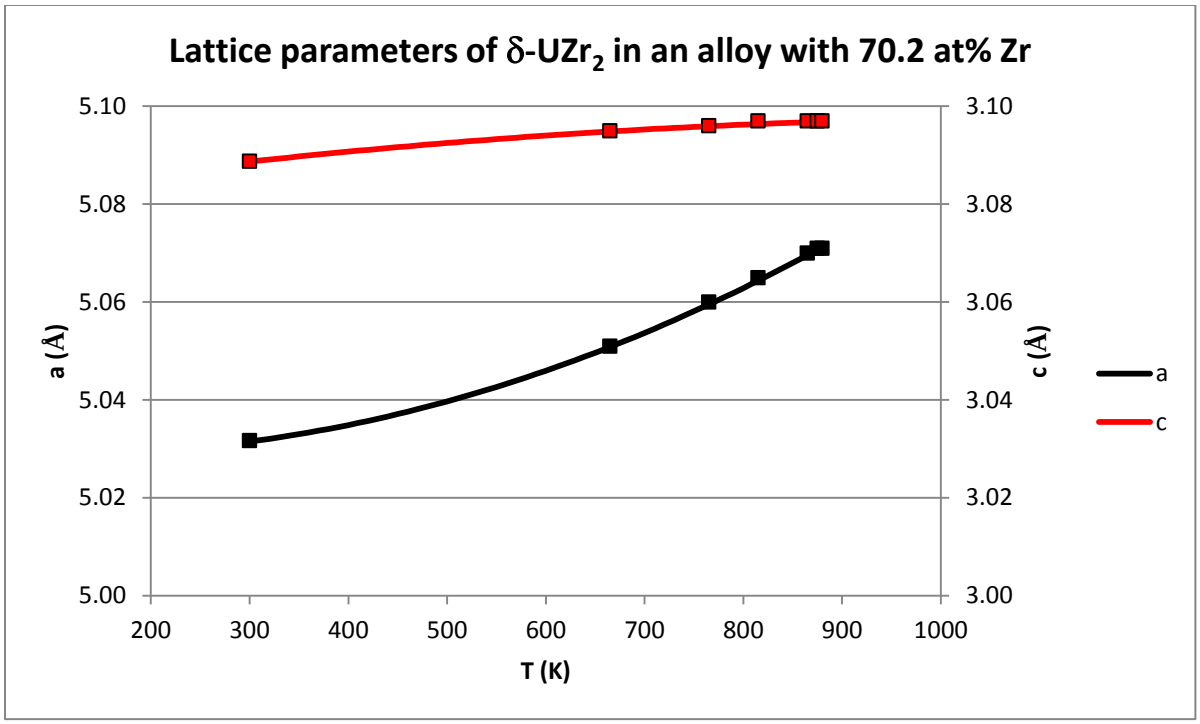

Figure 11. Variations in lattice parameters of δ-UZr_2 in U-70.7 at% Zr as a function of temperature (Equation 26 and Equation 27), with data points from Table 10.

2.1.1.5.2 Thermal Expansion of γ-(U,Zr)

The only available measurements of the thermal expansion of γ-(U,Zr) are from Rietveld refinement of high-temperature neutron-diffraction data from a sample with 70.7 at% Zr. Akabori et al. determined that the lattice parameters of this alloy were 3.589 Å at 925 K and 3.592 Å at 975 K [95].

2.1.1.5.3 Thermal Expansion of Polycrystalline U-Zr alloys with up to 20 wt% Zr

Thermal expansion measurements of three U-10Zr alloys show significant differences, particularly above ~700 K. Differences in thermal expansion measurements from samples with the same composition and different thermal and processing histories are likely because of the anisotropic thermal expansion of individual phases and perhaps because of different proportions of phases as a result of impurities. New measurements of samples with compositions and processing histories of interest for fuels are appropriate. [20]

Measurements of the thermal expansion of polycrystalline U-Zr alloys with up to ~20 wt% Zr were originally reported in four publications (Saller et al. 1956 [60], which was the source of all of the data from this composition range in the review of Touloukian et al. [61]), Basak et al. 2009 [62], and two publications by Kaity et al. [63, 64]). Although all of the measurements show increases in thermal expansion with increasing temperature, data from Saller and Touloukian show that thermal expansion decreases with Zr content, while data from Basak show that it increases (Figure 12 and Figure 13). Data from Kaity et al. involve only one composition.

Figure 12 shows older measurements of the linear thermal expansion of polycrystalline U-Zr alloys with up to ~15.5 wt% Zr [61]. The figure also shows polynomial fits for well-annealed alloys with 10 and 20% Zr (Equation 28 and Equation 29), which Touloukian et al. considered accurate to within ±7% for the entire temperature range. Thermal expansion curves for U and Zr are shown for comparison. Although individual measurements vary slightly, the curves in Figure 12 show a strong tendency for thermal expansion to decrease with increasing proportion of Zr. This tendency is consistent with the thermal

expansion of U and Zr and the existence of a continuous high-temperature solid solution between γ-U and β-Zr (Section 2.1.1.2.1.1.4).

Equation 28. Thermal expansion of U-10 wt%-Zr from 293 to 900 K according to Touloukian et al. [61]

$$(L-L_0)/L_0 = -0.424 + 1.658 \times 10^{-3} \times T - 1.052 \times 10^{-6} \times T^2 + 1.115 \times 10^{-9} \times T^3$$

where $(L-L_0)/L_0$ is thermal expansion in %, T is temperature in K, T is between 293 and 900 K, L is the length at temperature T, and L_0 is length at 293 K

Equation 29. Thermal expansion of U-20 wt%-Zr from 293 to 900 K according to Touloukian et al. [61]

$$(L-L_0)/L_0 = -0.301 + 1.160 \times 10^{-3} \times T - 7.790 \times 10^{-7} \times T^2 + 1.080 \times 10^{-9} \times T^3$$

where $(L-L_0)/L_0$ is thermal expansion in %, T is temperature in K, T is between 293 and 900 K, L is the length at temperature T, and L_0 is length at 293 K

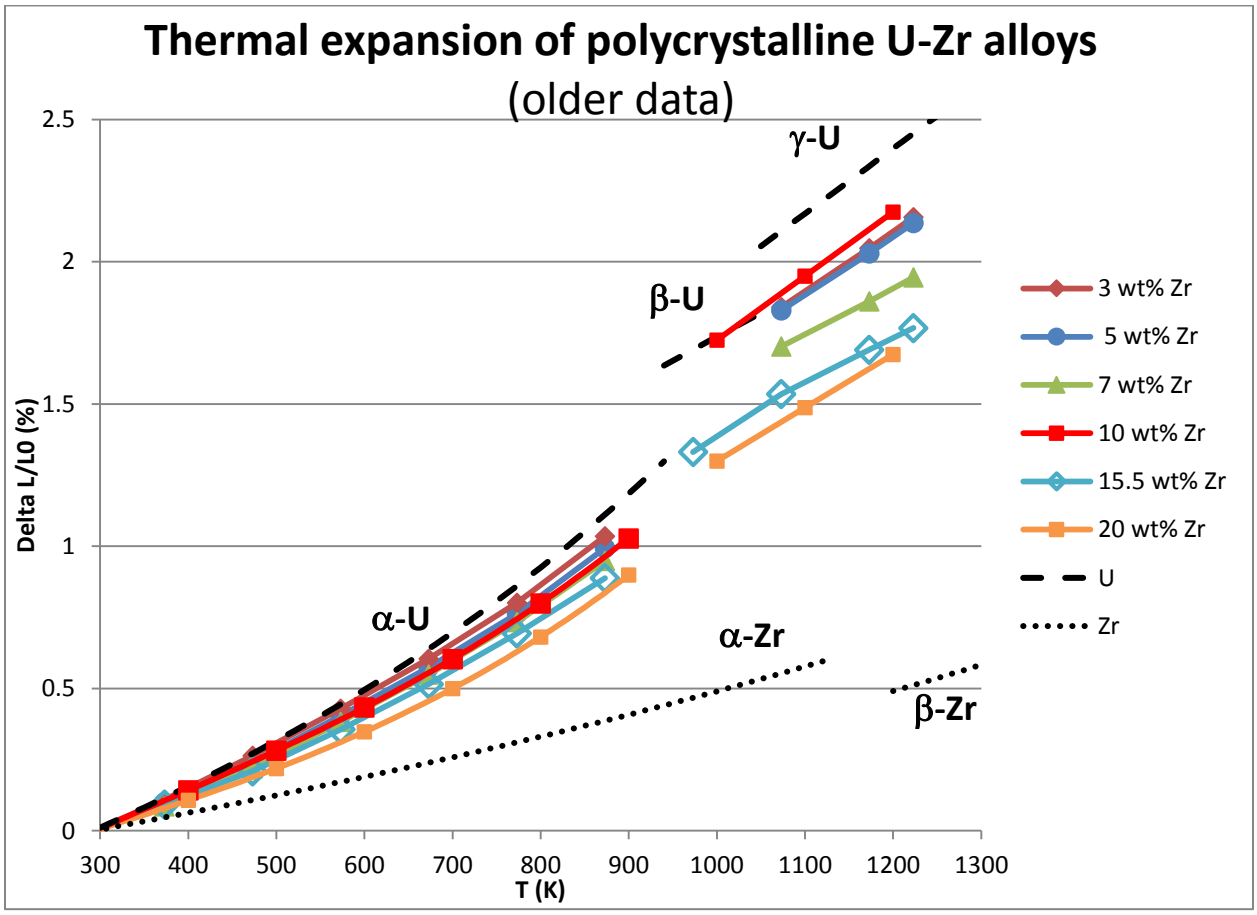

Figure 12. Thermal expansion of U-Zr alloys according to Saller et al. and Touloukian et al. [60, 61], with thermal expansion of U and Zr [61, 119] for comparison. Values for 10 wt% and 20 wt% Zr are polynomial fits to tabulated data from Touloukian et al. [61] (Equation 28 and Equation 29)

Figure 13 shows newer data, all of which was published after 2008. Thermal expansion shown by these data are generally higher than that in the older data. The 2009 data of Basak et al [62] shows increases in thermal expansion with higher Zr contents in alloys with up to 10 wt% Zr. This relationship is reversed in another paper by Basak and colleagues, in which the thermal expansion of an alloy with

2 wt% Zr is below that of U (Figure 2 of reference [76]). Equation 30 through Equation 37 express the thermal expansion measurements of Basak et al.

Equation 30. Thermal expansion of (α-U) in U-2 wt%-Zr from 323 to 923 K according to Basak et al. [62]

$$(L-L_0)/L_0 = -0.381 + 12.238 \times 10^{-4} \times T - 2.793 \times 10^{-7} \times T^2 + 9.904 \times 10^{-10} \times T^3$$

where $(L-L_0)/L_0$ is thermal expansion in %, T is temperature in K, T is between 323 and 923 K, L is the length at temperature T, and L_0 is length at 323 K

Equation 31. Thermal expansion of (γ-U) in U-2 wt%-Zr from 998 to 1173 K according to Basak et al [62]

$$(L-L_0)/L_0 = -7.775 + 2.405 \times 10^{-2} \times T - 2.105 \times 10^{-5} \times T^2 + 0.669 \times 10^{-8} \times T^3$$

where $(L-L_0)/L_0$ is thermal expansion in %, T is temperature in K, and T is between 998 and 1173 K

Equation 32. Thermal expansion of (α-U) in U-5 wt%-Zr from 323 to 923 K according to Basak et al. [62]

$$(L-L_0)/L_0 = -0.539 + 2.181 \times 10^{-3} \times T - 2.1 \times 10^{-6} \times T^2 + 2.087 \times 10^{-9} \times T^3$$

where $(L-L_0)/L_0$ is thermal expansion in %, T is temperature in K, T is between 323 and 923 K, L is the length at temperature T, and L_0 is length at 323 K

Equation 33. Thermal expansion of (γ-U) in U-5 wt%-Zr from 998 to 1173 K according to Basak et al. [62]

$$(L-L_0)/L_0 = -55.041 + 14.778 \times 10^{-2} \times T - 12.804 \times 10^{-5} \times T^2 + 3.737 \times 10^{-8} \times T^3$$

where $(L-L_0)/L_0$ is thermal expansion in %, T is temperature in K, and T is between 998 and 1173 K

Equation 34. Thermal expansion of (α-U) in U-7 wt%-Zr from 323 to 923 K according to Basak et al. [62]

$$(L-L_0)/L_0 = -0.62 + 2.732 \times 10^{-3} \times T - 3.386 \times 10^{-6} \times T^2 + 3.055 \times 10^{-9} \times T^3$$

where $(L-L_0)/L_0$ is thermal expansion in %, T is temperature in K, T is between 323 and 923 K, L is the length at temperature T, and L_0 is length at 323 K

Equation 35. Thermal expansion of (γ-U) in U-7 wt%-Zr from 998 to 1173 K according to Basak et al. [62]

$$(L-L_0)/L_0 = -42.52 + 11.369 \times 10^{-2} \times T - 9.709 \times 10^{-5} \times T^2 + 2.804 \times 10^{-8} \times T^3$$

where $(L-L_0)/L_0$ is thermal expansion in %, T is temperature in K, and T is between 998 and 1173 K

Equation 36. Thermal expansion of (α-U) in U-10 wt%-Zr from 323 to 923 K according to Basak et al. [62]

$$(L-L_0)/L_0 = -0.73 + 3.489 \times 10^{-3} \times T - 5.154 \times 10^{-6} \times T^2 + 4.39 \times 10^{-9} \times T^3$$

where $(L-L_0)/L_0$ is thermal expansion in %, T is temperature in K, T is between 323 and 923 K, L is the length at temperature T, and L_0 is length at 323 K

Equation 37. Thermal expansion of (γ-U) in U-10 wt%-Zr from 998 to 1173 K according to Basak et al. [62]

$$(L-L_0)/L_0 = -25.252 + 6.669 \times 10^{-2} \times T - 5.441 \times 10^{-5} \times T^2 + 1.518 \times 10^{-8} \times T^3$$

where $(L-L_0)/L_0$ is thermal expansion in %, T is temperature in K, and T is between 998 and 1173 K

In attempting to interpret and assess the thermal expansion data, it is important to recognize that thermal expansion may be strongly influenced by the thermal and processing histories and microstructures of individual samples because of the anistropic thermal expansion of some of the phases that may be present and possible changes in phase boundary compositions as a result of impurities. In the absence of new experiments, it seems reasonable to assume that the thermal expansion of U-Zr alloys with up to ~20 wt% Zr is consistent with the range of variation shown in Figure 12 and Figure 13. If greater precision is required, new measurements of specific alloys of interest may be appropriate.

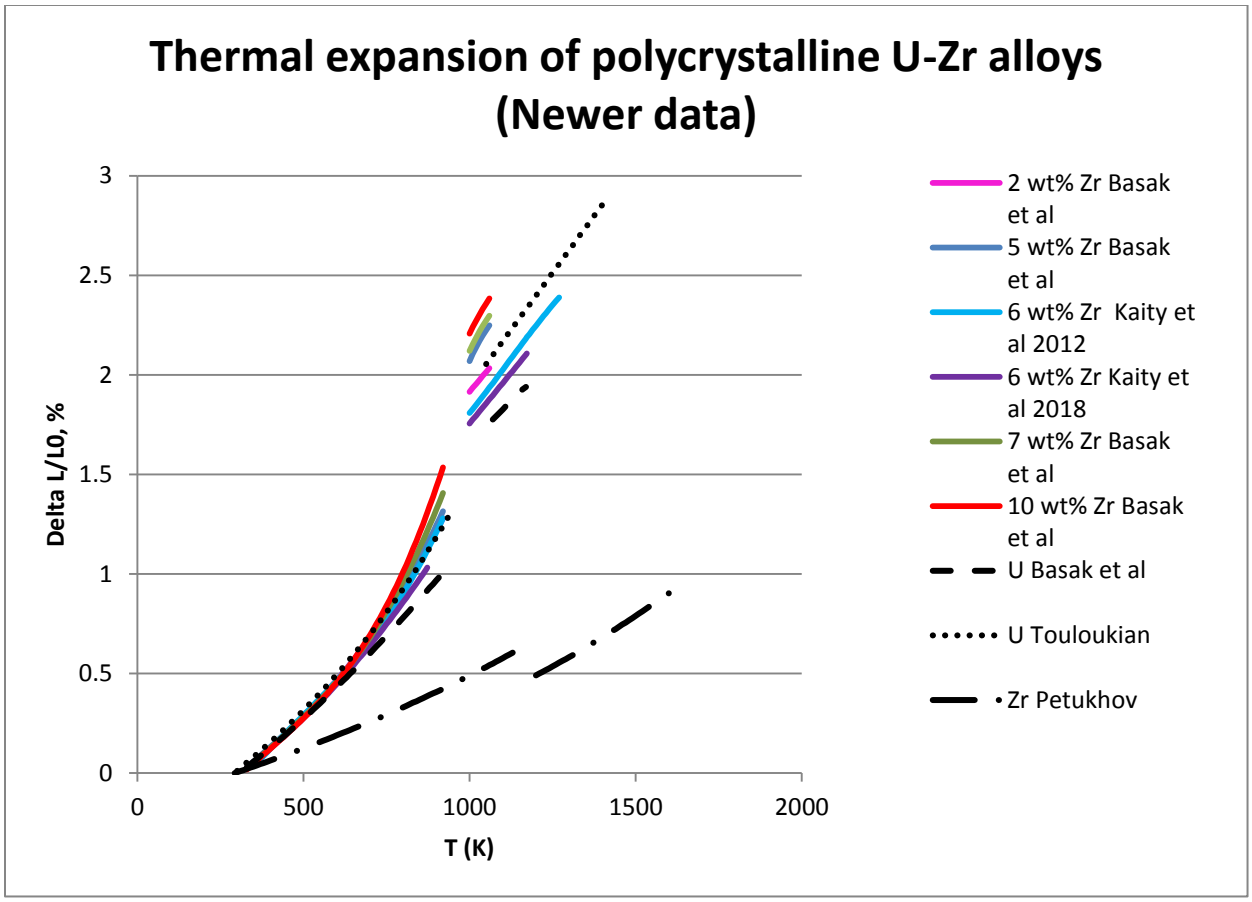

Figure 13. Thermal expansion of U and U-Zr alloys according to Basak et al. [62] (Equation 30 through Equation 37) and Kaity et al. [63, 64]

2.1.1.5.4 Coefficients of Thermal Expansion

Thermal expansion coefficients corresponding to Equation 28 and Equation 29 (which approximate the thermal conductivity of alloys with 10 and 20 wt% Zr) can be found in reference [61]. Basak et al. published thermal expansion coefficients for an alloy with 50 wt% Zr [26], and Rough published single values expressing coefficients of thermal expansion across relatively wide temperature ranges for U-59 wt% Zr and U-78 wt% Zr [103]. In view of the inconsistencies in the thermal expansion data and the relative lack of interest in high-Zr alloys for fuels, it seems appropriate to postpone summaries of thermal expansion coefficients until further high-quality measurements are available.

2.1.1.5.5 Densities

Reported densities of cast U-10 wt % Zr alloys are between 15.5 to slightly more than 16 g/cm^3, which is close to the theoretical density calculated from proportions and densities of U and Zr in the alloys [20].

2.1.1.5.5.1 Room-temperature Density of δ-UZr_2

Measurements of the room-temperature densities of single-phase samples of δ-UZr_2 are not available. However, Equation 5 can be used to calculate densities from crystal structures and lattice parameters which have been published in a number of references (e.g., [26-28, 88, 89, 92-95]. Data in reference [27] are apparently repeated from reference [26], and lattice parameters in reference [93] were determined by re-indexing data from reference [89]). Some early references (e.g., [89] and [92]) used a large cubic unit cell with 54 atoms; however, a hexagonal unit cell with 3 atoms has generally been accepted since it was proposed in 1957 [93, 94]. Densities calculated from the cubic and hexagonal unit cells are equivalent.

Table 11 and Figure 14 show the room-temperature densities of δ-UZr_2 in samples for which compositions and lattice parameters were published, calculated using Equation 5. Densities from references [92, 94] are generally consistent with those in Table 11 and Figure 14 but were not included because these references did not specify compositions. Densities reported by Basak et al. [26] are about 0.3 g/cm^3 higher than those in Table 11. The reason for this discrepancy is unknown, as Basak et al. said they had calculated their densities from the compositions and lattice parameters in Table 11.

Despite the absence of obvious systematic relationships between lattice parameters and compositions in measurements of δ-UZr_2 (Section 2.1.1.2.1.1.5), densities of δ-UZr_2 decrease approximately linearly as a function of composition. All of the calculated densities are smaller than would be predicted from a linear relationship between densities of α-U and α-Zr by a few tenths of a gram per cubic centimeter (Figure 14), possibly indicating that the structure of δ-UZr_2 is less closely packed than those of α-U and α-Zr.

The alloys considered in Table 11 and Figure 14 have a variety of thermal histories. In particular, values from references [26] and [28] are from samples with complex processing histories that may have included hot rolling, several cycles of quenching and heating, or lengthy holds at intermediate temperatures. None of these variations in thermal and processing history caused significant changes in the density of the δ-UZr_2.

If a single value for the density of δ-UZr_2 is needed, a value of 9.87 g/cm^3 is the most defensible choice. In addition to representing an intermediate composition (70.7 at% Zr), this density was calculated from lattice parameters from high-resolution neutron-diffraction data, which the authors believed were more accurate than lattice parameters from their X-ray diffraction data [95].

Table 11. Room-temperature lattice parameters and densities of δ-UZr_2.

Wt% Zr	Wt% U	At% Zr	At% U	*a* (Å)	*c* (Å)	Density (g/cm^3)	Reference
40	60	64	36	5.0369	3.0851	10.64	[26], Sample 35Zr240h
40	60	64	36	5.0342	3.0913	10.63	[26], Sample 7Zr2880h
44	56	67	33	5.025	3.086	10.32	[88]—
48	52	70	30	5.028	3.09	9.94	[88]—
48	52	701	29	5.0317	3.0888	9.87	[95]—
50	50	72	28	5.0429	3.1052	9.60	[28], Sample quenched from 875°C
50	50	72	28	5.0429	3.1043	9.61	[28], Sample quenched from 720°C
50	50	72	28	5.0419	3.0938	9.64	[28], Sample aged at 550°C and quenched
50	50	72	278	5.0343	3.0938	9.67	[28], Sample aged at 300°C and quenched
54	46	75	25	5.03	3.097	9.38	[88]—

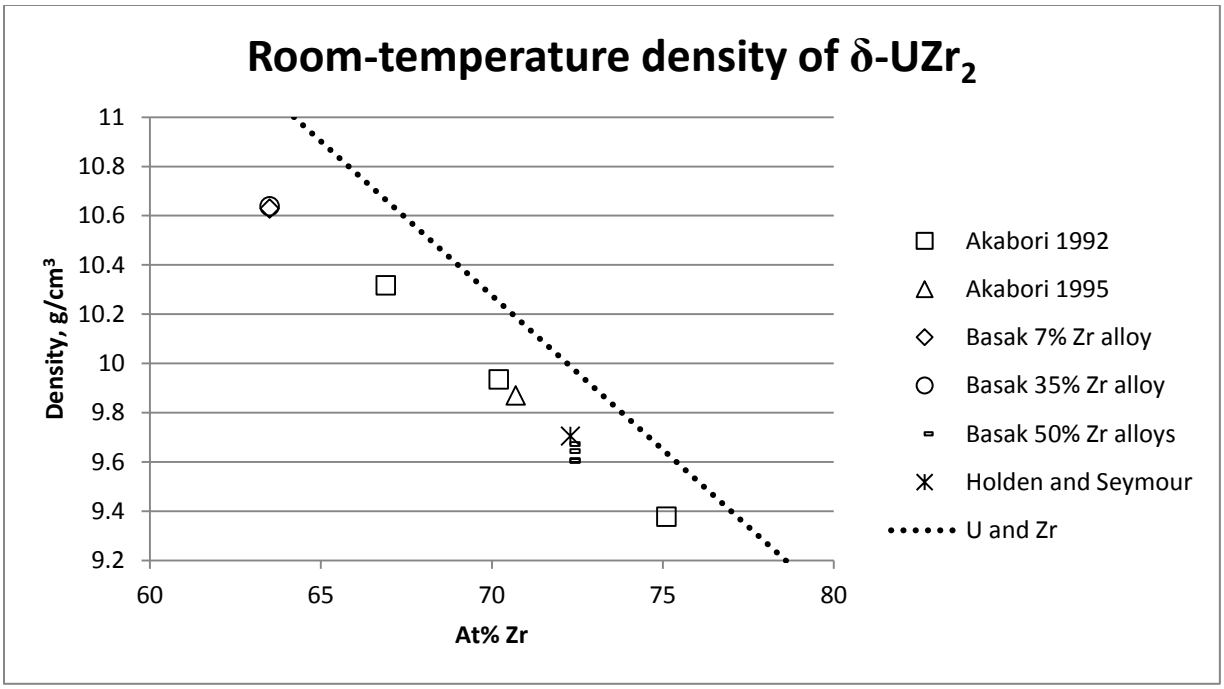

Figure 14. Room-temperature density of δ-UZr_2 calculated from lattice parameters in references [26, 28, 88, 89, 95]

2.1.1.5.5.2 Room-Temperature Densities of (α-U) Solid Solutions:

Measurements of the room-temperature densities of single-phase samples of U-Zr solid solution phases with the α-U structure have apparently not been published. Lattice parameters were published numerically by Basak et al. [26] and Rai et al. [75] and presented graphically by Basak et al. [76] and Zhang et al. [24].

Table 12 and Figure 15 show the densities of (α-U) solid solutions in U-Zr alloys with lattice parameters published numerically, calculated using Equation 5 with 4 atoms per unit cell [120]. The densities decrease approximately linearly as a function of composition. Despite differences in crystal structure between α-U and α-Zr, densities of (α-U) solid solutions can be approximated by interpolation between the room-temperature densities of α-U and α-Zr (sections 2.1.4.3 and 2.9.4.3 of reference [5]) , following the dotted line in Figure 15. This somewhat surprising result is apparently a consequence of the large differences in the atomic masses of U and Zr, which means that differences in density due to variations in lattice parameters are insignificant relative to differences caused by variations in composition.

Densities in Table 12 and Figure 15 are from samples with a variety of thermal and processing histories, some of which include hot rolling, several cycles of quenching and heating, or lengthy holds at intermediate temperatures Although Basak et al. determined that unit-cell volumes of samples with 2 wt% Zr increased with the rate at which samples were cooled, the corresponding variation in density was only ~0.1 g/cm^3 (0.5%). All of these data suggest that any differences in room-temperature densities of (α-U) solid solutions in U-Zr alloys as a result of variations in thermal or processing history are insignificant relative to differences caused by variations in composition.

Table 12. Room-temperature lattice parameters and densities of (α-U) solid solutions in U-Zr alloys, calculated from lattice parameters in specified references using Equation 5.

Wt % Zr	Wt % U	At% Zr	At% U	a (A)	b (A)	c (A)	Density (g/cm3)	Reference
1.1	0.989	2.820415	97.17958	2.8535	5.8629	4.9579	18.72	[26], Sample 7Zr2880h
2	0.98	5.056066	94.94393	2.8616	5.8565	4.9648	18.40	[75]
5	0.95	12.07532	87.92468	2.8652	5.8548	4.9688	17.55	[75]
10	0.9	22.47665	77.52335	2.8702	5.8503	4.9702	16.31	[75]
11.6	0.884	25.50715	74.49285	2.8539	5.8656	4.9681	16.01	[26], Sample 35Zr240h

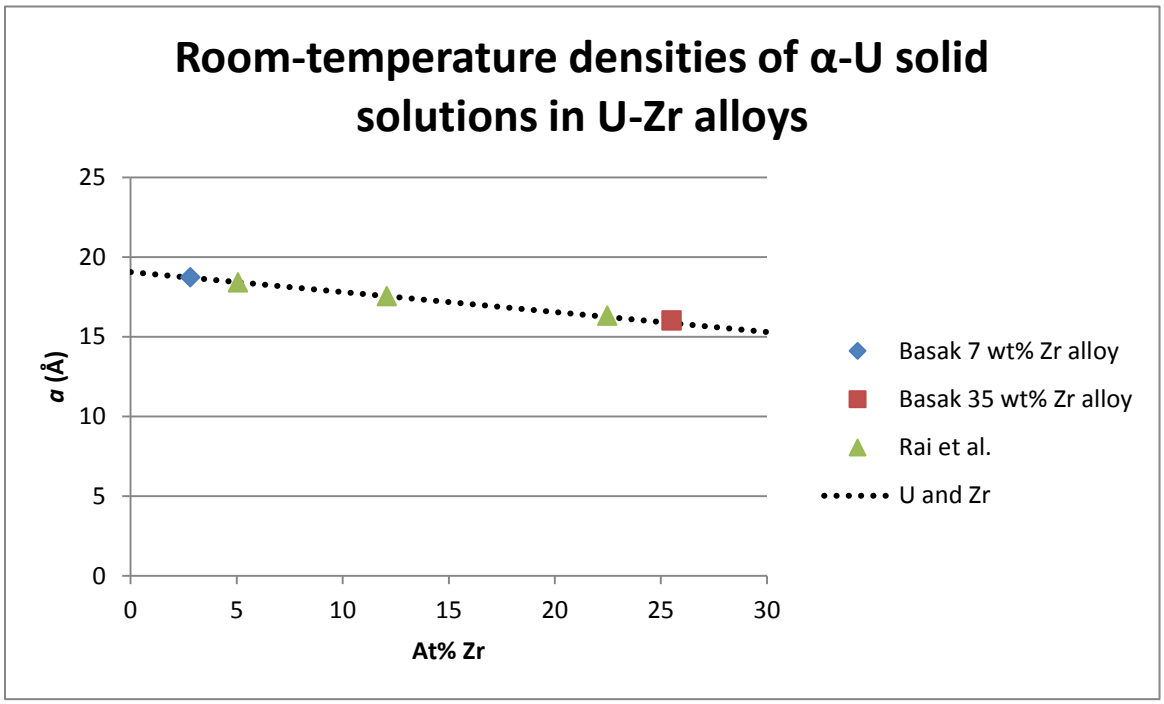

Figure 15. Room-temperature densities of (α-U) solid solutions in U-Zr alloys, calculated from data in references [26, 75] using Equation 5. Dotted line connects densities of α-U and α-Zr.

2.1.1.5.5.3 Room-Temperature Densities of γ-(U,Zr) Solid Solutions:

Room-temperature densities of γ-(U,Zr) solid solutions have apparently not been measured directly. Table 13 and Figure 16 show room-temperature densities of γ-(U,Zr) solid solutions in alloys with 25-80 at% Zr (11.3-60.5 wt% Zr), calculated from lattice parameters from X-ray diffraction using Equation 5 with two atoms per unit cell. Despite differences in crystal structure between γ-U and α-Zr, densities of γ-(U,Zr) solid solutions can be approximated by interpolation between the density of γ-U at 1060 K and the room-temperature density of α-Zr (sections 2.1.4.3 and 2.9.4.3 of reference [5]), as shown by the dotted line in Figure 16. This somewhat surprising result is apparently a consequence of the large differences in the atomic masses of U and Zr, which means that differences in density due to variations in lattice parameters are insignificant relative to differences caused by variations in composition.

Table 13. Room-temperature molar masses, lattice parameters, unit cell volumes, and densities of γ-(U,Zr) solid solutions.

At% Zr	molar mass (g)	*a* (Å)	Unit cell volume (Å^3)	Density (g/cm^3)	Reference
25	201.33	3.55	44.74	14.94	[84]
30	193.99	3.543	44.47	14.48	[84]
30	193.99	3.543	44.47	14.48	[58]
40	179.31	3.533	44.10	13.50	[84]
50	164.63	3.546	44.59	12.26	[84]
50	164.63	3.546	44.59	12.60	[84]
60	149.94	3.546	44.50	11.16	[84]
70	135.26	3.563	45.23	9.93	[84]
72.29	131.89	3.5765	45.75	9.57	[27, 28], Sample quenched from 635°C
72.29	131.89	3.5817	45.95	9.53	[28], Sample quenched from 875°C
72.29	131.89	3.5784	45.82	9.56	[28], Sample quenched from 720°C
74.9	128.07	3.57	45.50	9.34	[84]
80	120.58	3.572	45.58	8.78	[84]

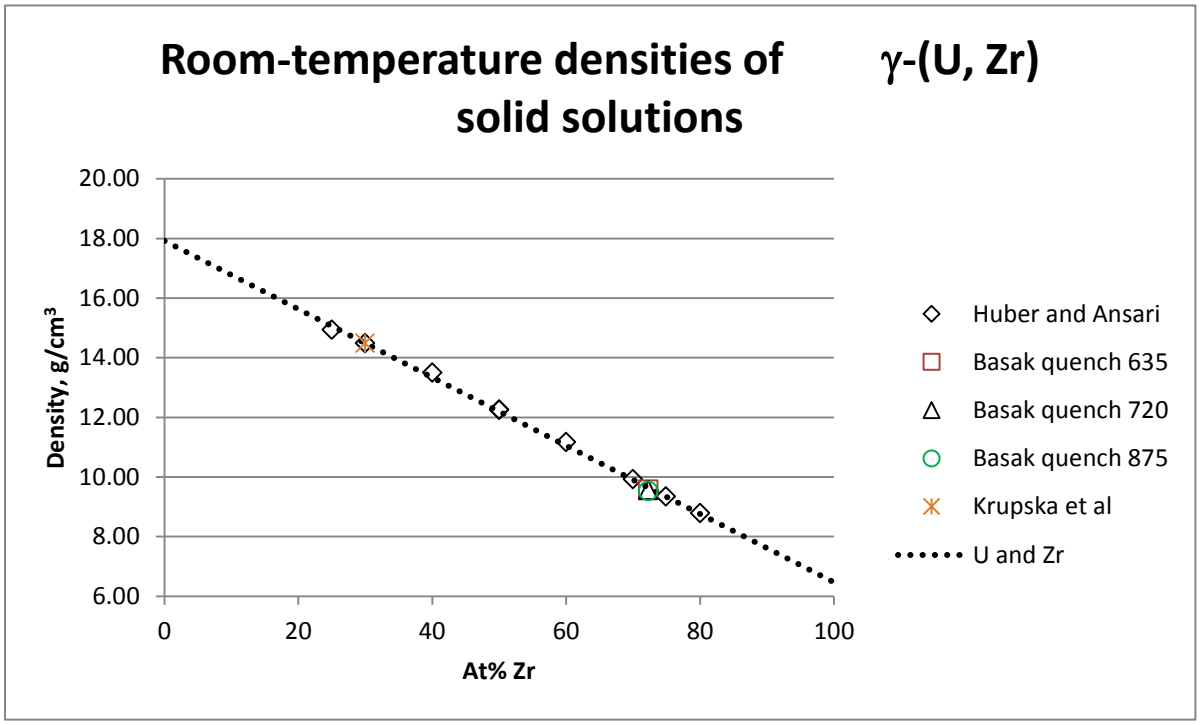

Figure 16. Room-temperature lattice parameters and densities of γ-(U,Zr) solid solutions calculated from lattice parameters in references [27, 28, 58, 84]. Dotted line connects the density of γ-U at 1060 K and the room-temperature density of α-Zr.

2.1.1.5.5.4 Room-Temperature Densities of As-cast U-Zr Alloys

Reported densities of cast U-10Zr alloys are between 15.5 and slightly more than 16 g/cm^3, which is close to the theoretical density calculated from proportions and densities of U and Zr in the alloys [20].

Figure 17 shows the published measurements of the room-temperature densities of as-cast U-Zr alloys. The dotted line shows a curve fitted to more than 20 measured densities [103]. The theoretical density is provided for comparison. Many of the measured densities from U-Zr alloys are smaller than the theoretical densities, with a maximum difference of ~ 1 g/cm^3. Differences between actual and theoretical densities are commonly attributed to casting flaws such as porosity and inclusions of low-density impurity phases.

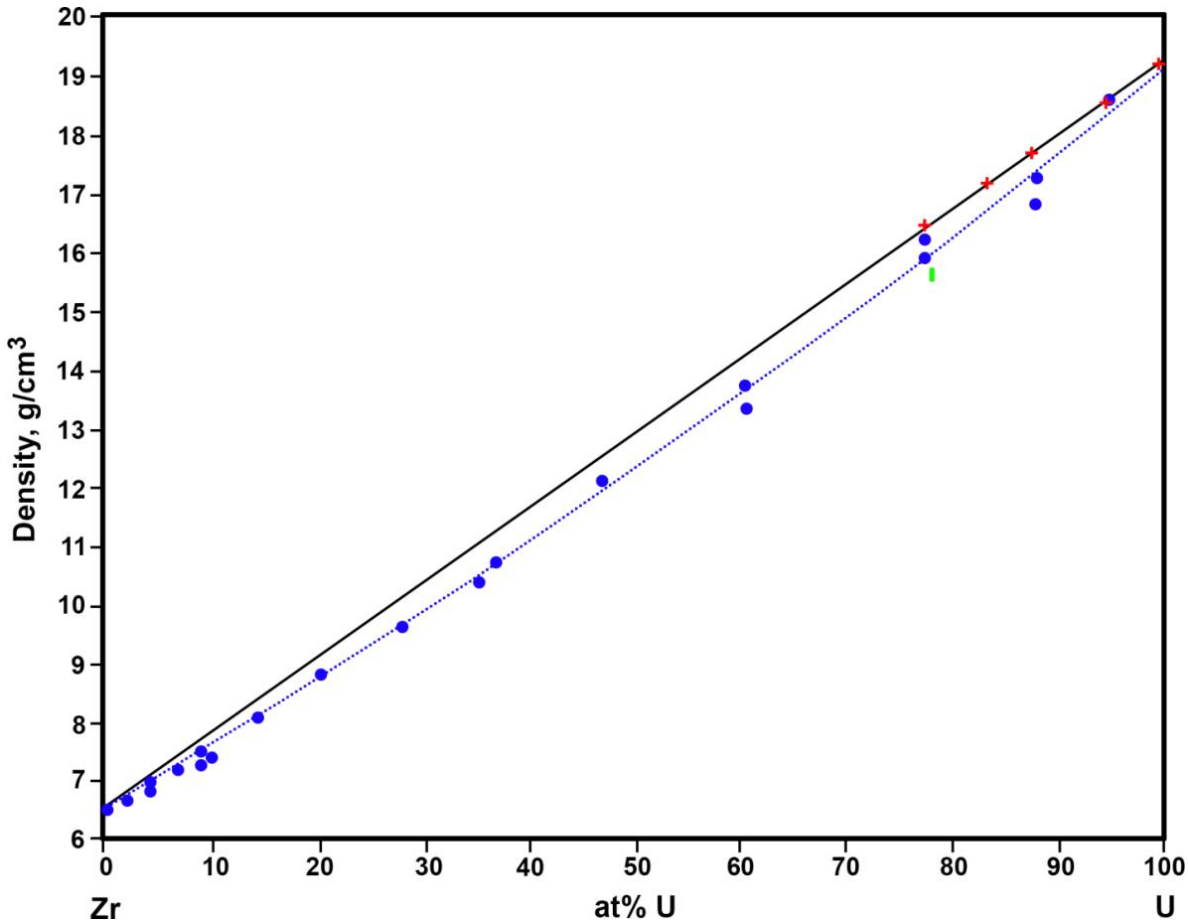

Figure 17. Room-temperature densities of as-cast U-Zr alloys. Blue circles and dotted line: Data from reference [103]. Red "+" symbols: Data from Figure 6d of reference [62]. Green vertical bar: Range of densities of U-10Zr (wt%) alloys produced using different casting methods [121-123]. Solid black line: Theoretical density.

2.1.1.6 Thermal Conductivity

Experimentally determined thermal conductivity values have been reported for U-Zr alloys with ~1-2, 5, 6, 9, 11, 17, 20, 29, 40, 52, 60, and 79 wt% Zr [63, 66, 110, 115, 124, 125]. Thermal conductivity was measured directly by ANL [125] and Kaity et al. [63], while thermal conductivity measurements reported by Takahashi et al. [66] Matsui et al. [110], and Gaiduchenko [115] were calculated from densities, thermal diffusivities, and heat capacities. Other researchers have attempted to use the Wiedemann-Franz law to estimate thermal conductivity from the Lorenz number and electrical resistivity; however, it

appears that the actual Lorenz number of the sample material may not be known well enough for this approach to be successful [70, 103, 110].

Figure 18 summarizes published thermal conductivity data for U-Zr alloys. The thermal conductivity of each alloy increases with temperature within the measurement range. Although there is considerable scatter, comparing thermal conductivity data from individual references shows that thermal conductivity decreases with as Zr content increases for samples with less than ~40-50 at% Zr and is essentially independent of composition for samples with ~50-90 at% Zr. Takahashi et al. suggested that the thermal conductivity of U-Zr alloys had a minimum at ~72.4 at% because of the low thermal conductivity of δ-(UZr_2) [66]. In the absence of reported thermal conductivity measurements of well-characterized single-phase samples of δ-(UZr_2), this suggestion cannot be verified.

Several measurements of the thermal conductivity of alloys with approximately 10 wt% Zr have been reported, with good agreement. Equation 38 is a polynomial fit to thermal conductivity measurements from an alloy with 11.4 wt% Zr [20].

Equation 38. Thermal conductivity of a U-Zr alloy with 11.4 wt% Zr (equation 8 of reference [125]). λ is thermal conductivity in W/m-K and T is temperature in K.

$$\lambda = -1.763 + 4.871\times10^{-2}\times T - 1.330\times10^{-5}\times T^2$$

The thermal conductivities of most compositions are smaller than that of Zr at relatively low temperatures (below ~300 K for alloys with~4 at% Zr, and below ~675 K for alloys with ~ 40 at% Zr). It is not clear why this pattern occurs.

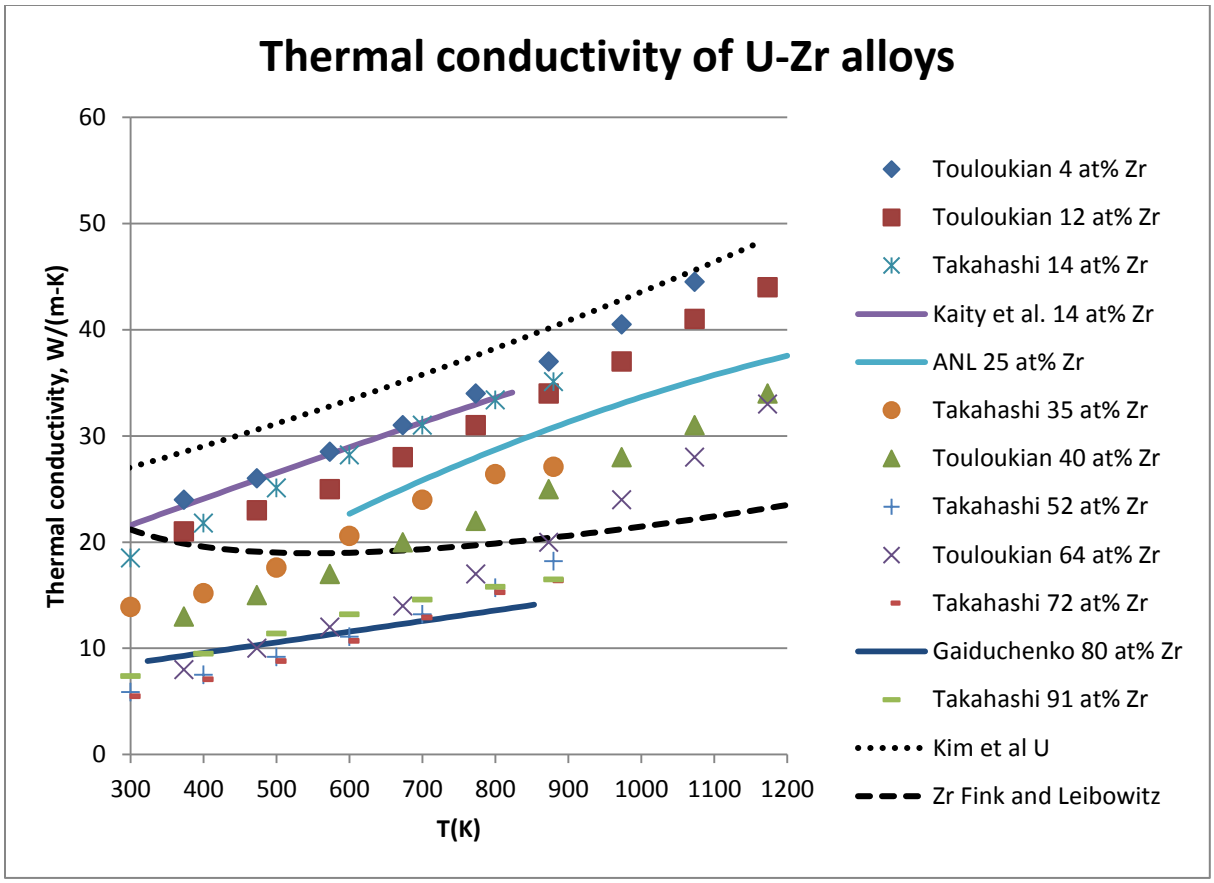

Figure 18. Thermal conductivity of U-Zr alloys [63, 66, 124, 125]. Data from [115] at temperatures between 650 and 1000°C are not included because individual measurements were not presented and because of significant differences between the polynomial fit to the data and the graphical presentation of the same data. Thermal conductivities of U [126] and Zr [127] are included for comparison.

Billone et al. [128], Ogata [49], and Kim et al. [126] developed equations to represent the thermal conductivities of arbitrary U-Zr alloys as functions of temperature and composition. (The Ogata equation is reprinted in reference [48] with a change in sign of one of the terms. Comparison to the data suggests that the equation in reference [49] is correct.) The Billone et al. equation is not considered further because it was developed too early to consider the extensive measurements made by Takahashi et al. [66].

The equations proposed by Kim et al. and Ogata produce similar results for alloys with concentrations of interest for nuclear fuels (~10 wt% Zr) (Figure 19), and both are plausible approximations to the actual thermal conductivity of alloys with this composition. The Ogata equation (Equation 39) [49] is far simpler, and, therefore, is preferred based on the currently available data for compositions with relatively low concentrations of Zr. However, the non-linear shape and built-in adjustment factor of the Kim et al. equation may make it worth considering if adjustments to accommodate new data are required.

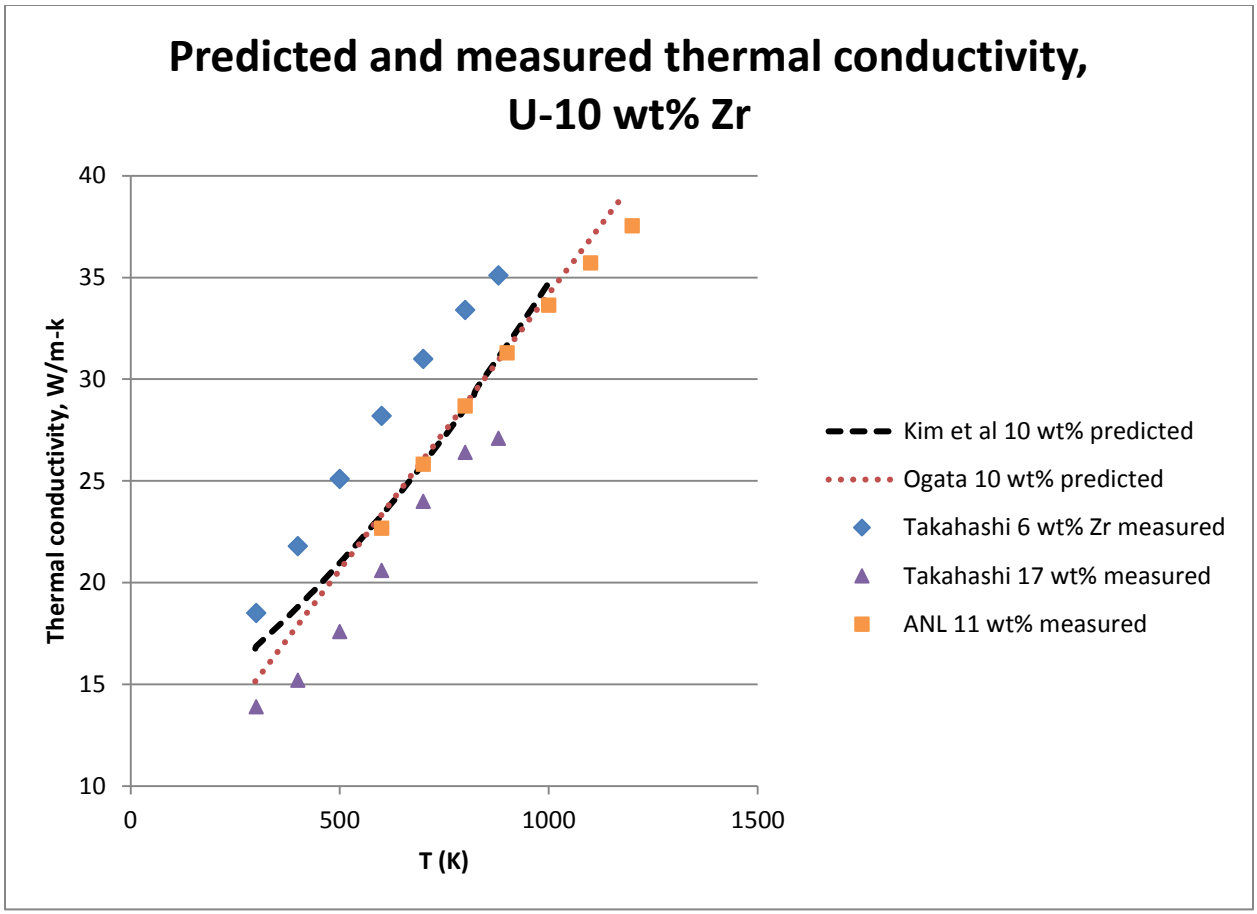

Figure 19. Measured and predicted thermal conductivity for U-Zr alloys with 6-17 wt% Zr. Ogata's predicted value is from Equation 39.

Equation 39. Estimated thermal conductivity of U-Zr alloys according to Ogata [49]

$$k = 16.309 + 0.02713 \times T - 46.27 \times C_{Zr} + 22.985 \times C_{Zr}^2$$

where k is thermal conductivity in W/m·K, C_{Zr} is atomic fraction of Zr, C_{Zr} is < 0.72, T is temperature in K, and T is < 1173 K

2.1.1.6.1 Lorenz Number

The thermal conductivity of an alloy with 20 at% Zr (~8.74 wt% Zr) determined from electrical resistivity using the Wiedemann-Franz Law with the theoretical value of the Lorenz number is lower than the thermal conductivity of the same alloy determined from heat capacity and thermal diffusivity [110], suggesting that the actual Lorenz number of the alloy is higher than the theoretical value.

2.1.1.7 Mechanical properties

2.1.1.7.1 Tensile Properties

Several researchers measured tensile properties of U-Zr alloys across the entire range of compositions, using samples that had been subjected to a variety of heat treatments [129]. Table 14 summarizes the results. Marsh attributes differences between injection-cast alloys made with Fernald uranium and arc-melted alloys made with Derby uranium (notes a and b, respectively) to uptake of carbon from the graphite crucibles used in injection casting [130, 131].

Table 14. Room-temperature tensile properties of uranium-zirconium alloys.

Composition (wt%)	0.2% Yield Strength, psi	Ultimate Strength, psi	Elongation in 1 inch, %	Elongation in 2 inches, %	Reduction of Area, %	Vickers Hardness	Notes	References
U	65900	117300	—	3.5	4.9	265	a	[130, 131]
U	48400	123000	—	11	—	263	b	[130, 131]
U-2.4Zr	47300	133000	—	18	21	283	b	[130, 131]
U-5.5Zr	88000	162000	—	6	7.5	307	b	[130, 131]
U-5.8Zr	97200	166200	—	5	6	347	a	[130, 131]
U-10.9Zr	110600	163200	—	5	6	363	a	[130, 131]
U-11.5Zr	145000	199000	—	9	—	359	b	[130, 131]
U-20.5Zr	—	—	—	—	—	411	b	[130, 131]
U-21.9Zr	140000	179000	—	4	5.8	291	a	[130, 131]
U-31.4Zr	132700	161600	—	2	4	350	b	[130, 131]
U-39.7Zr	118700	157300	—	1.5	1.6	384	a	[130, 131]
U-41.7Zr	95000	103300	—	1	—	279	b	[130, 131]
U-50.5Zr	84300	11800	—	4.5	8	272	b	[130, 131]
U-59Zr	83600	133000	5	—	5	—	c,d	[132]
U-59Zr	80200	126200	4	—	4	—	c,e	[132]
U-59Zr	53600	73400	2	—	5	—	c,f	[132]
U-59Zr	—	92000	0	—	0	—	c,g	[132]
U-59Zr	111600	144400	4	—	1	—	c,h	[132]
U-59.5Zr	80700	116500	—	3.6	6.2	302	a	[130, 131]
U-60.6Zr	80800	131800	—	9	14	295	b	[130, 131]
U-70.4Zr	71300	115000	—	14	16	243	b	[130, 131]
U-71.7Zr	87700	110000	—	4	4	298	a	[130, 131]
U-78Zr	102800	120200	16	—	23	—	c,d	[132]
U-78Zr	94000	101900	17	—	25	—	c,e	[132]
U-78Zr	59700	103500	23	—	24	—	c,i	[132]
U-78Zr	81400	106600	3	—	2	—	c,j	[132]
U-78Zr	—	83400	0	—	0	—	c,k	[132]
U-80.0Zr	86800	101800	—	24	41	235	b	[130, 131]
U-80.8Zr	85500	103900	—	10	8	252	a	[130, 131]
U-89.4Zr	60500	70200	—	—	—	246	b	[130, 131]
U-90Zr	77800	109200	8	—	13	—	c,l	[132]
U-90Zr	54500	79900	17	—	20	—	c,m	[132]
U-90Zr	40800	71800	32	—	32	—	c,n	[132]
U-90Zr	88100	105600	8	—	10	—	c,o	[132]
U-90Zr	58800	84300	—	16	27	197	a	[130, 131]
Zr	26700	53800	—	34	27	138	a	[130, 131]
Zr	18000	36700	—	43	56	113	b	[130, 131]

Table 14. (continued).

Composition (wt%)	0.2% Yield Strength, psi	Ultimate Strength, psi	Elongation in 1 inch, %	Elongation in 2 inches, %	Reduction of Area, %	Vickers Hardness	Notes	References
NOTE a: Alloys were prepared by induction melting using uranium feedstock from Fernald, then cast, hot rolled, and annealed for 24 hours at 575°C. Interpretation of mechanical properties from this alloy suggested that it had a high content of impurities, particularly carbon from the crucible. References: [130, 131]								
NOTE b: Alloys were prepared by arc melting using uranium feedstock from Derby, then cast, hot rolled, and annealed for 24 hours at 575°C. References: [130, 131]								
NOTE c: Alloys were made by arc-melting U and Zr feedstocks. The U feedstock was 99.9% pure with about 100 ppm each of C, O, and N. The zirconium feedstock had at most 0.2 wt% impurities and 200 ppm O. Values in the table are the average of two measurements, which were collected using a strain rate of approximately 0.007 inches/minute. Reference: [132]								
NOTE d: Sample was hot rolled at 700°C and furnace-cooled. Reference: [132]								
NOTE e: Sample was hot rolled at 700°C and furnace-cooled, then reheated to 575°C for 24 hours and furnace cooled. Reference: [132]								
NOTE f: Sample was rolled at 700°C and furnace-cooled, then reheated to 900°C and water-quenched, then reheated to 575°C for 24 hours and furnace cooled. Reference: [132]								
NOTE g: Sample was hot rolled at 700°C and furnace-cooled, then reheated to 700°C for 4 hours and water-quenched. Reference: [132]								
NOTE h: Sample was hot rolled at 700°C and furnace-cooled, then reheated to 700°C for 4 hours and air-cooled in a Vycor capsule. Reference: [132]								
NOTE i: Sample was hot rolled at 700°C and furnace-cooled, then reheated to 800°C for 1 hour and furnace cooled. Reference: [132]								
NOTE j: Sample was hot rolled at 700°C and furnace-cooled, then reheated to 800°C for 1 hour and air-cooled in a Vycor capsule. Reference: [132]								
NOTE k: Sample was hot rolled at 700°C and furnace-cooled, then reheated to 800°C for 1 hour and water-quenched. Both specimens failed in a brittle manner. Reference: [132]								
NOTE l: Sample was hot rolled at 700°C and air cooled. Reference: [132]								
NOTE m: Sample was hot rolled at 700°C and air cooled, then reheated to 700°C for 4 hours and furnace cooled. Reference: [132]								
NOTE n: Hot rolled at 700°C and air cooled, then reheated to 800°C for 1 hour and furnace cooled. Reference: [132]								
NOTE o: Hot rolled at 700°C and air cooled, then reheated to 900°C for 1 hour and water-quenched. Reference: [132]								

Fedorov et al. measured the elastic (Young's) modulus of alloys with 14.1, 27.7, 41.6, 60.5, 87.9, and 94 at% U (85.9, 72.3, 58.4, 39.5, 12.1, and 6 at% Zr) at temperature of 77.4 and 295 K using a method based on resonance bending vibrations at a frequency of ~ 1 kHz [133]. Feedstocks were described as "pure" uranium and zirconium. Samples were annealed by heating to 1000°C and cooling them slowly. Figure 20 shows the measurements at 295 K. Fedorov et al. attributed the deviation from linearity in their plots in alloys with ~30 at% Zr to the presence of δ-UZr_2.

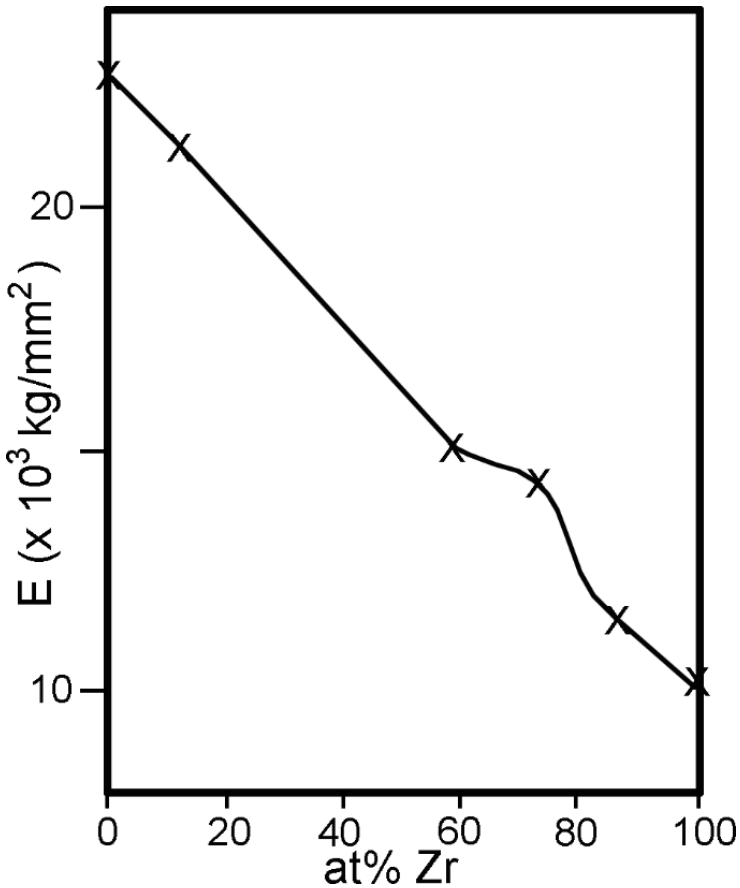

Figure 20. Elastic modulus for U-Zr alloys at 295 K (redrawn from refrence [133]).

Figure 21 compares measured tensile properties at room temperature and 370°C for U-Zr alloys with a range of compositions. Details of alloy preparation and some quantitative room-temperature measurements are in Table 14 (including notes c and e). The alloys were hot-rolled, annealed at 575°C for 24 hours, and machined to produce tensile-test specimens. Consideration of phase-transition temperatures in Table 7 suggests that the 575°C annealing temperature is slightly below the lowest-temperature phase transitions for all alloy compositions. Thus, there is no reason to believe that either the annealing or the heating during the tensile test produced changes in the equilibrium phase assemblages for the alloys.

Figure 21 suggests that U-Zr alloys become less strong and more ductile when heated at temperatures between room temperature and the lowest-temperature phase transitions. The data for yield strength and ultimate tensile stress suggest that alloys with ~70-80 at% Zr are less strong and ductile than alloys with lower Zr contents, possibly because of differences in the proportions of α-U and δ-UZr_2.

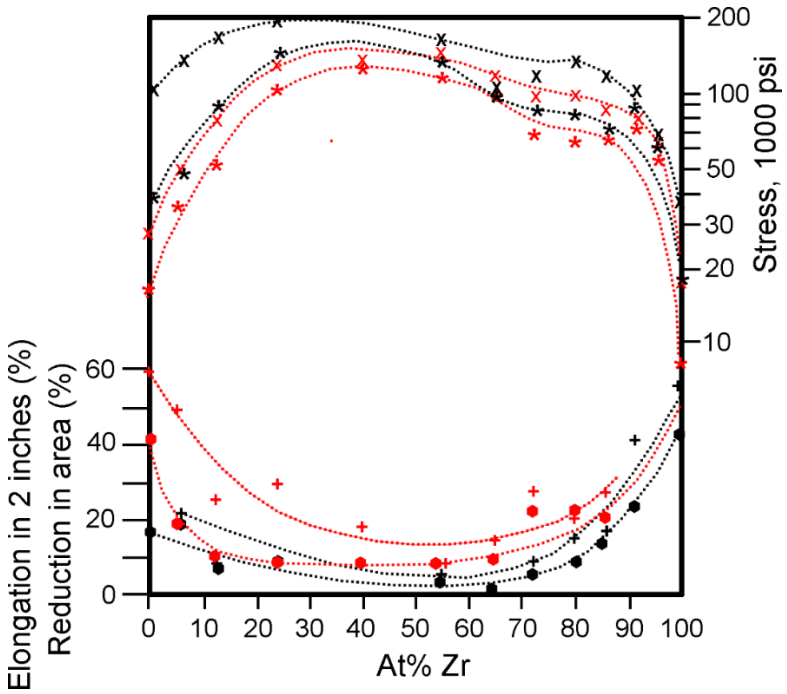

Figure 21. Tensile properties of U-Zr alloys at room temperature (black) and 375°C (red), after Figure 11 and Figure 12 from reference [132]. Different measurements use different symbols, which are the same for room-temperature and high-temperature data. Asterisks: Yield strength (0.2% offset), psi × 1000. "X" symbols: ultimate tensile strength, psi × 1000. "+" symbols: reduction in area, %. Dots: elongation in 2 inches, %.

Table 15. Hot-hardness values for injection-cast alloys made with uranium from Fernald (I-F) and arc-cast alloys made with uranium from Derby (A-D) [130, 131]. Refer to data from references [130, 131] in Table 14 for more information about these alloys.

Composition (wt%)	0.2% Yield Strength, psi	Ultimate Strength, psi	Elongation in 2 inches, %	Reduction of Area, %	Source
U	65900	117300	3.5	4.9	I-F
U	48400	123000	11		A-D
U-10.9Zr	110600	163200	5	6	I-F
U-11.5Zr	145000	199000	9	—	I-F
U-2.4Zr	47300	133000	18	21	I-F
U-20.5Zr	—	—	—	—	A-D
U-21.9Zr	140000	179000	4	5.8	I-F
U-31.4Zr	132700	161600	2	4	A-D
U-39.7Zr	118700	157300	1.5	1.6	I-F
U-41.7Zr	95000	103300	1	—	A-D
U-5.5Zr	88000	162000	6	7.5	A-D
U-5.8Zr	97200	166200	5	6	I-F
U-50.5Zr	84300	11800	4.5	8	A-D

Table 15. (continued).

Composition (wt%)	0.2% Yield Strength, psi	Ultimate Strength, psi	Elongation in 2 inches, %	Reduction of Area, %	Source
U-59.5Zr	80700	116500	3.6	6.2	I-F
U-60.6Zr	80800	131800	9	14	A-D
U-70.4Zr	71300	115000	14	16	A-D
U-71.7Zr	87700	110000	4	4	I-F
U-80.0Zr	86800	101800	24	41	A-D
U-80.8Zr	85500	103900	10	8	I-F
U-89.4Zr	60500	70200	—	—	A-D
U-90Zr	58800	84300	16	27	I-F
Zr	26700	53800	34	27	I-F
Zr	18000	36700	43	56	A-D

2.1.1.7.2 Creep

Much of the available data on creep of U-Zr alloys was reported in the 1950s. However, several researchers have used results of impression creep tests to determine the high-temperature creep stress rates of U-Zr alloys with 6, 7, and 50 wt% Zr within the last ten years [73, 134-136]. Kutty et al. developed a method for calculating creep stress curves from hot hardness data [137] and applied it to alloys with 5, 10, and 15 wt% Zr but did not calculate creep rates.

Only values from recent publications in which creep stress has been calculated are included in this Handbook. Researchers interested relationships between hot hardness and its relationship to creep in U-5Zr, U-10Zr, and U-15Zr (wt%) should consult reference [137]. Those interested in older data or data from alloys with other compositions should consult reference [131].

Table 16 lists recent measurements of the indentation creep behavior of U-6Zr, U-7Zr, and U-50Zr (wt%). As summarized in references [73, 134, 135, 138, 139], indentation creep measurements are collected using a cylindrical, flat-bottomed punch whose penetration depth near the sample surface is measured as a function of time for a given stress and sample temperature. The penetration depth is plotted against time to produce a creep curve, which shows the impression velocity. After an initial transient period, the impression velocity reaches a steady state. The creep rate is approximated by dividing the steady-state impression velocity by the diameter of the punch, and the power-law stress exponent is determined as the slope of a log-log plot of creep rate vs stress. The creep activation enthalpy can be calculated from the steady-state stress rate and the temperature. The stress exponent and activation enthalpy determined from indentation creep are comparable to values obtained from tensile creep tests.

The U-6Zr alloy used in the indentation creep testing was prepared by arc-melting nuclear-grade uranium and zirconium, turning and re-melting the alloy six times to improve homogeneity. The alloy was homogenized at 900°C for 24 hours, water quenched, hot rolled at 750°C, soaked at 875°C for ten minutes, and furnace cooled. Chemical analyses showed that the alloy had 6.12 wt% Zr, 450 ppm C, 60 ppm N, 580 ppm O, and 204 ppm Y, as well as lower contents of several other metallic impurities. X-ray diffraction data showed only peaks from α-U [73]. Creep curves at 575°C showed indications that the impression depth had “waves” of in which impression depth increased and decreased over time. This unusual behavior was explained by reactions leading to the separation of δ-UZr_2 from the original α’ solid solution phase occurring during the creep test [135, 136]. The creep activation enthalpy for U-6Zr was independent of stress, with an average value of 157 kJ/mol [73].

The U-7Zr alloy used in the indentation creep testing was prepared by arc-melting nuclear-grade uranium and zirconium, turning and re-melting the alloy six times to improve homogeneity. The alloy was homogenized at 800°C for 8 hours, water quenched, hot rolled at 750°C, soaked at 850°C for ten minutes, and water quenched. X-ray diffraction data showed only peaks from α-U [134].

The U-50Zr alloy samples used in the indentation creep testing were prepared by arc-melting 99.9% pure uranium and 99.95% pure zirconium, turning and re-melting the alloy six to eight times to improve homogeneity. The alloy was homogenized at 800°C for 24 hours and water quenched. Different samples were used for data at different temperatures. Each sample was annealed at the temperature at which it would be creep tested for 48 hours. Chemical analyses showed that the samples had 50.06 wt% Zr, 450 ppm C, 60 ppm N, 580 ppm O, and 204 ppm Y, as well as lower contents of several other metallic impurities. X-ray diffraction data showed only peaks from δ-UZr_2. The creep activation energy was independent of stress, with an average value of 106 kJ/mol [135].

No reliable information about creep in cast U-10Zr (wt%) alloys is available.

Table 16. Indentation creep of U-6Zr, U-7Zr, and U-50Zr (reference [73] Table 2, reference [134] Table 1 and Table 2, and reference [135] Table 2.)

Composition (wt%)	**Temperature (°C)**	**Stress, MPa**	**Steady-state Impression Velocity (μm/hour)**	**Creep Rate (per second)**	**Stress Exponent**	**Reference**
U-6Zr	550	18.51	6.93	1.284×10^{-6}	3.10	[73]
—	—	22.22	12.35	2.287×10^{-6}	—	—
—	—	27.77	24.29	4.450×10^{-6}	—	—
—	600	14.81	43.15	7.990×10^{-6}	8.40	[73]
—	—	18.51	399.44	7.397×10^{-5}	—	—
—	—	22.22	1511.46	2.799×10^{-4}	—	—
—	630	11.11	31.32	5.80×10^{-6}	8.00	[73]
—	—	14.81	303.58	5.622×10^{-5}	—	—
—	—	18.51	1720.44	3.186×10^{-4}	—	—
—	—	22.22	8299.8	1.540×10^{-3}	—	—
—	650	11.11	88.78	1.644×10^{-5}	8.21	[73]
—	—	14.81	749.52	1.388×10^{-4}	—	—
—	—	18.51	6015.6	1.110×10^{-3}	—	—
U-7Zr	630	22.2	2.105	1.4033×10^{-3}	—	[134]
—	700	22.2	2.4414	1.6276×10^{-3}	—	—
U-50Zr	525	18.52	1.749	3.238×10^{-7}	6.90	[135]
—	—	24.08	18.225	3.375×10^{-6}	—	—
—	—	27.79	20.936	3.877×10^{-6}	—	—
—	—	31.49	64.692	1.198×10^{-5}	—	—
—	—	37.04	267.462	4.953×10^{-5}	—	—
—	550	14.82	1.603	2.968×10^{-7}	6.92	[135]
—	—	18.52	3.920	7.259×10^{-7}	—	—
—	—	24.08	49.750	9.213×10^{-6}	—	—
—	—	27.79	93.528	1.732×10^{-5}	—	—

Table 16. (continued).

Composition (wt%)	Temperature (°C)	Stress, MPa	Steady-state Impression Velocity (µm/hour)	Creep Rate (per second)	Stress Exponent	Reference
—	575	12.97	2.946	5.455×10^{-7}	6.58	[135]
—	—	14.82	1.893	3.506×10^{-7}	—	—
—	—	18.52	14.855	2.751×10^{-6}	—	—
—	—	24.08	152.172	2.818×10^{-5}	—	—
—	—	27.79	402.732	7.458×10^{-5}	—	—

2.1.2 U-Zr-Np

2.1.2.1 Introduction

The earliest investigation of the U-Zr-Np phase diagram was published by Rodríguez et al. in 1997 [140]. This investigation included tentative isothermal sections of the U-Zr-Np phase diagram at temperatures of 520, 595, and 700°C. These sections were based on dilatometry, metallography, and microprobe analysis of eleven alloys, all but two of which had 67-88 wt% U. No diffraction data were used, and some of the microprobe analyses of fine-grained phases were described as "relatively inaccurate." Despite several questionable features (discussed below), these isothermal sections remain the only available attempt to determine the U-Zr-Np phase diagram from experimental data.

In 2018, Xie and Morgan used CALPHAD and *ab initio* methods to develop a model of the U-Zr-Np phase diagram and published isothermal sections at temperatures corresponding to those used by Rodríguez et al.[141]. Phase boundaries in the two sets of isothermal sections differ significantly. Although the calculated sections appear to be more plausible than the experimental sections, Xie and Morgan emphasized that further work is required, particularly for lower-temperature sections where reliable experimental data are lacking.

No information about heat capacity, density, or thermal conductivity of U-Zr-Np alloys is available.

Information on thermal expansion is limited to a single figure showing a dilatometric curve with 39.9 wt% U, 20.4 wt% Zr, and 39.7 wt% Np [140 (Figure 2)]. This figure is presented as an example of data used to investigate the U-Zr-Np phase diagram and does not have a quantitative thermal-expansion axis.

2.1.2.2 Phases and Phase Transformations

In the absence of diffraction data, Rodríguez et al. tentatively identified the phases in their samples using a combination of metallography, microprobe analyses, and information about phases in binary systems. They presented observed compositions and tentative isothermal phase diagrams on which measurements from individual alloys were identified, but did not otherwise address the properties of individual phases.

Rodríguez et al. used dilatometry to identify temperatures of phase transitions, and reported that all of their alloys had solid-state phase transitions at temperatures of 567-598 and 614-655°C. Solidus temperatures were between 955 and 1170 degrees. No clear systematic correlations between alloy compositions and phase transition or liquidus temperatures were apparent.

Researchers are encouraged to refer to the original paper [140] for data on compositions of alloys and phases, phase-transformation temperatures, and tentative phase identifications.

2.1.2.3 Phase Diagrams

Rodríguez et al. presented tentative partial isothermal sections at temperatures of 520, 595, and 700°C (Figure 22a, Figure 23a, and Figure 24a). Phase designations correspond to those in the U-Zr, U-Np, and Np-Zr binary phase diagrams (Section 2.1.1.3 in this document and Sections 3.1.2.3 and 6.1.2.3 in reference [5]), except that the U-Np phase that Rodríguez et al. called "ζ" in their phase diagrams is called "δ-(U,Np)" for consistency with earlier phase diagrams and other sections of this Handbook.

Several features of the sections developed by Rodríguez et al. are inconsistent with the current understanding of the U-Zr-Np system:

- The designation "γ" refers to a body-centered cubic solid solution between γ-U, γ-Np, and β-Zr. Although Rodríguez et al. believed that γ-Np and β-Zr form a continuous solid solution, more recent data indicate that these phases are not miscible (Section 6.1.2 in reference [5]). Thus, the boundaries of the "γ" field in Figure 22a and Figure 23a need revision.
- The isothermal sections at 520 and 595°C (Figure 23a and Figure 24a) show a single phase identified as "δ," which appears to be a solid solution between δ-UZr_2, δ-$NpZr_2$, and δ-(U,Np). Because δ-UZr_2 and δ-$NpZr_2$ have similar crystal structures and lattice parameters (Section 2.1.1.2.1.1.5 in this document and Section 6.1.2.1 in reference [5]), a solid solution between them is plausible. Although the structure of δ-(U,Np) has not been determined, it is apparently not like that of δ-UZr_2 and δ-$NpZr_2$ but instead may resemble the structure of ζ-(U,Pu) (Section 2.3.1.2.1). A solid solution between δ-(U,Np) and δ-UZr_2 or δ-$NpZr_2$ seems implausible, and it is likely that the "δ" field includes at least two distinct phases.

Figure 22b, Figure 23b, and Figure 24b show the calculated isothermal sections from the model of Xie and Morgan [141]. This model was based on *ab initio* calculations and extrapolation from binary phase diagrams of the U-Zr, Np-Zr, and Np-U systems developed using the CALPHAD method (references [46], [142], and [141], respectively). The model assumes that all tertiary interactions are negligible. The authors emphasize that their model is "uncertain for the lower-temperature part of the Np-U-Zr system," which is included only for the sake of completeness (reference [141] page 506).

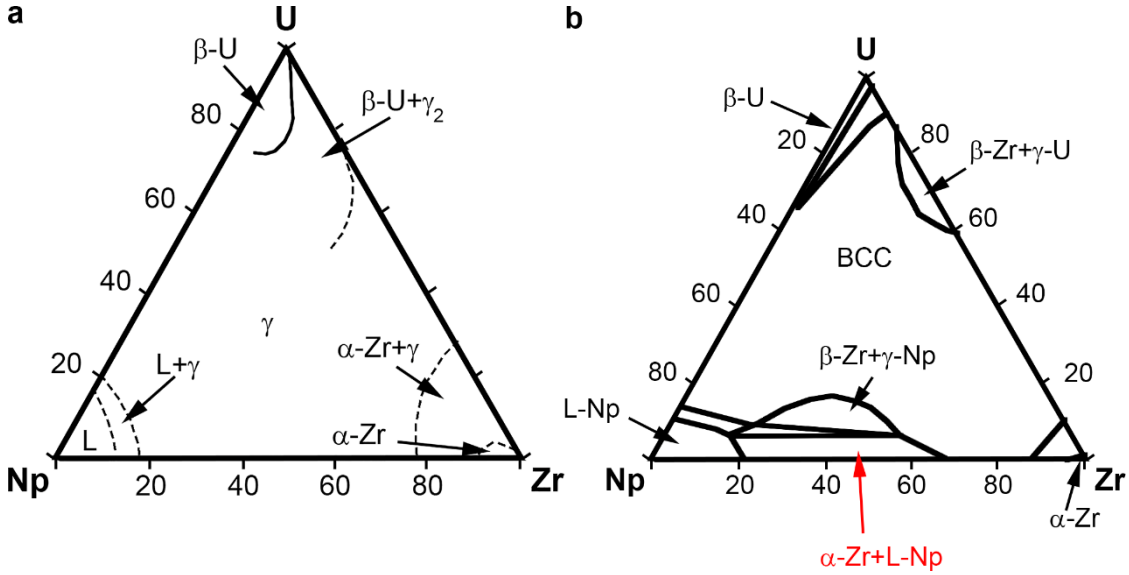

Figure 22. a: Tentative partial isothermal section of the U-Np-Zr system at 700°C suggested by Rodríguez et al. [140]. b: Isothermal section of the U-Np-Zr system at 700°C calculated by Xie and Morgan [141]. Phase identifications in black are from reference [141]; identifications in red were added for this Handbook to assist in interpretation.

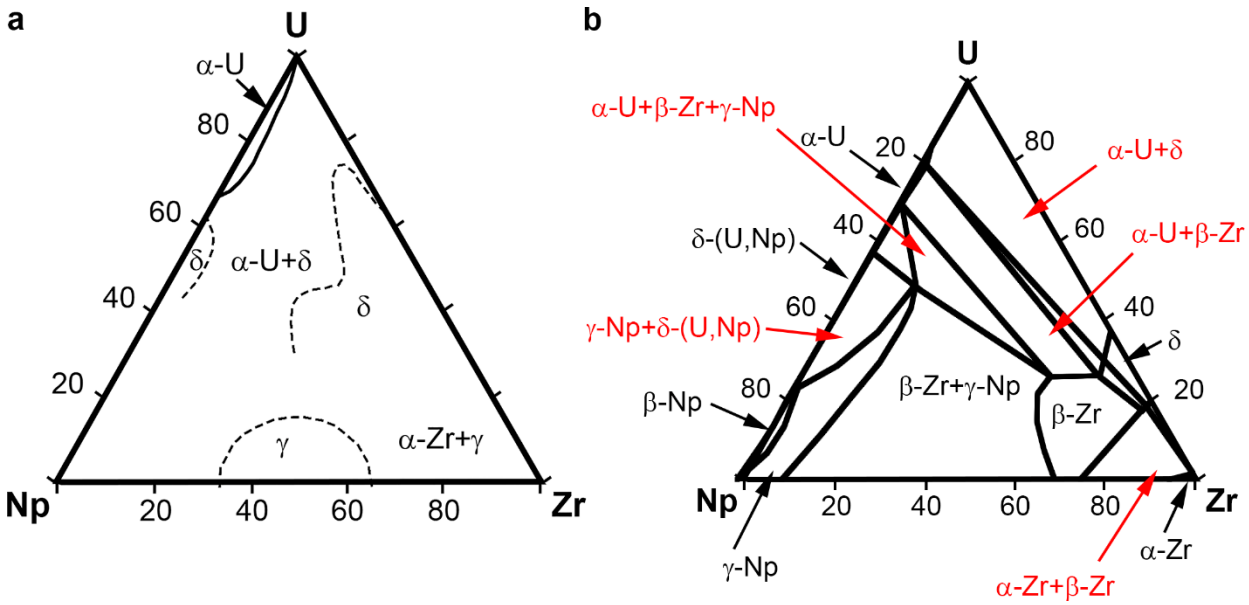

Figure 23. a: Tentative partial isothermal section of the U-Np-Zr system at 595°C suggested by Rodríguez et al. [140]. b: Isothermal section of the U-Np-Zr system at 595°C calculated by Xie and Morgan [141]. Phase identifications in black are from reference [141], except that the phase identified as "ζ"in the reference is called δ-(U, Np) for consistency with earlier research and the rest of this Handbook. Identifications in red were added for this Handbook to assist in interpretation.

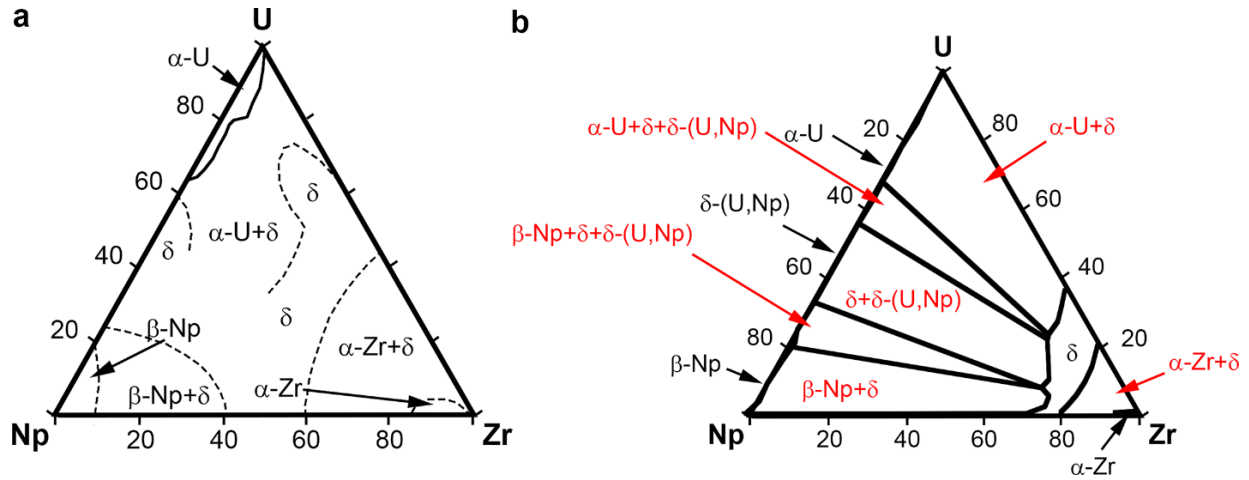

Figure 24. a: Tentative partial isothermal section of the U-Np-Zr system at 520°C suggested by Rodríguez et al. [140]. b: Isothermal section of the U-Np-Zr system at 520°C calculated by Xie and Morgan [141]. Phase designations in black are from reference [141], except that the phase identified as "ζ" in the reference is called δ-(U, Np) for consistency with earlier research and the rest of this Handbook. Identifications in red were added for this Handbook to assist in interpretation.

2.1.3 U-Zr-Ce

Much of the information about properties of U-Zr-Ce alloys was obtained during research on diffusion of rare-earth elements in U-Zr alloys [143, 144], although a limited amount of information addressing the specific heat and thermal expansion of U-Zr-Ce alloys is available [145, 146]. All of the available information is from alloys with at most 6 wt% Ce.

No information about U-Zr-Ce phase diagrams is available, although the data suggest very limited miscibility between Ce and U-Zr phases. The available information indicates that Ce occurs in small precipitates in a U-Zr matrix [143-146]. Phase-transition temperatures in U-Ce-Zr alloys are similar to those in U-Zr alloys.

Although small differences in heat capacity between U-10 wt% Zr alloys with 0, 4, and 6 wt% Ce have been reported [145], further work is needed to determine whether the reported differences are significant and indicate systematic trends.

No differences in thermal expansion were observed in comparisons between U-10 wt% Zr alloys with 2 and 6 wt% Ce [145].

The thermal conductivity of an alloy with 6 % Ce and 10% Zr was determined using experimental measurements of thermal diffusivity and density and a heat capacity estimated using the Kopp-Neumann law (Section 1.6.1). These results suggested that the thermal conductivity of these alloys was lower than that of U-10 wt% Zr, and that the difference in thermal conductivities was less than 5% [146]. As the sample contained "stringers" 50-100 μm long of a high-Zr phase that could affect the thermal conductivity [146], it is not clear how much of the difference in thermal conductivity is due to the Ce and how much to the microstructures.

Further investigation of alloys with compositions (including impurities), microstructures, and processing histories similar to those in nuclear fuels is required.

2.1.4 U-Zr-La-Ce-Pr-Nd

2.1.4.1 Introduction

A number of recent papers have presented limited characterization data from U-10Zr (wt%) alloys that also contain up to 10 wt% of a rare-earth alloy consisting of 53 wt% Nd, 25 wt% Ce, 16% wt% Pr, and 6 wt% La [122, 123, 147, 148]. The primary emphasis of these papers is development and evaluation of casting techniques. Because all of the techniques resulted in significant loss of rare-earth elements during casting, actual and nominal compositions of these alloys differ.

No information about heat capacities, thermal expansion, or thermal conductivity of these alloys is available.

2.1.4.2 Phases and Phase Transformations

All of the U-Zr-La-Ce-Pr-Nd alloys had globular or irregularly shaped particles with high concentrations of rare earth elements [122, 123, 147, 148]. The number and size of these precipitates increased with increasing concentrations of the rare-earth alloy in the starting composition. High-Zr inclusions were also commonly reported.

No detailed identification or characterization of the matrix and rare-earth phases is available, and no experimental data that could be used to determine whether rare-earth elements were present in the matrix has been reported.

No information about phase transitions in these alloys is available.

2.1.4.3 Density

Table 17 summarizes the available data on densities of as-cast U-Zr-La-Ce-Pr-Nd alloys. Differences between theoretical and as-cast densities are attributed primarily to loss of rare-earth elements during casting.

Table 17. As-cast and theoretical densities of U-Zr-La-Ce-Pr-Nd alloys with 0-7 wt% of a rare-earth alloy consisting of 53% Nd, 25% Ce, 16% Pr, and 6% La by weight.

Composition (wt%)	As-cast density (g/cm^3)	Theoretical density (g/cm^3) from reference	Casting method	Reference
U-10Zr-3RE	15.2	15.1	Injection	[123]
U-10Zr-3RE	15.1	15.1	Gravity	[122]
U-10Zr-5RE	14.7	—	Low-pressure gravity	[147]
U-10Zr-7RE	15.0	14.4	Injection	[123]

2.1.5 U-Zr-Ce-Nd-Y

The only available information about U-Zr alloys that also have rare-earth elements and yttrium is from METAPHIX Alloy CR1. This alloy was cast as part of a study intended to examine effects of rare-earth elements in U-Pu-Zr fuel alloys that also contain minor actinides. It has 62.7 wt% U, 5.2 wt% Ce, 16.1 wt% Nd, 15.0 wt% Zr, and 1.0 wt% Y (corresponding to ~44.8% U, 28% Zr, 6.3% Ce, 19% Nd, and 1.9% Y in atomic percentages) [149].

The matrix of an arc-melted sample of Alloy CR1 separated into distinct regions, one of which had a high concentration of rare-earth elements and one of which had a high concentration of uranium [149]. No further details about the compositions of the regions are available.

No information about phases, heat capacity, thermal expansion, or thermal conductivity of this alloy is available.

2.2 Alloys Based on Pu-Zr, Including Pu-Zr and Pu-Zr Alloys with Minor Actinides (Np, Am)

2.2.1 Pu-Zr

2.2.1.1 Introduction

Pu-Zr alloys have been investigated for almost 60 years, with much of the currently available experimental data collected during the 1950s and 1960s. The data were synthesized by Okamoto [150, 151] to produce a single phase diagram whose key features include continuous solubility between the body-centered cubic phases β-Zr and ε-Pu, extensive solubility of Zr in the fcc phase δ-Pu, limited solubility of Zr in α-Pu, β-Pu, γ-Pu, and δ′-Pu, and the existence of the intermediate phase θ-(Pu,Zr). However, many details of the phase diagram remain poorly known, particularly those involving temperatures below ~400°C or concentrations of Zr below ~30 at% or above ~65 at%.

A calculated Pu-Zr phase diagram by Kurata [34, 38] is in reasonable agreement with the experimentally determined data for temperatures above ~500°C.

The only available data on heat capacities of Pu-Zr alloys was measured at INL and initially reported in Revision 1 of this Handbook [2 (Section 3.2.5)]. A small amount of additional data are available in reference [152]. These preliminary measurements indicate that specific heats of alloys with 30 and 40 wt% Zr are similar and that the specific heat of the alloy with 30% Zr is slightly smaller than that of the alloy with 40 wt% Zr.

The thermal expansion of δ-(Pu, Zr) solid solutions varies with composition: thermal expansion is negative for compositions with less than ~7.5 at% Zr and positive for compositions with ~12 at% Zr. δ-(Pu, Zr) solid solutions with ~8-10 at% Zr show relatively little thermal expansion. The available data on ε-(Pu, Zr) solid solutions suggest that their thermal expansion is positive. No experimental data about the thermal expansion of other Pu-Zr phases is available.

The only available data on the thermal conductivity or diffusivity of Pu-Zr alloys was measured at INL and initially reported in Revision 1 of this Handbook [2 (Section 3.4.5)]. Preliminary measurements of alloys with 10 and 30 wt% Zr indicate that the thermal diffusivity of both alloys increases with temperature (although perhaps not smoothly), and that the diffusivity of the alloy with 30% Zr is lower than that of the alloy with 10% Zr.

Experimental work on Pu-Zr alloys is complicated by sluggish kinetics, high sensitivity to low concentrations of oxygen and other impurities, possible formation of oxygen-stabilized Pu-Zr phases, and the metallurgical complexity and unique characteristics of Pu. As a result of these difficulties, the existence of some Pu-Zr phases is controversial, and there is little published data on phase transformations.

2.2.1.2 Phases and Phase Transformations

2.2.1.2.1 Phases

The generally accepted Pu-Zr phases are:

- (α-Pu): Solid solution of α-Pu with a maximum Zr concentration that Taylor determined to be ~0.25 at% at room temperature [153]. In an earlier study, Marples reported a maximum concentration of 1.5-2 at% Zr but described this value as "very approximate" [154]. The maximum concentration determined by Taylor seems more likely to be accurate because it was based on a larger number of low-Zr compositions and used material of higher purity. No information about the lattice parameters of (α-Pu) solid solutions with Zr is available; however, in view of the low concentration of Zr in this phase, it seems reasonable to assume that its lattice parameters are similar to those of α-Pu (Section 2.3.2.1 of reference [5]).
- (β-Pu): Solid solution of β-Pu with a maximum Zr concentration that Taylor determined to be below 1 at% [153]. In an earlier study, Marples reported a maximum concentration of ~7 at% Zr but described this value as "somewhat uncertain" [154]. The maximum concentration determined by Taylor seems more likely to be accurate because it was based on larger number of low-Zr compositions and used material of higher purity.) No information about the lattice parameters of (β-Pu) solid solutions with Zr is available; however, in view of the low concentration of Zr in this phase, it seems reasonable to assume that its lattice parameters are similar to those of β-Pu (Section 2.3.2.1 of reference [5]).

  Although pure β-Pu cannot be quenched to room temperature, it was possible to obtain room-temperature X-ray diffraction from a phase with the β-U structure and a small but unspecified Zr content [155].
- (γ-Pu): Solid solution of γ-Pu with a maximum Zr concentration that Taylor determined to be below 1 at% [153]. No information about the lattice parameters of (γ-Pu) solid solutions with Zr is available; however, in view of the low maximum concentration of Zr, it seems reasonable to assume that they are similar to those of γ-Pu (Section 2.3.2.1 of reference [5]).
- δ-(Pu,Zr): Solid solution of δ-Pu with an extensive solubility for Zr. The crystal structure is fcc (space group $Fm\bar{3}m$). Lattice parameters decrease with increasing concentrations of Zr from a ~ 4.637 Å for an alloy with 4 at% Zr to a ~ 4.558 Å for an alloy with 70 at% Zr (Figure 25). According to Ellinger and Land, this phase can be retained at room temperature in quenched samples with ~4-40 at% Zr and is stable at room temperature in samples with more than 40 at% Zr. The maximum concentration of Zr in δ-(Pu,Zr) is at least ~70 at% [154, 156, 157].

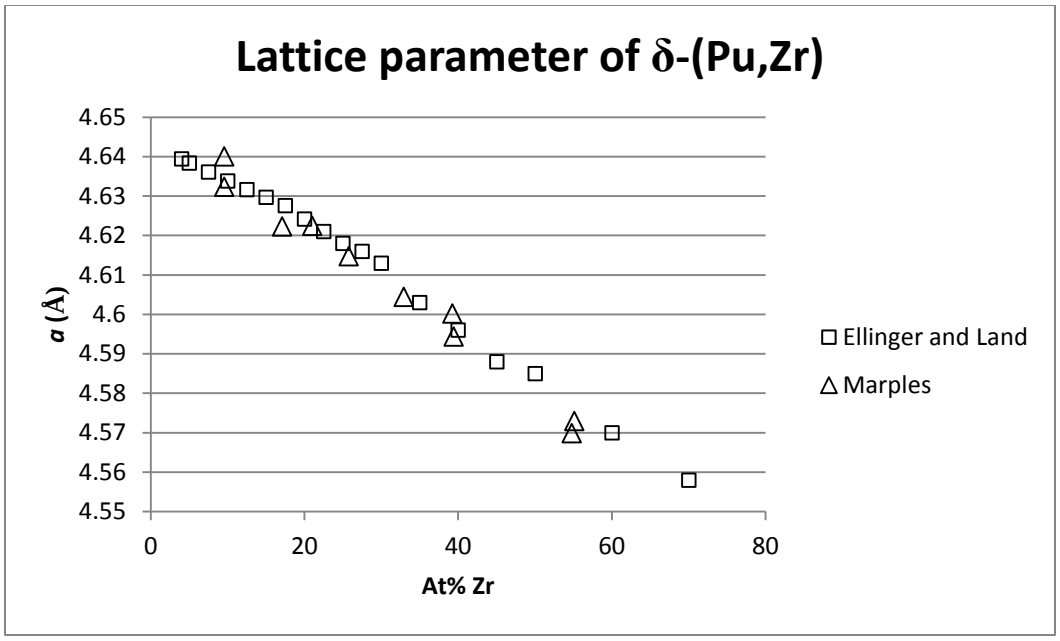

Figure 25. Variations in the room-temperature value of the lattice parameter, δ-(Pu,Zr). Data are from Marples [154] and Ellinger and Land [156].

- (δ'-Pu): Solid solution of δ'-Pu with a low solubility (probably ~1.5 at%) for Zr [154, 156]. No information about lattice parameters is available; however, in view of the low maximum concentration of Zr, it seems reasonable to assume that the lattice parameters of (δ'-Pu) solid solutions with Zr are similar to those of δ'-Pu (Section 2.3.2.1 of reference [5]).
- (α-Zr): Solid solution of α-Zr with a maximum solubility of ~13 at% Pu at ~620°C [154, 156]. The *c* lattice parameter decreases linearly with composition (Figure 26). The *a* lattice parameter also decreases (Figure 27), although the decrease is small enough that differences between samples with he same nominal composition and different thermal histories are comparable to differences between samples with different nominal compositions. Orientation relationships between (α-Zr) crystals formed from (β-Zr) that contains 0.3 to 3 wt% Pu are like those in pure Zr [158].

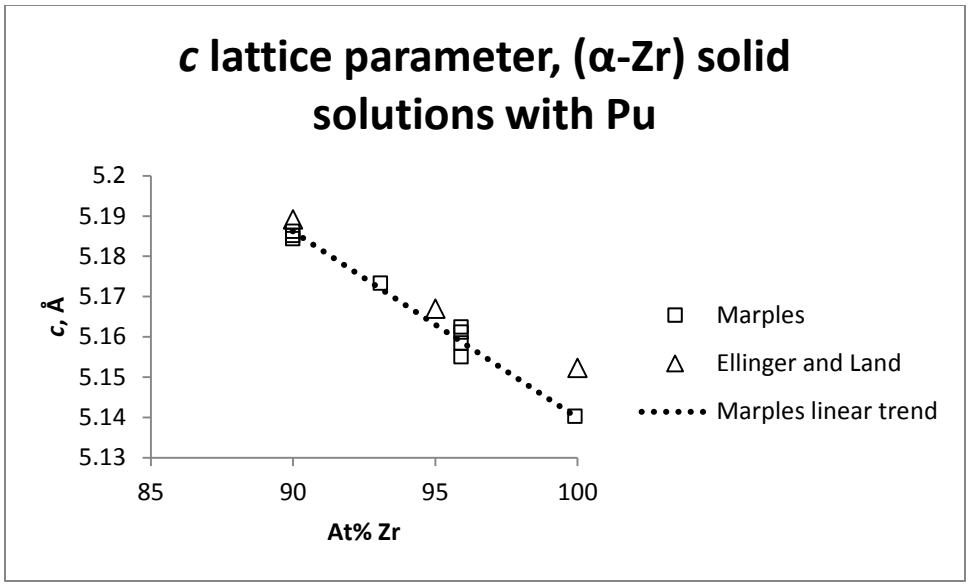

Figure 26. Variations in the room-temperature value of the *c* lattice parameter, (α-Zr) solid solutions with Pu. Data are from Marples [154] and Ellinger and Land [156]. Multiple data points with the same composition in data from Marples are from samples with different thermal histories.

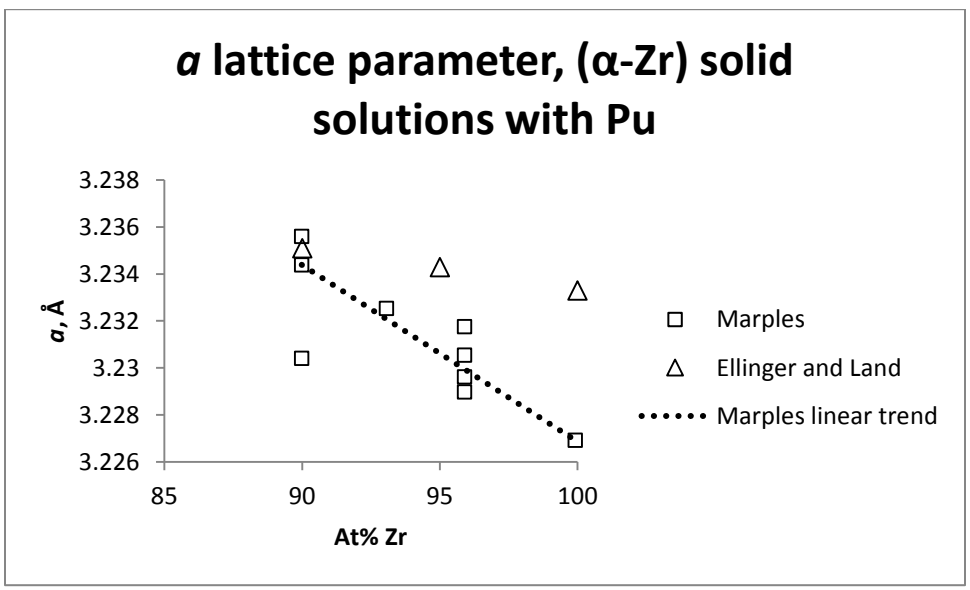

Figure 27. Variations in the room-temperature value of the *a* lattice parameter, (α-Zr) solid solutions with Pu. Data are from Marples [154] and Ellinger and Land [156]. Multiple data points with the same composition in data from Marples are from samples with different thermal histories.

- ε-(Pu,Zr): Body-centered cubic (space group $Im\bar{3}m$) solid solution between ε-Pu and β-Zr. Data from alloys with less than ~14 at% Zr at 500, 600, and 700°C shows that lattice parameters increase with increasing concentration of Zr, contrary to predictions from Vegard's law [159 Figure 8].
- θ-(Pu,Zr): Intermediate solid-solution phase sometimes called Pu_4Zr or Pu_6Zr. Different phase diagrams show different composition ranges: Marples lists the composition of this phase as ~10-30 at% Zr [154], the phase diagram of Bochvar et al. shows it as ~12-21 at%, and Ellinger and Land list it as 6-14 at% Zr. The unit cell was originally indexed as orthorhombic with 56 atoms (8 formula

units of Pu_6Zr) per unit cell [160] based on X-ray diffraction data from a sample with 21 at% Zr [154]. A later study indicated that the same data could be better represented by tetragonal unit cell (space group P_4/ncc) with lattice parameters a = 10.89 Å and c = 14.89 Å and 80 atoms (16 formula units of Pu_4Zr) per unit cell [161]. Positions of individual atoms have not been refined.

Other phases that have been suggested but generally do not appear in Pu-Zr phase diagrams include:

- ζ-$Pu_{28}Zr$, which has reported compositions between ~2.5 and 5 at% Zr [153, 156, 162]. The unit cell is body-centered tetragonal (space group $I4_1/a$) with a = 18.1899 Å, c = 7.8576 Å, and four formula units (116 atoms) per unit cell [163]. A careful study by Taylor [153] indicated that the compositional range of this phase is ~2.5-3 at% Zr, and that it decomposes peritectoidally to (γ-Pu) and (δ-Pu) at ~270-275°C [153, 156] rather than to (δ-Pu) and θ-(Pu,Zr) as reported by Kutaitsev et al. [162]; however, phase relationships in this part of the phase diagram are poorly understood and further experimental confirmation is recommended. Taylor stated that this phase is stable at room temperature [153], while Kutsaitsev et al. [162] indicated that it occurs only within a limited temperature range and decomposes to (β-Pu) and θ-(Pu,Zr) at ~220°C during cooling, although it is likely to be present as a metastable phase in room-temperature samples.

  ζ-$Pu_{28}Zr$ does not appear in the phase diagrams of Marples et al. [154] and Bochvar et al. [160], possibly because of a complex series of peak overlaps with other phases likely to be present in the same alloys in X-ray diffraction data [153]. This phase also does not appear in the phase diagrams of Okamoto, which follow the phase diagram of Bochvar et al. for solids with less than 50 at% Zr [150, 151].

- κ-$PuZr_2$: Hexagonal intermediate phase with ~75 at% Zr (space group P_6/mmm, a = 5.055 Å, c = 3.123 Å [154, 164]). This phase is isostructural with δ-UZr_2 (Section 2.1.1.2.1.1.5) and δ-$NpZr_2$ (Section 6.1.2.1 of reference [5]). Marples, who synthesized κ-$PuZr_2$ from filings, reported that it was slow to form and decomposed peritectoidally to α-Zr and δ-(Pu,Zr) at 380°C during heating [154]. Although κ-$PuZr_2$ appears in early phase diagrams [154, 160], later researchers have been unable to synthesize it and have suggested that it is oxygen-stabilized [156, 157, 165-167].

- ι-(Pu,Zr) (structure unknown). Ellinger and Land [156] reported that this phase has ~19-24 at% Zr, occupying part of the composition range of θ-(Pu,Zr) in other phase diagrams, and that it decomposes congruently into δ-(Pu, Zr) at ~335°C. They reported X-ray diffraction data from this phase. There are apparently no other published reports of this phase.

Pu-Zr alloys commonly have Pu-bearing high-Zr inclusions in alloys that phase diagrams indicate have too little Zr to form α-Zr or β-Zr (e.g., [168]). These inclusions are commonly referred to as "oxygen-stabilized α-Zr." Little is known about them, and further research is needed to determine why they form and whether they are stable.

2.2.1.2.2 Phase Transitions

Preliminary INL measurements of phase-transition temperatures in alloys with 10, 30, and 40 wt% Zr from DSC data were first reported in Revision 1 of this Handbook [2 (Section 3.2.5)]. Although the phase-transition temperatures were not quantified, they are reportedly consistent with predictions from the Pu-Zr phase diagrams (Section 2.2.1.2.3). The enthalpy determined from peaks at ~900-910 K, which were interpreted as representing the transition from δ-(Pu,Zr) to ε-(Pu,Zr), is 8.19 J/g for Pu-30Zr and 10.37 J/g for Pu-40Zr.

2.2.1.2.3 Phase Diagrams

Experimental phase diagrams of the entire Pu-Zr system based on original research were proposed by Bochvar et al. in 1958 [160], Marples and colleagues in 1960 and 1961 [154, 164], Kutaitsev et al. in 1965 and 1967 [162, 169], and Ellinger and Land in 1971 [156]. Although no later experimentally based phase diagrams of the entire system have been published, later research addressing specific aspects of the phase diagram indicated that none of the available phase diagrams was accurate. Changes required as a result of this later research include:

- Eliminating κ-$PuZr_2$ from the phase diagrams because of evidence indicating that it is oxygen-stabilized (Section 2.2.1.2.1).
- Incorporating new measurements of solidus and liquidus temperatures [153, 170]
- Incorporating new results from investigations of compositions with 0-10 and 50-100 at% Zr [153, 157]

No information about the purity of the materials used by Bochvar et al. [160] and Kutaitsev et al. is available. Kutaitsev et al. used data from some alloys that had been annealed at high pressure to establish equilibrium conditions [162, 169]. The Zr feedstock used by Marples contained about 2% Hf, and the Pu feedstock had been previously cast in graphite molds [154]. Ellinger and Land used electrorefined Pu with less than 300 ppm impurities and Zr with less than 0.1 wt% total impurities, including 105 ppm oxygen and less than 1000 ppm Hf [156]. The alloys studied by Taylor had less than ~575 ppm impurities, of which 230 ppm were Am. Samples used by Maeda, Suzuki and colleagues were prepared using powder metallurgy from zirconium hydride and plutonium. Their zirconium feedstock was 99.2% pure, with several thousand ppm of Fe and Mg, and the plutonium feedstock had 725 ppm impurities, primarily C and N [157, 170].

In 1993, Okamoto compared the phase diagrams of Bochvar et al. [160] and Marples [154] and determined that the primary differences involved the relationship between δ-(Pu,Zr) and ε-(Pu,Zr), which Bochvar et al. considered congruent and Marples considered eutectoid, and the relationships between κ-$PuZr_2$, δ-(Pu,Zr), and (α-Zr), which Okamoto considered irrelevant as a criterion for deciding which phase diagram was more accurate because of accumulated evidence that κ-$PuZr_2$ is an oxygen-stabilized phase. Okamoto suggested a composite phase diagram [150] in which the liquidus and solidus are from thermodynamic calculations by Leibowitz et al. [42], solid-state reactions in compositions with at least 50 at% Zr are from the experimental work of Suzuki et al. [157], and solid-state reactions in compositions with less than 50 at% Zr are from the experimental work of Bochvar et al. [160]. The calculated liquidus and solidus are consistent with the experimental solidus measurements of Marples, which include only compositions with up to ~35 at% Zr. Maximum concentrations of Zr in (α-Pu), (β-Pu), and (γ-Pu) in the 1993 Okamoto phase diagram are considered uncertain, but are higher than those determined in a careful study by Taylor [153]. ζ-($Pu_{28}Zr$) does not appear in the Okamoto phase diagram.

In 1995, Okamoto revised the liquidus and solidus to accommodate new research by Maeda et al. [170], who identified the liquidus and solidus temperatures from small changes in plots of vapor pressures for Pu in three alloys with 60-94 at% Zr and developed a new thermodynamic model to match their data. The model of Maeda et al. assumes ideal behavior of the liquid phase and regular solid solution behavior for the solid phase. The liquidus determined by Maeda et al. is comparable to that in the model of Leibowitz et al., but the solidus temperature is about 100 K higher for compositions with ~30-60 at% Zr.

Despite several areas of uncertainty (particularly involving low-Zr phases), the 1995 Okamoto phase diagram [151] (Figure 28 and Figure 29) is probably the best available approximation to the entire Pu-Zr phase diagram. Further research is needed to determine the liquidus temperature and phase boundaries indicated by dotted lines, and to resolve disagreements with the more detailed work of Taylor [153] involving low-Zr phases (Figure 30).

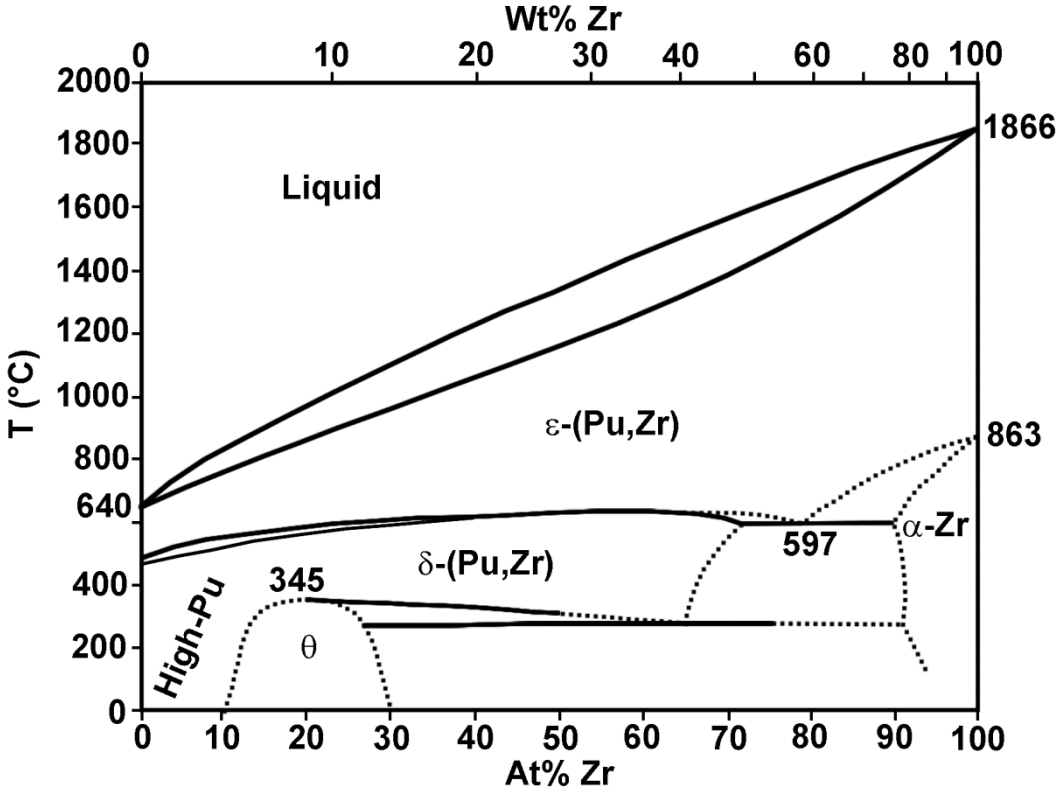

Figure 28. Pu-Zr phase diagram simplified from Okamoto 1995 [151]. See Figure 29 and Figure 30 for details of high-Pu phases.

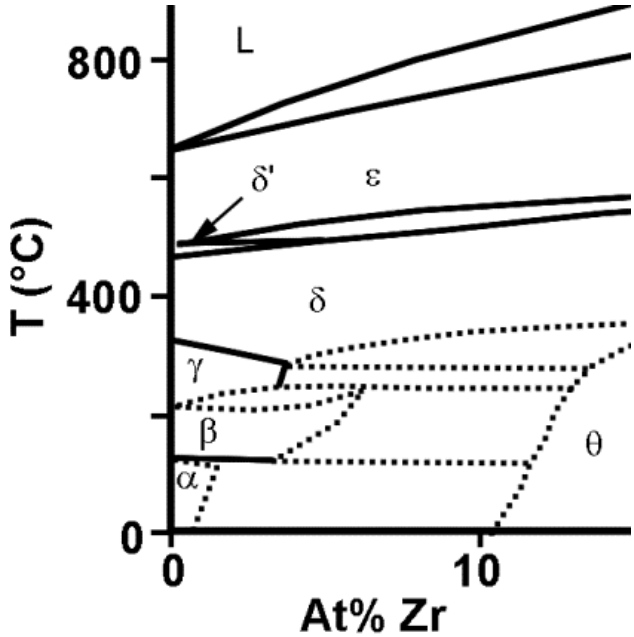

Figure 29. Identities and boundaries of high-Pu phases according to the 1995 Okamoto phase diagram [151]. α, β, γ, δ, δ', ε, and θ refer to (α-Pu), (β-Pu), (γ-Pu), (δ-Pu), (δ'-Pu), (ε-Pu), and θ-(Pu,Zr) respectively. ζ-$Pu_{28}Zr$ is not shown.

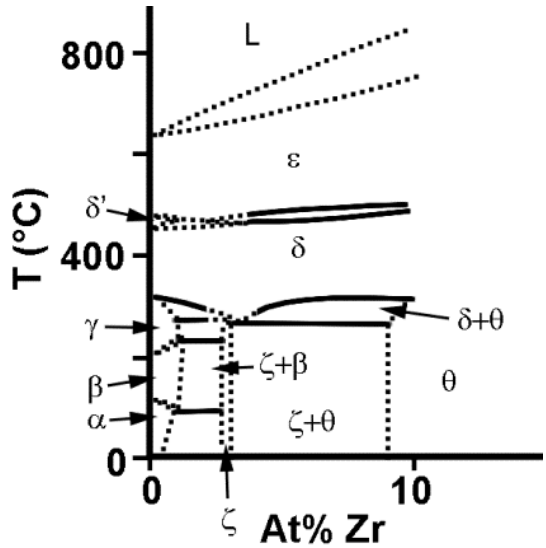

Figure 30. Identities and boundaries of high-Pu phases according to Taylor [153]. α, β, γ, δ, δ', ε, θ, and ζ refer to (α-Pu), (β-Pu), (γ-Pu), (δ-Pu), (δ'-Pu), (ε-Pu), θ-(Pu,Zr), and ζ-$Pu_{28}Zr$, respectively. Maximum concentrations of Zr in (α-Pu), (β-Pu), and (γ-Pu) are smaller than in Figure 29, and there are additional two-phase fields involving ζ-$Pu_{28}Zr$.

2.2.1.3 Heat Capacity and Related Properties

The only available information on heat capacities of Pu-Zr alloys is from preliminary measurements by researchers at INL [2 (Section 3.2.5), 152]. These measurements indicate that the specific heats of Pu-30Zr and Pu-40Zr (wt%) are similar and that the specific heat of Pu-30Zr is lower than that of Pu-40Zr.

2.2.1.4 Thermal Expansion and Density

Thermal expansion measurements of three U-10Zr (wt%) alloys show significant differences, particularly above ~700 K. Differences in thermal expansion between samples with different thermal and processing histories are likely because of the anisotropic thermal expansion of individual phases and perhaps because of different proportions of phases as a result of impurities. New measurements of samples with compositions and processing histories of interest for fuels are appropriate [20].

2.2.1.4.1 Thermal Expansion

Reference [171] is the primary source for experimental data on thermal expansion of δ-(Pu,Zr) alloys with Zr concentrations from ~5-12 at% (~2-5 wt%). It includes measurements of thermal expansion calculated from high-temperature X-ray diffraction data and from dilatometry. Results obtained using the two kinds of data appear consistent. Reference [172] appears to be an earlier publication of results of some of the experiments in reference [171].

Gschneidner et al. [171] developed polynomial equations that expressed sample lengths (for dilatometer data) or lattice parameters (for X-ray data) as functions of temperature (Table 18). Figure 31 shows thermal expansion calculated from these equations, using a reference temperature of 400°C for convenience. The figure shows a consistent pattern in which thermal expansion of δ-(Pu-Zr) solid solutions increases with increasing concentration of Zr. Alloys with less than 10 at% Zr show negative thermal expansion. Alloys with ~8 at% Zr show relatively little expansion, and may change between negative and positive expansion depending on temperature. Alloys with 10 or 12 at% Zr show positive expansion that increases with the concentration of Zr.

Thermal expansion data from high-temperature X-ray diffraction of nine Pu-Zr alloys are plotted in [159 Table 6], but are not tabulated in the reference. These results appear qualitatively consistent with results from reference [171], but suggest that positive thermal expansion occurs only in alloys with at least ~15 at% Zr.

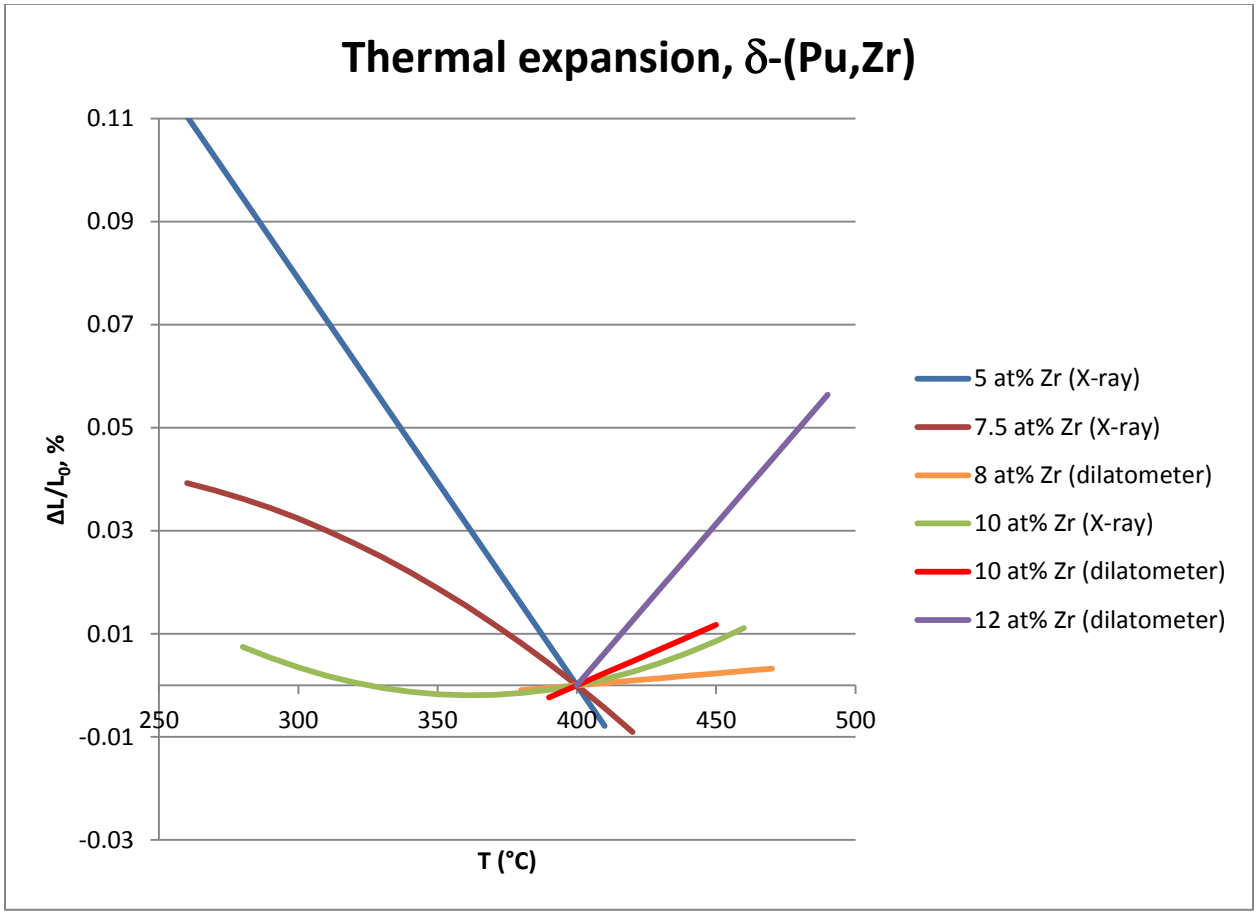

Figure 31. Thermal expansion of δ-Pu-Zr alloys, calculated from data in Table 18 [171] using a reference temperature of 400°C.

Table 18. Coefficients for equations expressing lengths of U-Pu alloys, $L = a + b \times T + c \times T^2$, where L is a length (for dilatometer data) or lattice parameter in Å(for X-ray data) and T is a temperature in °C [171]. The authors emphasize that these coefficients should only be used within the stated temperature ranges.

Composition (at% Zr)	Measurement Type	a	b	c	T Range (°C)
5	X-ray	4.6495	-3.656×10^{-5}	—	259-410
7.5	X-ray	4.6379	1.986×10^{-5}	-4.98×10^{-8}	260-425
8.0	Dilatometer	0.98598	0.460×10^{-6}	—	380-440
10.0	X-ray	4.6459	-4.634×10^{-5}	6.39×10^{-8}	275-462
10.0	Dilatometer	0.97372	2.284×10^{-6}	—	391-440
12.0	Dilatometer	1.00776	2.284×10^{-6}	—	401-499

The only available data on solid solutions between ε-Pu and β-Zr indicate that the thermal expansion of this phase is positive, like that of both ε-Pu and β-Zr [159].

2.2.1.4.2 Thermal Expansion Coefficients

Table 19 has thermal expansion coefficients corresponding to the thermal expansion values in Table 18 and Figure 31. A thermal expansion coefficient for δ-Pu is included for comparison. The thermal expansion coefficients are negative for compositions with less than ~8 at% Zr, small for samples with ~8-10 at% Zr, and positive for samples with 12 at% Zr.

Table 19. Coefficients of thermal expansion for δ-(Pu, Zr). Data for Pu are from reference [173]; other data are from reference [171]. Coefficients should not be used outside the listed temperature ranges.

Composition (at% Zr)	**$\bar{\alpha} \times 10^6$ /°C**	**Temperature Range For $\bar{\alpha}$ (°C)**	**Measurement Type**
0	-8.6	320-440	—
5.0	-7.88	300-401	X-ray diffraction
7.5	-3.50	300-425	X-ray diffraction
8.0	0.47	380-440	Dilatometer
10.0	0.21	300-440	X-ray diffraction
10.0	2.34	391-440	Dilatometer
12.0	6.28	401-440	Dilatometer

Thermal expansion coefficients for ε-Pu/β-Zr solid solutions were reported by Marples [159]. The data show considerable scatter, but suggest that the thermal expansion coefficient decreases from 27×10^{-6}/ °C for pure ε-Pu to ~20.5×10^{-6}/ °C for alloys with 20 at% Zr. This value for the thermal expansion coefficient of ε-Pu is significantly lower than the commonly accepted value of 36.5×10^{-6}/°C [173], suggesting that the reported thermal expansion coefficients for ε-Pu/β-Zr solid solutions may be too low.

2.2.1.4.3 Density

Figure 32 shows densities of (α-Zr) solid solutions with Pu, calculated from the lattice parameters in Figure 26 and Figure 27. Although the densities appear to follow a linear trend with composition, the decrease in density with increasing concentration of Pu is smaller than would be predicted by linear interpolation between the room-temperature densities of α-Pu (19.84 g/cm^3) and α–Zr (6.52 g/cm^3) (sections 2.3.4.3 and 2.9.4.3 of reference [5]).

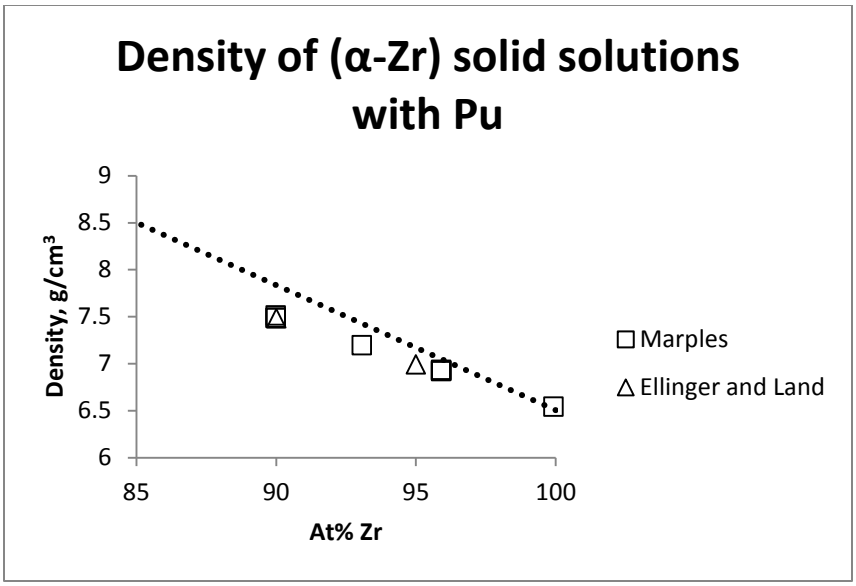

Figure 32. Densities of (α-Zr) solid solutions with Pu [154, 156]. Dotted line shows values that would be predicted by linear interpolation from the room-temperature densities of α-Pu and α-Zr.

Figure 33 shows densities of δ-(Pu,Zr) solid solutions, calculated from the values of the lattice parameter in Figure 25. The densities follow a linear trend with composition between the density of δ-Pu at 593 K (15.92 g/cm^3) and the room-temperature density of α-Zr (6.52 g/cm^3) (sections 2.3.4.3 and 2.9.4.3 of reference [5]).

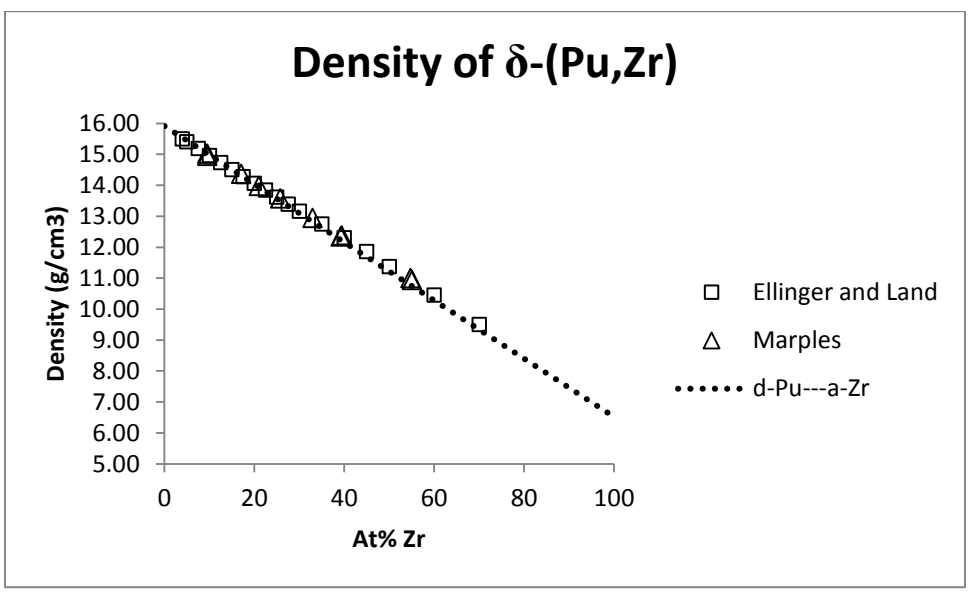

Figure 33. Densities of δ-(Pu,Zr) solid solutions [154, 156].

The calculated density of θ-(Pu-Zr) with 17.9 at% Zr is 15.76 g/cm^3 based on the structure refinement of Berndt [161]. This density is slightly lower than the measured values, which indicated that the density is at least 15.86 g/cm^3 [154]. As it is not clear that the experimental data was from a single-phase material, the calculated density is probably more accurate.

The calculated density of ζ-$Pu_{28}Zr$ with 2.8 at% Zr is 17.39 g/cm^3 based on the structure refinement of Cromer [163].

2.2.1.4.4 Changes in Length Due to Phase Transitions

Marples [154] reported that dilatometer data showed a contraction of ~0.5% during the transformation from δ-(Pu-Zr) to ε-(Pu,Zr). The amount of contraction appears to be independent of composition; however, the data show "considerable" scatter, which Marples attributed to sample creep.

2.2.1.5 Thermal Conductivity and Related Properties

INL researchers have made three preliminary laser-flash diffusivity measurements of Pu-Zr alloys: two measurements of an alloy with 10 wt% (23 at%) Zr and one of an alloy with 30 wt% (53 at%) Zr [2 (Section 3.4.5)]. The data suggest that thermal diffusivity increases with temperature for both compositions, and that the diffusivity of the alloy with 30 wt% is smaller than that of the alloy with 10 wt% Zr by up to ~0.005 cm^2/s (Figure 34).

Consideration of the Pu-Zr phase diagram (Section 2.2.1.2.3) suggests that the "hump" in the Pu-30Zr data at about 200°C may be due to formation of the δ-(Pu-Zr) phase. The upward curve in data for this alloy at ~650°C does not correspond to an obvious phase transformation in Pu-Zr alloys but is approximately the melting temperature of pure Pu.

Lee et al. measured the electrical resistivity of U-Pu alloys with 4 and 50 at% Zr [174]. In the absence of accurate information about the Lorenz number, it is not currently possible to compare the INL data to thermal conductivities calculated using the Wiedemann-Franz Law (Section 1.6.2).

Elliott and Hill [175] studied the low-temperature electrical resistivity of Pu-Zr alloys with hcp structures and up to 16 at% Pu that had been annealed at 600°C for at least a week and quenched. They reported that alloys with 5, 7.5, 10, and 12.5 at% Pu exhibited the Kondo effect (a low-temperature minimum in the electrical resistivity), while alloys with 0 and 16 at% Zr did not.

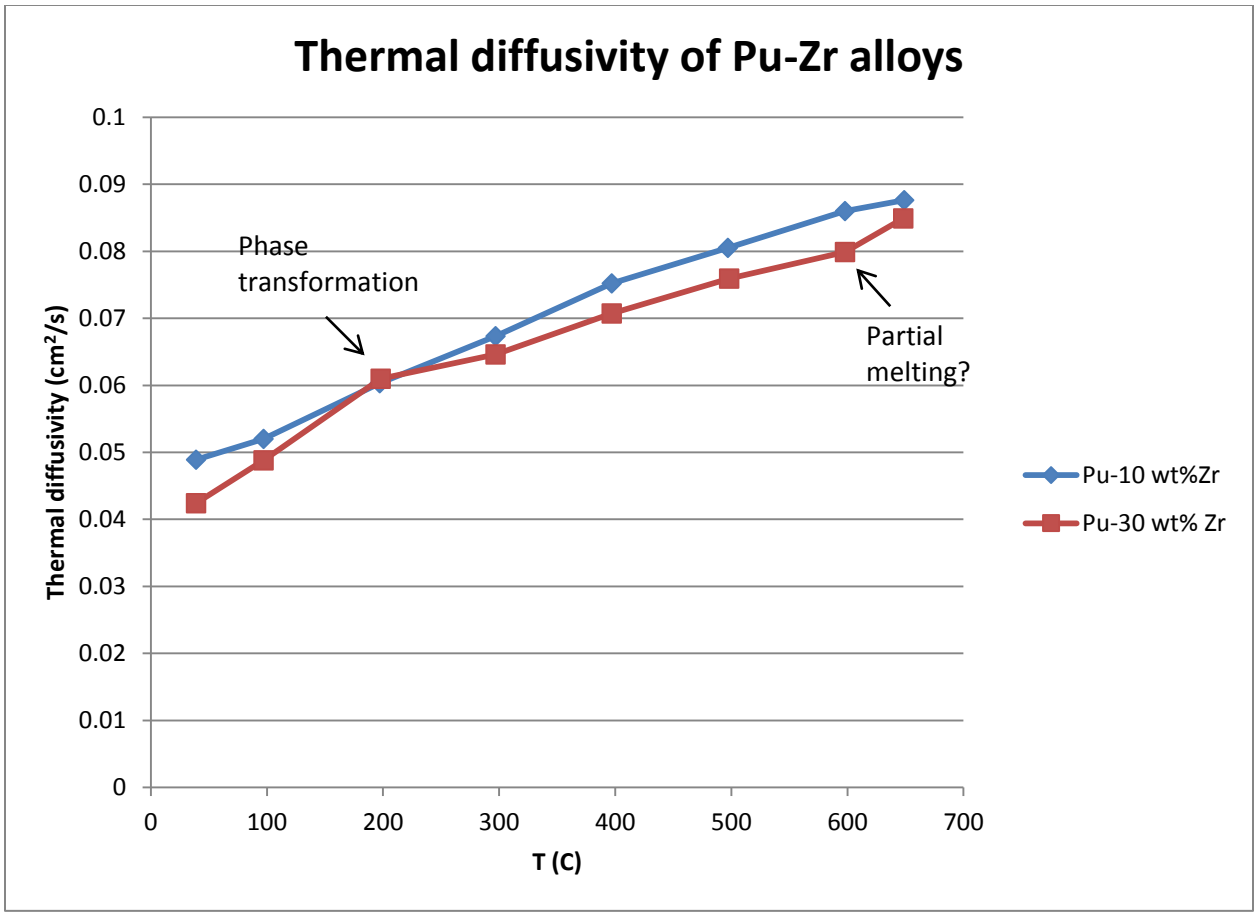

Figure 34. Thermal diffusivity of Pu-10 wt% Zr and Pu-30 wt% Zr alloys (INL preliminary data from reference [3], also available in reference). Data for Pu-10 wt% alloy are the average of two measurements.

2.2.2 Pu-Zr-Np (Alloy AFC1-MB)

2.2.2.1 Introduction

All of the available data on Pu-Zr-Np alloys is from Alloy AFC1-MB, whose nominal composition is 50 wt% Pu, 40 wt% Zr, and 10 wt% Np (corresponding to ~30 at% Pu, 64 at% Zr, and 6 at% Np). This alloy was cast and characterized at Idaho National Laboratory (INL) as part of a study of non-fertile fuel forms for accelerator transmutation of plutonium and minor actinides [176-180].

The actual composition of alloy AFC1-MB based on two analyses was ~8.3 wt% Np, 50 wt% Pu, and 41 wt% Zr [176, 177]. The alloy also contained ~0.24 wt% Am and up to ~1000 ppm O [177].

No information about the Pu-Zr-Np phase diagram or about heat capacities, thermal expansion, and thermal conductivities of Pu-Zr-Np alloys is available.

2.2.2.2 Phases

X-ray diffraction patterns from as-cast samples of Alloy AFC1-MB show peaks consistent with a mixture of two solid-solution phases [177 Figure 1]:

- δ-(Np,Pu,Zr): Face-centered cubic solid solution similar to δ-Pu, with lattice parameter a = 4.57 Å [176]. The lattice parameter of 45.5 pm in reference [177] is smaller than the atomic radii of Np, Pu, and Zr [181], and is not plausible.

- δ-(Np,Pu)Zr_2: Hexagonal solid solution phase similar to δ-UZr_2, δ-$NpZr_2$ and κ-$PuZr_2$, with lattice parameters a = 5.07 Å and c = 3.10 Å [176]. Lattice parameters of 50.6 and 31.2 pm in reference [177] are smaller than the atomic radii of Np, Pu, and Zr [181], and are not plausible.

SEM images such as [177 Figure 2] suggest that crystallites of individual phases in the matrix may be smaller than the analytical volumes of individual SEM microchemical analyses (typically a few μm across and deep). The SEM images also suggest that the sample contains a precipitate phase whose composition is unknown. Thus, the SEM data should not be interpreted as providing information about compositions of individual phases, and interpretations involving associations between specific matrix phases and areas with different contrast in SEM images should be treated with caution.

δ-$NpZr_2$ and κ-$PuZr_2$ are isostructural (Section 6.1.2.1 of reference [5] and Section 2.2.1.2.1 of this document, respectively), and Pu-Zr phase diagrams show a δ-Pu solid solution that can contain up to ~70 at% Zr (Section 2.2.1.2.3). However, the Np-Pu phase diagram shows very limited miscibility between δ-Pu and Np (Section 3.3.2 of reference [5]), and neither of the proposed Np-Zr phase diagrams indicates the possibility of a fcc solid solution between Np and Zr (Section 6.1.2 of reference [5]).

In the absence of new experimental information, it seems reasonable to assume that the reported structures and lattice parameters of the two phases in this sample are approximately correct, and that one of the phases is a δ-$NpZr_2$ solid solution that contains a significant fraction of Pu. A δ-Pu solid solution phase with a significant fraction of Zr is also likely, although it is less certain that this phase also contains Np.

2.2.2.3 Phase Transformations

TMA and DSC/DTA data from Alloy AFC1-MB suggest phase transitions at ~500, 550-580, and possibly ~910°C [176]. These transformations have been tentatively interpreted as indicating reactions leading to the disappearance of the δ-(Np,Pu)Zr_2 phase and the formation of a high-temperature bcc phase.

The identification of the lower-temperature transition as the disappearance of a (Np,Pu)Zr_2 solid solution phase is generally consistent with both of the proposed Np-Zr phase diagrams (Section 6.1.2 of reference [5])and with older Pu-Zr phase diagrams that show κ-$PuZr_2$ [154, 160], although these phase diagrams show the reaction leading to the disappearance of pure κ-$PuZr_2$ at a significantly lower temperature than the reported phase transitions in Alloy AFC1-MB. The interpretation of the higher-temperature reaction as formation of a bcc solid solution is consistent with the Np-Pu and Pu-Zr phase diagrams (Section 3.3.2 of reference [5]) and Section 2.2.1.2.3 of this document, respectively) and with the tentative Np-Zr phase diagram of Rodríguez et al. [140], but not with the tentative Np-Zr phase diagram of Gibson et al. [182], which shows limited miscibility between the bcc phases γ-Np and β-Zr (Section 6.1.2 of reference [5]). The identity and structure of the phase(s) between the transformations in Alloy AFC1-MB is unknown.

2.2.3 Pu-Zr-Am (Alloys AFC1-MC and DOE2)

2.2.3.1 Introduction

All of the published information about phases in Pu-Zr-Am alloys is from Alloys AFC1-MC and DOE2. These alloys have the same nominal composition, which consists of 48% wt% Pu, 40 wt% Zr, and 12% wt% Am (corresponding to ~29.1 at% Pu, 63.7 at% Zr, and 7.2 at% Am). Both alloys were cast and characterized by researchers at Argonne National Laboratory and Idaho National Laboratory [183-185]. Alloy AFC1-MC was part of a study of non-fertile transmutation fuels intended to allow rapid destruction of minor actinides in an accelerator-driven transmutation system [180]. Alloy DOE2 was included in the FUTURIX-FTA experiment. Although all of the Pu-40Zr-12Am alloys were arc-melted and cast in silica glass tubes, several casting techniques were used. It is generally not clear which technique was used to produce the samples from which results were reported.

No information on the Pu-Zr-Am phase diagram or the heat capacities and thermal conductivity of Alloys AFC1-MC and DOE2 is available.

2.2.3.2 Phases and Phase Transformations

X-ray diffraction data from Alloy DOE2 suggest that it consists primarily of a single fcc phase with lattice parameter a = 4.57 Å [185]. (The lattice parameter of 45.7 pm in references [180, 183] is smaller than the atomic radii of Np, Pu, and Zr [181], and is not plausible.) This phase has been tentatively identified as a ternary solid solution between δ-(Pu,Zr) and (β-Am).

DSC/DTA and TMA data showed a reversible phase transformation at ~700°C, which was tentatively interpreted as a transition between the fcc solid solution and a bcc solid solution [179, 183]. Transformations at 1319 and 1361°C were tentatively identified as the solidus and liquidus.

Although it seems plausible that the single phase in Alloys AFC1-MC and DOE2 is an fcc solid solution that transforms to a bcc solid solution at ~700°C, further work is required to understand the relationships between the ternary solid solutions suggested by the Pu-Am-Zr data and the reported limited miscibility of Am with Zr and perhaps Pu (Sections 3.5.2 and 6.2 of reference [5]).

2.2.3.3 Thermal Expansion and Density

2.2.3.3.1 Coefficients of Thermal Expansion

TMA data during heating of as-cast Pu-40Zr-12Am shows two temperature ranges with approximately linear thermal expansion: one from room temperature to the onset of the phase transition at ~700°C and one between the phase transition and ~900°C. The average linear coefficient of thermal expansion has been reported as 8×10^{-6}/K or 8.73×10^{-6}/K (reference [183] and INL internal data) below the phase transition and as 5×10^{-6}/K or 15.6×10^{-6}/K above it (reference [183] and INL internal data). Examination of the TMA curves (e.g., [183 Figure 1]) indicates that the coefficient of thermal expansion is somewhat smaller above the phase transition than below it, and the value of 15.6×10^{-6}/K above the phase transition should be disregarded.

2.2.3.3.2 Densities

Densities of five rods of Alloy AFC1-MC were measured by immersion. Values ranged from 9.732 to 9.952 g/cm^3, with an average value of ~9.88 g/cm^3.

2.2.3.3.3 Changes Due to Phase Transitions

TMA data indicates that the phase transition at ~700°C involves a pronounced contraction during heating. The amount of the contraction has not been quantified; however, consideration of TMA curves (e.g., [183 Figure 1] suggest that the sample length after the transition is only ~80% of the length before the transition.

2.2.4 Pu-Zr-Np-Am (Alloy AFC1-MD)

2.2.4.1 Introduction

All of the available data on Pu-Zr-Np-Am alloys is from Alloy AFC1-MD, whose nominal composition consists of 50 wt% Pu, 40 wt% Zr, 10 wt% Np and 10 wt% Am (corresponding to ~24.2 at% Pu, 63.65 at% Zr, 6 at% Np, and 6 at% Am). This alloy was part of a study of non-fertile transmutation fuels intended to allow rapid destruction of minor actinides in an accelerator-driven transmutation system [180]. It was cast and characterized at Idaho National Laboratory [176-179].

Samples of this alloy were fabricated by a procedure involving arc-melting the material several times on a copper hearth to homogenize it, then melting it a final time and casting it in a quartz mold to produce a cylinder ~4 mm in diameter.

No information about the heat capacity, thermal expansion, density, or thermal conductivity of any Pu-Zr-Np-Am alloy is available.

2.2.4.2 Phases and Phase Transformations

Microstructures in Alloy AFC1-MD resemble those in Pu-40Zr-10Np [179], with a fine-grained matrix surrounding small dark precipitates. X-ray diffraction patterns are consistent with a combination of two phases: a major phase with a face-centered cubic structure and lattice parameter a = 4.57Å and a minor phase with a hexagonal structure similar to that of δ-UZr_2 and lattice parameters a = 5.06Å and c = 3.10Å. Consideration of the sample composition and binary phase diagrams suggests that the fcc material is a δ-Pu solid solution and the hexagonal material is an actinide-Zr solid solution with a structure similar to that of δ-UZr_2, δ-$NpZr_2$, and κ-$PuZr_2$ (Section 2.1.1.2.1.1.5 of this document, Section 6.1.2.1 of reference [5], and Section 2.2.1.2.1 of this document, respectively).

Compositions of phases have not been identified, and the available images suggest that the sample is too fine-grained to allow measurements of individual phases using SEM.

2.3 Alloys Based on U-Pu, Including U-Pu and U-Pu Alloys with Minor Actinides (Np, Am)

2.3.1 U-Pu

2.3.1.1 Introduction

A phase diagram proposed by Peterson and Foltyn [186] is generally accepted despite inconsistencies with phase diagrams based on thermodynamic models [187-189]. The phase diagram of Peterson and Foltyn is supported by later measurements of solid-state phase transition temperatures [190, 191]. DTA measurements [190] suggest that relatively minor revisions in the liquidus and solidus may be needed for compositions with more than ~20 at% U.

The U-Pu system has two intermediate phases: ζ-(U,Pu), which can have ~25-74 at% U and is stable at room temperature, and η-(Pu-Zr), which can have between ~3 and 70 at% U and is stable at temperatures between 278 and 705°C. With the exception of a continuous solid solution between γ-U and ε-Pu, no Pu phase can incorporate more than a few at% U, and no U phase can incorporate more than ~20 at% Pu. The solidus and liquidus have minima at the same composition and temperature (~9-12 at% U and ~610-620°C) [186].

Almost all of the published experimental data about the heat capacity of U-Pu alloys is from a single paper in which specific heats were calculated from incremental enthalpies measured with drop calorimetry for an alloy with 10 wt% Pu. Although a small number of other values have been published, it is not clear whether they are based on independent measurements.

Kinetics of phase transformations are sluggish, and experimental results are likely to vary between samples with different thermal histories (e.g., [165, 192]). Samples of U-Pu alloys may exhibit marked changes as a result of thermal cycling. For example, one sample of an alloy with 10 wt% Pu that was cycled between 450 and 700°C experienced a 25% increase in length and 30% decrease in density, even though the sample was held at temperature for long enough to assure completion of phase transformations between cycles [193].

Published data on thermal expansion of U-Pu alloys is limited to a single report with information about an alloy with 15 wt% (~15 at%) Pu, early reports of average coefficients of thermal expansion for alloys with 10 and 20 at% Pu, and measurements of changes in lattice parameters in ζ-(U,Pu) in an alloy with 60 at% Pu. No data about the thermal expansion of η-(U,Pu) or any U-Pu alloy with more than 60 at% Pu is available.

Data on the thermal conductivity of U-Pu alloys is limited to a small number of measurements of the thermal conductivity of an alloy with 10 wt% (10 at%) Pu.

Models of the U-Pu phase diagram based on thermodynamic properties include those of Leibowitz et al. [42, 194], Ogawa [195], Chan et al. [196], and Y. Okamoto et al. [190]. Kurata [34, 38, 197] developed an internally consistent database of thermodynamic properties and used the CALPHAD approach to calculate a phase diagram that agrees well with the experimental data. Landa and colleagues modeled U-Pu alloys using *ab initio* and density functional theory approaches [198-200]. More recently, Dorado and colleagues used first-principles calculations to investigate the influence of point defects and impurities on the dynamical stability of δ-(U-Pu) [201].

2.3.1.2 Phases and Phase Transformations

2.3.1.2.1 Phases

U-Pu phases include a continuous solid solution between γ-U and ε-Pu, solid solutions of other U and Pu phases, and the intermediate phases ζ-(U,Pu) and η-(U,Pu). The U-Pu phases are:

- (α-Pu): Solid solution of α-Pu with a maximum solubility of ~0.2 at% U [186].
- (β-Pu): Solid solution of β-Pu with a maximum solubility of 2 at% U [186]. Lattice parameters of an alloy with 2 at% U at 186°C are a = 9.264 Å, b = 10.439 Å , c = 7.841 Å , and β= 92.22° [155].
- (γ-Pu): Solid solution of γ-Pu with a maximum solubility of 0.7 at% U [186]
- (δ-Pu): Solid solution of δ-Pu with a maximum solubility of 0.3 at% U [186]
- (δ′-Pu): Solid solution of δ′-Pu with a maximum solubility of 1.5 at% U [186]
- (α-U): Solid solution of α-U with a maximum solubility of 15 at% Pu [165, 186, 202]. Berndt measured the lattice parameters of α-U and eight alloys with Pu concentrations between ~2 and 15% in samples that had been furnace-cooled from 400°C. The a and c lattice parameters increased, and the b lattice parameter decreased, with increasing concentration of Pu [202]. However, values of each lattice parameter varied by at most ~0.01 Å, suggesting that both variations in the lattice parameters of (α-U) solid solutions in U-Pu alloys and differences from the lattice parameters of pure α-U can be neglected for most purposes.
- (β-U): Solid solution of β-U with a maximum solubility of 20 at% Pu [186]. Ellinger et al. [192] reported the room-temperature lattice parameters of a (β-U) alloy with 15 at% Pu as a = 10.61 Å and c = 5.605 Å, suggesting that incorporation of Pu may decrease both lattice parameters of (β-U) solid solutions. They also reported that U-Pu alloys with at least 10 at% Pu retained the β–U structure if they were water-quenched from the temperature range in which β-U is stable but had the α-U structure if they were quenched from temperatures where γ-U is stable.
- γ-(U,Pu): A continuous bcc solid solution between γ-U and ε-Pu [186].
- ζ-(U,Pu): This phase has 25-74 at% U and is stable at room temperature [186]. Although some early references (e.g., [91]) indexed it with a primitive cubic unit cell, a neutron-diffraction structure refinement indicates that ζ-(U,Pu) has a primitive rhombohedral unit cell with 58 atoms per unit cell and a lattice angle close to 90 degrees (space group $R\bar{3}m$, a = 10.6583 Å, α = 89.736° at 29°C for a sample with 60 at% Pu) [203]. The room-temperature value of the lattice parameter a decreases with increasing concentration of U (Figure 35).

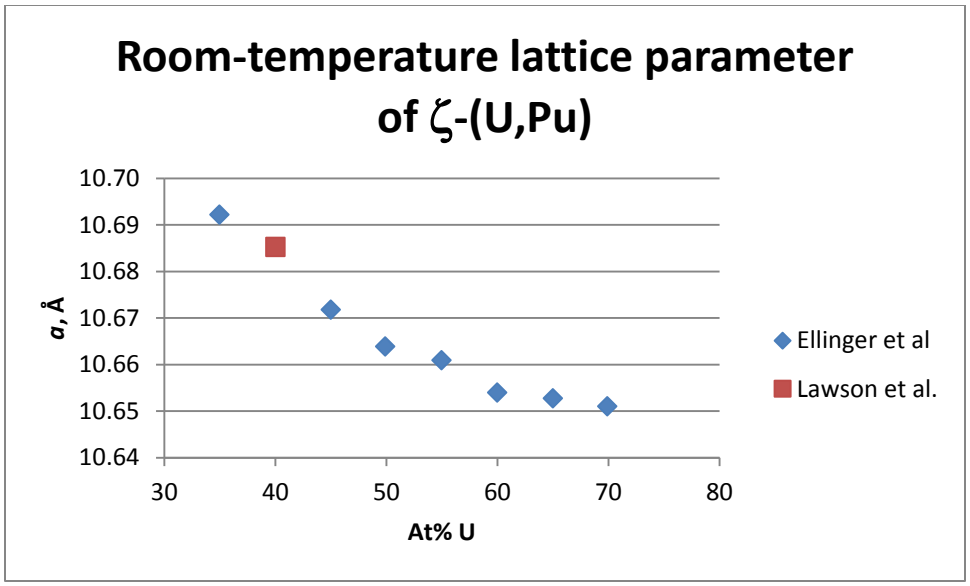

Figure 35. Variations in the room-temperature lattice parameter of ζ-(U,Pu) as a function of composition [192 (Figure 7), 203]. Although Ellinger et al. indexed their data based on a cubic unit cell and Lawson et al. used a rhombohedral unit cell, lattice parameters from these references are comparable because the rhombohedral lattice angle α is approximately 90 degrees.

- η-(U,Pu), a high-temperature phase with 4 to 70 at% U [186]. The crystal structure of this phase has not been determined, although Ellinger et al. [192] suggested that it might be tetragonal with a = 10.57 and c = 10.76 Å for a sample with 25 at% U that had been quenched from 500°C.

2.3.1.2.2 Phase Transformations

Direct measurements of phase-transition enthalpies are lacking. However, differences between incremental enthalpies for a sample with 10 wt% (~10 at%) Pu and those for pure U are negligible [118], suggesting that phase-transition enthalpies for this alloy are similar to those for pure U (Section 2.1.2.2 of reference [5]).

Savage [204] reported that the heat of fusion of a U-10Pu alloy is 2.4 kcal/g-atom (~10 kJ/mol), as compared to his measurement of 2.9 kcal/g-atom (~12.1 kJ/mol) for pure U. This value for the heat of fusion of pure U is at the maximum of the range of experimental values (Section 2.1.2.2 of reference [5]), and it seems likely that the heat of fusion of U-10Pu in the same publication is also high. In the absence of new experimental data, it seems reasonable to assume that the difference between the heats of fusion of U and U-10Pu (a decrease of ~2 kJ/mol) is accurate.

2.3.1.2.3 Phase Diagrams

Numerous researchers have suggested U-Pu phase diagrams (e.g., [91, 160, 165, 190-192, 205-207]). The basic topology of these phase diagrams is similar, although the phase diagram of Bochvar et al. [160] shows far lower minimum concentrations of U in ζ-(U,Pu) and β-U and higher concentrations of U in α-Pu and β-Pu than other phase diagrams.

In 1989, Peterson and Foltyn [186] assessed the available data and suggested a phase diagram based primarily on the work of Ellinger et al. [192]. This phase diagram (Figure 36) is widely accepted. More recent measurements by Y. Okamoto et al. [190] are consistent with sub-solidus phase-transition temperatures in the Peterson and Foltyn phase diagram, but suggest that the solidus may be slightly higher and the liquidus may be lower by ~30°C or more than the temperatures shown in the Peterson and Foltyn phase diagram. It has been suggested that the Peterson and Foltyn phase diagram should be modified as a result of these measurements and

to obtain better agreements with the results of thermodynamic models [187, 188]; however, no modified phase diagram has been published and recent publications (e.g., [38, 191, 208]) continue to use the phase diagram of Peterson and Foltyn.

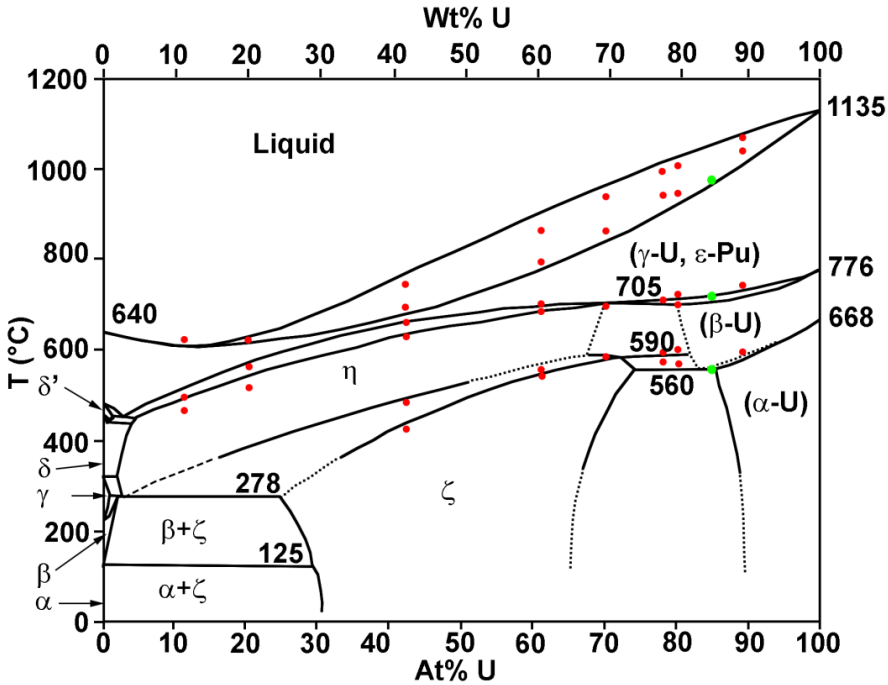

Figure 36. 1989 U-Pu phase diagram of Peterson and Foltyn [186], with more recent measurements from Y. Okamoto et al. [190] (red dots) and Kaity et al. [191] (green dots). α, β, γ, δ, and δ' refer to solid solutions of the corresponding Pu phases, ζ is ζ-(U,Pu), and η is η-(U,Pu).

2.3.1.3 Heat capacity and Related Properties

2.3.1.3.1 Incremental Enthalpy of U-10Pu

Almost all of the published experimental data about the heat capacity of U-Pu alloys is from a single paper by Savage [204], who calculated specific heats from incremental enthalpies measured with drop calorimetry. Savage concluded that the heat capacity of an alloy with 10 wt% Pu was similar to that of pure U. He presented quadratic equations representing heat capacities of individual phases as functions of temperature. Chiotti et al. [118] proposed Equation 40 through Equation 43 as alternative equations matching the same data. These equations were accepted by Peterson and Foltyn (with modifications to express heat capacity in J/mol·K rather than cal/mol·K) in their assessment of the phase diagram [186].

Figure 37 shows the incremental enthalpy of U-10Pu, as represented by Peterson and Foltyn's polynomial fit to Savage's experimental results [186, 204]. The incremental enthalpies of (β-U), (γ-U), and liquid are linear functions of temperature.

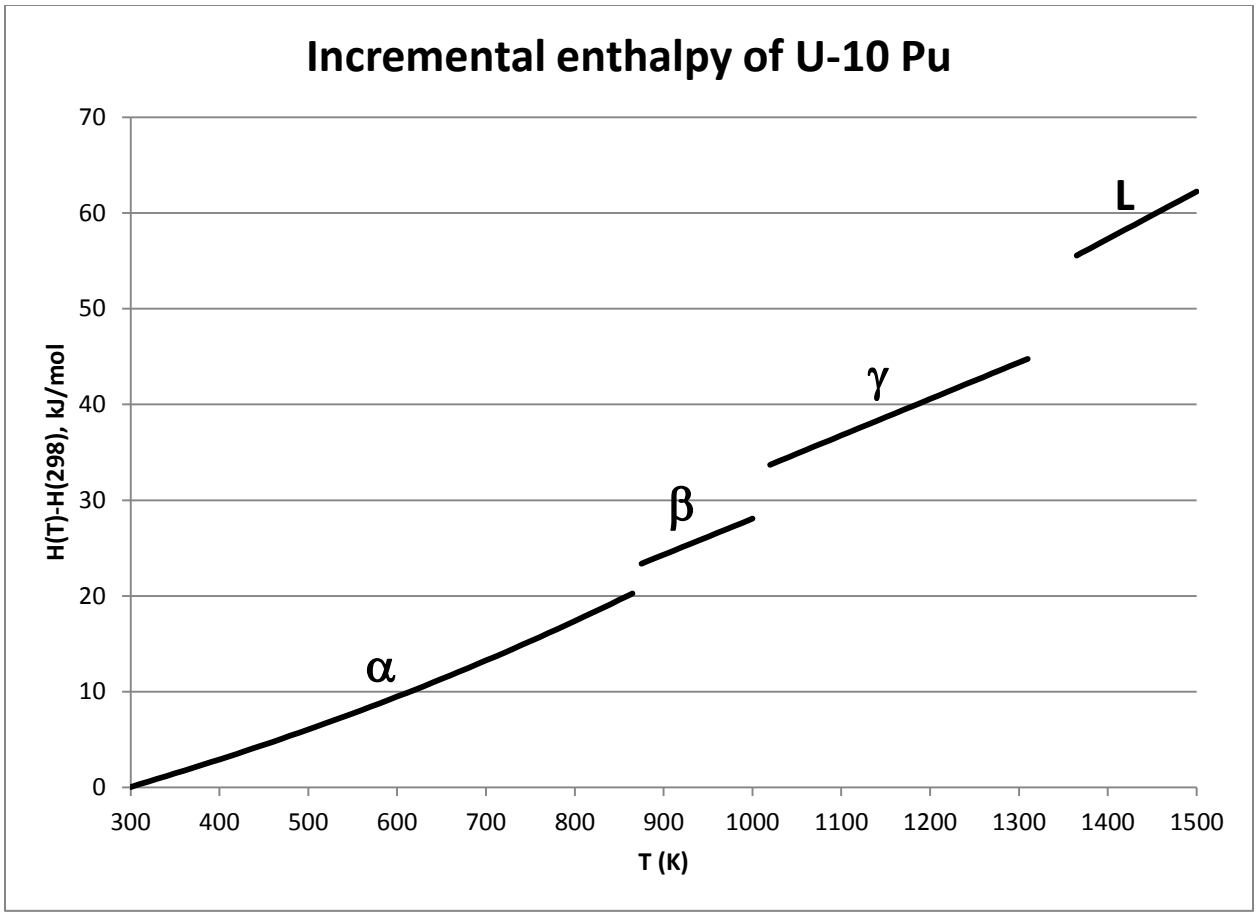

Figure 37. Incremental enthalpy (H(T) – H(298)) of U-10Pu, calculated from Equation 40 through Equation 43.

Equation 40. Incremental enthalpy of (α-U) phase in U-10Pu between 298 and 865 K [186]

H(T) - H(298) = -3948+12.196 × T+3.774 × 10-2 × T2/2-4.074 × 105 × T-1

where H is enthalpy at temperature T in J/mol, H(298) is enthalpy at 298 K in J/mol, T is temperature in K, and T is between 298 and 865 K

Equation 41. Incremental enthalpy of (β-U) phase in U-10Pu between 875 and 1000 K [186]

H(T) - H(298) =-9517.3+37.572 × T

where H is enthalpy at temperature T in J/mol, H(298) is enthalpy at 298 K in J/mol, T is temperature in K, and T is between 875 and 1000 K

Equation 42. Incremental enthalpy of (γ-U) phase in U-10Pu between 1020 and 1310 K [186]

H(T) - H(298) = -5189.4+38.116 × T

where H is enthalpy at temperature T in J/mol, H(298) is enthalpy at 298 K in J/mol, T is temperature in K, and T is between 1020 and 1310 K

Equation 43. Incremental enthalpy of U-10Pu liquid between 1365 and 1500 K [186]

H(T) - H(298) = -11867+49.371 × T

where H is enthalpy at temperature T in J/mol, H(298) is enthalpy at 298 K in J/mol, T is temperature in K, and T is between 1365 and 1500 K

A slightly earlier paper by Kelman et al. [193 Table VII] reported the enthalpy difference between 25°C and melting for a U-10Pu alloys as 46 cal/g (~45.8 kJ/mol, consistent with the results published by Savage [204]). These data were repeated by Kittel [209]. Because Savage was an author of the Kelman et al. paper, the enthalpies in all three publications [193, 204, 209] may represent the same experimental results.

2.3.1.3.2 Heat Capacity of U-10Pu

Although Savage presented quadratic equations representing heat capacities of individual phases as functions of temperature [204], Chiotti et al. [118] noted that these equations did not produce "sensible" heat capacities for β-U and γ-U solid solutions and could not be extrapolated to 298 K. Chiotti et al. therefore proposed alternative equations to fit Savage's data. These equations were accepted by Peterson and Foltyn (with modifications to express heat capacity in J/mol·K rather than cal/mol·K) in their assessment of the phase diagram [186].

It is important to note that Savage's conclusion that the heat capacities of U and U-10 Pu are similar was based on measurements of U that were available at the time of his research. Savage's measurements for the heat capacity of α-U and the average heat capacity of γ-U are similar to the recommended values for pure U in reference (Section 2.1.3.2 of reference [5]), but his values for β-U and liquid U are not. In the absence of new experimental data, it seems reasonable to qualitatively accept Savage's conclusion that heat capacities of U and U-10 Pu are similar even when this leads to disagreement with his quantitative values. Further research is needed to test this suggestion, and to investigate thermophysical properties of other U-Pu alloys.

Figure 38 shows the heat capacity of U-10Pu, as represented by Peterson and Foltyn's polynomial fit to Savage's experimental results [186, 204] (Equation 44 through Equation 47). Recommended values for the heat capacity of pure U from Konings and Beneš (reference [210] and Section 2.1.3.2 of reference [5]) are shown for comparison. The heat capacities of (α-U) in U-10Pu is similar to the heat capacity of pure α-U, and the average heat capacity for (γ-U) in U-10Pu is slightly smaller than that of pure γ-U. Heat capacities of (β-U) in U-10 Pu and of liquid U-10Pu are independent of temperature, as they are for U. However, the reported values of the heat capacities of (β-U) and liquid U-10Pu differ significantly from those for pure U. Further research is needed to understand why these differences occur, and to measure the heat capacities of other U-Pu alloys.

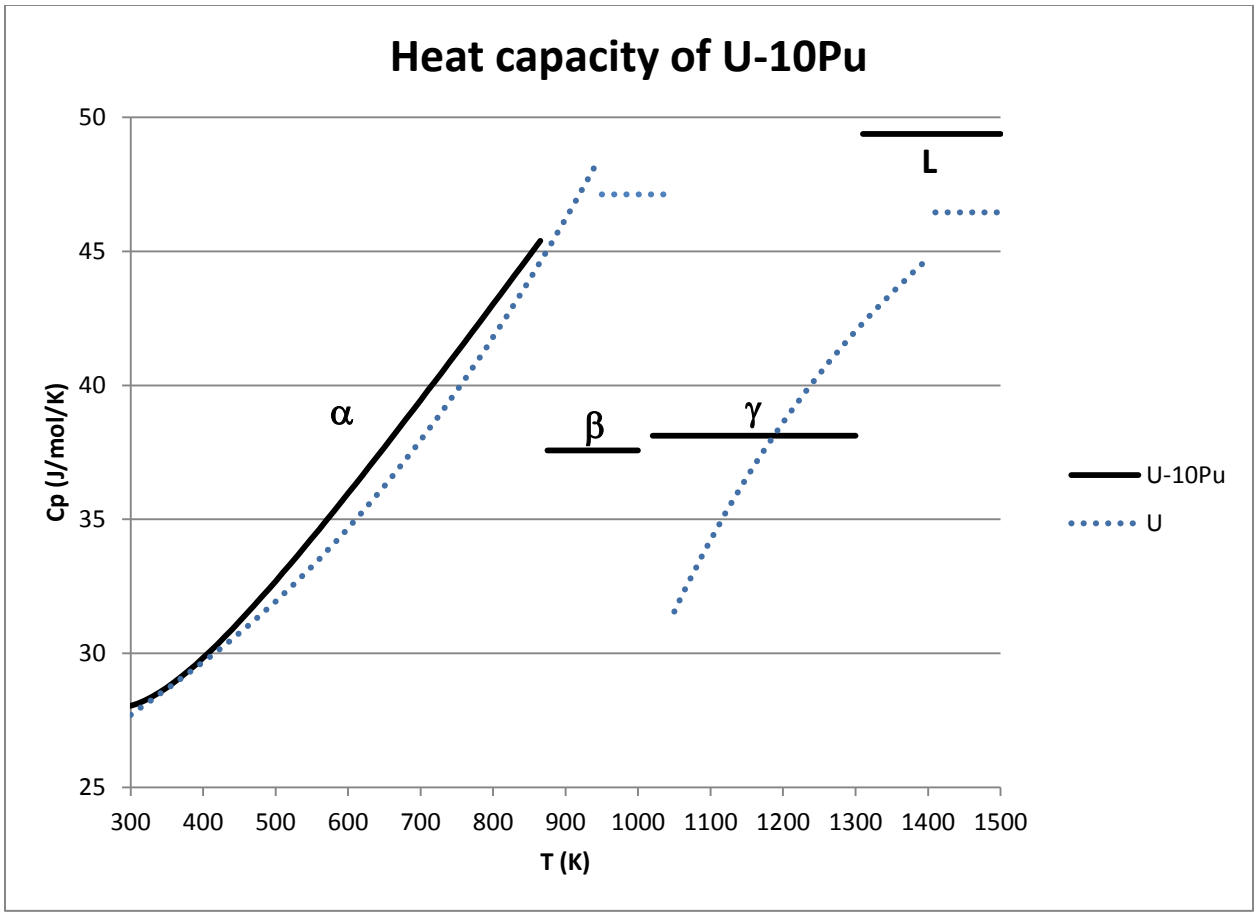

Figure 38. Heat capacity of U-10Pu (calculated from Equation 44 through Equation 47), with the heat capacity of U [210] for comparison.

Equation 44. Heat capacity of (α-U) phase in U-10Pu between 298 and 865 K [186]

$C_p = 12.196 + 3.774 \times 10^{-2} \times T + 4.074 \times 10^{5} \times T^{-2}$

where C_p is constant-pressure heat capacity in J/mol·K, T is temperature in K, and T is between 298 and 865 K

Equation 45. Heat capacity of (β-U) phase in U-10Pu between 875 and 1000 K [186]

$C_p = 37.572$

where C_p is constant-pressure heat capacity in J/mol·K

Equation 46. Heat capacity of (γ-U) phase in U-10Pu between 1020 and 1310 K [186]

$C_p = 38.116$

where C_p is constant-pressure heat capacity in J/mol·K

Equation 47. Heat capacity of U-10Pu liquid between 1365 and 1500 K [186]

$C_p = 49.371$

where C_p is constant-pressure heat capacity in J/mol·K

2.3.1.4 Thermal Expansion and Density

2.3.1.4.1 Thermal Expansion

2.3.1.4.1.1 Thermal Expansion of U-15Pu (wt%)

Kaity et al. [191] measured changes in length of a sample of a U-15wt% Pu alloy with a high-temperature dilatometer. They divided their thermal expansion data into three temperature ranges, separated by two phase transformations: the transformation from (α-U) to (β-U) beginning at 842K and the transformation from (β-U) to (γ-U) between 992 and 1009K. Kaity et al. fitted their data using three polynomials (Equation 48, Equation 49, and Equation 50), which are shown in Figure 39.

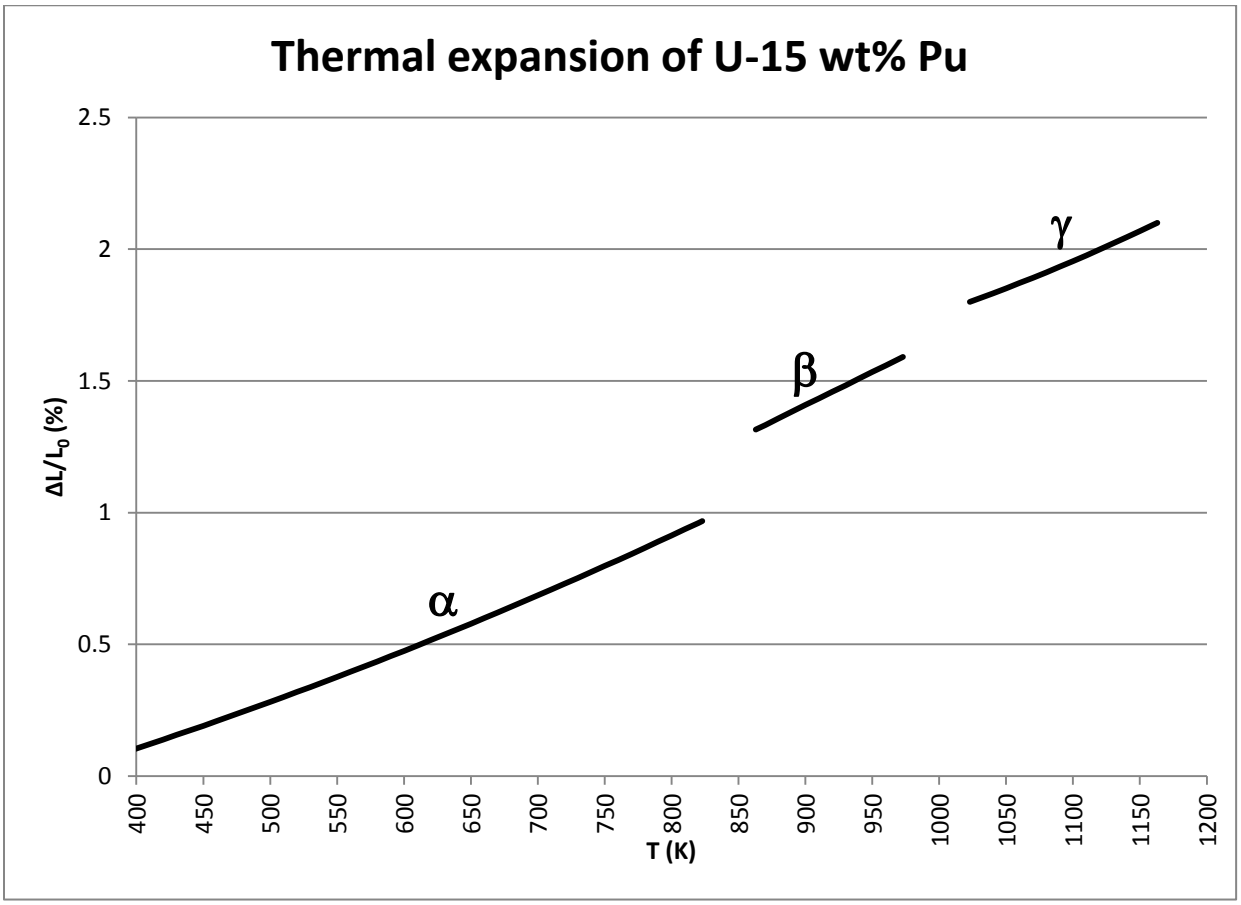

Figure 39. Thermal expansion of U-15 wt% (15 at%) Pu, calculated using Equation 48, Equation 49, and Equation 50.

Equation 48. Thermal expansion of (α-U) in U-15 wt%-Pu from 393 to 823 K according to Kaity et al. [191]

$$(L-L_0)/L_0 = -0.431 + 1.000 \times 10^{-3} \times T + 8.509 \times 10^{-7} \times T^2$$

where $(L-L_0)/L_0$ is thermal expansion in %, T is temperature in K, T is between 393 and 893 K, L is the length at temperature T, and L_0 is length at 300 K

Equation 49. Thermal expansion of (β-U) in U-15 wt%-Pu from 863 to 973 K according to Kaity et al. [191]

$$(L-L_0)/L_0 = -0.976 + 2.790 \times 10^{-3} \times T - 1.562 \times 10^{-7} \times T^2$$

where $(L-L_0)/L_0$ is thermal expansion in %, T is temperature in K, T is between 863 and 973 K, L is the length at temperature T, and L_0 is length at 300 K

Equation 50. Thermal expansion of (γ-U) in U-15 wt%-Pu from 1023 to 1163 K according to Kaity et al. [191]

$$(L-L_0)/L_0 = 2.249 - 2.710 \times 10^{-3} \times T + 22.204 \times 10^{-7} \times T^2$$

where $(L-L_0)/L_0$ is thermal expansion in %, T is temperature in K, T is between 393 and 893 K, L is the length at temperature T, and L_0 is length at 300 K

2.3.1.4.1.2 Thermal Expansion of ζ-(U,Pu)

Lattice parameters of ζ-(U,Pu) in a sample with composition $Pu_{0.60}U_{0.40}$ were measured at temperatures between ~302 and 650 K using high-resolution neutron diffraction [203 Figure 8]. The lattice parameter *a* increased with temperature, and the rhombohedral angle α decreased, changing the shape of the unit cell and increasing its volume slightly (Table 20).

Table 20. Lattice parameters and unit-cell volumes for ζ-(U,Pu) as a function of temperature, based on data read from [203 Figure 8].

T (K)	*a* (Å)	α (degrees)	Volume (Å^3)
302	10.684	89.74	1220
430	10.704	89.71	1226
580	10.756	89.53	1244
630	10.772	89.45	1250
675	10.783	89.33	1254

Based on this table, the mean volumetric coefficient of expansion $\Delta V/(V_0 \times \Delta T)$ is ~7.5×10^{-5}/K for temperatures between 302 and 675 K.

2.3.1.4.2 Coefficients of Thermal Expansion

The mean coefficient of thermal expansion for the U-15Pu alloy between 300 and 823 K is $18.58 \times 10^{-6} K^{-1}$ [191]. This value is smaller than those reported for U-10 Pu by Kelman et al. (19.4×10^{-6}/°C from 25°C to the first phase transformation, and 25.6×10^{-6}/°C from the end of the transformation to 720°C) [193, 209] and the value reported for U-20 Pu by Boucher et al. (21×10^{-6}/°C from 20-500°C) [211, 212]. However, all of the determinations of the thermal expansion coefficient agree closely enough that it seems reasonable to consider the average coefficient of thermal expansion determined by Kaity et al. [191] to be a reasonable estimate for U-Pu alloys with up to ~20% Pu.

Principal linear coefficients of thermal expansion for a U-Pu alloy with 98 wt% Pu and the β-Pu structure are available in reference [155].

2.3.1.4.3 Density

2.3.1.4.3.1 Densities of (α-Pu) Solid Solutions In U-Pu Alloys

No measurements of the density of this phase are available. Kittel et al. report that the addition of 2 at% U decreases the lattice parameters by 0.1 to 0.3% without significantly changing the lattice angle β. Decreasing the *a*, *b*, and *c* lattice parameters by 0.3% relative to the lattice parameters of pure α–Pu from

Section 2.3.2.1 of reference [5]) decreases the unit-cell volume by ~0.9%, which increases the density of the alloy to ~20.03g/cm^3 (as compared to the density of 19.84 g/cm^3 for α-Pu from Section 2.3.4.3 of reference [5]).

2.3.1.4.3.2 Densities of (β-Pu), (γ-Pu), (δ-Pu), and (δ'-Pu) Solid Solutions in U-Pu Alloys

No information about the densities of these phases is available. Because maximum concentrations of U are low, it seems reasonable to approximate the densities of these solid-solution phases by the densities of the corresponding phases in pure Pu (Section 2.3.4.3 of reference [5]).

2.3.1.4.3.3 Densities of (α-U) Solid Solutions in U-Pu Alloys

Densities of (α-U) solid solutions in U-Pu alloys can be calculated from lattice parameters measured by Berndt [202]. Although the densities decrease slightly with increasing concentrations of Pu, the maximum difference in densities is only ~0.05 g/cm^3. Thus, it seems reasonable to approximate the room-temperature densities of α-U solid solutions in U-Pu alloys by the density of α-U (Section 2.1.4.3 of reference [5]).

2.3.1.4.3.4 Densities of (β-U) Solid Solutions in U-Pu alloys

No measurements of the densities of (β-U) solid solutions with Pu are available. However, Ellinger et al. calculated the room-temperature density of β-U with 15 at% Pu as 18.78 g/cm^3 [192] based on crystallographic data. As pure β-U is not retained at room temperature in quenched samples, no data on its room-temperature density is available for comparison.

2.3.1.4.3.5 Density of ζ-(U,Pu)

Data on the densities of U-Pu alloys with the ζ-(U,Pu) structure are limited and somewhat contradictory. Ellinger et al. [192] reported that densities of this phase measured by liquid displacement were 18.5-18.8 g/cm^3. However, densities calculated from their lattice parameters using Equation 5 with 58 atoms per unit cell and the assumption that the isotopes in their alloy were U-238 and Pu-239 are somewhat higher: 18.8 g/cm^3 for an alloy with 35 at% U and lattice parameter a = 10.692 Å and 19.0 g/cm^3 for an alloy with 70 at% U and a = 10.651 Å. (Figure 40).

Lawson et al. [203] refined the structure of ζ-(U,Pu) in an alloy with 40 at% U using neutron diffraction. They determined that this phase has a rhombohedral unit cell with lattice parameters a = 10.6853 Å and α = 89.736 ° at room temperature and confirmed that there are 58 atoms in a unit cell. Based on these lattice parameters, the unit-cell volume is 1219.96 Å^3 and the density is 18.83 g/cm^3 for an alloy of U-238 and Pu-239. This density is consistent with values calculated from Ellinger's X-ray diffraction data (Figure 40), although the actual density of the alloy used by Lawson et al. was higher than this value because 95% of the Pu in their sample was Pu-242. The isotopes in Ellinger's samples are not specified.

Based on this comparison, it seems likely that the densities calculated from the X-ray data of Ellinger et al. [192] represent the actual density of ζ-(U,Pu) better than the densities determined from the liquid immersion measurements reported in the same paper. As Ellinger et al. did not present details of their immersion measurements, it these measurements may have been intended primarily to assist with structure determinations.

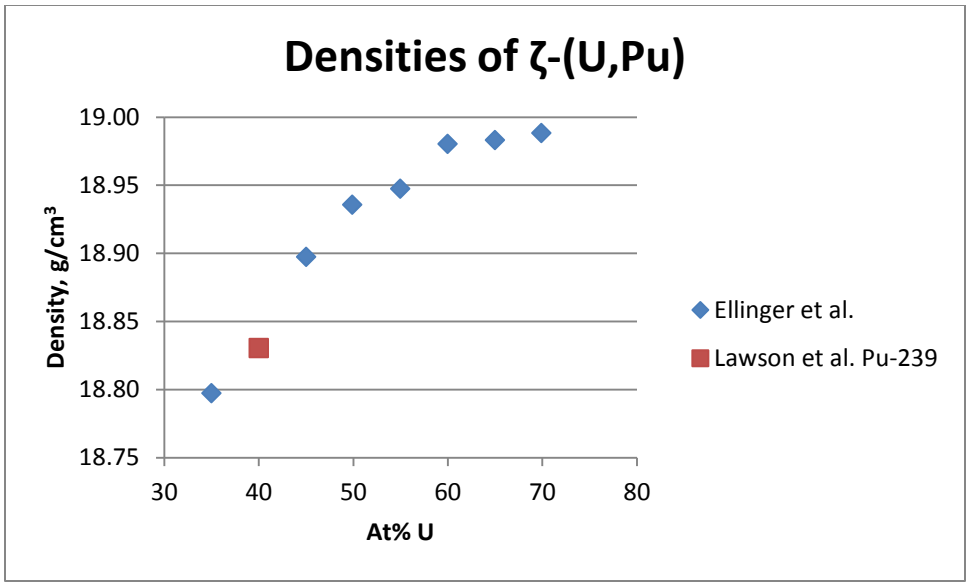

Figure 40. Calculated densities of ζ-(U,Pu) alloys assuming isotopes present are U-238 and Pu-239 based on structure data from references [192, 203].

2.3.1.4.3.6 Density of η-(U,Pu)

Data on the density of η-(U,Pu) is limited, and calculating densities from crystallographic information is complicated by the unknown crystal structure and variety of unit cells that have been suggested to describe it. Bochvar et al. [160] and Ellinger et al. [192] both suggested tetragonal unit cells with comparable volumes for alloys with 20-25 at% U; however, Bochvar et al. thought there were 56 atoms per unit cell, and Ellinger et al. thought there were 52 based on a density of 17.3 g/cm^3 deduced from dilatometer data.

As a result of this difference in the number of atoms per unit cell, the calculated density for an alloy with 25 at% U based on the unit cell of Ellinger et al. and assuming U-238 and Pu-239 is 17.14 g/cm^3, and the calculated density for an alloy with 20 at% U based on the unit cell of Bochvar et al. and the same isotopes is 18.47 g/cm^3. Further measurements of the density of this phase are clearly needed.

2.3.1.4.3.7 Densities of (U,Pu) Liquids

Researchers at Mound Laboratory measured the liquid densities of four U-Pu alloys with 77.6 to 94.5 at% Pu at temperatures from slightly above the liquidus to at least 845°C and provided least-squares fits to their experimental data [205]. Table 21 shows the lowest-temperature data for each alloy, the liquidus temperature, and the results of extrapolating the least-squares equations to the liquidus temperature determined by the Mound Laboratory researchers.

Table 21. Room-temperature densities of U-Pu liquids at the liquidus based on extrapolation of higher-temperature data from the specified temperature downwards to the liquidus.

At% Pu	Liquidus T (°C)	Density at liquidus (g/cm^3)
77.6	651	17.2
83.4	632	17.2
89.2	621	17.0
94.5	627	16.8

2.3.1.4.3.8 Densities of Solid U-Pu Alloys

Densities of a number of U-Pu alloys were reported by Ellinger et al. [192], by Boucher and colleagues [211, 212], and by Kittel et al. [193] (Figure 41). Ellinger et al. attributed the minimum in their data at ~10-15 at% U as due to retention of a relatively large fraction of (β-Pu), whose density is low relative to those of ζ-(U-Pu) and of other Pu phases. They also noted that the density of alloys with 10 at% U varied markedly as a result of thermal history: an alloy quenched from 300°C consisted of (α-Pu) and ζ-(U,Pu) and had a measured density of 18.55 g/cm^3, while an alloy with the same composition quenched from 250°C consisted of (β-Pu) and ζ-(U,Pu) and had a measured density of 17.94 g/cm^3.

Ellinger et al. described the samples used to determine their curve in Figure 41 as "as cast," which apparently means the samples were induction melted in a vacuum and allowed to solidify in the crucible. Weights of individual ingots varied between 3 and 40 g, and cooling rates were not specified.

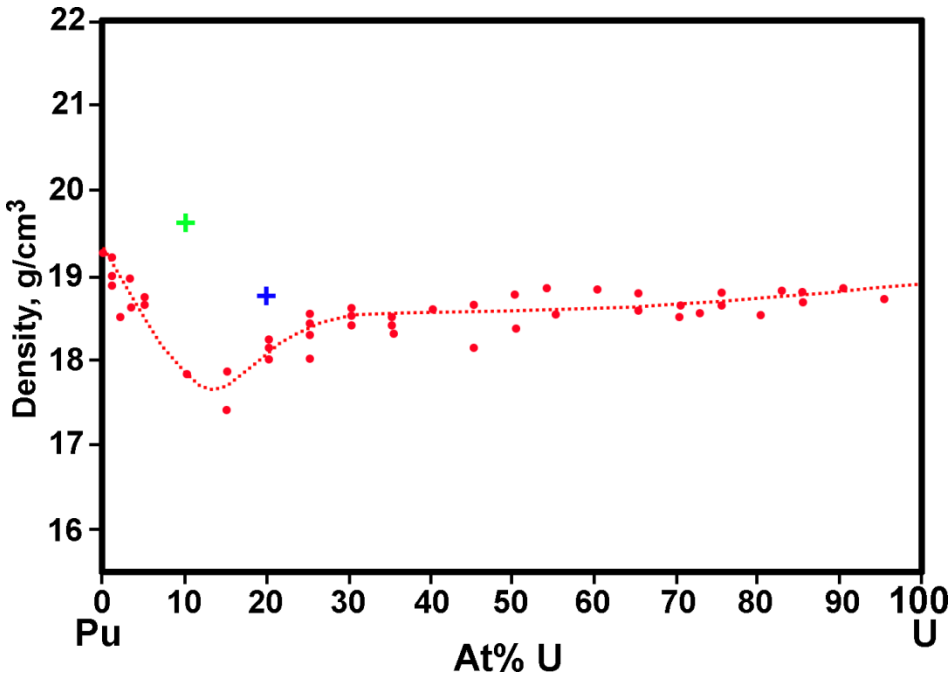

Figure 41. As-cast densities of U-Pu alloys. Red symbols and dotted line are from Ellinger et al. [192], blue "+" symbol is from Boucher and colleagues [211, 212], and green "+" symbol is from Kelman et al. [193].

2.3.1.4.4 Changes in Length Due to Phase Transitions

The (α-U) to (β-U) transformation was associated with a length increase ($\Delta L/L_0$) of 0.275%, and the (β-U) to (γ-U) transformation was associated with a length increase of 0.14%.

2.3.1.5 Thermal Conductivity and Related Properties

The only available thermal conductivity data for any U-Pu alloy was reported by Kelman et al. [193, 213 (Figure 7)]. Kittel et al. [209 (Table 17)] repeated these data except for the thermal conductivity at 200°C, which they appear to have erroneously carried over from an adjacent column of the same table.

According to Kelman et al., the thermal conductivity of an alloy with 10 wt% (10 at%) Pu is ~15% below that of the thermal conductivity of pure U. Since the thermal conductivity of pure U reported by Kelman et al. [193] is in good agreement with recent publications [63, 126], it seems likely that the thermal conductivity values for U-10Pu in Table 22 represent the actual behavior of U-10Pu.

Table 22. Thermal conductivity of U-10Pu [193].

T (°C)	Thermal Conductivity (W/m·K)
200	23.43
400	28.86
600	36.39
800	41.83

2.3.2 U-Pu-Np

2.3.2.1 Introduction

U-Pu-Np alloys have been proposed as nuclear fuels for long-life reactor cores and for production of ^{238}Pu as part of a Np-burning fuel cycle (e.g., [214, 215]). Despite this interest, the only available information about properties of these alloys considered in this Handbook is a calculated isothermal section at 923K.

2.3.2.1.1 Phases and Phase Transformations

Kurata [38 Figure 29] published a calculated isothermal section of the U-Pu-Np system at 923 K, based in part on unpublished data showing compositions of phases in an alloy whose bulk composition included ~10 at% Np, 25% Pu, and 65% U (Figure 42). The phase identifications in Figure 42 are tentative, and were added to the original figure based on comparison to binary phase diagrams. The identification of β-U is particularly tentative, as the temperature of Figure 42 is close to the phase-transformation temperature between α-U and β-U.

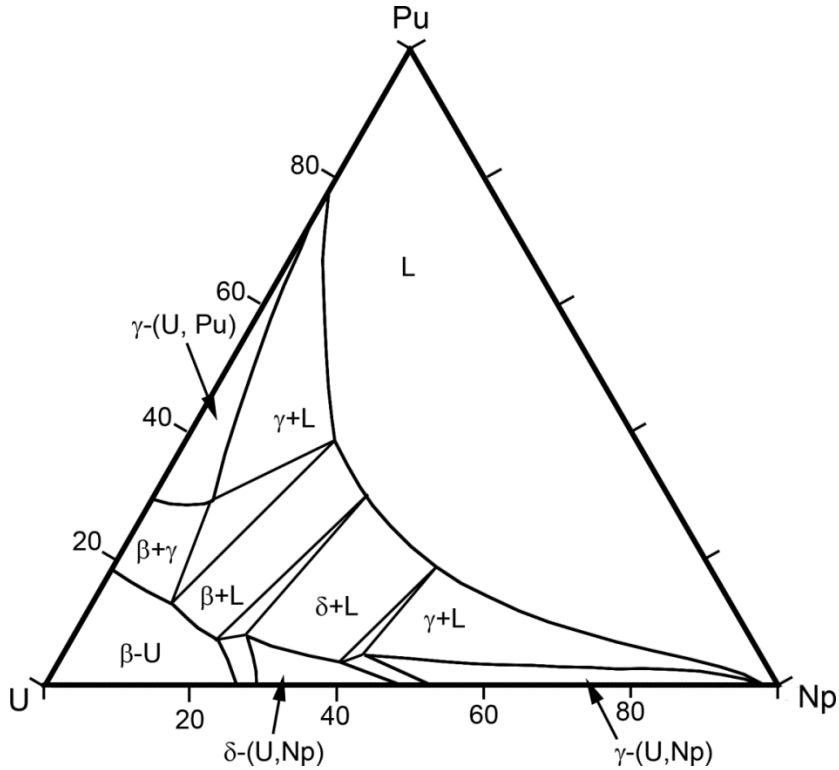

Figure 42. Calculated U-Np-Pu phase diagram [38], with phase identifications suggested by comparison to binary phase diagrams. β refers to β-U solid solutions, δ refers to δ-(U,Np) solid solutions, and γ refers to γ-(U,Np) or γ-(U,Pu) depending on composition.

2.3.3 U-Pu-Am

2.3.3.1 Introduction

Although some information on the U-Pu, U-Am, and Pu-Am binary systems is presented in Section 2.3.1 of this document and Sections 3.2 and 3.5 of reference [5], there is apparently no published experimental data on ternary phases in the U-Pu-Am system. The system was modeled by Ogawa [195], Kurata [216], and Perron et al. [199]. All three models agree that incorporation of Pu increases the mutual solubility of high-U and high-Am liquids. However, there are significant differences between the isothermal sections produced by the models at lower temperatures. Some of these differences probably reflect underlying differences in the phase diagrams for the U-Am and Pu-Am binary systems, neither of which is well known. In the almost total absence of experimental data, the isothermal sections of Perron et al. may be the best available representation of the U-Pu-Am system.

No information about heat capacity, thermal expansion, or thermal conductivity of U-Pu-Am alloys is available.

2.3.3.1.1 Phase Diagrams

No experimentally determined phase diagrams of the U-Pu-Am system are available. Ogawa used “a regular solution model with interaction parameters derived from the Brewer valence bond theory” to calculate a liquidus projection and an isothermal section at 1200 K [195]. This model considered only the liquid, fcc, and bcc phases.

Kurata developed a CALPHAD model for the U-Pu-Am system using a consistent database of thermodynamic properties for the U-Np-Pu-Am-Fe-Zr system [34, 216]. This model included low-temperature phases not considered in Ogawa’s model. Kurata published an isothermal section at

897 K (624°C) calculated using this model [38 (Figure 30), 216 (Figure 8)]. Perron et al. calculated additional isothermal sections at 1500, 1200, 900, 600, and 300 K using the thermodynamic data published by Kurata [199 (Figure 7)].

Perron et al. developed a model using CALPHAD for thermodynamic calculations, supplemented by *ab initio* electronic-structure calculations to determine needed parameters in the absence of experimental data. They used this model to calculate isothermal sections at 1500, 1200, 900, 600, and 300 K. In view of uncertainties about the existence of a continuous solid solution between γ-Am and ε-Pu (Section 3.5 of reference [5]), Perron et al. included two variations: a preferred model with a solid solution and an alternate model with a miscibility gap. Comparison of the isothermal sections from these variations shows little difference except in high-Pu compositions, and only the model preferred by Perron et al. is presented here.

Figure 43 shows isothermal sections at 1200 K calculated from the three models. Comparison with binary phase diagrams indicates that the fcc phase is a solid solution that includes β-Am and that the bcc phase(s) are ternary modifications of the (γ-U, ε-Pu) solid solution from the U-Pu binary system and (in the sections from the models of Ogawa and of Perron et al.) the (γ-Am, ε-Pu) solid solution from the Pu-Am binary system. The Ogawa model shows far more miscibility in ternary compositions than the models of Kurata and Perron et al., and also suggests that addition of Pu increases miscibility in the bcc phase. The isothermal sections from the models of Kurata and Perron et al. are topologically similar, although specific phase boundaries vary significantly.

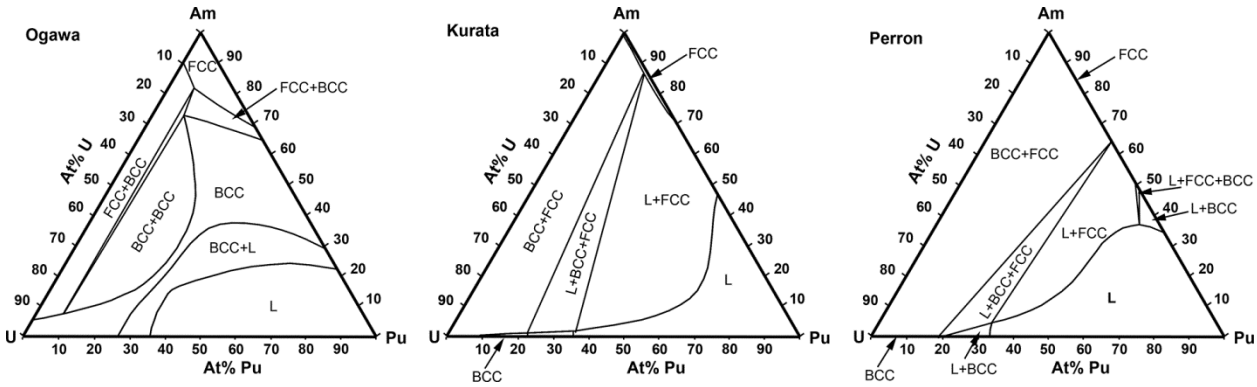

Figure 43. Calculated isothermal sections at 1200 K based on the models of Ogawa [195], Kurata [216] (as calculated by Perron et al. [199 (Figure 7)]), and the preferred model of Perron et al. [199 (Figure 8)].

Figure 44 shows isothermal sections at 900 K calculated from the models of Kurata and Perron et al. (The Ogawa model cannot be used at this temperature because it considers only liquid, fcc, and bcc phases.) Comparison with binary phase diagrams indicates that the fcc phase is the (β-Am, δ-Pu) solid solution with a low concentration of Pu, the bcc phase is the (γ-U, ε-Pu) solid solution with a low concentration of Am, and η is the η-(U,Pu) solid solution with a negligible concentration of Am. The isothermal sections in Figure 44 are generally similar to one another except in high-Pu compositions, where the phase diagram calculated by Perron et al. from Kurata's model does not match the phase diagram published by Kurata [216 Figure 8] and neither of the isothermal sections published by Perron et al. is entirely consistent with the commonly accepted U-Pu phase diagram (Section 2.3.1).

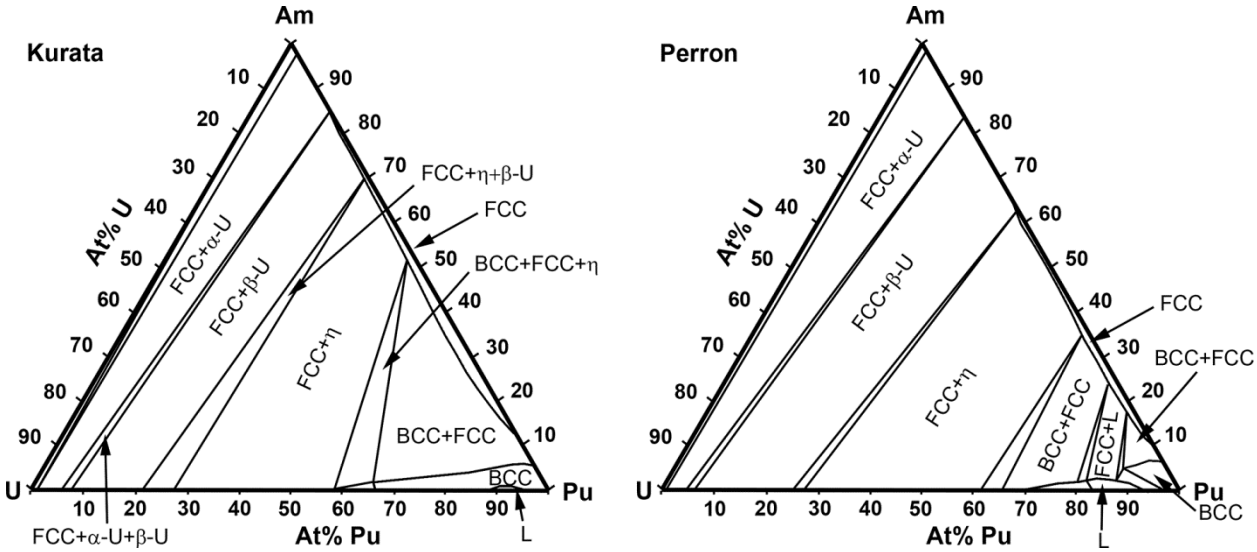

Figure 44. Calculated isothermal sections at 900 K based on the model of Kurata [216] (as calculated by Perron et al. [199 (Figure 7)]) and the preferred model of Perron et al. [199 (Figure 8)].

Figure 45 shows isothermal sections at 600 K calculated from the Kurata and Perron models. Comparison with binary phase diagrams indicates that the fcc phase is the (β-Am, δ-Pu) solid solution with a low concentration of Pu, the dhcp phase is α-Am with low concentrations of U and of Pu, η is the η-(U,Pu) solid solution with a negligible concentration of Am, and ζ is the ζ-(U,Pu) solid solution with a negligible concentration of Am. Although the isothermal sections from the Kurata and Perron models both indicate very limited miscibility in this system, definitions of two- and three-phase fields differ significantly between the two models.

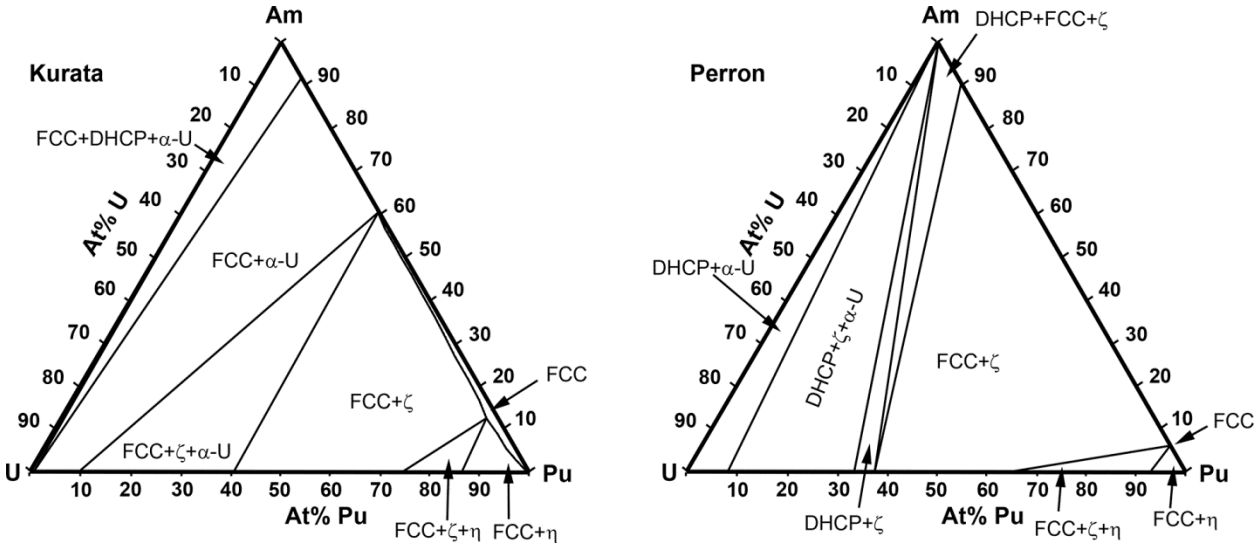

Figure 45. Calculated isothermal sections at 600 K based on the model of Kurata [216] (as calculated by Perron et al. [199 (Figure 7)]) and the preferred model of Perron et al. [199 (Figure 8)].

Figure 46 shows isothermal sections at 300 K calculated from the models of Kurata and Perron et al. Comparison with binary phase diagrams indicates that the fcc phase is the (β-Am, δ-Pu) solid solution with a low concentration of Pu, the dhcp phase is α-Am with low concentrations of U and Pu, and ζ is the ζ-(U, Pu) solid solution with a negligible concentration of Am. Although the isothermal sections both

indicate very low miscibility in this system, definitions of two- and three-phase fields differ significantly between the two models.

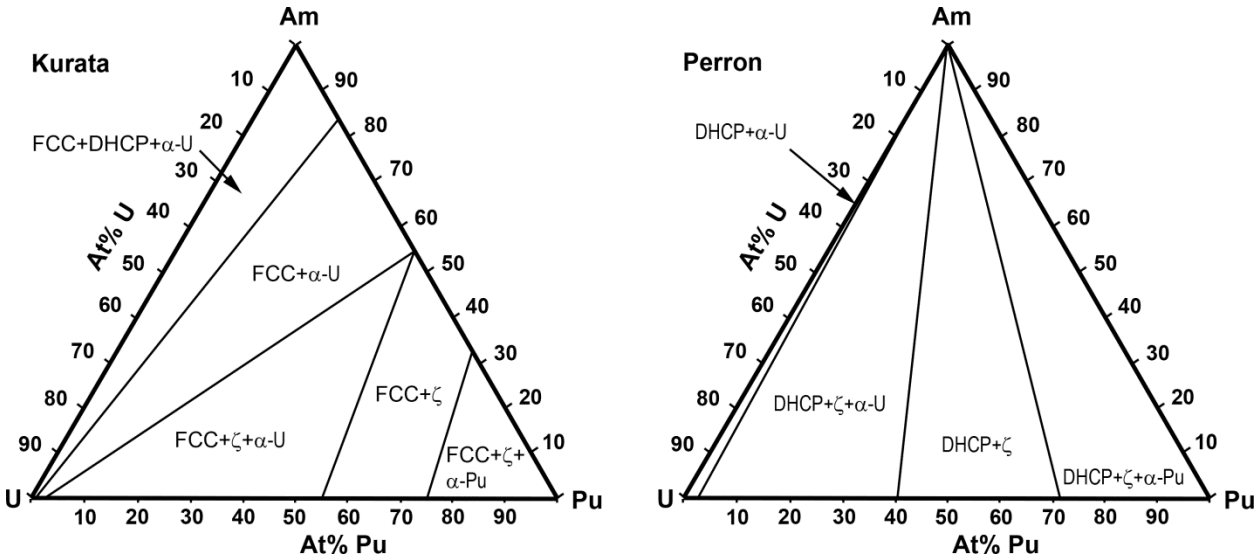

Figure 46. Calculated isothermal sections at 300 K based on the model of Kurata [216] (as calculated by Perron et al. [199 (Figure 7)]) and the preferred model of Perron et al. [199 (Figure 8)].

2.4 Alloys Based On U-Pu-Zr, including U-Pu-Zr and U-Pu-Zr Alloys with Minor Actinides (Np, Am, Cm), Rare-Earth Elements (La, Ce, Pr, Nd, Gd), and Y

2.4.1 U-Pu-Zr

2.4.1.1 Introduction

U-Pu-Zr alloys have been investigated extensively. At least 50 measurements of sub-solidus phase transformation temperatures [149, 166, 205, 217-219] and 75 determinations of phases in annealed samples [77, 81, 211, 212] have been reported, although many of these measurements are described as "preliminary."

Only two partial phase diagrams based on experimental data have been published. Researchers at Mound Laboratory suggested a sequence of possible solid-state transformations and presented a single figure showing transformations from a the high-temperature bcc solid solution to lower temperature phases [166, 220]. Slightly later, O'Boyle and Dwight considered all of the available data (apparently including that from Mound Laboratory) and suggested an alternate sequence of possible transformations and a series of isothermal sections at temperatures between 500 and 700°C [81]. The isothermal sections of O'Boyle and Dwight remain the most complete experimentally-based depiction of the U-Pu-Zr phase diagram and are widely used to assist in phase identifications for other kinds of data.

Experimental research since the publication of the O'Boyle and Dwight phase diagram is limited, but includes phase analyses from high-temperature neutron diffraction of U-8Pu-10Zr and U-19Pu-10Zr (wt%) [77, 78], measurements of the liquidus and solidus of U-13Pu-16Zr and U-12Pu-29Zr (at%) [42], measurements of phase transition temperatures in seven alloys [1, 2, 149], observations of constituent redistribution in samples of U-19Pu-10Zr (wt%) as a result of thermal gradients [218, 221], identification of phases in annealed U-23Pu-9Zr (wt%) from electron-diffraction data [222], and comparison of microstructures in as-cast and annealed samples [223].

There is general agreement that all of the phases in the U-Pu-Zr system at temperatures above ~500°C are solid solutions of phases in the U-Pu, U-Zr, and Pu-Zr systems. The first phase to crystallize for all U-Pu-Zr ternary compositions is a bcc solid solution between γ-U, ε-Pu, and β-Zr, which transforms to a number of lower-temperature phases by solid-state reactions. These reactions are characteristically slow, and annealing times of 25 days at 700°C and five months at 590°C were required to obtain grains large enough for microprobe analyses [81]. Thus, it is likely that none of the samples were at equilibrium and that characterization results are influenced by the thermal histories of specific samples.

Most of the available data on heat capacities of U-Pu-Zr alloys are from DSC data collected by researchers at INL from six alloys. The incremental enthalpy and heat capacity of a U-15Pu-10Zr (wt%) alloy based on drop-calorimetry data have also been reported by other researchers. Although the reported heat capacities show some variability, there are no obvious systematic relationships between heat capacities and compositions, and all of the reported heat capacities are generally similar to the heat capacity of U.

Only two measurements of thermal expansion coefficients for U-Pu-Zr alloys have been reported, although both have been widely repeated. Densities of as-cast U-Pu-Zr alloys vary but tend to decrease with increasing concentrations of Zr.

Despite reports of "catastrophic" events (including density losses of almost 0.7 g/cm^3 and samples catching fire) at temperatures as low as ~650-750°C during thermal cycling experiments [211, 217], systematic investigations indicate that thermal cycling does not cause a significant change in density. Thermal cycling phenomena are strongly dependent on the starting microstructure, particularly centerline porosity and preferred orientation [217], which were not specified in the thermal-cycling experiments.

Data on thermal conductivity of U-Pu-Zr alloys are limited to compositions with ~15-20 wt% Pu and ~3.4-14 wt% Zr. All of the available quantitative data were originally reported before ~1970. Although the original measurements show significant variation, they indicate that thermal conductivity increases with temperature for a given composition and suggest that increasing the concentration of Pu may lower the thermal conductivity. The thermal conductivity of any given sample is microstructure-dependent because of temperature drops at phase boundaries [224], and attempts to determine unique values for the thermal conductivities of U-Pu-Zr alloys as functions of composition and temperature alone may be unsuccessful.

None of the available empirical equations is an accurate representation of all of the experimental measurements of thermal conductivity of U-Pu-Zr alloys with 15-20 wt% Pu and 10-15 wt% Zr. Although it has been suggested that the thermal conductivity of U-Pu-Zr alloys can be modeled using a modification of the Bruggeman method [126], the large number of empirical fitting parameters make it difficult to use this model, and it may be appropriate to develop new equations to fit thermal conductivity values selected for specific applications.

Recent research on the U-Pu-Zr system has emphasized modeling. Landa and colleagues developed density functional theory models [55], Wenzhong and Unal [225] and Galloway et al. [226] addressed ways to incorporate U-Pu-Zr phase diagrams into the MOOSE-BISON fuel performance code, and Kurata [34, 197] compiled a thermodynamic database and used it to calculate isothermal diagrams that are in reasonably good agreement with the isothermal sections of O'Boyle and Dwight. Researchers at Idaho National Laboratory have recently published new data on microstructures in U-Pu-Zr alloys [222, 223, 227] and a review of fuel-cladding chemical interaction (FCCI) [228].

2.4.1.2 Phases and Phase Transitions

2.4.1.2.1 Phases

All of the known phases in the U-Pu-Zr ternary system are solid solutions of phases in the U-Pu, U-Zr, and Pu-Zr binary systems. Information about solid solutions that include all three elements is very

limited, and it is often necessary to assume that the properties of these phases are similar to those in binary alloys.

Generally accepted phases in U-Pu-Zr alloys are:

- (α-U): Solid solution of α-U (Section 2.1.2.1 of reference [5]) that can contain up to ~15 at% Pu and a small amount of Zr [81]. The only available information about the lattice parameters of a phase with the α–U structure in any U-Pu-Zr alloy was obtained by Mueller et al. using high-temperature neutron diffraction of U-8Pu-10Zr (wt%). Lattice parameters of this phase differed from those of α-U by ~0.04 Å at room temperature, with differences between the two phases decreasing with increasing temperature [77, 78].
- (β-U): Solid solution of β-U (Section 2.1.2.1 of reference [5]) that can contain up to ~20 at% Pu and a small amount of Zr [81]. No measurements of lattice parameters of β-U solid solutions in U-Pu-Zr alloys are available.
- γ-(U,Pu,Zr): Body-centered cubic (space group $Im\bar{3}m$) solid solution between γ-U, β-Zr, and ε-Pu (Sections 2.1.2.1, 2.3.2.1, and 2.9.2.1 of reference [5], respectively). This phase is sometimes referred to as "gamma," "γ,", or "γ phase." The reaction that leads to the separation of γ into γ_1 and γ_2 in U-Zr alloys (section 2.1.1.2.1.1.4) extends to compositions with up to ~17 at% Pu [81].

  In the absence of experimental data, it is tempting to assume that lattice parameters of solid solutions of γ-U, β-Zr, and ε-Pu can be approximated by interpolation between the lattice parameters of the pure phases. However, this assumption is inconsistent with measurements of lattice parameters in (β-Zr, ε-Pu) solid solutions (Section 2.2.1.2.1). Lattice parameters of (γ–U, β-Zr) solid solutions vary linearly with composition (Section 2.1.1.2.1.1.4).
- (α-Zr): Solid solution of α-Zr (Section 2.9.2.1 of reference [5]). Consideration of data from U-Zr and Pu-Zr alloys (Sections 2.1.1.2.1.1.2 and 2.2.1.2.1) suggests that the maximum equilibrium concentrations of U and Pu in α-Zr may be ~0.5 at% and ~13 at%, respectively. No measurements of lattice parameters of equilibrium α-Zr in U-Pu-Zr alloys are available. Ellinger and Land reported that both the *a* and *c* lattice parameters of α-Zr in Pu-Zr alloys increase with the concentration of Zr [156], while Marples reported that *c* increased and *a* was not significantly affected [154].

  High-Zr inclusions are commonly observed in U-Pu-Zr alloys with compositions that apparently have too little Zr to form stable α-Zr or β-Zr (e.g., [42, 81, 213, 229]). Some analyses show that these inclusions contain a few percent of U and Pu (e.g., [81]), while others indicate that no actinides are present (e.g., [213]). High-actinide sub-inclusions have been reported within the high-Zr inclusions [42]. The volume fraction of the high-Zr inclusions increases with the oxygen content in the alloy [81, 213], leading to the idea that the inclusions are "oxygen-stabilized α-zirconium." This identification is inconsistent with the data of Leibowitz et al., who believed that the high-Zr inclusions in their U-Pu-Zr alloys were liquid below 1500°C and might represent a previously unknown phase [42 (p. 151)]. Further research is needed to understand these high-Zr inclusions.
- (δ-Pu): Solid solution of δ-Pu (Section 2.3.2.1 of reference [5]). Consideration of data from Pu-Zr and U-Pu alloys (Sections 2.2.1.2.1 and 2.3.1.2.1) suggests that the maximum equilibrium concentrations of Zr and U in δ-Pu solid solutions may be ~70 at% and ~0.3 at%, respectively. No information about properties of δ-Pu solid solutions in U-Pu-Zr alloys is available.
- (α-Pu), (β-Pu), (γ-Pu), or (δ′-Pu): Solid solutions of the corresponding Pu phases (reference [5] Section 2.3.2.1). Consideration of data from Pu-Zr and U-Pu alloys (Sections 2.2.1.2.1 and 2.3.1.2.1) suggests that maximum Zr and U contents in these phases are low.

- η-(U,Pu): Solid solution of η-(U,Pu) (Section 2.3.1.2.1). O'Boyle and Dwight reported that solubility of Zr in this phase is limited [81]. No other information about this phase is available from U-Pu-Zr alloys.
- ζ-(U,Pu): Solid solution of ζ-(U,Pu) (Section 2.3.1.2.1). O'Boyle and Dwight indicate that the maximum Zr content in this phase is ~5 at% Zr, and that the solubility of Zr decreases at lower temperatures [81]. In contrast, researchers from Mound Laboratory believed that this phase can contain up to 9 at% Zr at 675°C and that the solubility of Zr increases at lower temperatures to a maximum of ~20 at% at 640°C [220]. O'Boyle and Dwight reported the lattice parameter of ζ-(U,Pu) in a U-30Pu-2.5Zr (at%) alloy as 10.658 Å, which is ~0.02% larger than the value of 10.651 Å reported by Ellinger et al. [192] from a U-30Pu (at%) alloy. O'Boyle and Dwight interpreted this difference as indicating that the lattice parameter of ζ-(U,Pu) solid solutions increased with increasing concentrations of Zr; however, consideration of the scatter in the reported lattice parameters of ζ-(U,Pu) in U-Pu alloys with different compositions (Figure 35) suggests that a difference of 0.02% may be smaller than the experimental errors in the measurements.
- (δ-UZr_2): Solid solution of (δ-UZr_2) and perhaps (κ-$PuZr_2$) (Sections 2.1.1.2.1.1.5 and 2.2.1.2.1). Experimental results reported by O'Boyle and Dwight [81] indicated that the maximum concentration of Pu in this phase is at least 20 at% in U-Pu-Zr alloys with 70 at% Zr, and it has been suggested that there is a continuous solid solution between δ-UZr_2 and the isostructural phase κ-$PuZr_2$ (e.g., [81, 230, 231]).

2.4.1.2.2 Phase Transitions

2.4.1.2.2.1 Liquidus and Solidus

Measured solidus and liquidus temperatures in U-Pu-Zr alloys have been reported by a number of research groups [42, 149, 193, 205, 209, 213, 217]. Other researchers were unable to measure solidus temperatures because these temperatures were above the high-temperature limits of their instruments (e.g., [211, 219]). Many of the measurements were considered preliminary, and many represent temperatures well above those of the standards used for instrument calibration. Some values are repeated in what appear to be multiple presentations of the same measurements. Figure 47 and Figure 48 show the measured liquidus and solidus temperatures, which are included in Table 23 and Table 24. Data for an alloy whose nominal composition are listed as U-15Pu-15Zr (at%) and U-17.1Pu-3.4Zr (wt%) in reference [213] are not included because the compositions in weight and atomic percent are inconsistent, and because other early references that generally repeat the same measurements list this as a U-Pu-Ti alloy [193, 209].

Researchers at Mound Laboratory measured solidus temperatures from seven U-Pu-Zr alloys with at least 70 at% Pu and liquidus temperatures from four [205, 232]. These temperatures are not included here because the samples were wrapped in Ta foil, and Mound Laboratory reported that data from other samples wrapped in Ta foil showed evidence that hydrogen produced in the furnace had penetrated the foil and contaminated the samples [205]. Solidus temperatures for Pu-Zr alloys in the Mound Laboratory data are comparable to those accepted by other researchers (e.g.,[151]), although liquidus temperatures appear anomalously high for alloys with more than ~5 at% Zr (as noted by Leibowitz et al. [233]). Solidus and liquidus temperatures for U-Pu alloys in the Mound Laboratory data are within ~30°C of those accepted by other researchers (e.g., [186, 190]. In the absence of other experimental data, it may be necessary to use the Mound Laboratory solidus and liquidus temperatures when information about high-Pu compositions is needed.

Liquidus and solidus temperatures in binary U-Zr and Pu-Zr alloys increase with increasing concentrations of Zr (Sections 2.1.1.2.2.1 and 2.2.1.2.3). The liquidus and solidus temperatures of U-Pu alloys decrease to a minimum at ~12 at% U and 610°C and increase monotonically with increasing concentrations of U above that value (Section 2.3.1.2.3). All U-Pu-Zr alloys crystallize with a

body-centered cubic structure, forming a continuous solid solution (Section 2.4.1.2.1). Thus, it seems likely that both the liquidus and solidus temperatures of U-Pu-Zr alloys increase from the melting temperature of Pu (640°C) to that of Zr (1854°C) except in compositions close to the minimum in the U-Pu binary.

Consideration of the data in Figure 47 shows that the measured liquidus temperatures are not consistent with this expectation, even after consideration of the reported errors. Most of the data were collected using DTA, and the reported values were above the temperatures of common calibration standards and almost certainly at the upper temperatures limits of the instruments. Measurements using dilatometry are likely to have experienced challenges due to partial melting of the sample at temperatures above the solidus. Thus, it seems reasonable to assume that the actual errors in liquidus measurements may have been significantly larger than the reported error estimates.

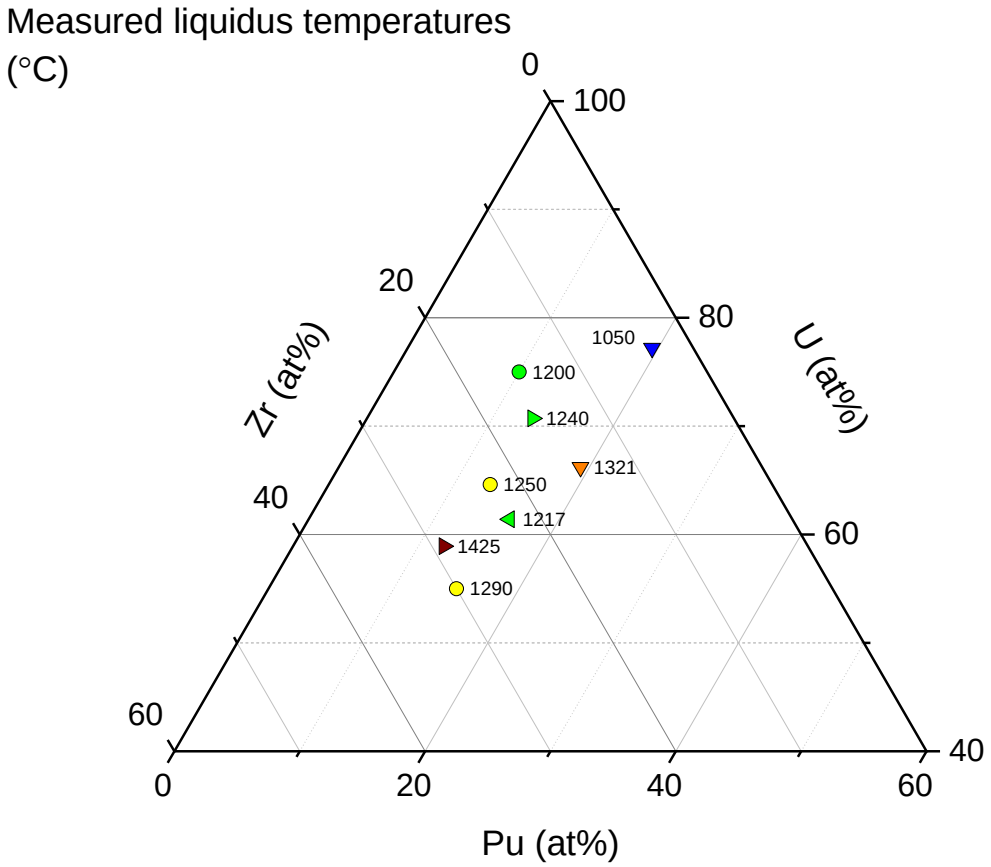

Figure 47. Measured liquidus temperatures for U-Pu-Zr alloys with at least 40 at% U (Table 23). Shapes indicate sources of data: circles are from references [193, 209, 213], right-pointing triangles are from reference [217], left-pointing triangle is from reference [149], and downward-pointing triangles are from reference [42]. Colors indicate temperature ranges: blue is 1050-1100°C, light green is 1200-1250, yellow is 1250-1290, orange is 1300-1350, and brown is 1400-1450. Numbers next to data points are temperatures.

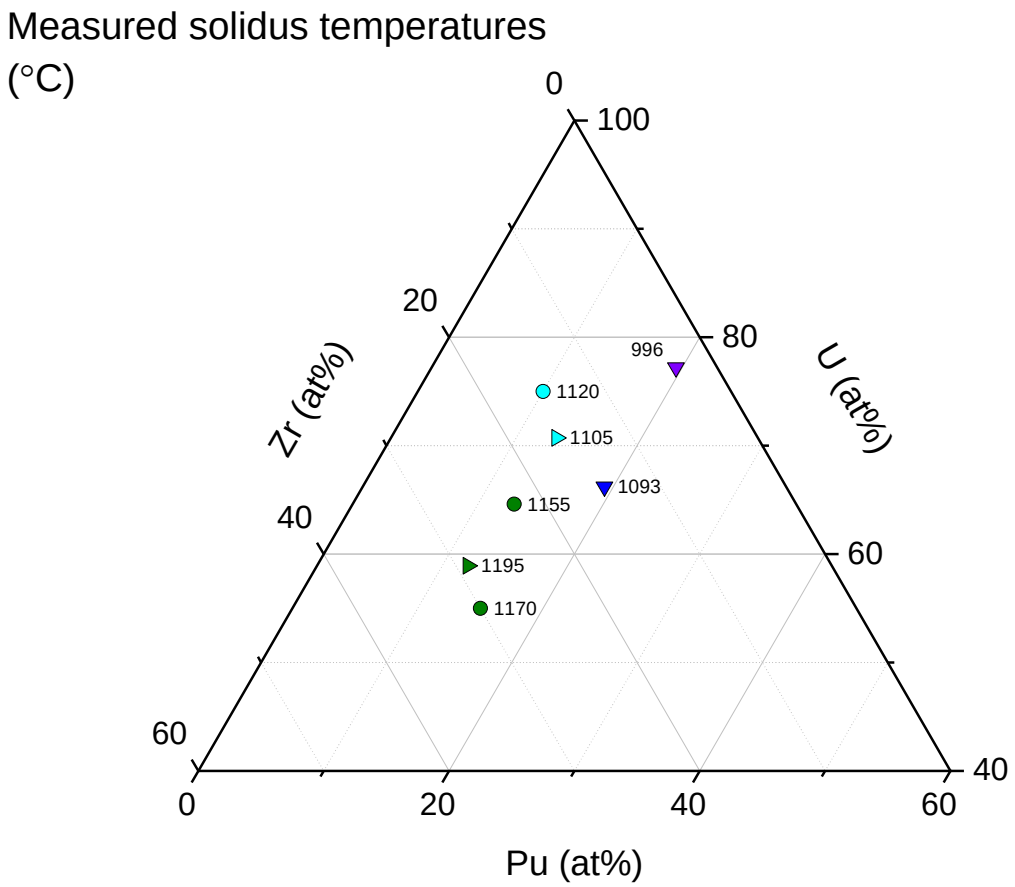

Figure 48. Measured solidus temperatures for U-Pu-Zr alloys with at least 40 at% U (Table 23). Shapes indicate sources of data: circles are from references [193, 209, 213], right-pointing triangles are from reference [217], and downward-pointing triangles are from reference [42]. Colors indicate temperature ranges: purple is < 1000°C, blue is 1050-1100, turquoise is 1100-1150, and green is 1150-1200. Numbers next to data points are temperatures.

Figure 48 shows that the measured solidus temperatures generally increase with increasing proportions of Zr, as expected. Although new measurements using high-purity samples with a wider range of compositions are desirable, it seems likely that any revisions required by new measurements of samples with compositions similar to the currently available data will be relatively small.

With the exception of the questionable Mound Laboratory data for high-Pu alloys, measurements of liquidus and solidus temperatures for other U-Pu-Zr alloys are lacking. Three approaches to estimating solidus and liquidus temperatures have been suggested. In the earliest approach, Leibowitz et al. [42] developed thermodynamic models for the liquidus and solidus. Later analyses by Kurata [197] were used by Ogata [48, 49] to derive analytical expressions for liquidus and solidus temperatures for compositions with less than 80 at% Zr and more U than Pu. These expressions match experimental data on the U-Zr and U-Pu-Zr systems [42, 105, 193, 217] to within 60°C for the solidus and 130°C for the liquidus. Somewhat later, Kurata [34, 38] calculated liquid and solidus temperatures using CALPHAD, and obtained agreement with the experimental data in references [217] and [42] to within ±20°C.

Figure 49, Figure 50, Table 23, and Table 24 compare experimental measurements with liquidus and solidus temperatures calculated using the three models. Solidus and liquidus temperatures from the

models generally agree with each other better than they do with the data for compositions with more than ~50 at% U, but differ by up to ~100°C for some compositions. The currently available data are not adequate to determine which model is best, but suggest caution in relying on thermodynamic models based on the currently available data.

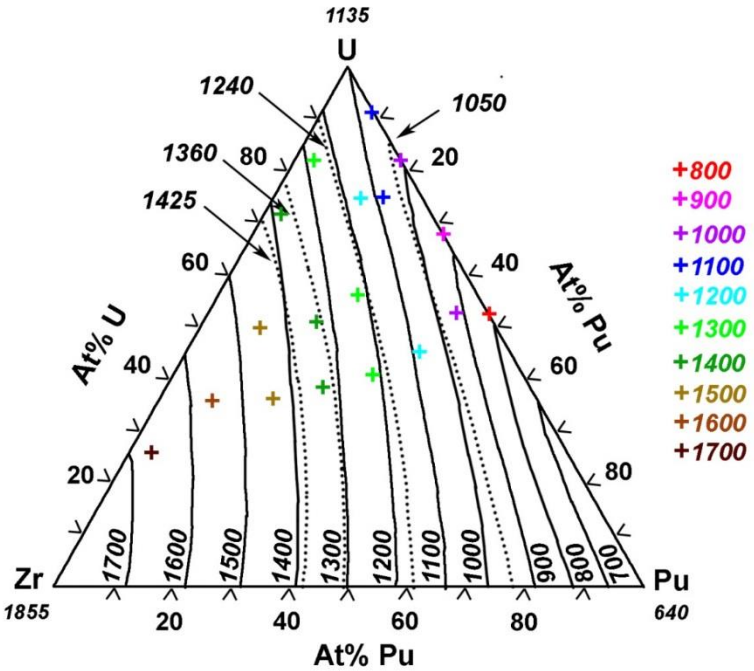

Figure 49. Liquidus temperatures (°C) from models of Leibowitz et al. [42] (solid lines), Kurata [38] (dotted lines), and Ogata [48] (colored symbols showing examples of calculated points, with each color indicating a different temperature). Reference [38] also includes a curve corresponding to a temperature of 1321°C, which is not shown here for clarity. Melting temperatures of U, Pu, and Zr are shown for comparison.

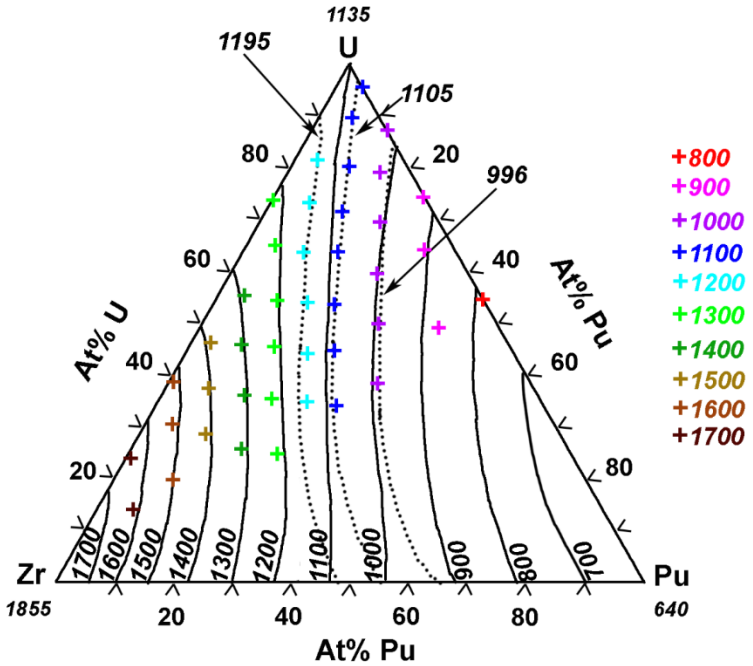

Figure 50. Solidus temperatures (°C) from models of Leibowitz et al. [42] (solid lines), Kurata [38] (dotted lines), and Ogata [48] (colored symbols showing examples of calculated points).

Table 23. Comparison of experimental and calculated liquidus temperatures (°C) for U-Pu-Zr alloys.

Composition (wt%)	**Composition (at%)**	**Liquidus Temperature (°C)**			
		Experimental [reference]	**Ogata [48]**	**Kurata [38]**	**Leibowitz et al. [42]**
U-15Pu-6.8Zr	U-13Pu-16Zr	1240±20 [217]	1281	~1250	1268
U-15Pu-13.5Zr	U-12Pu-29Zr	1425±20 [217]	1413	~1390	1394
U-20Pu-1.3Zr	U-19.5Pu-3.3Zr	1050±4 [42]	1063	~1060	1060
U-22Pu-6Zr	U-19.3Pu-14.5Zr	1321±23 [42]	1246	~1230	1216
U-11.1Pu-6.3Zr	U-10Pu-15Zr	1200 [193, 209, 213]	1280	~1250	~1225
U-15Pu-10Zr	U-12.9Pu-22.5Zr	1250 [193, 209, 213]	1353	~1330	~1310
U-18.5Pu-14.1Zr	U-15Pu-30Zr	1290 [193, 209, 213]	1413	~1380	~1350
U-19Pu-10Zr	U-16Pu-22.6Zr	1217±10 [149]	1346	~1350	~1310

Table 24. Comparison of experimental and calculated solidus temperatures (°C) for U-Pu-Zr alloys.

Composition (wt%)	**Composition (at%)**	**Solidus Temperature (°C)**			
		Experimental [reference]	**Ogata [48]**	**Kurata [38]**	**Leibowitz et al. [42]**
U-15Pu-6.8Zr	U-13Pu-16Zr	1105±10 [217]	1098	~1105	1121
U-15Pu-13.5Zr	U-12Pu-29Zr	1195±10 [217]	1213	~1195	1187
U-20Pu-1Zr	U-19.5Pu-3.3Zr	996±5 [42]	961	<996	1012
U-22Pu-6Zr	U-19.3Pu-14.5Zr	1093±8 [42]	1038	~1040	1071
U-11.1Pu-6.3Zr	U-10Pu-15Zr	1120 [193, 209, 213]	1124	~1110	~1095
U-15Pu-10Zr	U-12.9Pu-22.5Zr	1155 [193, 209, 213]	1154	~1150	~1115
U-18.5Pu-14.1Zr	U-15Pu-30Zr	1170 [193, 209, 213]	1195	~1190	~1140

2.4.1.2.2.2 Solid-state Transitions

Four approaches have been used to understand solid-state phase transitions in U-Pu-Zr alloys: measurement of phase-transition temperatures, identification of coexisting phases in annealed samples, identification of coexisting phases using high-temperature diffraction, and identification of zones representing different phase assemblages that developed as a result of thermal gradients in thermotransport experiments.

2.4.1.2.2.2.1 Transition Temperatures

Original measurements of temperatures of phase transitions occurring below the solidus in U-Pu-Zr alloys have been reported by researchers at CEA [211], Argonne National Laboratory [219], Mound Laboratory [166, 205], Los Alamos National Laboratory [217], and Idaho National Laboratory, and as part of the METAPHIX Programme [149] (Figure 51). The reported values are summarized in Table 25.

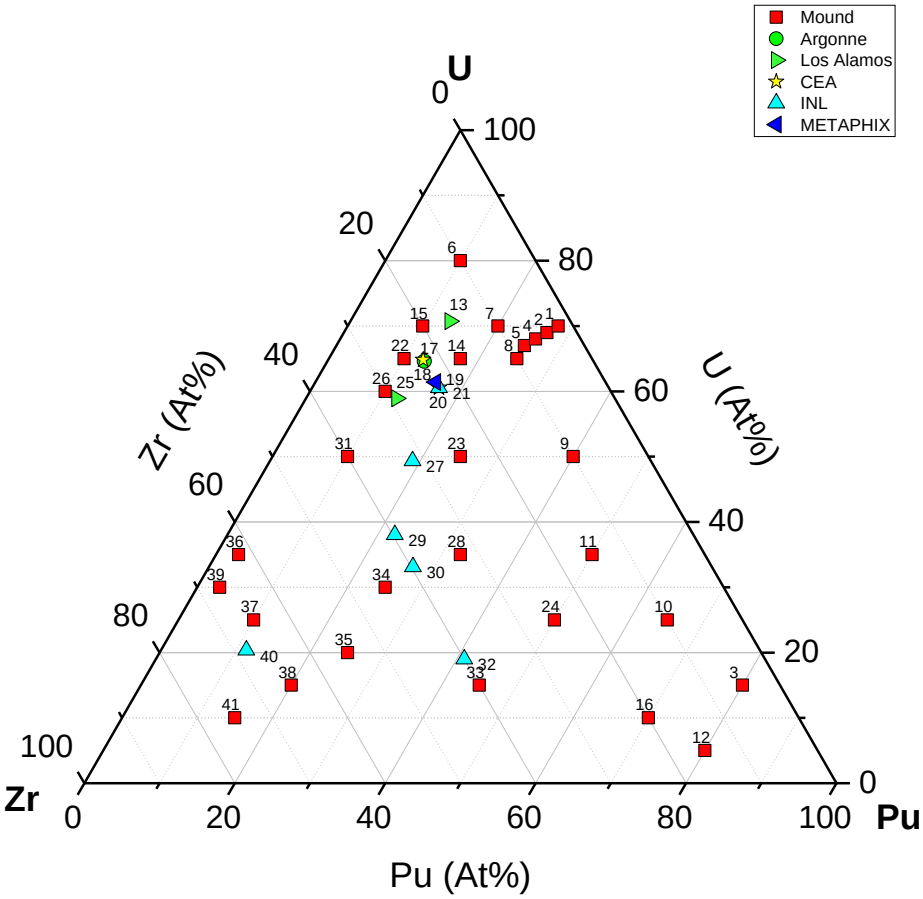

Figure 51. Compositions of U-Pu-Zr alloys with measurements of sub-solidus phase-transition temperatures, with point numbers from Table 25. Data are from Mound Laboratory [166], Argonne National Laboratory [219], Los Alamos National Laboratory [217], CEA [211], Idaho National Laboratory, and the METAPHIX programme [149]. Colors and symbols indicate data from different laboratories.

The vast majority of the measurements are in reports from national laboratories in the United States and have not been published in the peer-reviewed literature. Most of these measurements were described as preliminary. Descriptions of experimental methods are commonly incomplete or contradictory, and information about actual sample composition and purity is rarely provided. A number of researchers reported that some peaks in their DTA data probably represented more than one phase transition.

In the absence of a well-defined phase diagram for the U-Pu-Zr system, attempts to assess the consistency of the data in Table 25 by comparing transition temperatures of "similar" compositions are likely to be misleading. It is encouraging to note that phase-transition temperatures in U-15Pu-10Zr (wt%) by Argonne National Laboratory in the USA and by CEA in France agree to within a few degrees. The similarity between transition temperatures reported by the METAPHIX Programme and by CEA for alloys with 19-20 wt% Pu and 10 wt% Zr is also encouraging, although less close. However, further measurements with high-purity samples are needed.

Table 25. Measured sub-solidus transition temperatures in U-Pu-Zr alloys, sorted by increasing at% Zr.

Point Number	Composition (at%)	Composition (wt%)	Highest T (°C)	Second Highest T (°C)	Third Highest T (°C)	Reference	Notes
1	U-28Pu-2Zr	U-28.9Pu-0.8Zr	695	645	—	[166]	a
2	U-27Pu-4Zr	U28.2Pu-1.6Zr	690	675	665	[166]	a
3	U-80Pu-5Zr	U-83.2Pu-1.9Zr	560	515	—	[166]	a
4	U-26Pu-6Zr	U-27.5Pu-2.4Zr	690	675	655	[166]	a
5	U-25Pu-8Zr	U-26.8Pu-3.2Zr	675	—	—	[166]	a
6	U-10Pu-10Zr	U-10.9Pu-4.1Zr	668	660	600	[166]	a
7	U-20Pu-10Zr	U-21.7Pu-4.1Zr	675	582	—	[166]	a
8	U-25Pu-10Zr	U-27.1Pu-4.1Zr	672	572	—	[166]	a
9	U-40Pu-10Zr	U-43.2Pu-4Zr	650	587	—	[166]	a
10	U-65Pu-10Zr	U-69.8Pu-4Zr	592	560	—	[166]	a
11	U-50Pu-15Zr	U-55.7Pu-6.3Zr	628	594	530?	[166]	a
12	U-80Pu-15Zr	U-88.4Pu-6.2Zr	485	420	—	[166]	a
13	U-13.2Pu-16.1Zr	U-15Pu-6.8Zr	643	588	—	[217]	b
14	U-17.5Pu-17.5Zr	U-21.7Pu-4.1Zr	665	590	—	[166]	a
15	U-10Pu-20Zr	U-11.7Pu-8.7Zr	670	662	610	[166]	a
16	U-70Pu-20Zr	U-80.3Pu-8.6Zr	535	510	485?	[166]	a
17	U-12.9Pu-22.5Zr	U-15Pu-10Zr	654	596	—	[219]	c
18	U-12.6Pu-22.6Zr	U-15Pu-10Zr	645	600	—	[211]	d
19	U-16Pu-22.6Zr	U-19Pu-10Zr	630	580	—	[149]	e
20	U-16.9Pu-22.6Zr	U-20Pu-10Zr	650	586	—	[211]	d
21	U-17Pu-23Zr	U-20Pu-10Zr	654	580	—	INL	f
22	U-10Pu-25Zr	U-12.1Pu-11.3Zr	668	660	608	[166]	a
23	U-25Pu-25Zr	U-30.1Pu-11.2Zr	655	600	575	[166]	a
24	U-50Pu-25Zr	U-59.7Pu-11.2Zr	605?	595?	537	[166]	a
25	U-12.1Pu-29Zr	U-15Pu-13.5Zr	638	588	—	[217]	b
26	U-10Pu-30Zr	U-12.5Pu-14.1Zr	665	655	605	[166]	a
27	U-19Pu-32Zr	U-24Pu-15Zr	637	574	—	INL	f
28	U-32.5Pu-32.5Zr	U-41.3Pu-15.4Zr	642	605	570	[166]	a
29	U-22Pu-40Zr	U-30Pu-20Zr	598	570	—	INL	f
30	U-27Pu-40Zr	U-36.5Pu-20Zr	570	551	—	INL	f
31	U-10Pu-40Zr	U-13.6Pu-20.3Zr	665	655	610	[166]	a
32	U-41Pu-40Zr	U-55Pu-20Zr	518	502	—	INL	f
33	U-45Pu-40Zr	U-60.3Pu-20.1Zr	575?	535	—	[166]	a
34	U-25Pu-45Zr	U-41.3Pu-15.4Zr	640	585	—	[166]	a
35	U-25Pu-55Zr	U-38.4Pu-31.6Zr	575	—	—	[166]	a
36	U-3Pu-62Zr	U-5.2Pu-43.7Zr	625	—	—	[166]	a
37	U-10Pu-65Zr	U-17Pu-41.4Zr	610	—	—	[166]	a

Table 25. (continued).

Point Number	Composition (at%)	Composition (wt%)	Highest T (°C)	Second Highest T (°C)	Third Highest T (°C)	Reference	Notes
38	U-20Pu-65Zr	U-33.9Pu-41.2Zr	—	580	—	[166]	a, g
39	U-3Pu-67Zr	U-5.2Pu-43.7Zr	612	—	—	[166]	a
40	U-12Pu-68Zr	U-20Pu-45Zr	591	—	—	INL	f
41	U-15Pu-75Zr	U-28.4Pu-53.1Zr	—	580	—	[166]	a, g

NOTE a: Transition temperatures measured by researchers at Mound Laboratory appear in reports MLM-1402 [205], which reports data from 22 U-Pu-Zr alloys, and MLM-1445 [166], which reports data from 29. Most of the alloy compositions in the reports are identical, and phase transition temperatures for each of these alloys commonly differ by at most a degree or two between the two reports. The reports indicate slightly different sample histories: MLM-1402 says that phase-transition data were collected from crushed, arc-melted alloy buttons that were annealed for a minimum of 3 hours at 750°C followed by annealing at 550°C for at least 3 days, while MLM-1445 says that the data were collected from alloys that were arc-melted and inverted at least 15 times to ensure homogeneity, checked for homogeneity using metallographic analyses of cross-sections of the as-cast alloys, and annealed at 700°C for a minimum of 24 hours followed by annealing at 500°C for three days. Both reports indicated that the data were collected using DTA and that the samples were encapsulated in molybdenum to avoid earlier problems with hydrogen contamination in Ta-encapsulated alloys (as reported in reference [205]). No information about the actual sample compositions or impurities was provided in either report.

Because of the similarity in alloy compositions and results, it has been assumed here that MLM-1402 and MLM-1445 report the same experimental results despite the different descriptions of sample histories, and that differences between the two reports represent either collection of new data for MLM-1445 or re-evaluation of data in MLM-1402. Thus, Table 25 includes only transition temperatures from MLM-1445.

NOTE b: Reference [217] is a report from Los Alamos Scientific Laboratory. It contains DTA data collected from alloys that had been inductively melted and stirred, cast, and extruded. Compositions listed appear to be actual rather than nominal. Major impurities in U-15Pu-6.8Zr (wt%) were Fe (240 ppm by weight), C (130 ppm), and O (90 ppm). Major impurities in U-14.6Pu-13.5Zr (wt%) were Fe (240 ppm) and O (65-80 ppm). Values in Table 25 are transition onset temperatures during heating; temperature ranges and onset temperatures during cooling are available in the original reference. Cooling data from the higher-temperature transition in the U-15Pu-13.5Zr (wt%) alloy showed two overlapping peaks.

NOTE c: Reference [219] is a monthly report from the Reactor Development Program at Argonne National Laboratory. Data in this report is described as "preliminary and subject to change." This report contains DTA results from solid-state transformations in a single alloy. Plots of phase-transition temperatures measured during heating and cooling at rates between 0.4 and 4°C/minute were extrapolated to lower heating and cooling rates to obtain the "equilibrium" transformation temperatures listed in Table 25. No information about actual composition or impurities was provided.

NOTE d: Reference [211] is the English translation of a Commissariat a L'Energie Atomique (CEA) report. Phase transition temperatures were identified by dilatometry in alloys prepared by arc-melting U, Pu, and Zr feedstocks in purified argon, then inverting and re-melting the alloys at least four times. The alloys were cast in a copper mold and annealed for 150 hours at 900°C in a vacuum. No information about the actual compositions or impurities was provided.

NOTE e: Data are from METAPHIX alloy CR13, which was prepared by arc-melting and mixing U-Pu and Zr liquids. Phase-transition temperatures were identified using dilatometry and are reported as "approximate." No information about the actual composition or impurities was provided [149].

NOTE f: Data in Table 25 should be considered as preliminary. Values in the table represent DTA measurements of onset temperatures of phase transitions during heating in alloys that were arc-melted and drop-cast. No information about actual compositions or impurities was provided.

NOTE g: Mound Laboratory data specifically indicates that the highest solid-state transition temperature in this alloy was not reported [166].

2.4.1.2.2.2.2 Transition Enthalpies

Data on phase-transformation enthalpies are generally lacking. However, researchers at Idaho National Laboratory measured phase-transition temperatures and enthalpies for six alloys. These data appear in previous revisions of this Handbook [1-3] but are otherwise unpublished.

The measurements were made in an air-atmosphere glovebox. Despite a flowing cover gas with oxygen concentration below the parts per billion range, the samples developed visible oxide layers during data collection. Because of peak overlaps in the DSC curves, it was not possible to separate peaks from individual transformations, and total enthalpies were calculated from the areas under all of the peaks corresponding to temperatures between 400 and 800°C.

Although they did not provide quantitative enthalpies, Harbur and colleagues reported relative energies of transitions between ~590 and 650°C in U-15Pu-6.8Zr and U-15Pu-13.5Zr (both in wt%) (Table V of reference [217]). These researchers identified two transitions in DTA data from the U-15Pu-6.8Zr alloy. The lower-temperature transition occurred between 588 and 598°C during heating and between 596 and 594°C during cooling, and the higher-temperature transition occurred between 643 and 658°C during heating and 634-626°C during cooling. The energy of the higher-temperature transition was about 4 times that of the lower-temperature transition.

Harbur and colleagues identified two transitions during heating of the U-15Pu-13.5Zr alloy, and three during cooling. The lower-temperature transition occurred between ~588 and 593°C during heating, and between 593 and 588°C during cooling. The higher-temperature transition occurred between ~638 and 653°C during heating. DSC data collected during cooling showed that this was not a single transition, but instead, consisted of overlapping peaks corresponding to transitions occurring between 626 and 618°C and between 618 and 610°C. The energy of the transition between 618 and 610°C was about four times that of the transition between 626 and 618°C, and the combined energies of these higher-temperature transitions were approximately equal to the energy of the lower-temperature transition for this alloy.

Figure 52 and Table 26 summarize the available data for phase-transition enthalpies in U-Pu-Zr alloys. Savage did not explicitly specify the phase-transition enthalpy or provide measurements that were at temperatures immediately above and below the phase transition [204]. The value in Table 26 is calculated from polynomials expressing the incremental enthalpy values above and below the phase transition(s) in reference [204], assuming that all transitions occurred in the temperature interval between the equations (600 and 650°C). The phase-transition enthalpy from reference [204] appears significantly higher than enthalpies from INL data, for reasons that need to be investigated.

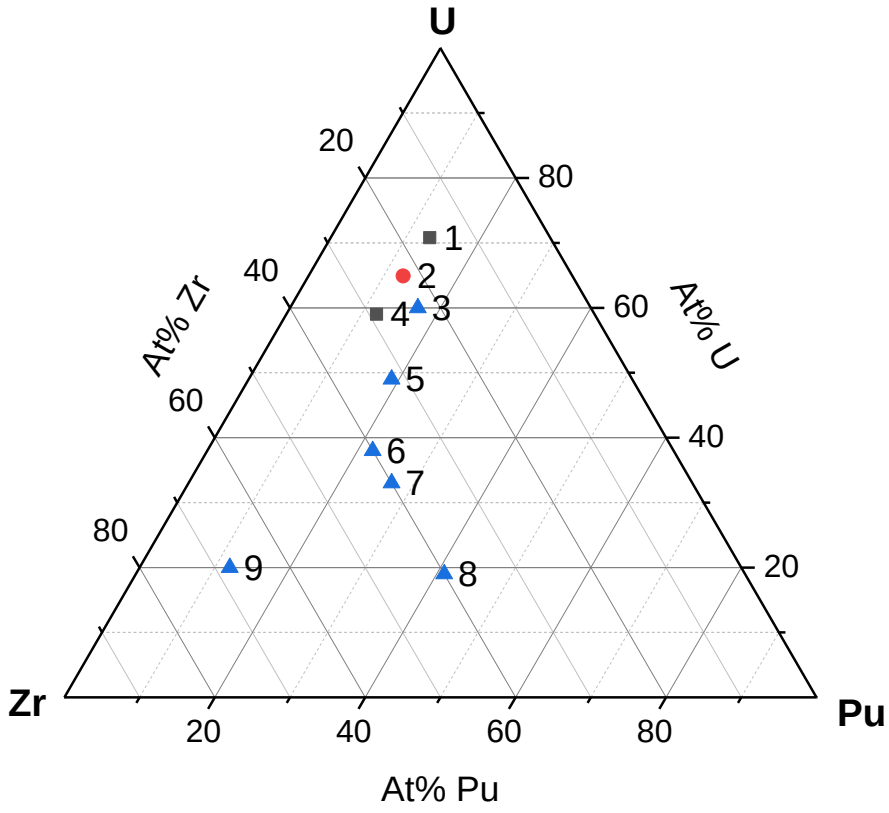

Figure 52. Compositions of alloys whose phase-transition temperatures and enthalpies were measured at INL. Colors and symbols indicate sources of data (dark gray squares: Harbur et al., red circle: Savage, blue triangles: INL). Numbers indicate point numbers from Table 26.

Table 26. Combined enthalpies of transitions between 400 and 800°C.

Point No.	Composition (wt%)	Composition (at%)	ΔH_{Tr} (J/g)	Source
1	U-15Pu-6.8Zr	U-13.2Pu-16Zr	Not reported	Reference [217]
2	U-15Pu-10Zr	U-12.6Pu-22.5Zr	39.13	Reference [204]
3	U-20Pu-10Zr	U-17Pu-23Zr	30.54±0.3	INL (alloy AFC2-E1)
4	U-15Pu-13.5Zr	U-12Pu-29Zr	Not reported	Reference [217]
5	U-24Pu-15Zr	U-19Pu-32Zr	29.07±0.36	INL (alloy AFC2-B7)
6	U-30Pu-20Zr	U-22Pu-40Zr	32.28±0.71	INL (alloy AFC2-B1)
7	U-36.5Pu-20Zr	U-27Pu-40Zr	27.76±0.1	INL (alloy AFC2-B8)
8	U-55Pu-20Zr	U-41Pu-40Zr	35.75±0.57	INL (alloy AFC2-B2)
9	U-20Pu-45Zr	U-12Pu-68Zr	32.37±0.07	INL (alloy AFC2-B3)

2.4.1.2.2.2.3 Coexisting Phases

Several research groups have attempted to infer the reactions corresponding to transition temperatures by identifying coexisting phases in U-Pu-Zr alloys and assuming that these phases represent equilibrium assemblages. Most of the data are from room-temperature analyses of annealed samples in which phases were identified using some combination of X-ray diffraction, microprobe analyses, metallography, and transmission electron microscopy. Smaller amounts of data from high-temperature neutron diffraction and from analyses of samples that were held in thermal gradients are also available.

2.4.1.2.2.2.3.1 Coexisting Phases in Annealed Samples

Identification of equilibrium phase assemblages from annealed samples is complicated by peak overlaps in X-ray diffraction (e.g., [20, 153]), difficulties in distinguishing between phases in metallographic analyses (e.g., [166]), fine-grained microstructures that may require annealing times of months to allow development of single-phase areas large enough for microprobe analyses (e.g., [81, 223]), and the complex thermal histories and relatively short annealing times of some samples. Non-equilibrium phases that are believed to be retained from higher temperatures are commonly reported (e.g., [211, 222]).

Table 27 summarizes coexisting phases identified in room-temperature analyses of annealed samples. Thermal histories of individual samples are described in the notes. Although a thorough assessment of the data requires better knowledge of the U-Pu-Zr phase diagram than is currently available, consideration of the variety of phases reported in U-Pu-Zr alloys with 19-20 wt% Pu and 10 wt% Zr (samples 19-28 in Table 27) suggests that the relationship between the reported phases and compositions is complex. Annealing times and temperatures and cooling rates vary widely. If the lengthy annealing times needed to obtain crystals 4 mm across reported by O'Boyle and Dwight [81] are typical, it is likely that very few of the samples in Table 27 have equilibrium phase assemblages.

Table 27. Coexisting phases from room-temperature analyses of annealed samples[a].

Sample No.	Composition, at% Composition, wt% Reference (sample No.)	T (°C)[b]																			
		350	500	570	580	590	595	605	620	630	640	650	660	670	680	700	750	850	900	950	1000
1	U-9Pu-3Zr U-9Pu-1Zr [81] (7)[c]	—	—	—	—	α, γ	—	α, γ	—	—	—	β, γ	—	β, γ	β, γ	—	—	—	—	—	—
2	U-29Pu-3Zr U-30Pu-1Zr [81] (10)[c]	—	—	—	—	—	—	—	—	—	—	—	—	η	—	—	—	—	—	—	—
3	U-28Pu-5Zr U-29Pu-2Zr [81] (11)[c]	—	—	—	—	—	—	ζ	—	ζ	—	—	ζ	η, γ	γ	γ	—	—	—	—	—
4	U-19Pu-7Zr U-20Pu-3Zr O&D (1)[c]	—	—	—	—	ζ, γ	—	ζ, γ	—	—	ζ, γ	ζ, γ	ζ, γ	—	—	γ	—	—	—	—	—
5	U-28Pu-8Zr U-30Pu-3Zr [81] (12)[c]	—	—	—	—	—	—	ζ, γ	—	—	—	ζ, γ	ζ, γ	γ	—	—	—	—	—	—	—
6	U-27Pu-11Zr U-29Pu-4Zr [81] (13)[c]	—	—	—	—	—	—	ζ, γ	—	—	—	ζ, γ	ζ, γ	γ	—	—	—	—	—	—	—
7	U-14Pu-12Zr U-15Pu-5Zr [81] (6)[c]	—	—	—	—	—	—		—	—	—	—	—	β, γ	—	—	—	—	—	—	—
8	U-17Pu-14Zr U-19Pu-6Zr [81] (2)[c]	—	—	—	—	ζ, γ	—	ζ, γ	—	—	ζ, γ	ζ, γ	γ_1	γ	—	γ	—	—	—	—	—
9	U-20Pu-20Zr U-23.3Pu-8.7Zr [222][d]	—	—	—	—	—	—	—	—	—	—	—	—	—	—	—	—	γ, β-Pu, α-Zr (incl), δ, ζ	—	—	—

Table 27. (continued).

Sample No.	Composition, at% Composition, wt% Reference (sample No.)	T (°C)[b]																			
		350	500	570	580	590	595	605	620	630	640	650	660	670	680	700	750	850	900	950	1000
10	U-8Pu-23Zr U-10Pu-10Zr [81] (8)[c]	—	—	—	—	—	—	—	—	—	—	β, γ		β, γ	γ_1	γ	—	—	—	—	—
11	U-13Pu-22Zr U-15Pu-10Zr [211][e, f]	—	—	—	—	—	—	—	—	—	—	—	—	—	—	—	—	—	—	—	γ, unk (sm)
12	U-13Pu-22Zr U-15Pu-10Zr [211][e, g]	—	—	—	—	—	—	—	—	—	—	—	—	—	—	—	—	—	—	γ, unk (sm)	—
13	U-13Pu-22Zr U-15Pu-10Zr [211][e, h]	—	—	—	—	—	—	—	β, γ, ζ	—	—	—	—	—	—	—	—	—	—	—	—
14	U-13Pu-22Zr U-15Pu-10Zr [211][e, i]	—	α, β, γ, ζ	—	—	—	—	—	—	—	—	—	—	—	—	—	—	—	—	—	—
15	U-13Pu-22Zr U-15Pu-10Zr [211][e, j]	—	α (tr), γ, δ (sm), ζ (subst)	—	—	—	—	—	—	—	—	—	—	—	—	—	—	—	—	—	—
16	U-13Pu-22Zr U-15Pu-10Zr [211][e, k]	—	α (tr), γ, δ (sm), ζ (subst)	—	—	—	—	—	—	—	—	—	—	—	—	—	—	—	—	—	—
17	U-13Pu-22Zr U-15Pu-10Zr [211][e, l]	α (tr), γ, δ (sm), ζ (subst)	—	—	—	—	—	—	—	—	—	—	—	—	—	—	—	—	—	—	—

Table 27. (continued).

Sample No.	Composition, at% Composition, wt% Reference (sample No.)	T (°C)[b]																			
		350	500	570	580	590	595	605	620	630	640	650	660	670	680	700	750	850	900	950	1000
18	U-13Pu-22.5Zr U-15Pu-10Zr [213][m]	—	—	—	—	—	—	—	—	—	—	—	—	—	—	—	—	—	—	δ, α, Zr (imp)	—
19	U-16Pu-23Zr U-19Pu-10Zr [81] (3) [c]	—	—	—	—	ζ, γ	—	ζ, γ	—	—	ζ, γ	ζ, γ	γ_1	γ	—	—	—	—	—	—	—
20	U-16Pu-23Zr U-19Pu-10Zr [221] (C) [n, o]	—	—	—	—	—	—	—	—	—	—	—	—	—	—	—	ζ, δ	—	—	—	—
21	U-16Pu-23Zr U-19Pu-10Zr [221] (D) [n, p]	—	—	—	—	—	—	—	—	—	—	ζ, δ	—	—	—	—	—	—	—	—	—
22	U-16Pu-23Zr U-20Pu-10Zr [211][e, f]	—	—	—	—	—	—	—	—	—	—	—	—	—	—	—	—	—	—	—	γ, unk (sm)
23	U-16Pu-23Zr U-20Pu-10Zr [211][e, g]	—	—	—	—	—	—	—	—	—	—	—	—	—	—	—	—	—	—	γ, unk (sm)	—
24	U-16Pu-23Zr U-20Pu-10Zr [211][e, h]	—	—	—	—	—	—	—	β, γ, ζ	—	—	—	—	—	—	—	—	—	—	—	—
25	U-16Pu-23Zr U-20Pu-10Zr [211][e, i]	—	α, β, γ, ζ	—	—	—	—	—	—	—	—	—	—	—	—	—	—	—	—	—	—
26	U-16Pu-23Zr U-20Pu-10Zr [211][e, j]	—	α (tr), γ, δ (sm), ζ (subst)	—	—	—	—	—	—	—	—	—	—	—	—	—	—	—	—	—	—

Table 27. (continued).

Sample No.	Composition, at% Composition, wt% Reference (sample No.)	T (°C)[b]																			
		350	500	570	580	590	595	605	620	630	640	650	660	670	680	700	750	850	900	950	1000
27	U-16Pu-23Zr U-20Pu-10Zr [211][e, k]	—	α (tr), γ, δ (sm), ζ (subst)	—	—	—	—	—	—	—	—	—	—	—	—	—	—	—	—	—	—
28	U-16Pu-23Zr U-20Pu-10Zr [211][e, l]	α (tr), γ, δ (sm), ζ (subst)	—	—	—	—	—	—	—	—	—	—	—	—	—	—	—	—	—	—	—
29	U-12Pu-26Zr U-15Pu-12Zr [217][q, r]	—	—	—	—	—	—	—	—	—	—	—	—	—	—	—	γ, α-Zr	—	—	—	—
30	U-12Pu-26Zr U-15Pu-12Zr {Harbur, 1970 #382[q, s]	—	—	—	—	—	—	—	—	—	—	α or β, δ	—	—	—	—	—	—	—	—	—
31	U-12Pu-26Zr U-15Pu-12Zr {Harbur, 1970 #382[q, t]	—	α, δ, ζ	—	—	—	—	—	—	—	—	—	—	—	—	—	—	—	—	—	—
32	U-14Pu-30Zr U-18Pu-14Zr [81] (4) [c]	—	—	—	—	—	—	ζ, γ	—	—	ζ, γ	ζ, γ	γ_1, γ_2	—	—	—	—	—	—	—	—
33	U-8Pu-32Zr U-10Pu-15Zr [81] (9) [c]	—	—	—	—	α, δ	—	α, γ	—	—	—	β, γ	β, γ	—	γ_1, γ_2	—	—	—	—	—	—
34	U-12Pu-40Zr U-16Pu-20Zr [81] (5) [c]	—	—	—	—	—	—	ζ, γ	—	—	ζ, γ	ζ, γ	γ_1, γ_2	—	—	—	—	—	—	—	—

NOTE a: α and β refer to α-U and β-U; γ refers to bcc solid solutions between γ-U, β-Zr, and ε-Pu; η refers to η-(U,Pu), ζ refers to ζ-(U,Pu), δ refers to δ-UZr_2, "incl" indicates a phase that occurs as inclusions, "imp" indicates a phase that includes impurities, "unk" indicates an unidentified phase, "tr" indicates trace quantities, "sm" indicates small quantities, and "subst" indicates substantial quantities. It should be assumed that all phases may include elements not specified in the identifications given here.

Table 27. (continued).

Sample No.	Composition, at% Composition, wt% Reference (sample No.)	T (°C)[b]																			
		350	500	570	580	590	595	605	620	630	640	650	660	670	680	700	750	850	900	950	1000

NOTE b: The value in this column is the last reported annealing temperature for each sample. Complex thermal profiles (e.g., thermal cycling or multiple stages of annealing) are described in notes.

NOTE c: Samples were prepared by triple arc-melting electrolytic uranium, electrolytic plutonium, and crystal bar zirconium on a water-cooled copper hearth. All samples were homogenized by holding them for 7 days at a temperature approximately 100 °C below the solidus, annealing for times that varied with the alloy composition, and water quenching. Annealing times for individual samples varied from 25 days (600 hours) at 700 C to 150 days (3600 hours) at 590 C. These annealing times allowed grains to grow to 4 micrometers or larger, making it possible to perform quantitative microprobe analyses.

With the exception of O'Boyle and Dwight's Sample 7 (Sample number 1 in Table 27), sample compositions were read from a ternary plot. It was stated that nominal and actual compositions of analyzed samples agreed to within 0.5 wt%, although O'Boyle and Dwight's Sample 7 reportedly changed composition from approximately U-9Pu-12Zr to U-9Pu-3Zr (in at%) as a result of copper contamination during arc melting. Actual proportions of Zr in samples are slightly lower than those in the table because some of the Zr was in high-Zr inclusions and high-Zr layers on the outer surfaces of the annealed materials. Interstitial impurities in U-Pu-Zr alloys were reported as 40-110 ppm C, 4-20 ppm H, 60-220 ppm O, and 1-27 ppm N. (Reference [81])

NOTE d: Sample was arc-melted, homogenized by re-melting and inverting twice, melted again, cast in a zirconia-coated quartz glass tube to form a cylinder, annealed at 850°C for 96 hours (4 days), and furnace-cooled for one day. The cylinder was sectioned, embedded in acrylic resin, polished, and coated with a thin layer of gold. After SEM examination, several sections were extracted and thinned for TEM analysis using a FIB instrument. Phases were identified by comparing experimental electron diffraction patterns to calculated patterns based on published crystal structures. No information about the sample purity, actual bulk composition, or compositions of individual phases was provided. (Reference [222])

NOTE e: Samples were prepared by arc-melting U, Pu, and Zr, inverting and re-melting the samples four more times. The alloys were cast in the furnace using a copper mold. Phases were identified using metallography and X-ray diffraction. No information about actual compositions, details of analytical techniques, or sample purity was provided. (Reference [211])

NOTE f: Sample was annealed at 1000°C for 90 hours (3.75 days), then quenched in oil. (Reference [211])

NOTE g: Sample was annealed at 950°C for 165 hours (6.9 days), then quenched in oil. (Reference [211])

NOTE h: Sample was annealed at 620°C for 5 hours, then quenched in oil. (Reference [211])

NOTE i: Sample was annealed at 500°C for 50 hours (~2 days), then quenched in oil. (Reference [211])

NOTE j: Sample was annealed at 500°C for 900 hours (37.5 days), then slowly cooled to 20°C. (Reference [211])

NOTE k: Sample was cycled 115 times between 500 and 750°C, held at 500°C for 240 hours (10 days), and slowly cooled to 20°C. (Reference [211])

NOTE l: Sample was held at 900°C for 2 hours, slowly cooled to 350°C, held for 340 hours (~14 days), and slowly cooled to 20°C. (Reference [211])

NOTE m: Sample was described as "homogenized and quenched from the γ-temperature region (950°C)." No other information about the sample was provided. (Reference [213])

NOTE n: Samples were cut from an injection-cast cylindrical rod. Chemical analyses adjacent to the samples showed that actual compositions were within 0.5 wt% of nominal compositions. No information about sample purity was provided. Microstructures in both of the annealed samples discussed in this reference were interpreted as having ζ along prior grain boundaries from the earlier γ phase and fine intergrowths of ζ and δ in the interiors of the original γ-phase grains (Reference [221])

NOTE o: Sample was annealed at 750°C for 10 hours (Reference [221], Sample C)

NOTE p: Sample was annealed at 650°C for 10 hours (Reference [221], Sample D)

NOTE q: Samples were inductively melted and stirred, cast, and extruded. Reported sample compositions appear to be actual rather than nominal. Phases were identified from microprobe images and linescans, which were not quantified to determine absolute concentrations. (Reference [217])

NOTE r: Sample was held at 750°C for 17 days (408 hours). Density decreased by ~0.07 g/cm^3 during the heat treatment. No information about cooling rate was provided. The alloy contained 300 ppm O. (Reference [217])

NOTE s: Sample was held at 650°C for 18 days (432 hours). Density decreased by ~0.09 g/cm^3 during the heat treatment. No information about cooling rate was provided. The sample contained δ and a uranium phase; unfortunately, the text is contradictory about whether the U phase was α or β (the text is contradictory). (Reference [217])

NOTE t: Sample was held at 500°C for 19 days (456 hours). Density decreased by ~0.02 g/cm^3 during the heat treatment. No information about cooling rate was provided. (Reference [217])

2.4.1.2.2.2.3.2 Coexisting Phases from High-temperature Neutron-Diffraction Data

Mueller et al. reported identities of coexisting phases in U-8Pu-10Zr and U-19Pu-10Zr (in wt%, corresponding to U-7Pu-23Zr and U-16Pu-23Zr in at%) from high-temperature neutron-diffraction data in a conference proceedings paper that appeared in two places [77, 78] (their Table 2 and Figure 7b). The same data appear in references [234] and [221], although the label corresponding to the highest-temperature data from U-19Pu-10Zr is 660°C in references [77, 78] and 650°C in references [234] and [221].

The results of the neutron-diffraction analyses are summarized in Table 28. No information about the origin of the samples was provided, although they may have been from fuel pins intended for irradiation in the Integral Fast Reactor (IFR). The samples were as-cast material, which was heated at an unspecified rate. Phase identifications were based on Rietveld refinements in which it was initially assumed that the phases in each sample were consistent with the isothermal sections of O'Boyle and Dwight [81]. At the time of the conference proceedings papers, analysis of the data from U-19Pu-10Zr (wt%) had just begun, and the identification of ζ should probably be regarded as tentative. The analysis results were apparently never finalized and published as a journal paper.

Table 28. Phases and volume percentages of coexisting phases from high-temperature neutron-diffraction data [77, 78]. α and β refer to α-U and β-U, δ refers to δ-UZr_2, ζ refers to ζ-(U,Pu), γ refers to the bcc solid solution between γ-U, ε-Pu, and β-Zr, and ? indicates unidentified peaks. Numbers in parentheses are volume percentages of phases.

Composition, at% Composition, wt%	**T (°C)**									
	25	**50**	**500**	**570**	**580**	**590**	**595**	**640**	**650**	**660**
U-7Pu-23Zr U-8Pu-10Zr	α (80), δ (20)	α (78), δ (22)	—	α (71), δ (29)	—	α (12), β (66), δ (22)	—	—	α (3), β (77), γ (20)	—
U-16Pu-23Zr U-19Pu-10Zr	δ, ζ,?	—	δ, ζ	—	δ, ζ	—	δ, ζ	γ, δ	—	γ

2.4.1.2.2.2.3.3 Coexisting Phases and Transition Temperatures in Thermal Gradients

Three research groups reported results of thermotransport experiments in which U-Pu-Zr alloys were held in thermal gradients [217, 218, 221]. Temperatures were measured at a small number of points (typically the ends of the samples, and possibly one point in the middle), and reported temperatures of phase transitions at intermediate locations may have been calculated from sample positions using the average thermal gradient calculated from the temperatures at the ends of the samples. Changes in sample compositions between regions with different phase assemblages as a result of element migration were observed by several researchers.

The earliest study was reported by Harbur et al. in 1970 [217]. Their sample was a 1" long rod of U-15Pu-13.4Zr (wt%) whose ends were kept at temperatures of 500 and 750°C for 17 days. Although Harbur et al. did not report the thermal gradient in their experiment, the sample length and end temperatures suggest an average gradient of ~10°C/mm. Harbur et al. reported an abrupt change between a single-phase region at the hot end of the sample and a two-phase region in which the approximate compositions of the phases were U-15Pu and U-15Pu-20Zr (in wt%). Within the two-phase region, grain sizes decreased with decreasing temperature, and microstructures at the cooler end of the sample resembled those in a sample that had been annealed at 500°C for 19 days (possibly sample 31 in Table 25 of this paper). Harbur et al. did not identify the phases, but the composition of the U-15Pu-20Zr phase suggests that it was γ. The absence of Zr in the U-15Pu phase suggests that it may have been ζ-(U,Pu),

although it has a smaller proportion of Pu than would be expected from the information in Section 2.3.1.2.1.

In 1994, Kurata et al. reported observations from a sample of METAPHIX Alloy CR13 (U-19Pu-10Zr in wt%) that had been held in a temperature gradient between 623 and 1123 K (350 and 850°C) for 663 hours (almost 28 days). The average thermal gradient for this sample was 21K/mm. Kurata et al. used metallographic analysis to divide their sample into four regions, with boundaries at the ends of the sample and at 750, 840, and 940 K (477, 567, and 667°C). Kurata et al. tentatively identified phases within each region as δ-UZr_2 and ζ-(U,Pu) between 750 and 840 K, γ and ζ-(U,Pu) between 840 and 940 K, and γ above 940 K based on consideration of the isothermal sections of O'Boyle and Dwight [81]. They reported a "drastic" composition change at ~840 K, with higher proportions of U and lower proportions of Zr above this temperature.

Somewhat later, Sohn et al. reported observations from a sample whose nominal composition was U-19Pu-10Zr (wt%) that had been held in a temperature gradient of 22°C/mm for 41 days [221]. Chemical analyses of materials adjacent to the thermal gradient sample showed that actual compositions and nominal compositions of the alloy agreed to within 0.5 wt%. Phases and microstructures in the thermal gradient samples were reportedly similar to those in samples that had been annealed at comparable temperatures (Samples 20 and 21 in Table 25 of this paper).

2.4.1.2.3 Phase Diagrams

A number of different kinds of data that can be used to assess and develop phase diagrams for sub-solidus reactions have been published. They include microprobe measurements of the composition of γ coexisting with other phases in annealed samples [81], phase transition temperatures, generally measured using DTA (Table 25), coexisting phases in annealed samples (Table 27), coexisting phases in high-diffraction data (Table 28), and thermotransport experiments in which changes in phase assemblages are noted in samples that are held in thermal gradients (Section 2.4.1.2.2.2.3.3). Individual references generally emphasize only one kind of data, and no single reference presents phase-transition temperatures and identifications of coexisting phases in the same samples. Assessment of existing phase diagrams, therefore, requires comparing different kinds of data reported in different references.

Only two attempts at determining the sub-solidus part of the U-Pu-Zr phase diagram from experimental data have been reported. Both were based in part on binary phase diagrams available at the time.

The first attempt to determine the U-Pu-Zr phase diagram was reported by researchers at Mound Laboratory in 1968. It consists of a contour plot of the temperatures and possible reactions by which the gamma phase transforms to lower-temperature phases and a reaction scheme. The contour plot was published in a Mound Laboratory report and a short conference paper [166, 220]. The reaction scheme was apparently never published beyond the original Mound Laboratory report [166] and was described as "tentative." No information about actual sample compositions or impurities was provided.

The Mound Laboratory contour plot and reaction scheme were based primarily on phase transition temperatures from thirty ternary alloys measured using DTA (data from reference [166] in Table 25 of this paper), supplemented in some cases by X-ray diffraction, microprobe analyses, and dilatometry. Mound Laboratory researchers attempted to identify the phases involved in each transition by metallographic examination of samples that had been annealed below the transition temperatures for two to three weeks. Phase identifications were complicated by fine-grained microstructures and by the lack of a satisfactory chemical etchant, and were considered "tentative." Although a few phase assemblages appear in the reaction scheme, it is not possible to associate them with sample compositions, and there is no systematic presentation of relationships between phases, annealing temperatures, and sample compositions in the Mound Laboratory data.

The second attempt to determine the sub-solidus part of the U-Pu-Zr phase diagram was published by O'Boyle and Dwight in 1970 as an extended conference presentation paper (reference [81]), and was based in part on consideration of phase-transition temperatures from reference [205] and the Mound Laboratory depiction of the gamma solvus [220]. The O'Boyle and Dwight paper includes a contour plot showing new microprobe measurements of the compositions of the γ phase in alloys annealed at a variety of temperatures, a reaction scheme, identifications of coexisting compositions in thirteen alloys annealed at temperatures between 590 and 700°C (data from reference [81] in Table 27 of this paper), and a series of nine isothermal sections representing temperatures from 500 to 700°C. The O'Boyle and Dwight paper does not include measurements of phase-transition temperatures, and results of the microprobe analyses of phases other than γ and high-Zr inclusions were not presented.

A number of other phase diagrams have been published since the work of O'Boyle and Dwight. Thermodynamically based models (including the CALPHAD approach) have been developed for the liquidus and solidus (e.g., [34, 38, 42, 49, 197, 235]). CALPHAD has also been used to develop isothermal sections that are generally consistent with the work of O'Boyle and Dwight (e.g., [34, 38, 197]). Tentative room-temperature U-Pu-Zr phase diagrams based on extrapolation from the U-Pu, U-Zr, and Pu-Zr binary phase diagrams and the isothermal sections of O'Boyle and Dwight have been suggested (e.g., [222, 230, 231, 236]). At least two pseudo-binary diagrams with fixed proportions of plutonium have been published [237, 238]. None of these research activities represents a new experimental investigation of the U-Pu-Zr phase diagram.

2.4.1.2.3.1 Gamma Solvus

The existence of a bcc solid solution between γ-U, β-Zr, and ε-Pu that incorporates U, Pu, and Zr in all proportions and transforms to lower-temperature phases on cooling led researchers to construct a ternary surface representing the lowest temperatures at which the bcc phase is stable. This surface also represents the highest-temperature solid-state phase transition for each composition. It is sometimes referred to as the "gamma solvus."

Figure 53a shows a depiction of the gamma solvus developed by researchers at Mound Laboratory [166, 220]. Dashed black lines with arrows are not discussed in the original references, but should probably be interpreted as indicating changes in coexisting compositions by analogy to liquidus projections (e.g., [239]). In practice, however, kinetics of solid-state phase transitions are sufficiently sluggish that it seems unlikely that the indicated reaction paths would be followed except in very slowly cooled samples.

Figure 53b is a composite figure showing the gamma solvus from the work of O'Boyle and Dwight [81]. Compositions with more than 30 at% U are from Figure 2 of reference [81]. The black symbols represent microprobe measurements of the composition of the bcc solid solution phase in alloys that had been annealed at temperatures corresponding to contour lines in the figure. Compositions of the alloys were not specified. The figure apparently shows two kinds of measurements, as indicated by square and circular symbols, but the distinction between the two was not explained in the original reference. Contours for compositions with less than ~30 at% U are based on boundaries of single-phase γ fields in isothermal sections (Figures 4, 5, and 6 in reference [81]).

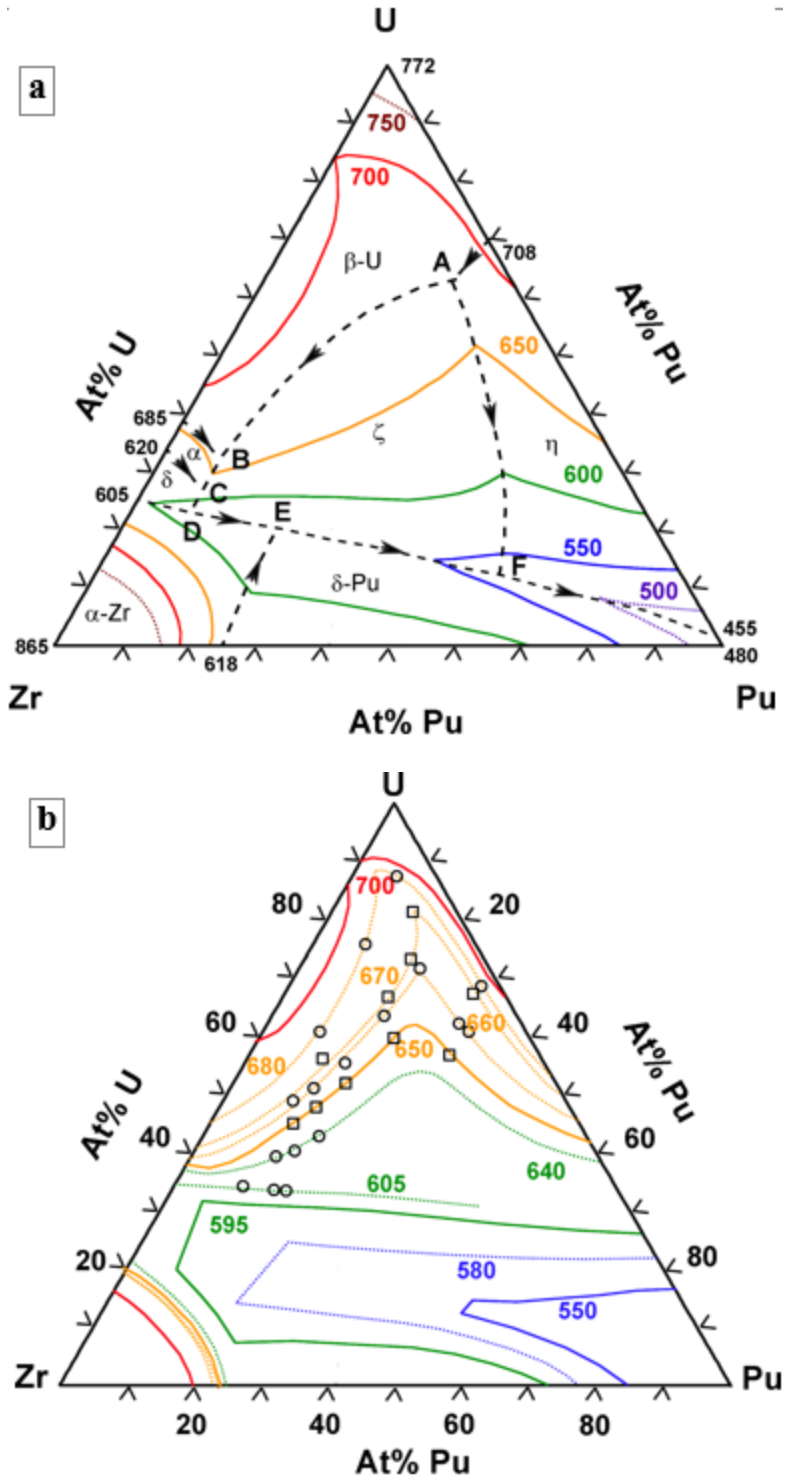

Figure 53. The gamma solvus in the U-Pu-Zr ternary system. Contours indicate solvus temperatures in °C. Colors indicate corresponding temperatures in both parts of the figure. a. As interpreted by researchers at Mound Laboratory [166, 220]. α indicates α-U, δ indicates δ-UZr_2, η indicates η-(U,Pu), ζ indicates ζ-(U,Pu), and all phases are ternary solid solutions. Capital letters indicate four-phase reactions identified in Section 2.4.1.2.3.2. b. Composite phase diagram from O'Boyle and Dwight [81]. The truncated 605-degree contour line is an artifact of the way the figure was constructed.

2.4.1.2.3.2 Reaction Schemes

Researchers at Mound Laboratory tentatively identified six four-phase reactions in ternary U-Pu-Zr alloys at temperatures between ~535 and 675°C (Figure 2 of reference [166]). O'Boyle and Dwight identified five four-phase reactions within the same temperature range (Figure 3 of reference [81]). Researchers at Mound Laboratory also suggested lower-temperature reactions that are not considered here because they were apparently based on interpretation of binary phase diagrams rather than experimental data from U-Pu-Zr alloys.

The reactions suggested by both research groups are summarized below. In this summary, α refers to α-U, β refers to β-U, δ refers to δ-UZr_2, κ refers to κ-$PuZr_2$, η refers to η-(U,Pu), ζ refers to ζ-(U,Pu), and γ refers to the bcc solid solution between γ-U, β-Zr, and ε-Pu. The first reaction listed is a Class III reaction as defined by Rhines [240], and the remaining reactions are Class II. The reactions are:

- β +γ+η→ζ (label "A" in Figure 53a): O'Boyle and Dwight suggested that this reaction occurs at 670°C. Mound Laboratory suggested that it occurs at 675°C. The Mound Laboratory reaction scheme indicates that this reaction represents a transition from the single phase assemblage β+γ+η to the three phase assemblages η+β+ζ, β+γ+ζ, and γ+η+ζ during cooling.
- γ+β→α+ζ (label "B" in Figure 53a): O'Boyle and Dwight suggested that this reaction occurs at 650°C. Mound Laboratory suggested that it occurs at 660°C. The Mound Laboratory reaction scheme indicates that this reaction represents a transition from the two phase assemblages γ+α+β and β+γ+ζ to the two phase assemblages α+β+ζ and α+γ+ζ during cooling.
- γ+α→δ+ζ (label "C" in Figure 53a): O'Boyle and Dwight suggested that this reaction occurs at 595°C. Mound Laboratory suggested that it occurs at 610°C. The Mound Laboratory reaction scheme indicates that this reaction represents a transition from γ+δ+α and γ+ζ+α to δ+ζ+α and δ+ζ+γ during cooling.
- γ+δ→α-Zr+ζ (label "D" in Figure 53a): Mound Laboratory suggested that this reaction occurs at 585°C. It does not appear in the reaction scheme of O'Boyle and Dwight. The Mound Laboratory reaction scheme indicates that this reaction represents a transition from γ+δ+α–Zr and γ+δ+ζ to γ+ζ+α-Zr and δ+ζ+α-Zr during cooling.
- γ+α-Zr→δ+δ-Pu: O'Boyle and Dwight suggested that this reaction occurs at 580°C. Mound Laboratory thought that it might occur at 585°C and considered it as an alternative to reaction "D."
- γ+α-Zr→δ-Pu+ζ (label "E" in Figure 53a): Mound Laboratory suggested that this reaction occurs at 580°C. It does not appear in the reaction scheme of O'Boyle and Dwight. The Mound Laboratory reaction scheme indicates that this reaction represents a transition from β+δ-Pu+α-Zr and γ+ζ+α-Zr to α-Zr+δ-Pu+ζ and γ+δ-Pu+ζ during cooling.
- γ+δ→δ-Pu+ζ: This reaction does not appear in either reaction scheme. Mound Laboratory thought that it might occur at 580°C and considered it as a possible alternative to reaction "E."
- γ+ζ→δ+η: O'Boyle and Dwight suggested that this reaction occurs at 550°C. It does not appear in the Mound Laboratory reaction scheme.
- γ+ζ→δ-Pu+η (label "F" in Figure 53a); Mound Laboratory suggested that this reaction occurs at 535°C. It does not appear in the reaction scheme of O'Boyle and Dwight. The Mound Laboratory reaction scheme indicates that this reaction represents a transition from γ+η+ζ and γ+δ-Pu+ζ to γ+δ-Pu+η and δ-Pu+η+ζ during cooling.

2.4.1.2.3.3 Isothermal Sections

Figure 54 shows the nine isothermal sections developed by O'Boyle and Dwight [81], which include temperatures from 500 to 700°C. The high-Pu section of the 500-degree section is incomplete. Despite their age, limited temperature range, and limited discussion of relationships to experimental data in the original references, these sections are the most complete experimentally determined representation of the U-Pu-Zr phase diagram. They are still widely cited, and are commonly used to interpret experimental data such as phase transition temperatures, diffraction patterns, and metallographic observations.

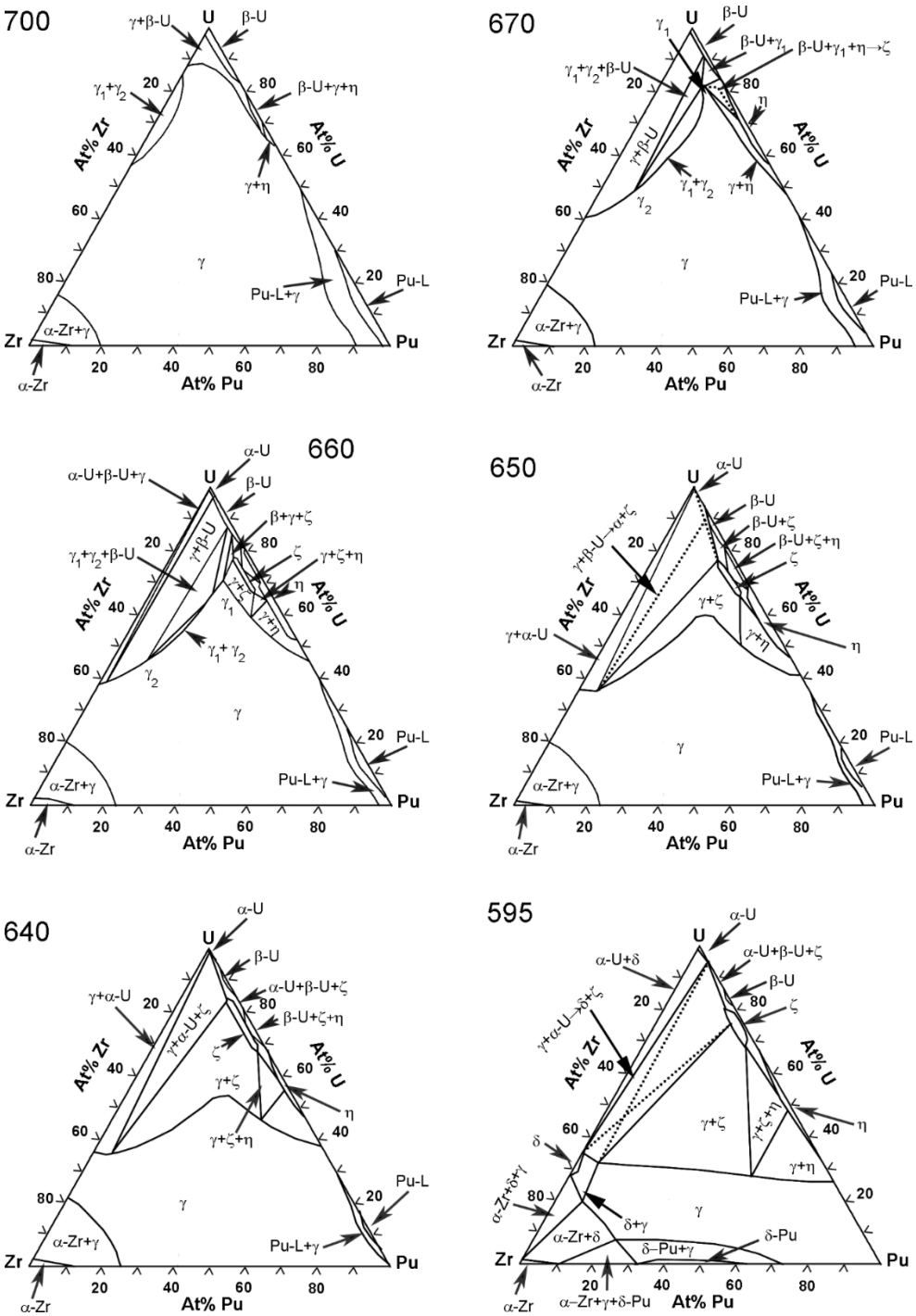

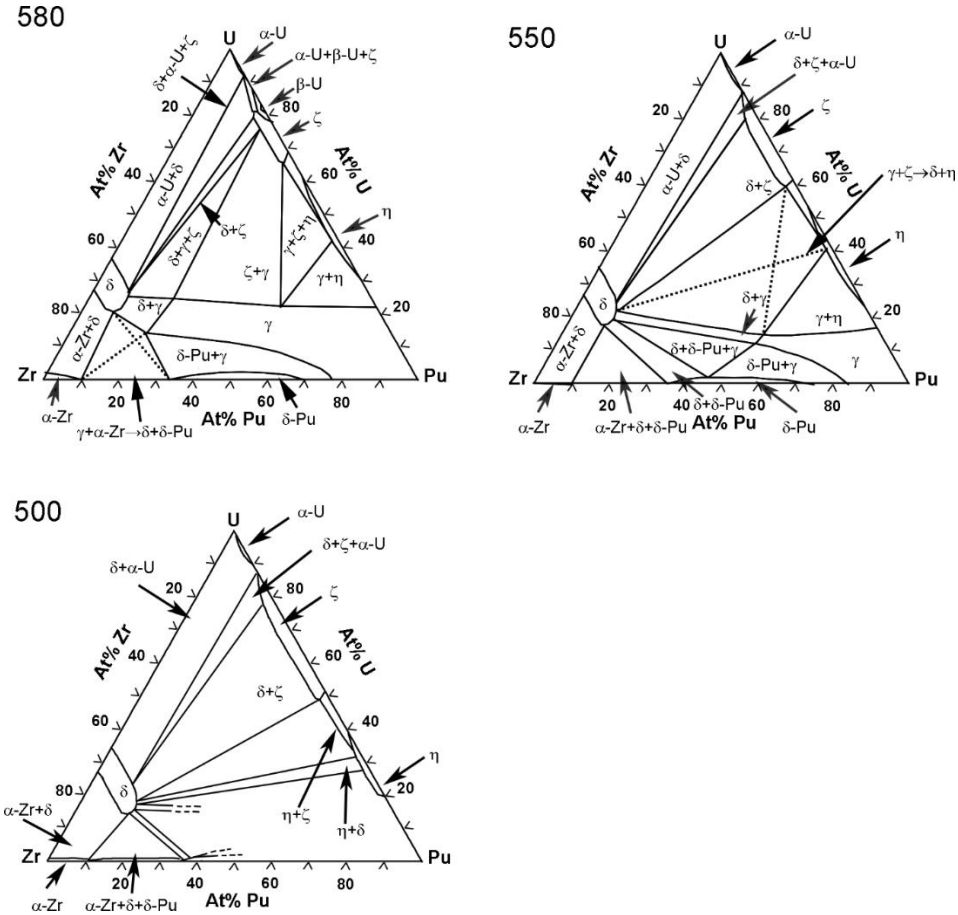

Figure 54. Isothermal sections of O'Boyle and Dwight , based on figures 4-6 of reference [81]. δ refers to δ-UZr_2, ζ refers to ζ-(U,Pu), η refers to η-(U,Pu), and Pu-L is liquid Pu. Dotted lines indicate four-phase reactions. Large numbers adjacent to each section indicate its temperature in °C.

Assessing the accuracy of the isothermal sections developed by O'Boyle and Dwight is complicated by the limited discussion about the relationships between the isothermal sections and experimental data in the original references [81, 241]. O'Boyle and Dwight presented new microprobe measurements of the compositions of γ in alloys annealed at various temperatures, which are shown by squares and circles in Figure 53b. These measurements are generally consistent with O'Boyle and Dwight's presentation of the gamma solvus and with boundaries of single-phase γ regions in their isothermal sections. However, comparisons between their data and measurements by other researchers is impossible because O'Boyle and Dwight did not present information about the alloys used in their measurements.

O'Boyle and Dwight also presented new information about coexisting phases in thirteen alloys (Figure 1 and Table 1 of reference [81]). This information is included in Table 27 of this paper. It is entirely consistent with phase boundaries in the isothermal sections.

Comparisons between the isothermal sections and phase-transition temperatures is more complicated. O'Boyle and Dwight indicated that they considered data from references [219] and [166] (their references 12 and 13), which include most of the measurements of phase-transition temperatures in Table 25.

Figure 55 is a graphical depiction of the relationships between reported phase transition temperatures (Table 25) and the isothermal sections of O'Boyle and Dwight (Figure 54). Colored symbols in each row of Figure 55 show compositions that have reported phase transitions within the temperature range

indicated by numbers in parentheses, which is the same for all three diagrams in each row. The first diagram in each row shows the isothermal section at the upper end of the temperature range, the second diagram shows the isothermal section at the lower end of the temperature range, and the third diagram shows the isothermal section corresponding to the next lower temperature. If the phase transition temperatures and isothermal sections are consistent, each of the colored data points in Figure 55 should have a different phase assemblage in the left and middle isothermal sections in each row. Colored points that have the same phase assemblage in the left and middle sections indicate inconsistencies between the phase-transition temperatures and the isothermal sections. These points generally have different phase assemblages in the middle and right isothermal sections, indicating a phase transition between the temperatures of these sections.

For example, in the first row of Figure 55, the colored symbol labeled "8" indicates that the entry for point 8 in Table 25 has at least one phase transition temperature between 670 and 700°C. The first row of Figure 55 shows that the point 8 is single-phase γ at both 670 and 700°C and is in the two-phase $\gamma+\delta$ region at 660°C. Thus, the transition temperatures for point 8 in Table 25 are inconsistent with the isothermal sections of O'Boyle and Dwight because the Table 25 indicates a phase transition at 672°C and the isothermal sections indicate that the transition occurs between 660 and 670°C. Similar inconsistencies occur in the data for point 14 in the second row of Figure 55, points 28 and 34 in the fourth row, and points 24, 34, and 37 in the fifth row.

Despite these examples, measured phase transition temperatures in Table 25 are generally consistent with transition temperatures inferred from pairs of isothermal sections in Figure 54. Many of the inconsistencies can be resolved by assuming errors of a few percent in the compositions of the points, the positions of the contours, or the measured temperatures. Nonetheless, Figure 55 shows a pattern in which measured transition temperatures are consistently higher than transition temperatures inferred from isothermal sections. All of the inconsistencies involve temperatures measured by Mound Laboratory and phase transitions at the gamma solvus. It is not possible to determine the source of the inconsistencies. It is important to note, however, that consistency between measured transition temperatures and isothermal sections does not mean that the transition temperatures are accurate or the phases involved in each transition have been identified correctly.

New experimental research is needed to investigate essentially all aspects of the U-Pu-Zr phase diagram. It is important to combine phase-transition temperatures with identification and characterization of coexisting phases in equilibrium phase assemblages. As kinetics of phase transitions are poorly known but are generally considered to be sluggish, it may be appropriate to examine similar samples that have been annealed for different periods to determine the needed annealing times, and to investigate the extent to which results of high-temperature diffraction studies are influenced by heating rate and by isothermal holds. In this context, it may be important to differentiate between sluggish nucleation and sluggish coarsening, as that distinction may be crucial in interpreting observations of fine-scale microstructures using techniques such as TEM.

Phase boundaries in U-Zr alloys are known to be sensitive to low concentrations of impurities (e.g., [21]) and have been shown to differ between alloys that contain oxygen in concentrations of 160 and 355 ppm [25]. Thermodynamic calculations suggest that differences between experimentally determined Pu-Am phase diagrams may be due to impurities in the samples [242]. Although no comparable studies have investigated the influence of impurities in U-Pu-Zr alloys, it seems prudent to assume that these alloys also are highly sensitive to impurities. Therefore, it is important that future experimental research involves high-purity samples and careful documentation of actual compositions including impurities. Further experimental investigation of the entire phase diagram using high-purity samples with careful control of gaseous impurities such as O and N is needed.

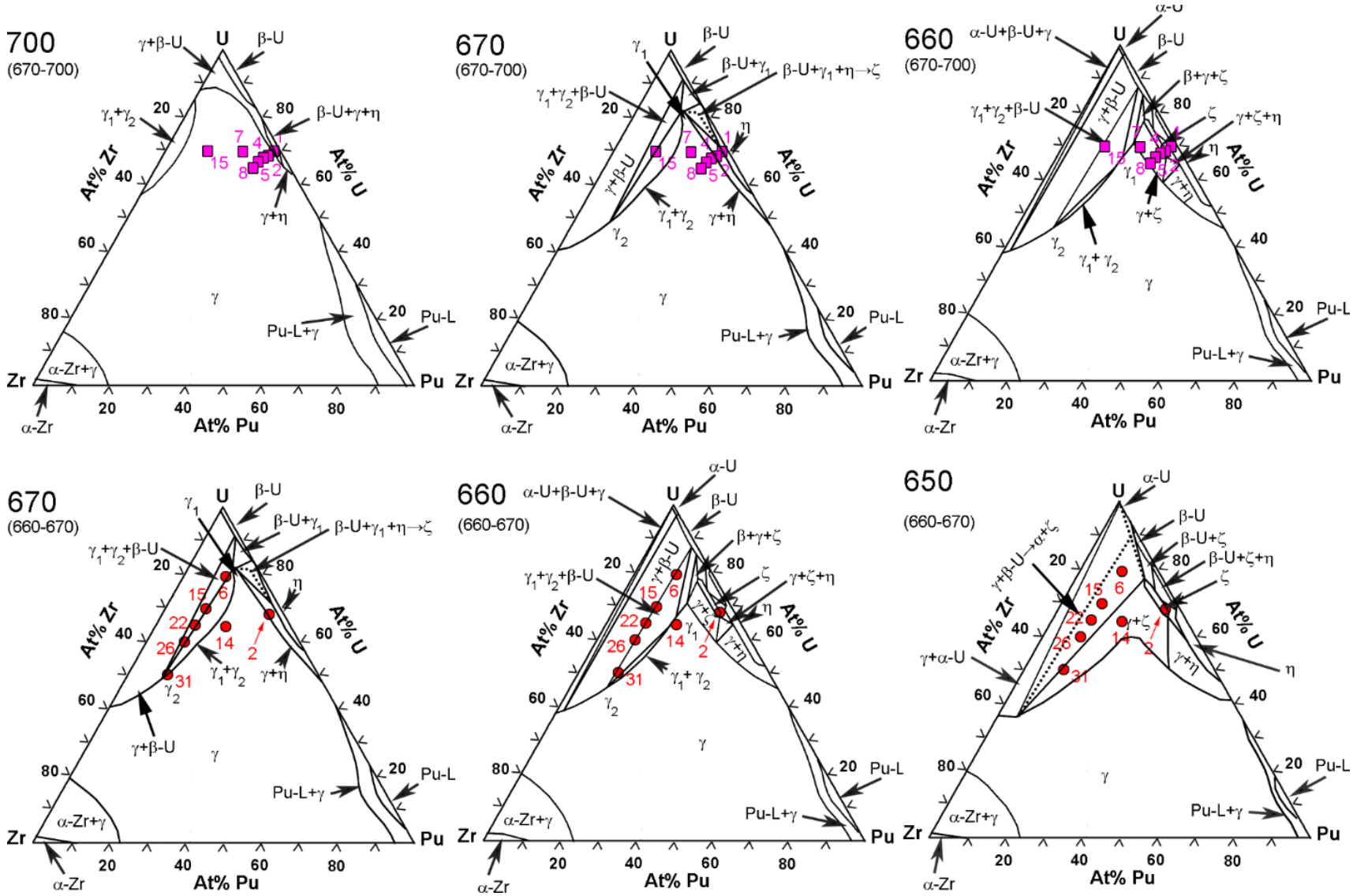
700
(670-700)
670
(670-700)
660
(670-700)
670
(660-670)
660
(660-670)
650
(660-670)
U
Zr
Pu
At% Zr
At% U
At% Pu
α-Zr
α-Zr+γ
Pu-L
Pu-L+γ
γ
γ+β-U
β-U
β-U+γ+η
γ+η
β-U+γ1+η→ζ
β+γ+ζ
γ+ζ+η
γ+ζ
α-U+β-U+γ
α-U
γ+β-U→α+ζ
β-U+ζ
β-U+ζ+η
γ+α-U

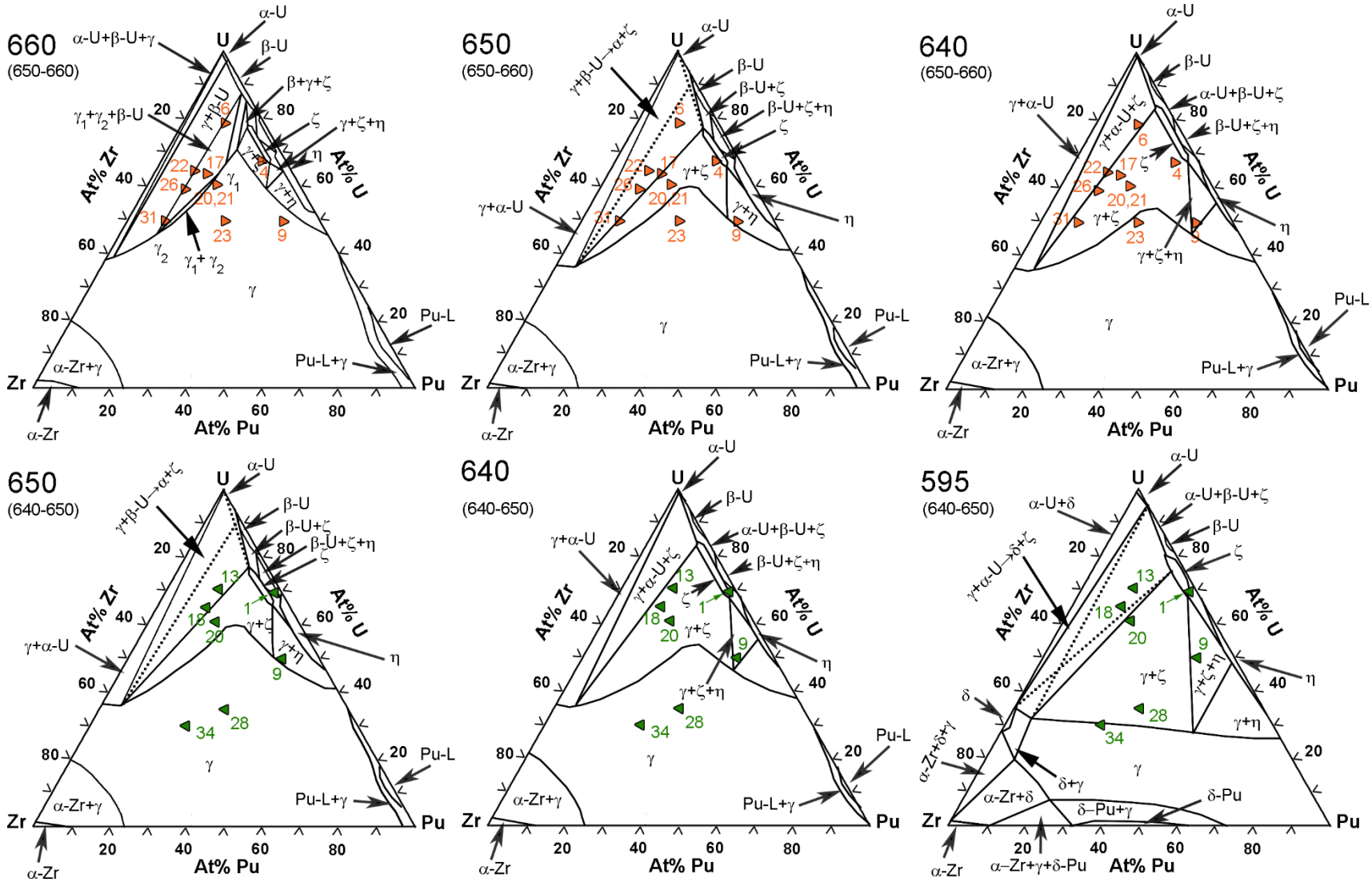
660
(650-660)
α-U+β-U+γ
α-U
β-U
β+γ+ζ
γ1+γ2+β-U
γ+β-U
ζ
γ+ζ+η
η
At% Zr
At% U
γ1
γ2
γ1+γ2
γ
γ+η
Pu-L
Pu-L+γ
α-Zr+γ
Zr
Pu
α-Zr
At% Pu
650
(650-660)
γ+β-U→α+ζ
β-U+ζ
β-U+ζ+η
γ+α-U
γ+ζ
640
(650-660)
α-U+β-U+ζ
γ+α-U+ζ
γ+ζ+η
650
(640-650)
640
(640-650)
595
(640-650)
α-U+δ
γ+α-U→δ+ζ
δ
α-Zr+δ+γ
δ+γ
α-Zr+δ
δ-Pu
δ-Pu+γ
α-Zr+γ+δ-Pu

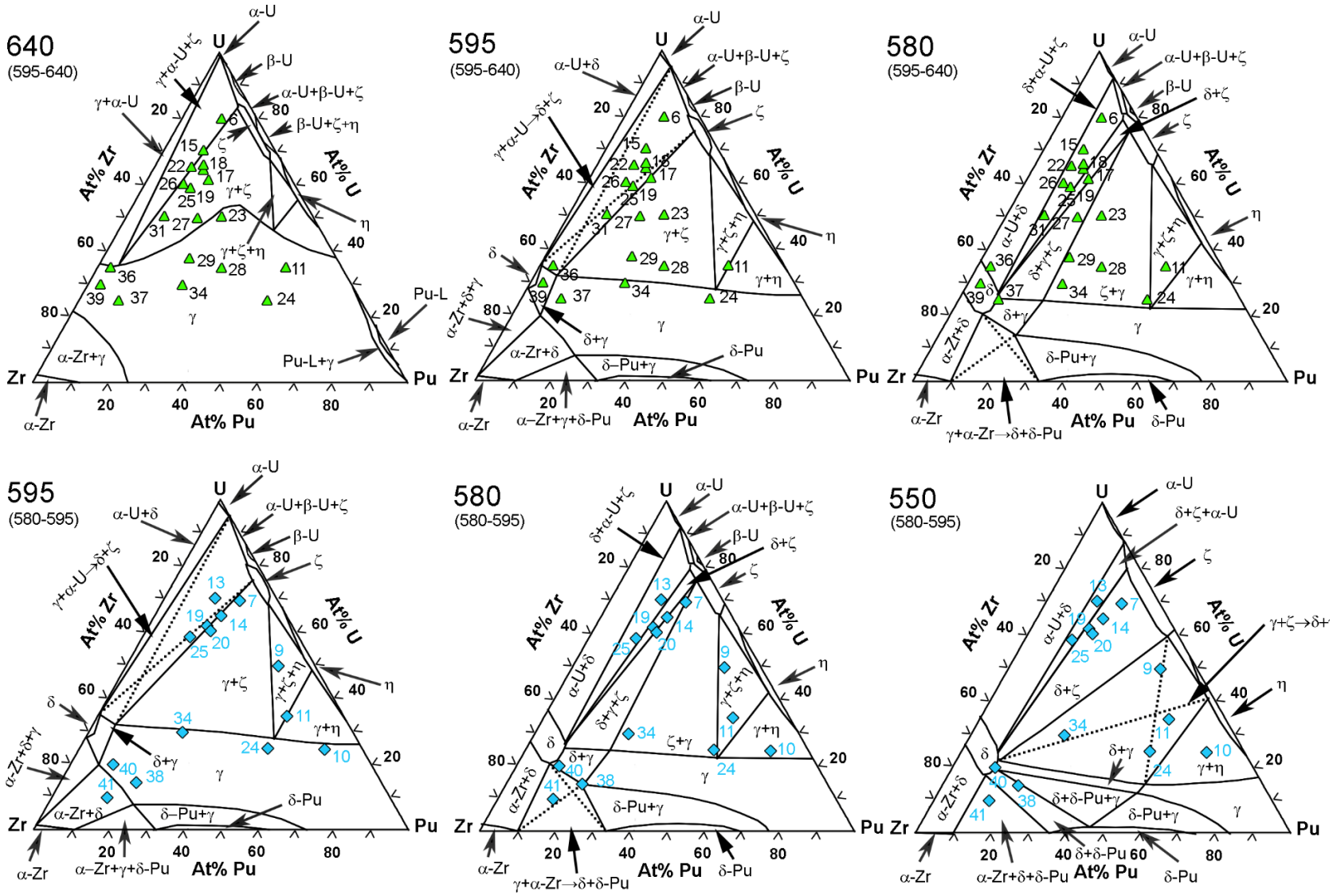
640
(595-640)
595
(595-640)
580
(595-640)
595
(580-595)
580
(580-595)
550
(580-595)
U
Zr
Pu
At% Zr
At% U
At% Pu
α-U
β-U
α-U+β-U+ζ
β-U+ζ+η
γ+α-U+ζ
γ+α-U
γ+ζ
γ+ζ+η
η
ζ
δ
Pu-L
Pu-L+γ
α-Zr+γ
α-Zr
γ
α-U+δ
γ+α-U→δ+ζ
α-Zr+δ+γ
δ+γ
α-Zr+δ
δ-Pu+γ
δ-Pu
α–Zr+γ+δ-Pu
γ+α-Zr→δ+δ-Pu
δ+ζ
δ+α-U+ζ
α-U+δ
δ+γ+ζ
γ+η
ζ+γ
δ+δ-Pu+γ
α-Zr+δ+δ-Pu
γ+ζ→δ+γ

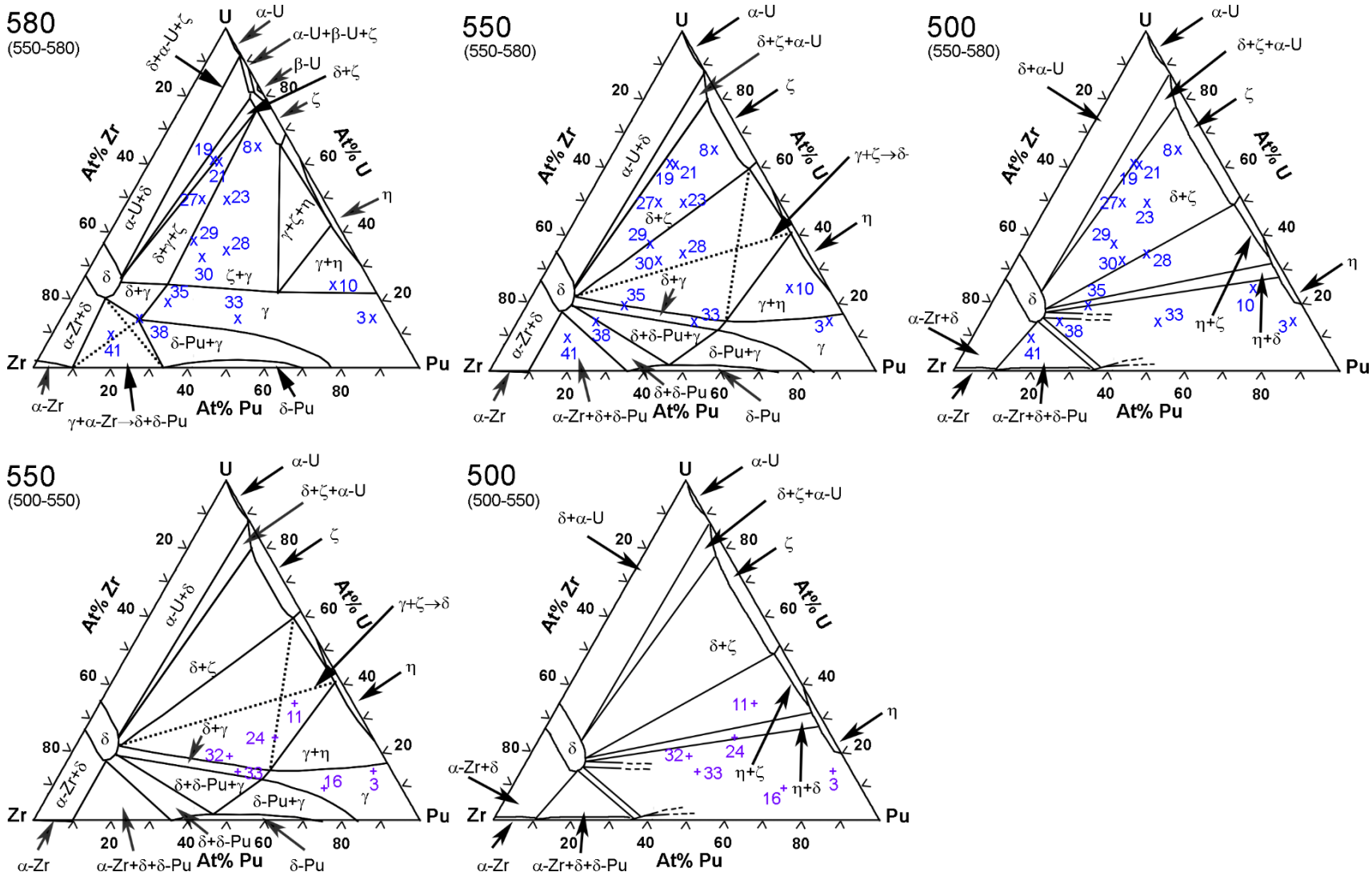

Figure 55. Comparison of measured phase-transition temperatures (Table 25) with transition temperatures from the isothermal sections of O'Boyle and Dwight (Figure 54). Large numbers adjacent to each isothermal section identify the temperature of the section. Smaller numbers in parentheses indicate a range of measured temperatures. Colored symbols represent compositions that have reported phase transitions in the specified temperature ranges. Numbers adjacent to the symbols correspond to point numbers in Table 25.

2.4.1.3 Heat Capacity and Related Properties

Experimental data about heat-capacities of seven U-Pu-Zr alloys are available. The earliest data were published by Savage in 1968 [204], and were calculated from measurements of incremental heat capacity of an alloy with composition U-20Pu-10Zr in wt% (U-12.6Pu-22.5Zr in at%) using drop calorimetry These values remain the only experimental values of the heat capacity of any U-Pu-Zr alloy at temperatures above 600°C. Equation 51, Equation 52, and Figure 56 express the incremental enthalpy measurements. Savage attributed the abrupt rise in the incremental enthalpy between 600 and 650°C to the transformation from (α-U) to (γ-U) and disappearance of (δ-UZr_2).

Equation 53 and Equation 54 express the corresponding heat capacities as linear functions of temperature.

Equation 51. Incremental enthalpy of U-15Pu-10Zr between 25 and 600°C [204]

$$H(T) - H(25) = -0.185+0.00636 \times T+0.00000318 \times T^2$$

where H is enthalpy at temperature T in kcal/mol, H(25) is enthalpy at 25°C in kcal/mol, T is temperature in °C, and T is between 25 and 600°C

Equation 52. Incremental enthalpy of U-15Pu-10Zr between 650 and 1150°C [204]

$$H(T) - H(25) = 2.91+0.00379 \times T+0.00000312 \times T^2$$

where H is enthalpy at temperature T in kcal/mol, H(25) is enthalpy at 25°C in kcal/mol, T is temperature in °C, and T is between 650 and 1150°C

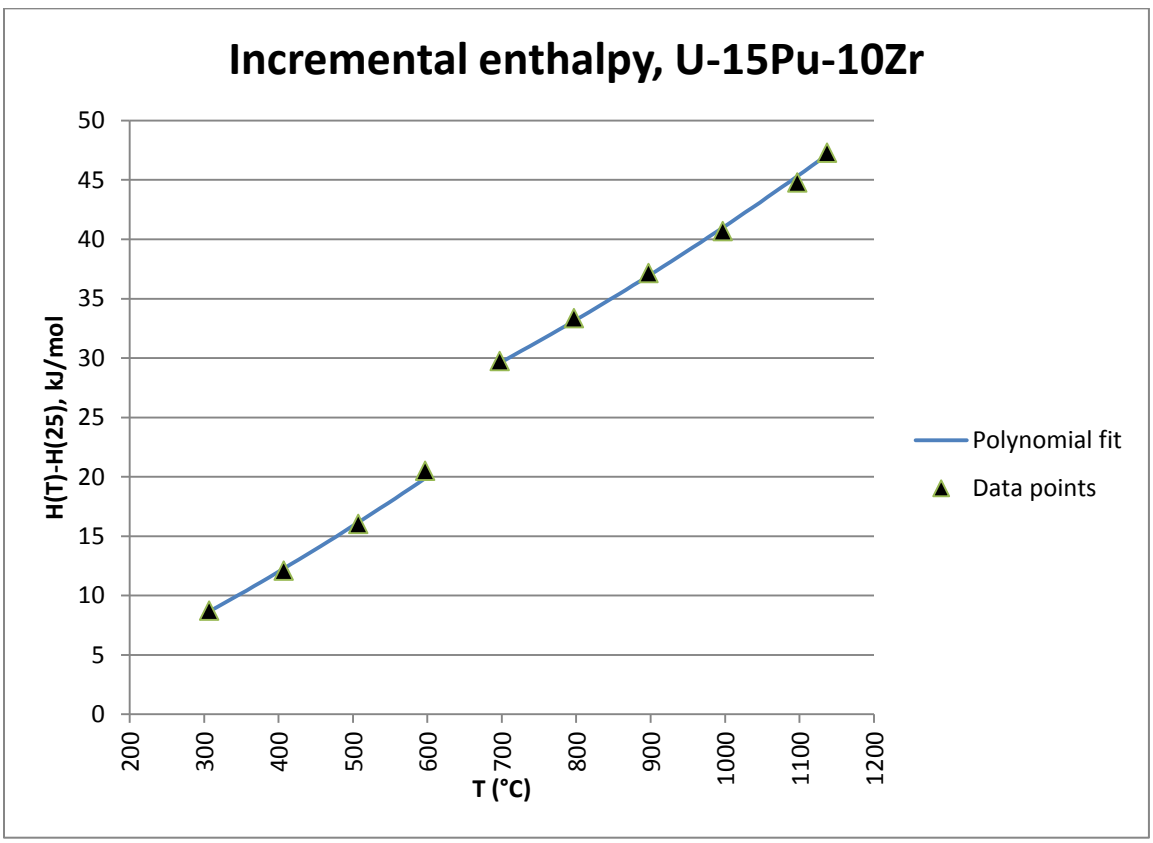

Figure 56. Incremental enthalpy (H(T) – H(25)) of U-15Pu-10Zr [204]. Triangles are measured data points, and the polynomial fit is calculated from Equation 53 and Equation 54.

Equation 53. Heat capacity of U-15Pu-10Zr between 25 and 600°C [204]

$C_p = 6.36+0.00636 \times T$

where C_p is constant-pressure heat capacity in cal/ mol·°C, T is temperature in °C, and T is between 25 and 600°C

Equation 54. Heat capacity of U-15Pu-10Zr between 650 and 1150°C [204]

$C_p = 3.79+0.00623 \times T$

where C_p is constant-pressure heat capacity in cal/ mol·°C, T is temperature in °C, and T is between 650 and 1150°C.

More recently, researchers at INL measured the heat capacities of an additional six alloys using DSC/DTA. These alloys are the same as those used to measure phase-transition enthalpies (Table 26). The INL measurements were made in an air-atmosphere glovebox. Despite a flowing cover gas of high-purity argon with oxygen concentration below the parts per billion range, some samples developed visible oxide layers during data collection. Attempts to obtain reliable heat-capacity measurements at higher temperatures were unsuccessful. The INL data were expressed as polynomials (Equation 55 through Equation 60).

Equation 55. Heat capacity (in J/g-K) of INL Alloy AFC2-E1 (U-20Pu-10Zr in wt%, U-17Zr-23Zr in at%) for temperatures between room temperature and 550°C

$C_p = -9\times10^{-8}\times T^2 + 0.0001\times T + 0.1368$

Equation 56. Heat capacity (in J/g-K) of INL Alloy AFC2-B7 (U-24Pu-15Zr in wt%, U-19Pu-32Zr in at%) for temperatures between 100 and 540°C

$C_p = -3.54\times10^{-8}\times T^2 + 1.18\times10^{-4} \times T + 0.130$

Equation 57. Heat capacity (in J/g-K) of INL Alloy AFC2-B1 (U-30Pu-20Zr in wt%, U-22Pu-40Zr in at%) for temperatures between 100 and 540°C

$C_p = -8.48\times10^{-8}xT^2 + 2.22\times10^{-4}\times T + 0.135$

Equation 58. Heat capacity (in J/g-K) of INL Alloy AFC2-B8 (U-36.5Pu-20Zr in wt%, U-27Pu-40Zr in at%) for temperatures between 100 and 540°C

$C_p = -5\times10^{-8}T^2 + 0.0001\times T + 0.1285$

Equation 59. Heat capacity (in J/g-K) of INL Alloy AFC2-B2 (U-55Pu-20Zr in wt%, U-41Pu-40Zr in at%) for temperatures between 100 and 460°C

$C_p = -6.61\times10^{-8}xT^2 + 1.17x10^{-4}\times T + 0.127$

Equation 60. Heat capacity (in J/g-K) of INL Alloy AFC2-B3 (U-20Pu-45Zr in wt%, U-12Pu-68Zr in at%) for temperatures between 100 and 575°C.

$C_p = -4.69\times10^{-8}T^2 + 1.74x10^{-4}\times T + 0.177$

Figure 57 shows the heat capacities of the U-Pu-Zr alloys measured by Savage and by researchers at INL. Although there is some variation in heat capacities, there is no obvious relationship between heat capacities and compositions. New measurements with careful control of oxygen and nitrogen in the samples and glovebox atmosphere are clearly required. In the absence of these measurements, it seems reasonable to approximate the heat capacities of these U-Pu-Zr alloys by that of U, as suggested by Savage [204].

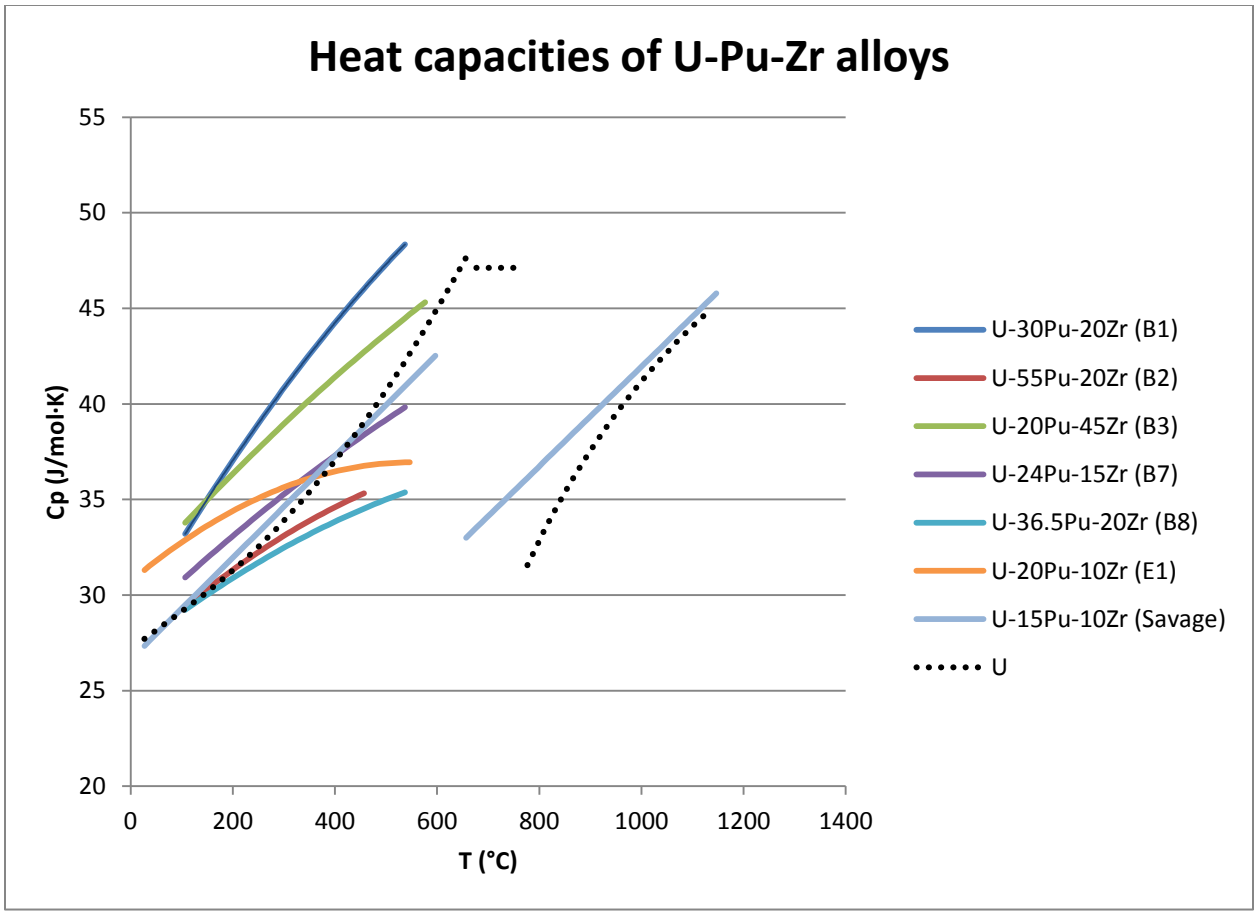

Figure 57 (corrects Figure 61 of reference [3]). Heat capacities of U-Pu-Zr alloys, calculated from Equation 55 through Equation 60, and converted to J/mol-K. Compositions in legend are in wt%. The heat capacity of pure U [210] is provided for comparison.

2.4.1.4 Thermal Expansion and Density

2.4.1.4.1 Thermal Expansion Coefficients

Published measurements of thermal expansion coefficients for U-Pu-Zr alloys were originally reported by researchers at CEA and Argonne National Laboratory [211, 213]. Other publications (e.g., [48, 193, 209, 212, 243]) repeat these measurements. All of the available data are from alloys with 11-20 wt% Pu and 6-15 wt% Zr. Within this composition range, there is generally good agreement about thermal expansion coefficients.

The published measurements generally fall within two temperature ranges separated by phase transformations: room temperature to ~600°C, and above ~660°C (Table 29, Table 30). Reported coefficients of thermal expansion below the phase transformations range from 16.3×10^{-6}/°C to 18.3×10^{-6}/°C, and reported coefficients of thermal expansion above the phase transformations range from 18.1×10^{-6}/°C to 20.1×10^{-6}/°C. In view of the relatively small variation in the reported values and the lack of an obvious correlation between thermal expansion coefficients and compositions, it seems reasonable to estimate the thermal expansion coefficients of alloys with ~10-20 wt% Pu and 5-15 wt% Zr by using the average values of the reported data (17.5×10^{-6}/°C below the phase transformations and 20.1×10^{-6}/°C above).

Table 29 and Table 30 do not include data for an alloy whose nominal composition is listed as U-15Pu-15Zr (at%) and U-17.1Pu-3.4Zr (wt%) in reference [213]. Compositions in wt% and at% for this alloy are inconsistent, and other early references that generally repeat the same measurements list this as a U-Pu-Ti alloy [193, 209].

Table 29. Thermal expansion coefficients for U-Pu-Zr alloys between room temperature and ~600°C.

Composition (wt%)	**Composition (at%)**	**Coefficient of Thermal Expansion × 10^6 (per °C)**	**Temperature Range (°C)**	**References**
U-11.1Pu-6.3Zr	U-10Pu-15Zr	18.3	25-595	[48, 193, 209, 213]
U-15Pu-10Zr	U-13Pu-22.5Zr	17.6	25-595	[48, 193, 209, 213]
U-15Pu-10Zr	U-13Pu-22.5Zr	16.3	20-600	[48, 209, 211, 212]
U-20Pu-10Zr	U-17Pu-23Zr	17.3	20-586	[48, 209, 211, 212, 243]
U-17Pu-14Zr	U-14Pu-30Zr	18.2	25-596	[244]
U-18.5Pu-14.1Zr	U-15Pu-30Zr	17.5	25-595	[48, 193, 209, 213]
Average		17.5	20-586	—

Table 30. Thermal expansion coefficients for U-Pu-Zr alloys at higher temperatures.

Composition (wt%)	**Composition (at%)**	**Coefficient of Thermal Expansion × 10^6 (per °C)**	**T Range (°C)**	**References**
U-11.1Pu-6.3Zr	U-10Pu-15Zr	18.1	680-950	[193, 209, 213]
U-15Pu-10Zr	U-12.9Pu-22.5Zr	20.1	665-950	[48, 193, 209, 213]
U-17Pu-14Zr	U-14Pu-30Zr	22.3	665-950	[244]
U-18.5Pu-14.1Zr	U-15Pu-30Zr	20.0	660-950	[48, 193, 209, 213]
Average		**20.1**	**660-950**	**—**

2.4.1.4.2 Changes In Length Due to Phase Transitions

Table 31 shows reported changes in length associated with phase transformations in U-Pu-Zr alloys. Data for an alloy whose nominal composition is listed as U-15Pu-15Zr (at%) and U-17.1Pu-3.4Zr (wt%) in reference [213] are not included because the compositions in wt% and at% are inconsistent, and because other early references that generally repeat the same measurements list this as a U-Pu-Ti alloy [193, 209].

The change in length associated with phase transformations between ~585 and 680°C is generally reported as an increase of ~0.5% in data originally published by ANL [213] and ~0.3% in data originally published by CEA [211]. However, reference [211] recognizes two phase transformations within this temperature range and only reports expansion due to the larger of the two, while reference [213] reports only one transformation. Thus, it seems reasonable to assume that the total thermal expansion ($\Delta L/L_0$) related to all of the phase transformations between ~585 and 680°C is ~0.5% for alloys with ~10-20 wt% Pu and 5-15 wt% Zr. Further measurements may be desirable, particularly if the phases involved in the transitions can be reliably identified.

Table 31. Length changes (in %) from phase transformations in U-Pu-Zr alloys.

Composition (wt%)	Length Change ($\Delta L/L_0$, %)	Temperature Range (°C)	References
U-11.1Pu-6.3Zr	0.51	595-680	[193, 209, 213]
U-15Pu-10Zr	0.52	595-665	[193, 209, 213]
U-15Pu-10Zr	0.31[a]	645	[211]
U-20Pu-10Zr	0.31[a]	650	[211]
U-17Pu-14Zr	0.58	595-665	[244]
U-18.5Pu-14.1Zr	0.50	595-660	[193, 209, 213]
a. Refers to only one of two transformations.			

2.4.1.4.3 Density

Experimental measurements of room-temperature densities of U-Pu-Zr alloys were originally published in several reports [211, 213, 217] and summarized in a recent review [48]. Data for an alloy whose nominal composition is listed as U-15Pu-15Zr (at%) and U-17.1Pu-3.4Zr (wt%) in reference [213] is not included because compositions in wt% and at% for this alloy are inconsistent, and because other early references that generally repeat the measurements from reference [213] list it as a U-Pu-Ti alloy [193, 209].

Table 32 and Figure 58 present the experimental data, with theoretical densities for comparison. The theoretical densities were calculated using Equation 8, assuming that the phases present are α-U with a density of 19.05 g/cm^3, α-Pu with a density of 19.84 g/cm^3, and α-Zr with a density of 6.52 g/cm^3 (Sections 2.1.4.3, 2.3.4.3, and 2.9.4.3 of reference [5]). The theoretical density of a specific alloy may be slightly different from the value presented here depending on the isotopes present.

Table 32 and Figure 58 present the experimental data. All of the measured densities are below the theoretical density, but generally only by a few percent (Figure 58). Some differences between measured and actual densities may be explained by differences between nominal and actual compositions, by differences between isotopes used to calculate theoretical densities and those actually present, and (at least in principle) by densities of phases actually present. The data from Harbur et al. (red lines in Figure 58) suggest that extrusion may increase the density of an alloy slightly. Data from Boucher and Barthelemy [211, 212] suggest that differences in thermal history have little effect on density. Some researchers have suggested that the concentrations of impurities such as carbon and oxygen are important, and that alloys with ~500 ppm impurities are ~3-5% lower than in alloys without impurities [213].

Despite these possible sources of differences between theoretical and actual densities, it seems reasonable to approximate densities of actual U-Pu-Zr alloys by their theoretical densities.

Table 32. Room-temperature densities of U-Pu-Zr alloys, listed in order of increasing atomic fraction of Zr.

Composition (wt%)	Composition (at%)	T (°C)	Measured density (g/cm^3)	Theoretical density (g/cm^3)	Comments	Reference
U-11.1Pu-6.3Zr	U-10Pu-15Zr	25	17.0	17.06	As-cast	[213 Table 1]
U-15Pu-10Zr	U-12.6Pu-22.6Zr	25	16.0	16.06	As-cast	[213 Table 1]
U-15Pu-10Zr	U-12.6Pu-22.6Zr	20	15.67	16.06	As-cast	[211]
U-15Pu-10Zr	U-12.6Pu-22.6Zr	20	15.74	16.06	Quenched from 500°C	[211]

Table 32. (continued).

Composition (wt%)	Composition (at%)	T (°C)	Measured density (g/cm^3)	Theoretical density (g/cm^3)	Comments	Reference
U-15Pu-10Zr	U-12.6Pu-22.6Zr	20	15.79	16.06	Quenched from 900°C	[211]
U-19Pu-10Zr	U-16Pu-22.6Zr		15.80	16.08	As-cast	[149]
U-20Pu-10Zr	U-16.9Pu-22.6Zr	20	15.73	16.09	As-cast	[211]
U-20Pu-10Zr	U-16.9Pu-22.6Zr	20	15.64	16.09	Quenched from 500°C	[211, 212]
U-20Pu-10Zr	U-16.9Pu-22.6Zr	20	15.65	16.09	Quenched from 900°C	[211]
U-20Pu-10Zr	U-16.9Pu-22.6Zr	Room T	15.31	16.09	As-cast	INL unpublished
U-18.4Pu-14.1Zr	U-15Pu-30Zr	25	15.1	15.09	As-cast	[213 Table 1]
U-24Pu-15Zr	U-19Pu-32Zr	Room T	13.3	14.90	As-cast	INL
U-30Pu-20Zr	U-22Pu-40Zr	Room T	13.15	13.89	As-cast	INL unpublished
U-36.5Pu-20Zr	U-27Pu-40Zr	Room T	13.15	13.91	As-cast	INL unpublished
U-55Pu-20Zr	U-41Pu-40Zr	Room T	13.43	13.98	As-cast	INL unpublished
U-20Pu-45Zr	U-11Pu-68Zr	Room T	9.87	10.26	As-cast	INL unpublished

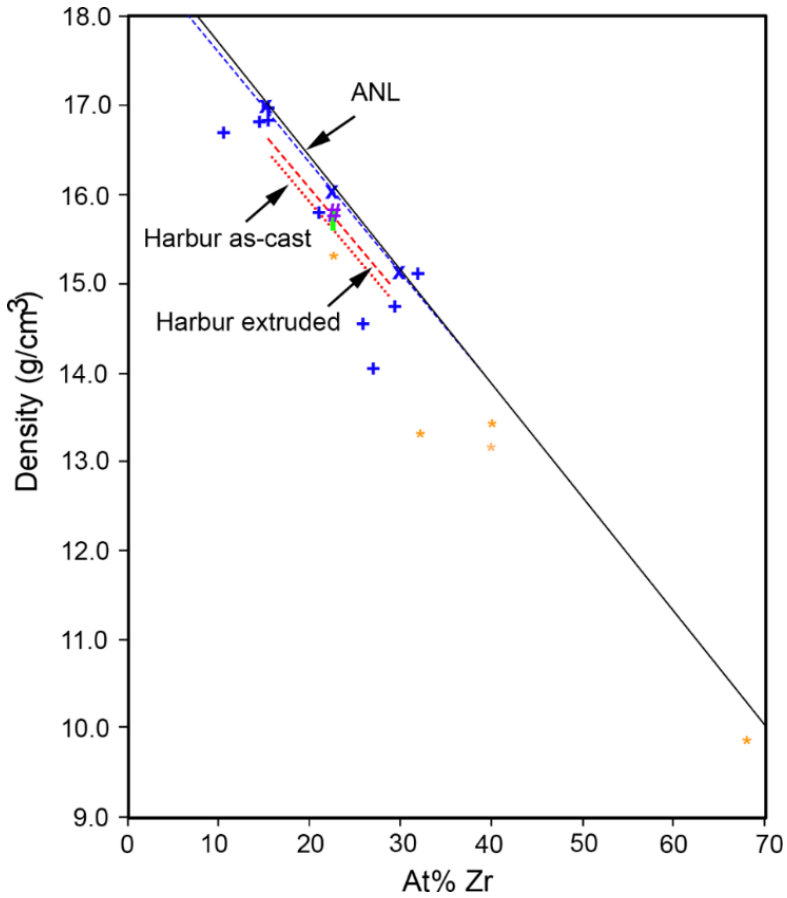

Figure 58 (corrects and updates Figure 62 of reference [3]). Room-temperature densities of U-Pu-Zr alloys (blue line and "+" symbols are from Figure 5 of reference [213], blue "x" symbols are from Table 1 of reference [213], purple "#" symbol is from [149], orange "*" symbols are INL data, dotted and dashed red lines are from [217], green line indicates range of values in data from references [211, 212], black line is theoretical density).

2.4.1.5 Thermal Conductivity and Related Properties

Several studies of the thermal conductivity of U-Pu-Zr alloys are available [211, 213, 217, 244, 245]. All of the alloys have ~15-20 wt% Pu and ~6-15 wt% Zr, and two of the studies involve only one or two data points.

The thermal conductivity values are summarized in Table 33 and Figure 59. Data for an alloy whose nominal composition is listed as U-15Pu-15Zr (at%) and U-17.1Pu-3.4Zr (wt%) in reference [213] are not included because compositions in wt% and at% for this alloy are inconsistent, and because other early references that generally repeat the measurements from reference [213] list it as a U-Pu-Ti alloy [193, 209]

As noted by researchers at Argonne National Laboratory, increasing the amount of Zr lowers the thermal conductivity for alloys with the same Pu content [245]. Although there are exceptions, the available data also show that thermal conductivity tends to be lower in materials with higher Pu contents.

Table 33. Thermal conductivities of U-Pu-Zr alloys (W/cm-K).

T (°C)	**Composition (wt% Zr)** **Composition (at% Zr)** **References**						
	U-16.2Pu-6.2Zr ~U-14.7Pu-15Zr [245] (Casting D44)	**U-15Pu-6.8Zr ~U-13Pu-16Zr [217]**	**U-14.7Pu-9.7Zr U-12.7Pu-21.9Zr [245] (Casting D54)**	**U-15Pu-10Zr ~U-12.6Pu-22.6Zr [213]**	**U-20Pu-10Zr ~U-16.9Pu-22.6Zr [211]**	**U-18.4Pu-11.5Zr ~U-15.5Pu-25.3Zr [245] (Casting D50)**	**U-18.4Pu-14.1Zr ~U-14.7-30.1Zr [213]**
23	—	—	—	—	0.084a	—	—
100	0.109	—	0.100	—	—	0.092	—
110	—	0.128	—	—	—	—	—
200	0.142	—	0.132	0.12	—	0.117	0.11
300	0.177	—	0.164	—	—	0.144	—
400	0.210	—	0.196	0.18	—	0.171	0.17
500	0.241	—	0.225	—	—	0.197	—
600	0.264	—	0.253	0.22	—	0.219	0.21
700	0.280	—	0.278	—	—	0.234	—
800	0.293	—	0.301	0.25	—	0.248	0.24
892	—	0.317	—	—	—	—	—
900	~0.301	—	~0.323	—	—	~0.260	—

NOTE a: Calculated from electrical resistivity (86 μΩ-cm at 23°C) and the Wiedemann-Franz law (Section 1.6.2)

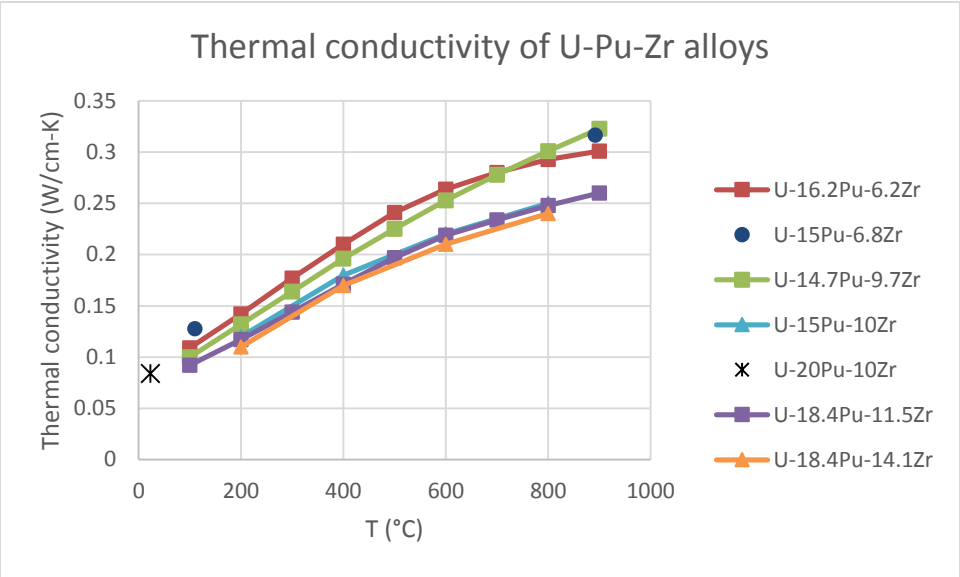

Figure 59. Thermal conductivity of U-Pu-Zr alloys (data from Table 33). Compositions are in wt%. Symbols indicate sources of data: squares are from [245], circles are from [217], triangles are from [213], and asterisk is from [211].

Billone et al. [128], Ogata [48, 49], and Kim et al. [126] developed equations to predict the thermal conductivity of U-Pu-Zr alloys. The Billone et al. model was developed to allow the LIFE-METAL fuel performance code to be used for U-Pu-Zr alloys, and represents the thermal conductivity of an alloy as a quadratic equation in T. The Ogata model is purely empirical, and represents the thermal conductivities of compositions with less than 72 at% Zr and 16 at% Pu as linear functions of temperature. The Kim et al. model incorporates "fitting factors" to extend the Bruggeman model for thermal conductivity of two-phase materials to solid solutions, which makes it possible to calculate an approximate thermal conductivity for an alloy based on temperature, composition, and the thermal conductivities of the elements involved.

Figure 60 compares the Billone et al. and Ogata models to measured thermal conductivity for alloys with compositions close to U-15Zr-10Pu (green) and U-18Pu-20Zr (turquoise). The Kim et al. model is not included because the practical difficulties involved in calculating it do not seem justified without a better knowledge of the required elemental thermal conductivity values. The Billone et al. model is a reasonable representation of the available data for U-15Zr-10Pu, but neither model is a good approximation for the U-18.4Pu-14.1Zr data. Given the widespread availability of curve-fitting software, the best approach may be to fit a curve to the desired thermal conductivity values rather than using a previously published model.

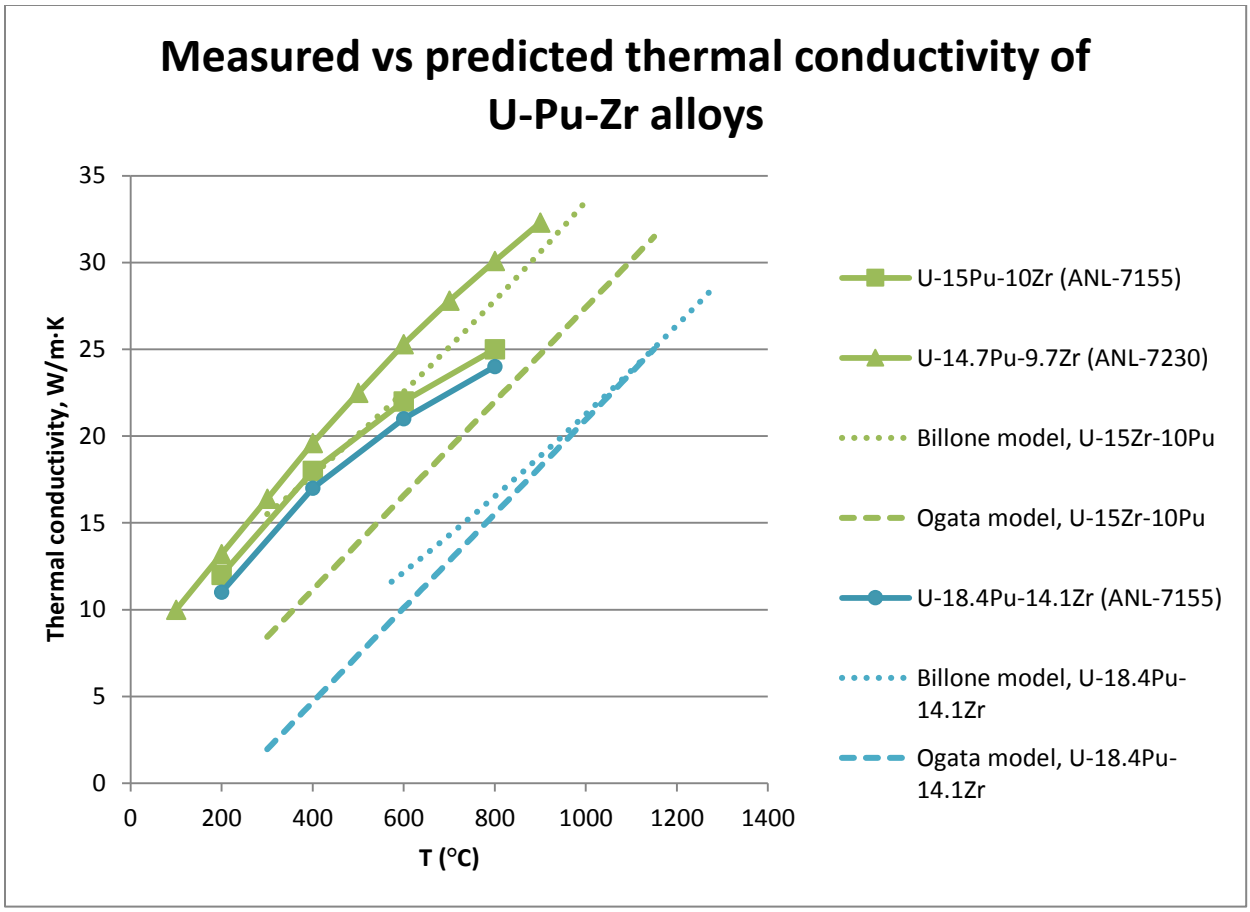

Figure 60. Comparison of measured and predicted thermal conductivity of U-Pu-Zr alloys (compositions in wt%)

There are no measurements of thermal conductivities of individual U-Pu-Zr phases. However, R.J. Dunworth suggested that the thermal conductivity of α-(U,Pu) and δ-(U,Pu)Zr_2 is about twice that of ζ-(U,Pu) based on a comparison between thermal conductivity measurements and volume fractions of phases determined from an isothermal section of the U-Pu-Zr phase diagram at 500°C [213 page 19]. Since Dunworth believed that increasing the concentration of Pu should increase the proportion of ζ-(U,Pu) and decrease that of α-(U,Pu), he inferred that alloys with higher proportions of Pu would have lower thermal conductivities. This suggestion is qualitatively consistent with the data in Figure 59.

2.4.1.6 Mechanical Properties

2.4.1.6.1 Yield stress, ultimate tensile stress, and elastic (Young's) modulus

Data on tensile properties of U-Pu-Zr alloys are available from sources including:

- A table in a 1971 review by Kittel et al. (Table 26 of [209]), which includes information about the composition, temperature, ultimate tensile strength (UTS), yield strength, modulus of elasticity, area reduction, and total elongation. Some of the same information also appears in two Argonne National Laboratory reports (Table VII of reference [219] and Table 4 of reference [213]). Reference [209] indicates that the samples were homogenized at 950°C for a week and oil quenched. Although reference [213] indicates that the sample were homogenized, it does not specify the time or temperature. If it is assumed that the homogenization conditions were the same for samples used in tensile and compression testing, alloys with >10 wt% Zr were homogenized at 1050°C, not 950°C

(footnote to Table 3, reference[213]). According to the Argonne reports, tensile properties were measured on samples that had previously been used to measure creep properties, and, therefore, contained some (<5%) hot work. No other information about sample properties or test procedures was provided.

- A report of the ultimate tensile strength, yield strength, elongation, and elastic modulus of six U-Pu-Zr alloys tested at Los Alamos National Laboratory [217]. All of the alloys were cast, and five were then extruded. Oxygen contents were reported for three of the alloys, with a maximum value of 180 ppm. The initial strain rate for the tests was 0.015/min; however, tests were carried out with a contant load, and strain rates during ductile deformation were not controlled. It was not possible to read the units in which the elastic modulus was reported in any of the available copies; however, assistance from librarians at INL and Los Alamos Scientific Laboratory clarified that the units were psi × 10^6. These units are consistent with those implicitly assumed in a 2012 review by Ogata [48].
- A single value for the elastic modulus of METAPHIX alloy CR13 (U-19Pu-10Zr by weight) (Table 3 of reference [149]). This measurement was intended to allow comparisons between U-Pu-Zr alloys and U-Pu-Zr alloys with minor actinides and rare earth elements. It was made using an ultrasonic method. No other details about the testing and measurement procedures (including measurement temperature) were provided.

Table 34, Figure 61, Figure 62, and Figure 63 summarize the available measurements of tensile properties of U-Pu-Zr alloys. Samples for which yield strengths are not reported experienced brittle failure.

Figure 61 shows a clear difference between the ultimate tensile strengths in measurements reported by Kittel et al. and by Harbur et al, even for samples with similar compositions (e.g., compare sample number 3 with 4, and 9 with 10 and 11 in Table 34). In the absence of detailed information about the samples and measurement procedures used by Kittel et al., it is not clear whether these differences are due to differences in sample compositions (particularly impurities) or testing conditions.

Although measurements of tensile properties of individual phases are not available, the decrease in yield strength in all samples with increasing temperatures is generally interpreted as indicating that the γ phase is weak and ductile. Although it is possible that the small increase in yield strengths at between ~525 and 625°C is a consequence of phase transitions at the gamma solvus (Section 2.4.1.2.3.1), this interpretation should be treated with caution because measurements below this temperature range were reported by Harbur et al. and those above it were reported by Kittel et al.

Table 34. Tensile properties of U-Pu-Zr alloys.

Sample No.	**Composition (wt%)**	**Composition, at%**	**T (°C)**	**Ultimate tensile strength, kg/mm^2**	**Yield strength (0.2% offset), kg/mm^2**	**Elastic modulus, kg/mm^{2}x10^{-3}**	**References**
	Wt% U	At% U	—	—	—	—	—
1	U-11.1Pu-6.3Zr	U-9.85Pu-15Zr	25	18.1	—	17.4	[209, 213, 219]
1	—	—	500	30.1	—	6.8	[209]
1	—	—	625	9.5	8.7	3	[209]
1	—	—	675	1.2	1.1	1.4	[209, 213, 219]
2	U-16.6Pu-6.3Zr	U-14.8Pu-15Zr	25	4	—	10.6	[209, 213, 219]
2	—	—	500	15.8	—	—	[209]
2	—	—	625	8.9	4.1	2.1	[209]
2	—	—	675	1.2	1.1	1.6	[209, 213, 219]
2	—	—	700	1.2	1.6	1.7	[209]

Table 34. (continued).

Sample No.	Composition (wt%)	Composition, at%	T (°C)	Ultimate tensile strength, kg/mm^2	Yield strength (0.2% offset), kg/mm^2	Elastic modulus, kg/mm^{2}x10^{-3}	References
3	U-15Pu-10Zr	U-12.6Pu-22.6Zr	25	6.7	—	12.5	[209]
3	—	—	500	13.3	—	6.6	[209]
3	—	—	625	8.1	7.2	1.6	[209]
3	—	—	675	2.1	1.7	3.3	[209]
4	U-15Pu-10Zr	U-12.6Pu-22.6Zr	25	49.2	—	1.5	[217]
4	—	—	300	27.4	—	1.4	[217]
4	—	—	350	30.9	30.9	0.6	[217]
4	—	—	400	9.8	7.0	0.3	[217]
5	U-19Pu-10Zr	U-16Pu-22.6Zr	—	—	—	8.7	[149]
6	U-14Pu-11.7Zr	U-11.6Pu-26Zr	25	53.4	—	1.6	[217]
6	—	—	100	56.2	—	1.5	[217]
7	U-15Pu-12.2Zr	U-12.3Pu-26.7Zr	25	42.9	—	1.0	[217]
8	U-15Pu-12.2Zr	U-12.3Pu-26.7Zr	25	67.3	—	1.9	[217]
8	—	—	300	59.6	—	1.8	[217]
8	—	—	350	39.2	38.7	1.7	[217]
8	—	—	450	5.7	4.8	0.3	[217]
8	—	—	525	4.0	2.9	0.3	[217]
9	U-15Pu-13.5Zr	U-12.1Pu-29Zr	25	59.1	—	0.7	[217]
10	U-12.3Pu-14.1Zr	U-9.8Pu-30.1Zr	25	4.9	—	10.2	[209]
11	U-18.5Pu-14.1Zr	U-14.8Pu-30.1Zr	25	7.7	—	13	[209, 213, 219]
11	—	—	675	2.9	2.8	1.9	[209, 213, 219]

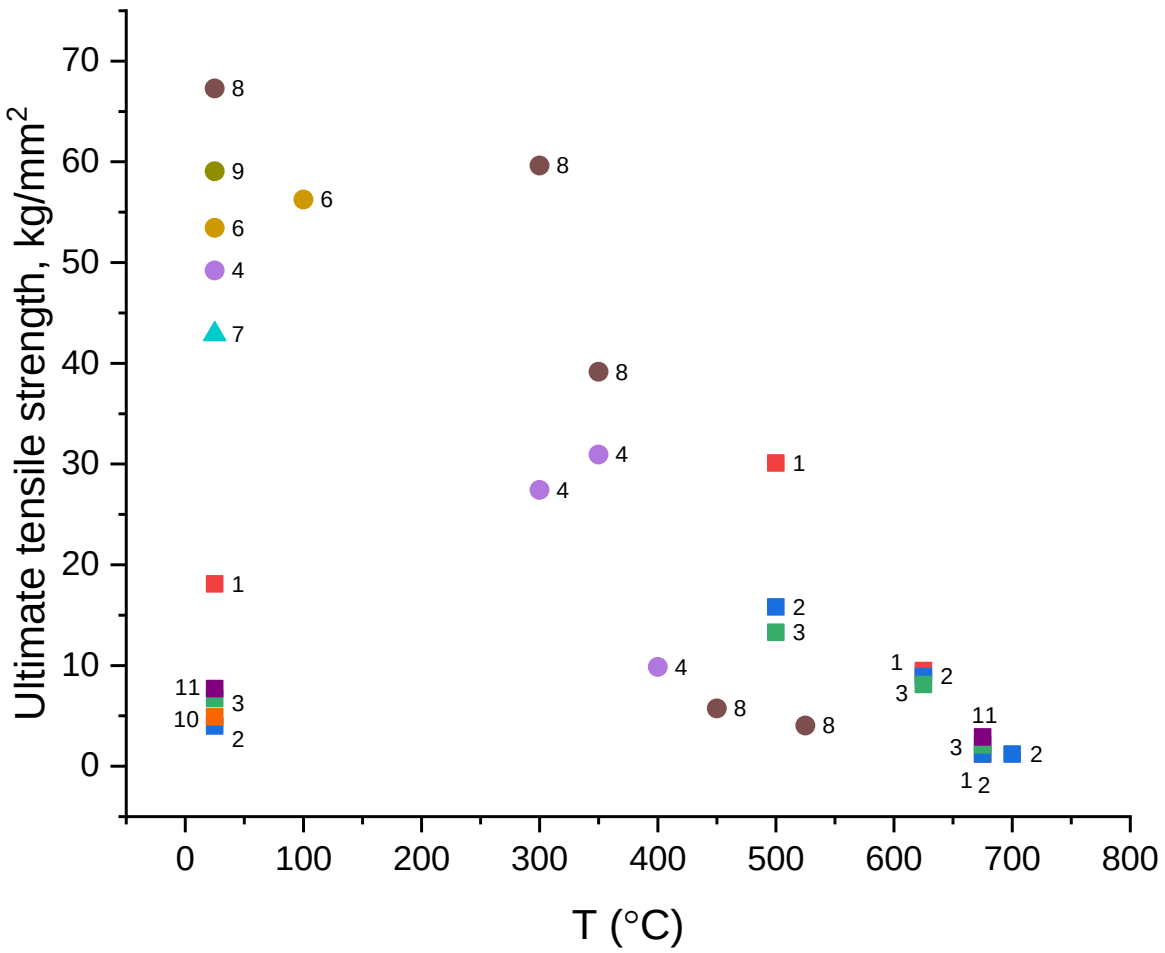

Figure 61. Ultimate tensile strength of U-Pu-Zr alloys. Data values are in Table 34. Different shapes indicate different data sources (circle: reference [209], squares: as-extruded data from reference [217], triangle: as-cast data from reference [217]. Numbers and colors indicate individual samples.

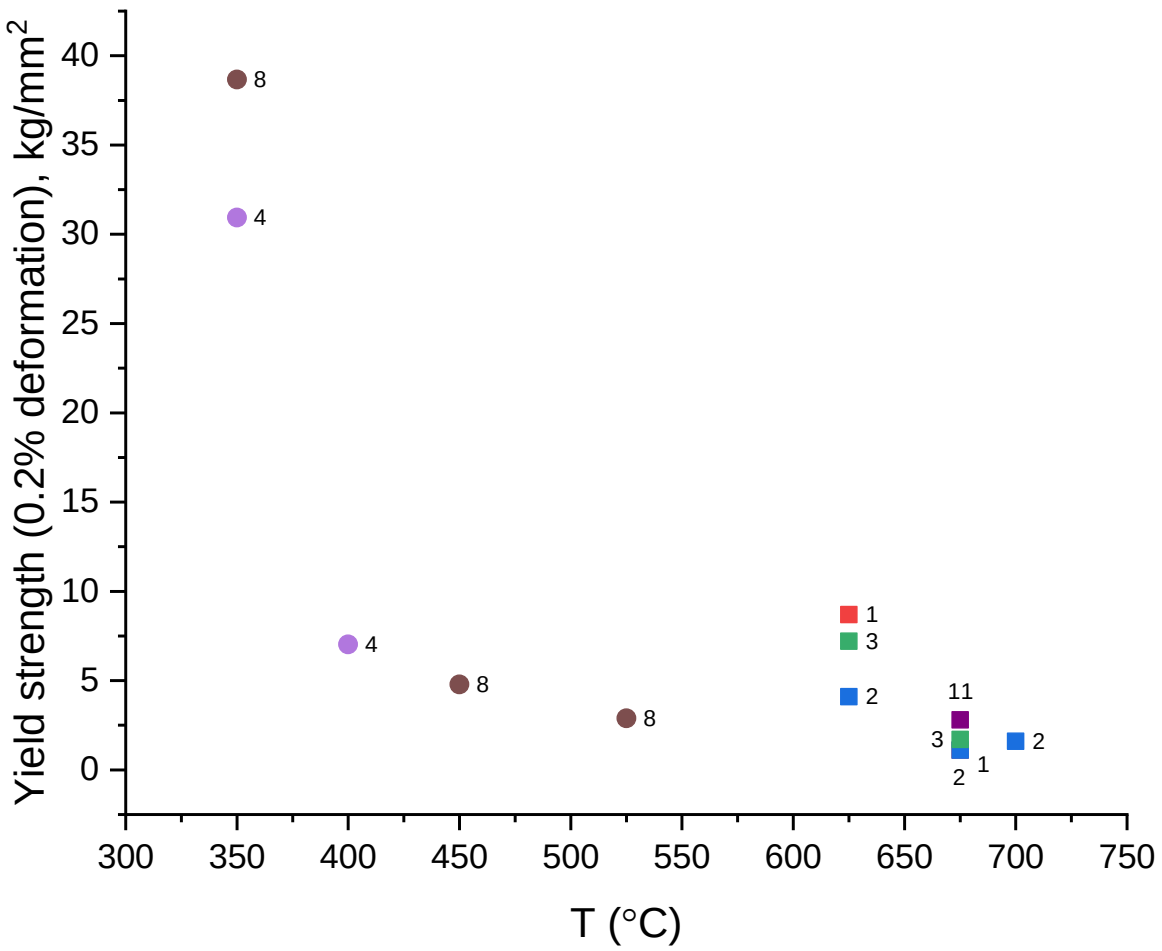

Figure 62. Yield strength of U-Pu-Zr alloys (0.2% deformation). Data values are in Table 34. Shapes, colors, and sample numbers are like those in Figure 61.

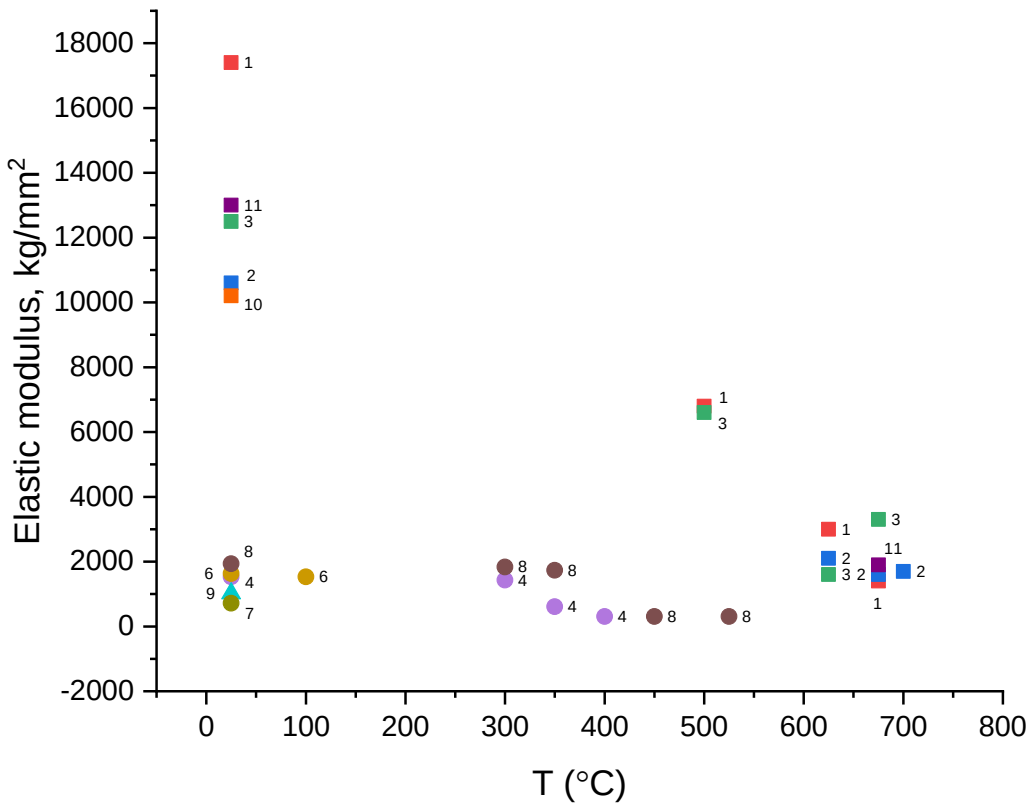

Figure 63. Elastic modulus of U-Pu-Zr alloys. Data values are in Table 34. Shapes, colors, and sample numbers are like those in Figure 61.

2.4.1.6.2 Poisson's Ratio

The only available measurement of Poisson's ratio for any U-Pu-Zr alloy is from METAPHIX Alloy CR13 (U-19Pu-10Zr in wt%), which indicates that the Poisson's ratio of this alloy is 0.31 [149]. The measurement was made using an ultrasonic method. No further information about the testing procedure (including testing temperature) was provided.

A small amount of information about reductions in areas of four U-Pu-Zr alloys at various temperatures is available in a review by Kittel et al. (Table 26 of reference [209]). The information was apparently collected during measurement of tensile properties, and no other information about the samples or measurement procedures was provided.

2.4.1.6.3 Compressive Strength

Kittel et al. summarized measurements of the ultimate compressive strengths of five U-Pu-Zr alloys [209]. The same information appears in reference [213], except that greater than (>) and less than (<) signs have been exchanged. Reference [213] also provides additional detail about homogenization temperatures. Table 35 summarizes the compressive-strength data from reference [209] (which is preferred to data from reference [213] because it is more recent and appeared in a peer-reviewed journal), with additional information about the homogenization temperature of the U-18.5Pu-14.1Zr (wt%) alloy from reference [213].

Table 35. Ultimate compressive strengths of U-Pu-Zr alloys.

Composition (wt%)	Composition, at%	T (°C)	Ultimate compressive strength, kg/mm^2	Homogenization
U-11.1Pu-6.3Zr	U-9.9Pu-15Zr	25	164	1 week at 950°C, oil quenched
		625	12	
		675	4	
U-12.3Pu-14.1Zr	U-9.8Pu-30Zr	25	166	1 week at 1050°C, oil quenched
		675	6.9	
		750	4.2	
12.3Pu-14.1Zr	U-9.8Pu-30Zr	25	164	As-cast
		500	<55	
		625	12	
		675	5.2	
U-16.6Pu-6.3Zr	U-14.8Pu-15Zr	25	127	As-cast
		500	<55	
		625	11	
		675	2.5	As-cast
U-15Pu-10Zr	U-12.7Pu-22.6Zr	25	129	
		500	48	
		625	11	
		675	5.6	
U-18.5Pu-14.1Zr	U-14.8Pu-30Zr	25	116	1 week at 1050°C, oil quenched
		675	5.6	

2.4.1.6.4 Shear Modulus

The only available measurement of the shear modulus for any U-Pu-Zr alloy is from METAPHIX Alloy CR13 (U-19Pu-10Zr in wt%), which indicates that the shear modulus of this alloy is 32.56 GPa [149]. The measurement was made using an ultrasonic method. No further information about the testing procedure (including the testing temperature) was provided.

2.4.1.6.5 Creep

Primary references for information about measured creep stress rates in U-Pu-Zr alloys are:

- A 1971 review by Kittel et al.[209] in which most values are repeated from two earlier Argonne National Laboratory reports [213, 219]. Values in references [209] and [213] differ from those in reference [219] for U-18.5Pu-14.1Zr (wt%) at a strain rate of 2 kg/mm^2 and temperature of 650°C, and for all strain rates at temperatures of 675 and 700°C. Although the reasons for the differences are not explained in any of the references, the values in reference [219] have been disregarded because it seems likely that were revised in references [209] and [213]. No details of sample properties or testing procedures were provided.
- A 1970 report by Harbur and colleagues, which tabulates data from three alloys that were cast and extruded. Oxygen contents were reported for two of the alloys, with a maximum of 180 ppm.

- A paper presented at a 1965 conference by Kelman and colleagues [193] that reports creep data at low stresses for a single alloy at temperatures of 600, 675, and 700°C. The same values for creep at 675 and 700°C also appear in two Argonne National Laboratory reports, but reported times to attain 1% strain at 725°C in the conference paper are significantly longer than those in the Argonne reports. It is not clear why the values differ or which publication has the most reliable values. Reference [246] was issued in May of 1965, reference [247] was issued in June of 1966, and reference [193] reports a 1965 conference presentation but was not published until 1967. As the value in reference [246] was clearly early, it seems likely that the creep data for 600°C from reference [193] has been revised from earlier references and, therefore, is preferred.

Table 36 summarizes data from Kittel et al. [209] and Harbur et al. [217], which report the time to achieve a 2% change in length. The times reported by Harbur are consistently shorter than those reported at higher temperatures by Kittel et al. for similar stresses. It is not possible to determine from the currently available data whether this difference is due to differences in sample composition (particularly impurities), different processing histories, or the occurrence of different phase assemblages or microstructures at different temperatures.

Table 36. Time (in minutes) to attain 2% strain in U-Pu-Zr alloys.

Composition (wt%)	Composition (at%)	Stress (kg/mm^2)	T (°C)									References
			290	350	400	500	600	625	650	675	700	
U-11.1Pu-6.3Zr	U-9.9Pu-15Zr	0.5	—	—	—	—	—	—	—	15	—	[209, 213, 219]
		1	—	—	—	—	—	—	—	5	—	[209, 213, 219]
		2	—	—	—	—	—	—	—	3	—	[209, 213, 219]
		4	—	—	—	—	—	5	—	1	—	[209, 213, 219]
U-16.6Pu-6.3Zr	U-14.8Pu-15Zr	0.5	—	—	—	—	—	—	—	10	—	[209, 213, 219]
		1	—	—	—	—	—	5000	—	1	—	[209, 213, 219]
		2	—	—	—	—	—	210	—	—	—	[209, 213, 219]
		4	—	—	—	—	—	10	—	—	—	[209, 213, 219]
U-15Pu-10Zr	U-12.6Pu-22.6Zr	0.5	—	—	—	—	—	—	5000	—	—	[209, 213, 219]
		1	—	—	—	—	—	5000	80	—	—	[209, 213, 219]
		2	—	—	—	—	—	210	1	—	—	[209, 213, 219]
		4	—	—	—	—	—	10	—	—	—	[209, 213, 219]
U-18.5Pu-14.1Zr	U-14.8Pu-30Zr	0.5	—	—	—	—	100000	—	5000	60	55	[209, 213]
		1	—	—	—	—	10000	—	80	10	10	[209, 213]
		2	—	—	—	—	800	—	2	2	3	[209, 213]
		4	—	—	—	—	70	—	—	—	—	[209, 213, 219]
U-15Pu-10Zr	U-12.6Pu-22.6Zr	1.4	—	—	—	20	—	—	—	—	—	[217]
		2.1	—	—	—	5	—	—	—	—	—	[217]
		5.6	—	—	30	Failed	—	—	—	—	—	[217]
		7.0	—	—	9	Failed	—	—	—	—	—	[217]
		7.7	—	—	3	Failed	—	—	—	—	—	[217]
		14.1	—	300	Failed	Failed	—	—	—	—	—	[217]
		21.1	—	20	Failed	Failed	—	—	—	—	—	[217]
		28.1	—	9	Failed	Failed	—	—	—	—	—	[217]
U-15Pu-12.5Zr	U-12.2Pu-27.2Zr	1.4	—	—	—	8	—	—	—	—	—	[217]
		2.1	—	—	—	4	—	—	—	—	—	[217]
		10.5	—	—	15	Failed	—	—	—	—	—	[217]
		12.0	—	—	8	Failed	—	—	—	—	—	[217]
		13.4	—	—	4	Failed	—	—	—	—	—	[217]
U-15Pu-6Zr	U-13.4Pu-14.3Zr	0.7	—	—	—	0.3	—	—	—	—	—	[217]
		3.5	30	Failed	Failed	Failed	—	—	—	—	—	[217]
		4.2	9	Failed	Failed	Failed	—	—	—	—	—	[217]

Table 37. Time (in minutes) to attain 1% strain in U-18.5Pu-14Zr (wt%) (Table 22-VIII of reference [193])

Stress (kg/mm^2)	Temperature (°C)		
	600	**675**	**700**
0.28	—	94	70
0.42	38000	27	32
0.56	37000	13	12

2.4.1.6.6 Hardness

Primary references for hardness measurements in U-Pu-Zr alloys are:

- A CEA report by Boucher and Barthelemy [211], which has hardness measurements from samples of U-15Pu-10Zr and U-20Pu-10Zr (wt%) with different annealing histories. Data were collected with a 10 kg load. The maximum relative error in the hardness measurements is estimated at 2%.
- An Argonne National Laboratory report (reference [213]) that lists hardness measurements from four U-Pu-Zr alloys. No information about sample purity is available. Data from U-17.1Pu-3.4Zr (wt%) have been disregarded because compositions in wt% and at% for this alloy are inconsistent and because other early references list this as a U-Pu-Ti alloy in presentations of other properties [193, 209].
- A 1971 review by Kittel et al.[209], which repeats information from Boucher and Barthelemy and from a conference paper by Kelman [248]. A 1965 review by Kelman et al. contains similar data [193], although hardness values in the two reviews differ by ~1%. Neither review includes new data. Although the Kittel review commonly repeats information from reference [213] with small differences that have been interpreted as revisions for this Handbook, the review by Kittel et al. did not include the data from the Argonne report in this case, for unknown reasons. No information about sample purity is available.
- A 1970 report by Harbur and colleagues at Los Alamos National Laboratory [217], includes data from four U-Pu-Zr alloys. This report compares hardness of as-cast and extruded alloys and contains the only available high-temperature hardness measurements for any U-Pu-Zr alloy. Although sample-purity data were not provided for the alloys used in hardness testing, alloys used to measure other properties had <200 ppm O. The U feedstock had ~200 ppm total detected impurities, including 50-100 ppm of carbon, the Pu feedstock had ~200 ppm detected impurities, and the Zr feedstock had ~110 ppm C and 170 ppm O.

Harbur and colleagues also reported that their samples contained small (1-5 μm) globular inclusions of a high-Zr material that they believed to be the "oxygen-stabilized α-Zr" reported by O'Boyle and Dwight [81], even in areas with only ~80 ppm oxygen. These inclusions were "extremely hard," with Vickers hardness values as high as 2500 [217]. This maximum value is an order of magnitude higher than the Vickers hardness of 110 for commercially available Zr ([249]).

All of the available measurements are from samples with ~10-20 wt% Pu and 5-10 wt% Zr. None of these references contains detailed information about sample preparation or testing procedures. Although only reference [211] reported the units for their hardness measurements, it seems likely that all of the measurements are in kg/mm^2.

Table 44 shows that hardness values for U-15Pu-10Zr (wt%) differ widely, for reasons that cannot be determined. The data of Boucher and Barthelemy suggests that alloys that have been annealed at 900°C (above the gamma solvus) and quenched are harder than those that have been annealed and quenched from temperatures below the gamma solvus. Although the causes of these differences in hardness cannot be determined with certainty, it seems likely that they may result from differences in phase assemblages before quenching.

Table 38. Hardness measurements (Vickers) of U-Pu-Zr alloys.

Nominal Composition (wt%)	Nominal Composition (at%)	Hardness (HV)	References	Notes
U-16Pu-6Zr	U-14Pu-30Zr	440	[217]	a
U-11.1Pu-6.3Zr	U-9.9Pu-15Zr	470	[213]	—
U-15Pu-10Zr	U-12.6Pu-22.6Zr	539	[209, 248]	b
U-15Pu-10Zr	U-12.6Pu-22.6Zr	540	[213]	—
U-15Pu-10Zr	U-12.6Pu-22.6Zr	440	[217]	a
U-15Pu-10Zr	U-12.6Pu-22.6Zr	426	[209, 211]	c, d
U-15Pu-10Zr	U-12.6Pu-22.6Zr	428	[209, 211]	c, e
U-15Pu-10Zr	U-12.6Pu-22.6Zr	488	[209, 211]	c, f
U-20Pu-10Zr	U-17Pu-23Zr	417	[209, 211]	c, d
U-20Pu-10Zr	U-17Pu-23Zr	415	[209, 211]	c, e
U-20Pu-10Zr	U-17Pu-23Zr	480	[209, 211]	c, f
U-15Pu-13.5Zr	U-12Pu-29Zr	380	[217]	a
U-18.5Pu-14.1Zr	U-14.8Pu-30.1Zr	410	[213]	—
U-18.5Pu-14.1Zr	U-14.8Pu-30.1Zr	406	[209, 248]	b

NOTE a: Hardness values for as-cast and as-extruded samples are identical

NOTE b: As-cast sample

NOTE c: Alloys were prepared by arc-melting U, Pu, and Zr, inverting and remelting four times, and casting in a copper mold.

NOTE d: Annealed at 500°C for 50 hours and quenched in oil.

NOTE e: Annealed at 620°C for 5 hours and quenched in oil.

NOTE f: Reference [211] says the sample was annealed at 900°C and quenched but does not specify the annealing time or quenching method. Reference [209] says the sample was annealed at 900°C for two hours and quenched in oil.

Table 39 and Figure 64 are the only available measurements of the hot hardness of any U-Pu-Zr alloy. A hardness value of 4.3 at a stated temperature of 725°C has not been included because the temperature is out of order, suggesting that it may be an error. The dramatic change at ~600°C is consistent with the temperatures of the reactions at the gamma solvus (Section 2.4.1.2.3.1).

Table 39. Hot hardness of U-15Pu-6.8Zr (wt%) (data from Table IV of reference [217])

T (°C)	Hardness
800	3.4
725	4.3
730	5.4
720	5.6
710	7.4

Table 39. (continued).

T (°C)	Hardness
700	6.4
690	8.8
680	8.8
670	10
650	11
625	18.2
610	20.2
600	39.6
590	46.6
580	59.1
570	60.9
550	83.5
500	148
450	202
400	256

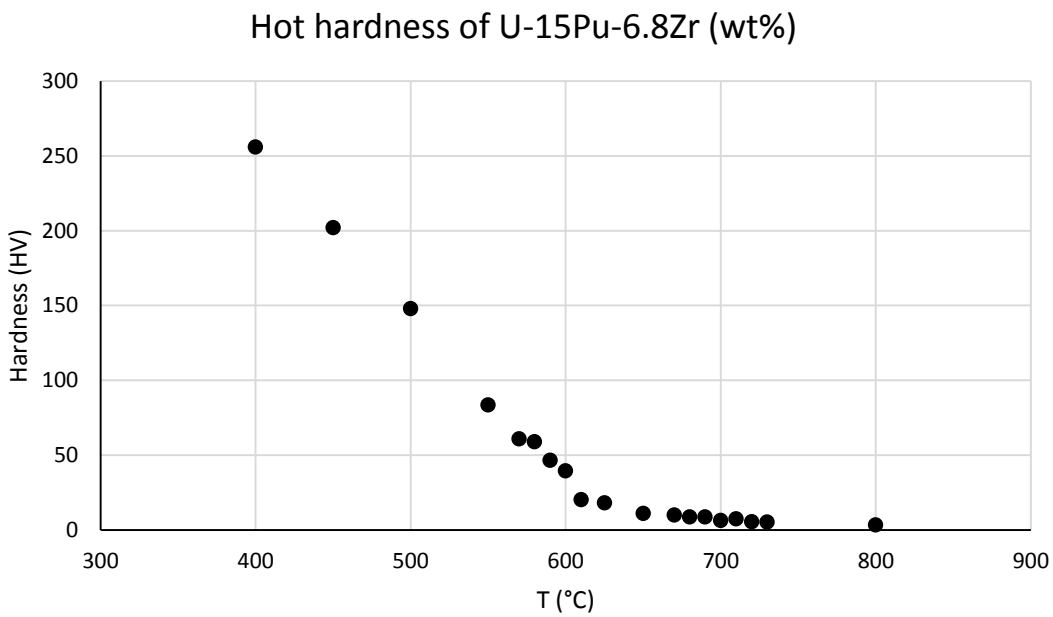

Figure 64. Hot hardness of U-15Pu-6.8Zr (wt%) (data from Table IV of reference [217].)

2.4.2 U-Pu-Zr Alloys with Minor Actinides (Np, Am, Cm), Sorted by Increasing Weight Percentage of Zr

2.4.2.1 U-20Pu-10Zr-2Am

2.4.2.1.1 Introduction

Nishi and colleagues [250] recently reported the heat capacity, thermal diffusivity, and thermal conductivity of two pieces of an alloy whose nominal composition has 68 wt% U, 20 wt% Pu, 2 wt% Am, and 10 wt% Zr (corresponding to 59 at% U, 17 at% Pu, 22.4 at% Zr, and 1.7 at% Am). The actual compositions had 67.3-68.3 wt% U, 20.0-20.5% Pu, 1.6-1.9% Am, and 10.1-10.4% Zr.

Two examples of this alloy were fabricated by injection-casting into a zirconia-coated quartz glass tube to form cylinders ~3 mm in diameter. The examples had identical nominal compositions but used Am feedstocks produced using different refinement techniques. Samples for thermal diffusivity measurements, microstructural analysis, and chemical analysis were produced by slicing discs from the as-cast cylinders.

These measurements provide the only available data on the heat capacity, thermal diffusivity, and thermal conductivity of any U-Pu-Zr-Am alloy. No information about the thermal expansion or as-cast density of this alloy is available.

2.4.2.1.2 Phases and Phase Transformations

SEM data indicated that the as-cast alloys consisted of two phases. The phases were not identified or characterized in detail, but were assumed to be similar to δ-UZr_2 and ζ-(U,Pu). The data suggested that Am was present in both phases; however, it is not clear that the spatial resolution of the SEM data was high enough to provide reliable single-phase measurements.

Although no specific phase-transition temperatures were reported, a phase transition between ~773 and 923 K was suggested by the heat-capacity and thermal-diffusivity data.

2.4.2.1.3 Heat Capacity and Related Properties

Nishi et al. [250] measured the incremental enthalpies of both 68U-20Pu-10Zr-2Am alloys at temperatures from 335 to 827 K using drop calorimetry and calculated the corresponding heat capacities (Figure 65 and Figure 66).

Equation 61 and Equation 62 express the incremental enthalpies of the individual alloys.

Equation 61. Incremental enthalpy of U-20Pu-2Am-10Zr Alloy 1 from 335 to 827 K [250]

$$H_T - H_{298.15} = 7.966 \times 10^{-6} \times T^2 + 2.649 \times 10^{-2} \times T - 9.528 + 2.752 \times 10^2 \times T^{-1}$$

Equation 62. Incremental enthalpy of U-20Pu-2Am-10Zr Alloy 2 from 335 to 827 K [250]

$$H_T - H_{298.15} = 9.442 \times 10^{-6} \times T^2 + 2.661 \times 10^{-2} \text{ x } T - 9.536 + 2.276 \times 10^2 \times T^{-1}$$

Where H_T is the enthalpy at temperature T in kJ/mol, $H_{298.15}$ is the enthalpy at 298.15 K, and T is a temperature in K, $335 \leq T \leq 827$. (Reference [250] lists the first term in Equation 62 as $9.442 \times 10^{-9} \times T^2$, which is inconsistent with tabulated values of enthalpies in its Table 4. The exponent in Equation 62 has been adjusted to match the enthalpy measurements in the table.)

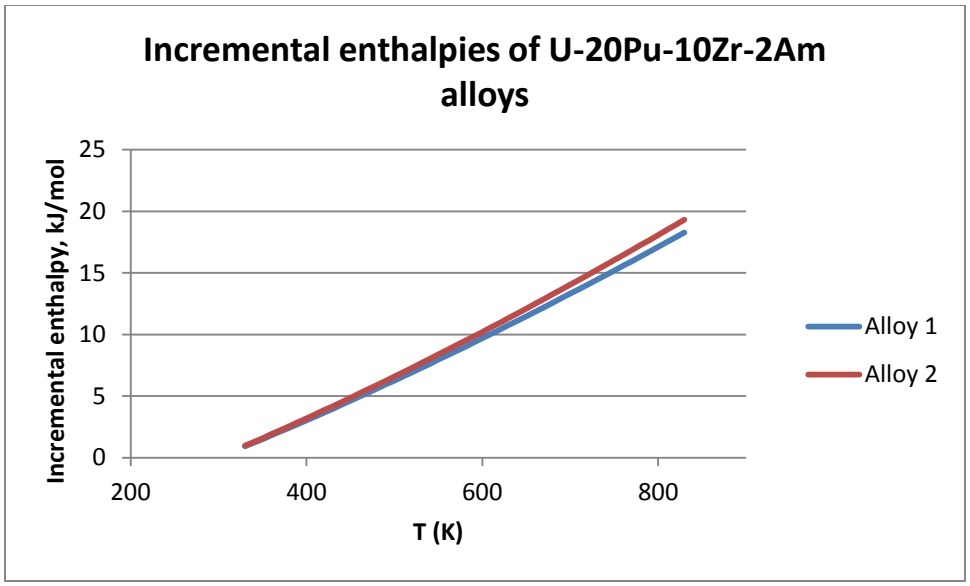

Figure 65. Incremental enthalpies of U-20Pu-10Zr-2Am alloys (Equation 61 and Equation 62).

Equation 63, Equation 64, and Figure 66 express the heat capacities of the individual alloys.

Equation 63. Heat capacity of U-20Pu-2Am-10Zr Alloy 1 [250]

$C_p = 1.593\times10^{-2}\times T + 26.49 - 2.752\times10^{5}\times T^{-2}$

Equation 64. Heat capacity of U-20Pu-2Am-10Zr Alloy 2 [250]

$C_p = 1.888\text{x}10^{-2}\times T + 26.61 - 2.276\times10^{5}\times T^{-2}$

Where C_p is the heat capacity at temperature T in J/mol-K and T is a temperature in K, $335 \leq T \leq 827$

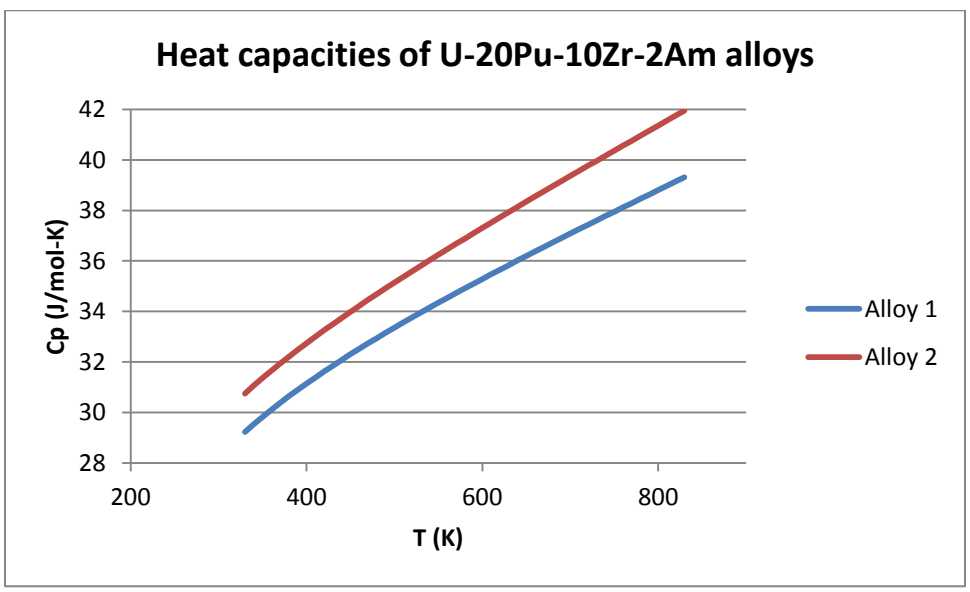

Figure 66. Heat capacities of U-20Pu-10Zr-2Am alloys from Equation 63 and Equation 64.

2.4.2.1.4 Thermal Conductivity and Related Properties

Nishi et al. determined the thermal conductivity of two alloys with the same nominal composition and slightly different bulk compositions at temperatures from 300 to 773 K and from 923 to 1073 K (Equation 65 and Equation 66). The thermal conductivities were determined from new measurements of heat capacity and thermal diffusivity and from a previously published bulk density value of 15.8×10^3 kg/m^3 for U-20Pu-10Zr (by weight). Heat capacities were based on measurements of incremental enthalpies made using drop calorimetry for temperatures below 773 K and were extrapolated at higher temperatures. Thermal diffusivities were measured with a laser-flash instrument.

Although the differences in thermal conductivities of the samples were within the estimated errors of the conductivities, Nishi et al. speculated that the difference in the thermal conductivities of their alloys was due to differences in the concentration of oxygen (0.277 wt% in Alloy 1, 0.484 wt% in Alloy 2). They assumed a linear relationship between thermal conductivity and oxygen content, and developed Equation 67 to represent the speculative thermal conductivity of an "oxygen-free" 68U-20Pu-2Am-10Zr alloy.

Equation 65. Thermal conductivity of 68U-20Pu-2Am-10Zr Alloy 1 [250 Equation 8]

$\lambda = 1.07 \times 10\text{-}5 \times T2 + 0.0204 \times T + 0.707$

Where λ is thermal conductivity in W/(m·K), T is a temperature in K, and either $300 \leq T \leq 773$ or $923 \leq T \leq 1073$. The estimated error for this equation is ± 11%.

Equation 66. Thermal conductivity of 68U-20Pu-2Am-10Zr Alloy 2 [250 Equation 9]

$\lambda = 1.00 \times 10\text{-}5 \times T2 + 0.0195 \times T + 0.637$

Where λ is thermal conductivity in W/(m·K), T is a temperature in K, and either $300 \leq T \leq 773$ or $923 \leq T \leq 1073$. The estimated error for this equation is ± 12%.

Equation 67. Speculative thermal conductivity of oxygen-free 68U-20Pu-2Am-10Zr [250 Equation 10]

$\lambda = 1.15 \times 10\text{-}5 \times T2 + 0.0226 \times T + 0.459$

Where λ is thermal conductivity in W/(m·K), T is a temperature in K, and either $300 \leq T \leq 773$ or $923 \leq T \leq 1073$. The estimated error for this equation is ± 17%.

Figure 67 shows thermal conductivities and estimated errors from all three equations. Thermal conductivities from Alloys 1 and 2 are the same to within the estimated errors, and the speculative thermal conductivity for the oxygen-free alloy is only slightly outside the estimated errors for the experimentally determined thermal conductivities.

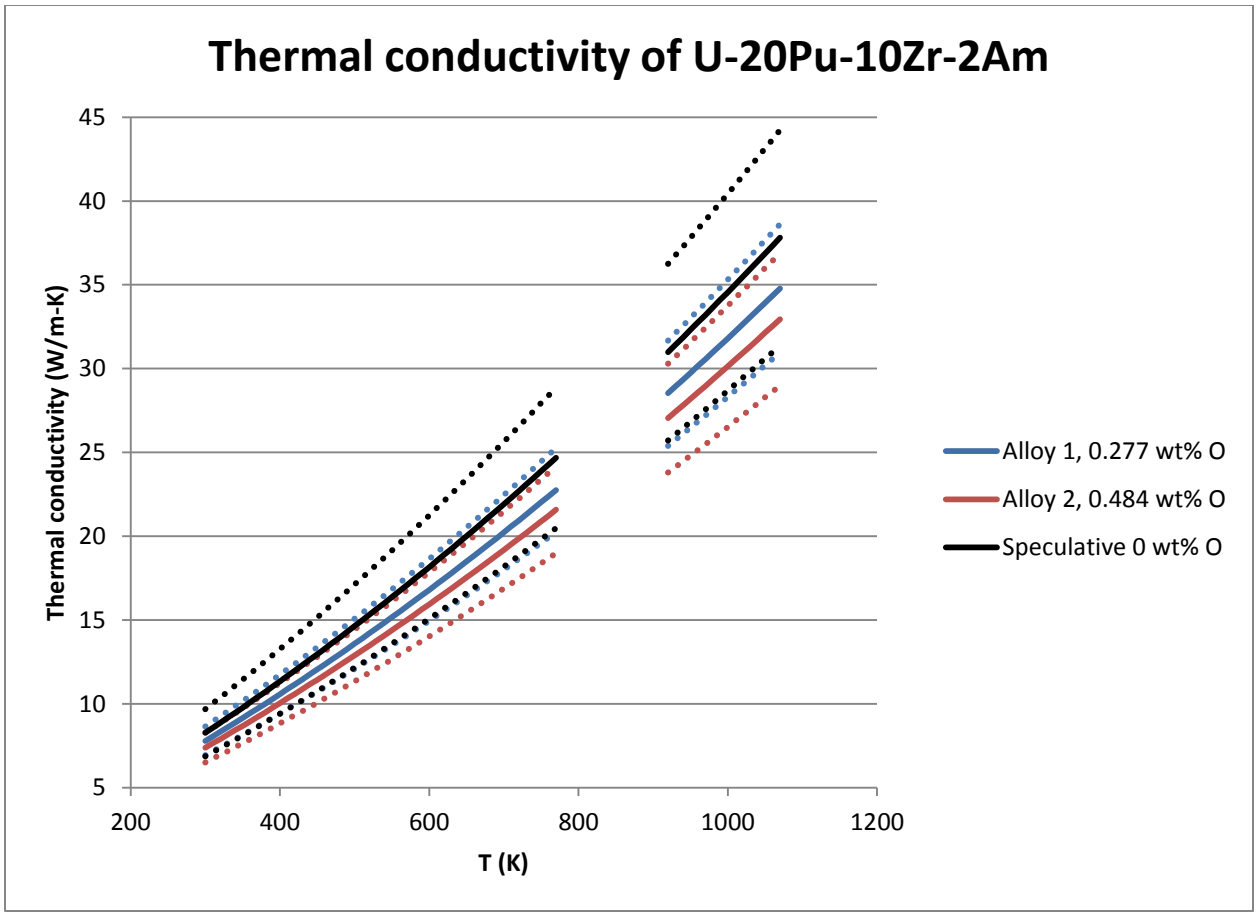

Figure 67. Thermal conductivity of U-20Pu-10Zr-2Am alloys with varying concentrations of oxygen (Equation 65, Equation 66, and Equation 67). Dotted lines indicate upper and lower boundaries for each equation based on errors of ±11% for Equation 65, ±12% for Equation 66, and ±17% for Equation 67 [250]. Thermal conductivities at temperatures above 923K are based on heat capacities extrapolated from lower temperatures. Thermal conductivities between 773 and 973 K were not determined.

2.4.2.2 U-20Pu-10Zr-2Np-3Am (Alloys AFC2-E3, AFC2-E5, X501, and Historical EBR-II)

2.4.2.2.1 Introduction

Alloys AFC2-E3 and AFC2-E5 were cast and characterized at Idaho National Laboratory as part of a series of experiments that also included U-20Pu-10Zr rodlets. The experiments were intended to provide quantitative information about the benefits of minor actinides on fuel performance [251]. The nominal compositions of Alloys AFC2-E3 and AFC2-E5 are identical except for the isotopic makeup of the uranium, and are similar to the compositions of EBR-II fuels and of fuels that were irradiated as part of the X501 minor actinide burning experiment [252, 253].

The nominal composition of Alloys AFC2-E3 and AFC2-E5 consists of 65 wt% U, 20 wt%Pu, 10 wt% Zr, 2 wt% Np, and 3 wt% Am, corresponding to approximately 56 at% U, 17.2 at% Pu, 22.5 at% Zr, 1.7 at% Np, and 2.6 at% Am.

No information about the thermal conductivity of these alloys is available.

2.4.2.2.2 Phases and Phase Transformations

2.4.2.2.2.1 Phases

SEM images from Alloy E3 show dark high-Zr inclusions in a light-colored matrix (Figure 68). Some of the high-Zr dark inclusions also contain detectable concentrations of Si, which is not present in the nominal composition of the alloy. The SEM images show polygonal boundaries that commonly surround areas 10-20 μm across. The areas inside the boundaries contain parallel lamellae, which sometimes appear in two nearly perpendicular directions. It is not possible to determine the nature of the lamellae from the available data, although it seems likely that the polygonal boundaries are derived from the original grain boundaries formed when the alloy first crystallized from a liquid.

In the absence of diffraction data, it is not possible to identify the phases in this material.

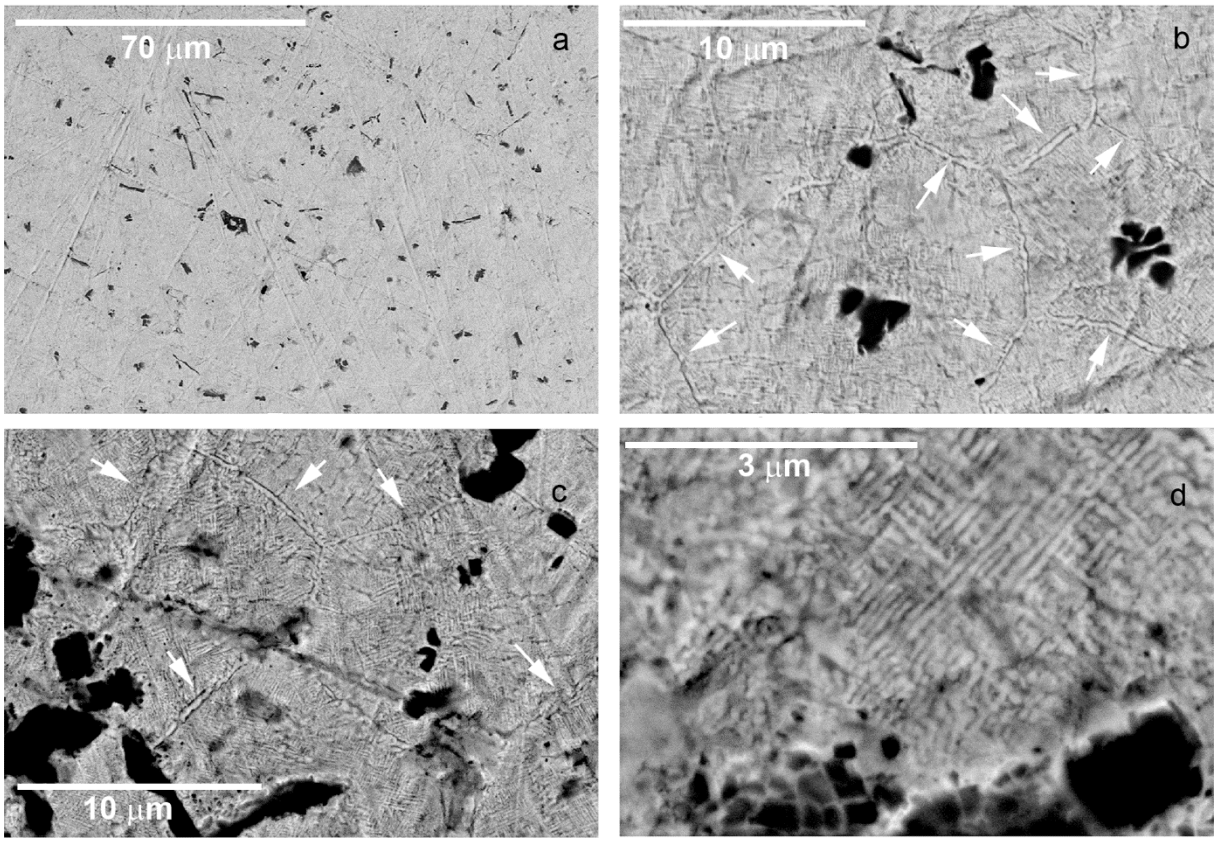

Figure 68. SEM BSE images of U-20Pu-2Np-3Am-10Zr (FCRD alloy AFC2-E3). Black areas are high-Zr inclusions. Arrows indicate examples of polygonal boundaries.

2.4.2.2.2.2 Phase Transitions

DSC data from this alloy show two peaks between room temperature and ~800°C (Table 40). Changes in slope during the onset of the higher-temperature peak during cooling suggest that it represents at least three phase transitions, which have not been deconvoluted. The total enthalpy represented by all of the phase transitions is 31.14±0.8 J/g measured during heating, and -31.17±0.2 J/g measured during cooling.

Table 40. Phase-transformation temperatures in Alloy AFC2-E3 (U-20Pu-10Zr-2Np-3Am).

	Lower-T peak		Higher-T peak	
	Heating (Peak A)	**Cooling (Peak D)**	**Heating (Peak B)**	**Cooling (Peak C)**
Onset temperature (K)	837	835	933	906

2.4.2.2.3 Heat Capacity and Related Properties

The heat capacity of Alloy AFC2-E3 was determined as the average of heat capacities from three DSC/TGA cycles. Each cycle involved heating and cooling the sample between room temperature and ~800°C at a rate of 10°C per minute. Heat capacities from temperatures above the onset of the lower-temperature phase transition at ~ 564°C (Section 2.4.2.2.2.2) should be disregarded.

Heat capacities below ~550°C can be approximated by Equation 68 and Figure 69.

Equation 68. Heat capacity of Alloy AFC2-E3

$C_p = 0.0179 + 0.0001xT - 2 \times 10^{-8} \times T^2$

Where C_p is a heat capacity in J/g-K and T is a temperature in °C, room temperature ≤ T ≤ 550

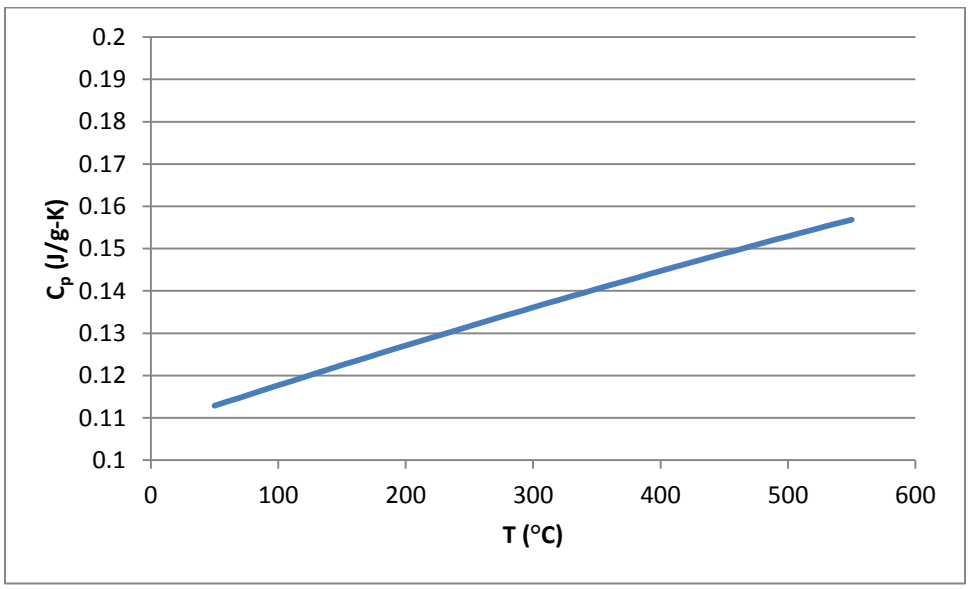

Figure 69. Heat capacity of Alloy AFC2-E3 (Equation 68).

2.4.2.2.4 Thermal Expansion and Density

No information about the thermal expansion of this alloy is available.

The room-temperature density of as-cast Alloy AFC2-E3 is 15.11 g/cm^3.

2.4.2.3 U-20Pu-15Zr-2Np-3Am (Alloy AFC2-A1)

2.4.2.3.1 Introduction

Alloy AFC2-A1, whose nominal composition is 60 wt% U, 2% Np, 20% Pu, 3% Am, and 15% Zr (~48.5 at% U, 1.6 at% Np, 16 at% Pu, 2.4 at% Am, and 31.5 at% Zr) was cast and characterized at Idaho National Laboratory. It is part of a series of related alloys with differing concentrations of uranium and rare-earth elements that was intended to investigate properties of fuels recycled using a pyrochemical process that did not completely remove the rare-earth elements. Other alloys in the series are Alloy

AFC2-A2 (1% rare-earth elements, Section 2.4.4.4), AFC2-A3 (1.5% rare-earth elements, Section 2.4.4.5), and AFC2-A7 (8% rare-earth elements, Section 2.4.4.6).

Samples of Alloy AFC2-A1 were produced by mixing feedstock materials in appropriate proportions, arc-melting three times to homogenize the alloy, then melting the alloy a final time, and drawing it into a silica glass ("quartz") tube using a suction-casting process. This process produced a cylinder with an approximate diameter of ~4 mm. Analyses of as-cast alloys showed differences between actual and nominal concentrations of several wt% for U and Zr, 1 wt% for Np, 1.5-2 wt% for Pu, and 0.l5 wt% for Am, [254, 255].

No information about the thermal conductivity of this alloy is available.

2.4.2.3.2 Phases and Phase Transformations

2.4.2.3.2.1 Phases

SEM images of Alloy AFC2-A1 show high-Zr inclusions, a small fraction of which also contain Si, surrounded by a matrix with a lower concentration of Zr (Figure 70) [10, 230 (Figure 1b), 231 (Figure 1), 254]. Contrast variations in the matrix can be correlated to local variations in the proportions of U and Zr [254], and suggest either a single-phase matrix with a wide range of compositions or a fine-grained matrix consisting of several phases with significantly different compositions and locally varying proportions. Concentrations of Np, Pu, and Am in the matrix generally appear uniform at the spatial scale of the SEM data, although a few small high-Am inclusions (possibly oxides) were observed [254].

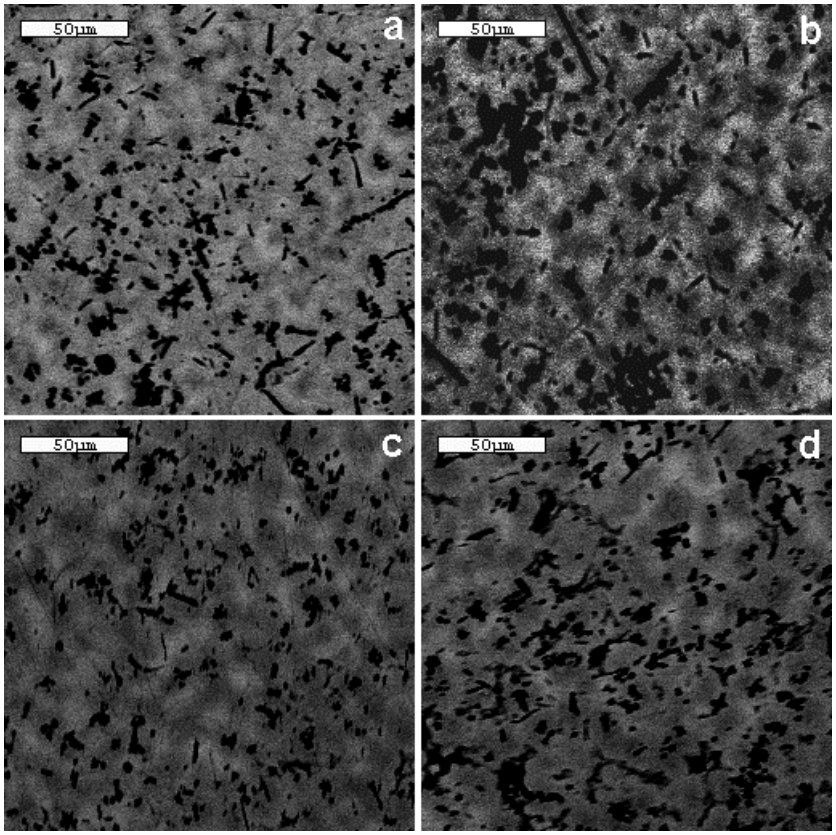

Figure 70. BSE SEM images of Alloy AFC2-A1. Black spots are high-Zr inclusions, light areas are relatively high in U and low in Zr, and dark areas are relatively high in Zr and low in U. Concentrations of other actinides show little variation in the matrix. Image b was also published by Janney and Kennedy [254], and image c was also published in references [10, 230, 231].

X-ray diffraction patterns from this alloy have low peak-to-background ratios and are dominated by peaks from the LaB_6 (NIST SRM 660a) used as an internal standard [230 (Figure 2 Pattern A), 231 (Figure 2 Pattern A)].

All of the published information about phases and lattice parameters in this alloy is apparently based on two Rietveld refinement analyses of a single X-ray diffraction pattern. One of the analyses indicated that the alloy consisted primarily of a phase with a structure similar to that of δ-UZr_2 and lattice parameters a = 5.060 Å and c = 3.088 Å [256 (Alloy A1)]. The second analysis showed results of a Rietveld refinement in which it was assumed that the phases present were LaB_6 (the internal standard), ζ-(U,Pu), δ-(U,Pu)Zr_2, α-U, and γ-U. This refinement indicated that ~29.4% of the material represented by the diffraction pattern was the LaB_6 internal standard. When proportions of other phases in the refinement were re-normalized without the LaB_6, the analysis results showed that the sample contained ~86% ζ-(U,Pu) with lattice parameters a = 10.718 Å and α = 89.42°, ~6% δ-(U,Pu)Zr2 with a = 5.057 Å and c = 3.102 Å, ~8% γ-U with a = 3.592 Å, and no α-U [230 (Alloy A; Figure 5, Tables 3 and 4), 231 (Alloy A; Figures 2 and 3, Tables 2 and 3)].

In attempting to understand why two Rietveld refinements of the same data are consistent with two different primary phases, it is important to recognize that Rietveld refinements are based on adjusting parameters to minimize differences between experimental and calculated diffraction patterns, and that a close match between the experimental and calculated diffraction patterns does not guarantee a result that accurately represents the actual properties of the material [257]. The Rietveld refinement algorithm assumes that all of the phases in the material have been identified correctly and that all of the phases in the refinement are actually present in the material. Violations of these assumptions are likely to lead to erroneous results.

The only available X-ray diffraction data from ζ-(U,Pu) indicates that X-ray diffraction patterns from this phase shows one strong peak corresponding to a d-spacing of 2.496 Å, one moderate-intensity peak corresponding to a d-spacing of 1.446 Å, and a large number of weak, moderately weak, or very weak peaks [192]. d-spacings of the strong and moderate peaks are similar to those of the strongest and second-strongest peaks from δ-UZr_2 (at ~2.51 and ~1.45 Å, respectively) [88], making it difficult to qualitatively confirm the presence of ζ-(U,Pu) in samples that also have δ-UZr_2. Further complications in analysis of the present data arise because the X-ray patterns show only a few, relatively small, peaks from the sample.

In interpreting the X-ray diffraction results, it is also important to consider that the data were obtained from slices of as-cast alloys rather than powders, that the number of phases and lattice parameters included in the refinement is large relative to the number of peaks from the sample, that some of the phases might be solid solutions with lattice parameters that vary as a result of variations in composition, and that the identification of phases for the Rietveld refinement was qualitatively incorrect because it did not include phases corresponding to the high-Zr inclusions shown in the SEM data.

Despite these considerations, the conclusion that the major phases in Alloy AFC2-A1 are structurally similar to ζ-(U,Pu) and δ-UZr_2 seem plausible based on phase identifications from electron-diffraction data from as-cast Alloy AFC2-A7 [258], although errors in phase proportions and lattice parameters are likely to be significantly larger than the published values. Inferences about compositions of individual phases should be treated with caution, as they are not supported by single-phase chemical measurements or high-quality lattice parameter measurements.

2.4.2.3.2.2 Phase Transitions

DSC/DTA measurements of Alloy AFC2-A1 between room temperature and ~800°C show two peaks [10 (Figure 86), 230 (Figure 6), 231 (Figure 4)]. Shapes of both peaks during cooling suggest that each peak includes more than one reaction. Deconvolution of the higher-temperature peak showed that it represents two reactions whose onset temperatures differ by ~13 degrees [230, 231]. The reactions represented by the lower-temperature peak have apparently not been deconvoluted.

TMA data from Alloy AFC2-A1 shows two phase transitions [10]. Onset temperatures of both transitions are higher than indicated by the DSC/DTA data.

Table 41 and Table 42 summarize the reported phase-transformation temperatures and enthalpies for Alloy AFC2-A1. In the absence of data in which possible multiple reactions in the lower-temperature peak have been deconvoluted, the results of Burkes et al. [230, 231] are probably the most accurate values available.

Table 41. Phase-transformation temperatures in U-20Pu-3Am-2Np-15Zr (Alloy AFC2-A1).

Reaction 1		**Reaction 2**		**Reaction 3**		**Method**	**Reference**
Heating T (K)	**Cooling T (K)**	**Heating T (K)**	**Cooling T (K)**	**Heating T (K)**	**Cooling T (K)**		
833	829	920	894	933	912	DSC/TGA with deconvolution of higher-T peak	[230, 231]
830	821	927	909	—	—	DSC/TGA	[256]
860	848	953	913	—	—	TMA	[10]

Table 42. Phase-transformation enthalpies in U-20Pu-3Am-2Np-15Zr (Alloy AFC2-A1).

Reaction 1		**Reaction 2**		**Reaction 3**		**Reference**
Enthalpy during heating (J/g)	**Enthalpy during cooling (J/g)**	**Enthalpy during heating (J/g)**	**Enthalpy during cooling (J/g)**	**Enthalpy during heating (J/g)**	**Enthalpy during cooling (J/g)**	
6.0 ±0.31	-5.9±0.24	8.6±0.55	-7.9±0.35	10.1±0.50	-10.9±0.24	[230, 231]
4.27±0.34	-4.80±0.41	20.54±2.95	-22.58±3.36	—	—	[256]

2.4.2.3.3 Heat Capacity and Related Properties

The specific heat of Alloy AFC2-A1 was determined as the average of heat capacities from three DSC/TGA cycles. Each cycle involved heating and cooling the sample between room temperature and ~1100°C at a rate of 10°C per minute. The sample lost approximately 1.76% of its mass during the experiment and showed evidence of oxidation and reaction with the alumina crucible liner, and the baseline appeared unstable at higher temperatures [259]. Thus, heat capacities from temperatures above the onset of the lower-temperature phase transition at ~ 830 K (557°C) (Section 2.4.2.3.2) should be disregarded.

The specific heat of Alloy AFC2-A1 below ~550°C can be approximated by Equation 69 and Figure 71)

Equation 69. Heat capacity of Alloy AFC2-A1 [256]

$$C_p = 0.21 - 0.23\times10^{-3}\times T - 0.05\times10^{5}\times0.05T^{-2} + 0.23\times10^{-6}\times T^{2}$$

Where C_p is a heat capacity in J/g-K and T is a temperature in K, $323 \leq T \leq 823$

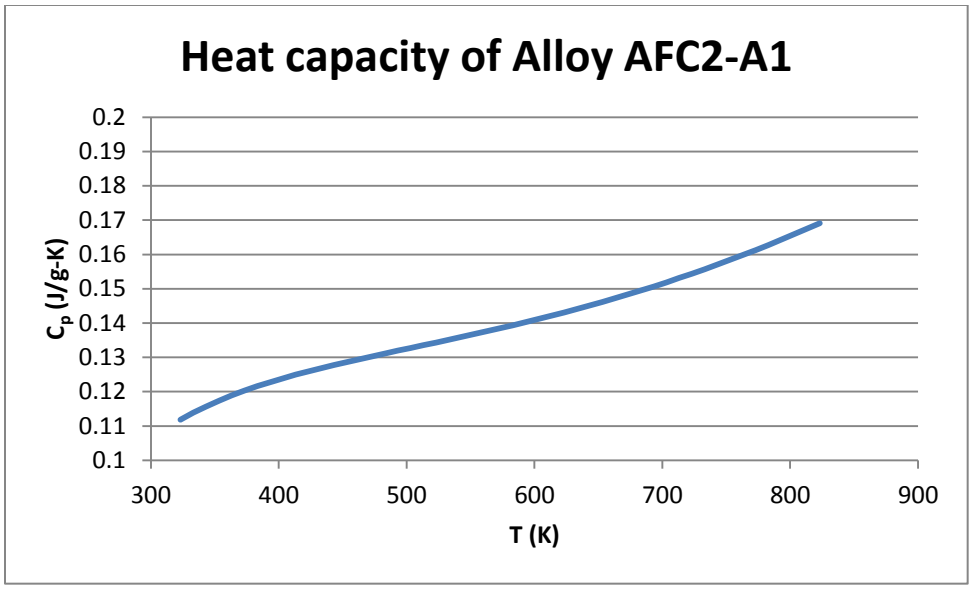

Figure 71. Specific heat of Alloy AFC2-A1 (Equation 69).

2.4.2.3.4 Thermal Expansion and Density

2.4.2.3.4.1 Thermal Expansion

The linear thermal expansion of Alloy AFC2-A1 was measured using a TMA instrument. Measurements from three cycles during which the samples were heated and cooled between room temperature and 800°C showed lower reproducibility than measurements from other alloys in the AFC2-A series. Some probe movement was observed during measurements, and surface oxidation was observed after the third cycle [10].

Despite these problems, the data show that thermal expansion of Alloy AFC2-A1 is similar to that of Alloys AFC2-A2, AFC2-A3, AFC2-A4, AFC2-A5, and AFC2-A6 [10 (Figure 54)]. This thermal expansion can be represented by Equation 70.

Equation 70. Linear thermal expansion of Alloys AFC2-A1, AFC2-A2, AFC2-A3, AFC2-A4, AFC2-A5, and AFC2-A6 between 20 and 550°C in percent [10 (Equation 3)]

$\Delta L/L_0 = 0.0015019xT - 0.03003$

where $\Delta L/L_0$ is the linear thermal expansion of the sample in percent, ΔL is the difference in sample length as a result of differences in temperature, L_0 is the length of the sample at 20°C, L is the length of the sample at temperature T, T is a temperature in °C, and $20 \leq T \leq 550$

2.4.2.3.4.2 Coefficients of Thermal Expansion

The coefficient of linear thermal expansion corresponding to Equation 70 is approximately 1.5×10^{-5}/°C for temperatures between 20 and 550°C. Assuming isotropic thermal expansion, the corresponding coefficient of volumetric thermal expansion is approximately 4.5×10^{-5}/°C.

2.4.2.3.4.3 Density

Room-temperature densities of four pieces of as-cast Alloy AFC2-A1 were measured using the Archimedes method. The densities varied between 13.74 and 14.50 g/cm^3, with an average value of ~14.05 g/cm^3 [255 (Table 3)]. Volumes and densities at temperatures between 20 and 550°C can be approximated using Equation 6, Equation 7, and Equation 70.

2.4.2.4 U-30Pu-20Zr-3Np-5Am (Alloy AFC2-A6)

2.4.2.4.1 Introduction

Alloy AFC2-A6, whose nominal composition is 42 wt% U, 3% Np, 30% Pu, 5% Am, and 20% Zr (corresponding to approximately 32 at% U, 2.3 at% Np, 22.6 at% Pu, 3.7 at% Am, and 39.5 at% Zr) was cast and characterized at Idaho National Laboratory. It is part of a series of related alloys with differing concentrations of uranium and rare-earth elements that were intended to investigate properties of fuels recycled using a pyrochemical process that did not completely remove the rare-earth elements. Other alloys in the series are Alloy AFC2-A5 (1% rare-earth elements, Section 2.4.4.7), AFC2-A4 (1.5% rare-earth elements, Section 2.4.4.8), and AFC2-A8 (8% rare-earth elements, Section 2.4.4.9).

Samples of Alloy AFC2-A6 were produced by mixing feedstock materials in appropriate proportions, arc-melting three times to homogenize the alloy, then melting the alloy a final time and casting it into a silica glass ("quartz") tube to produce a cylinder with an approximate diameter of ~4 mm. Analyses of as-cast alloys showed differences between actual and nominal concentrations of several wt% for U, 0.3 wt% for Np, 1.5wt% for Pu, 0.4 wt% for Am, and 1 wt% for Zr [254, 255].

No information about the heat capacity or thermal conductivity of this alloy is available.

2.4.2.4.2 Phases and Phase Transformations

2.4.2.4.2.1 Phases

SEM images of alloy AFC2-A6 show high-Zr inclusions, a small fraction of which also contain Si, surrounded by a matrix with a lower concentration of Zr (Figure 72) [10, 230 (Figure 1B), 236 (Figure 1), 254]. Some images also show pores, two of which have been mistakenly identified as high-Zr inclusions in previously published images [230 (Figure 1B), 236 (Figure 1)]. Contrast variations in BSE images of the matrix can be correlated to local variations in the proportions of U and Zr [254], and suggest either a single-phase matrix with a wide range of compositions or a fine-grained matrix consisting of several phases with significantly different compositions and locally varying proportions. Concentrations of Np, Pu, and Am in the matrix appear uniform at the scale of the SEM data.

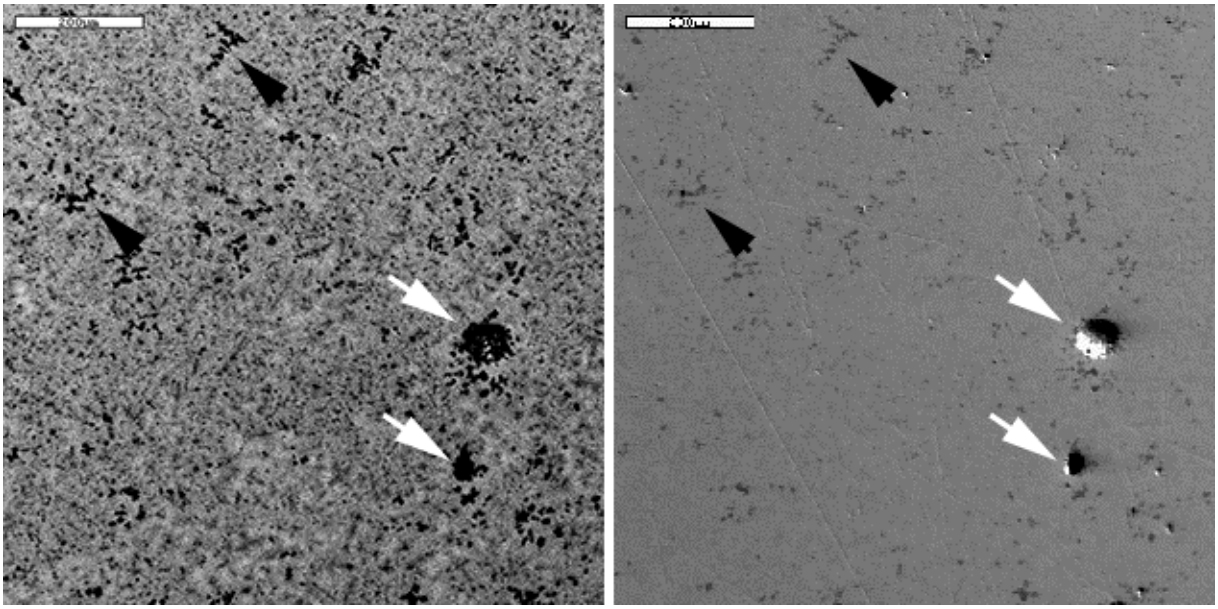

Figure 72. BSE (left) and SE (right) SEM images of U-30Pu-5Am-3Np-20Zr (FCRD alloy AFC2-A6). Black arrows show clusters of high-Zr inclusions; white arrows indicate pores that have been mistakenly identified as inclusions in other publications.

X-ray diffraction patterns from this alloy have low peak-to-background ratios and are dominated by sharp peaks from the LaB_6 used as an internal standard [230 (Figure 4, Pattern B), 236 (Figure 2, Pattern F)]. A Rietveld refinement in which it was assumed that the phases present were LaB_6, ζ–(U,Pu), δ-(U,Pu)Zr_2, α-U, and γ-U indicated that almost 75% of the material represented by the diffraction pattern is LaB_6 [236 (Figure 3)]. When proportions of other phases in the refinement were re-normalized to a total of 100%, the results showed that the sample consists of ~57% ζ-(U,Pu) with lattice parameters a = 10.744 Å and a = ~89.4°, ~28% δ-(U,Pu)Zr_2 with a = 5.057 Å and c = 3.113 Å, 2.2% α-U with a = 2.844 A, b = 5.861 A, and c = 5.136 Å, and ~13% γ-U with a = 3.596 Å [230 (Alloy B)].

In assessing the Rietveld refinement results, it is important to recognize that the number of phases and lattice parameters included in the Rietveld refinement is large relative to the number of peaks in the data. The refinement did not include the high-Zr phase identified in the SEM data. Based on these considerations, it seems likely that errors in the phase proportions and lattice parameters from the Rietveld refinement are significantly larger than the published uncertainties [230], which appear to be based on counting statistics. Detailed interpretations of the Rietveld-refinement results, including inferences about compositions of individual phases from lattice parameters, should be treated with caution unless verified by further experiments.

The identification of the major phases in as-cast Alloy AFC2-A6 as similar to δ-(U,Pu) and δ-UZr_2 is nonetheless plausible based on U-Pu-Zr phase diagrams and phases identified by electron diffraction in as-cast Alloy AFC2-A7 [258].

2.4.2.4.2.2 Phase Transitions

DSC/DTA measurements at temperatures up to ~800°C show two peaks [236 Figure 6]. Deconvolution of the higher-temperature peak showed that it represents two reactions whose onset temperatures differ by ~20-30 degrees (Table 43).

TMA data from Alloy AFC2-A6 shows two phase transitions [10]. The onset temperatures of the lower-temperature reaction in the TGA and DSC/DTA data are similar, as are the onset temperatures of the higher-temperature reaction during cooling.

Table 43 and Table 44 summarize reported phase-transformation temperatures and enthalpies for Alloy AFC2-A6. The deconvoluted phase-transformation temperatures are probably the more accurate of the two values currently available.

Table 43. Phase-transformation temperatures in U-3Np-30Pu-5Am-20Zr (Alloy AFC2-A6).

Reaction 1		**Reaction 2**		**Reaction 3**			
Heating T (K)	**Cooling T (K)**	**Heating T (K)**	**Cooling T (K)**	**Heating T (K)**	**Cooling T (K)**	**Method**	**References**
826±2.6	819±0.6	879±7.2	877±1.2	912±12.5	896±0.2	DSC/DTA with deconvolution	[230, 236]
823	848	943	893	—	—	TMA	[10]

Table 44 Phase-transformation enthalpies in U-3Np-30Pu-5Am-20Zr (Alloy AFC2-A6).

Reaction 1		**Reaction 2**		**Reaction 3**		
Enthalpy during heating (J/g)	**Enthalpy during cooling (J/g)**	**Enthalpy during heating (J/g)**	**Enthalpy during cooling (J/g)**	**Enthalpy during heating (J/g)**	**Enthalpy during cooling (J/g)**	**Reference**
15.3 ±1.08	-16.0±0.14	7.5±1.98	-8.9±0.34	4.2±1.67	-5.9±0.29	[230, 236]

2.4.2.4.3 Thermal Expansion and Density

2.4.2.4.3.1 Thermal Expansion

The linear thermal expansion of Alloy AFC2-A6 was measured using a TMA instrument. The sample was cycled three times between room temperature and 800°C. Data from all three cycles were similar during heating and cooling [10].

The thermal expansion of Alloy AFC2-A6 is similar to that of Alloys AFC2-A1, AFC2-A2, AFC2-A3, AFC2-A4, and AFC2-A5 [10 (Figure 54)]. This thermal expansion can be represented by Equation 70 (Section 2.4.2.3.4.1).

2.4.2.4.3.2 Coefficients of Thermal Expansion

The coefficient of linear thermal expansion corresponding to Equation 70 is approximately 1.5×10^{-5}/°C for temperatures between 20 and 550°C. Assuming isotropic thermal expansion, the corresponding coefficient of volumetric thermal expansion is approximately 4.5×10^{-5}/°C. These coefficients are like those of Alloy AFC2-A1 (Section 2.4.2.3.4.2).

2.4.2.4.3.3 Density

Room-temperature densities of as-cast material from four castings of as-cast Alloy AFC2-A6 were determined using the Archimedes method. These densities ranged from 12.83 to 12.93 g/cm^3, with an average value of ~12.88 g/cm^3. Volumes and densities at temperatures between 20 and 550°C can be approximated using Equation 6, Equation 7, and Equation 70.

2.4.2.5 U-34Pu-20Zr-2Np-4Am (Alloy AFC1-MG)

2.4.2.5.1 Introduction

Phases and microstructures in Alloy AFC1-MG (nominal composition 40U-2Np-34Pu-4Am-20Zr in weight percentages, ~30.4U-1.5Np-25.6Pu-3.0Am-39.6Zr in atomic percentages) were investigated by researchers at Argonne and Idaho National Laboratories as part of a study of low-U fuels for transmutation of minor actinides. Key results from SEM and XRD analyses were summarized in review papers by Keiser et al. [179] and Burkes et al. [230]. In reading these papers, it is important to note that the image of this alloy in the review by Burkes et al. [230 (Figure 1c)] is from a sample that had been repeatedly heated in a DSC experiment.

Samples of Alloy AFC1-MG were prepared by a procedure that involved arc-melting the material several times on a copper hearth to homogenize it, followed by gravity drop casting to produce cylinders ~4 mm in diameter. Transverse slices were cut and ground to produce flat surfaces for analysis [179, 230].

No information about the heat capacity, thermal expansion, or thermal conductivity of this alloy is available.

2.4.2.5.2 Phases and Phase Transformations

2.4.2.5.2.1 Phases

SEM images of an as-cast sample of this alloy show small, dark-contrast, globular inclusions of a high-Zr phase surrounded by a matrix with contrast variations on a scale of a few tens of micrometers. The high-Zr inclusions occur preferentially in darker areas of the matrix. Contrast is correlated with Pu content: brighter areas have higher concentrations of Pu, and darker areas have lower ones. Concentrations of other actinides have the same pattern as Pu, although differences between areas with relatively high and relatively low concentrations appear smaller than for Pu. Bright-contrast linear or curved features (arrows in Figure 73 parts b and c) appear preferentially in lighter-contrast areas of the matrix, bounding irregularly shaped areas a few tens of micrometers across. These curved features have

been described as “grain boundaries,” although they may be retained from early stages of crystallization rather than representing grain boundaries in the present, finer-grained, microstructure.

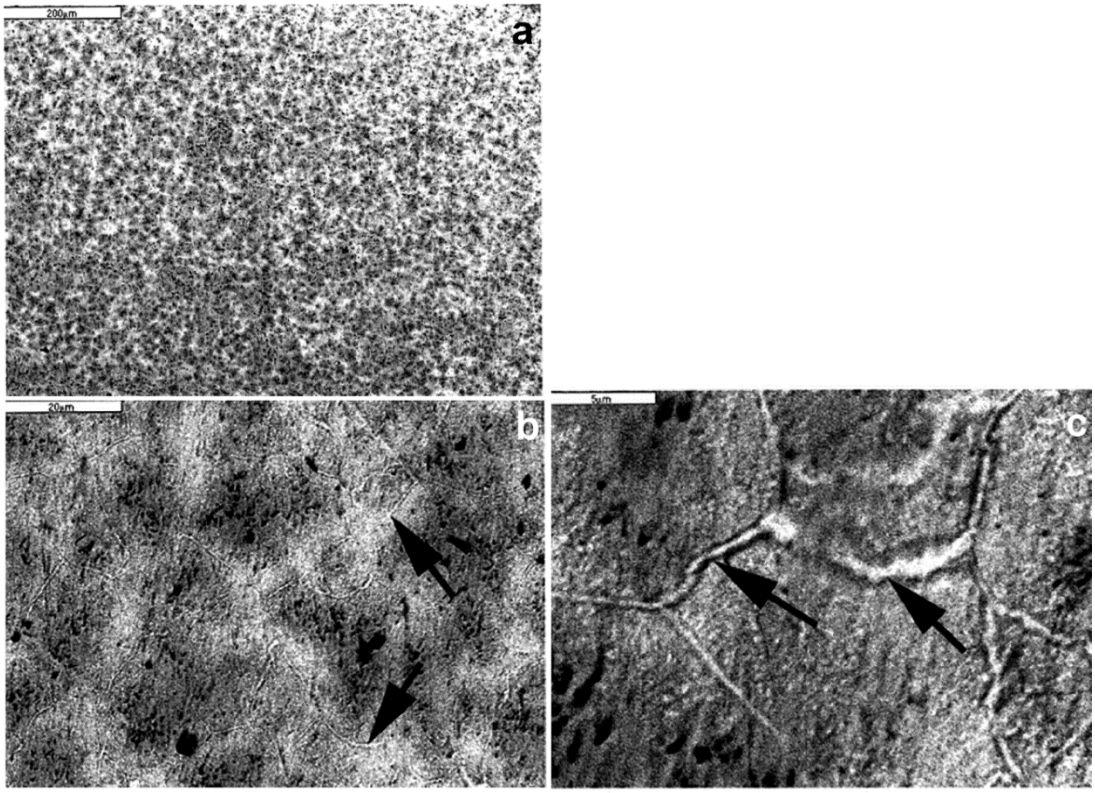

Figure 73. SEM images of as-cast U-2Np-34Pu-4Am-20Zr (Alloy AFC1-MG). Arrows indicate linear features that may have originated as grain boundaries in higher-temperature phases.

SEM data were also collected from a sample that had been cycled three times between room temperature and 1000°C in a DSC experiment. Images of this sample show a network of bright-contrast features bounding polygons a few tens of micrometers across [230 (Figure 1C)]. X-ray maps show that the polygonal boundaries are enriched in U and depleted in Am relative to adjacent areas, and suggest that darker areas in the interiors of the polygons may be higher in Am and lower in U than lighter areas.

X-ray diffraction patterns from as-cast samples of this alloy show small, broad peaks corresponding to d-spacings similar to those of δ-UZr_2 (Figure 74). A Rietveld refinement based on the assumption that the phases in the sample are δ-UZr_2, ζ-(U,Pu), α-U, and γ-U indicated that about 50% of the sample had a structure similar to that of δ-UZr_2 with lattice parameters a = 5.085 Å and c = 3.110 Å and about 50% of the sample had a structure similar to that of ζ-(U,Pu) with lattice parameters a = 10.723 Å and α = 90.28°. γ-U was included in the refinement because it was believed that it might be retained in the sample and α-U was apparently included for consistency with other alloys in the same publication. Neither of these phases produced qualitatively identifiable peaks, and the Rietveld refinement did not indicate a significant concentration of either α-U or γ-U [230 (Tables 3 and 4, Alloy C)].

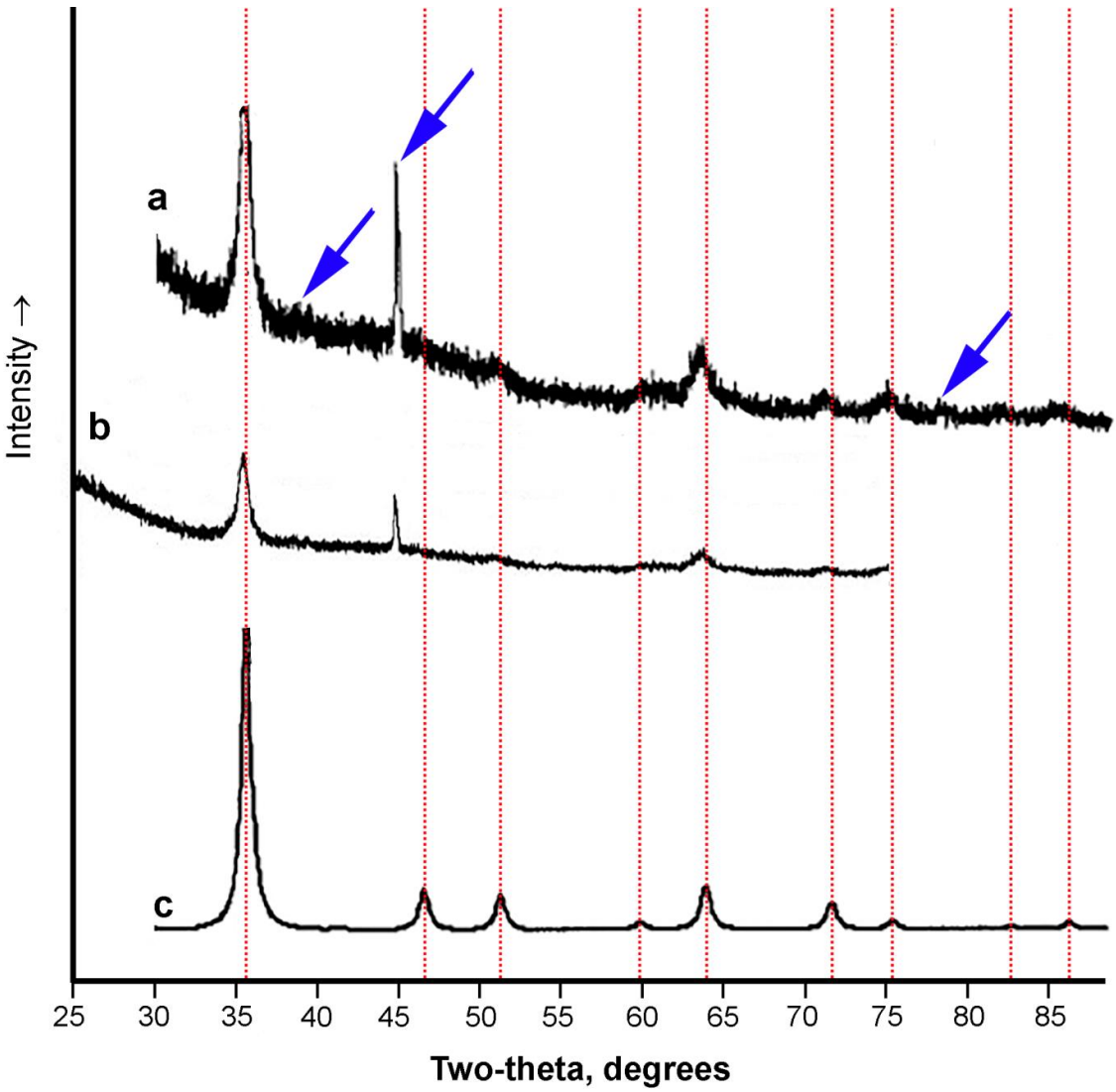

Figure 74. Experimental X-ray diffraction patterns from U-2Np-34Pu-4Am-20Zr (Alloy AFC1-MG) with simulated pattern from δ-UZr_2 for comparison. a: Experimental pattern. b: Experimental pattern [230 (Figure 4, Pattern C)]. c. Simulated pattern from d-UZr_2. Dashed red lines indicate positions of peaks from δ-UZr_2; blue arrows indicate positions of peaks from the aluminum sample holder, which was used as an internal standard. Patterns were measured with Cu K_α X-rays.

In assessing the Rietveld refinement results, it is important to recognize that the number of phases and lattice parameters included in the Rietveld refinement is large relative to the number of peaks in the data. The refinement included two phases that were not present in significant quantities and did not include the high-Zr phase identified in the SEM data. Based on these considerations, it seems likely that errors in the phase proportions and lattice parameters from the Rietveld refinement are significantly larger than the published uncertainties, which appear to be based on counting statistics [230]. Detailed interpretations of the Rietveld refinement results should be treated with caution unless verified by further experiments. Inferences about compositions of individual phases should be regarded as speculative in the absence of single-phase chemical measurements.

The identification of the major phases in as-cast Alloy AFC1-MG as structurally similar to δ-(U,Pu) and δ-UZr2 is plausible based on U-Pu-Zr phase diagrams and phases identified by electron diffraction in as-cast Alloy AFC2-A7 [258].

2.4.2.5.2.2 Phase Transitions

The only available data on phase-transition temperatures and enthalpies were obtained by deconvolution of peaks in DTA data [230, Alloy C]. These data show three phase transitions whose onset temperatures and enthalpies are summarized in Table 45. As no high-temperature diffraction or microchemical data to support phase identifications are available, attempts to identify the reactions responsible for the transitions shown by the DSC data should be treated with caution.

Table 45. Phase-transformation temperatures and enthalpies in Alloy AFC1-MG (U-2Np-34Pu-4Am-20Zr) [230 (Table 7)].

	Transformation 1		**Transformation 2**		**Transformation 3**	
	Heating	**Cooling**	**Heating**	**Cooling**	**Heating**	**Cooling**
Onset temperature (K)	815±2.2	804±1.2	837±10.9	866±10.3	889±3.6	883±0.5
Enthalpy (J/g)	7.2 ±1.70	-9.2±0.19	2.4±1.56	-4.0±1.57	3.6±0.41	-2.9±1.60

2.4.2.6 U-28Pu-30Zr-7Am (Alloy AFC1-MF)

2.4.2.6.1 Introduction

Alloy AFC1-MF was investigated at Idaho National Laboratory as part of a research program that investigated alloys with relatively low concentrations of uranium as fast-reactor fuels intended for transmutation of minor actinides. The nominal composition of this alloy is 35 wt% U, 28 wt% Pu, 7 wt% Am, and 30 wt% Zr (corresponding to 23.7 at% U, 18.8 at% Pu, 4.7 at% Am, and 52.9 at% Zr).

Key characterization results from Alloy AFC1-MF were published in review papers by Burkes et al. [230 (Alloy E)] and Keiser et al. [179].

Samples of Alloy AFC1-MF were prepared by a procedure that involved arc-melting the material several times on a copper hearth to homogenize it, followed by gravity drop casting to produce cylinders ~4 mm in diameter Transverse slices were cut and ground to produce flat surfaces for analysis using scanning electron microscopy, X-ray diffraction, and DSC/TGA.

X-ray diffraction results suggest that this alloy consist primarily of a phase with a structure similar to that of δ-UZr_2 and also contains a significant fraction of a phase with a structure similar to that of ζ-(U,Pu). Phase transition temperatures and enthalpies are not available, but are reported to be similar to those of Alloy AFC1-MI (Section 2.4.2.7).

No information about the heat capacity, thermal expansion, density, or thermal conductivity of this alloy is available.

2.4.2.6.2 Phases and Phase Transformations

2.4.2.6.2.1 Phases

SEM images of as-cast alloy AFC1-MF show uniform microstructures with numerous small high-Zr precipitates. Contrast variations in the matrix suggest that it consists of more than one phase [179, 230 Figure 1E]. However, there are no SEM measurements of the compositions of individual phases in this alloy.

The obvious peaks in X-ray diffraction patterns of this alloy are similar to those of δ-UZr_2. A Rietveld refinement based on the assumption that the phases in the alloy are ζ-(U,Pu), δ-(U, Pu) Zr_2, α-U,

and γ-U indicated that the sample consists primarily of two phases: one similar to ζ-(U,Pu) with lattice parameters *a* = 10.692 Å and α = 90.52° (~27% of the sample) and one similar to δ-UZr_2 with lattice parameters a = 5.062 and c = 3.092 Å (~70% of the sample). The Rietveld refinement showed small amounts of α–U (which was apparently included in the refinement for consistency with other alloys in the paper) and γ–U (a possible retained phase stable at higher temperatures). The refinement did not include a high-Zr phase corresponding to the precipitates in the SEM data [230 (Tables 3 and 4)]

Because the number of phases and lattice parameters in the Rietveld refinement is large relative to the number of peaks in the data, it is likely that errors in phase proportions and lattice parameters are larger than the published estimated errors [230], which appear to be based on counting statistics. In particular, the identification and lattice parameters of α-U and γ-U require further verification.

The identification of the major phases in as-cast U-29Pu-30Zr-7Am as similar to δ-(U,Pu) and δ-UZr_2 is nonetheless plausible based on consideration of U-Pu-Zr phase diagrams. It is also consistent with phases identified by electron diffraction in the matrix of an as-cast sample of Alloy AFC2-A7 (nominal composition 52U-20Pu-15Zr-3Am-2Np-8.0RE, Section 2.4.4.6).

2.4.2.6.2.2 Phase Transitions

Measured phase transition temperatures and enthalpies for this alloy are not available, but are reportedly similar to those from U-29Pu-2Np-4Am-30Zr (Alloy AFC1-MI, Section 2.4.2.7).

2.4.2.7 U-29Pu-30Zr-2Np-4Am (Alloys AFC1-MI, AFC1-MJ, and DOE1)

2.4.2.7.1 Introduction

Alloys with nominal composition 35U-2Np-29Pu-4Am-30Zr (where numbers represent weight percentages of each element) were cast and characterized at Idaho National Laboratory. Alloy AFC1-MI was part of a study of transmutation fuels with low concentrations of U. Alloy AFC1-MJ, which has the same nominal composition, is also known as Alloy DOE1, and was intended for irradiation in the Phénix reactor as part of the FUTURIX-FTA project. Because properties of Alloys AFC1-MI and AFC1-MJ are similar, it is sometimes not possible to tell which alloy is represented in reported experimental results.

Alloy AFC1-MI was cast into cylinders ~4 mm diameter by arc-melting and homogenizing the alloy, then melting it a final time and pouring it into zirconia-coated quartz tubes. Alloy AFC1-MJ was cast into cylinders ~5 mm diameter by arc-melting and homogenizing the alloy, then melting it a final time and sucking it up into a quartz tube with a syringe [179, 185]. The average composition of this alloy determined from two castings is ~ 34.8 wt% U, 2.2% Np, 28.9% Pu, 3.6% Am, and 30.7% Zr [184].

No reliable information about the heat capacity or thermal conductivity of this alloy is available.

2.4.2.7.2 Phases and Phase Transformations

2.4.2.7.2.1 Phases

SEM images of the interior portions of as-cast samples of Alloys AFC1-MI and AFC1-MJ show high-Zr inclusions and small pores. The distribution of U, Np, Pu, Am, and Zr appears relatively homogeneous, although some images show variations in contrast as a result of small differences in relative proportions of Zr and actinides (Figure 75a). Some SEM images show contrast variations in the matrix in areas a few tens of micrometers across (Figure 75b and c). These variations can be correlated to local differences in the concentration of Zr [185, 230].

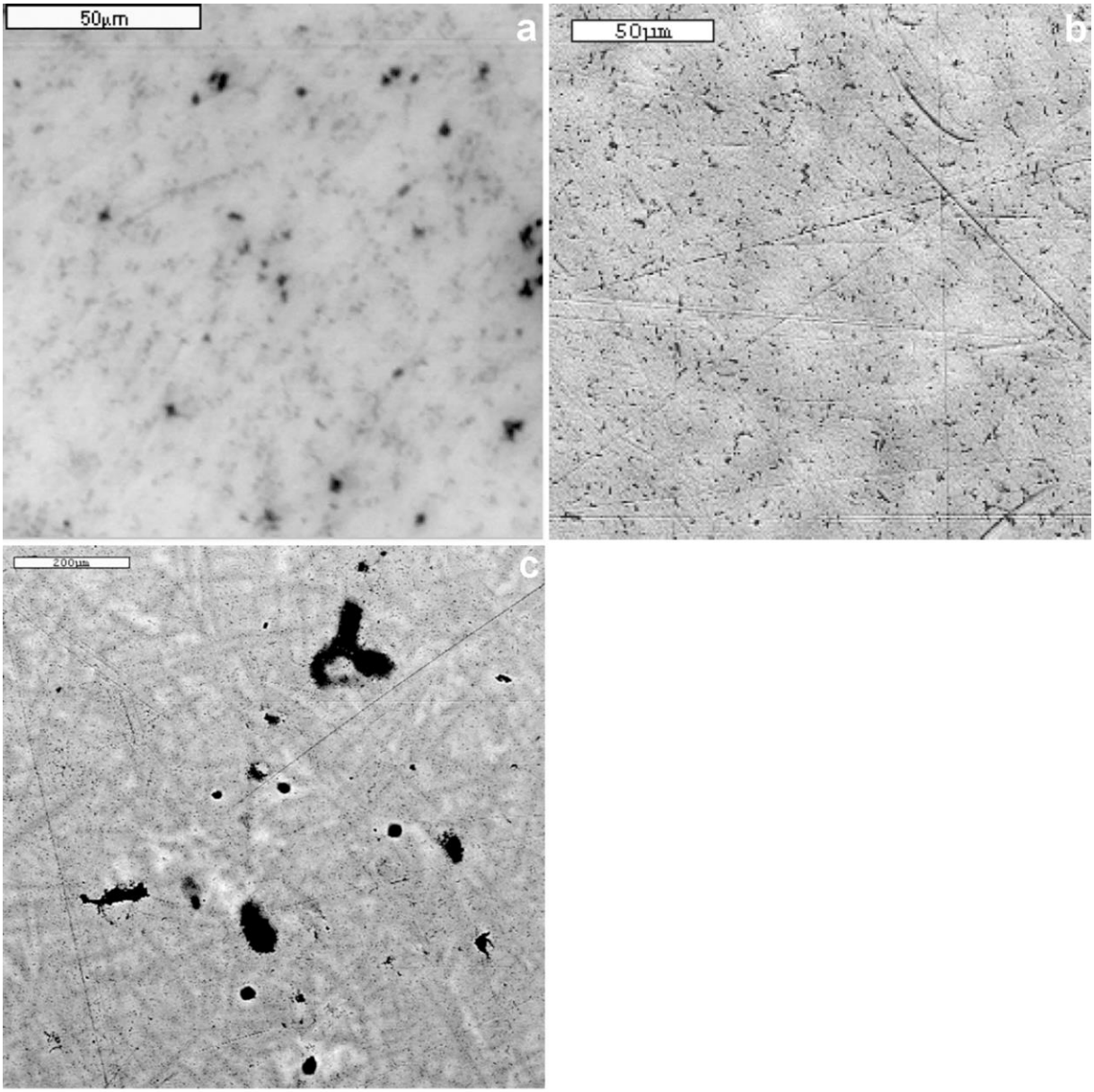

Figure 75. BSE images of U-29Pu-4Am-2Np-30Zr. a: Alloy AFC1-MI [230] b: Alloy AFC1-MJ (DOE1) [185] c: Alloy AFC1-MJ (DOE1). Large black areas in Part C are pores.

A Rietveld refinement based on the assumption that the phases in the sample were δ-UZr_2, ζ-(U,Pu), α-U, and γ-U determined that the sample contains ~11.4% ζ-(U,Pu) with lattice parameters a = 10.686 Å and α = 89.36° and ~88.5% δ-UZr_2 with lattice parameters a = 5.059 Å and c = 3.099 Å [230]. γ-U was included in the refinement because it was believed that it might be retained in the sample and α-U was apparently included for consistency with other alloys in the same publication. Neither of these phases produced qualitatively identifiable peaks, and the Rietveld refinement did not indicate a significant concentration of either α-U or γ-U [230 (Tables 3 and 4, Alloy D)].

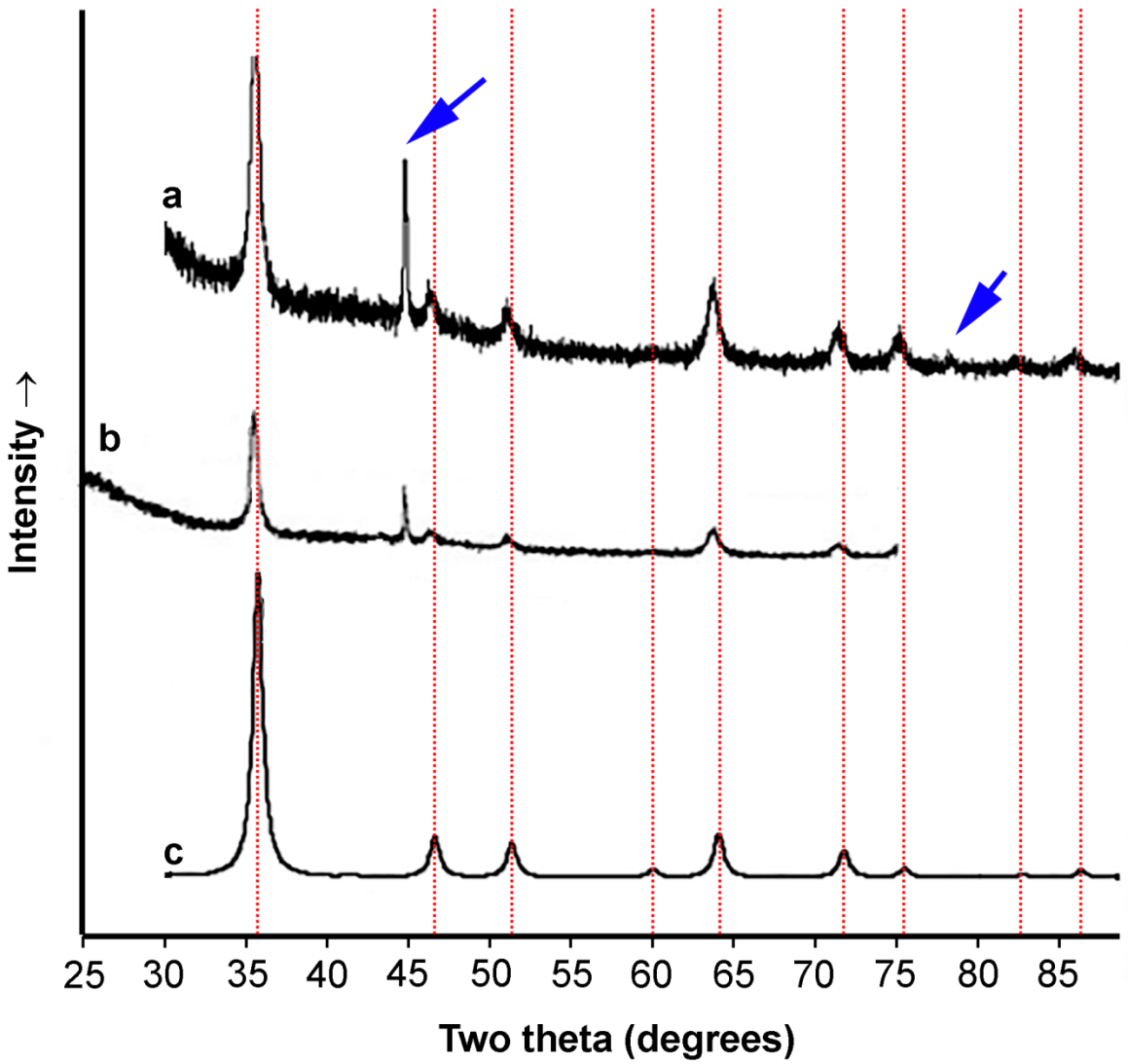

Figure 76. Experimental X-ray diffraction patterns from U-29Pu-4Am-2Np-30Zr with simulated pattern from δ-UZr_2 for comparison. a: Experimental pattern. b: Experimental pattern [230 (Figure 4, Pattern D)]. c. Simulated pattern from δ-UZr_2. Dashed red lines indicate positions of peaks from δ-UZr_2; blue arrows indicate positions of peaks from the Al used as an internal standard. Patterns were measured with Cu K_α X-rays.

In assessing the Rietveld refinement results, it is important to recognize that the number of phases and lattice parameters included in the Rietveld refinement is large relative to the number of peaks in the data. The refinement included two phases that were not present in significant quantities and did not include the high-Zr phase identified in the SEM data. Based on these considerations, it seems likely that errors in the phase proportions and lattice parameters from the Rietveld refinement are significantly larger than the published uncertainties [230], which appear to be based on counting statistics. Detailed interpretations of the Rietveld refinement results should be treated with caution unless verified by further experiments.

The identification of the major phases in as-cast Alloy AFC1-MG as structurally similar to δ-(U,Pu) and δ-UZr_2 is plausible based on U-Pu-Zr phase diagrams and phases identified by electron diffraction in

as-cast Alloy AFC2-A7 [258]. Inferences about compositions of individual phases should be regarded as speculative in the absence of single-phase chemical measurements.

2.4.2.7.2.2 Phase Transitions

The only available data on phase-transition temperatures and enthalpies in this alloy were obtained by deconvolution of peaks in DTA data [230]. These data show three phase transitions whose onset temperatures and enthalpies are summarized in Table 46. As no high-temperature diffraction or microchemical data to support phase identifications are available, attempts to identify the reactions responsible for the transitions shown by the DSC data should be treated with caution.

Table 46. Phase transition temperatures from Alloys AFC1-MI and AFC1-MJ [230 (Table 8)].

	Transformation 1		**Transformation 2**		**Transformation 3**	
	Heating	**Cooling**	**Heating**	**Cooling**	**Heating**	**Cooling**
Onset temperature (K)	820±1.4	796±0.6	832±3.4	835±14.5	855±0.5	836±0.3
Enthalpy (J/g)	5.8 ±2.27	-2.0±0.869	13.7±2.13	-8.0±3.02	3.8±1.23	-13.5±2.17

2.4.2.7.3 Thermal Expansion and Density

2.4.2.7.3.1 Coefficient of Linear Thermal Expansion

The linear thermal expansion from two pieces of Alloy AFC1-MJ was measured using TMA. The coefficient of linear thermal expansion is approximately 1.322×10^{-5}/°C between room temperature and the onset of the lowest-temperature phase transition and 2.059×10^{-5}/°C from the end of the highest-temperature phase transition to ~1000°C.

2.4.2.7.3.2 Density

Room-temperature densities of pieces from three rods of Alloy AFC1-MJ were measured using the Archimedes method. The densities were 11.46, 11.23, 11.551 g/cm3, with an average value of ~14.05 g/cm^3.

2.4.2.7.3.3 Changes in Volume Due to Phase Transitions

The TMA data indicates that the phase transition at ~600°C is associated with an increase in length. Assuming isotropic expansion, this change in length indicates a corresponding increase in volume.

2.4.2.8 U-25Pu-40Zr-2Np-3Am (Alloy AFC1-MH)

2.4.2.8.1 Introduction

Phases and microstructures in Alloy AFC1-MH (nominal composition 30U-2Np-25Pu-3Am-40Zr in weight percentages, ~18.3U-1.2Np-15.1Pu-1.8Am-53.6Zr in atomic percentages) were investigated by researchers at Idaho National Laboratory as part of a study of low-U fuels for transmutation of minor actinides. Key results from SEM and XRD analyses were summarized in review papers by Burkes et al. [230] and Keiser et al. [179].

Samples of Alloy AFC1-MH were prepared by a procedure that involved arc-melting the material several times on a copper hearth to homogenize it, followed by gravity drop casting to produce cylinders ~4 mm in diameter. Transverse slices were cut and ground to produce flat surfaces for analysis [179].

No information about the heat capacity, thermal expansion, or thermal conductivity of this alloy is available.

2.4.2.8.2 Phases and Phase Transformations

2.4.2.8.2.1 Phases

Very little SEM data from this alloy is available, although microstructures generally resemble those in other U-Np-Pu-Am-Zr alloys [179]. X-ray maps suggest a homogeneous distribution of actinides and Zr.

X-ray diffraction patterns from as-cast samples of this alloy show small, broad peaks corresponding to d-spacings similar to those of δ-UZr_2 (Figure 77). A Rietveld refinement based on the assumption that the phases in the sample are δ-UZr_2, ζ-(U,Pu), α-U, and γ-U indicated that ~16% of the sample had a structure similar to that of ζ-(U,Pu) with lattice parameters a = 10.685 Å and α = 89.69° and ~82% of the sample had a structure similar to that of δ-UZr_2 with lattice parameters a = 5.048 and c = 3.105 Å. γ-U was included in the refinement because it was believed that it might be retained in the sample and α-U was apparently included for consistency with other alloys in the same publication. Neither of these phases produced qualitatively identifiable peaks, and the Rietveld refinement did not indicate a significant concentration of either phase [230 (Tables 3 and 4, Alloy F)].

In interpreting the Rietveld refinement results, it is important to recognize that the number of phases and lattice parameters included in the refinement is large relative to the number of peaks in the data. The refinement included two phases that were not present in significant quantities and did not include the high-Zr phase identified in the SEM data. Based on these considerations, it seems likely that errors in the phase proportions and lattice parameters from the Rietveld refinement are significantly larger than the published uncertainties, which appear to be based on counting statistics [230]. Detailed interpretations of the Rietveld refinement results should be treated with caution unless verified by further experiments. Inferences about compositions of individual phases should be regarded as speculative in the absence of single-phase chemical measurements.

The identification of the major phases in as-cast Alloy AFC1-MH as structurally similar to δ–(U,Pu) and δ-UZr_2 is plausible based on U-Pu-Zr phase diagrams and phases identified by electron diffraction in as-cast Alloy AFC2-A7 [258].

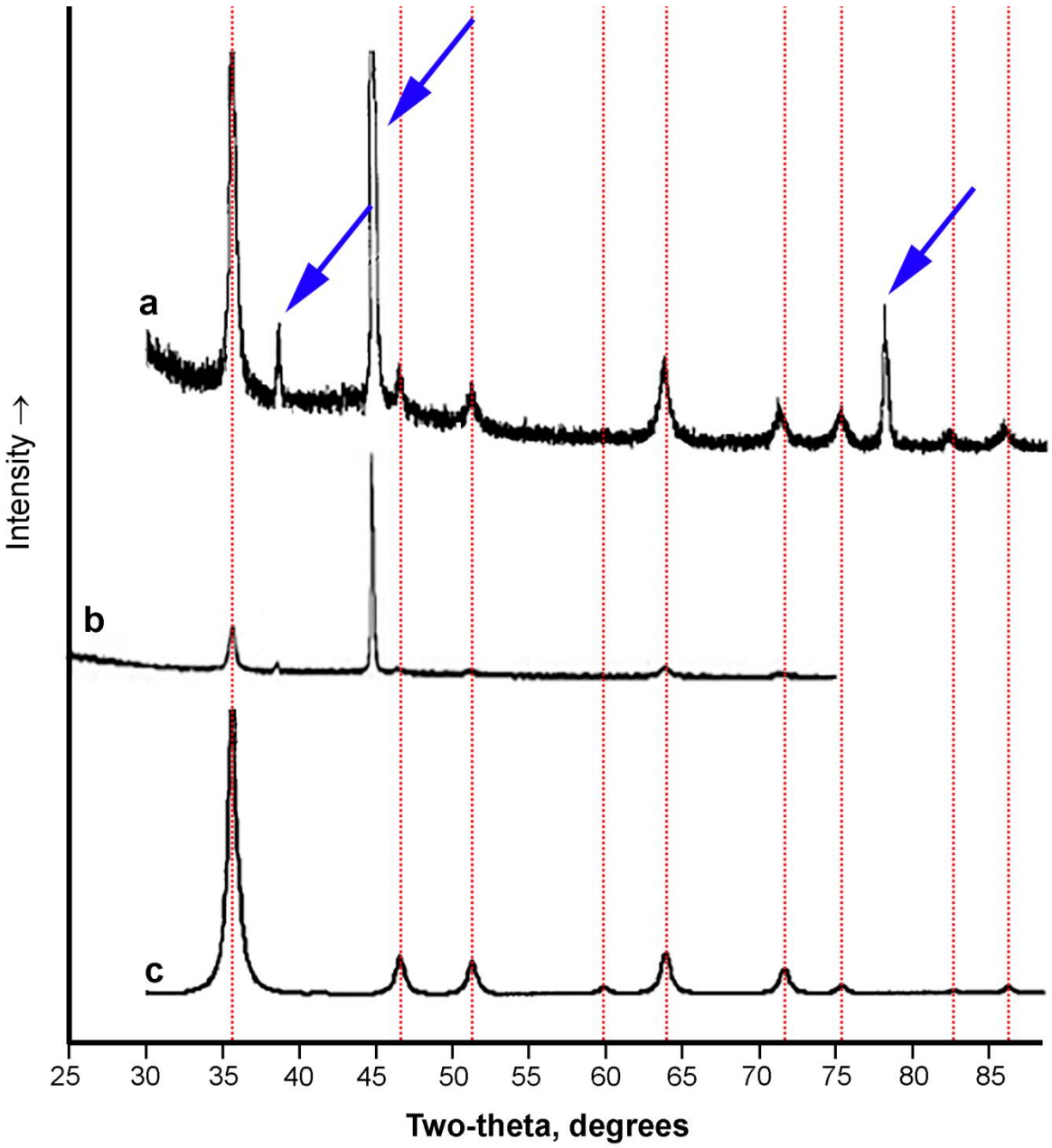

Figure 77. Experimental X-ray diffraction patterns from Alloy AFC1-MH with simulated pattern from δ-UZr_2 for comparison. a: Experimental pattern. b: Experimental pattern [230 (Figure 4, Pattern F)]. c: Simulated pattern from δ-UZr_2. Dashed red lines indicate positions of peaks from δ-UZr_2; blue arrows indicate positions of peaks from the Al used as an internal standard. Patterns were measured with Cu K_α X-rays.

2.4.2.8.2.2 Phase Transitions

The only available data on phase-transition temperatures and enthalpies were obtained by deconvolution of peaks in DTA data [230 (Alloy F)]. These data show three phase transitions whose onset temperatures and enthalpies are summarized in Table 47. As no high-temperature diffraction or microchemical data to support phase identifications are available, attempts to identify the reactions responsible for the transitions shown by the DSC data should be treated with caution.

Table 47. Phase-transition temperatures in 30U-2Np-25Pu-3Am-40Zr (Alloy AFC1-MH) [230 (Table 9)]

	Transition 1		**Transition 2**		**Transition 3**	
	Heating	**Cooling**	**Heating**	**Cooling**	**Heating**	**Cooling**
Onset temperature (K)	839±1.3	831±0.2	850±3.9	839±0.7	861±3.5	846±0.5
Enthalpy (J/g)	10.1±6.87	-8.4±1.02	11.2±2.53	-12.8±0.37	4.5±0.08	-5.2±4.03

2.4.2.9 U-19Pu-10Zr-3.0Np-1.6Am-0.4Cm (METAPHIX Alloy U-19Pu-10Zr-5MA)

Alloy U-Pu-Zr-5MA (also referred to as U-19Pu-10Zr-5MA, U-Pu-Zr-5MA, and U-Pu-Zr-MA) was irradiated as part of the METAPHIX Programme. The nominal composition of this alloy consists of 66 wt% U, 19 wt% Pu, 10 wt% Zr, 3.0 wt% Np, 1.6 wt% Am, and 0.4 wt% Cm [260]. The actual average composition of the alloy includes 66.30 wt% U, 19.35 wt% Pu, 8.97 Zr, 2.97 wt% Np, 1.45 wt% Am, 0.32 wt% Cm, and less than 0.3 wt% impurities [260].

Samples of Alloy U-Pu-Zr-5MA were prepared by arc-melting U, Np, Pu, Am, and Cm feedstocks in an argon atmosphere and mixing with molten Zr and casting into fuel rods in yttria molds [261].

Characterization of un-irradiated Alloy U-Pu-Zr-5MA has been limited, and few results have been published. No information about identities and properties of individual phases is available, although the alloy is reported to be homogeneous based on examination using microprobe and metallographic techniques [261].

The as-cast density of the alloy is 15.32 g/cm^3 [149].

No information about phase transitions, heat capacity, or thermal conductivity of this alloy is available.

Results of post-irradiation examination have been published in a number of journal papers (e.g., [149, 260, 262, 263]

2.4.3 U-Pu-Zr alloys with rare-earth elements (La, Ce, Pr, Nd)

2.4.3.1 U-20Pu-15Zr-1.5RE (Alloy AFC2-B4)

2.4.3.1.1 Introduction

Researchers at Argonne and Idaho National Laboratories investigated Alloy AFC2-B4 to assist in understanding possible fuels for destruction of transuranic alloys by transmutation. This alloy was not intended for irradiation.

The nominal composition of Alloy AFC2-B4 contains 63.5 wt% U, 20 wt% Pu, 15 wt% Zr, and 1.5 wt% of a rare-earth alloy consisting of 6 wt% La, 16 wt% Pr, 25 wt% Ce, and 53 wt% Nd (~0.09 wt% La, 0.24 wt% Ce, 0.375 wt% Pr, and 0.795 wt% Nd in the entire alloy). This composition corresponds to approximately 50.8 at% U, 15.9 at% Pu, 31.3 at% Zr, 0.l12 at% La, 0.33 at% Ce, 0.5 at% Pr, and 1.05 at% Nd.

Alloy AFC2-B4 was prepared by arc-melting, then cast into fused silica tubes in an argon-atmosphere glovebox to form cylinders approximately 4 mm in diameter [223, 264].

No information about the heat capacity, thermal expansion, or thermal conductivity of this alloy is available.

2.4.3.1.2 Phases and Phase Transformations

To a first approximation, SEM images of as-cast Alloy AFC2-B4 show a U-Pu-Zr matrix surrounding high-Zr and high-RE inclusions. Polygonal features bounding irregular hexagons are visible in some images, as are series of elongated, closely spaced parallel features (Figure 78). X-ray maps indicate that the RE elements occur in separate inclusions, and that there are small inversely correlated variations in the proportions of U and Zr (Figure 79). The distribution of Pu in the matrix appears homogeneous at the spatial scale of the SEM data.

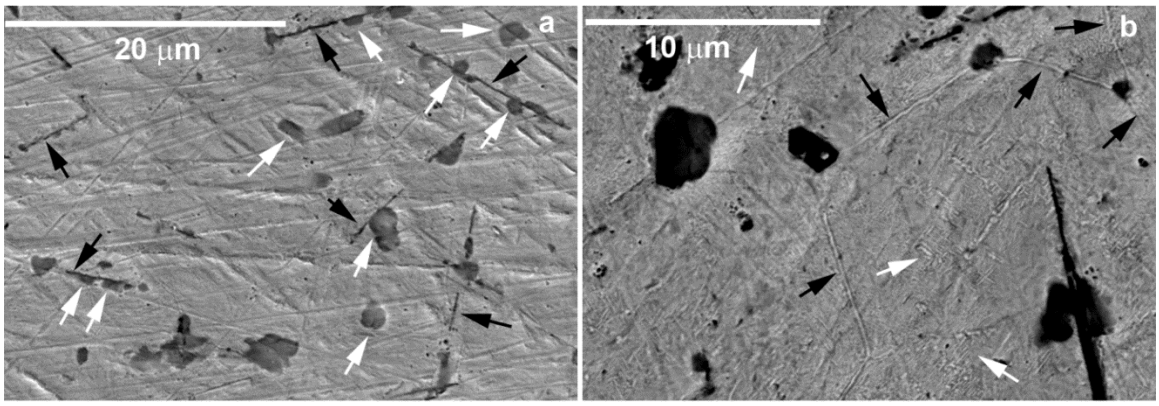

Figure 78. SEM images of as-cast alloy AFC2-B4. a: SE image. Black arrows show examples of high-Zr inclusions; white arrows show examples of high-RE inclusions. Note that small high-RE inclusions are commonly adjacent to high-Zr inclusions. b: BSE image with contrast adjusted to emphasize features in matrix. Black arrows show examples of polygonal boundaries; white arrows show examples of areas with fine parallel microstructures.

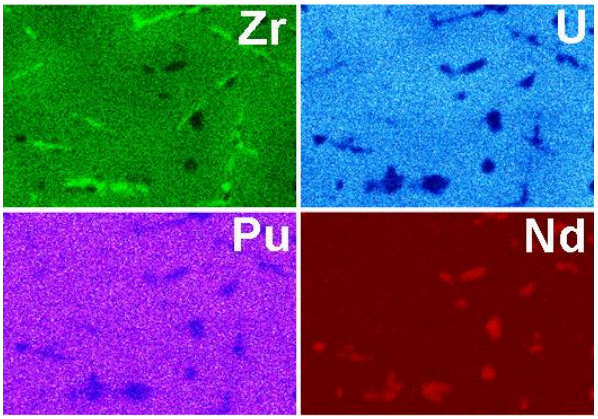

Figure 79. X-ray maps from the area of Figure 78 Part a, showing Nd as a representative rare-earth element. Contrast was adjusted independently for individual maps. Brighter areas indicate higher concentrations of the indicated elements.

Microstructures in transverse slices of annealed samples prepared by holding sections of as-cast cylinders at a temperature of 500°C for 1 week and cutting transverse slices from the middle portions of the cylinders show segregation of the matrix into high-U and high-Zr regions. Polygonal features bounding irregularly shaped hexagonal areas are broader than those in the as-cast material, and show longitudinal separation into regions with different compositions (Figure 80). The distribution of Pu in the matrix appears homogeneous, and the rare-earth elements occur in separate inclusions.

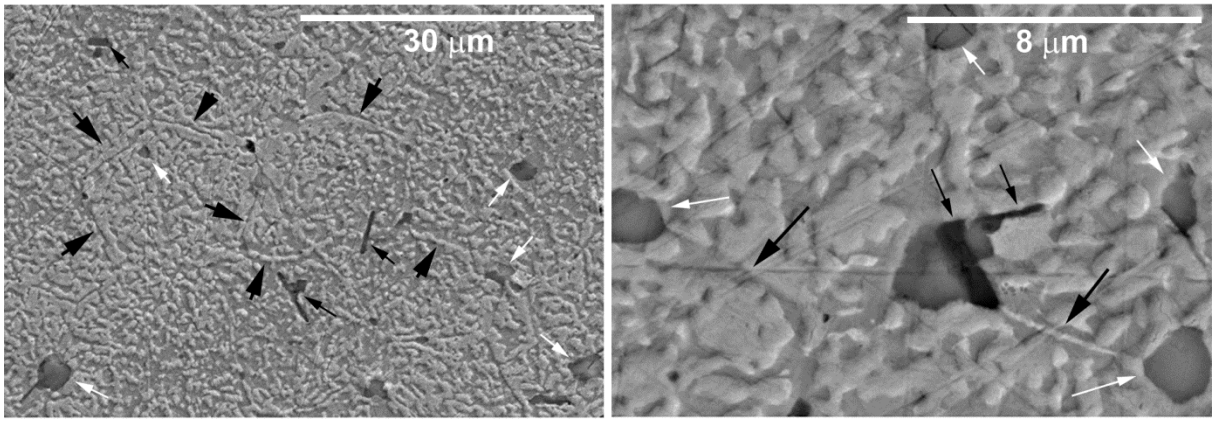

Figure 80. SEM SE images of annealed alloy AFC2-B4. Large black arrows show examples of polygonal boundaries. Small black arrows show examples of high-Zr inclusions. Small white arrows show examples of high-RE inclusions.

No information about identities or quantitative chemical compositions of individual phases or about phase transitions in Alloy AFC2-B4 is available.

2.4.4 U-Pu-Zr Alloys with Minor Actinides (Np, Am) and Rare-Earth Elements (La, Ce, Pr, Nd), Sorted by Increasing Weight Percentage of Zr

2.4.4.1 U-18Pu-10Zr-1.2Np-0.8Am-0.5Ce-1.4Nd (METAPHIX Alloy CR11)

2.4.4.1.1 Introduction

Alloy CR11 was cast by the METAPHIX Programme as part of a study intended to examine effects of rare-earth elements in U-Pu-Zr fuel alloys that also contain minor actinides. Its nominal composition has 61.8 wt% U, 1.2 wt% Np, 18.0 wt% Pu, 0.8 wt% Am, 0.5 wt% Ce, 1.4 wt% Nd, and 10.0 wt% Zr, (corresponding to ~58.1 at% U, 15.2 at% Pu, 22.2 at% Zr, 1 at% Np, 0.7 at% Am, 0.7 at% Ce, and 2 at% Nd) [149]. Proportions of elements in Alloy CR11 are similar to those in METAPHIX Alloy U-19Pu-10Zr-2MA-2RE (Section 2.4.5.2), except that Alloy CR11 has a slightly lower concentration of Pu, Alloy U-19Pu-10Zr-2MA-2RE includes low concentrations of Cm, Gd, and Y that are not present in Alloy CR11, and the concentration of U in Alloy CR11 is lower than that in Alloy U-19Pu-10Zr-2MA-2RE by ~5 wt%.

No information about the heat capacity or thermal conductivity of this alloy is available.

2.4.4.1.2 Phases and Phase Transformations

2.4.4.1.2.1 Phases

Information on phases in as-cast Alloy CR11 is limited. An arc-melted sample of this alloy did not form high-RE and low-RE regions like those in alloys CR6 and CR10 (Sections 2.4.4.3 and 2.4.4.2, respectively), but instead had RE- and Am-rich precipitates that were “homogeneously dispersed” in a U-Pu-Zr-Np matrix [149].

Matrices of rapidly quenched samples of Alloy CR11 that had been annealed at 773 K for 28 hours, at 773 K for 97 hours, or at 873 K for an unspecified time between 3.5 and 100 hours had two-phase matrices, while matrices of rapidly quenched samples that had been annealed at 923K for 3.5 or 100 hours or at 1123 K for an unspecified time between 3.5 and 100 hours had a single matrix phase. The annealed samples had RE inclusions ~3 μm across, which were dispersed “almost homogeneously” in samples annealed at 773 and 873 K. Although the RE inclusions occurred at grain boundaries in samples annealed at 973 and 1123 K, their distribution was “homogeneously dispersed” [149].

No experimental data about crystal structures or compositions of phases in this alloy are available.

2.4.4.1.2.2 Phase Transitions

Dilatometry data shows that temperatures of phase transitions in Alloy CR11 are similar to those in METAPHIX Alloys CR12 (Section 2.4.5.1) and CR13 (U-19Pu-10Zr, Section 2.4.1) [149 (Figure 4)], and occur at ~853 and 903 K. Although the melting temperature of Alloy CR11 was not reported, it seems likely that this temperature is similar to the melting temperatures of Alloys CR12 (~1480 K) and CR13 (~1490 K, [149]).

2.4.4.1.3 Thermal Expansion and Density

The only available data on thermal expansion of Alloy CR11 is a single dilatometric curve that does not provide quantitative information about thermal expansion [149 (Figure 4)]. This curve shows changes in slope at approximately 853 and 903 K, which were attributed to specific reactions based on phase diagrams and comparison to other alloys. Although other changes in slope are visible in the dilatometric curve between 853 and 903 K, no further information is available about these changes.

2.4.4.2 U-18.3Pu-10.2Zr-9.3Np-4.7Am-3.2Ce-10.2Nd (METAPHIX Alloy CR10)

Alloy CR10 was cast by the METAPHIX Programme as part of a study intended to examine effects of rare-earth elements in U-Pu-Zr fuel alloys that also contain minor actinides. It has 43.9 wt% U, 9.3 wt% Np, 18.3 wt% Pu, 4.7 wt% Am, 3.2 wt% Ce, 10.2 wt% Nd, and 10.2 wt% Zr, (corresponding to approximately 35.2 at% U, 14.6 at% Pu, 21.3 at% Zr, 3.7 at% Am, 4.3 at% Ce, and 13.5 at% Nd) [149].

Ohta et al. [149] reported that an arc-melted sample of Alloy CR10 separated into high-RE and low-RE regions similar to those in Alloy CR6 (Section 2.4.4.3) and that most of the Am was in the high-E material.

No information about the heat capacity, thermal expansion, room-temperature density, or thermal conductivity of this alloy is available.

2.4.4.3 U-19.3Pu-10.7Zr-9.7Np-3.7Ce-11.6Nd (METAPHIX Alloy CR6)

Alloy CR6 was cast by the METAPHIX Programme as part of a study intended to examine effects of rare-earth elements in U-Pu-Zr fuel alloys that also contain minor actinides. It has 45.0 wt% U, 9.7% Np, 19.3% Pu, 9.7% Np, 11.6% Nd, 3.7% Ce, and 10.7% Zr, (corresponding to 35.4 at% U, 7.6 at% Np, 15 at% Pu, 22 at% Zr, 5 at% Ce, and 15 at% Nd) [149].

Ohta et al. [149] reported that an arc-melted sample of this alloy formed a high-RE layer along the upper surface during casting, and that the rest of the alloy was depleted in Ce and Nd. The composition of the high-Ce, high-Nd layer was ~22Ce-65Nd-12Pu (by weight), and the composition of the low-Ce, low-Nd areas was ~50U-14Zr-22Pu-13Np. Although Ohta et al. referred to these materials as “phases,” an image of the alloy suggests that each “phase” may contain more than one material.

No information about identifications and properties of individual phases, phase transitions, heat capacities, thermal expansion, as-cast densities, or thermal conductivity of this alloy is available.

2.4.4.4 U-20Pu-15Zr-2Np-3Am-1RE (Alloy AFC2-A2)

2.4.4.4.1 Introduction

Alloy AFC2-A2 was cast and characterized at Idaho National Laboratory. It is part of a series of related alloys with differing concentrations of uranium and rare-earth elements that were intended to investigate properties of fuels recycled using a pyrochemical process that did not completely remove the rare-earth elements. Other alloys in the series are Alloy AFC2-A1 (no rare-earth elements, Section 2.4.2.3), AFC2-A3 (1.5% rare-earth elements, Section 2.4.4.5), and Alloy AFC2-A7 (8% rare-earth elements, Section 2.4.4.6).

The nominal composition of Alloy AFC2-A2 contains 59 wt% U, 20 wt% Pu, 15 wt% Zr, 2 wt% Np, 3 wt% Am, and 1% of a rare-earth alloy consisting of 6 wt% La, 16 wt% Pr, 25 wt% Ce, and 53 wt% Nd (corresponding to 0.06 wt% La, 0.25 wt% Ce, 0.16 wt% Pr, and 0.53 wt% Nd in the entire alloy. This composition corresponds to ~47.4 at% U, 1.6 at% Np, 16 at% Pu, 2.4 at% Am, 0.08% at% La, 0.34 at% Ce, 0.32% at Pr, 0.70 at % Nd, and 31.4 at% Zr. Analyses of as-cast samples of Alloy AFC2-A2 showed that the actual composition was ~59.1 wt% U, 2.07% Np, 19.43% Pu, 3.28% Am, 1.02% RE, and 14.0% Zr [231 (Alloy B), 254].

No information about the heat capacity or thermal conductivity of this alloy is available.

2.4.4.4.2 Phases and Phase Transformations

2.4.4.4.2.1 Phases

SEM images and X-ray maps of Alloy AFC2-A2 show an actinide-zirconium matrix surrounding high-Zr and high-RE inclusions (Figure 81) [10, 254 (Figures 1a, 1b, 2c)]. A number of the high-Zr inclusions also contain Si, which is not present in the nominal composition of the alloy. X-ray maps show a strong correlation between Am and RE inclusions; however, it is not possible to determine whether the Am and RE elements are in the same phases. High-Zr and high-RE inclusions commonly occur adjacent to one another.

Contrast variations in BSE images of the matrix can be correlated to local variations in the proportions of U and Zr, and suggest either a single-phase matrix with a wide range of compositions or a fine-grained matrix consisting of several phases with significantly different compositions and locally varying proportions. Concentrations of Np and Pu in the matrix appear uniform. Am is depleted adjacent to high-Am inclusions (e.g., [254 (Figure 4)], but otherwise appears to be uniformly distributed in the matrix.

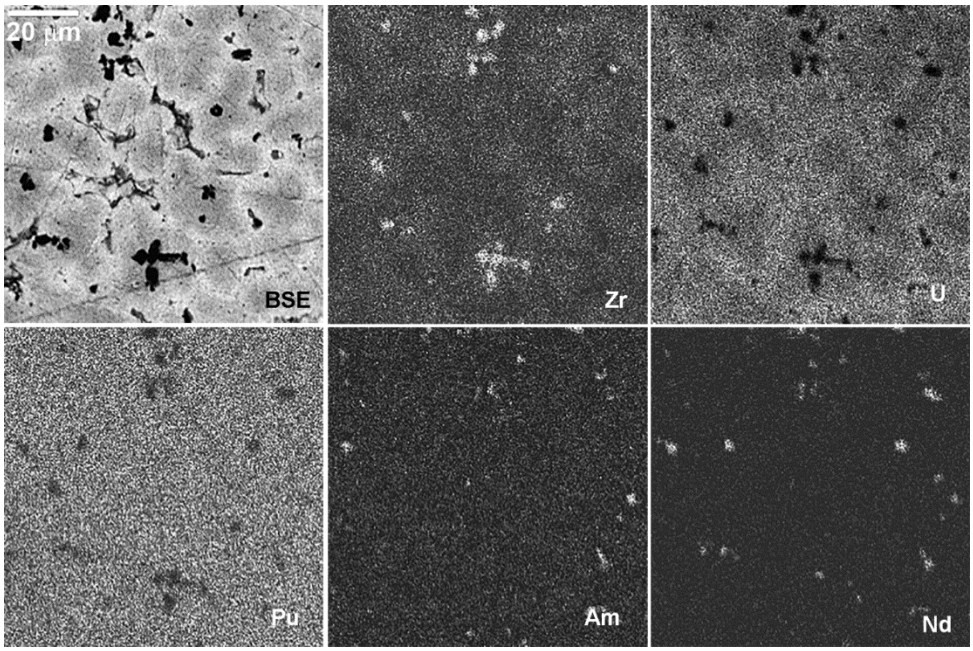

Figure 81. SEM BSE image and X-ray maps showing distributions of selected elements from Alloy AFC2-A2. Concentrations of U and Zr vary inversely and are correlated to contrast in BSE image. Concentration of Pu is homogeneous at the spatial scale of the data except in high-Zr inclusions. The Np map is similar to the Pu map, but has a very low number of total counts. Distributions of La, Ce, and Pr are similar to that of Np. The Am map resembles those of the rare-earth elements more closely than those of other actinides.

The X-ray diffraction pattern from this alloy is dominated by the LaB_6 internal standard and has only a small number peaks that can be clearly attributed to the sample (Figure 82). A Rietveld refinement based on the assumption that the sample contained LaB_6 (used as an internal standard), δ-UZr_2, ζ-(U,Pu), α-U, and γ-U showed that the pattern represented ~80% LaB_6, 1% δ-UZr_2 with lattice parameters $a \approx 5.047$Å and $c \approx 3.101$ Å, 16% ζ-(U,Pu) with lattice parameters $a \approx 10.723$ Å and $\alpha \approx 89.40°$, 2.6% γ-U with lattice parameter $a \approx 3.585$ Å, and less than 0.1% α-U with lattice parameters $a \approx 2.739$ Å, $b \approx 5.623$ Å, and $c \approx 5.027$ Å. When re-normalized without the LaB_6, these phase proportions correspond to ~81% ζ-(U,Pu), ~6% δ-UZr2, 1% α-U, and ~13 % γ-U [231 (Tables 2 and 3, Alloy B)].

In interpreting the X-ray diffraction results, it is important to consider that the data were obtained from slices of as-cast alloys rather than powders, that the number of phases and lattice parameters included in the Rietveld refinement was large relative to the number of peaks from the sample in the data, that some of the phases might be solid solutions with lattice parameters that vary as a result of differences in composition, and that the identification of phases for the Rietveld refinement was qualitatively incorrect because it did not include any phases that might correspond to the inclusions shown in the SEM data. It is also important to recognize that there are no chemical measurements from individual phases.

Although the identification of the major phases in this alloy as similar to ζ-(U,Pu) and δ-(UZr_2) is consistent with the U-Pu-Zr phase diagrams of O'Boyle and Dwight (2.4.1.2.3) and with phases identified by electron diffraction of as-cast Alloy AFC2-A7 [258], it seems likely that the actual errors in phase proportions and lattice parameters in the X-ray diffraction data are larger than the published error estimates [236], which appear to be based on counting statistics. Unless confirmed by further measurements, detailed interpretation of lattice parameters and phase proportions from the X-ray diffraction data for purposes such as determining compositions of individual phases or developing detailed phase diagrams should be regarded with caution. The presence and reported concentration of γ-U (a retained higher-temperature phase) and the identification of α-U in the sample should be treated with particular caution unless confirmed by further analyses.

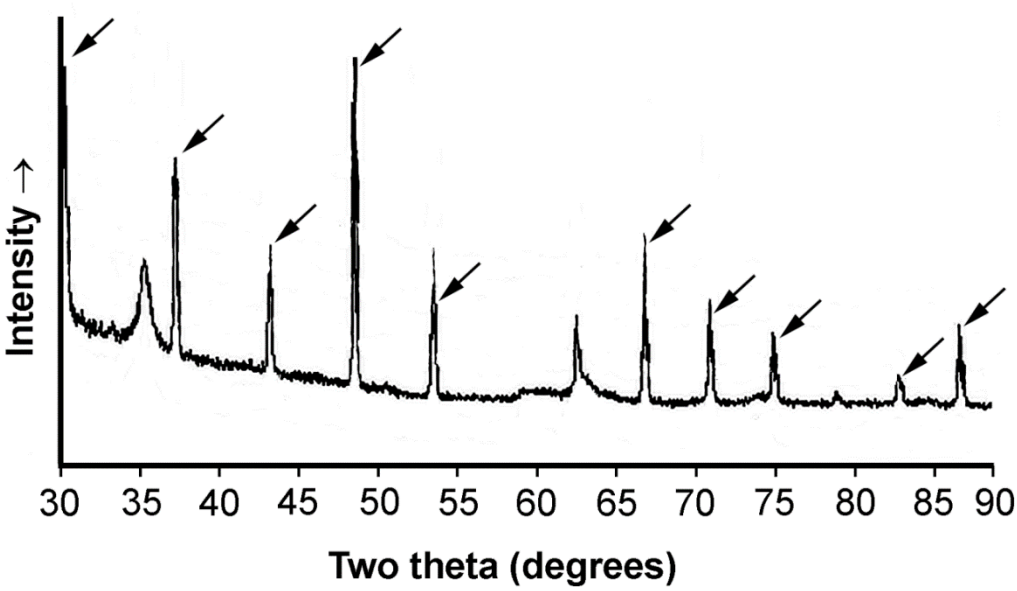

Figure 82. Experimental X-ray diffraction patterns from Alloy AFC2-A2 [231 (Figure 2, Pattern B)]. Arrows indicate peaks from the LaB_6 internal standard. The pattern was collected using Cu K_α radiation.

2.4.4.4.2.2 Phase Transitions

DTA heating and cooling curves from as-cast Alloy AFC2-A2 show two peaks between room temperature and ~800°C. The shape of the higher-temperature peak during cooling suggests that it represents more than one reaction. Burkes et al. deconvoluted the higher-temperature peak based on initial phase-transition estimates from phase-diagram analysis and determined that it represents two reactions [231].

TMA data from Alloy AFC2-A2 also show two phase transitions [10]. Onset temperatures for the lower-temperature reaction during heating and cooling are generally consistent with the DTA data, but onset temperatures for the higher-temperature reaction are significantly higher in the TMA data than in the DTA data.

Table 48 and Table 49 summarize the available data on phase-transformation temperatures and enthalpies in Alloy AFC2-A2. Although differences between DTA and TMA data suggest that further experimental research is needed to understand phase transitions in this alloy, the deconvoluted DTA data from Burkes et al. [231] are probably the most accurate values available.

Table 48. Phase-transformation temperatures in 59U-20Pu-3Am-2Np-1.0RE-15Zr (Alloy AFC2-A2) [10, 231 (Tables 4 and 5, Alloy B)].

Reaction 1		**Reaction 2**		**Reaction 3**			
Heating T (K)	**Cooling T (K)**	**Heating T (K)**	**Cooling T (K)**	**Heating T (K)**	**Cooling T (K)**	**Method**	**Reference**
846±1.6	841±0.1	918±2.2	892±2.1	935±1.6	919±5.9	DTA	[231]
860	848	953	913	—	—	TMA	[10]

Table 49. Phase-transformation enthalpies in 59U-20Pu-3Am-2Np-1.0RE-15Zr [10 (Table 10, Alloy A2), 231 (Tables 4 and 5, Alloy B)] determined by DTA.

Reaction 1		**Reaction 2**		**Reaction 3**		
Enthalpy during heating (J/g)	**Enthalpy during cooling (J/g)**	**Enthalpy during heating (J/g)**	**Enthalpy during cooling (J/g)**	**Enthalpy during heating (J/g)**	**Enthalpy during cooling (J/g)**	**Reference**
10.0 ±0.08	-9.6±0.17	11.3±1.78	-12.4±0.76	6.3±1.61	-6.2±0.71	[230, 236]

2.4.4.4.3 Thermal Expansion and Density

2.4.4.4.3.1 Linear Thermal Expansion

The only available measurements of the thermal expansion of Alloy AFC2-A2 were made using a TMA instrument. Measurements two cycles during which the samples were heated and cooled between room temperature and 800°C showed good reproducibility [10].

The thermal expansion of Alloy AFC2-A2 is generally similar to that of Alloys AFC2-A1, AFC2-A3, AFC2-A4, AFC2-A5, and AFC2-A6 [10 (Figure 54)]. This thermal expansion can be represented by Equation 70 (Section 2.4.2.3.4.1).

2.4.4.4.3.2 Coefficients of Thermal Expansion

The coefficient of linear thermal expansion corresponding to Equation 70 is approximately 1.5×10^{-5}/°C for temperatures between 20 and 550°C. Assuming isotropic thermal expansion, the corresponding coefficient of volumetric thermal expansion is approximately 4.5×10^{-5}/°C. These coefficients are like those of Alloy AFC2-A1 (Section 2.4.2.3.4.2).

2.4.4.4.3.3 Density

Room-temperature densities of two pieces of as-cast Alloy AFC2-A2 were determined from dimensional analysis. The densities were 14.10 and 14.16 g/cm^3, with an average value of ~14.13 g/cm^3 [10 (Table 13), 255 (Table 3)]. Volumes and densities at temperatures between 20 and 550°C can be approximated using Equation 6, Equation 7, and Equation 70.

2.4.4.5 U-20Pu-15Zr-2Np-3Am-1.5RE (Alloy AFC2-A3)

2.4.4.5.1 Introduction

Alloy AFC2-A3 was cast and characterized at Idaho National Laboratory. It is part of a series of related alloys with differing concentrations of uranium and rare-earth elements that were intended to investigate properties of fuels recycled using a pyrochemical process that did not completely remove the rare-earth elements. Other alloys in the series are Alloy AFC2-A1 (no rare-earth elements, Section 2.4.2.3), AFC2-A2 (1.0% rare-earth elements, Section 2.4.4.4), and Alloy AFC2-A7 (8% rare-earth elements, Section 2.4.4.6).

The nominal composition of Alloy AFC2-A3 contains 58.5 wt% U, 20% Pu, 15% Zr, 2% Np, 3% Am, and 1.5 wt% of a rare-earth alloy consisting of 6 wt% La, 16 wt% Pr, 25 wt% Ce, and 53 wt% Nd (corresponding to 0.09% La, 0.38% Ce, 0.24% Pr, and 0.795% Nd in the entire alloy. This composition corresponds to ~46.9 at% U, 1.6 at% Np, 15.9 at% Pu, 2.4 at% Am, 0.12% La, 0.51% Ce, 0.32% Pr, 1.05% Nd, and 31.3 at% Zr. Analyses of as-cast samples of Alloy AFC2-A3 showed that the actual composition was ~57.6 wt% U, 2.01% Np, 19.9% Pu, 3.60% Am, 1.53% RE, and 15.6% Zr [231 (Alloy C), 254].

Casting involved mixing feedstock materials in appropriate proportions, arc-melting three times to homogenize the alloy, then melting the alloy a final time and casting it into a silica glass ("quartz") tube to produce a cylinder with an approximate diameter of ~4 or 5 mm [231 (Alloy C), 254]

No information about the heat capacity or thermal conductivity of this alloy is available.

2.4.4.5.2 Phases and Phase Transformations

2.4.4.5.2.1 Phases

SEM images and X-ray maps of as-cast alloy AFC2-A3 show a high-actinide matrix with a significant concentration of Zr and three common kinds of inclusions: high-Zr inclusions, some of which also have Si, high-RE inclusions, and high-Am inclusions [10, 254] (Figure 83; see also [254 (Figure 3)]). High-Zr and high-RE inclusions commonly occur adjacent to each other. Am occurs in small inclusions adjacent to some (but not all) high-RE inclusions.

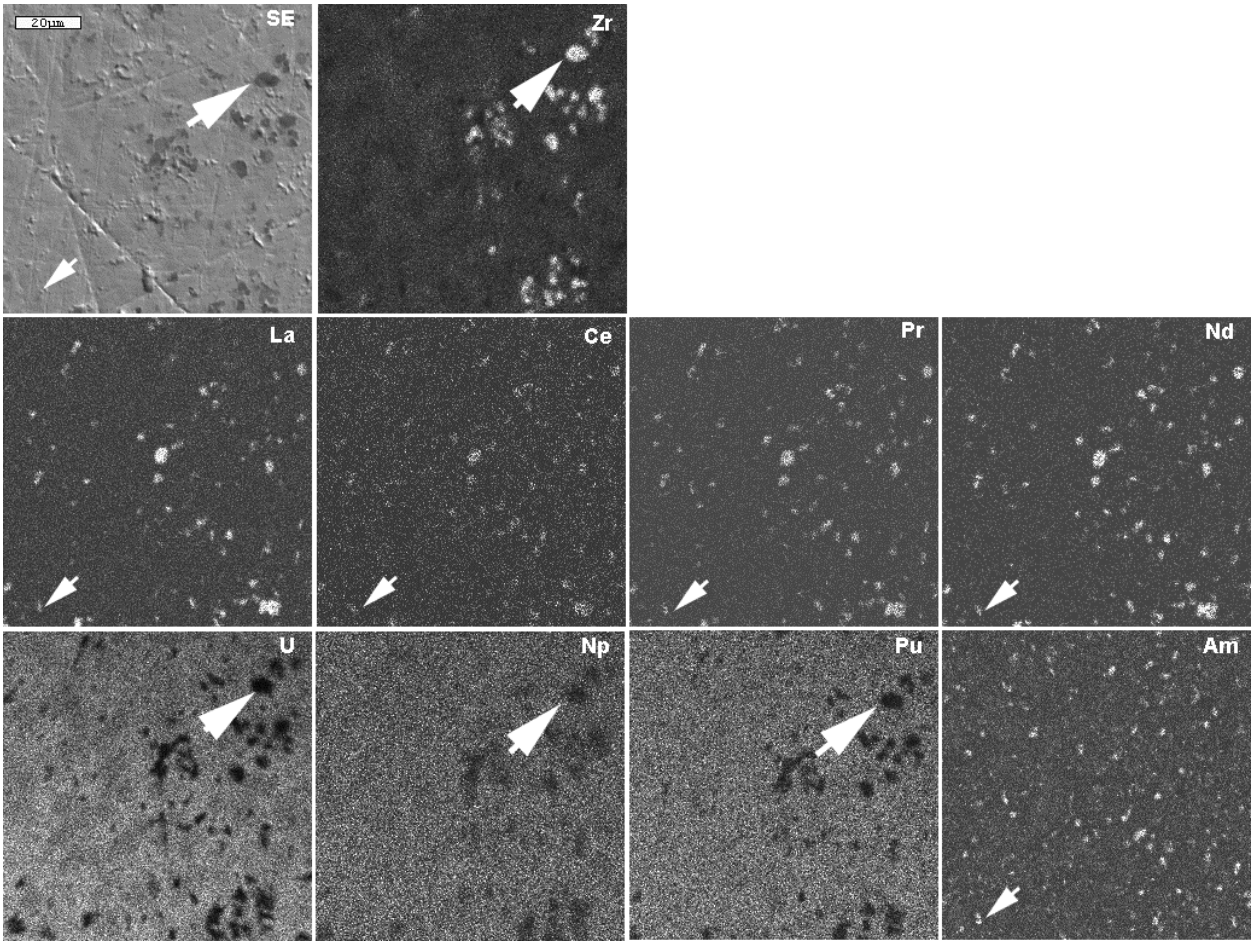

Figure 83. SEM images and X-ray maps from as-cast Alloy AFC2-A3. Black arrows indicate the same high-Zr inclusion; white arrows indicate the same small high-RE inclusion and adjacent high-Am inclusion.

Contrast variations in BSE images of the matrix in as-cast samples can be correlated to local variations in the proportions of U and Zr [254], and suggest either a single-phase matrix with a wide range of compositions or a fine-grained matrix consisting of several phases with significantly different compositions and locally varying proportions. Concentrations of Np and Pu in the matrix appear uniform. Am appears to be depleted adjacent to high-Am inclusions, but otherwise appears to be uniformly distributed in the matrix.

SEM images of a sample of as-cast Alloy AFC2-A3 that had been cycled three times between room temperature and 1100°C in DSC experiments showed thin features bounding polygonal areas, many of which contained elongated, approximately parallel features. X-ray maps showed that the polygonal boundaries were enriched in U relative to the adjacent material, and that the elongated features inside the polygons corresponded to variations in concentrations of U and Zr [265]. Gradual variations in U and Zr similar to those in the as-cast sample were no longer visible.

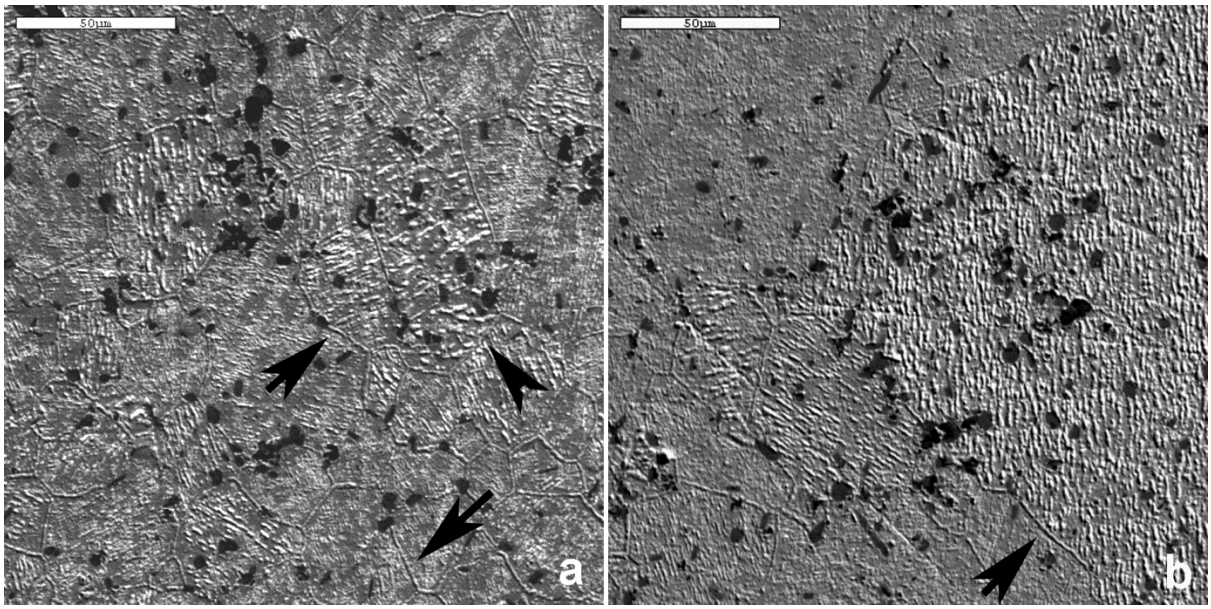

Figure 84. SEM images from Alloy AFC2-A3 after DSC experiment [265]. Black arrows indicate high-U polygonal boundaries.

Two Rietveld refinement analyses of phases and lattice parameters in this alloy have been published. One of these analyses determined that the major phase in the alloy was δ-UZr_2 with lattice parameters a = 5.03 Å and c = 3.08 Å [256]. The second analysis assumed that the sample contained LaB_6 (used as an internal standard), δ-UZr_2, ζ-(U,Pu), α-U, and γ-U, and determined that the pattern represented 57.16% LaB_6, 33.78% ζ-(U, Pu), 5.55% γ-U, and 3.51% δ-UZr_2. When the analysis was repeated without the LaB_6, the refinement results showed that the sample consists of approximately 81.1% ζ-(U,Pu) with lattice parameters a = 10.712 Å and α = 89.37°, 6.9% δ-UZr_2 with lattice parameters a = 5.045 Å and c = 3.111 Å, 11.4% γ-U with lattice parameter a = 3.587 Å, and 0.6% α-U with lattice parameters a = 2.741 Å, b = 5.634 Å, and c = 5.021 Å [231].

In attempting to understand why two Rietveld refinements from the same material are consistent with two different primary phases, it is important to recognize that Rietveld refinements are based on adjusting parameters to minimize differences between experimental and calculated diffraction patterns, and that a close match between the two diffraction patterns does not guarantee a result that accurately represents the phases that are actually present in the material (e.g. [257]). Rietveld refinements assume that all of the phases in the material have been identified correctly as a part of setting up the refinements, and that all of the phases in the refinements are actually present in the material. Violations of these assumptions are likely to lead to erroneous results.

It seems likely that differences between the results of the two refinements from Alloy AFC2-A3 are primarily consequences of the initial assumptions about the phases in the sample. Qualitatively distinguishing whether the X-ray diffraction data shows ζ-(U,Pu) in addition to δ-UZr_2 is difficult because each of the two strongest peaks from ζ-(U,Pu) is within ~0.3° of one of the two peaks from δ-UZr_2 [88, 192].

Although γ-U is not stable at room temperature, it has been reported in rapidly quenched U-Zr alloys [27, 28, 84]. Its presence as a retained higher-temperature phase in Alloy AFC2-A3 is therefore plausible.

α-U was apparently included in the refinement in reference [231] because its possible presence was suggested by postulated room-temperature phase diagrams (e.g., [230]). The proportion of this phase reported in the refinement results is insignificant.

In interpreting the X-ray diffraction results, it is important to consider that the data were obtained from slices of as-cast alloys rather than powders, that the number of phases and lattice parameters included in both of the refinements was large relative to the number of peaks from the sample, that some of the phases might be solid solutions with lattice parameters that vary as a result of variations in composition, and that the identification of phases for the Rietveld refinement was qualitatively incorrect because it did not include phases corresponding to any of the inclusions shown in the SEM data. It is also important to recognize that there were no measurements of compositions of individual phases.

Despite these considerations, U-Pu-Zr phase diagrams (Section 2.4.1.2.3) and electron-diffraction data from Alloy AFC2-A7 (Section 2.4.4.6) both suggest that alloy AFC2-A3 is likely to have both δ-UZr_2 and ζ-(U,Pu), and that the lattice parameters from the refinement that assumed that the sample was single-phase δ-UZr_2 [256] should be disregarded. It seems likely that the actual errors in phase proportions and lattice parameters in the X-ray diffraction data are larger than the estimated errors indicated by reference [236], which appear to be based on counting statistics. The presence and reported concentration of γ-U and α-U and detailed interpretation of relatively small variations in phase proportions or lattice parameters should be treated with caution unless confirmed by further analyses.

2.4.4.5.2.2 Phase Transitions

DTA heating and cooling curves from as-cast Alloy AFC2-A3 show two peaks at temperatures between room temperature and ~800°C [231 (Figure 6)]. The shape of the higher-temperature peak indicates that it represents more than one reaction. Burkes et al. deconvoluted the higher-temperature peak based on initial phase-transition estimates from phase-diagram analysis and determined that this peak represents two reactions whose onset temperatures during heating differ by ~24 degrees. The lower-temperature peak has apparently not been deconvoluted.

Table 50 and Table 51 summarize the reported phase-transformation temperatures and enthalpies from Alloy AFC2-A3. Temperatures from references [231] and [256] were apparently both determined from the DSC traces in reference [231 (Figure 6)].

Table 50. Reported Phase-transformation temperatures in 58.5U-20Pu-3Am-2Np-1.5RE-15Zr [10, 231 (Tables 4 and 5, Alloy C), 256 (Table 3)].

Transformation 1		**Transformation 2**		**Transformation 3**			
Heating T (K)	**Cooling T (K)**	**Heating T (K)**	**Cooling T (K)**	**Heating T (K)**	**Cooling T (K)**	**Method**	**Reference**
845±0.6	841±0.1	919±0.9	892±2.1	—	—	DTA	[256]
851±1.9	845±0.1	908±7.3	879±1.1	932±2.4	901±0.4	DTA	[231]
858	798-923	953	868	—	—	TMA	[10]

Onset temperatures of the lowest-temperature transformation during heating and cooling from DTA and TMA data are in reasonably good agreement. Onset temperatures for the higher-temperature peak (transformation 2) show wider differences. Although the reasons for these discrepancies are unclear, they suggest that the actual errors in onset temperatures in Table 50 may be larger than the error estimates for the individual measurements. Further experimental data are clearly required to understand phase-transformation temperatures in this alloy. In the absence of these data, the deconvoluted transformation temperatures from reference [236] are probably the best available values.

Each of the references in Table 51 reports that enthalpies for individual transformations measured during cooling are generally larger than those measured during heating by ~1-2 J/g, which is larger than indicated by the error estimates for individual measurements but still typically less than ~10%. (Transformation 2 in the data of reference [231] is an exception; however, the combined enthalpies of Transformations 2 and 3 are larger during cooling than during heating.). Further work is needed to understand these data.

Table 51. Phase-transformation enthalpies in 58.5U-20Pu-3Am-2Np-1.5RE-15Zr [10 (Table 10), 231 (Tables 4 and 5, Alloy C), 256 (Table 3)] determined by DTA.

Transformation 1		Transformation 2		Transformation 3		
Enthalpy during heating (J/g)	**Enthalpy during cooling (J/g)**	**Enthalpy during heating (J/g)**	**Enthalpy during cooling (J/g)**	**Enthalpy during heating (J/g)**	**Enthalpy during cooling (J/g)**	**Reference**
16.50±2.19	-14.47±1.95	21.72±2.31	-24.01±2.94	—	—	[256]
10.5 ±0.08	-10.4±0.09	7.7±0.62	-6.6±0.45	5.1±0.27	-8.5±0.51	[231]

2.4.4.5.3 Thermal Expansion and Density

2.4.4.5.3.1 Linear Thermal Expansion

The thermal expansion of Alloy AFC2-A3 was measured using a TMA instrument. Measurements from three cycles during which the samples were heated and cooled between room temperature and 800°C showed differences between the beginning and final sample lengths for each cycle, which were attributed to mechanical movement during each heating cycle [10].

Despite these problems, the thermal expansion of Alloy AFC2-A3 is generally similar to that of Alloys AFC2-A1, AFC2-A2, AFC2-A4, AFC2-A5, and AFC2-A6 [10 (Figure 54)]. This thermal expansion can be represented by Equation 70 (Section 2.4.2.3.4.1).

2.4.4.5.3.2 Coefficients of Thermal Expansion

The coefficient of linear thermal expansion corresponding to Equation 70 is approximately 1.5×10^{-5}/°C for temperatures between 20 and 550°C. Assuming isotropic thermal expansion, the corresponding coefficient of volumetric thermal expansion is approximately 4.5×10^{-5}/°C. These coefficients are like those of Alloy AFC2-A1 (Section 2.4.2.3.4.2).

2.4.4.5.3.3 Density

Room-temperature densities of three pieces of as-cast Alloy AFC2-A3 were measured using the Archimedes method. The densities were 13.54, 13.77, and 13.93 g/cm^3, with an average value of ~13.75 g/cm^3 [10 (Table 13), 255 (Table 3)]. Volumes and densities at temperatures between 20 and 550°C can be approximated using Equation 6, Equation 7, and Equation 70.

2.4.4.6 U-20Pu-15Zr-2Np-3Am-8RE (Alloy AFC2-A7)

2.4.4.6.1 Introduction

Alloy AFC2-A7 was cast and characterized at Idaho National Laboratory. It is part of a series of related alloys with differing concentrations of uranium and rare-earth elements that were intended to investigate properties of fuels recycled using a pyrochemical process that did not completely remove the rare-earth elements. Other alloys in the series are Alloy AFC2-A1 (no rare-earth elements, Section 2.4.2.3), AFC2-A2 (1% rare-earth elements, Section 2.4.4.4), and AFC2-A3 (1.5% rare-earth elements, Section 2.4.4.5). Weight percentages of minor actinides in Alloy AFC2-A7 are similar to the highest percentages in the METAPHIX alloys, and the weight percentage of rare-earth elements was intended to approximate a U-Pu-Zr fuel that had been previously reprocessed and irradiated to high burnups [258]. Although techniques used to cast Alloy AFC2-A7 were similar to those used for fuel pins, it was not intended for irradiation.

The nominal composition of Alloy AFC2-A7 is 52 wt% U, 20 wt% Pu, 15 wt% Zr, 2 wt% Np, 3 wt% Am, and 8.0 wt% of a rare-earth alloy consisting of 6 wt% La, 16 wt% Pr, 25 wt% Ce, and 53 wt% Nd (corresponding to ~0.48 wt% La, 2 wt% Ce, 1.28 wt% Pr, and 4.24 wt% Nd in the entire alloy). This composition corresponds to ~30 at% U, 22.5 at% Zr, 11.4 at% Pu, 1.2 at% Np, 1.7 at% Am, 0.47% at% La, 1.95 at% Ce, 1.24% at Pr, and 4.02 at% Nd. Analyses of as-cast alloys showed that the actual composition of the alloy was ~51.6 wt% U, 2.54 wt% Np, 16.5 wt% Pu, 3.74 wt% Am, 15.9 wt% Zr, and 7.04 wt% RE alloy based on an analytical total of 97.3 wt% of the sample [258]. Oxygen was not included in the analysis, but was identified in TEM data [258, 266].

No information about the heat capacity, density, thermal expansion, or thermal conductivity of this alloy is available.

2.4.4.6.2 Phases and Phase Transformations

SEM images of Alloy AFC2-A7 show an actinide-zirconium matrix surrounding four kinds of inclusions: high-Zr inclusions, high-Si inclusions, high-RE inclusions that also have significant concentrations of Am, and high-RE inclusions that do not have significant concentrations of Am [266]. The matrix has linear features bounding irregular polygons a few tens of micrometers across, but otherwise generally appears homogeneous in SEM images. FIB images suggest that the matrix is nanocrystalline and contains more than one phase [258]. X-ray maps show inverse variations in the concentrations of U and Zr [266].

TEM data shows that the matrix consists primarily of two phases occurring in highly elongated, parallel regions. Electron diffraction patterns indicate that one of these phases has a structure similar to that of ζ-(U,Pu) and one has a structure similar to that of δ-UZr_2. Some of the TEM diffraction patterns also indicate the presence of a nanocrystalline phase with a structure similar to that of UO_2. Although the presence of the oxide phase complicates interpretation of the chemical data, TEM-EDX analyses indicate that the phase similar to ζ-(U,Pu) consists of ~70 at% U, 5% Np, 14% Pu, 1% Am, and 10% Zr and the phase similar to δ-UZr2 has ~25 at% U, 2% Np, 10-15% Pu, 1-2% Am, and 55-60% Zr [258].

SEM and TEM data show that the high-Am RE inclusions consist of ~2-5 at% La, 15-20 at% Ce, 5-10 at% Pr, 25-45 at% Nd, 1 at% Np, 5-10 at% Pu, and 10-20 at% Am. Some analyses showed up to ~40 at% O; however, others showed much lower concentrations. These inclusions have a face-centered cubic structure with a lattice parameter of ~ 5.4 Å (consistent with RE oxides but too large for RE metals), and show evidence of a high degree of internal strain. These observations were interpreted as suggesting that the high-Am RE inclusions consist of a complex, spatially heterogeneous Pu-Am-RE alloy that may contain small oxide domains [266].

SEM and TEM data show that the low-Am RE phase is an oxide with a structure similar to that of trigonal Nd_2O_3, and that it contains small sub-inclusions with large concentrations of actinides and Zr. This phase should not be present based on the nominal composition of the sample, which does not include O, but apparently formed during casting. TEM analyses of this phase show that it contains ~35-45 at% O, 1-2% Zr, 4-5% La, 9-10% Ce, 6-7% Pr, and 40-45% Nd [266].

Electron diffraction data from two adjacent high-Zr crystals at the edge of a TEM sample showed that they were not α-Zr, but instead had a face-centered cubic structure [267]. Analysis of other high-Zr inclusions in this alloy suggested that they might have nucleated at the interfaces between immiscible liquids that later crystallized to form high-RE and high-Zr inclusions, and that similar inclusions in other alloys might have nucleated at small crystallites of carbides, nitrides, or oxides. The data also suggested that the inclusions might have crystallized as actinide-Zr solid solutions that un-mixed during cooling [268]. However, further investigations of these inclusions are clearly required.

No information about phase transitions in this alloy is available.

2.4.4.7 U-30Pu-20Zr-3Np-5Am-1RE (AFC2-A5)

2.4.4.7.1 Introduction

Alloy AFC2-A5 was cast and characterized at Idaho National Laboratory. It is part of a series of related alloys with differing concentrations of uranium and rare-earth elements that were intended to investigate properties of fuels recycled using a pyrochemical process that did not completely remove the rare-earth elements. Other alloys in the series are FCRD Alloys A6 (U-30Pu-20Zr-5Am-3Np, Section 2.4.2.4), A4 (U-30Pu-20Zr-3Np-5Am-1.5RE, Section 2.4.4.8), and A8 (U-30Pu-20Zr-3Np-5Am-8RE, Section 2.4.4.9).

The nominal composition of Alloy AFC2-A5 has 41 wt% U, 30 wt% Pu, 20 wt% Zr, 3 wt% Np, 5 wt% Am, and 1 wt% of a rare-earth alloy consisting of 6 wt% La, 16 wt% Pr, 25 wt% Ce, and 53 wt% Nd (corresponding to concentrations of 0.06 wt% La, 0.25 wt% Ce, 0.16 wt% Pr, and 0.53 wt% Nd in the entire alloy. This composition corresponds to ~31 31 at% U, 2.3 at% Np, 22.5 at% Pu, 3.7 at% Am, 0.08% at% La, 0.32 at% Ce, 0.20% at Pr, 0.66 at % Nd, and 39.3 at% Zr.

Casting of Alloy AFC2-A5 involved mixing feedstock materials in appropriate proportions, arc-melting three times to homogenize the alloy, then melting the alloy a final time and casting it into a silica glass (“quartz”) tube to produce a cylinder with an approximate diameter of ~4 mm. Analyses of as-cast alloys showed that the actual composition of the alloy was ~39 wt% U, 3.2% Np, 28.5% Pu, 5% Am, 23% Zr, and 1.1% rare-earth elements (La, Ce, Pr, and Nd) [254].

No information about the heat capacity or thermal conductivity of this alloy is available.

2.4.4.7.2 Phases and Phase Transformations

2.4.4.7.2.1 Phases

SEM images and X-ray maps of Alloy AFC2-A5 show an actinide-Zr matrix surrounding high-Zr and high-RE inclusions (Figure 85) [10, 254]. A number of the high-Zr inclusions also contain Si, which is not present in the nominal composition of the alloy Although some X-ray maps (not including Figure 85) show a strong correlation between Am and RE inclusions, it is not possible to determine whether the Am and RE elements are in the same phases. High-Zr and high-RE inclusions commonly occur adjacent to one another.

Some BSE images of Alloy AFC2-A5 show subtle contrast variations in the matrix. Comparison to other alloys suggests that these contrast variations are correlated to local differences in the proportions of U and Zr. Concentrations of Np and Pu in the matrix appear uniform.

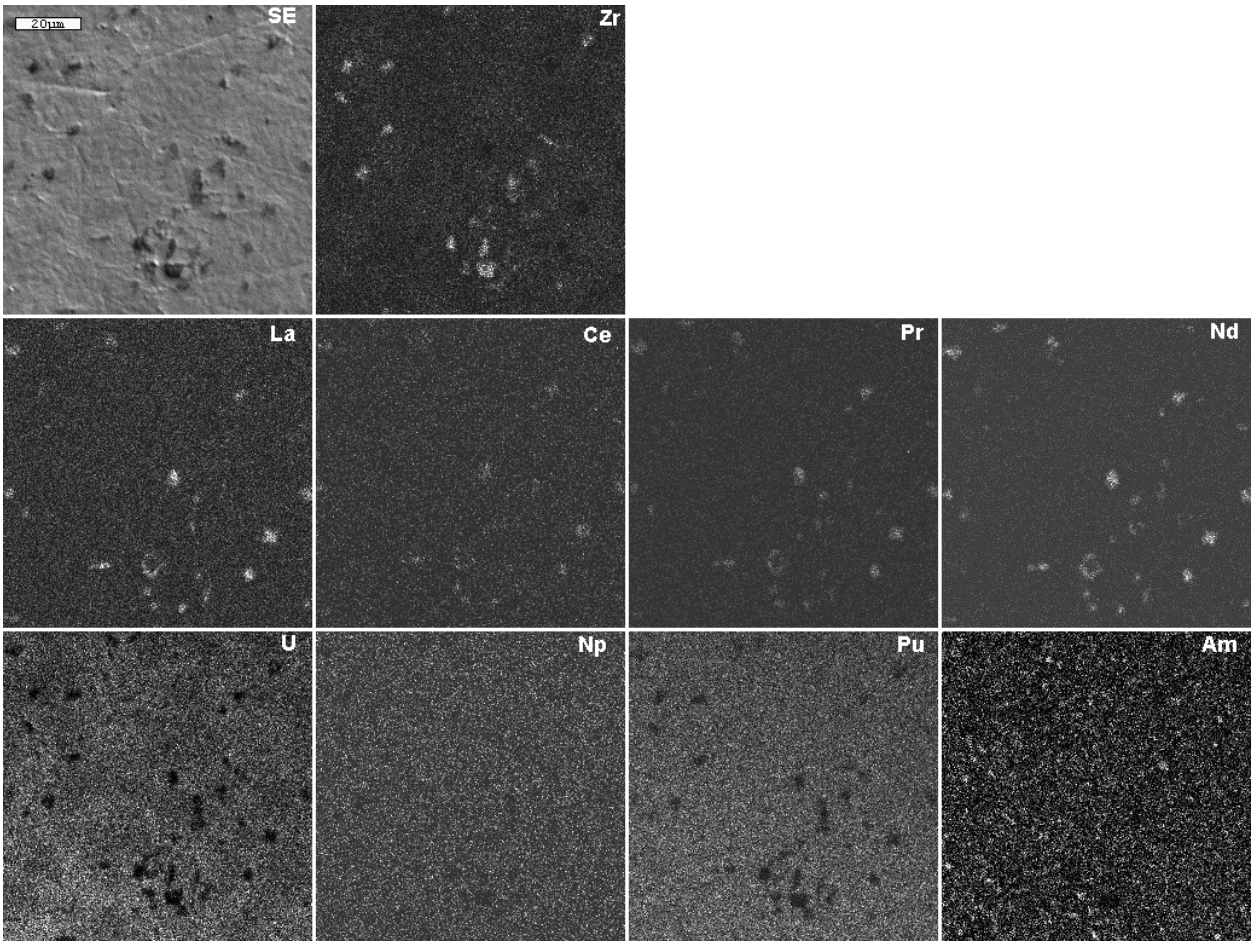

Figure 85. X-ray maps showing distributions of elements in as-cast AFC2-A5.

The X-ray diffraction pattern from this alloy is dominated by the LaB_6 internal standard and has only a few peaks that can be clearly attributed to the sample (Figure 86). A Rietveld refinement based on the assumption that the sample contained LaB_6, δ-UZr_2, ζ-(U,Pu), α-U, and γ-U showed that the pattern represents ~76.6% LaB_6, 5.5% δ-UZr_2 with lattice parameters a = 5.092±0.007 Å and c = 3.109±0.004 Å, 13.3% ζ-(U,Pu) with lattice parameters a = 10.716±0.005 Å and α = 89.33±0.06°, 0.32% α-U with lattice parameters a = 2.565±0.001, b = 5.478±0.002, and c = 4.962±0.001, and 4.31% γ-U with lattice parameter a = 3.578±0.001 Å. When re-normalized without the LaB_6, these phase proportions correspond to ~57% ζ–(U,Pu), ~28% δ-UZr_2, 1.4% α-U, and ~18 % γ-U) [236 (Tables 2 and 3, Alloy E)].

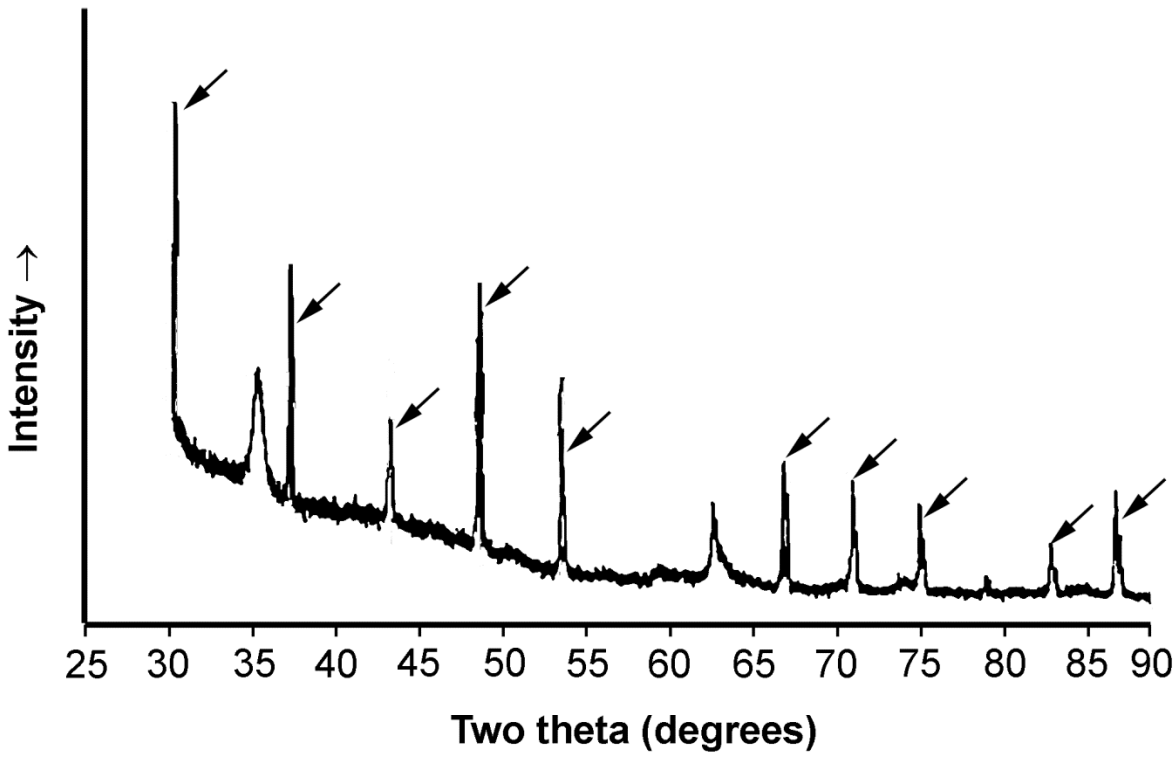

Figure 86. Experimental X-ray diffraction patterns from Alloy AFC2-A5 (re-drawn from [236 (Figure 2, Pattern E)]). Arrows indicate peaks from the LaB_6 internal standard. The pattern was collected with Cu K_α radiation.

In interpreting the X-ray diffraction results, it is important to consider that the data were obtained from slices of as-cast alloys rather than powders, that the number of phases and lattice parameters included in the Rietveld refinement was large relative to the number of peaks from the sample in the data, that some of the phases might be solid solutions with lattice parameters that vary as a result of differences in composition, and that the identification of phases for the Rietveld refinement was qualitatively incorrect because it did not include phases that might correspond to any of the inclusions shown in the SEM data.

Although the identification of the major phases in this alloy as similar to ζ-(U,Pu) and δ-(UZr_2) is consistent with U-Pu-Zr phase diagrams (Section 2.4.1.2.3) and with phases identified by electron diffraction of a more complex alloy [258], it seems likely that uncertainties in proportions and lattice parameters in the X-ray diffraction data are far larger than the estimated errors indicated by reference [236], which appear to be based on counting statistics. Detailed interpretations of phase identifications, concentrations, and lattice parameters (particularly for α-U and γ-U) should be regarded with caution unless confirmed by further analyses.

2.4.4.7.2.2 Phase Transitions

DTA heating and cooling curves from as-cast Alloy AFC2-A5 show two peaks at temperatures between room temperature and ~800°C [236 Figure 5]. Burkes et al. deconvoluted the higher-temperature peak based on initial phase-transition estimates from phase-diagram analysis and determined that this peak represents two reactions whose onset temperatures during heating differ by ~30 K.

TMA measurements of this alloy also show two phase transitions [10]. The onset temperature for the lower-temperature transition during cooling is consistent with the DTA data, but onset temperatures for the higher-temperature transition during both heating and cooling are significantly higher in the TMA data than in the DSC data.

Table 52 and Table 53 summarize the available data on phase-transformation temperatures and enthalpies in Alloy AFC2-A5. Although differences between DTA and TMA data suggest that further experimental research is needed to understand phase transitions in this alloy, the deconvoluted DTA data from Burkes et al. [231] are probably the most accurate values available.

Table 52. Phase-transformation temperatures in 41U-30Pu-5Am-3Np-1.0RE-20Zr (Alloy AFC2-A5) [10, 236 (Tables 4 and 5, Alloy E)].

Transformation 1		**Transformation 2**		**Transformation 3**			
Heating T (K)	**Cooling T (K)**	**Heating T (K)**	**Cooling T (K)**	**Heating T (K)**	**Cooling T (K)**	**Method**	**Reference**
822±2.8	820±0.1	870±4.7	872±0.2	900±9.7	897±0.4	DTA	[236]
843	823	923	898	—	—	TMA	[10]

Table 53. Phase-transformation enthalpies in 41U-30Pu-5Am-3Np-1.0RE-20Zr (Alloy AFC2-A5) [236 (Tables 4 and 5, Alloy E)] determined by DTA.

Reaction 1		**Reaction 2**		**Reaction 3**		
Enthalpy during heating (J/g)	**Enthalpy during cooling (J/g)**	**Enthalpy during heating (J/g)**	**Enthalpy during cooling (J/g)**	**Enthalpy during heating (J/g)**	**Enthalpy during cooling (J/g)**	**Reference**
12.4 ±0.47	-12.6±0.04	3.0±1.16	-3.4±0.22	5.2±0.99	-6.9±0.19	[236]

2.4.4.7.3 Thermal Expansion and Density

2.4.4.7.3.1 Linear Thermal Expansion

The thermal expansion of Alloy AFC2-A5 was measured using a TMA instrument. The sample was cycled twice between room temperature and 800°C. Data from the first heating was not recorded because of instrument failure. The remaining measurements were similar during heating and cooling [10].

The available data indicate that the thermal expansion of Alloy AFC2-A5 is essentially identical to that of Alloys AFC2-A1, AFC2-A2, AFC2-A3, AFC2-A4, and AFC2-A6 [10 (Figure 54)]. This thermal expansion can be represented by Equation 70 (Section 2.4.2.3.4.1).

2.4.4.7.3.2 Coefficients of Thermal Expansion

The coefficient of linear thermal expansion corresponding to Equation 70 is approximately 1.5×10^{-5}/°C for temperatures between 20 and 550°C. Assuming isotropic thermal expansion, the corresponding coefficient of volumetric thermal expansion is approximately 4.5×10^{-5}/°C. These coefficients are like those of Alloy AFC2-A1 (Section 2.4.2.3.4.2).

2.4.4.7.3.3 Density

Room-temperature densities of as-cast material from four castings of as-cast Alloy AFC2-A5 were determined using dimensional analysis. These densities ranged from 12.41 to 13.38 g/cm^3, with an average value of ~12.86 g/cm^3 [10 (Table 13), 255 (Table 3)]. Volumes and densities at temperatures between 20 and 550°C can be approximated using Equation 6, Equation 7, and Equation 70.

2.4.4.8 U-30Pu-20Zr-3Np-5Am-1.5RE (Alloy AFC2-A4)

2.4.4.8.1 Introduction

Alloy AFC2-A4 was cast and characterized at Idaho National Laboratory. It is part of a series of related alloys with differing concentrations of uranium and rare-earth elements that were intended to investigate properties of fuels recycled using a pyrochemical process that did not completely remove the rare-earth elements. Other alloys in the series are Alloys AFC2-A6 (U-30Pu-20Zr-5Am-3Np, Section 2.4.2.4), AFC2-A5 (U-30Pu-20Zr-3Np-5Am-1RE, Section 2.4.4.7), and AFC2-A8 (U-30Pu-20Zr-3Np-5Am-8RE, Section 2.4.4.9).

The nominal composition of Alloy AFC2-A4 has 40.5 wt% U, 30 wt% Pu, 20 wt% Zr, 3 wt% Np, 5 wt% Am, and 1.5 wt% of a rare-earth alloy consisting of 6 wt% La, 16 wt% Pr, 25 wt% Ce, and 53 wt% Nd% (corresponding to concentrations of 0.09 wt% La, 3.375 wt% Ce, 0.24 wt% Pr, and 0.795 wt% Nd, in the entire alloy). This composition corresponds to approximately 30.5 at% U, 22.4 at% Pu, 39.2 at% Zr, 2.3 at% Np, 3.7 at% Am, 0.12 at% La, 0.48 at% Ce, 0.3 at% Pr, and 1 at % Nd.

Casting of Alloy AFC2-A4 involved mixing feedstock materials in appropriate proportions, arc-melting three times to homogenize the alloy, then melting the alloy a final time and casting it into a silica glass (“quartz”) tube to produce a cylinder with an approximate diameter of ~4 mm. Analyses of as-cast alloys showed that the actual composition of the alloy was ~44 wt% U, 2.6% Np, 29.7% Pu, 4.2% Am, 17.3% Zr, and 1.4% rare-earth elements (La, Ce, Pr, and Nd) [254].

No information about the heat capacity or thermal conductivity of this alloy is available.

2.4.4.8.2 Phases and Phase Transformations

2.4.4.8.2.1 Phases

SEM images and X-ray maps Alloy AFC2-A4 show an actinide-Zr matrix surrounding high-Zr and high-RE inclusions. A number of the high-Zr inclusions also contain Si, which is not present in the nominal composition of the alloy [10, 254]. Although X-ray maps show a strong correlation between Am and RE inclusions (Figure 87), the spatial resolution of the maps is too low to determine whether the Am and RE elements are in the same phases. High-Zr and high-RE inclusions may occur adjacent to one another. Contrast variations in BSE images of the matrix can be correlated to local variations in the proportions of U and Zr [254], and suggest either a single-phase matrix with a wide range of compositions or a fine-grained matrix consisting of several phases with significantly different compositions and locally varying proportions. Concentrations of Np and Pu in the matrix appear uniform. Am is depleted adjacent to high-Am inclusions, but otherwise appears to be uniformly distributed in the matrix.

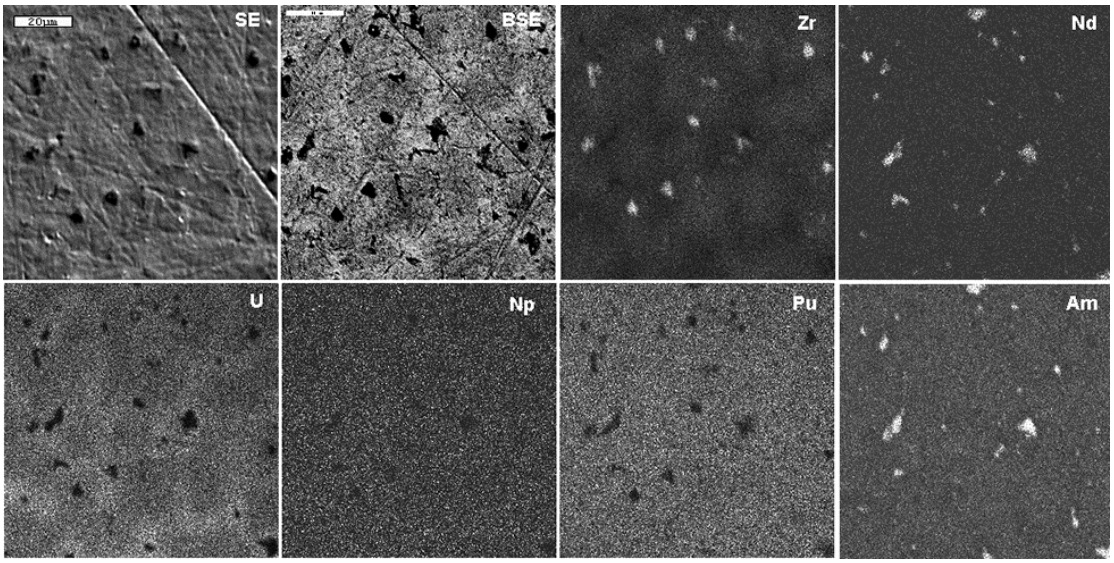

Figure 87. SEM images and X-ray maps from Alloy AFC2-A4. Distributions of La, Ce, and Pr are similar to that of Nd.

The X-ray diffraction pattern from this alloy is dominated by the LaB_6 internal standard and has only a small number peaks that can be clearly attributed to the sample (Figure 88). A Rietveld refinement based on the assumption that the sample contained LaB_6, δ-UZr_2, ζ-(U,Pu), α-U, and γ-U showed that the pattern represented ~66.7% LaB_6, 10.5% δ-UZr_2 with lattice parameters $a \approx 5.078$ Å and $c \approx 3.106$ Å, 19% ζ-(U,Pu) with lattice parameters $a \approx 10.719$ Å and $\alpha = 89.59°$, 4% γ-U with lattice parameter $a \approx 3.592$ Å, and no α-U. When re-normalized without the LaB_6, these phase proportions correspond to ~57% ζ-(U,Pu), ~31% δ-UZr_2, and ~11 % γ-U [236].

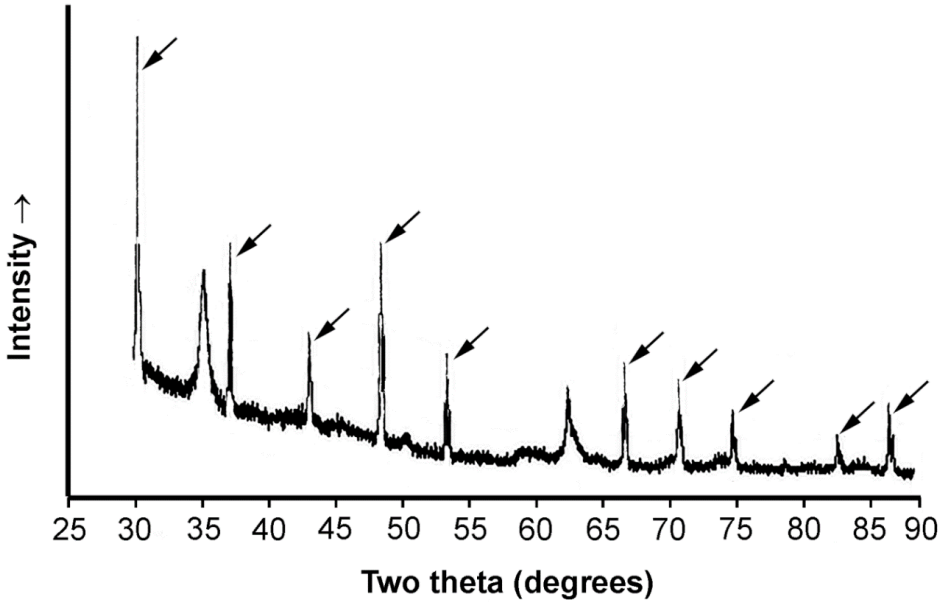

Figure 88. Experimental X-ray diffraction patterns from Alloy AFC2-A4 (re-drawn from [236 (Figure 2, Pattern D)]). Arrows indicate peaks from the LaB_6 internal standard. Two-theta angles correspond to Cu K_a radiation.

In interpreting the X-ray diffraction results, it is important to consider that the data were obtained from slices of as-cast alloys rather than powders, that the number of phases and lattice parameters included in the refinement was large relative to the number of peaks from the sample in the data, that some of the phases might be solid solutions with lattice parameters that vary as a result of variations in composition, and that the identification of phases for the Rietveld refinement was qualitatively incorrect because it included a phase that was not present and did not include phases that might correspond to any of the inclusions shown in the SEM data.

Although the identification of the major phases in this alloy as similar to ζ-(U,Pu) and δ-(UZr_2) is consistent with U-Pu-Zr phase diagrams (Section 2.4.1.2.3) and with phases identified by electron diffraction of a more complex alloy [258], it seems likely that error estimates in phase proportions and lattice parameters in the X-ray diffraction data should be far larger than indicated by either the number of significant digits in data presented here or the error estimates in reference [236]. In particular, the presence and reported properties of γ-U require further experimental confirmation, and detailed interpretation of relatively small variations in phase proportions or lattice parameters should be treated with caution unless confirmed by further analyses.

2.4.4.8.2.2 Phase Transitions

DTA heating and cooling curves from as-cast Alloy AFC2-A4 show two peaks at temperatures between room temperature and ~800°C [236 (Figure 4)]. Shapes of both peaks suggest that each may represent more than one reaction. Burkes et al. deconvoluted the higher-temperature peak based on initial phase-transition estimates from phase-diagram analysis and determined that this peak represents two reactions whose onset temperatures during heating differ by ~38 degrees. The lower-temperature peak has apparently not been deconvoluted.

TMA measurements clearly show one phase transition, and a second is suggested by a small change in slope of the data collected during heating [10]. Onset temperatures from both reactions are higher than those in the deconvoluted DTA data.

Table 54 and Table 55 summarize the available data on phase-transformation temperatures and enthalpies in Alloy AFC2-A4. Although differences between DTA and TMA data suggest that further experimental research is needed to understand phase transitions in this alloy, the deconvoluted DTA data from Burkes et al. [231] are probably the most accurate values available.

Table 54. Phase-transformation temperatures in 40.5U-3Np-30Pu-5Am-1.5RE-20Zr (Alloy AFC2-A4) [10, 236 (Tables 4 and 5, Alloy D)].

Transformation 1		**Transformation 2**		**Transformation 3**			
Heating T (K)	**Cooling T (K)**	**Heating T (K)**	**Cooling T (K)**	**Heating T (K)**	**Cooling T (K)**	**Method**	**Reference**
816±1.4	818±0.1	875±3.6	886±2.4	913±1.1	901±1.4	—	[236]
843	848	923	—	—	—	—	[10]

Table 55. Phase-transformation enthalpies in 40.5U-3Np-30Pu-5Am-1.5RE-20Zr [236 (Tables 4 and 5, Alloy D)].

Transformation 1		**Transformation 2**		**Transformation 3**		
Enthalpy during heating (J/g)	**Enthalpy during cooling (J/g)**	**Enthalpy during heating (J/g)**	**Enthalpy during cooling (J/g)**	**Enthalpy during heating (J/g)**	**Enthalpy during cooling (J/g)**	**Reference**
11.3 ±0.07	-10.7±0.12	7.4±1.27	-7.2±1.14	5.1±0.56	-8.2±1.03	[236]

2.4.4.8.3 Thermal Expansion and Density

2.4.4.8.3.1 Linear Thermal Expansion

The thermal expansion of Alloy AFC2-A4 was measured using a TMA instrument. Curves collected during a single cycle during which the sample was heated and cooled between room temperature and 800°C were similar during heating and cooling [10].

The available data indicate that the thermal expansion of Alloy AFC2-A4 is essentially identical to that of Alloys AFC2-A1, AFC2-A2, AFC2-A3, AFC2-A5, and AFC2-A6 [10 (Figure 54)]. This thermal expansion can be represented by Equation 70 (Section 2.4.2.3.4.1).

2.4.4.8.3.2 Coefficients of Thermal Expansion

The coefficient of linear thermal expansion corresponding to Equation 70 is approximately 1.5×10^{-5}/°C for temperatures between 20 and 550°C. Assuming isotropic thermal expansion, the corresponding coefficient of volumetric thermal expansion is approximately 4.5×10^{-5}/°C. These coefficients are like those of Alloy AFC2-A1 (Section 2.4.2.3.4.2).

2.4.4.8.3.3 Density

Room-temperature densities of as-cast material from two castings of as-cast Alloy AFC2-A4 were determined using dimensional analysis. These densities were 12.97 and 13.40 g/cm^3, with an average value of ~13.2 g/cm^3 [10 (Table 13), 255 (Table 3)]. Volumes and densities at temperatures between 20 and 550°C can be approximated using Equation 6, Equation 7, and Equation 70.

2.4.4.9 U-30Pu-20Zr-3Np-5Am-8RE (Alloy AFC2-A8)

2.4.4.9.1 Introduction

Alloy AFC2-A8 was cast and characterized at Idaho National Laboratory. It is part of a series of related alloys with differing concentrations of uranium and rare-earth elements that was intended to investigate properties of fuels recycled using a pyrochemical process that did not completely remove the rare-earth elements. Other alloys in the series are FCRD Alloys A6 (U-30Pu-20Zr-5Am-3Np, Section 2.4.2.4), A5 (U-30Pu-20Zr-3Np-5Am-1.0RE, Section 2.4.4.7), and A4 (U-30Pu-20Zr-3Np-5Am-1.5RE, Section 2.4.4.8). The concentrations of minor actinides and rare-earth elements in Alloy AFC2-A8 are both higher than the maximum concentrations in the irradiated METAPHIX alloys, and this alloy was not intended for irradiation.

The nominal composition of Alloy AFC2-A8 contains 34 wt% U. 30 wt% Pu, 20 wt% Zr, 3 wt% Np, 5 wt% Am, and 8.0 wt% of a rare-earth alloy consisting of 6 wt% La, 16 wt% Pr, 25 wt% Ce, and 53 wt% Nd (corresponding to 0.48 wt% La, 2 wt% Ce, 1.28 wt% Pr, and 4.24 wt% Pr in the entire alloy). This composition corresponds to 24.8 at% U, 21.7 at% Pu, 38 at% Zr, 2.19 at% Np, 3.6 at% Am, 0.6 at% La, 2.47 at% Ce, 1.57 at% Pr, and 5.09 at% Nd.

No information about the phase transition temperatures and enthalpies, heat capacity, thermal expansion, density, or thermal conductivity of this alloy is available.

2.4.4.9.2 Phases and Phase Transformations

SEM images of microstructures in Alloy AFC2-A8 show an actinide-zirconium matrix surrounding four kinds of inclusions: high-Zr inclusions, high-Si inclusions, high-RE inclusions that also have significant concentrations of Am, and high-RE inclusions that do not have significant concentrations of Am (Figure 89). SEM images and X-ray maps of the matrix show a network consisting of elongated high-RE inclusions and narrow high-U features bounding irregularly shaped polygonal areas of a material that contains numerous small, approximately equant, light-contrast areas. High-Zr inclusions occur in a variety of shapes, and commonly have variations in contrast within a single inclusion. Many RE

inclusions contain both high-Am and low-Am RE materials. High-Si inclusions are far less common than high-Zr or high-RE inclusions and generally occur either surrounded by or at the edges of RE inclusions.

Although individual phases in this alloy have not been identified, it seems plausible that the rare-earth inclusions in Alloy AFC2-A8 are similar to those in AFC2-A7 [266]. If so, the dark rare-earth inclusions in Alloy AFC2-A8 are oxides, which imply the presence of significant concentrations of oxygen during casting.

High-Zr inclusions in a variety of actinide-Zr alloys (including AFC2-A7) are known to have significant concentrations of actinides [267, 268] and it seems possible that contrast variations in the high-Zr inclusions in Alloy AFC2-A8 are related to local differences in actinide concentration. However, in the absence of crystal-structure and microchemical information from these inclusions, this interpretation remains speculative.

Although no TEM data from Alloy AFC2-A8 are available, the SEM data are not consistent with a matrix consisting of highly elongated, parallel domains of δ-(U,Np.Pu,Am)Zr_2 and ζ-(U,Np,Pu,Am) similar to those observed in Alloy AFC2-A7 [258]. The phase-transformation history suggested by U-Pu-Zr phase diagrams [81] indicates that Alloy AFC2-A8 may once have had a much higher proportion of the high-temperature phase η-(U,Pu) than Alloy AFC2-A7 did. Ellinger et al. believed they could distinguish between ζ-(U,Pu) formed from γ-(U,Pu-Zr) and ζ-(U,Pu) formed from η-(U,Pu) [192]. Although they did not provide details, it seems plausible that differences in matrix microstructures in Alloys AFC2-A7 and AFC2-A8 result from differences in the transformations leading to formation of ζ-(U,Pu) rather than to different matrix phases in the room-temperature alloys. However, further investigation is clearly required.

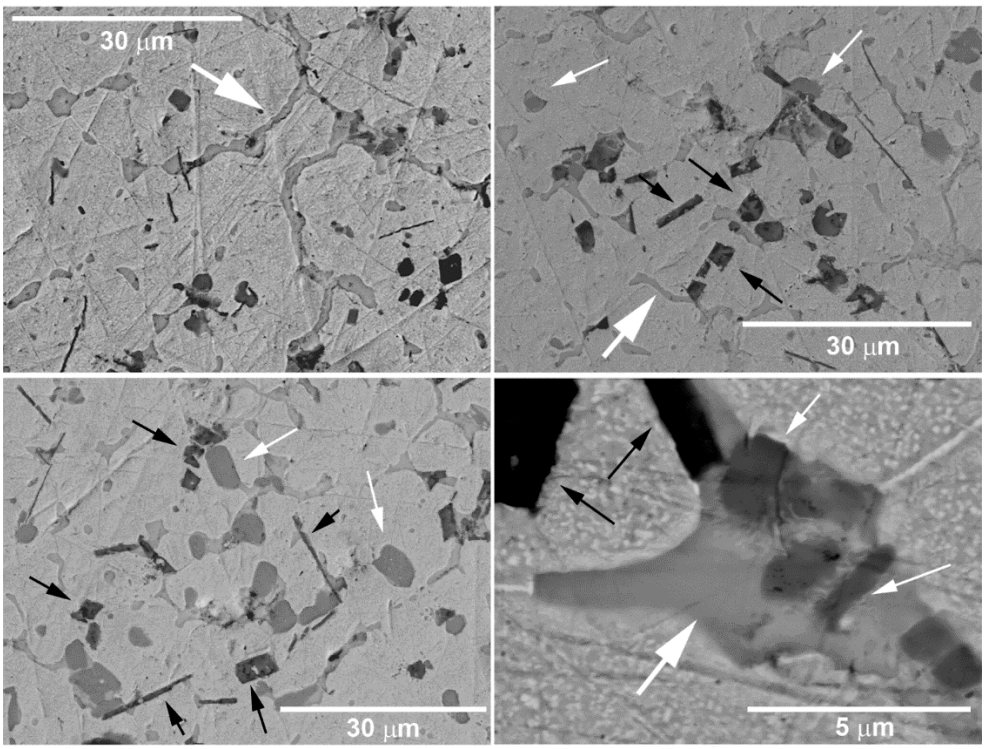

Figure 89. SEM images of Alloy AFC2-A8. Large white arrows indicate examples of high-Am RE inclusions, small white arrows indicate examples of low-Am RE inclusions, and black arrows indicate high-Zr inclusions. Note variations in high-Zr inclusion indicated by black arrows in parts b and c. Also note small bright spots in matrix and polygonal boundaries in upper right and center left of Part d.

2.4.5 U-Pu-Zr Alloys with Minor Actinides (Np, Am, Cm), Rare-Earth Elements (La, Ce, Pr, Nd, and Y

2.4.5.1 U-19Pu-10Zr-3Np-2Am-1.2Ce-3.6Nd-0.2Y (METAPHIX Alloy CR12)

2.4.5.1.1 Introduction

Alloy CR12 was cast by the METAPHIX Programme as part of a study intended to examine effects of rare-earth elements in U-Pu-Zr fuel alloys that also contain minor actinides. The nominal composition of this alloy consists of composition has 61.0 wt% U, 3.0 wt% Np, 19.0 wt% Pu, 2.0 wt% Am, 1.2 wt% Ce, 3.6 wt% Nd, and 10.0 wt% Zr [149], (corresponding to approximately 51.1 at% U, 15.8 at% Pu, 21.8 at% Zr, 2.5 at% Np, 1.65 at% Am, 1.7 at% Ce, 5 at% Nd, and 0.5 at% Y). Proportions of elements in Alloy CR12 are similar to those in METAPHIX Alloy U-19Pu-10Zr-5MA-5RE (Section 2.4.5.3), which also includes low concentrations of Cm, Gd, and Y.

Ohta et al. studied phases and phase transitions in this alloy using metallography, dilatometry, and microprobe analysis [149]. Kurata et al. also studied this alloy, but used samples held in thermal gradients to investigate element migration [218]. Although direct comparisons are difficult because of changes in local composition as a result of element migration in Kurata's samples, both research groups reached similar conclusions.

No information about the heat capacity or thermal conductivity of this alloy is available.

2.4.5.1.2 Phases and Phase Transformations

2.4.5.1.2.1 Phases

Information on phases in as-cast Alloy CR12 is limited. Ohta et al. [149] reported that an arc-melted sample of this alloy did not form high-RE and low-RE regions like those in alloys CR6 and CR10, but instead had RE- and Am-rich precipitates distributed uniformly in a U-Pu-Zr-Np matrix. Sari et al. reported similar microstructures in their as-cast samples and indicated that most of the Np was in the matrix [269].

Quenched samples of Alloy CR12 that had been annealed at 773 K for 28 or 97 hours or at 873 K for an unspecified time between 3.5 and 100 hours had two-phase matrices. Microprobe analyses showed that one of these phases had ~40-50 wt% U, ~22% Pu, and ~25-30% Zr, as well as ~2.5-3.5% Np and 1% Am, and the other had ~75% U, 4% Np, 17-19% Pu, 2-3% Zr, and 0.1-0.3% Am. Analyses from both phases showed low concentrations (≤ 0.5 wt%) of Ce and Nd [149 (Table 2)].

Quenched samples that had been annealed at 923K for 3.5 or 100 hours or at 1123 K for an unspecified time between 3.5 and 100 hours had a single matrix phase. Microprobe analyses showed that this phase had ~66.5% U, 20% Pu, 3.7% Np, 0.4% Am, 9% Zr, and ≤ 0.3% Ce and Nd [149 (Table 2)].

The annealed samples had RE inclusions ≥ 10 μm across, which were dispersed almost homogeneously in samples annealed at 773 and 873 K. Although the RE inclusions occurred at grain boundaries in samples annealed at 973 and 1123 K, Ohta et al. described their distribution as "homogeneously dispersed" [149]. Microprobe analyses of inclusions in the annealed samples showed compositions of ~ 8% Pu, 18-25% Ce, and 50-60% Nd, with low concentrations (≤ 0.5) of U, Np, and Zr. Concentrations of Am in the RE inclusions were ~19-23% in samples annealed at 723 K, but decreased to ~5% in the sample annealed at 1123 K [149, Table 2]. Ohta et al. suggested this decrease in the concentration of Am might represent Am lost due to from evaporation during annealing [149].

Ohta et al. presumed that matrix phases in the sample annealed at 773 K were similar to ζ-(U,Pu) and δ-UZr_2, and matrix phases in the sample annealed at 873 K were similar to ζ-(U,Pu) and either δ-UZr_2 or γ-(U,Pu,Zr). The single matrix phase in samples annealed at 923 K or 1123 K was presumed to be γ-(U,Pu,Zr). These phase identifications were apparently based on analysis of phase diagrams and comparison to phases identified in other publications rather than on crystallographic data and should not be interpreted as experimental results.

2.4.5.1.2.2 Phase Transitions

Dilatometry measurements by Ohta et al. indicated that Alloy CR12 has solid-state phase transitions at ~853 and 903 K and melts at 1480 +/- 10 K [149]. These transition temperatures are similar to those in METAPHIX Alloys CR11 (Section 2.4.4.1) and CR13 (71.0U-19.0Pu-10.0 Zr, Section 2.4.1.2.1 [149]), and are consistent with inferred phase transitions based on changes in composition in the thermal-gradient research of Kurata et al. [218].

2.4.5.1.3 Thermal Expansion and Density

The only available data on thermal expansion of Alloy CR12 is a single dilatometric curve that does not have a quantitative thermal-expansion axis [149 Figure 4]. This curve shows changes in slope at approximately 853 and 903 K, which were attributed to specific reactions based on phase diagrams and comparison to other alloys. Although other changes in slope are visible in the dilatometric curve between 853 and 903 K, no further information is available about these changes.

2.4.5.2 U-19Pu-10Zr-1.2Np-0.6Am-0.2Cm-1.4Nd-0.2Ce-0.2Gd-0.2Y (METAPHIX Alloy U-19Pu-10Zr-2MA-2RE)

2.4.5.2.1 Introduction

Alloy U-19Pu-10Zr-2MA-2RE (sometimes called UPuZrMA2%RE2%) was fabricated by the METAPHIX Programme as part of an experiment to study behavior of minor actinides and rare-earth elements in U-Pu-Zr fuel alloys during irradiation. The alloy was fabricated by a series of steps involving mixing powdered materials and arc melting of the starting materials, then cast in heated yttria molds [261, 262].

The average actual composition of Alloy U-19Pu-10Zr-2MA-2RE is 66.85% U, 19.80% Pu, 9.46% Zr, 1.23% Np, 0.67% Am, 0.18% Cm, 0.20% Ce, 1.25% Nd, 0.16% Gd and 0.12% Y by weight [260, 263], corresponding to approximately 57.5% U, 19.95% Pu, 21.26% Zr, 1.06% Np, 0.57% Am, 0.15% Cm, 0.29% Ce, 1.78% Nd, 0.21% Gd and 0.28% Y in atomic percent). The composition of this alloy is similar to METAPHIX Alloy CR11 (Section 2.4.4.1), which was not intended for irradiation.

Alloy U-19Pu-10Zr-2MA-2RE has been irradiated to peak target burnups of ~1.5, 7, and 10 at% fissions per initial metal atom (FIMA) in the Phénix fast reactor. Publications with details of the irradiation experiments and PIE results include [149, 260, 262, 263].

No information about the heat capacity or thermal expansion of this alloy is available.

2.4.5.2.2 Phases and Phase Transformations

Capriotti et al. tentatively identified a phase similar to z-(U,Pu) in as-cast Alloy U-19Pu-10Zr-2MA-2RE based on preliminary analysis of X-ray diffraction data [270]. No other information about phases or phase transformations in un-irradiated samples of this alloy is available. However, because of the similarity in compositions to Alloy CR11 (Section 2.4.4.1), it seems likely that properties of Alloy CR11 are similar to those of Alloy U-19Pu-10Zr-2MA-2RE.

2.4.5.2.3 Thermal Expansion and Density

The average density of as-cast Alloy U-19Pu10Zr-2MA-2RE is ~14.73 g/cm^3 [149]. No other information about thermal expansion and related properties of this alloy is available.

2.4.5.3 U-19Pu-10Zr-3Np-1.6Am-0.4Cm-0.5Ce-3.5Nd-0.5Gd-0.5Y (METAPHIX Alloy U-19Pu-10Zr-5MA-5RE)

Alloy U-19Pu-10Zr-5MA-5RE (sometimes called UPuZrMA5%RE5%) was fabricated and irradiated by the METAPHIX Programme as part of an experiment to study behavior of minor actinides and rare-earth elements in U-Pu-Zr fuel alloys during irradiation. This alloy was fabricated by a series of steps involving mixing and arc melting powdered starting materials, and was then then cast in heated yttria molds [261, 262].

The average actual composition of Alloy U-19Pu-10Zr-5MA-5RE is 63.5% U, 3.04% Np, 19.75% Pu, 1.52% Am, 0.31% Cm, 0.45% Ce, 2.3% Nd, 0.32% Gd, 0.31% Y, and 8.19% Zr by weight [260] (corresponding to approximately 55.40% U, 2.65% Np, 17.09% Pu, 1.3% Am, 0.26% Cm, 0.72% Y, 18.61% Zr, 0.66% Ce, and 3.3% Nd in atomic percent). The composition of Alloy U-19Pu-10Zr-5MA-5RE is similar to METAPHIX Alloy CR12 (Section 2.4.5.1), which was not intended for irradiation.

Alloy U-19Pu10Zr-5MA-5RE has been irradiated to peak target burnups of ~1.5, 7, and 10 at% fissions per initial metal atom (FIMA) in the Phénix fast reactor. Publications with details of the irradiation experiments and PIE results include [149, 260, 262, 263].

The only available information about phases, heat capacity, thermal expansion, or thermal conductivity of this alloy is the room-temperature density of the as-cast material (~14.67 g/cm^3, [149]). However, because of the similarity in compositions to Alloy CR12 (Section 2.4.5.1), it seems likely that properties of Alloy U-19Pu10Zr-5MA5RE are similar to those of Alloy CR12.

3. REFERENCES

[1] D.E. Janney, C.A. Papesch, FCRD Transmutation Fuels Handbook 2015 (Idaho National Laboratory Report INL/EXT-15-36520 revision 0), Idaho Falls, ID, 2015.

[2] D.E. Janney, C.A. Papesch, S.C. Middlemas, FCRD Advanced Reactor (Transmutation) Fuels Handbook (Idaho National Laboratory Report INL/EXT-15-36520 revision 1), Idaho Falls, ID, 2016.

[3] D.E. Janney, Metallic Fuels Handbook, Part 1: Alloys based on U-Zr, Pu-Zr, U-Pu, or U-Pu-Zr, including those with minor actinides (Np, Am, Cm), rare-earth elements (La, Ce, Pr, Nd, Gd), and Y (Idaho National Laboratory Report INL/EXT-15-36520 rev 2 part 1), Idaho Falls, ID, 2017.

[4] D.E. Janney, Metallic Fuels Handbook, Part 2: Elements and Alloys not Based on U-Zr, Pu-Zr, U-Pu, or U-Pu-Zr (Idaho National Laboratory Report INL/EXT-15-36520 Revision 2 Part 2), Idaho Falls, ID, 2017.

[5] D.E. Janney, Metallic Fuels Handbook, Part 2: Elements and Alloys not Based on U-Zr, Pu-Zr, U-Pu, or U-Pu-Zr (Idaho National Laboratory Report INL/EXT-15-36520 Revision 3 Part 2), Idaho Falls, ID, 2018.

[6] W.M. Haynes, ed., Conversion factors, in: CRC Handbook of Chemistry and Physics, 96th Edition (Internet Version 2016), CRC Press/Taylor and Francis, Boca Raton, FL, 2016.

[7] W.L. Bragg, E.A. Wood, The conversion factor for kX units to Ångstrom units, Journal of the American Chemical Society, 69 (1947) 2919.

[8] F. Foote, E.R. Jette, The fundamental relation between lattice constants and density, Physical Review, 58 (1940) 81-86.

[9] P. Hirsch, A. Howie, R. Nicholson, D.W. Pashley, M.J. Whelan, Electron Microscopy of Thin Crystals, Robert E. Krieger Publishing Co., Inc., Malabar, FL, 1977.

[10] T.A. Hyde, Fabrication and Pre-irradiation Characterization of a Minor Actinide and Rare Earth Containing Fast Reactor Fuel Experiment for Irradiation in the Advanced Test Reactor, 2012.

[11] T. Tsuji, Heat Capacity of Solids, in: S.L. Chaplot, R. Mittal, N. Choudhury (Eds.) Thermodynamic Properties of Solids: Experiment and Modeling, WILEY-VCH Verlag GmbH & Co. KGaA, Weinheim, Germany, 2010, pp. 159-196.

[12] G.S. Kumar, G. Prasad, R.O. Pohl, Experimental determinations of the Lorenz number, Journal of Materials Science, 28 (1993) 4261-4272.

[13] C.Y. Ho, R.W. Powell, P.E. Liley, Thermal conductivity of the elements: a comprehensive review, Journal of Physical and Chemical Reference Data, 3 (1974) 1-1 to 1-796.

[14] L. Binkele, Transport properties of yttrium and six rare-earth metals in the temperature range 300-1000 K, High Temperatures-High Pressures, 21 (1989) 131-137.

[15] K.A. Gschneidner Jr., Physical Properties of the Rare Earth Metals, in: W.M. Haynes (Ed.) CRC Handbook of Chemistry and Physics, 96th Edition (Internet Version 2016), CRC Press/Taylor and Francis, Boca Raton, FL, 2015.

[16] S.M. McDeavitt, A.A. Solomon, Preparation and performance of U-10Zr alloy nuclear fuel using powder metallurgy techniques, in: J.M. Capus (Ed.) Advances in Powder Metallurgy, Metal Powder Industries Federation : American Powder Metallurgy Institute, 1992, pp. 109-123.

[17] S.M. McDeavitt, A.A. Solomon, Hot-isostatic pressing of U-10Zr by a coupled grain boundary diffusion and creep cavitation mechanism, Journal of Nuclear Materials, 228 (1996) 184-200.

[18] Y. Xiong, P. Zhang, W. Jing, J. Ba, G. Zhang, Characterization of U-10%Zr alloy powders by a hydriding-dehydriding process, Rare Metal Materials and Engineering, 43 (2014) 2792-2795.

[19] A.M. Adamska, R. Springell, A.D. Warren, L. Picco, O. Payton, T.B. Scott, Growth and characterization of uranium-zirconium alloy thin films for nuclear industry applications, Journal of Physics D - Applied Physics, 47 (2014) 315301.

[20] D.E. Janney, S.L. Hayes, Experimentally known properties of U-10Zr alloys: a critical review, Nuclear Technology, 203 (2018) 109-126.

[21] R.I. Sheldon, D.E. Peterson, The U-Zr (uranium-zirconium) system, Bulletin of Alloy Phase Diagrams, 10 (1989) 165-171 and 205-206.

[22] R.I. Sheldon, D.E. Peterson, U-Zr (uranium-zirconium), in: T.B. Massalski (Ed.) Binary Alloy Phase Diagrams, II ed., 1990, pp. 3520-3523.

[23] J.T. McKeown, S. Irukuvarghula, S. Ahn, M.A. Wall, L.L. Hsiung, S. McDeavitt, P.E.A. Turchi, Coexistence of the α and δ phases in an as-cast uranium-rich U-Zr alloy, Journal of Nuclear Materials, 436 (2013) 100-104.

[24] Y. Zhang, X. Wang, G. Zeng, H. Wang, J. Jia, L. Sheng, P. Zhang, Microstructural investigation of as-cast uranium rich U-Zr alloys, Journal of Nuclear Materials, 471 (2016) 59-64.

[25] S.T. Zegler, The uranium-rich end of the uranium-zirconium system (Argonne National Laboratory Report ANL-6055), Argonne National Laboratory, Argonne, IL, 1962.

[26] C.B. Basak, Microstructural evolution of U-rich U-Zr alloys under near-equilibrium condition, Journal of Nuclear Materials, 416 (2011) 280-287.

[27] C.B. Basak, S. Neogy, D. Srivastava, G.K. Dey, S. Banerjee, Disordered BCC γ-phase to δ-phase transformation in Zr-rich U-Zr alloy, Philosophical Magazine, 91 (2011) 3290-3306.

[28] C.B. Basak, N. Prabhu, M. Krishnan, On the formation mechanism of UZr_2 phase, Intermetallics, 18 (2010) 1707-1712.

[29] S. Ahn, S. Irukuvarghula, S.M. McDeavitt, Thermophysical investigations of the uranium–zirconium alloy system, Journal of Alloys and Compounds, 611 (2014) 355-362.

[30] G.L. Hofman, S.L. Hayes, M.C. Petri, Temperature gradient driven constituent redistribution in U-Zr alloys, Journal of Nuclear Materials, 227 (1996) 277-286.

[31] T. Ogawa, T. Iwai, M. Kurata, Demixing of U-Zr alloys under a thermal-gradient, Journal of the Less-Common Metals, 175 (1991) 59-69.

[32] M. Paukov, I. Tkach, F. Huber, T. Gouder, M. Cieslar, D. Drozdenko, P. Minarik, L. Havela, U-Zr alloy: XPS and TEM study of surface passivation, Applied Surface Science, 441 (2018) 113-119.

[33] R. Mariani, L. Squires, T. Hartmann, D. Janney, S. Taylor, T. O'Holleran, J.R. Kennedy, Behavior of zirconium on passivated U-Zr based fuel alloys, in: 11th International Exchange Meeting on Partitioning and Transmutation (November 1-5, 2005), San Francisco, CA, 2005.

[34] M. Kurata, Thermodynamic database on U-Pu-Zr-Np-Am-Fe alloy system I - Re-evaluation of U-Pu-Zr alloy, IOP Conference Series: Materials Science and Engineering, 9 (Actinides 2009) (2010) 1-8.

[35] J. Belak, J.l. Fattebert, A. Landa, P. Söderlind, L. Zepeda-Ruiz, P. Turchi, Modeling UZr metallic fuels: coupling thermodynamics with microstructure, Transactions of the American Nuclear Society, 102 (2010) 841-842.

[36] P.Y. Chevalier, E. Fischer, B. Cheynet, Progress in the thermodynamic modelling of the O-U-Zr ternary system, CALPHAD: Computer Coupling Phase Diagrams and Thermochemistry, 28 (2004) 15-40.

[37] M. Kurata, T. Ogata, K. Nakamura, T. Ogawa, Thermodynamic assessment of the Fe-U, U-Zr, and Fe-U-Zr systems, Journal of Alloys and Compounds, 271/273 (1998) 636-640.

[38] M. Kurata, Phase diagrams of actinide alloys, in: R.J.M. Konings (Ed.) Comprehensive Nuclear Materials, volume 2, Elsevier, 2012, pp. 139-195.

[39] A. Landa, P. Söderlind, B. Grabowski, P.E.A. Turchi, A.V. Ruban, L. Vitos, Ab Initio Study of Advanced Metallic Nuclear Fuels for Fast Breeder Reactors, Actinides and Nuclear Energy Materials, 1444 (2012) 67-78.

[40] A. Landa, P. Söderlind, P.E.A. Turchi, Density-functional study of the U-Zr system, Journal of Alloys and Compounds, 478 (2009) 103-110.

[41] A. Landa, P. Söderlind, P.E.A. Turchi, Density-functional study of U-Mo and U-Zr alloys, Journal of Nuclear Materials, 414 (2011) 132-137.

[42] L. Leibowitz, E. Veleckis, R.A. Blomquist, A.D. Pelton, Solidus and liquidus temperatures in the uranium-plutonium-zirconium system, Journal of Nuclear Materials, 154 (1988) 145-153.

[43] L. Leibowitz, R.A. Blomquist, A.D. Pelton, Thermodynamics of the uranium-zirconium system, Journal of Nuclear Materials, 167 (1989) 76-81.

[44] T. Ogawa, J.K. Gibson, R.G. Haire, M.M. Gensini, M. Akabori, Thermodynamic analysis of Zr-U and Zr-Np alloys in view of f-d interaction, Journal of Nuclear Materials, 223 (1995) 67-71.

[45] T. Ogawa, T. Iwai, Thermochemical modelling of U-Zr alloys, Journal of the Less-Common Metals, 170 (1991) 101-108.

[46] W. Xiong, W. Xie, C. Shen, D. Morgan, Thermodynamic modeling of the U-Zr system -- a revisit, Journal of Nuclear Materials, 443 (2013).

[47] A.P. Moore, B. Beeler, C. Deo, M.I. Baskes, M.A. Okuniewski, Atomistic modeling of high temperature uranium-zirconium alloy structure and thermodynamics, Journal of Nuclear Materials, 467 Part 2 (2015) 802-819.

[48] T. Ogata, Metal Fuel, in: R.J.M. Konings (Ed.) Comprehensive Nuclear Materials, volume 3, Elsevier, 2012, pp. 1-40.

[49] T. Ogata, Irradiation behavior and thermodynamic properties of metallic fuel, Journal of Nuclear Science and Technology, 39 Supplement 3 (2002) 675-681.

[50] A.P. Moore, C. Deo, M.I. Baskes, M.A. Okuniewski, Atomistic mechanisms of morphological evolution and segregation in U-Zr alloys, Acta Materialia, 115 (2016) 178-188.

[51] W. Xie, C.A. Marianetti, D. Morgan, Response to letter Electron correlation and relativity of the 5*f* electrons in the U-Zr alloy system, Journal of Nuclear Materials, 476 (2016) 110-112.

[52] P.S. Ghosh, A. Arya, G.K. Dey, Ab-initio study of high temperature lattice dynamics of BCC zirconium (β-Zr) and uranium (γ-U), AIP Conference Proceedings, 1591 (2014) 1062-1064.

[53] P. Söderlind, B. Sadigh, V. Lordi, A. Landa, P.E.A. Turchi, Electron correlation and relativity of the 5f electrons in the U–Zr alloy system, Journal of Nuclear Materials, 444 (2014) 356-358.

[54] W. Xie, W. Xiong, C.A. Marianetti, D. Morgan, Correlation and relativistic effects in U metal and U-Zr alloy: validation of *ab initio* approaches, Physical Review B, 88 (2013) 235128.

[55] A. Landa, P. Söderlind, P.E.A. Turchi, L. Vitos, A. Ruban, Density-functional study of Zr-based actinide alloys: 2. U-Pu-Zr system, Journal of Nuclear Materials, 393 (2009) 141-145.

[56] A. Landa, P. Söderlind, P.E.A. Turchi, L. Vitos, A. Ruban, Density-functional study of Zr-based actinide alloys, Journal of Nuclear Materials, 385 (2009) 68-71.

[57] C.-B. Zhang, X.-P. Li, W.-D. Li, P. Zhang, W. Yin, F. Wang, B.-T. Wang, Structural, electronic, and elastic properties of equiatomic UZr alloys from first-principles, Journal of Nuclear Materials, 496 (2017) 333-342.

[58] M. Krupska, N.-T.H. Kim-Ngan, S. Sowa, M. Paukov, I. Tkach, D. Drozdenko, L. Havela, Z. Tarnawski, Structure, Electrical Resistivity and Superconductivity of Low-alloyed γ-U phase retained to low temperatures by means of rapid cooling, Acta Metallurgica Sinica (English Letters), 29 (2016) 388-398.

[59] S. Sowa, N.-T.H. Kim-Ngan, M. Krupska, M. Paukov, I. Tkach, L. Havela, Superconductivity in U-T alloys (T = Mo, Pt, Nb, Zr) stabilized in the cubic γ-U structure, Acta Physica Polonica A, 130 (2016) 521-526.

[60] H.A. Saller, R.F. Dickerson, W.E. Murr, Uranium alloys for high-temperature application (Battelle Memorial Institute Report BMI-1098), Battelle Memorial Institute, Columbus, OH, 1956.

[61] Y.S. Touloukian, R.K. Kirby, R.E. Taylor, P.D. Desai, Thermal Expansion: Metallic elements and alloys (Thermophysical Properties of Matter vol. 12), IFI/Plenum, New York, 1975.

[62] C. Basak, G.J. Prasad, H.S. Kamath, N. Prabhu, An evaluation of the properties of as-cast U-rich U-Zr alloys, Journal of Alloys and Compounds, 480 (2009) 857-962.

[63] S. Kaity, J. Banerjee, M.R. Nair, K. Ravi, S. Dash, T.R.G. Kutty, A. Kumar, R.P. Singh, Microstructural and thermophysical properties of U-6 wt.%Zr alloy for fast reactor application, Journal of Nuclear Materials, 427 (2012) 1-11.

[64] S. Kaity, J. Banerjee, S.C. Parida, V. Bhasin, Structural, microstructural and thermal analysis of U-(6-*x*)Zr-*x*Nb alloys (*x* = 0, 2, 4, 6), Journal of Nuclear Materials, 504 (2018) 234-250.

[65] A.C. Bagchi, G.J. Prasad, K.B. Khan, A study on zirconium-rich uranium-zirconium alloys, Transactions of the Indian Institute of Metals, 67 (2014) 123-130.

[66] Y. Takahashi, M. Yamawaki, K. Yamamoto, Thermophysical properties of uranium-zirconium alloys, Journal of Nuclear Materials, 154 (1988) 141-144.

[67] Y. Park, R. Newell, A. Mehta, D.D. Keiser Jr., Y.H. Sohn, Interdiffusion and reaction between U and Zr, Journal of Nuclear Materials, 502 (2018) 42-50.

[68] S. Irukuvarghula, B. Blamer, S. Ahn, S.C. Vogel, A.S. Losko, S.M. McDeavitt, Texture evolution during annealing of hot extruded U-10wt% Zr alloy by in situ neutron diffraction, Journal of Nuclear Materials, 497 (2017) 10-15.

[69] H. Okamoto, Oxygen-uranium binary phase diagram (1990 Okamoto H), in: P. Villars, H. Okamoto, K. Cenzual (Eds.) ASM Alloy Phase Diagrams Database (https://madatada.asminternational.org/apd/index.aspx), consulted May 30, 2018, ASM International, Materials Park, OH, 2016.

[70] A.A. Bauer, ed., An evaluation of the properties and behavior of zirconium-uranium alloys (Battelle Memorial Institute Report BMI-1350), Battelle Memorial Institute, Columbus, OH, 1959.

[71] K. Ghoshal, S. Kaity, S. Mishra, A. Kumar, Microstructural investigation of uranium-rich U-Zr-Nb ternary alloy system, Journal of Nuclear Materials, 446 (2014) 217-223.

[72] S. Mukherjee, S. Kaity, M.T. Saify, S.K. Jha, P.K. Pujari, Evidence of zirconium nano-agglomeration in as-cast dilute U–Zr alloys, Journal of Nuclear Materials, 452 (2014) 1-5.

[73] T.R.G. Kutty, S. Kaity, C.B. Basak, A. Kumar, R.P. Singh, Creep behaviour of U-6%Zr alloy by impression creep technique, Nuclear Engineering and Design, 250 (2012) 125-133.

[74] S. Irukuvarghula, S. Ahn, S.M. McDeavitt, Decomposition of the γ phase in as-cast and quenched U-Zr alloys, Journal of Nuclear Materials, 473 (2016) 206-217.

[75] A.K. Rai, R. Subramanian, R.N. Hajra, H. Tripathy, M. Rengachari, S. Saibaba, Calorimetric study of phase stability and phase transformation in U-*x*Zr (*x* = 2, 5, 10 wt pct) alloys, Metallurgical and Materials Transactions A, 46 (2015) 4986-5001.

[76] C.B. Basak, R. Keswani, G.J. Prasad, H.S. Kamath, N. Prabhu, Phase transformations in U-2 wt% Zr alloy, Journal of Alloys and Compounds, 471 (2009) 544-552.

[77] M.H. Mueller, J.W. Richardson Jr., R.V. Strain, G.L. Hofman, Phase analysis of metallic plutonium-containing fuel alloys using neutron diffraction, in: C.S. Barrett, J.V. Gilfrich, I.C. Noyan, T.C. Huang, P.K. Predecki (Eds.) Advances in X-ray analysis, Plenum, Steamboat Springs, CO, 1991, pp. 447-457.

[78] M.H. Mueller, J.W. Richardson Jr., R.V. Strain, G.L. Hofman, Phase analysis of metallic plutonium-containing fuel alloys using neutron diffraction, in: 36th Annual Denver X-Ray Conference on Applications of X-ray Analysis, Steamboat Springs, CO, 1990.

[79] G. Xie, J. Yang, B. Zhang, W. Li, Study of phases in U-lowt% Zr alloy by neutron diffraction, Acta Metallurgica Sinica Series A, Physical Metallurgy & Materials Science, 8 (1995) 174-180.

[80] J.F. Duffey, C.A. Bruch, Delta phase field of the U-Zr equilibrium diagram, Transactions of the Metallurgical Society of AIME, 212 (1958) 17-19.

[81] D.R. O'Boyle, A.E. Dwight, The uranium-plutonium-zirconium ternary alloy system, in: W.N. Miner (Ed.) Plutonium 1970 and Other Actinides, Metallurgical Society of AIME, 1970, pp. 720-732.

[82] J. Donohue, H. Einspahr, The structure of β-uranium, Acta Crystallographica, B27 (1971) 1740-1743.

[83] A.C. Lawson, C.E. Olsen, J.W. Richardson Jr., M.H. Mueller, G.H. Lander, Structure of β-uranium, Acta Crystallographica, B44 (1988) 89-96.

[84] J.G. Huber, P.H. Ansari, The superconductivity of BCC U-Zr alloys, Physica, 135B (1985) 441-444.

[85] E. Epremian, Uranium alloy newsletter (Division of Research, AEC, report WASH-298(Del.), (1956).

[86] F.A. Rough, Physical properties and transformation studies, in: E. Epremian (Ed.) Uranium Alloy Newsletter (Division of Research, AEC, Report WASH-298(Del.), 1956, pp. 14-16.

[87] C.L. Komar Varela, L.M. Gribaudo, R.O. González, S.F. Aricó, Transformation behavior of the γU(Zr,Np) phase under continuous cooling conditions, Journal of Nuclear Materials, 453 (2014) 124-130.

[88] M. Akabori, A. Itoh, T. Ogawa, F. Kobayashi, Y. Suzuki, Stability and structure of the δ phase of the U-Zr alloys, Journal of Nuclear Materials, 188 (1992) 249-254.

[89] A.N. Holden, W.E. Seymour, Intermediate phase in the uranium-zirconium system, Journal of Metals, 8 (1956) 1312-1316.

[90] D. Summers-Smith, The constitution of uranium-zirconium alloys, Journal of the Institute of Metals, 83 (1954-1955) 277-282.

[91] F.A. Rough, A.A. Bauer, Constitution of uranium and thorium alloys (Battelle Memorial Institute Report BMI-1300), Battelle Memorial Institute, Columbus, OH, 1958.

[92] M.H. Mueller, The δ phase found in the U-Zr alloys, Acta Crystallographica, 8 (1955) 849-850.

[93] J.M. Silcock, Intermediate phase in the uranium-zirconium system by A.N. Holden and W.E. Seymour, Journal of Metals (Transactions AIME), 209 (1957) 521.

[94] E.R. Boyko, The structure of the δ phase in the uranium-zirconium system, Acta Crystallographica, 10 (1957) 712-713.

[95] M. Akabori, T. Ogawa, A. Itoh, Y. Morii, The lattice stability and structure of δ-UZr_2 at elevated temperatures, Journal of Physics: Condensed Matter, 7 (1995) 8249-8257.

[96] C. Basak, R. Keswani, G.J. Prasad, H.S. Kamath, N. Prabhu, S. Banerjee, Investigation on the martensitic transformation and the associated intermediate phase in U-2 wt%Zr alloy, Journal of Nuclear Materials, 393 (2009) 146-152.

[97] B.A. Hatt, The orientation relationship between the gamma and alpha structures in uranium-zirconium alloys, Journal of Nuclear Materials, 19 (1966) 131-141.

[98] J. Lehmann, R.F. Hills, Nomenclature proposee pour les phases des alliages d'uranium (Proposed nomenclature for phases in uranium alloys), Journal of Nuclear Materials, 2 (1960) 261-268 (in French and English).

[99] R.F. Hills, B.R. Butcher, B.W. Howlett, D. Stewart, The effect of cooling rate on the decomposition of the γ-phase in uranium-zirconium alloys, Journal of Nuclear Materials, 16 (1965) 25-38.

[100] G. Lagerberg, Phase transformations in a uranium-zirconium alloy containing 2 weight percent zirconium, Journal of Nuclear Materials, 9 (1963) 261-276.

[101] S. Irukuvarghula, S.M. McDeavitt, Formation mechanism of delta phase in the as-cast U-10 wt% Zr alloy, Transactions of the American Nuclear Society, 109 (2013) 612-615.

[102] K.-H. Kim, S.J. Oh, S. Kim, C. Lee, C. Lee, Microstructural characterization of U-Zr alloy fuel slugs for sodium-cooled fast reactor, Surface and Interface Analysis, 44 (2012) 1515-1518.

[103] F.A. Rough, An evaluation of data on zirconium-uranium alloys (Battelle Memorial Institute Report BMI-1030), Battelle Memorial Institute, Columbus, OH, 1955.

[104] M. Kanno, M. Yamawaki, T. Koyama, N. Morioka, Thermodynamic activity measurements of U-Zr alloys by Knudsen effusion mass spectrometry, Journal of Nuclear Materials, 154 (1988) 154-160.

[105] A. Maeda, Y. Suzuki, T. Ohmichi, Uranium activity of uranium-rich U-Zr alloys by Knudsen effusion mass spectrometry, Journal of Alloys and Compounds, 179 (1992) L21-L24.

[106] S. Balakrishnan, K. Ananthasivan, K.C. Hari Kumar, Measurement of the solidus and liquidus in the U-Zr system by the spot-technique, Journal of Alloys and Compounds, 689 (2016) 751-758.

[107] Reference points on the ITS-90 temperature scale, in: W.M. Haynes (Ed.) CRC Handbook of Chemistry and Physics, 97th Edition (Internet Version 2017), CRC Press/Taylor and Francis, Boca Raton, FL, 2017.

[108] H.A. Saller, F.A. Rough, A.A. Bauer, J.R. Doig, Constitution of delta-phase alloys of system U-Zr-Ti, Journal of Metals, 9 (1957) 878-881.

[109] B.-H. Lee, J.S. Cheon, Y.-H. Koo, J.-Y. Oh, J.-S. Yim, D.-S. Sohn, M. Baryshnikov, A. Gaiduchenko, Measurement of the specific heat of Zr-40wt% U metallic fuel, Journal of Nuclear Materials, 360 (2007) 315-320.

[110] T. Matsui, T. Natsume, K. Naito, Heat capacity measurements of $U_{0.80}Zr_{0.20}$ and $U_{0.80}Mo_{0.20}$ alloys from room temperature to 1300K, Journal of Nuclear Materials, 167 (1989) 152-159.

[111] S. Dash, K. Ghoshal, T.R.G. Kutty, Thermodynamic investigations of uranium-rich binary and ternary alloys, Journal of Thermal Analysis and Calorimetry, 112 (2013) 179-185.

[112] Y. Takahashi, K. Yamamoto, T. Ohsato, H. Shimada, T. Terai, M. Yamawaki, Heat capacities of uranium-zirconium alloys from 300 to 1100 K, Journal of Nuclear Materials, 167 (1989) 147-151.

[113] A. Virot, Caracteristiques de l'alliage uranium-zirconium a 6 % en poids de zirconium, Journal of Nuclear Materials, 5 (1962) 106-119 (in French with English abstract).

[114] G.B. Fedorov, E.A. Smirnov, Heat capacity of uranium-zirconium systems, Soviet Journal of Atomic Energy, 25 (1968) 795-797 (translated from Atomnaya Énergiya vol 725 no. 791 pp. 754-756, July 1968).

[115] A.B. Gaiduchenko, Thermophysical properties of irradiated uranium-zirconium fuel, Atomic Energy, 104 (2008) 5-10 (translated from Atomnaya Énergiya, vol 108, no 101, pp. 106-109, 2008).

[116] Y. Takahashi, K. Yamamoto, T. Ohsato, T. Terai, M. Yamawaki, Heat-capacities of uranium-zirconium alloys from 300-K to 1100-K, Journal of Metals, 40 (1988) A73.

[117] S. Ahn, S.M. McDeavitt, Transformation Enthalpies of Uranium-Zirconium Alloy System, Transactions of the American Nuclear Society, 106 (2012) 239-241.

[118] P. Chiotti, V.V. Akhachinskij, I. Ansara, M.H. Rand, The Chemical Thermodynamics of Actinide Elements and Compounds, Part 5: The actinide binary alloys, IAEA, Vienna, Austria, 1981.

[119] V. Petukhov, Thermal expansion of zirconium in the solid phase, High Temperatures-High Pressures, 35/36 (2003/2004) 15-23.

[120] M.H. Mueller, R.L. Hitterman, H.W. Knott, The atomic position parameter in alpha uranium -- room temperature and above, Acta Crystallographica, 15 (1962) 421-422.

[121] J.H. Kim, H. Song, K.H. Kim, C.B. Lee, Fabrication of uranium alloy fuel slug for sodium-cooled fast reactor by injection casting, Journal of Radioanalytical and Nuclear Chemistry, 301 (2014) 797-803.

[122] J.H. Kim, H. Song, K.H. Kim, C.B. Lee, Fabrication and evaluation of rare-earth bearing fuel slugs for sodium-cooled fast reactors, Journal of Radioanalytical and Nuclear Chemistry, 303 (2015) 615-621.

[123] J.-H. Kim, J.W. Lee, K.-H. Kim, J.-Y. Park, Injection casting of U-Zr and U-Zr-RE fuel slugs and their characterization, Journal of Nuclear Science and Technology, 54 (2017) 648-654.

[124] Y.S. Touloukian, R.W. Powell, C.Y. Ho, P.G. Klemens, Thermal Conductivity (Thermophysical Properties of Matter vol. 1), IFI/Plenum, New York, 1970.

[125] Argonne National Laboratory, Chemical Technology Division Annual Technical Report for 1986 (Argonne National Laboratory Report ANL-87-19), Argonne National Laboratory, Argonne, IL, 1987.

[126] Y.S. Kim, T.W. Cho, D.-S. Sohn, Thermal conductivities of actinides (U, Pu, Np, Cm, Am) and uranium-alloys (U-Zr, U-Pu-Zr, and U-Pu-TRU-Zr), Journal of Nuclear Materials, 445 (2014) 272-280.

[127] J.K. Fink, L. Leibowitz, Thermal conductivity of zirconium, Journal of Nuclear Materials, 226 (1995) 44.

[128] M.C. Billone, Y.Y. Liu, E.E. Gruber, T.H. Hughes, J.M. Kramer, Status of fuel element modeling codes for metallic fuels, in: Proceedings of the International Conference on Reliable Fuels for Liquid Metal Reactors, Tucson, AZ, 7-11 Sept, American Nuclear Society, La Grange Park, IL, 1986.

[129] W. Chubb, Physical properties of zirconium-uranium alloys, in: A.A. Bauer (Ed.) An Evaluation of the Properties and Behavior of Zirconium-Uranium Alloys (Report BMI-1350), Battelle Memorial Institute, Columbus, OH, 1959, pp. 78-88.

[130] L.L.J. Marsh, Strength characteristics of zirconium-uranium alloys, in: F.A. Rough (Ed.) An Evaluation of Data on Zirconium-Uranium Alloys (Report BMI-1030), Battelle Memorial Institute, Columbus, OH, 1955, pp. 47-68.

[131] L.L.J. Marsh, Strength characteristics of uranium-zirconium alloys, in: A.A. Bauer (Ed.) An Evaluation of the Properties and Behavior of Zirconium-Uranium Alloys (Report BMI-1350), Battelle Memorial Institute, Columbus, OH, 1959, pp. 55-77.

[132] W. Chubb, F.A. Rough, Mechanical properties and heat treatment response of zirconium-uranium alloys, American Society for Metals -- Transactions, 51 (1959) 697-716.

[133] G.B. Fedorov, M.T. Zuev, E.A. Smirnov, A. Kissil', E., Some physical and mechanical properties of uranium-zirconium alloys at low temperatures, Soviet Atomic Energy, 34 (1973) 111-114 (Translated from Atomnaya Énergiya, vol. 134, no. 112, pp. 185-188, February 1973).

[134] K. Ghoshal, T.R.G. Kutty, S. Mishra, A. Kumar, Creep studies on U-7% Zr, U-7% Nb, and U rich U-Nb-Zr alloys, Journal of Nuclear Materials, 432 (2013) 20-22.

[135] T.R.G. Kutty, C.B. Basak, A. Kumar, H.S. Kamath, Creep behaviour of delta-phase of U-Zr system by impression creep technique, Journal of Nuclear Materials, 408 (2011) 90-95.

[136] T.R.G. Kutty, S. Kaity, A. Kumar, Impression creep behaviour of U-6%Zr alloy: role of microstructure, 11th International Conference on the Mechanical Behavior of Materials, ICM11 (Como, Italy, June 5-9, 2011), 55 (2013) 561-565.

[137] T.R.G. Kutty, C. Ganguly, D.H. Sastry, Development of creep curves from hot indentation hardness data, Scripta Materialia, 34 (1996) 1833-1838.

[138] J.C.M. Li, Impression creep and other localized tests, Materials Science and Engineering A, 322 (2002) 23-42.

[139] D.H. Sastry, Impression-creep technique--an overview, Materials Science and Engineering A, 409 (2005) 67-75.

[140] R.J. Rodríguez, C. Sari, A.J.C. Portal, Investigation of the Np-Zr and U-Np-Zr systems, Journal of Alloys and Compounds, 209 (1994) 263-268.

[141] W. Xie, D. Morgan, CALPHAD modeling and ab initio calculations of the Np-U-Zr system, Computational Materials Science, 143 (2018) 505-514.

[142] W. Xiong, W. Xie, D. Morgan, Thermodynamic evaluation of the Np–Zr system using CALPHAD and ab initio methods, Journal of Nuclear Materials, 452 (2014) 569-577.

[143] T. Ogata, M. Akabori, A. Itoh, Diffusion of cerium in uranium-zirconium solid solutions, Materials Transactions, 44 (2003) 47-52.

[144] T. Ogata, K. Nakamura, A. Itoh, M. Akabori, Reactions between U-Zr alloys and Fe at 1003K, Journal of Nuclear Materials, 441 (2013) 579-582.

[145] S.-J. Oh, K.-H. Kim, C.-B. Lee, C.-T. Lee, S.-J. Jang, Effects of Ce element addition on the characteristics of U-Zr alloys, Transactions of the American Nuclear Society, 98 (2008) 1047-1048.

[146] J.-S. Cheon, S.-J. Oh, B.-O. Lee, C.-B. Lee, The effect of RE-rich phase on the thermal conductivity of U-Zr-RE alloys, Journal of Nuclear Materials, 385 (2009) 559-562.

[147] J.H. Kim, H. Song, H.T. Kim, K.H. Kim, C.B. Lee, R.S. Fielding, Development of a new casting method to fabricate U-Zr alloy containing minor actinides, Journal of Radioanalytical and Nuclear Chemistry, 299 (2014) 103-109.

[148] S.W. Kuk, K.H. Kim, J.H. Kim, H. Song, S.J. Oh, J.-Y. Park, C.B. Lee, Y.-S. Youn, J.-Y. Kim, Phase characteristics of rare earth elements in metallic fuel for a sodium-cooled fast reactor by injection casting, Journal of Nuclear Materials, 486 (2017) 53-59.

[149] H. Ohta, T. Ogata, D. Papaioannou, M. Kurata, T. Koyama, J.-P. Glatz, V.V. Rondinella, Development of fast reactor metal fuels containing minor actinides, Journal of Nuclear Science and Technology, 48 (2011) 654-661.

[150] H. Okamoto, Pu-Zr (plutonium-zirconium), Journal of Phase Equilibria, 14 (1993) 400-401.

[151] H. Okamoto, Pu-Zr (plutonium-zirconium), Journal of Phase Equilibria, 16 (1995) 287-288.

[152] C.A. Papesch, A. Aitkaliyeva, S. Middlemas, Phase verification and thermophysical properties evaluation of Pu-Zr alloys, Transactions of the American Nuclear Society, 116 (2017) 508-509.

[153] J.M. Taylor, Plutonium-zirconium equilibrium diagram from 0 to 10 at% Zr, Journal of Nuclear Materials, 30 (1969) 346-350.

[154] J.A.C. Marples, The plutonium-zirconium phase diagram, Journal of the Less-Common Metals, 2 (1960) 331-351.

[155] W.H. Zachariasen, F.H. Ellinger, The crystal structure of beta plutonium metal, Acta Crystallographica, 16 (1963) 369-375.

[156] F.H. Ellinger, C.C. Land, On the plutonium-zirconium phase diagram, Nuclear Metallurgy, 17 (1971) 686-698.

[157] Y. Suzuki, A. Maeda, T. Ohmichi, Phase diagram of the Pu-Zr system in the Zr-rich region, Journal of Alloys and Compounds, 182 (1992) L9-L14.

[158] J.F. Cornet, Etude cristallographique de la transformation allotropique $\beta \rightarrow \alpha$ du zirconium faiblement allie en plutonium, Journal of Nuclear Materials, 42 (1972) 325-338 (French with English abstract).

[159] J.A.C. Marples, The lattice parameters of some δ- and ε-plutonium alloys, Journal of Physics and Chemistry of Solids, 25 (1964) 521-534.

[160] A.A. Bochvar, S.T. Konobeevskii, V.I. Kutaitsev, T.S. Menshikova, N.T. Chebotarev, Interaction of plutonium and other metals in connection with their arrangement in Mendeleev's periodic table, in: Proceedings of the UN International Conference on Peaceful Uses of Atomic Energy, 1958, pp. 184-193.

[161] A.F. Berndt, The theta phase in the plutonium-zirconium system, Journal of the Less-Common Metals, 12 (1967) 82-83.

[162] V.I. Kutaitsev, N.T. Chebotarev, I.G. Lebedev, M.A. Andrianov, V.N. Konev, T.S. Menshikova, Phase diagrams of plutonium with the metals of groups IIA, IVA, VIIIA and IB, in: A.E. Kay, M.B. Waldron (Eds.) Plutonium 1965, Chapman and Hall for The Institute of Metals, 1965, pp. 420-449.

[163] D.T. Cromer, The crystal structure of ζ-Pu--Zr, ideal formula $Pu_{28}Zr$, Acta Crystallographica, B35 (1979) 14-19.

[164] D.M. Poole, M.G. Bale, P.G. Mardon, J.A.C. Marples, J.L. Nichols, Phase diagrams of some plutonium binary alloy systems, in: E. Grison, W.B.H. Lord, R.D. Fowler (Eds.) Plutonium 1960 (Proceedings of the second international conference on plutonium metallurgy, Grenoble, France, 19-22 April 1960), Cleaver-Hume Press Limited for Commissariat à l'énergie atomique, London, 1961, pp. 267-281.

[165] D. Calais, M. Dupuy, M. Mouchnino, A.Y. Portnoff, A. Van Craeynest, Diffusion of plutonium in the solid state, in: A.E. Kay, M.B. Waldron (Eds.) Plutonium 1965, Chapman and Hall, 1965, pp. 358-391.

[166] Monsanto Research Corporation, Reactor Fuels and Materials Development Plutonium Research: January-June, 1967 (Mound Laboratory Report MLM-1445), Miamisburg, OH, 1968.

[167] J.C. Lauthier, N. Housseau, A. Van Craeynest, D. Calais, Contribution a l'etude du diagramme de phases plutonium-zirconium, Journal of Nuclear Materials, 23 (1967) 313-319.

[168] J.C. Walden, P.L. Wallace, J.W. Magana, X-ray spectometric analysis of plutonium-zirconium alloys, Applied Spectroscopy, 29 (1975) 175-178.

[169] V.I. Kutaitsev, N.T. Chebotarev, M.A. Andrianov, V.N. Konev, I.G. Lebedev, V.I. Bagrova, A.V. Beznosikova, A.A. Kruglov, P.N. Petrov, E.S. Smotritskaya, Phase diagrams of plutonium with metals of groups IIA, IVA, VIII, and IB, Soviet Atomic Energy, 23 (1967) 1279-1287 (Translated from Atomnaya Énergiya, vol 1223, no. 1276, pp. 1511-1519, 1967).

[170] A. Maeda, Y. Suzuki, Y. Okamoto, T. Ohmichi, Vaporization behavior of plutonium-zirconium binary alloy, Journal of Alloys and Compounds, 205 (1994) 35-38.

[171] K.A. Gschneidner Jr., R.O. Elliott, J.T. Waber, Influence of alloying on the negative thermal expansion of delta plutonium, Acta Metallurgica, 11 (1963) 947-955.

[172] R.O. Elliott, K.A. Gschneidner Jr., C.A. Kempter, Thermal expansion of some delta plutonium solid solution alloys, in: E. Grison, W.B.H. Lord, R.D. Fowler (Eds.) Plutonium 1960, Cleaver-Hume Press, London, 1961, pp. 142-155 (Paper no. 134).

[173] D.L. Clark, S.S. Hecker, G.D. Jarvinen, M.P. Neu, Plutonium, in: L.R. Morss, N.M. Edelstein, J. Fuger (Eds.) The Chemistry of the Actinide and Transactinide Elements, Springer, Dordrecht, The Netherlands, 2010, pp. 813-1264.

[174] J.A. Lee, R.O.A. Hall, E. King, G.T. Meaden, Some properties of plutonium and plutonium-rich alloys, in: E. Grison, W.B.H. Lord, R.D. Fowler (Eds.) Plutonium 1960 (The proceedings of the second international conference on plutonium metallurgy, Grenoble, France, 19-22 April 1960), Cleaver-Hume Press Ltd., London, 1961, pp. 39-50.

[175] R.O. Elliott, H.H. Hill, Resistance minima in zirconium-plutonium alloys, Journal of the Less-Common Metals, 22 (1970) 123-126.

[176] J.R. Kennedy, Thermal characteristics of a neptunium-bearing Pu-40Zr based alloy, in: Global 2003: Atoms for prosperity: updating Eisenhower's global vision for nuclear energy, American Nuclear Society, 2003, pp. 2297-2298.

[177] J.R. Kennedy, J.R. Stuart, D.D. Keiser, S.M. Frank, M.K. Meyer, Phase relations in neptunium bearing plutonium-zirconium alloys, Transactions of the American Nuclear Society, 87 (2002) 357-359.

[178] D.D. Keiser, Jr., J.R. Kennedy, Characterization of as-cast transmutation alloys containing Pu, Zr, Am, and Np, in: G.D. Jarvinen (Ed.) Plutonium Futures--The Science, 2003, pp. 154-155.

[179] D.D. Keiser, Jr., J.R. Kennedy, B.A. Hilton, S.L. Hayes, The development of metallic nuclear fuels for transmutation applications: materials challenges, JOM, 60 (2008) 29-32.

[180] M.K. Meyer, D.D. Keiser, S.M. Frank, J.R. Kennedy, G. Knighton, Fabrication and characterization of Pu-Zr and Pu-Am-Zr alloys, Transactions of the American Nuclear Society, 87 (2002) 356-357.

[181] M. Mantina, R. Valero, C.J. Cramer, D.G. Truhlar, Atomic radii of the elements, in: W.M. Haynes (Ed.) CRC Handbook of Chemistry and Physics, 96th Edition (Internet Version 2016), CRC Press/Taylor and Francis, Boca Raton, FL, 2015.

[182] J.K. Gibson, R.G. Haire, M.M. Gensini, T. Ogawa, Alloying behavior in selected neptunium binary systems: the role of 5f bonding, Journal of Alloys and Compounds, 213/214 (1994) 106-110.

[183] J.R. Kennedy, Investigation of the thermal characteristics of an americium bearing Pu-40Zr-based alloy, in: Plutonium Futures--The Science. (Third topical conference on plutonium and actinides), Albuquerque, NM (6-10 July 2003), 2003.

[184] J.R. Kennedy, M.J. Lambregts, A.W. Maddison, Thermal conductivity of minor actinide doped Pu-Zr and U-Pu-Zr transmutation fuels, Transactions of the American Nuclear Society, 91 (2004) 457-458.

[185] J.I. Cole, D.D. Keiser Jr., J.R. Kennedy, Microstructural characterization of as-cast metallic transmutation fuels, in: Global 2007, American Nuclear Society, Boise, ID (September 9-13, 2007), 2007.

[186] D.E. Peterson, E.M. Foltyn, The Pu-U (plutonium-uranium) system, Bulletin of Alloy Phase Diagrams, 10 (1989) 160-164.

[187] H. Okamoto, Pu-U (plutonium-uranium), Journal of Phase Equilibria, 17 (1996) 372b.

[188] H. Okamoto, Pu-U (plutonium-uranium), Journal of Phase Equilibria, 13 (1992) 107-108.

[189] H. Okamoto, T.B. Massalski, Thermodynamically improbable phase diagrams, Journal of Phase Equilibria, 12 (1991) 148-168.

[190] Y. Okamoto, A. Maeda, Y. Suzuki, T. Ohmichi, Investigation of the Pu-U phase diagram, Journal of Alloys and Compounds, 213/214 (1994) 372-374.

[191] S. Kaity, J. Banerjee, K. Ravi, R. Keswani, T.R.G. Kutty, A. Kumar, G.J. Prasad, Characterization and property evaluation of U-15 wt% Pu alloy for fast reactor, Journal of Nuclear Materials, 433 (2013) 206-214.

[192] F.H. Ellinger, R.O. Elliott, E.M. Cramer, The plutonium-uranium system, Journal of Nuclear Materials, 1 (1959) 233-243.

[193] L.R. Kelman, H.V. Rhude, J.G. Schnizlein, H. Savage, Status of metallic plutonium fast power-breeder fuels, in: A.E. Kay, M.B. Waldron (Eds.) Plutonium 1965: Proceedings of the third international conference on plutonium, London, 1965, Chapman and Hall for The Institute of Metals, London, 1967, pp. 458-484.

[194] L. Leibowitz, R.A. Blomquist, A.D. Pelton, Thermodynamic modeling of the phase equilibria of the plutonium-uranium system, Journal of Nuclear Materials, 184 (1991) 59-64.

[195] T. Ogawa, Alloying behaviour among U, Np, Pu and Am predicted with the Brewer valence bond model, Journal of Alloys and Compounds, 194 (1993) 1-7.

[196] K.S. Chan, J.K. Lee, H.I. Aaronson, Kaufman approach calculations of partial phase diagrams amongst Th, U, Np and Pu, Journal of Nuclear Materials, 92 (1980) 237-242.

[197] M. Kurata, Thermodynamic assessment of the Pu-U, Pu-Zr, and Pu-U-Zr systems, CALPHAD-Computer Coupling of Phase Diagrams and Thermochemistry, 23 (1999) 305-337.

[198] A. Landa, P. Söderlind, P.E.A. Turchi, L. Vitos, O.E. Peil, A.V. Ruban, Density-functional study of bcc Pu-U, Pu-Np, Pu-Am, and Pu-Cm alloys, Journal of Nuclear Materials, 408 (2011) 61-66.

[199] A. Perron, P.E.A. Turchi, A. Landa, P. Söderlind, B. Ravat, B. Oudot, F. Delaunay, The Pu–U–Am system: An *ab initio* informed CALPHAD thermodynamic study, Journal of Nuclear Materials, 458 (2015) 425-441.

[200] A. Perron, P.E.A. Turchi, A. Landa, P. Söderlind, B. Ravat, B. Oudot, F. Delaunay, M. Kurata, Thermodynamic re-assessment of the Pu–U system and its application to the ternary Pu–U–Ga system, Journal of Nuclear Materials, 454 (2014) 81-95.

[201] B. Dorado, J. Bieder, M. Torrent, Influence of point defects and impurities on the dynamical stability of δ-plutonium, Journal of Physics: Condensed Matter, 29 (2017) 245402.

[202] A.F. Berndt, Room temperature lattice constants of alloys of plutonium in alpha-uranium, Journal of Nuclear Materials, 9 (1963) 53-58.

[203] A.C. Lawson, J.A. Goldstone, B. Cort, R.J. Martinez, F.A. Vigil, T.G. Zocco, J.W. Richardson Jr., M.H. Mueller, Structure of ζ-phase plutonium-uranium, Acta Crystallographica B: Structural Science, 52 (1996) 32-37.

[204] H. Savage, The heat content and specific heat of some metallic fast-reactor fuels containing plutonium, Journal of Nuclear Materials, 25 (1968) 249-259.

[205] Monsanto Research Corporation, Reactor Fuels and Materials Development Plutonium Research: 1966 Annual Report (Mound Laboratory Report MLM-1402), Miamisburg, OH, 1967.

[206] F.H. Ellinger, W.N. Miner, D.R. O'Boyle, F.W. Schonfeld, Constitution of Plutonium Alloys (Los Alamos National Laboratory Report LA-3870), Los Alamos National Laboratory, Los Alamos, NM, 1968.

[207] S. Rosen, M.V. Nevitt, J.J. Barker, The U-Pu-C ternary phase diagram below 50 atomic percent carbon, Journal of Nuclear Materials, 9 (1963) 128-136.

[208] S.S. Hecker, M. Stan, Properties of plutonium and its alloys for use as fast reactor fuels, Journal of Nuclear Materials, 383 (2008) 112-118.

[209] J.H. Kittel, J.E. Ayer, W.N. Beck, M.B. Brodsky, D.R. O'Boyle, S.T. Zegler, F.H. Ellinger, W.N. Miner, F.W. Schonfeld, R.D. Nelson, Plutonium and plutonium alloys as nuclear fuel materials, Nuclear Engineering and Design, 15 (1971) 373-440.

[210] R.J.M. Konings, O. Beneš, The Thermodynamic Properties of the *f*-Elements and Their Compounds. I. The Lanthanide and Actinide Metals, Journal of Physical and Chemical Reference Data, 39 (2010) 043102.

[211] R. Boucher, P. Barthelemy, Comparison of the Alloys U-Pu-Mo, U-Pu-Nb, U-Pu-Ti, U-Pu-Zr (Argonne National Laboratory Translation ANL-TRANS-138), translated from CEA Report CEA-R 2531, "Comparaison des alliages U-Pu-Mo, U-Pu-Nb, U-Pu-Ti, U-Pu-Zr," by B. Blumenthal, 1964.

[212] R. Boucher, P. Barthelemy, C. Milet, A study of plutonium-based alloys carried out at Fontenay-aux-Roses, in: A.E. Kay, M.B. Waldron (Eds.) Plutonium 1965: Proceedings of the third international conference on plutonium, London, 1965, Chapman and Hall for The Institute of Metals, London, 1965, pp. 485-509.

[213] Argonne National Laboratory, Metallurgy Division Annual Progress Report for 1965 (Argonne National Laboratory Report ANL-7155), Argonne National Laboratory, Argonne, IL, 1965.

[214] K. Nikitin, M. Saito, M. Kawashima, V. Artisyuk, A. Shmelev, Long-life water cooled small reactor with U-Np-Pu fuel, Journal of Nuclear Science and Technology, 38 (2001) 511-516.

[215] P. Wydler, W. Heer, P. Stiller, H.U. Wenger, A uranium-plutonium-neptunium fuel cycle to produce isotopically denatured plutonium, Nuclear Technology, 49 (1980) 115-120.

[216] M. Kurata, Thermodynamic database on U-Pu-Zr-Np-Am-Fe alloy system II - Evaluation of Np, Am, and Fe containing systems, IOP Conference Series: Materials Science and Engineering, 9 (Actinides 2009) (2010).

[217] D.R. Harbur, J.W. Anderson, W.J. Maraman, Studies on the U-Pu-Zr alloy system for fast breeder reactor applications (Los Alamos National Laboratory Report LA-4512), 1970.

[218] M. Kurata, T. Inoue, C. Sari, Redistribution behavior of various constituents in U-Pu-Zr alloy and U-Pu-Zr alloy containing minor actinides and rare-earths in a temperature-gradient, Journal of Nuclear Materials, 208 (1994) 144-158.

[219] Argonne National Laboratory, Reactor development program progress report, September 1965 (Argonne National Laboratory Report ANL-7105), Argonne, IL, 1965.

[220] P.A. Tucker, D.E. Etter, J.M. Gebhart, Phase study of uranium-plutonium-zirconium alloys, Transactions of the American Nuclear Society, 11 (1968) 99.

[221] Y.H. Sohn, M.A. Dayananda, G.L. Hofman, R.V. Strain, S.L. Hayes, Analysis of constituent redistribution in the gamma (bcc) U-Pu-Zr alloys under gradients of temperature and concentrations, Journal of Nuclear Materials, 279 (2000) 317-329.

[222] A. Aitkaliyeva, J.W. Madden, C. Papesch, J.I. Cole, TEM identification of subsurface phases in ternary U-Pu-Zr fuel, Journal of Nuclear Materials, 473 (2016) 75-82.

[223] D.E. Janney, B.H. Sencer, Microstructure changes caused by annealing of U-Pu-Zr alloys, Journal of Nuclear Materials, 486 (2017) 66-69.

[224] K. Pietrak, T.S. Wiśniewski, A review of models for effective thermal conductivity of composite materials, Journal of Power Technologies, 95 (2015) 14-24.

[225] Z. Wenzhong, C. Unal, U-Pu-Zr fuel properties and thermal performance modeling for sodium fast reactors, Transactions of the American Nuclear Society, 106 (2012) 264-264.

[226] J.D. Galloway, C. Unal, N.N. Carlson, Modeling Constituent Redistribution in U-Pu-Zr Metallic Fuel Using the Advanced Fuel Performance Code BISON, 2013.

[227] A. Aitkaliyeva, C. Papesch, M. Tonks, Coupling experiments and simulations to understand metallic fuel behavior, Transactions of the American Nuclear Society, 116 (2017) 479-480.

[228] C. Matthews, U. Cetin, J. Galloway, D.D. Keiser, S.L. Hayes, Fuel-cladding chemical interaction in U-Pu-Zr metal fuels: A critical review, Nuclear Technology, 198 (2017) 231-259.

[229] G.L. Hofman, R.G. Pahl, C.E. Lahm, D.L. Porter, Swelling behavior of U-Pu-Zr fuel, Metallurgical Transactions A (Physical Metallurgy and Materials Science), 21A (1990) 517-528.

[230] D.E. Burkes, J.R. Kennedy, T. Hartmann, C.A. Papesch, D.D. Keiser, Jr., Phase characteristics of a number of U-Pu-Am-Np-Zr metallic alloys for use as fast reactor fuels, Journal of Nuclear Materials, 396 (2010) 49-56.

[231] D.E. Burkes, J.R. Kennedy, T. Hartmann, C.A. Papesch, Phase characteristics of a U-20Pu-3Am-2Np-15Zr metallic alloy containing rare earths, Nuclear Engineering and Design, 239 (2009) 2747-2753.

[232] Monsanto Research Corporation, Reactor Fuels and Materials Development, Plutonium Research: January-March 1966 (Mound Laboratory report MLM-1346), Miamisburg, OH, 1966.

[233] L. Leibowitz, E. Veleckis, R.A. Blomquist, Solidus and liquidus temperatures in the uranium-plutonium-zirconium system, in: US-Japan Joint Seminar on the High Tempreature Chemistry of Current Light-Water Reactors and Advanced All-Metal Reactors, Tokyo, Japan, 1987.

[234] G.L. Hofman, L.C. Walters, Metallic fast reactor fuels, in: B.R.T. Frost, R.W. Cahn, P. Haasen, E.G. Kramer (Eds.) Materials Science and Technology, A Comprehensive Treatment, VCH Verlagsgesellschaft mbH, 1994, pp. 1-43.

[235] T. Ogata, Y.S. Kim, A.M. Yacout, Metal fuel performance modeling and simulation, in: R.J.M. Konings (Ed.) Comprehensive Nuclear Materials, Elsevier, 2012, pp. 713-753.

[236] D.E. Burkes, J.R. Kennedy, T. Hartmann, L.N. Squires, Phase characteristics of a U-22Pu-4Am-2Np-40Zr metallic alloy containing rare earths, Journal of Phase Equilibria and Diffusion, 30 (2009) 309-317.

[237] Y.S. Kim, S.L. Hayes, G.L. Hofman, A.M. Yacout, Modeling of constituent redistribution in U-Pu-Zr metallic fuel, Journal of Nuclear Materials, 359 (2006) 17-28.

[238] M. Ishida, T. Ogata, M. Kinoshita, Constituent migration model for U-Pu-Zr metallic fast reactor fuel, Nuclear Technology, 104 (1993) 37-51.

[239] D.R.F. West, N. Saunders, Ternary Phase Diagrams in Materials Science, 3rd Edition, Maney for the Institute of Materials, London, 2002.

[240] F.N. Rhines, Phase Diagrams in Metallurgy, McGraw-Hill, New York, 1956.

[241] D.R. O'Boyle, H.V. Rhude, Solid-state reactions in U-Pu-Zr system, Argonne National Laboratory Metallurgy Division Annual Progress Report for 1966 (Argonne National Laboratory Report ANL-7299), (1966) 18, 20-21.

[242] P.E.A. Turchi, A.I. Landa, P.A. Söderlind, Thermodynamic assessment of the Am-Pu system with input from *ab initio*, Journal of Nuclear Materials, 418 (2011) 165-173.

[243] Y.S. Kim, G.L. Hofman, A.M. Yacout, Migration of minor actinides and lanthanides in fast reactor metallic fuel, Journal of Nuclear Materials, 392 (2009) 164-170.

[244] L.E. Link, J.E. Ayer, D.K. Butler, K.A. Hub, W.B. Loewenstein, W.J. Mecham, D. Meneghetti, D.H. Thompson, V.G.J. Trice, J.T. Weills, 1000 MW(e) metal-fueled fast breeder reactor (Argonne National Laboratory Report ANL-7001), (1966).

[245] Argonne National Laboratory, Reactor Development Progress Report (Argonne National Laboratory Report ANL-7230), Argonne National Laboratory, Argonne, IL, 1966.

[246] Argonne National Laboratory, Reactor Development Program Progress Report, May, 1965 (Argonne National Laboratory Report ANL-7046), Argonne National Laboratory, Argonne, IL, 1965.

[247] L.J. Kelman, W.N. Beck, C.M. Walter, W.F. Murphy, C.C. Crothers, Uranium-plutonium alloys, in: L.E. Link, J.E. Ayer, D.K. Butler, K.A. Hub, W.B. Loewenstein, W.J. Mecham, D. Meneghetti, D.H. Thompson, V.G.J. Trice, J.T. Weills (Eds.) 1000-MW(e) Metal-Fueled Fast Breeder Reactor (Argonne National Laboratory report ANL-7001), Argonne National Laboratory, Argonne, Illinois, 1966, pp. 98-104.

[248] L.R. Kelman, Improved metallic fast power breeder fuels, Transactions of the American Nuclear Society, 8 (1965) 347-348.

[249] Alfa Aesar, Zirconium, in, Thermo Fisher Scientific, 2018.

[250] T. Nishi, K. Nakajima, M. Takano, M. Kurata, Y. Arita, Thermal conductivity of U-20wt%Pu-2wt%Am-10wt%Zr alloy, Journal of Nuclear Materials, 464 (2015) 270-274.

[251] L. Braase, Transmutation Fuels Campaign FY-09 Accomplishments Report (INL/EXT-09-16834), 2009.

[252] M.K. Meyer, S.L. Hayes, W.J. Carmack, H. Tsai, The EBR-II X501 Minor Actinide Burning Experiment, 2008.

[253] M.K. Meyer, S.L. Hayes, W.J. Carmack, H. Tsai, The EBR-II X501 minor actinide burning experiment, Journal of Nuclear Materials, 392 (2009) 176-183.

[254] D.E. Janney, J.R. Kennedy, As-cast microstructures in U-Pu-Zr alloy fuel pins with 5-8 wt% minor actinides and 0-1.5 wt% rare-earth elements, Materials Characterization, 61 (2010) 1194-1202.

[255] T.A. Hyde, Fabrication report for the AFC-2A and AFC-2B Capsule irradiations in the ATR (Idaho National Laboratory Report INL/EXT-07-13021), 2007.

[256] D.E. Burkes, J.R. Kennedy, T. Hartmann, C.A. Papesch, Characterization of 60U-20Pu-3Am-2Np-15Zr alloys with 1.5 wt% rare earth elements, Transactions of the American Nuclear Society, 98 (2008) 1062-1064.

[257] R.A. Young, ed., The Rietveld Method, Oxford University Press and the International Union of Crystallography, Oxford, England, 1993.

[258] D.E. Janney, J.R. Kennedy, J.W. Madden, T.P. O'Holleran, Am phases in the matrix of a U-Pu-Zr alloy with Np, Am, and rare-earth elements, Journal of Nuclear Materials, 456 (2015) 46-53.

[259] J.R. Kennedy, A. Maddison, D. Burkes, C. Papesch, Thermal Analysis of AFC-2A Metallic Transmutation Fuels, 2007.

[260] L. Capriotti, S. Brémier, K. Inagaki, P. Pöml, D. Papaioannou, H. Ohta, T. Ogata, V.V. Rondinella, Characterization of metallic fuel for minor actinides transmutation in fast reactor, Progress in Nuclear Energy, 94 (2017) 194-201.

[261] M. Kurata, A. Sasahara, T. Inoue, J. Betti, J.F. Babelot, J.C. Spirlet, L. Koch, Fabrication of U-Pu-Zr metallic fuel containing minor actinides, Proceedings of the International Conference on Future Nuclear Systems (Global '97), (1999) 1384-1389.

[262] H. Ohta, T. Ogata, S. Van Winckel, D. Papaioannou, V.V. Rondinella, Minor actinide transmutation in fast reactor fuels irradiated for 120 and 360 equivalent full-power days, Journal of Nuclear Science and Technology, 53 (2015) 968-980.

[263] H. Ohta, T. Ogata, D. Papaioannou, V.V. Rondinella, M. Masson, J.-L. Paul, Irradiation of minor actinide-bearing uranium-plutonium-zirconium alloys up to ~2.5 at. %, ~7 at. %, and ~10 at. % burnups, Nuclear Technology, 190 (2015) 36-51.

[264] D.E. Janney, J.R. Kennedy, Microstructure changes during annealing of unirradiated U-Pu-Zr metal fuels, Transactions of the American Nuclear Society, 103 (2010) 292-293.

[265] D.E. Janney, J.R. Kennedy, Microstructural changes in thermally cycled U-Pu-Zr-Am-Np metallic transmutation fuel with 1.5% lanthanides, Transactions of the American Nuclear Society, 98 (2008) 1058-1059.

[266] D.E. Janney, J.W. Madden, T.P. O'Holleran, High- and low-Am RE inclusion phases in a U-Np-Pu-Am-Zr alloy, Journal of Nuclear Materials, 458 (2015) 106-114.

[267] D.E. Janney, J.R. Kennedy, J.W. Madden, T. O'Holleran, Crystal structure of high-Zr inclusions in an alloy containing U, Pu, Np, Am, Zr and rare-earth elements, Journal of Nuclear Materials, 448 (2014) 109-112.

[268] D.E. Janney, T.P. O'Holleran, Zr inclusions in actinide-Zr alloys: New data and ideas about how they form, Journal of Nuclear Materials, 460 (2015) 13-15.

[269] C. Sari, C.T. Walker, M. Kurata, T. Inoue, Interaction of U-Pu-Zr alloys containing minor actinides and rare-earths with stainless-steel, Journal of Nuclear Materials, 208 (1994) 201-210.

[270] L. Capriotti, K. Inagaki, D. Papaioannou, S. Bremier, H. Ohta, T. Ogata, R. Eloirdi, F. Bocci, D. Bouexiere, V.V. Rondinella, Phase characterization in unirradiated and irradiated metallic fuel for minor actinides transmutation in fast reactor, Transactions of the American Nuclear Society, 110 (2014) 781-782.

INL/EXT-15-36520
Revision 3 Part 2

Metallic Fuels Handbook, Part 2:
Elements and Alloys not Based on U-Zr, Pu-Zr, U-Pu, or U-Pu-Zr

Dawn E. Janney

With special assistance from Cynthia A. Adkins and contributions from Douglas E. Burkes, James I. Cole, Randall S. Fielding, Steven M. Frank, Thomas Hartmann, Timothy A. Hyde, Dennis D. Keiser, Jr., J. Rory Kennedy, Andrew Maddison, Robert D. Mariani, Scott C. Middlemas, Thomas P. O'Holleran, Bulent H. Sencer, and Leah N. Squires

August 2018

NTRD-FUEL-2018-000085 / Part 2

The INL is a U.S. Department of Energy National Laboratory
operated by Battelle Energy Alliance

DISCLAIMER

This information was prepared as an account of work sponsored by an agency of the U.S. Government. Neither the U.S. Government nor any agency thereof, nor any of their employees, makes any warranty, expressed or implied, or assumes any legal liability or responsibility for the accuracy, completeness, or usefulness, of any information, apparatus, product, or process disclosed, or represents that its use would not infringe privately owned rights. References herein to any specific commercial product, process, or service by trade name, trade mark, manufacturer, or otherwise, does not necessarily constitute or imply its endorsement, recommendation, or favoring by the U.S. Government or any agency thereof. The views and opinions of authors expressed herein do not necessarily state or reflect those of the U.S. Government or any agency thereof.

INL/EXT-15-36520
Revision 3 Part 2

Metallic Fuels Handbook, Part 2: Elements and Alloys not Based on U-Zr, Pu-Zr, U-Pu, or U-Pu-Zr

Dawn E. Janney

With special assistance from Cynthia A. Adkins and contributions from
Douglas E. Burkes, James I. Cole, Randall S. Fielding, Steven M. Frank,
Thomas Hartmann, Timothy A. Hyde, Dennis D. Keiser, Jr., J. Rory Kennedy,
Andrew Maddison, Robert D. Mariani, Scott C. Middlemas, Thomas P. O'Holleran,
Bulent H. Sencer and Leah N. Squires

August 2018

Idaho National Laboratory
Idaho Falls, Idaho 83415

http://www.inl.gov

Prepared for the
U.S. Department of Energy
Office of Nuclear Energy
Under DOE Idaho Operations Office
Contract DE-AC07-05ID14517

INTENTIONALLY BLANK

SUMMARY

Transmutation of minor actinides such as Np, Am, and Cm in spent nuclear fuel is of international interest because of its potential for reducing the long-term health and safety hazards caused by the radioactivity of the spent fuel. One important approach to transmutation (currently being pursued by the DOE Fuel Cycle Research & Development Advanced Fuels Campaign) involves incorporating the minor actinides into U-Pu-Zr alloys, which can be used as fuel in fast reactors. U-Pu-Zr alloys are well suited for electrolytic refining, which leads to incorporation rare-earth fission products such as La, Ce, Pr, and Nd. It is, therefore, important to understand not only the properties of U-Pu-Zr alloys but also those of U-Pu-Zr alloys with concentrations of minor actinides (particularly Np and Am) and rare-earth elements (particularly La, Ce, Pr, and Nd) similar to those in reprocessed fuel.

In addition to requiring extensive safety precautions, alloys containing U, Pu, and minor actinides are difficult to study for numerous reasons, including their complex phase transformations, characteristically sluggish phase-transformation kinetics, tendency to produce experimental results that vary depending on the histories of individual samples, rapid oxidation, and sensitivity to contaminants such as oxygen in concentrations below a hundred parts per million. Although less toxic, rare-earth elements such as La, Ce, Pr, and Nd are also difficult to study for similar reasons. Many of the experimental measurements were made before 1980, and many of the references for data on the rare-earth elements were originally published in Soviet journals. The level of documentation for experimental methods and results varies widely. It is therefore not surprising that little is known with certainty about U-Pu-Zr alloys, particularly those that also contain minor actinides and rare-earth elements. General acceptance of results commonly indicates that there is only a single measurement for a particular property rather than multiple measurements with similar results.

The Metallic Fuels Handbook summarizes currently available information about phases and phase diagrams, heat capacity, thermal expansion, and thermal conductivity of elements and alloys in the U-Pu-Zr-Np-Am-La-Ce-Pr-Nd system. Many sections in this revision are updates of material in previous versions of the Handbook [1-4]. New material in this revision involves primarily additional details about U-Zr and U-Pu-Zr alloys, including some information about properties not included in earlier revisions of the Handbook. In addition to presenting information about materials properties, this handbook emphasizes data assessments and provides information about how well each property is known and how much variation exists between measurements. Although the Handbook includes some results from models, its primary focus is experimental data.

Because of its size, the Handbook has been split into two parts, which are presented as separate documents. Part 1 (reference [5]) contains introductory material and information about the U-Pu-Zr system (U-Zr, Pu-Zr, U-Pu, and U-Pu-Zr alloys, including those with minor actinides, rare-earth elements, and Y). Part 2 (this document) contains information about elements and the remaining alloys in the U-Np-Pu-Am-La-Ce-Pr-Nd-Zr system.

INTENTIONALLY BLANK

ACKNOWLEDGEMENTS

This Handbook would not have been possible without the dedication, enthusiastic help, and expertise of the staff of the INL Research Library. Their ability to find even the most obscure documents is truly outstanding.

I would like to thank Dr. Steven L. Hayes for his support and insightful comments, Dr. Pavel Medvedev for Russian translation, and Dr. Steven M. Frank for helpful discussions. Ms. Cynthia A. Adkins not only provided project management support and thorough proofreading, but contributed some data and provided invaluable assistance in assessing the quality of the thermochemical data.

Funding for researching and writing the handbook was provided by the U.S. Department of Energy, Office of Nuclear Energy, under DOE Idaho Operations Office Contract DE-AC07-05ID14517.

INTENTIONALLY BLANK

CONTENTS

SUMMARY iii

ACKNOWLEDGEMENTS v

ACRONYMS xxi

1. INTRODUCTION 1

2. ELEMENTS (U, Np, Pu, Am, La, Ce, Pr, Nd, and Zr) 6

2.1 U 6
2.1.1 Introduction 6
2.1.2 Phases and Phase Transformations 7
2.1.3 Heat Capacity and Related Properties 9
2.1.4 Thermal Expansion and Density 12
2.1.5 Thermal Conductivity and Related Properties 15

2.2 Np 17
2.2.1 Introduction 17
2.2.2 Phases and Phase Transformations 18
2.2.3 Heat Capacity and Related Properties 19
2.2.4 Thermal Expansion and Density 21
2.2.5 Thermal Conductivity and Related Properties 24

2.3 Pu 26
2.3.1 Introduction 26
2.3.2 Phases and Phase Transformations 27
2.3.3 Heat Capacity and Related Properties 31
2.3.4 Thermal Expansion and Density 34
2.3.5 Thermal Conductivity and Related Properties 36

2.4 Am 38
2.4.1 Introduction 38
2.4.2 Phases and Phase Transformations 39
2.4.3 Heat Capacity and Related Properties 40
2.4.4 Thermal Expansion and Density 41
2.4.5 Thermal Conductivity and Related Properties 44

2.5 La 44
2.5.1 Introduction 44
2.5.2 Phases and Phase Transformations 45
2.5.3 Heat Capacity and Related Properties 45
2.5.4 Thermal Expansion and Density 47
2.5.5 Thermal Conductivity and Related Properties 51

2.6 Ce 52
2.6.1 Introduction 52
2.6.2 Phases and Phase Transformations 53
2.6.3 Heat Capacity and Related Properties 54
2.6.4 Thermal Expansion and Density 55
2.6.5 Thermal Conductivity and Related Properties 58

2.7 Pr 60
2.7.1 Introduction 60

2.7.2 Phases and Phase Transformations 60
2.7.3 Heat Capacity and Related Properties 61
2.7.4 Thermal Expansion and Density 62
2.7.5 Thermal Conductivity and Related Properties 65

2.8 Nd 67
2.8.1 Introduction 67
2.8.2 Phases and Phase Transformations 67
2.8.3 Heat Capacity and Related Properties 67
2.8.4 Thermal Expansion and Density 69
2.8.5 Thermal Conductivity and Related Properties 72

2.9 Zr 74
2.9.1 Introduction 74
2.9.2 Phases and Phase Transformations 75
2.9.3 Heat Capacity and Related Properties 75
2.9.4 Thermal Expansion and Density 76
2.9.5 Thermal Conductivity and Related Properties 78

3. ALLOYS CONTAINING ONLY U, Np, Pu, and Am (Except U-Pu and U-Np-Pu, which are in Handbook Volume 1 (reference [5])) 80

3.1 U-Np 80
3.1.1 Introduction 80
3.1.2 Phases and Phase Transformations 80
3.1.3 Thermal Expansion and Density 82

3.2 U-Am 84
3.2.1 Introduction 84
3.2.2 Phases and Phase Transformations 84

3.3 Np-Pu 85
3.3.1 Introduction 85
3.3.2 Phases and Phase Transformations 86
3.3.3 Thermal Expansion and Density 89
3.3.4 Thermal Conductivity and Related Properties 89

3.4 Np-Am 92
3.4.1 Introduction 92
3.4.2 Phases and Phase Transformations 92

3.5 Pu-Am 93
Introduction 93
3.5.1 Phases and Phase Transformations 94
3.5.2 Heat Capacity and Related Properties 98
3.5.3 Thermal Expansion and Density 98
3.5.4 Thermal Conductivity and Related Properties 99

3.6 Np-Pu-Am 100
3.6.1 Introduction 100
3.6.2 Phases and Phase Transformations 100

4. ALLOYS CONTAINING ONLY La, Ce, Pr, and Nd 101

4.1 La-Ce 101
4.1.1 Introduction 101
4.1.2 Phases and Phase Transformations 102
4.1.3 Heat Capacity and Related Properties 105

4.1.4 Thermal Expansion and Density 105
4.1.5 Thermal Conductivity and Related Properties 107
4.2 La-Pr 107
4.2.1 Introduction 107
4.2.2 Phases and Phase Transformations 107
4.2.3 Thermal Expansion and Density 108
4.2.4 Thermal Conductivity and Related Properties 110
4.3 La-Nd 111
4.3.1 Introduction 111
4.3.2 Phases and Phase Transformations 111
4.3.3 Heat Capacity and Related Properties 113
4.3.4 Thermal Expansion and Density 113
4.4 Ce-Pr 114
4.4.1 Introduction 114
4.4.2 Phases and Phase Transformations 114
4.4.3 Thermal Conductivity and Related Properties 116
4.5 Ce-Nd 116
4.5.1 Introduction 116
4.5.2 Phases and Phase Transformations 117
4.6 Pr-Nd 118
4.6.1 Introduction 118
4.6.2 Phases and Phase Transformations 119
4.6.3 Heat Capacity and Related Properties 120
4.6.4 Thermal Expansion and Density 121
4.6.5 Thermal Conductivity and Related Properties 121
4.7 Mischmetals (Rare-earth alloys that include La, Ce, Pr, and Nd) 122

5. BINARY ALLOYS OF AN ACTINIDE (U, Np, Pu, Am) AND A RARE-EARTH ELEMENT (La, Ce, Pr, Nd) 122
5.1 U-La 122
5.1.1 Introduction 122
5.1.2 Phases and Phase Transformations 122
5.2 U-Ce 123
5.2.1 Introduction 123
5.2.2 Phases and Phase Transformations 123
5.3 U-Pr 124
5.3.1 Introduction 124
5.3.2 Phases and Phase Transformations 125
5.4 U-Nd 126
5.4.1 Introduction 126
5.4.2 Phases and Phase Transformations 126
5.5 Np-La 127
5.6 Np-Ce 127
5.7 Np-Pr 127
5.8 Np-Nd 128
5.9 Pu-La 128
5.9.1 Introduction 128

5.9.2 Phases and Phase Transformations 128
5.10 Pu-Ce 130
5.10.1 Introduction 130
5.10.2 Phases and Phase Transformations 130
5.10.3 Thermal Expansion and Density 134
5.10.4 Thermal Conductivity and Related Properties 140
5.11 Pu-Pr 140
5.11.1 Introduction 140
5.11.2 Phases and Phase Transformations 141
5.12 Pu-Nd 143
5.12.1 Introduction 143
5.12.2 Phases and Phase Transformations 144
5.13 Am-La 146
5.13.1 Introduction 146
5.13.2 Phases 146
5.14 Am-Ce 147

6. BINARY ALLOYS OF A MINOR ACTINIDE (Np, Am) WITH Zr 147
6.1 Np-Zr 147
6.1.1 Introduction 147
6.1.2 Phases and Phase Transformations 148
6.2 Am-Zr 151

7. BINARY ALLOYS OF A RARE-EARTH ELEMENT (La, Ce, Pr, Nd) With Zr 152
7.1 La-Zr 152
7.1.1 Introduction 152
7.1.2 Phases and Phase Transformations 153
7.2 Ce-Zr 154
7.2.1 Introduction 154
7.2.2 Phases and Phase Transformations 155
7.3 Pr-Zr 157
7.4 Nd-Zr 157
7.4.1 Introduction 157
7.4.2 Phases and Phase Transformations 158

8. REFERENCES 160

FIGURES

Figure 1. Heat capacities of solid and liquid U. Values from Konings and Beneš [7] (Equation 1, Equation 2, Equation 3, and Equation 4) are preferred. 10

Figure 2. Heat capacity of U as an ideal gas. Values from Konings and Beneš were calculated from Equation 5and Equation 6. 11

Figure 3. Thermal expansion of U. Lines represent thermal expansion of polycrystalline U, calculated using Equation 7 through Equation 11. Symbols represent recommended values for thermal expansion of single crystals of α-U in the indicated crystallographic directions from Touloukian et al. [55]. 12

Figure 4. Density of U. Data labeled "Klepfer and Chiotti," "Lawson et al.," and "Rohr and Wittenberg" are from references [18, 42, 61]. Data labeled "Touloukian" were calculated using Equation 12 and equations for Touloukian's thermal expansion (Equation 7, Equation 9, and Equation 10). Data labeled "Konings et al." were calculated using Equation 13. 15

Figure 5. Thermal conductivity of U (Equation 14, Equation 15, and Equation 16). 16

Figure 6. Heat capacity of α-Np [7, 84, 85]. 20

Figure 7. Estimated heat capacities of β-, γ-, and liquid Np, with the heat capacities of U and Pu phases on which the estimates are based. Heat-capacity values for Np are from Konings & Beneš [7]. Solid lines indicate tetragonal phases (space groups $P42_12$ for β-Np, $P42mnm$ for β-U, and $I4/mmm$ for δ'-Pu), dotted lines indicate bcc phases (space group $Im3m$), and dashed lines indicate liquids. Colors indicate different elements. 21

Figure 8. Instantaneous coefficients of thermal expansion for polycrystalline α- and β-Np at selected temperatures [81 Table 4]. 23

Figure 9. Density and molar volume of Np from Zachariasen's X-ray data [76]. 24

Figure 10. Thermal conductivity of Np calculated using the theoretical value of the Lorenz number (2.44×10^{-8} WΩ/K^2) and electrical resistivity data from Lee [93]. 26

Figure 11. Heat capacities of solid and liquid Pu. Values from Konings and Beneš [7] (solid black lines, Equation 18 through Equation 24) are preferred. 32

Figure 12. Heat capacity of ^{239}Pu as an ideal gas, calculated using Equation 25 and Equation 26. 33

Figure 13. Linear thermal expansion of polycrystalline Pu [148]. 34

Figure 14. Thermal conductivity of Pu. Data from Alexander and Wood were calculated from Equation 28 through Equation 32. 37

Figure 15. Estimated heat capacity of Am above 300 K, showing values from Oetting et al. [6], Konings [176], and Ward et al. [54 Table A.6] 41

Figure 16. Thermal expansion of α-Am. The *a* and *c* lattice parameters are from McWhan et al. (Equation 34 and Equation 35); "Konings" value is from Equation 36. 43

Figure 17. Heat capacity of La (references [196, 198, 199, 201, 202] and Equation **37**, Equation 38, Equation 39, and Equation 40)). 46

Figure 18. Thermal expansion of single crystals of α- and β-La, based on values calculated from Equation 41 through Equation 43 using a reference temperature of 300 K. Dotted line for β-La indicates that it is likely to be present (particularly during cooling) but is not thermodynamically stable. 48

Figure 19. Densities and molar volumes of La phases (reference [193] and Equation 44 and Equation 45). Dashed lines show properties of β-La at temperatures where it is thermodynamically unstable but likely to occur; dotted lines show extrapolation beyond the upper temperatures of the equations following [193 Figure 1]. 50

Figure 20. Thermal conductivity of La [95, 199, 202, 211, 212, 214]. 52

Figure 21. Heat capacity of Ce (references [7, 199, 200, 244, 245] and Equation 48 through Equation 51). 55

Figure 22. Thermal expansion of γ-Ce, based on values calculated from Equation 52 using a reference temperature of 300 K. 56

Figure 23. Densities and molar volumes of γ-Ce (lines calculated from Equation 53) and δ-Ce (squares) from reference [193]. 58

Figure 24. Thermal conductivity of Ce (references [62, 95, 199, 202, 214, 248-250]. 59

Figure 25. Heat capacity of Pr (references [196, 201, 202, 254, 255] and Equation 54 through Equation 56). 62

Figure 26. Thermal expansion of a and c lattice parameters of α-Pr, calculated from Equation 57 and Equation 58 with a reference temperature of 300 K. 64

Figure 27. Molar volumes of Pr phases (Equation 59 and references [193 (Table 2)] and [251 (Figure 4)]). 65

Figure 28. Thermal conductivity of α-Pr from references [202, 214, 248, 249, 256]. 66

Figure 29. Heat capacity of Nd (references [199, 200, 244] and Equation 61 through Equation 63 from [7]). 69

Figure 30. Thermal expansion of α-Nd. "a" and "c" are single-direction expansions in the *a* and *c* directions, based on values calculated from Equation 64 and Equation 65 using a reference temperature of 300 K. The "polycrystalline" value is a weighted average of the single-direction values. 71

Figure 31. Molar volumes and densities of α-Nd (curves) and β-Nd (squares) (Equation 66 and reference [193]). 72

Figure 32. Thermal conductivity of Nd [95, 199, 200, 211, 214, 248, 249, 259, 260]. 74

Figure 33. Heat capacities of solid Zr phases (IAEA data calculated using Equation 67 and Equation 68). 76

Figure 34. Thermal expansion of polycrystalline Zr, calculated from Equation 69 and Equation 70. 77

Figure 35. Thermal conductivity of Zr (Equation 74, reference [272]). 79

Figure 36. U-Np phase diagram proposed by Mardon and Pearce (re-drawn from [293]). 82

Figure 37. Thermal expansion of individual lattice parameters of Np-14.9 wt% U (solid lines), with β-Np lattice parameters for comparison (dotted lines) (after [292 Fig. 4]). 83

Figure 38. Room-temperature densities of U-Np alloys from pycnometry (re-drawn from [292 Figure 2]). Although Mardon and Pearce did not identify the phases involved, their phase diagram shows that the three room-temperature phases are (β-Np), δ-(U,Np), and (α-U). 84

Figure 39. Calculated U-Am phase diagram proposed by Perron et al. (re-drawn from [301]) 85

Figure 40. Np-Pu phase diagram of Sheldon and Peterson (re-drawn from [309]). 88

Figure 41. Electrical resistivity of Pu and Np-Pu alloys (after [314 (Figure 2.9)], with lower-temperature data not shown). Data for each material is expressed relative to R0, the resistivity of the material at 273 K. Numbers next to curves indicate compositions in at% Np. 90

Figure 42. Thermal conductivities (blue squares) and electrical resistivities (red diamonds) from Olsen and Elliott [313]. 91

Figure 43. Np-Am phase diagram calculated by Ogawa [73, 316]. Red arrows show compositions corresponding to experimental data. 93

Figure 44. Lattice parameters of (β-Am, δ-Pu) solid solutions [319, 325]. 95

Figure 45. Experimentally determined Pu-Am phase diagram according to Ellinger et al. [318, 319]. α, β, γ, δ, δ' and ε indicate Pu solid solution phases. Although this phase diagram is based on the most thoroughly documented experimental study of the Pu-Am system to date, it is no longer generally accepted. 96

Figure 46. Experimentally determined Pu-Am phase diagram according to Shushakov et al. [320]. α, β, γ, δ, δ' and ε indicate Pu phases. 96

Figure 47. Pu-Am phase diagram of Okamoto [330], which combines the experimental data of Ellinger et al. [319] with modeling by Ogawa [73]. α, β, γ, δ, δ' and ε indicate Pu phases 97

Figure 48. Calculated Pu-Am phase diagram of Gotcu-Freis et al. [321], which shows immiscibility of ε-Pu and γ-Am solid solutions. α, β, γ, δ, δ' and ε indicate Pu solid solution phases. 97

Figure 49. Calculated Pu-Am phase diagram of Turchi et al. [322], which shows a continuous solid solution between ε-Pu and γ-Am. This phase diagram has two "β+δ" fields because of a small miscibility gap in the (δ, β-Am) solid solution. α, β, γ, δ, δ' and ε indicate Pu solid solution phases. 98

Figure 50. Thermal expansion of Am-stabilized δ-Pu alloys based on changes in the *a* lattice parameter from high-temperature X-ray diffraction (re-drawn from [320 (Figure 2)]). Numbers next to the curves indicate percentages of Am in the alloys. 99

Figure 51. Isothermal sections calculated by Ogawa [73]. 100

Figure 52. Isothermal section calculated by Kurata [295, 300]. 101

Figure 53. Lattice spacings for (β-La, γ-Ce) solid solutions. Blue symbols indicate values summarized by Gschneidner and Calderwood [194], red symbols indicate values from Scott et al. [335] 104

Figure 54. La-Ce phase diagram after Gschneidner and Calderwood [194] with data from Bulanova et al. [336] (blue crosses) and equilibrium β-Ce to γ-Ce transformation temperature from Gschneidner and Pecharsky [240] (green circle). 104

Figure 55. Heat capacity of a La-Ce alloy with 50 at% La, estimated using the Kopp-Neumann Law and elemental heat capacities from the equations in Sections 2.5.3 and 2.6.3 of this handbook. Heat capacities of La and Ce are included for comparison. Colors indicate compositions and line types (dots, etc.) indicate phases. The fcc alloy is a solid solution between β-La and γ-Ce. 105

Figure 56. Densities of La-Ce liquids calculated using Equation 75 and Table 16. 106

Figure 57. Hypothetical La-Pr phase diagram (based on reference [350] with phase-transformation temperatures adjusted slightly to match the recommendations in Sections 2.5.2.2 and 2.7.2.2) 108

Figure 58. Densities of La-Pr liquids calculated using Equation 76 and Table 17. Solid lines show data from reference [351]; dotted lines show data from reference [340] 110

Figure 59. Suggested La-Nd phase diagrams. Red symbols represent data from Wu et al. [353]: plus symbols are (β-La), x symbols are (α-Nd), and superimposed symbols indicate that both phases were identified. Black lines are phase diagram suggested by Gschneidner

and Calderwood [194]. Green lines are from the calculated phase diagram of Yang et al. [354] and show only areas where the phase diagrams differ. 112

Figure 60. Densities of La-Nd liquids calculated using Equation 77 and Table 18 (after [340]). 114

Figure 61. Ce-Pr phase diagram after Gschneidner and Calderwood [194], with phase-transformation temperatures for Ce and Pr from Sections 2.6.2.2 and 2.7.2.2. The green dot is the most recent value of the equilibrium transition temperature between β-Ce and γ–Ce. 116

Figure 62. Proposed Ce-Nd phase diagrams. Dashed black lines are a tentative phase diagram suggested by Moffatt [364] and reproduced by Okamoto [350]. Dashed orange lines are sub-solidus phase boundaries calculated by Cacciamani et al. [369]. Symbols are experimental data from Speight et al. [361] (red; + indicates an alloy with reported fcc lattice parameters, * indicates an alloy with reported dhcp lattice parameters), Keiser [362] (green; x symbols indicate boundaries of the two-phase region), and Hachimi et al. [363] (blue; open circle indicates an alloy with predominantly fcc structure, filled circle indicates an alloy with dhcp structure). Liquidus temperatures in all of the proposed phase diagrams are identical. 118

Figure 63. Pr-Nd phase diagram after [373], with phase-transformation temperatures for La and Nd adjusted slightly for consistency with recommendations in Sections 2.7.2.2 and 2.8.2.2. 120

Figure 64. Heat capacity of a Pr-Nd alloy with 50 at% Pr, estimated using the Kopp-Neumann Law with heat capacities of Pr and Nd (Sections 2.7.3 and 2.8.3). Heat capacities of pure Pr and Nd are included for comparison. Colors indicate compositions, and line types (dots, etc.) indicate phases. The dhcp alloy is a solid solution of α-Pr and α-Nd, and the bcc alloy is a solid solution of β-Pr and β-Nd. 121

Figure 65. Tentative U-La phase diagram drawn for this Handbook based on the work of Okamoto [385], with experimental data from Haefling and Daane [381] (red "+" symbols), Rough and Bauer [380] (red squares), and Shoji et al. [382] (green circles). 123

Figure 66. U-Ce phase diagram after Gschneidner [207 Figure 120]. Colored symbols indicate phase boundaries from Haefling and Daane [381] (red "+" symbols), Rough and Bauer [380] (red squares), and Shoji et al. [382] (green circles). 124

Figure 67. Tentative partial U-Pr phase diagram drawn for this handbook, with experimental data from Haefling and Daane ([381], red "+" symbols) and Rough and Bauer ([380], red squares). Shapes of phase boundaries were assumed to be analogous to those in the U-Ce system. 126

Figure 68. Tentative partial U-Nd phase diagram based on that of Parnell et al. [392], displaying only the temperature range for which there is experimental data. Red "+" symbols indicate data from Haefling and Daane [381]. Red squares indicate data from Rough and Bauer [380]. 127

Figure 69. Pu-La phase diagram of Ellinger et al. (re-drawn from [400]). 129

Figure 70. Pu-Ce phase diagram of Ellinger et al. (re-drawn from [404]). 132

Figure 71. Pu-Ce phase diagram of Selle et al. (re-drawn from [405]). 133

Figure 72. Composite Pu-Ce phase diagram (re-drawn from Okamoto [411]). 133

Figure 73. Lattice parameters of δ-Pu alloys from X-ray diffraction data (Equation 78 and Table 20). 135

Figure 74. Linear thermal expansion from Equation 78, Equation 79, and Table 20, normalized to length at 370°C. 136

Figure 75. Coefficients of thermal expansion, Ce-stabilized δ-Pu alloys [413, 414]. The dashed line represents the "best fit" estimate of Goldberg et al. [414]. 138

Figure 76. Coefficient of thermal expansion of ε-Pu solid solutions in Pu-Ce alloys as a function of composition (re-drawn from [414 (Figure 7)]). 138

Figure 77. Densities of liquid Pu-Ce alloys in g/cm^3 (Equation 80 and Equation 81). 139

Figure 78. Change in length of Pu-Ce alloys associated with the transition from δ-Pu to ε-Pu structures as a function of composition [414 (Figure 6)]. 140

Figure 79. Pu-Pr phase diagram of Kutaitsev et al. (re-drawn from [419]). 142

Figure 80. Pu-Pr phase diagram of Ellinger et al. (re-drawn from [420]). 143

Figure 81. Pu-Nd phase diagram of Kutaitsev et al. [419]. 145

Figure 82. Pu-Nd phase diagram after Ellinger et al. [408, 420]. 146

Figure 83. Tentative Np-Zr phase diagram proposed by Gibson and Haire [425]. Colored symbols show data from Table 23. Red symbols are data from Gibson and Haire [426, 427]; blue symbols are data from Rodríguez et al. [424]. Note that this phase diagram expresses compositions in atomic % Zr. 150

Figure 84. Tentative Np-Zr phase diagram proposed by Rodríguez et al. [424], showing only temperatures from 100 to 1000°C. Colored symbols are as in Figure 83. Note that this phase diagram expresses compositions in weight percent Zr. 151

Figure 85. Calculated Am-Zr phase diagram (after [295]). 152

Figure 86. La-Zr phase diagram of Mattern et al. [437] 154

Figure 87. Commonly reproduced Ce-Zr phase diagram suggested by Moffatt [444], based on the assumption that the Ce-Zr and Ce-Ti phase diagrams are similar (redrawn from [447]). This diagram has been recently superseded by the new phase diagram of Mattern et al. (Figure 88). 156

Figure 88. Newer Ce-Zr phase diagram based on new experimental data and thermodynamic modeling (after Mattern et al. [441]). Solid lines indicate areas with new data. 157

Figure 89. Nd-Zr phase diagram after Mattern et al. [452]. Solid lines indicate areas with new data. 160

TABLES

Table 1. Contents of both volumes of the Handbook organized by material group. References are to sections in this document unless otherwise noted. Reference [5] is Part 1 of this Handbook. 2

Table 2. Contents of Handbook organized by composition. . References are to sections in this document unless otherwise noted. Reference [5] is Part 1 of this Handbook. 3

Table 3. Contents of Handbook organized by alloy name. All references are to Part 1 of this Handbook. 5

Table 4. Coefficients of thermal expansion for polycrystalline Np. 22

Table 5. Onset temperatures of solid-state phase transitions in high-purity Pu, °C. 29

Table 6. Enthalpies of solid-state transformations in Pu. Samples are the same as in Table 5. Values are assumed to be measured during heating unless indicated in the notes. Units vary between references. 30

Table 7. Thermal expansion coefficients (10^{-6}/K) of solid and liquid Pu [55, 98, 148]. 35

Table 8. Mean linear coefficients of thermal expansion along single directions for anisotropic Pu phases [98]. 35

Table 9. Lattice parameters, unit-cell volumes, and calculated densities for Pu phases. 36

Table 10. Coefficients of thermal expansion for La. Coefficients with ranges of temperatures are averages across the temperature ranges. 49

Table 11. Coefficients of thermal expansion for γ-Ce (single crystals and polycrystals). 57

Table 12. Coefficients of thermal expansion for α-Pr. 63

Table 13. Coefficients of thermal expansion for α-Nd. 70

Table 14. Electrical resistivity and thermal conductivity of Np-Pu alloys with the (α-Pu) structure at 300 K. Resistivity data are from Olsen and Elliott [313]; conductivity values were calculated assuming a Lorenz number of 3.15×10^{-8} WΩK^{-2} 91

Table 15. Electrical resistivities and thermal conductivity of Pu-Am alloys at 300 K. Electrical resistivities were read from reference [325 (Figure 4)]. Thermal conductivities were calculated using the Wiedemann-Franz Law with the recommended value of the Lorenz number for Pu (3.15×10^{-8} WΩK^{-2}) 99

Table 16. Coefficients for calculating densities of La-Ce liquids (after [340]). 106

Table 17. Coefficients for calculating densities of La-Pr liquids 109

Table 18. Coefficients for calculating densities of La-Nd liquids (after [340]). 113

Table 19. Principal linear thermal expansion coefficients for Pu-1Ce (at%) from 133 to 202°C [126, 150]. α_1, α_2, and α_3 are mutually orthogonal, with α_1 parallel to the direction of maximum thermal expansion, α_2 parallel to the *b* crystallographic axis, and α_3 approximately perpendicular to the (101) crystallographic plane. α is the average of α_1, α_2, and α_3. φ is the angle between α_1 and the *b* crystallographic axis measured in the obtuse angle β and has a value of 38° 134

Table 20. Coefficients for calculating thermal expansion of Pu-Ce alloys using Equation 78 [413]. 135

Table 21. Average coefficients of linear thermal expansion for Ce-stablized δ-Pu alloys [413]. 137

Table 22. Lattice parameters of arc-melted La and Am-La alloys [421]. 147

Table 23. Phase-transformation temperatures in Np-Zr alloys. 148

Table 24. Phase-transformation enthalpies in Np-Zr alloys [426]. 149

Table 25. Phase transformations in the Nd-Zr system [451 (Table III), 452 (Table 3), 453 (Figure 4)]. Subscripts in the data from Mattern et al. indicate the calculated composition (at% Zr) in each phase 159

EQUATIONS

Equation 1. Heat capacity of α-U [7] 10
Equation 2. Heat capacity of β-U [7] 10
Equation 3. Heat capacity of γ-U [7] 10
Equation 4. Heat capacity of liquid U [7] 11
Equation 5. Heat capacity of U gas from 298.15 to 1800 K [7] 11
Equation 6. Heat capacity of U gas from 1800 to 4000 K [7] 11
Equation 7. Mean thermal expansion of polycrystalline α-U according to Touloukian et al. [55] 13
Equation 8. Measured thermal expansion of polycrystalline α-U according to Basak et al. [56] 13
Equation 9. Mean thermal expansion of polycrystalline β-U [8 Table 8] 13
Equation 10. Provisional values for mean thermal expansion of polycrystalline γ-U according to Touloukian et al. [55] 13
Equation 11. Mean thermal expansion of polycrystalline γ-U according to Basak et al. [56] 13
Equation 12. Density of solid U as a function of thermal expansion [8] 14
Equation 13. Density of liquid U [8, 21] 14
Equation 14. Thermal conductivity of U from 255 to 1173 K according to Kim et al. [19] 16
Equation 15. Thermal conductivity of U from 293 to 1405 K according to the IAEA [21] 16
Equation 16. Thermal conductivity of U from 298 to 823 K according to Kaity et al. [20] 16
Equation 17. Heat capacity of α-Np [7] 19
Equation 18. Heat capacity of α-Pu ([7] with temperature range from [145]) 31
Equation 19. Heat capacity of β-Pu [7, 69, 145] 31
Equation 20. Heat capacity of γ-Pu [7, 69, 145] 31
Equation 21. Heat capacity of δ-Pu [7, 69, 145] 31
Equation 22. Heat capacity of δ′-Pu [7, 69] 31
Equation 23. Heat capacity of ε-Pu [7, 69] 31
Equation 24. Heat capacity of liquid Pu [7] 32
Equation 25. Heat capacity of Pu gas from 298.15 to 1400 K [7] 33
Equation 26. Heat capacity of Pu gas from 1400 to 4000 K [7] 33
Equation 27. Thermal expansion of α-Pu [55] 34
Equation 28. Thermal conductivity of α-Pu from 294 to 394 K according to Alexander and Wood [104] 37
Equation 29. Thermal conductivity of β-Pu from 415 to 490 K according to Alexander and Wood [104] 38
Equation 30. Thermal conductivity of γ-Pu from 491 to 595 K according to Alexander and Wood [104] 38

Equation 31. Thermal conductivity of δ-Pu from 602 to 696 K according to Alexander and Wood [104] 38

Equation 32. Thermal conductivity of ε-Pu from 750 to 822 K according to Alexander and Wood [104] 38

Equation 33. Approximate thermal conductivity of Pu from 400 to 820 K according to Alexander and Wood [104] 38

Equation 34. Lattice parameter of α-Am parallel to the *a* crystallographic direction [163] 41

Equation 35. Lattice parameter of α-Am parallel to the *c* crystallographic direction [163] 41

Equation 36. Thermal expansion of Am [8] 42

Equation 37. Heat capacity of α-La [7] 46

Equation 38. Heat capacity of β-La (after [7], but with the last coefficient multiplied by T rather than T^2 for consistency with data from Berg et al. [196]) 46

Equation 39. Heat capacity of γ-La [7] 46

Equation 40. Heat capacity of La liquid (C_p in J/mol-K) [7] 46

Equation 41. *a* lattice parameter of α-La between 20 and 293°C [193 Table IV] 47

Equation 42. *c* lattice parameter of α-La between 20 and 293°C [193 Table IV] 47

Equation 43. Lattice parameter of β-La between 20 and 598°C [193 Table IV] 47

Equation 44. Molar volume of α-La between 20 and 293°C [193 Table IV] 49

Equation 45. Molar volume of β-La between 20 and 598°C [193 Table IV] 49

Equation 46. Heat capacity of Ce liquid between 1400 and 1700 K [245] 54

Equation 47. Heat capacity of Ce liquid between 1700 and 2500 K [245] 54

Equation 48. Heat capacity of γ-Ce between 373 and 998 K [7] 54

Equation 49. Heat capacity of δ-Ce between 998 and 1070 K [7] 54

Equation 50. Heat capacity of Ce liquid between 1070 and 2500 K [7] 54

Equation 51. Heat capacity of Ce liquid above 2500 K [7] 55

Equation 52. Values of the *a* lattice parameter of γ-Ce between 20 and 619 °C [193 Table IV] 55

Equation 53. Density of γ-Ce between 20 and 619°C [193 (Table IV)] 57

Equation 54. Heat capacity of α-Pr [7] 61

Equation 55. Heat capacity of β-Pr [7] 61

Equation 56. Heat capacity of Pr liquid [7] 61

Equation 57. *a* lattice parameter of α-Pr between 20 and 449°C [193 Table IV] 62

Equation 58. *c* lattice parameter of α-Pr between 20 and 449°C [193 Table IV] 62

Equation 59. Molar volume of α-Pr between 20 and 293 °C [193 (Table IV)] 64

Equation 60. Thermal diffusivity of liquid Pr [254] 66

Equation 61. Heat capacity of α-Nd [7] 68

Equation 62. Heat capacity of β-Nd (in J/mol-K) [7] 68

Equation 63. Heat capacity of Nd liquid (in J/mol-K) [7] 68
Equation 64. *a* lattice parameter of α-Nd 20 and 969°C [193 Table IV] 69
Equation 65. *c* lattice parameter of α-Nd between 20 and 969°C [193 Table IV] 69
Equation 66. Molar volume of α-Nd between 20 and 696°C [193 Table IV] 72
Equation 67. Heat capacity of α-Zr from 298 to 1100 K [21] 76
Equation 68. C_p of β-Zr from 1100 to 2128 K [21] 76
Equation 69. Thermal expansion of α-Zr [271] 77
Equation 70. Thermal expansion of β-Zr [271] 77
Equation 71. Mean linear thermal expansion coefficient for polycrystalline α-Zr from 293 to 1130 K [271] 78
Equation 72. Mean linear thermal expansion coefficient for polycrystalline β-Zr (α in units of 10^{-6}/K, T in K, T from 1200 to 1830 K) [271] 78
Equation 73. Density of solid Zr from 298 to 2128 K [21] 78
Equation 74. Approximate thermal conductivity of Zr according to Fink and Leibowitz [272] 79
Equation 75. Densities of La-Ce liquids as functions of temperature (after [340]) 106
Equation 76. Density of La-Pr alloys (after [340, 351]) 108
Equation 77. Density of La-Nd alloys (after [340]) 113
Equation 78. Lattice parameter (for X-ray diffraction data) or sample length (for dilatometer data) for Pu-Ce alloys, to be used with coefficients from Table 20 [413] 134
Equation 79. Linear thermal expansion of Ce-stabilized δ-Pu, referenced to 370°C 136
Equation 80. Density of a liquid Pu-Ce alloy with 4.8 at% Ce [417] 139
Equation 81. Density of a liquid Pu-Ce alloy with 75 at% Ce [417] 139

ACRONYMS

AFC	Advanced Fuels Campaign
ANL	Argonne National Laboratory
bcc	Body-centered cubic (a crystal structure)
CALPHAD	CALculation of PHAse Diagrams
CEA	Commissariat a l'Energie Atomique (French Atomic Energy Commission)
dhcp	Double hexagonally close packed (a crystal structure)
DFT	Density Functional Theory
DOE	U. S. Department of Energy
DSC	Differential scanning calorimetry
DTA	Differential thermal analysis
fcc	Face-centered cubic (a crystal structure)
FCRD	Fuel Cycle Research and Development
FIB/SEM	Focused ion beam/scanning electron microscope
hcp	Hexagonally close packed (a crystal structure)
IAEA	International Atomic Energy Agency
INL	Idaho National Laboratory
NIST-JANAF	National Institute of Standards and Technology – Joint Army, Navy, Air Force
OECD/NEA	Organisation for Economic Co-Operation and Development/Nuclear Energy Agency
SI	Systeme International d'Unites (French) (International System of Units)
TMA	Thermomechanical analysis

INTENTIONALLY BLANK

Metallic Fuels Handbook, Part 2: Elements and Alloys not Based on U-Zr, Pu-Zr, U-Pu, or U-Pu-Zr

1. INTRODUCTION

Transmutation of minor actinides such as Np, Am, and Cm in spent nuclear fuel is of international interest because of its potential for reducing the long-term health and safety hazards caused by the radioactivity of the spent fuel. For this reason, the DOE Fuel Cycle Research & Development (FCRD) Advanced Fuels Campaign (AFC) has been performing research on nuclear fuel technologies that could be used in conjunction with a future actinide transmutation mission. One important approach to transmutation involves incorporating the minor actinides into U-Pu-Zr alloys, which can be used as fuel in fast reactors. U-Pu-Zr alloys are well suited for electrolytic refining, which leads to retention of rare-earth fission products such as La, Ce, Pr, and Nd. It is, therefore, important to understand not only the properties of U-Pu-Zr alloys but also those of U-Pu-Zr alloys with concentrations of minor actinides (Np, Am) and rare-earth elements (La, Ce, Pr, and Nd) similar to those in reprocessed fuel.

The Metallic Fuels Handbook reviews and summarizes the available data on phases, heat capacities, thermal expansion, and thermal conductivity of elements and alloys in the U-Pu-Zr-Np-Am-La-Ce-Pr-Nd system. Many sections are revisions and updates of material in previous versions of the Handbook [1-4]. New material in this revision involves primarily additional details about U-Zr and U-Pu-Zr alloys, including some information about mechanical properties, vapor pressures, and thermodynamic properties. In addition to presenting information about materials properties, this handbook emphasizes data assessments and provides information about how well each property is known and how much variation exists between measurements. Although the Handbook includes some results from models, its primary focus is experimental data.

Because of its size, the Handbook has been split into two parts. Part 1 (reference [5]) contains introductory material and information about alloys in the U-Pu-Zr system, including those with rare-earth elements and minor actinides. Part 2 (this document) contains information about elements and about alloys that are part of the U-Pu-Zr-Np-Am-La-Ce-Pr-Nd system but not the U-Pu-Zr system. Three tables have been provided at the beginning of this document to help readers find the information they are looking for in the Handbook.

As in past years, the focus of the Handbook is the U-Pu-Zr system, which is defined for purposes of this Handbook as consisting of U-Zr, Pu-Zr, and U-Pu-Zr alloys, including those with minor actinides (Np, Am, and Cm), rare-earth elements (La, Ce, Pr, Nd, and Gd), and Y. To emphasize this focus, the first elements to be listed for alloys that are part of this system are U, Pu, and Zr, followed by the minor actinides, rare-earth elements, and Y. This scheme is generally consistent with that used by the METAPHIX Programme.

The Handbook is intended to serve three audiences. One audience is researchers, who may find it useful to know what has been measured, where it has been published, and what kinds of information are needed. A second audience is modelers, who need a concise summary of information about specific properties and the accuracy with which they are known. The third audience is project managers, who need information to help them identify gaps in knowledge. These audiences have different needs and interests, and the Handbook is a compromise intended to be useful to all of them. It includes extensive references and summaries of research results and needs, but is not intended to be a complete presentation of the original data. The Handbook also includes numerous graphs and, where available, equations that provide convenient approximations to materials properties for modelers. It is important to understand that many of the equations provided in the Handbook were developed by fitting polynomials to data and have no

physical basis; while they can be used with caution for design studies, fuel modelers should refer to the original experimental data in the references cited by the handbook to develop or validate their own equations and/or models. Although the Handbook includes some citations to research involving development of models, its primary focus is experimental data. Although the Handbook is intended to provide a comprehensive overview and assessment of the data, all users of the Handbook are expected to consult the original references for details not presented here.

The Handbook includes information about properties of elements and alloys of interest for FCRD fuels. It is not intended to be a comprehensive guide to all properties and materials. In particular, it does not include fuel types not specifically intended for transmutation in a fast neutron spectrum (e.g., fuels for light-water and high-conversion water reactors), properties not relevant to fuels (e.g., measurements at high pressures), issues involved in materials supplies and fuel fabrication, alloys that include elements other than U, Np, Pu, Am, La, Ce, Pr, Nd and Zr (with the exception of low concentrations of Y, Cm, and Gd in alloys investigated by the METAPHIX Programme) and (to the extent that they can be avoided) sample-specific properties such as microstructures whose values depend on fabrication parameters, characteristics, or histories of specific samples.

The metals and alloys in this edition of the Handbook are uniquely difficult to study for a number of reasons. Experimental designs may be constrained by radioactive and other hazards of some of the materials. Kinetics of phase transformations are commonly sluggish, and it is highly unlikely that all of the samples in previous research had equilibrium phases and microstructures. Thermal cycling effects (changes in sample characteristics during heating that are not fully reversed during cooling) are commonly reported and may be significant. Careful control of impurities (particularly oxygen) during sample fabrication and data collection is both crucial and difficult, and oxygen contents below 100 ppm in samples may significantly affect thermophysical properties. Many of the measurements presented in this Handbook were made before 1980, and documentation of sample compositions and experimental methods may be incomplete. For all of these reasons, differences between measured values for similar alloys are commonly far larger than the estimated errors for individual measurements. Further research on well-characterized materials with careful control of impurities is needed for almost all of the alloys and properties presented here.

Table 1. Contents of both volumes of the Handbook organized by material group. References are to sections in this document unless otherwise noted. Reference [5] is Part 1 of this Handbook.

Material	Handbook Section
U-Pu-Zr system, including U-Pu, U-Zr, Pu, Zr, and U-Pu-Zr alloys with and without minor actinides (Np, Am, Cm), rare-earth elements (La, Ce, Pr, Nd, Gd) and Y	Reference [5] Section 2
Alloys based on U-Zr, including U-Zr and U-Zr alloys with minor actinides (Np, Am), rare-earth elements (La, Ce, Pr, Nd), and Y	Reference [5] Section 2.1
Alloys based on Pu-Zr, including Pu-Zr and Pu-Zr alloys with minor actinides (Np, Am)	Reference [5] Section 2.2
Alloys based on U-Pu, including U-Pu and U-Pu alloys with minor actinides (Np, Am)	Reference [5] Section 2.3
Alloys based on U-Pu-Zr, including those with minor actinides (Np, Am, Cm), rare-earth elements (La, Ce, Pr, Nd, Gd), and Y	Reference [5] Section 2.4
U-Pu-Zr	Reference [5] Section 2.4.1
U-Pu-Zr alloys with minor actinides (Np, Am, Cm), sorted by increasing weight percentage of Zr	Reference [5] Section 2.4.2
U-Pu-Zr alloys with rare-earth elements (La, Ce, Pr, Nd)	Reference [5] Section 2.4.3

Table 1. (continued).

Material	Handbook Section
U-Pu-Zr alloys with minor actinides (Np, Am) and rare-earth elements (La, Ce, Pr, Nd), sorted by increasing weight percentage of Zr	Reference [5] Section 2.4.4
U-Pu-Zr alloys with minor actinides (Np, Am, Cm), rare-earth elements (La, Ce, Pr, Nd, Gd), and Y	Reference [5] Section 2.4.5
Elements (U, Np, Pu, Am, La, Ce, Pr, Nd, and Zr)	Section 2
Alloys containing only actinides (U, Np, Pu, Am), except those based on U-Pu	Section 3
Alloys containing only rare-earth elements (La, Ce, Pr, Nd) and mischmetals	Section 4
Binary alloys of an actinide (U, Np, Pu, Am) and a rare-earth element (La, Ce, Pr, Nd)	Section 5
Binary alloys of a minor actinide (Np, Am) and Zr	Section 6
Binary alloys of a rare-earth element (La, Ce, Pr, Nd) and Zr	Section 7

Table 2. Contents of Handbook organized by composition. . References are to sections in this document unless otherwise noted. Reference [5] is Part 1 of this Handbook.

Element(s)	Handbook Section
U	Section 2.1
Np	Section 2.2
Pu	Section 2.3
Am	Section 2.4
La	Section 2.5
Ce	Section 2.6
Pr	Section 2.7
Nd	Section 2.8
Zr	Section 2.9
U-La	Section 5.1
U-Ce	Section 5.2
U-Pr	Section 5.3
U-Nd	Section 5.4
U-Np	Section 3.1
U-Pu	Reference [5] Section 2.3.1
U-Am	Section 3.2
U-Zr	Reference [5] Section 2.1.1
Np-La	Section 5.5
Np-Ce	Section 5.6
Np-Pr	Section 5.7
Np-Nd	Section 5.8
Np-Pu	Section 3.3

Table 2. (continued).

Element(s)	Handbook Section
Np-Am	Section 3.4
Np-Zr	Section 6.1
Pu-La	Section 5.9
Pu-Ce	Section 5.10
Pu-Pr	Section 5.11
Pu-Nd	Section 5.12
Pu-Am	Section 3.5
Pu-Zr	Reference [5] Section 2.2.1
Am-La	Section 5.13
Am-Ce	Section 5.14
Am-Zr	Section 6.2
La-Ce	Section 4.1
La-Pr	Section 4.2
La-Nd	Section 4.3
La-Zr	Section 7.1
Ce-Pr	Section 4.4
Ce-Nd	Section 4.5
Ce-Zr	Section 7.2
Pr-Nd	Section 4.6
Pr-Zr	Section 7.3
Nd-Zr	Section 7.4
U-Pu-Np	Reference [5] Section 2.3.2
U-Pu-Am	Reference [5] Section 2.3.3
U-Pu-Zr	Reference [5] Section 2.4.1
U-Zr-Ce	Reference [5] Section 2.1.3
U-Zr-Np	Reference [5] Section 2.1.2
Np-Pu-Am	Section 3.6
Pu-Zr-Np	Reference [5] Section 2.2.2
Pu-Zr-Am	Reference [5] Section 2.2.3
U-Pu-Zr-Am	Reference [5] Sections 2.4.2.1 and 2.4.2.6
Pu-Zr-Np-Am	Reference [5] Section 2.2.4
U-Pu-Zr-Np-Am	Reference [5] Sections 2.4.2.2 through 2.4.2.5, 2.4.2.7, and 2.4.2.8
U-Zr-Ce-Nd-Y	Reference [5] Section 2.1.5
U-Pu-Zr-Np-Ce-Nd	Reference [5] Section 2.4.4.3
U-Zr-La-Ce-Pr-Nd	Reference [5] Section 2.1.4
U-Pu-Zr-La-Ce-Pr-Nd	Reference [5]9 Section 2.4.3.1

Table 2. (continued).

Element(s)	Handbook Section
U-Pu-Zr-Np-Am-Ce-Nd	Reference [5] Section 2.4.4.1 and 2.4.4.2
U-Pu-Zr-Np-Am-Ce-Nd-Y	Reference [5] Section 2.4.5.1
U-Pu-Zr-Np-Am-La-Ce-Pr-Nd	Reference [5] Section 2.4.4.4 through 2.4.4.9
U-Pu-Zr-Np-Am-Ce-Nd-Gd-Y	Reference [5] Section 2.4.5.2 and 2.4.5.3
Mischmetals (rare-earth alloys that include La, Ce, Pr, and Nd)	Section 4.7

Table 3. Contents of Handbook organized by alloy name. All references are to Part 1 of this Handbook.

Name	Nominal composition (wt%)	Handbook Section
FCRD DOE1	U-29Pu-30Zr-2Np-4Am	Reference [5] Section 2.4.2.7
FCRD DOE2	Pu-40Zr-12Am	Reference [5] Section 2.2.3
FCRD AFC1-MB	Pu-40Zr-10Np	Reference [5] Section 2.2.2
FCRD AFC1-MC	Pu-40Zr-12Am	Reference [5] Section 2.2.3
FCRD AFC1-MD	Pu-40Zr-10Np-10Am	Reference [5] Section 2.2.4
FCRD AFC1-MF	U-28Pu-30Zr-7Am	Reference [5] Section 2.4.2.6
FCRD AFC1-MG	U-34Pu-20Zr-2Np-4Am	Reference [5] Section 2.4.2.5
FCRD-AFC1-MH	U-25Pu-40Zr-2Np-3Am	Reference [5] Section 2.4.2.8
FCRD AFC1-MI and MJ	U-29Pu-30Zr-2Np-4Am	Reference [5] Section 2.4.2.7
FCRD AFC2-A1	U-20Pu-15Zr-2Np-3Am	Reference [5] Section 2.4.2.3
FCRD AFC2-A2	U-20Pu-15Zr-2Np-3Am-1RE[a]	Reference [5] Section 2.4.4.4
FCRD AFC2-A3	U-20Pu-15Zr-2Np-3Am-1.5RE[a]	Reference [5] Section 2.4.4.5
FCRD AFC2-A4	U-30Pu-20Zr-3Np-5Am-1.5RE[a]	Reference [5] Section 2.4.4.8
FCRD AFC2-A5	U-30Pu-20Zr-3Np-5Am-1RE[1]	Reference [5] Section 2.4.4.7
FCRD AFC2-A6	U-30Pu-20Zr-3Np-5Am	Reference [5] Section 2.4.2.4
FCRD AFC2-A7	U-20Pu-15Zr-2Np-3Am-8RE[a]	Reference [5] Section 2.4.4.6
FCRD AFC2-A8	U-30Pu-20Zr-3Np-5Am-8RE[a]	Reference [5] Section 2.4.4.9
FCRD AFC2-B1	U-30Pu-20Zr	Reference [5] Section 2.4.1
FCRD AFC2-B2	U-55Pu-20Zr	Reference [5] Section 2.4.1
FCRD AFC2-B3	U-20Pu-45Zr	Reference [5] Section 2.4.1
FCRD AFC2-B4	U-20Pu-15Zr-1.5RE[a]	Reference [5] Section 2.4.3.1
FCRD AFC2-B7	U-24Pu-15Zr	Reference [5] Section 2.4.1
FCRD AFC2-B8	U-36.5Pu-20Zr	Reference [5] Section 2.4.1
FCRD AFC2-E3 and E5	U-20Pu-10Zr-2Np-3Am	Reference [5] Section 2.4.2.2
METAPHIX CR1	U-5.2Ce-16.1Nd-15.0Zr-1.0Y	Reference [5] Section 2.1.5
METAPHIX CR6	U-19.3Pu-10.7Zr-9.7Np-3.7Ce-11.6Nd	Reference [5] Section 2.4.4.3
METAPHIX CR10	U-18.3Pu-10.2Zr-9.3Np-4.7Am-3.2Ce-10.2[Nd]	Reference [5] Section 2.4.4.2

Table 3. (continued).

Name	Nominal composition (wt%)	Handbook Section
METAPHIX CR11	U-18Pu-10Zr-1.2Np-0.8Am-0.5Ce-1.4Nd	Reference [5] Section 2.4.4.1
METAPHIX CR12	U-19Pu-10Zr-3Np-2Am-1.2Ce-3.6Nd-0.2Y	Reference [5] Section 2.4.5.1
METAPHIX CR13	U-19.0Pu-10.0Zr	Reference [5] Section 2.4.1
METAPHIX U-19Pu-10Zr-5MA	U-19Pu-10Zr-3.0Np-1.6Am-0.4Cm	Reference [5] Section 2.4.2.9
METAPHIX U-19Pu-10Zr-2MA-2RE	U-19Pu-10Zr-1.2Np-0.6Am-0.2Cm-1.4Nd-0.2Ce-0.2Gd-0.2Y	Reference [5] Section 2.4.5.2
METAPHIX U-19Pu-10Zr-5MA-5RE	U-19Pu-10Zr-3Np-1.6Am-0.4Cm-0.5Ce-3.5Nd-0.5Gd-0.5Y	Reference [5] Section 2.4.5.3
a. RE is a rare-earth alloy whose nominal composition (by weight) is 6La-16Pr-25Ce-53Nd		

2. ELEMENTS (U, Np, Pu, Am, La, Ce, Pr, Nd, and Zr)

2.1 U

2.1.1 Introduction

Uranium has been investigated for decades, and most of its properties are better understood than those of other materials in this Handbook. Uranium has three solid phases (α-U, β-U, and γ-U) that are stable at atmospheric pressure. The crystal structures and lattice parameters of all three phases are well known, although the space group and atomic positions in β-U were only resolved by the use of high-resolution neutron-diffraction data.

The heat capacity of U has been extensively studied, with most measurements originally published between 1947 and 1980 and independent critical reviews of the available data in 1976 and 2010 [6, 7]. Recommended values for the heat capacity of α-U are similar in both reviews. Although both agree that the heat capacities of β-U and liquid U are independent of temperature, their recommended values differ by 5-10%. The reviews also disagree about the possible temperature dependence of the heat capacity of γ-U. The major reason for the differences between the reviews is that the 1976 review [6] used primarily measurements of heat capacity, while the 2010 review [7] also considered measurements of incremental enthalpy, which is more reliable for high-temperature measurements. The recommendations of the 2010 review are presented here and were reprinted in a third major review [8]; recommendations from the 1976 review can be found in a number of sources (e.g., [6, 9, 10]). All three reviews contain extensive citations to the original experimental data.

The low-temperature heat capacity of U was reviewed by Konings and Beneš [7]. More recent information has been published by Krupska et al. [11] and by Kim-Ngan et al. [12].

Heat capacities and a variety of thermodynamic properties have been calculated, with generally good agreement with the experimental literature [13].

The thermal expansion of α-U is highly anisotropic, with increases in length along two of three mutually orthogonal directions and a decrease in length along the third during heating. Numerous measurements of thermal expansion of single crystals have been published, with generally good agreement. The thermal expansion of single crystals of α-U has been modeled, with generally good agreement with the experimental literature [13]. Korn [14] developed ways to calculate the direction of zero thermal expansion and depict it as a three-dimensional surface. Although only a few measurements of thermal expansion of single crystals of β-U

have been published, they are in good agreement. Data on thermal expansion of γ-U are sufficiently rare that it is not possible to meaningfully assess their agreement.

It is commonly assumed that the thermal expansion of a polycrystalline U sample can be predicted from single-crystal data. In practice, however, polycrystalline U samples develop surface roughness, change shape, and increase in volume (and therefore decrease in density) as a result of thermal cycling, presumably because of internal strains from differential expansion of adjacent crystals with different orientations in the sample (e.g., [15-18]). This effect can be large, as shown by a 100% increase in the length of one sample [18]. Consequences of thermal cycling are highly sample-dependent and may be influenced by factors such as grain size, preferred orientation, sample fabrication and processing, and thermal history.

At least 100 measurements of the thermal conductivity of U have been made, with most of them published before 1970. Recommended values in a 2014 review by Kim et al. [19] are in excellent agreement with a 2012 measurement not included in the review [20]. There is also excellent agreement that the thermal conductivity increases by ~0.02 W/m·K between ~290 and 1173 K, a temperature range that includes the α-β phase transition. However, a 2008 compilation of data by the IAEA [21] recommends thermal conductivity values that are 10-20% lower than those recommended by Kim et al. The good agreement between the new measurements and the recommended values of Kim et al. suggests that the Kim et al. review [19] may be a better representation of the actual thermal conductivity than the values in the IAEA tabulation. However, more research is needed to resolve this issue.

Recent efforts to understand the thermal conductivity of U include molecular dynamics modeling to understand the possible role of discrete breathers [22] and detailed consideration of the behavior of solitons during phase transitions [23].

Most of the recent research on pure U involves either modeling (e.g., [24-30]) or studies of deformation mechanisms and corresponding development of microstructures and preferred orientation (e.g., [17, 31-36]). Jacobsen and Velisavljevic recently reported experimental results from high-pressure experiments [37], Chung et al. demonstrated a technique for three-dimensional microstructural characterization using a dual-beam FIB/SEM instrument [38], and Serezhkin et al. used Voronoi-Dirichlet tessellation to analyze crystal structures [39].

Early researchers and fuel developers recognized that the irradiation stability and other properties of U may be influenced by alloying elements such as C, Fe, Al, and Si in concentrations of a few hundred ppm. This recognition led to development of "adjusted uranium" alloys (e.g., [40, 41]).

2.1.2 Phases and Phase Transformations

2.1.2.1 Phases

U has three phases that are stable at atmospheric pressure. With the exception of the space group for β-U, crystal structures and lattice parameters have been known for decades, and there is little variation between reported measurements. The values presented here are based on one of the few new studies since the 1970s and were obtained using Rietveld refinement of data from high-resolution neutron powder diffraction.

The atmospheric-pressure U phases are:

- α-U, orthorhombic (space group *Cmcm* with four atoms per unit cell), a = 2.8539 Å, b = 5.8678 Å, c = 4.9554 Å at 298 K [42]

  α-U has an *A*20 structure with a C-centered orthorhombic unit cell. Each unit cell has four atoms, located at (0, y, ¼), (0, –y, ¾), (½, ½+y, ¼), and (½, ½-y, ¾). The value of the position parameter y is ~0.1025 at room temperature [43-46], and rises to ~0.1058 at ~625°C [45]. Below room temperature, the value of y decreases to a minimum at 43 K then increases at lower temperatures [43]. The structure has been described as distorted hexagonal close packing involving "corrugated" or

"puckered" sheets perpendicular to the *b* axis [9, 45, 47]. The depth of the corrugation increases and the distortion of the hexagonal close packing decreases with increasing values of *y* [45].

Information about local atomic environments, Debye-Waller factors, and the low-temperature charge density wave modulation in α-U can be found in references [48] and [49].

- β-U, tetragonal (space group $P4_2/mnm$ with 30 atoms per unit cell), a = 10.7589 Å, c = 5.6531 Å at 955 K [42]

  Although it has been known for decades that β-U has a tetragonal unit cell containing 30 atoms, it was not possible to distinguish between three candidate space groups based on X-ray diffraction data (e.g., [9, 50]). Because pure β-U cannot be quenched to room temperature, early studies of the crystal structure and lattice parametes of β-U used alloys stabilized by small amounts of elements such as Cr [46]. Lawson et al. eventually determined that the space group of β-U is $P4_2/mnm$ and identified positions of 30 atoms in six crystallographically independent positions in each unit cell using high-temperature, high-resolution neutron diffraction data [42].

- γ-U, bcc (space group $Im\bar{3}m$), a = 3.5335 Å at 1060 K [42]. Although pure γ-U is not retained at room temperature even in splat-cooled samples [11, 51], Summers-Smith suggested that the room-temperature lattice parameter of γ-U is 3.51 kX (3.52 Å) based on extrapolation from a series of U-Zr alloys with the γ–U structure [52].

  γ-U has a body-centered cubic structure [42, 53]. Because this phase cannot be quenched to room-temperature, high-temperature techniques are required to study it.

2.1.2.2 Phase Transformations

Most of the experimental measurements of phase-transformation and melting temperatures in U were made before 1970, and later references are based on new interpretations of the original data. Major reviews include those by Oetting et al. [6] for the IAEA, Ward et al. [54], Grenthe et al. [10] for the OECD/NEA, and Konings and Beneš ([7], with key results repeated in [8]). Recommended transformation temperatures and enthalpies from all of the reviews are similar.

Recommended phase-transformation temperatures and ranges of measured values are [7]:

- α-β, 941±2 K (668 ±2 °C), based on 10 publications with original measurements that range from 933 to 943 K (660 to 670 °C).
- β-γ, 1049±2 K (776±2 °C), based on 9 publications with original measurements that range from 1037 to 1050 K)
- γ-liquid, 1407±2 (based on 7 publications with original measurements, which range from 1401 to 1406 K).

Recommended phase-transformation enthalpies and ranges of measured values are [7]:

- α-β, 2.85±0.15 kJ/mol (based on 6 publications with original measurements that range from 2.63 to 3.26 kJ/mol)
- β-γ, 4.62±0.5 kJ/mol (based on 6 publications with original measurements that range from 4.18 to 4.87 kJ/mol)
- γ-liquid, 8.47±1.00 kJ/mol (based on 6 publications with original measurements that range from 7.03 to 12.1 kJ/mol).

2.1.3 Heat Capacity and Related Properties

2.1.3.1 Standard Thermodynamic Values

The standard entropy of solid U is a CODATA Key Value. The standard entropy of uranium gas and enthalpy of formation of uranium gas are also generally accepted values. They are [7]:

- S^0(298.15 K) = 50.20 ± 0.20 J/mol·K for α-U
- S^0(298.15 K) = 199.79 ± 0.10 J/mol·K for U gas
- $\Delta_f H^0$(298.15 K) = 533 ± 8 kJ/mol for U gas.

2.1.3.2 Heat Capacities of Solid and Liquid Phases

Major reviews and assessments of measurements of the heat capacity of U include those by Oetting et al. [6] as part of an IAEA series on the chemical thermodynamics of actinide elements and compounds and by Konings and Beneš [7] as part of a recent critical review of thermodynamic properties of lanthanide and actinide metals. Grenthe et al. [10] fitted a new polynomial to the heat-capacity data for α-U in the review by Oetting et al. in their review of chemical thermodynamics for NEA/OECD, and Konings et al. [8] followed Konings and Beneš in a recent review of nuclear materials.

Figure 1 shows the heat capacities for solid and liquid U recommended by Oetting et al. [6] and by Konings and Beneš [7]. As shown in the figure, both reviews recommend similar values for the heat capacity of α-U at temperatures above ~300 K. The heat capacity of β-U in reference [7] is almost 10% larger than that in reference [6] (47.12 vs 42.3 J/mol·K), and the heat capacity of liquid U is almost 5% smaller (46.45 vs 48.69 J/mol·K). The average values for the heat capacity of γ-U are similar in both reviews (38.31 J/mol·K in reference [6] and 39.05 J/mol·K in reference [7]), although reference [6] suggests that the heat capacity of this phase is independent of temperature and reference [7] indicates that it is not.

Almost all of the original measurements of the heat capacities and incremental enthalpies of solid and liquid U were originally published between about 1947 and 1980. However, Oetting et al. [6] considered primarily measurements of heat capacity, while Konings and Beneš [7] also considered measurements of incremental enthalpy. In the absence of further experimental data, it seems reasonable to consider the recommendations of Konings and Beneš (Equation 1 through Equation 4) to be the more accurate representation of the heat capacities of solid and liquid U phases. This is because Konings and Beneš considered a larger amount of data collected using a wider variety of measurement techniques, including some techniques that are well-suited to collecting high-temperature data.

More recent research involves calculations of the pressure and temperature dependence of the heat capacity of α-U based on DFT calculations [13] and measurements of heat capacities at temperatures below 3 K [11, 12].

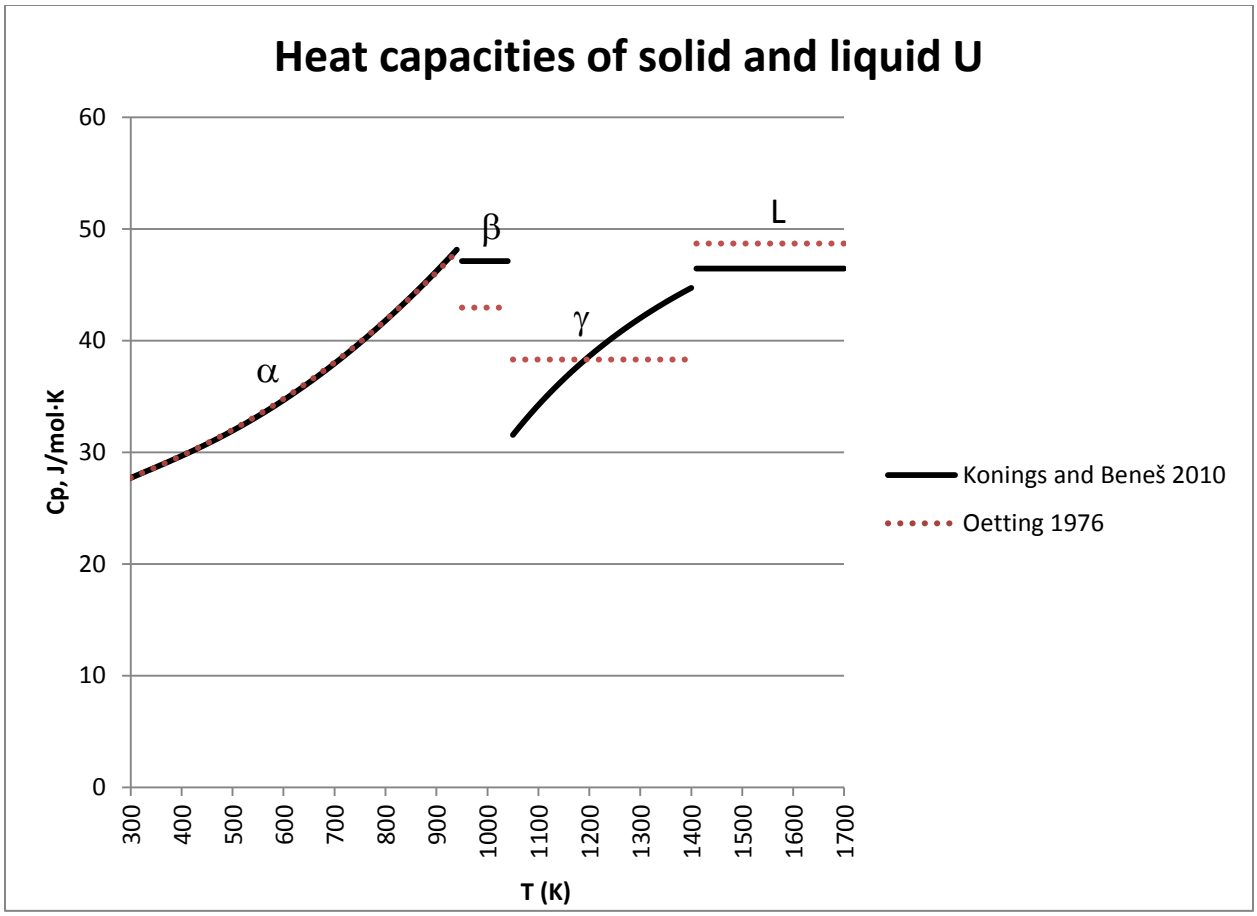

Figure 1. Heat capacities of solid and liquid U. Values from Konings and Beneš [7] (Equation 1, Equation 2, Equation 3, and Equation 4) are preferred.

Equation 1. Heat capacity of α-U [7]

$$C_p = 28.4264 - 6.9587 \times 10^{-3} \times T + 29.8744 \times 10^{-6} \times T^2 - 0.11888 \times 10^6 \times T^{-2}$$

where C_p is constant-pressure heat capacity in J/mol·K and T is temperature in K

Equation 2. Heat capacity of β-U [7]

$$C_p = 47.12$$

where C_p is constant-pressure heat capacity in J/mol·K

Equation 3. Heat capacity of γ-U [7]

$$C_p = 61.6420 - 33.1644 \times 10^6 \times T^{-2}$$

where C_p is constant-pressure heat capacity in J/mol·K and T is temperature in K

Equation 4. Heat capacity of liquid U [7]

C_p (liquid U) = 46.45

where C_p is constant-pressure heat capacity in J/mol·K

2.1.3.3 Heat Capacity of the Ideal Gas

Oetting et al. [6] calculated the heat capacity of uranium as an ideal gas from information on electronic levels available before 1975. They tabulated values at temperatures from 0 to 6000 K, although they described their values above 2000 K as "interim." Grenthe et al. [10] fitted a polynomial to Oetting's values for temperatures from 298.15 to 2500 K. More recently, Konings and Beneš [7] re-calculated the heat capacity of uranium gas, using newer data and a larger number of electronic energy levels, and fitted it with two polynomials (Equation 5 and Equation 6).

As shown in Figure 2, the two sets of data agree to within ~1% for temperatures between ~300 and 2000 K. If heat capacities above 4000 K are required, the "interim" values of Oetting et al. [6 (Table A1.6)] are the only available values.

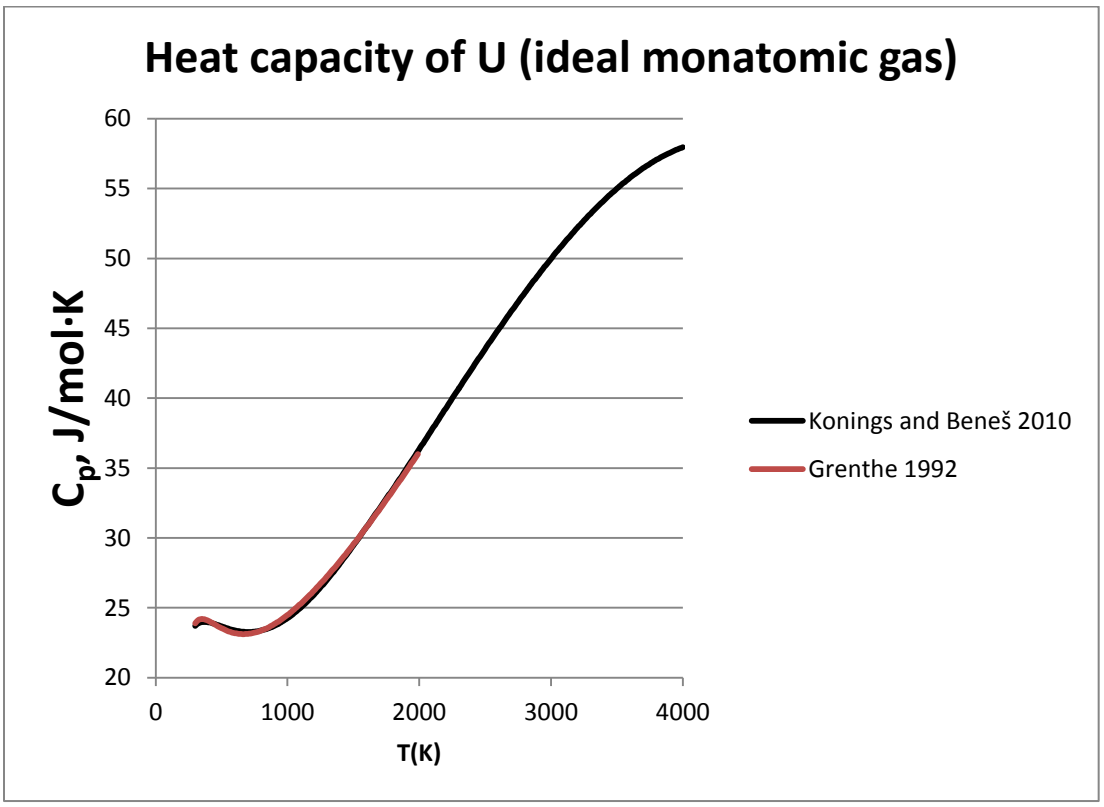

Figure 2. Heat capacity of U as an ideal gas. Values from Konings and Beneš were calculated from Equation 5and Equation 6.

Equation 5. Heat capacity of U gas from 298.15 to 1800 K [7]

$$C_p = 35.1688 - 32.2466 \times 10^{-3} \times T + 27.0474 \times 10^{-6} \times T^2 - 5.3433 \times 10^{-9} \times T^3 - 3.6652 \times 10^5 \times T^{-2}$$

where C_p is constant-pressure heat capacity in J/mol·K, T is temperature in K, and T is between 298.15 and 1800 K

Equation 6. Heat capacity of U gas from 1800 to 4000 K [7]

$$C_p = 4.9298 + 10.4892 \times 10^{-3} \times T + 3.7043 \times 10^{-6} \times T^2 - 0.7598 \times 10^{-9} \times T^3 + 6.8108 \times 10^6 \times T^{-2}$$

where C_p is constant-pressure heat capacity in J/mol·K, T is temperature in K, and T is between 1800 and 4000 K

2.1.4 Thermal Expansion and Density

2.1.4.1 Thermal Expansion

The thermal expansion of α-U is highly anistropic, with expansion parallel to the *a* and *c* crystallographic directions and contraction parallel to *b*. Touloukian et al. [55] published recommended thermal expansion values for single crystals and polycrystalline samples of α-U and provisional thermal expansion values for β-U and γ-U based on a review of 48 previously published measurements (Figure 3). Although these measurements were obtained using a variety of techniques and samples, they show relatively little scatter.

More recent thermal expansion measurements of α-U and γ-U from dilatometry of an as-cast sample of polycrystalline U by Basak et al. [56] are significantly below the values recommended by Touloukian et al., although the thermal expansion of α-U reported by Basak et al. is comparable to the lowest values reported by Touloukian et al.

Given the anisotropic thermal expansion of α-U and demonstrated dependence of the coefficient of thermal expansion for polycrystalline α-U on processing history (Section 2.1.4.2), it is not surprising that different samples have different thermal expansion behavior. Thus, new measurements of thermal expansion should be made using samples with the same processing history as the materials of interest.

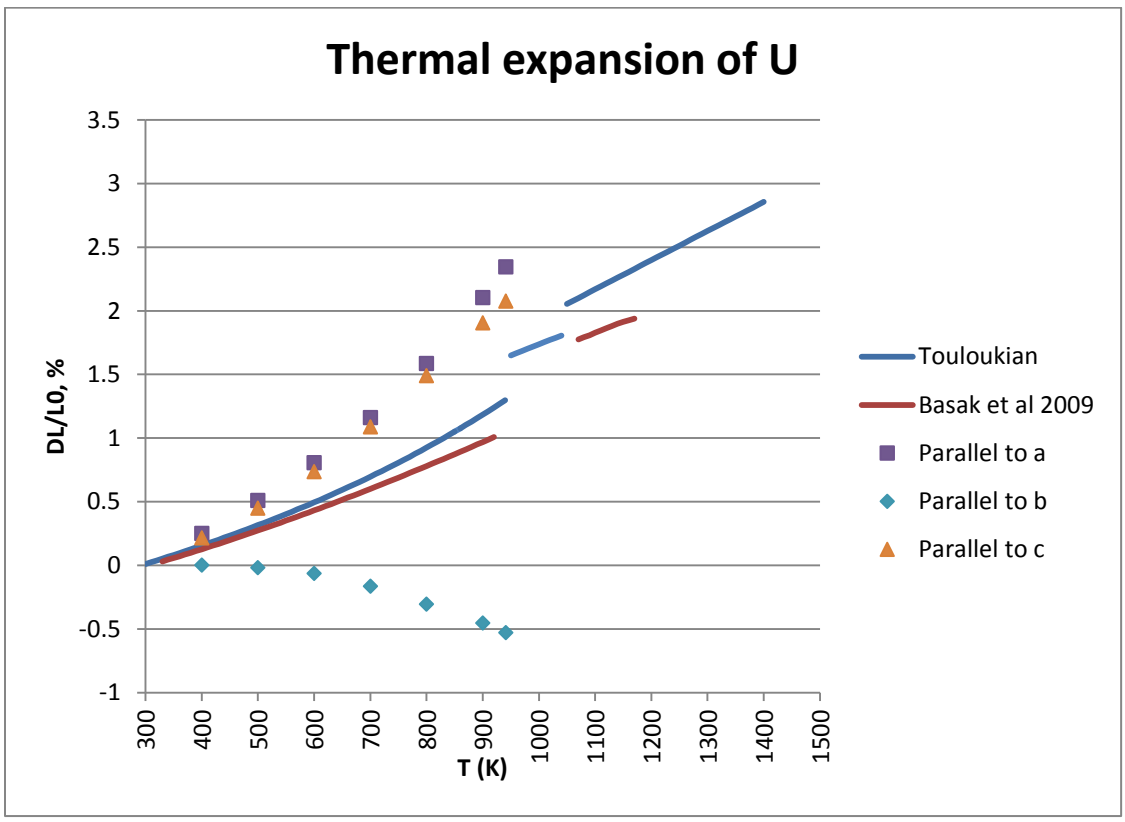

Figure 3. Thermal expansion of U. Lines represent thermal expansion of polycrystalline U, calculated using Equation 7 through Equation 11. Symbols represent recommended values for thermal expansion of single crystals of α-U in the indicated crystallographic directions from Touloukian et al. [55].

Two equations were developed to represent the mean thermal expansion of polycrystalline α-U:

Equation 7. Mean thermal expansion of polycrystalline α-U according to Touloukian et al. [55]

$(L-L_0)/L_0 = -0.379+1.264 \times 10^{-3} \times T - 8.982 \times 10^{-8} \times T^2 + 6.844 \times 10^{-10} \times T^3$

where $(L-L_0)/L_0$ is thermal expansion in %, T is temperature in K, T is between 293 and 941 K, L is the length at temperature T, and L_0 is length at 293 K

Equation 8. Measured thermal expansion of polycrystalline α-U according to Basak et al. [56]

$(L-L_0)/L_0 = -0.326+8.338 \times 10^{-4} \times T + 8.038 \times 10^{-7} \times T^2 – 1.465 \times 10^{-10} \times T^3$

where $(L-L_0)/L_0$ is thermal expansion in %, T is temperature in K, T is between 323 and 923 K, L is the length at temperature T, and L_0 is length at 323 K

Although Touloukian et al. [55] and Basak et al. [56] did not publish equations expressing the thermal conductivity of β-U, Konings et al. [8] developed Equation 9 to represent the data used to determine the provisional values of Touloukian et al. [55].

Equation 9. Mean thermal expansion of polycrystalline β-U [8 Table 8]

$(L-L_0)/L_0 = 8.04 \times 10^{-5} + 1.729 \times 10^{-5} \times T$

Where $(L-L_0)/L_0$ is thermal expansion in %, T is temperature in K, T is between 945 and 1045 K, L is the length at temperature T, and L_0 is length at 293 K

Polynomials representing the thermal expansion of γ-U are:

Equation 10. Provisional values for mean thermal expansion of polycrystalline γ-U according to Touloukian et al. [55]

$(L-L_0)/L_0 = -0.149 + 1.775 \times 10^{-3} \times T + 4.382 \times 10^{-7} \times T^2 - 1.239 \times 10^{-10} \times T^3$

Where $(L-L_0)/L_0$ is thermal expansion in %, T is temperature in K, T is between 1048 and 1400 K, L is the length at temperature T, and L_0 is length at 293 K

Equation 11. Mean thermal expansion of polycrystalline γ-U according to Basak et al. [56]

$(L-L_0)/L_0 = 81.794 – 21.986 \times 10^{-2} \times T + 19.985 \times 10^{-5} \times T^2 – 6.006 \times 10^{-8} \times T^3$

Where $(L-L_0)/L_0$ is thermal expansion in %, T is temperature in K, T is between 1063 and 1173 K, L is the length at temperature T, and L_0 is length at 323 K

2.1.4.2 Thermal Expansion Coefficients

Average values for linear thermal expansion coefficients of α-U parallel to the *a*, *b*, and *c* crystallographic directions have been tabulated in several reviews, of which the most recent is the 2010 review by Grenthe et al. [9]. This review indicates that the coefficient of thermal expansion for single crystals is 26.5×10^{-6}/K parallel to the *a* crystallographic direction, -2.4×10^{-6}/K parallel to *b*, and 23.9×10^{-6}/K parallel to *c*, over temperature ranges from 25-325°C [9]. An earlier review by Yakel [46] lists coefficients of thermal expansion as 35.6×10^{-6}/K parallel to α, -8.4×10^{-6}/K parallel to *b*, and 31.6×10^{-6}/K parallel to *c*, from 27 to 640°C [46]. Because the thermal expansion is not a linear function of temperature (Figure 3), different average coefficients of thermal expansion can be estimated from the same data by averaging over a different temperature range, and it is not clear whether the thermal expansion coefficients of Yakel and Grenthe are consistent.

Touloukian et al. [55] provide an extensive tabulation of older data from a number of individual samples, and Lawson et al. [42] published high-temperature neutron-diffraction data from a single sample.

The linear thermal expansion coefficients for β-U are ~23 × 10^{-6} K^{-1} parallel to *a* and ~5 × 10^{-6} K^{-1} parallel to *c* [18, 42, 57], corresponding to an average thermal expansion coefficient of ~17 × 10^{-6} K^{-1}.

The linear thermal expansion coefficient for γ-U is (22.5 ± 1.3) × 10^{-6} K^{-1} [18, 58] over the temperature range from 0 to 1100°C.

Coefficients of thermal expansion for polycrystalline U are strongly dependent on processing history, and the assumption that thermal expansion can be represented by a single average value for all samples may lead to significant errors [59].

2.1.4.3 Density

Densities of U phases calculated from information in Section 2.1.2.1 are:

- α-U, 19.05 g/cm^3 at 298 K
- β-U, 18.12 g/cm^3 at 955 K
- γ-U, 17.92 g/cm^3 at 1060K. This value is smaller than the density of 18.06 g/cm^3 quoted in a recent review by Edelstein [60]. Edelstein's density is consistent with on a lattice parameter of 3.524 Å from another chapter of the same review series [9], which did not give a reference for the lattice parameter. Although further research is needed to determine which value is more accurate, the density of 17.92 g/cm^3 is the more defensible value because the origin of the 3.524 Å lattice parameter is unknown.

The high-temperature density of solid U can be calculated from the room-temperature volume and thermal expansion (Equation 12) or from high-temperature diffraction data using Equation 5 from Reference [5] with values from Section 2.1.2.1. The density of liquid U can be calculated using Equation 13.

Equation 12. Density of solid U as a function of thermal expansion [8]

$$\rho(T) = \frac{M}{V_0(1 + 3\frac{\Delta L}{L_0(T)})}$$

Where ρ(T) is the density at temperature T, M is the atomic mass (238 for U-238), V_0 is the molar volume at the reference temperature (12.50 cm^3/mol near room temperature for α-U), and $\Delta L/L_0$ is the thermal expansion at temperature T

The density of liquid U can be calculated using an equation developed by the IAEA and repeated by Konings et al. (Equation 13).

Equation 13. Density of liquid U [8, 21]

$$\rho = 20.332 - 2.146 \times T$$

where ρ is the density in g/cm^3, T is temperature in K, and T is between 1405 and 2100 K

Figure 4 shows the density of U. If densities from more than one source of data are available, they are in good agreement.

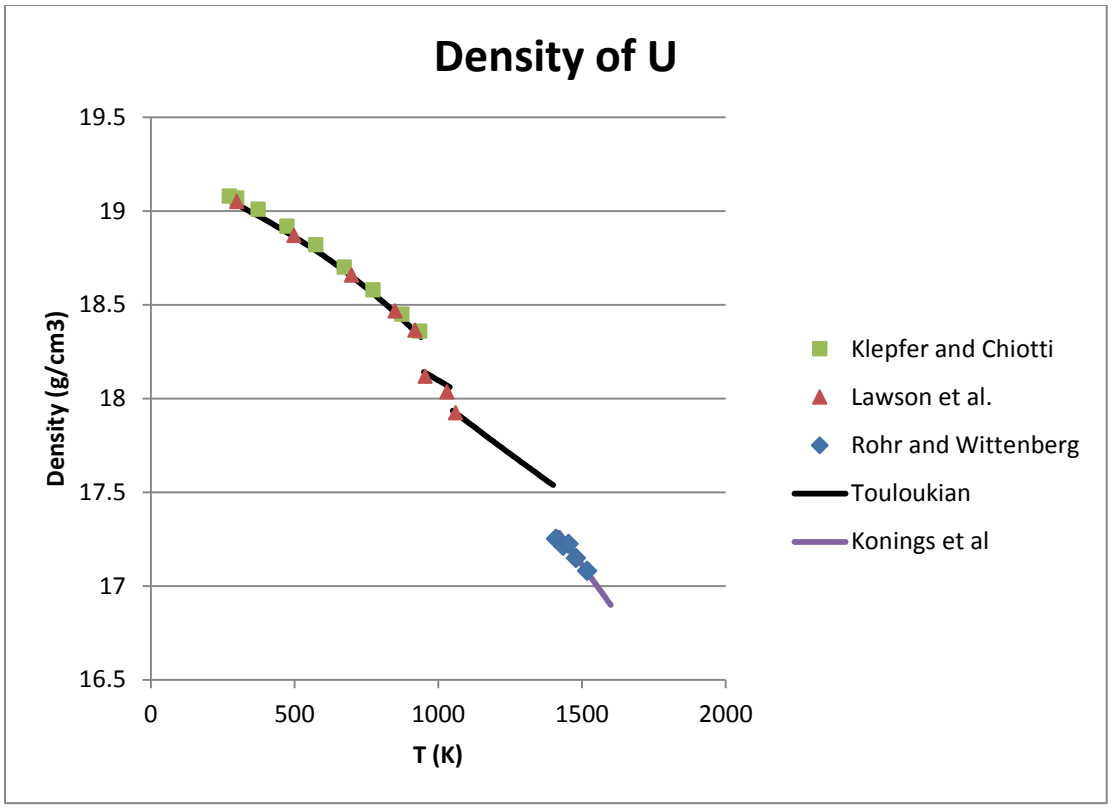

Figure 4. Density of U. Data labeled "Klepfer and Chiotti," "Lawson et al.," and "Rohr and Wittenberg" are from references [18, 42, 61]. Data labeled "Touloukian" were calculated using Equation 12 and equations for Touloukian's thermal expansion (Equation 7, Equation 9, and Equation 10). Data labeled "Konings et al." were calculated using Equation 13.

2.1.4.4 Changes in Volume as A Result of Phase Transitions

According to a review by Yakel, uranium increases in volume by 1.2% as a result of the α-β transition, and by 0.7% as a result of the β-γ transition [46]. The volume of uranium reportedly increases by 2.2% during melting [61].

2.1.5 Thermal Conductivity and Related Properties

2.1.5.1 Thermal Conductivity

Reviews of the thermal conductivity of U include those by Touloukian et al. [62], Kim et al. [19], and the IAEA [63]. The review of Kim et al. includes the data used by Touloukian et al. as well as data from Takahashi et al. [64], but does not include the measurements reported by Kaity et al. [20]. The IAEA review provides three estimates of thermal conductivity based on different weightings of the same data, with only one of the three being used in a recent IAEA compilation of data [21].

Figure 5 shows the thermal conductivity of U from the reviews by Kim et al. (Equation 14) and the IAEA (Equation 15) and shows recent measurements by Kaity et al. (Equation 16) that were not included in either of the reviews. Plotted values from all three sources have similar slopes, which indicate that the thermal conductivity increases by ~0.02 W/m-K within the range of each of the curves; however, the thermal conductivity from the IAEA tabulation is ~10-20% lower than either of the other curves. The good agreement between the new measurements of Kaity et al. [20] and the recommended thermal conductivity in the review by Kim et al. [19] suggests that the Kim et al. review may be a better representation of the actual thermal conductivity than the IAEA tabulation.

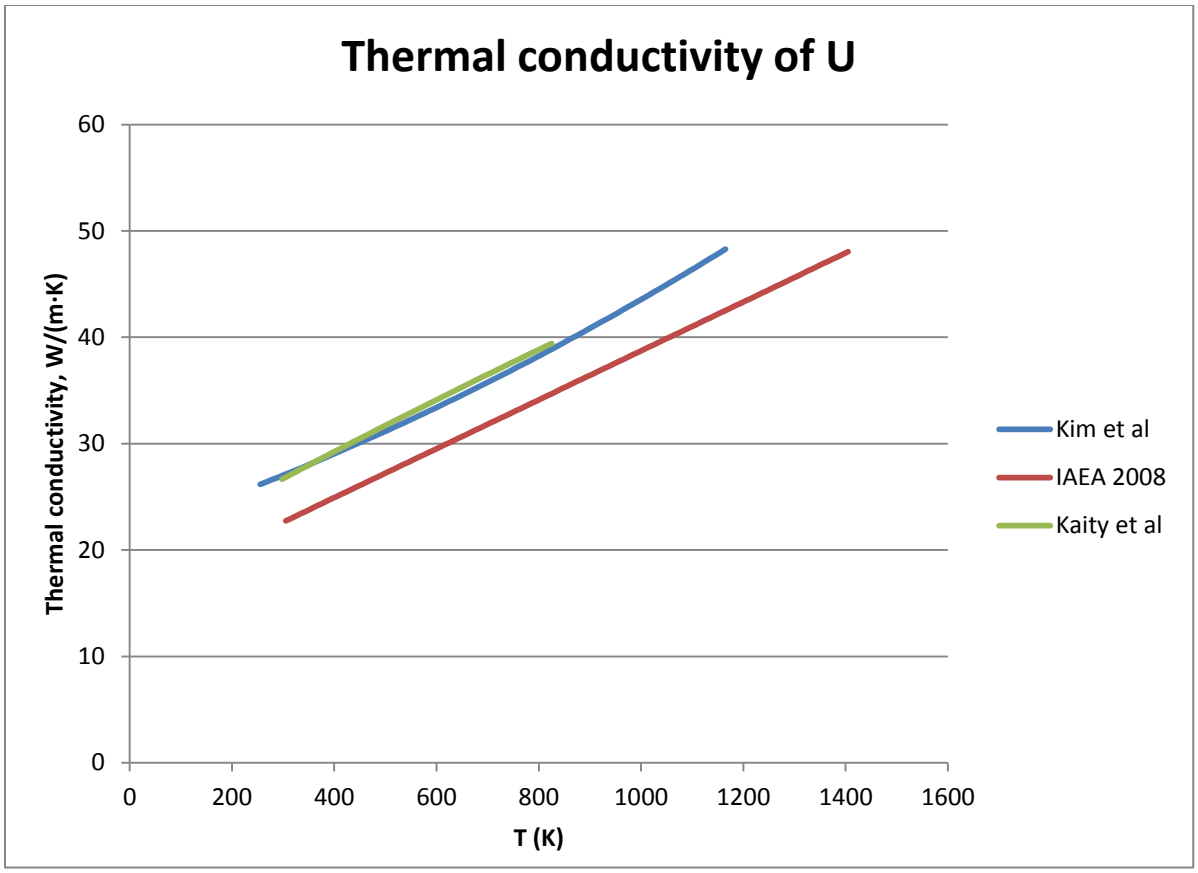

Figure 5. Thermal conductivity of U (Equation 14, Equation 15, and Equation 16).

The equations used to generate the data in the plot are:

Equation 14. Thermal conductivity of U from 255 to 1173 K according to Kim et al. [19]

$k = 21.73 + 1.591 \times 10^{-2} \times T + 5.907 \times 10^{-6} \times T^2$

where k is thermal conductivity in W/m·K, T is temperature in K, and T is between 255 and 1173 K

Equation 15. Thermal conductivity of U from 293 to 1405 K according to the IAEA [21]

$k = 22 + 0.023 \times (T-273)$

where k is thermal conductivity in W/m·K, T is temperature in K, and T is between 293 and 1405 K

Equation 16. Thermal conductivity of U from 298 to 823 K according to Kaity et al. [20]

$k = 18.890 + 2.678 \times 10^{-2} \times T-2.302 \times 10^{-6} \times T^2$

where k is thermal conductivity in W/m·K, T is temperature in K, and T is between 298 and 823 K.

2.2 Np

2.2.1 Introduction

In addition to being a nuclear material, Np is of scientific interest because of the behavior of its 5*f* electrons. This interest has led to research including collection of data at very high pressures and measurements using a variety of spectroscopic techniques. These aspects of actinide science are summarized in two comprehensive reviews [65, 66], and will not be considered further in this handbook because of their limited relevance for FCRD fuels. Modeling papers too recent to be considered in these reviews include those of Lukoyanov et al. [67] and Bajaj et al. [68].

There is general agreement about the existence and properties of three Np phases (α-Np, β-Np, and γ-Np) that are stable at atmospheric pressure. It has been suggested that there may be a fourth Np phase that has a very narrow temperature range of stability and forms only in high-purity samples [69-71]. Experimental measurements of high-purity Np at pressures up to 52 GPa did not show additional high-pressure phases [72]. Some references (e.g., [73, 74]) discuss the properties of a hypothetical fcc Np phase, which is not considered in this Handbook because there is no experimental evidence indicating that it actually exists.

Experimental measurements of the heat capacity of α-Np at temperatures above 300 K are available in two publications, which are in good agreement at the single temperature they have in common. As experimental measurements of the heat capacity of β-Np, γ-Np, and liquid Np are not available, these properties are commonly approximated by analogy to those of U and Pu phases. In the absence of experimental data, it is not possible to address the accuracy of these approximations.

The thermal expansion of single crystals of α-Np and β-Np is anisotropic, as reported in the single paper with experimental measurements. The thermal expansion of single crystals of γ-Np has not been reported.

The linear thermal expansion coefficient for polycrystalline α-Np has been experimentally measured by two research groups and modeled by a third group, with good agreement. Experimental measurements of the linear thermal expansion coefficient for polycrystalline β-Np were reported by the same research groups, with much less good agreement. It has been suggested that the lack of agreement is a consequence of the strongly anisotropic thermal expansion of β-Np, which would cause differences in thermal expansion coefficients for polycrystalline samples with different preferred orientations. The linear thermal expansion coefficient for polycrystalline γ-Np has been reported in a single publication, but may be higher than the reported value because of sample deformation during measurement.

Reported densities of Np phases at different temperatures are commonly quoted from a single X-ray diffraction study. Densities determined from thermal expansion are in good agreement with the X-ray data for β-Np. The density of γ-Np is less well known, and densities determined using different techniques differ by several percent.

The thermal conductivity of Np at 300 K has been determined using two measurement techniques, leading to four different values that differ by a factor of almost two. Measurements of thermal conductivity at higher temperatures are not available, and estimates using the Wiedemann-Franz Law (Section 1.6.2 in Reference [5]) differ by ~10%.

Recent research includes use of Voronoi-Dirichlet tessellation to understand thermal polymorphism of Np [39] and attempts to develop first-principles models of structural properties [75].

2.2.2 Phases and Phase Transformations

2.2.2.1 Phases

The currently accepted lattice parameters and crystal structures of α-Np and β-Np were first published in 1952 by Zachariasen [76, 77], and have been corroborated or repeated by later researchers (e.g., [8, 69, 70, 78]). Neutron-diffraction work by Lawson et al. [48] expanded on these results by measuring Debye-Waller factors and calculating effective Gruneisen constants for α-Np.

High-quality data on the structure of γ-Np is difficult to obtain because of oxidation of the sample and a high degree of overlap between x-ray patterns for γ-Np and NpO [70, 76]. The generally accepted lattice parameter was suggested by Lemire et al. [69] based on a review of the available data.

The generally accepted crystalline Np phases that are stable at atmospheric pressure are [69]:

- α-Np, orthorhombic (space group *Pnma*), 8 atoms per unit cell, a = 6.663 Å, b = 4.723 Å, c = 4.887 Å at 293 K. (The original structure refinement [77] used the non-standard setting *Pmcn*, which can be converted to *Pnma* by appropriate permutation of the axes.) As-cast α-Np commonly shows extensive twinning [79, 80], which may be due to stresses caused by the highly anisotropic thermal expansion of individual crystals [81].
- β-Np, tetragonal (space group $P42_12$), 4 atoms per unit cell, a = 4.897 Å, c = 3.388 Å at 586 K
- γ-Np, bcc (space group $Im\bar{3}m$), a = 3.518 Å at 873 K

Anomalies in thermal-analysis data suggest the possible existence of a fourth Np phase with a very narrow temperature range of stability near the β-γ phase transformation [69-71]. No information about its possible crystal structure and lattice parameters is available.

2.2.2.2 Phase Transformations

Measurements of phase-transformation and melting temperatures of Np are in good agreement. Phase-transformation mechanisms are less well known, but were investigated by Selle and Rechtien [82].

The recommended atmospheric-pressure phase-transformation temperatures and ranges of values from a recent assessment of the experimental data are [7]:

- α-β, 553±5 K (280±5°C) based on 10 published measurements that range from 544 to 559 K. This temperature rises slightly (~1.1 kbar/°C) for pressures up to a few kbars [83].
- β-γ, 850±3 K (577±3°C) based on 10 published measurements that range from 830 to 856 K.
- γ-liquid, 913±3 K (640±3°C) based on 8 published measurements that range from 870 to 913 K.

The corresponding recommended phase-transformation enthalpies and ranges of values are [7]:

- α-β, 4.7±0.5 kJ/mol based on 4 publications with original measurements that range from 4.73 to 8.37 kJ/mol
- β-γ, 3.0±0.5 kJ/mol based on 3 publications with original measurements that range from 2.99 to 5.27 kJ/mol
- γ-liquid, 3.2±0.5 kJ/mol (based on 6 publications with original measurements that range from 3.19 to 5.19 kJ/mol

2.2.3 Heat Capacity and Related Properties

Two publications report experimental measurements of the heat capacity of α-Np at room temperature and above. One of these publications (by Eldred and Curtis in 1957) is a half-page letter that reports the average heat capacity between 20 and 99 °C (293 and 372 K) as 0.0319 cal/g·°C (~31.65 J/mol·K) [84]. The other publication (by Evans and Mardon in 1959) reports heat capacities at five temperatures between 60 and 207 °C (333 and 480 K) [85]. The publications are in good agreement about the heat capacity of Np at the single temperature they have in common (~62°C) (Figure 6).

Konings and Beneš [7] expanded the work of Evans and Mardon [85] to other temperatures by fitting a quadratic equation to their data (Figure 6, Equation 17). The heat capacity at 298 K (29.63 J/mol-K) is the same as earlier estimates by Oetting et al. [6, 54], which were based on the same experimental data.

Equation 17. Heat capacity of α-Np [7]

$$C_p = 30.132 - 36.2372 \times 10^{-3} \times T + 115.89 \times 10^{-6} \times T^2$$

where C_p is constant-pressure heat capacity in J/mol·K and T is temperature in K

In the absence of experimental data, heat-capacity values for β-Np and γ-Np have been estimated based on analogies to U and Pu phases with similar crystallographic characteristics (e.g., [6, 7]). For example, the heat capacity of β-Np is estimated from the heat capacities of δ'-Pu and β-U because all three phases are tetragonal, and the heat capacity of γ-Np is estimated from the heat capacities of ε-Pu and γ-U because all three phases have bcc structures. Using this approach, Konings and Beneš estimated the heat capacity of β-Np as 40 J/mol-K, the heat capacity of γ-Np as 36 J/mol-K, and the heat capacity of liquid Np as 46 J/mol-K [7].

Although estimating the heat capacity of Np based on properties of structurally similar phases of other elements is perhaps the best approach given the available data, it has at least two significant disadvantages:

- It involves comparisons between materials with different space groups at different temperatures (Figure 7).
- It depends on the heat capacities of β-U, γ-U, δ'-Pu, ε-Pu, liquid U, and liquid Pu. Some of these heat capacities are also poorly known.

Heat capacities of α-Np and β-Np were recently modeled by Filanovich and Povzner [86]. Although this paper apparently used only data from temperatures below 300 K, its results for α-Np appear comparable to the polynomial suggested by Konings and Beneš (Equation 17). The modeled heat capacity of β-Np increases with temperature, with an average value that is similar to the constant value suggested by Konings and Beneš.

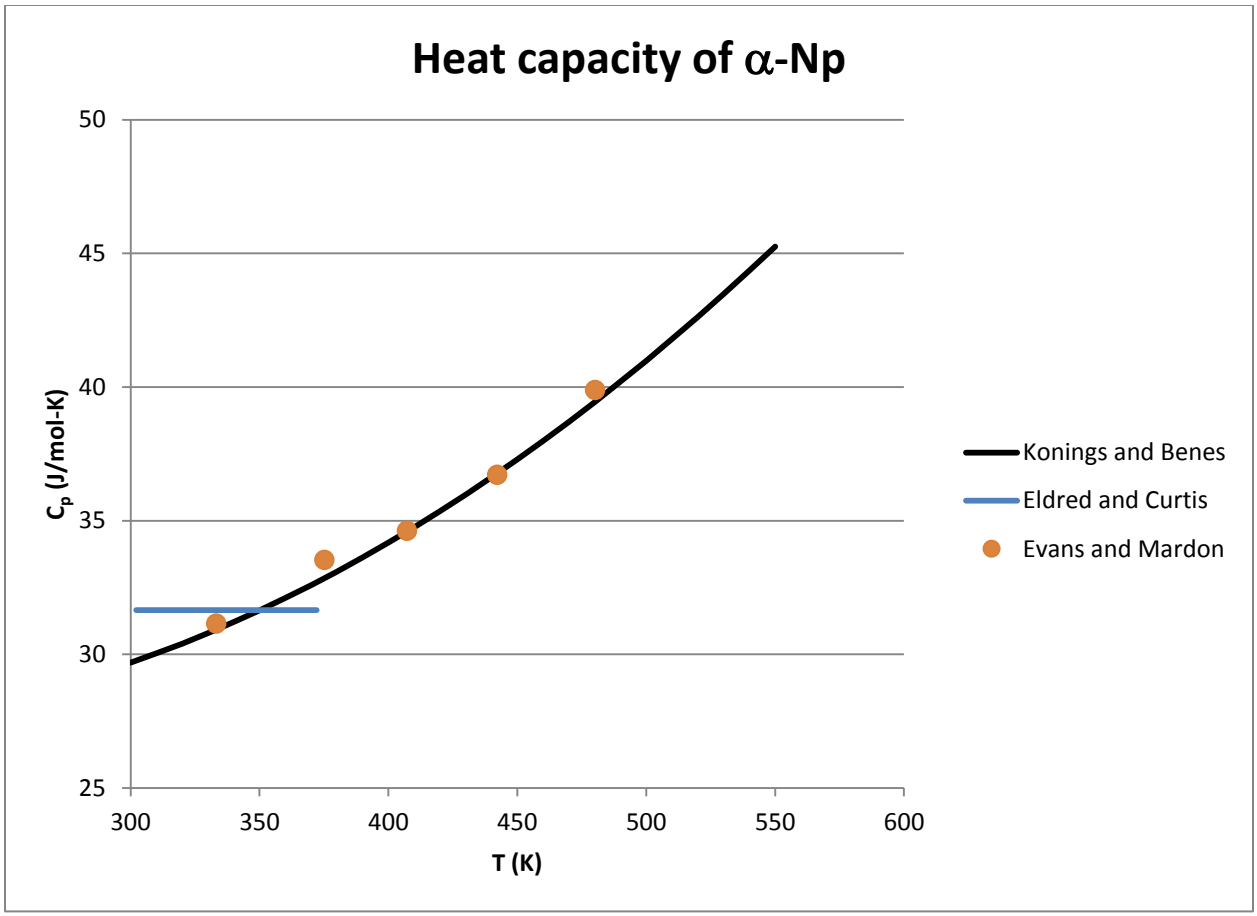

Figure 6. Heat capacity of α-Np [7, 84, 85].

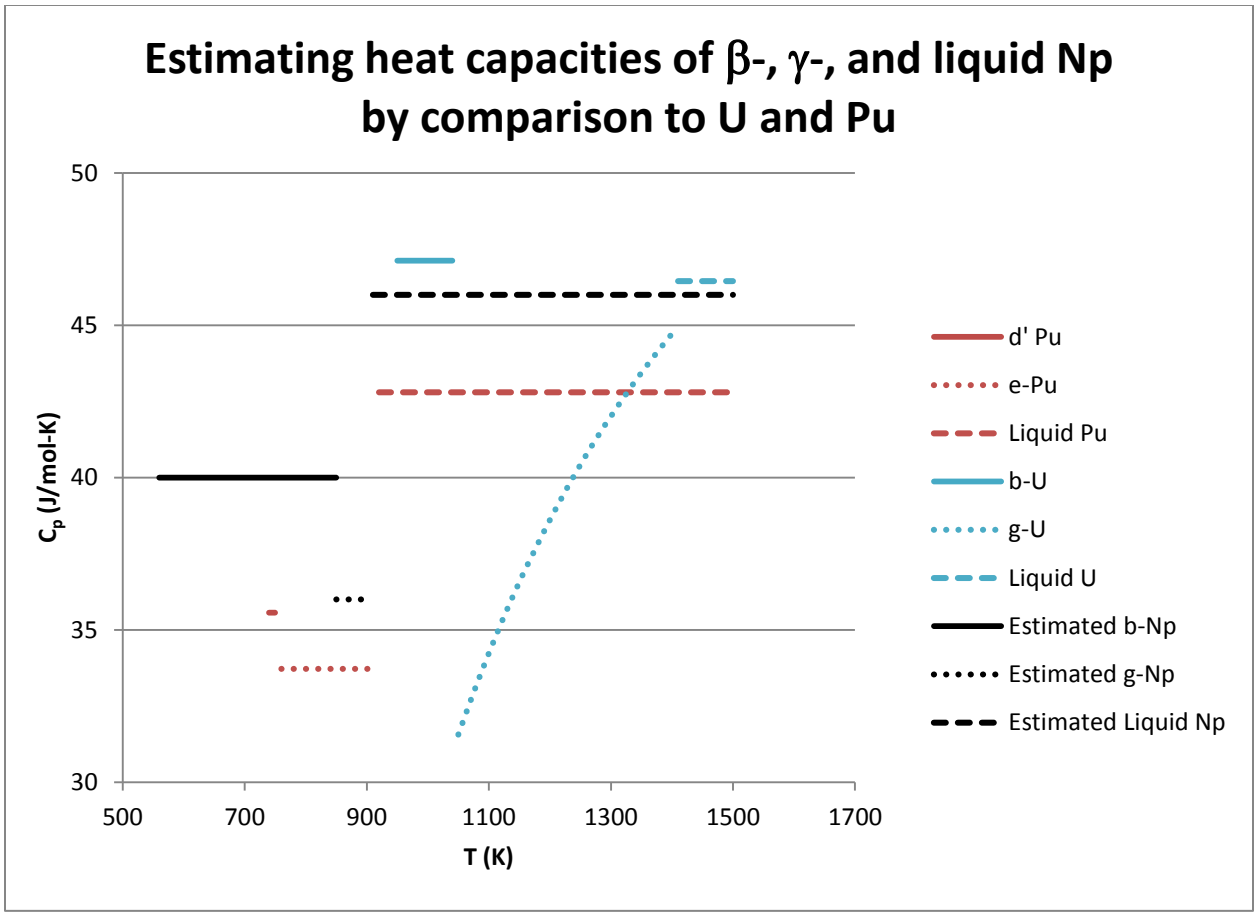

Figure 7. Estimated heat capacities of β-, γ-, and liquid Np, with the heat capacities of U and Pu phases on which the estimates are based. Heat-capacity values for Np are from Konings & Beneš [7]. Solid lines indicate tetragonal phases (space groups $P42_12$ for β-Np, $P42mnm$ for β-U, and $I4/mmm$ for δ'-Pu), dotted lines indicate bcc phases (space group $Im\bar{3}m$), and dashed lines indicate liquids. Colors indicate different elements.

2.2.4 Thermal Expansion and Density

2.2.4.1 Thermal Expansion of Single Crystals

The thermal expansion of single crystals of α-Np is anisotropic. Thermal expansion coefficients (in space group *Pnma*) are 34×10^{-6}/K parallel to the *a* axis, 24×10^{-6}/K parallel to *b*, and 25×10^{-6}/K parallel to *c*, for temperatures between ~300 and 550 K [76].

The thermal expansion of single crystals of β-Np is also anisotropic. Thermal expansion coefficients are 64×10^{-6}/K parallel to the *a* and *b* axes, and approximately 0 parallel to *c*, for temperatures between ~555 and 700 K [76].

No measurements of the thermal expansion of single crystals of γ-Np are available.

2.2.4.2 Coefficients of Thermal Expansion for Polycrystalline Neptunium

Original measurements of coefficients of thermal expansion for polycrystalline α-Np and β-Np were reported by Lee et al. [70] and by Cort [81] (Table 4). A recently developed model [86] produces values in good agreement with the data of Cort.

Table 4. Coefficients of thermal expansion for polycrystalline Np.

Phase	**T (K)**	**Coefficient of Thermal Expansion (K^{-1})**	**Reference**
α-Np	313-513	27.5×10^{-6}	[70]
α-Np	300-525	27.0×10^{-6}	[81]
β-Np	573-813	41×10^{-6}	[70]
β-Np	550-870	60.5×10^{-6}	[81]
γ-Np	~850-973?	33×10^{-6}	[87]

Although the measured coefficients of thermal expansion for α-Np in the two studies are similar, the measured coefficients of thermal expansion for β-Np are not. Cort suggests that the difference may be due to the thermal anisotropy of Np and preferred orientation in his samples. However, consideration of his measurements of phase-transformation temperatures and instantaneous coefficients of thermal expansion (Figure 8) suggests that his highest-temperature measurement, which he identified as β-Np, may actually represent γ-Np. If so, the thermal expansion coefficients for β-Np from the two references may be more similar than they appear in Table 4.

Attempts to measure thermal expansion at higher temperatures are difficult because of sample creep or "sagging" [70, 81], and only one measurement identified as the thermal expansion coefficient for γ-Np has been reported. This value may be too low as a result of experimental difficulties [87].

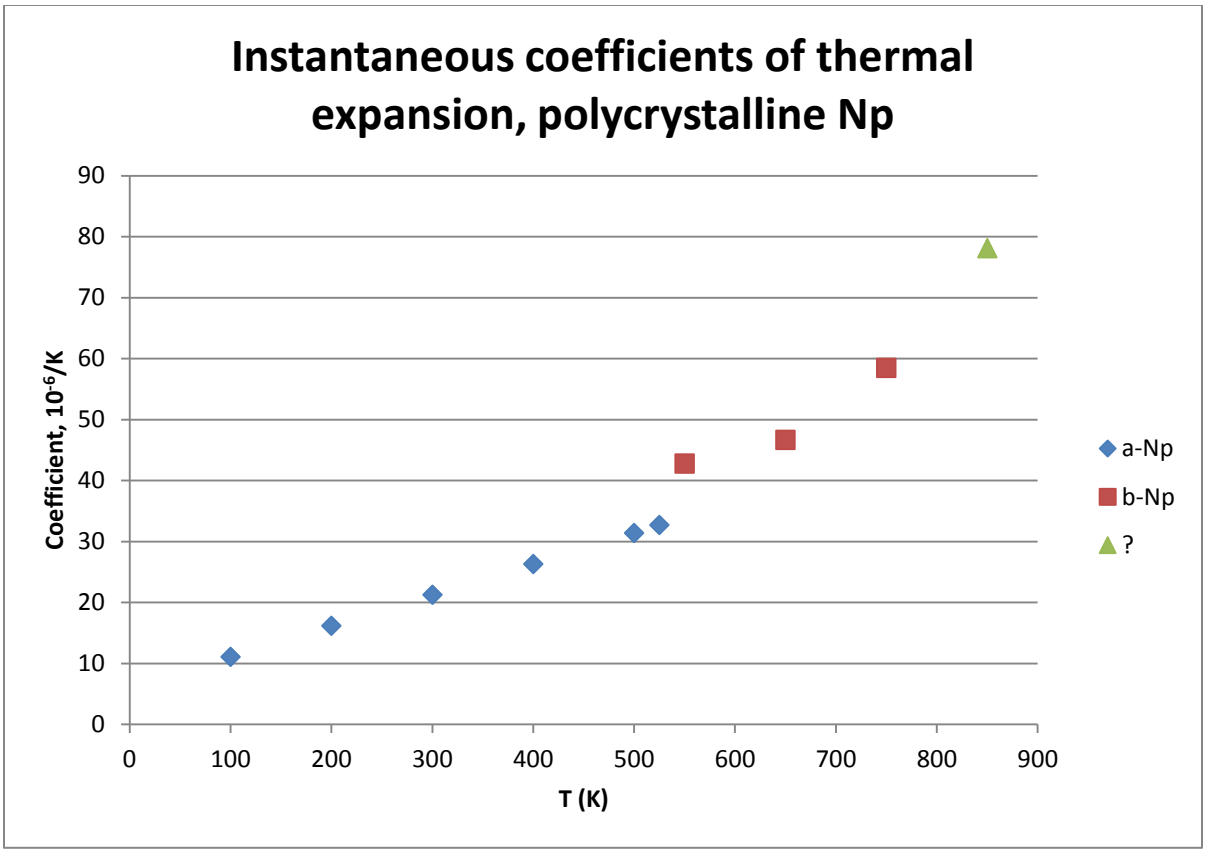

Figure 8. Instantaneous coefficients of thermal expansion for polycrystalline α- and β-Np at selected temperatures [81 Table 4].

2.2.4.3 Density and Volume

Densities calculated from X-ray diffraction of α-Np are ~ 20.45 to 20.48 g/cm^3 at 20°C [70, 76]. Measured values are lower (19.5 to 20.3 g/cm^3), possibly because the samples contain inclusions of lower-density materials [70, 84, 88].

Densities calculated from X-ray diffraction data from β-Np at ~290°C are 19.4 to 19.5 g/cm^3 [70, 76]. These densities are generally consistent with a density of 19.3 g/cm^3 at 302°C (575 K) determined from thermal expansion data [81].

The density of γ-Np is not well known. X-ray diffraction data suggests a density of ~18 g/cm^3 at 592°C, assuming a bcc structure that could not be reliably determined from the X-ray data [70, 76]. Thermal expansion data indicates a density of 18.30 g/cm^3 at 567°C (840 K) [81]. Foltyn calculated the density of γ-Np at 583°C as 18.40 g/cm^3 [71] using the Clausius-Clapeyron relation (Section 1.4 of reference [5]) with data on the enthalpy of the β-γ transition from new DTA measurements, high-pressure data from reference [89], and the density of β-Np from the X-ray diffraction data of Zachariasen [76]. In combination, these data suggest that the density of γ-Np at temperatures of ~580-600°C is slightly more than 18 g/cm^3. Further work is required to determine this density with greater precision and at other temperatures.

Figure 9 shows relationships between density and temperature for α, β, and γ-Np based on X-ray diffraction data [76], and the corresponding molar volumes calculated for ^{237}Np.

The density of liquid Np has not been reported.

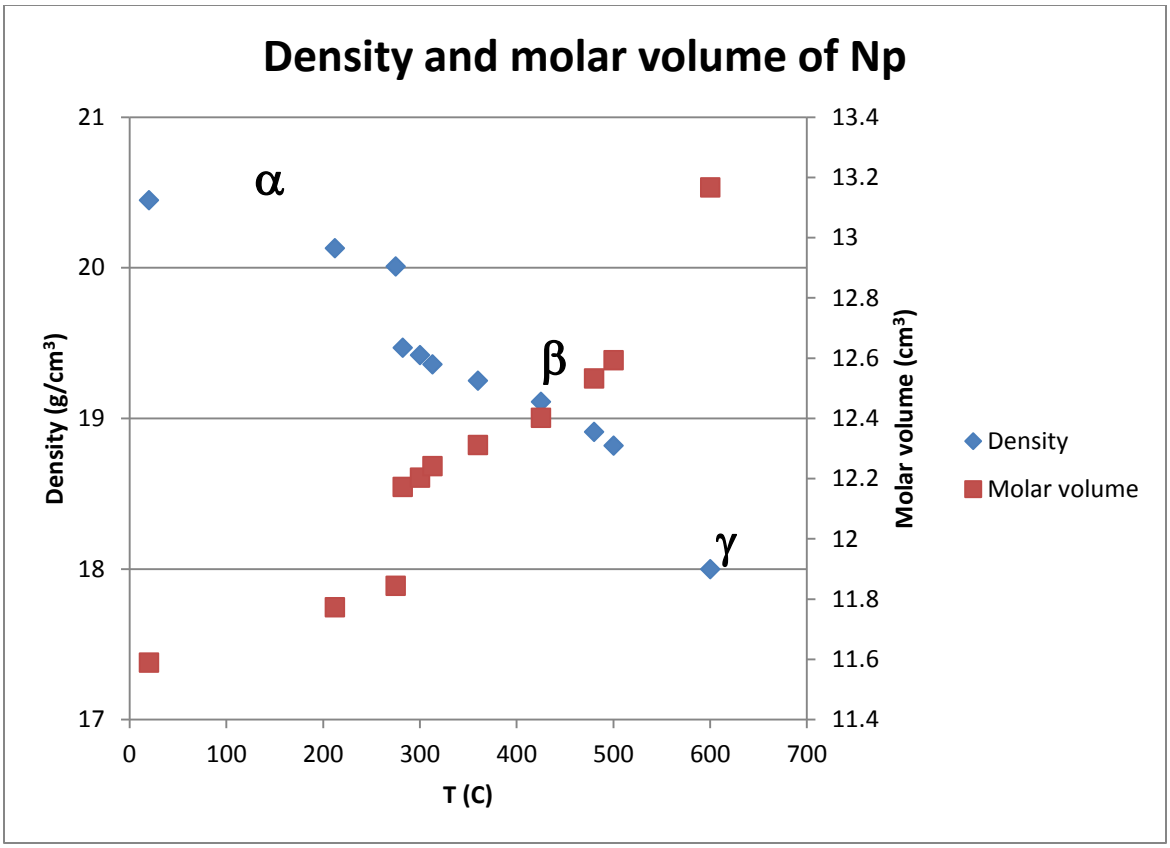

Figure 9. Density and molar volume of Np from Zachariasen's X-ray data [76].

2.2.4.4 Changes in Volume as a Result of Phase Transitions

Calculations based on the X-ray diffraction data of Zachariasen [76] show that the molar volume of Np increases by ~2.8% at the α-β transition, and by ~4.5% at the β-γ transition. These values differ from those presented by Wittenberg and colleagues (3.3 and 3.6% increases in volume at the α-β and β-γ transformations, respectively) [90, 91] and by Selle and Rechtien (increases of 2.85 and 3.25%) [82]. The reasons for these differences are not clear.

Wittenberg et al. reported that the volume of Np increases by ~1.5% during melting [90, 91].

2.2.5 Thermal Conductivity and Related Properties

2.2.5.1 Lorenz Number

Wagner [92] calculated the Lorenz number for Np at room temperature as 3.21×10^{-8} WΩ/K^2 using his thermal diffusivity data and previously published values for density, heat capacity, and electrical resistivity. Some of these values are no longer accepted, and Wagner's value of the Lorenz number should not be used.

Calculation of the room-temperature Lorenz number for Np using the best available data (thermal diffusivity of 0.027 cm^2/sec [92], electrical resistivity of 116.5 μΩ/cm [93], heat capacity of 29.7 J/mol-K (Section 2.2.3), and density of 20.48 g/cm^3 (Section 2.2.4.3)) gives a value of ~2.62×10^{-8} WΩ/K^2. This value is slightly larger than the theoretical value (2.44×10^{-8} WΩ/K^2), which in turn appears to be slightly larger than the Lorenz number for Np presented graphically (and without explanation of where the value comes from) in a 2012 review [8 (Figure 22)].

In the absence of compelling data indicating otherwise, it seems reasonable to assume that the room-temperature Lorenz number for Np can be approximated by the theoretical value. The temperature dependence of the Lorenz number is unknown.

2.2.5.2 Thermal Conductivity at 300 K

Althoug the thermal conductivity of Np at 300 K has not been measured, it can be estimated in four ways. Two of the four estimates were derived from electrical resistivity measurements by Lee et al. [93]. The earliest determination was that of Lee et al., who applied a method developed by Kannuluik [94] to the electrical resistivity data and concluded that the thermal conductivity of Np is "0.01 ± 0.001 c.g.s. units at 300°K" [87 p. 464]. Touloukian et al. [62] re-calculated the thermal conductivity using the same data and method and obtained a value of 4.18 W/m-K. This value appears in a recent review by Konings [8].

A second estimate of the thermal conductivity of Np based on the data of Lee et al. was published by Ho et al. [95]. They rejected Touloukian's value because it produced a Lorenz number that they believed was implausibly low, and instead estimated the thermal conductivity of Np at 300 K as 6.3 W/m-K. Although Ho et al. did not explain why they suggested this value, it can be obtained from the Wiedemann-Franz law (Section 1.6.2 in reference [5]) with Lee's resistivity data and the theoretical Lorenz number. This value for the thermal conductivity of Np appears in the CRC Handbook of Chemistry and Physics [96] and was recommended in a recent review by Kim et al. [19].

The remaining two estimates of thermal conductivity are based on the diffusivity data of Wagner [92]. Wagner estimated the room-temperature thermal conductivity of Np as 7.70 W/m-K at 300 K based on a thermal diffusivity of 0.027 cm^2/sec, a heat capacity of 32.9 J/mol-K, and a density of 20.4 g/cm^3. This value for heat capacity is significantly higher than the value of 29.63 J/mol-K recommended in Section 2.2.3, and this value for density is slightly lower than the theoretical density of 20.45-20.48 g/cm^3 (Section 2.2.4.3).

Re-calculating the thermal conductivity of Np based on Wagner's diffusivity data using a heat capacity of 29.7 J/mol-K and density of 20.48 g/cm^3 gives the fourth estimate of the thermal conductivity of Np, 6.92 W/m-K at 300 K.

Better experimental data is needed to determine the actual thermal conductivity of Np, although it seems likely that it is between 6 and 7 W/m-K. In the absence of this data, the value of 6.3 W/m-K proposed by Ho et al. [95] for the room-temperature thermal conductivity of Np seems the most defensible estimate.

2.2.5.3 Thermal Conductivity at Higher Temperatures

No measurements of the thermal conductivity of Np at temperatures above 300 K are available. However, this data can be approximated for temperatures up to 900 K by using the Wiedemann-Franz Law (Section 1.6.2 in reference [5]). Figure 10 shows thermal conductivity values calculated using electrical resistivity measurements reported by Lee et al. [93] and the theoretical value for the Lorenz number.

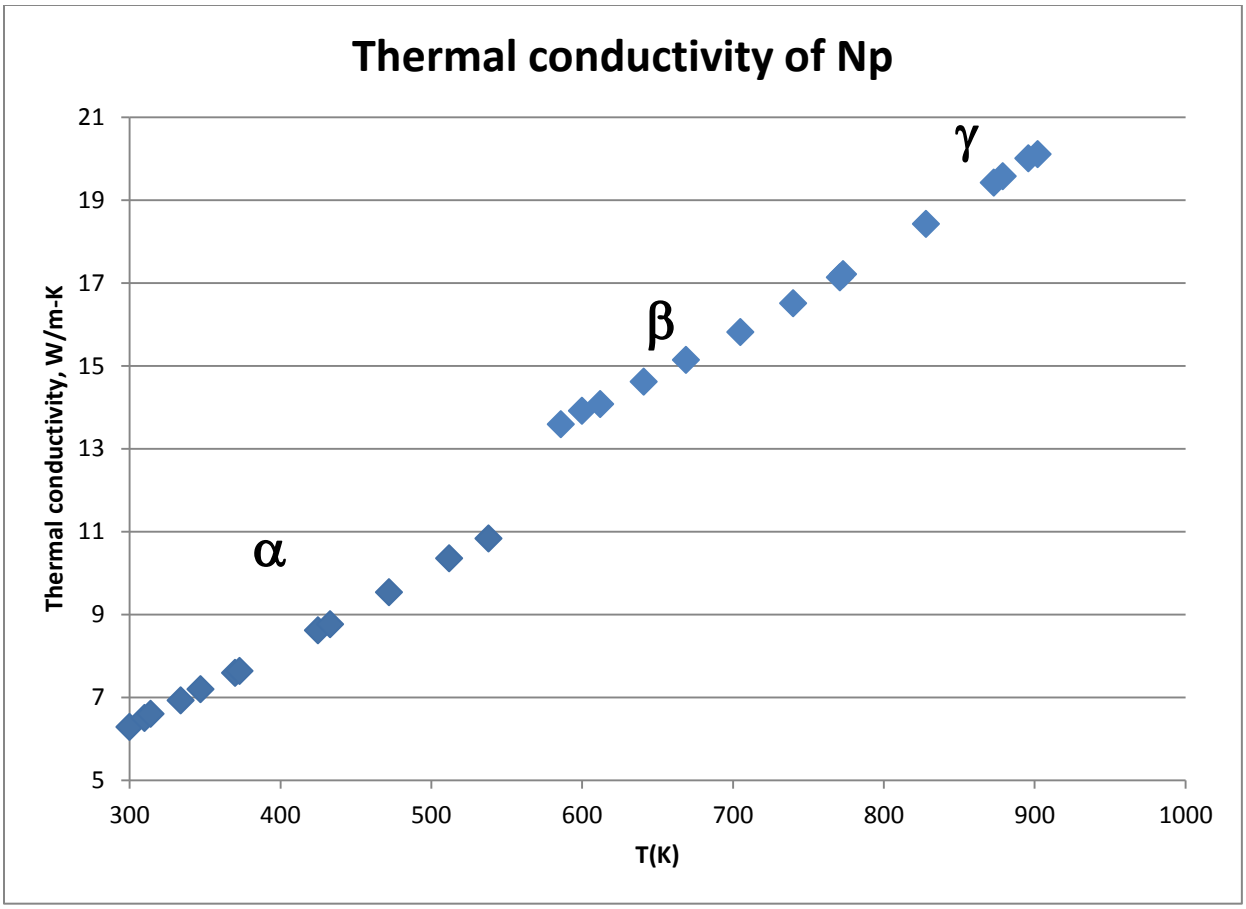

Figure 10. Thermal conductivity of Np calculated using the theoretical value of the Lorenz number (2.44×10^{-8} WΩ/K^2) and electrical resistivity data from Lee [93].

2.3 Pu

2.3.1 Introduction

Plutonium is a uniquely complicated element, with six solid phases (α-Pu, β-Pu, γ-Pu, δ-Pu, δ'-Pu, and ε-Pu) that are stable at atmospheric pressure. Volume changes during phase transitions are significant but poorly quantified, and two of the phases exhibit negative thermal expansion. Although these characteristics are not understood in detail, it is generally believed that they are due to the complex behavior of the 5*f* electrons (e.g., [65, 66, 97]).

Most of the experimental data for Pu was published before 1970, although later references have new interpretations of the earlier data. Major reviews include those by Oetting et al. [6] for the IAEA, Ward et al. [54], Lemire et al. [69] for the OECD/NEA, Konings and Beneš [7] (with key results repeated in [8]), and Clark et al. [98]. There is generally good agreement about many properties of Pu; however, it is important to recognize that there are only a small number of original measurements, and the good agreement between different references may reflect a lack of data rather than agreement between numerous measurements.

Measuring the thermal expansion of Pu is difficult, and only a small number of measurements have been published. These measurements show wide variations. Detailed studies of phase-transformation mechanisms by Ennaceur [99-103] show that transformations in individual samples are affected by factors such as previous thermal and phase-transformation history, and that the order in which

transformations occur may be different during heating and cooling. Understanding thermal expansion is further complicated by the anisotropic thermal expansion of α-Pu, β-Pu, γ-Pu, and δ′-Pu, and by the negative thermal expansion of δ-Pu and δ′-Pu. Even when phase transitions are not involved, thermal expansion of polycrystalline aggregates may vary between individual samples.

The thermal conductivity of Pu is relatively well known, thanks in part to new measurements from high-purity plutonium [104].

One important area of ongoing experimental research involves understanding changes in lattice parameters, electrical resistivity, and magnetic susceptibility at cryogenic temperatures due to irradiation from α-particles produced by radioactive decay of the sample. Results of this research indicate that effects of self-irradiation may be significant at temperatures below ~20 K but are annealed rapidly enough that they can be neglected at room temperature and above (e.g., [105-109]).

Other recent research on Pu includes investigation of the ground-state electron configuration of δ-Pu by neutron spectroscopy [110], demonstration of a technique for three-dimensional microstructural characterization using a dual-beam FIB/SEM instrument [38], studies of aging phenomena in δ–^{239}Pu [111], use of Voronoi-Dirichlet tessellation to analyze crystal structures [39], a detailed consideration of the behavior of solitons at phase transitions [23], and development of models [112-122].

2.3.2 Phases and Phase Transformations

2.3.2.1 Phases

Plutonium has six phases that are stable at atmospheric pressure. They are:

- α-Pu, monoclinic (space group $P2_1/m$, a = 6.183 Å, b = 4.822 Å, c = 10.963 Å, β = 101.79° at 294 K [98]). The atoms are arranged in layers of highly distorted hexagons perpendicular to the b axis. The α-Pu structure has 16 atoms per unit cell in 8 crystallographically unique positions. Positions of the individual atoms can be found the original structure refinements by Zachariasen and Ellison [123, 124] and the review by Clark et al. [98]. Information about Debye-Waller factors can be found in reference [49].
- β-Pu, monoclinic (space group $I2/m$, a = 9.284 Å, b = 10.463 Å, c = 7.859 Å, β = 93.13° at 463 K (190°C) [98]; the unconventional space group $I2/m$ is equivalent to space group $C2/m$ with origin choice 3 in the International Tables for Crystallography [125]). The β-Pu structure has 34 atoms per unit cell in 7 crystallographically unique atomic positions. Positions of the individual atoms can be found in the original structure refinement by Zachariasen and Ellison [126] and the review by Clark et al. [98].
- γ-Pu, orthorhombic (space group $Fddd$, a = 3.159 Å, b = 5.768 Å, c = 10.162 Å at 508 K [98]). The structure consists of two face-centered cubic lattices displaced by ¼ of the body diagonal. The γ-Pu structure has eight atoms per unit cell. Positions of the individual atoms can be found in the original structure refinement by Zachariasen and Ellison [127] and the review by Clark et al. [98].
- δ-Pu, fcc (space group $Fm\bar{3}m$), a = 4.6371 Å at 593 K [98].
- δ′-Pu, tetragonal (space group $I4/mmm$), a = 3.34 Å, c = 4.44 Å at 738 K [98]. The structure is body-centered tetragonal, with two atoms per unit cell [128].
- ε-Pu, bcc (space group $Im\bar{3}m$), a = 3.6361 Å at 763 K [98]. The structure is body-centered cubic [129].

Two high-pressure studies indicate that δ- and δ'-Pu both transform to γ-Pu at pressures somewhat below one kbar [130, 131], while a third study indicates that δ-, δ'-, and γ-Pu all transform to a seventh Pu phase (ζ-Pu) at pressures between 0.6 and 1.7 kbars [132]. None of these studies included diffraction

data, and all of the evidence for the existence of ζ-Pu is apparently from a single conference paper. Although investigation of this phase transformation is important for plutonium metallurgy, it is not relevant for metallic fuels because of the pressures at which it occurs.

2.3.2.2 Phase Transformations

Pu phase transformations are sensitive to alloying elements in low concentrations. Elements such as Al, Ga, Ce, Am, In, Tl, and Sc stabilize the δ-Pu structure so that it can be examined at room temperature, and elements such as Si, Zn, Zr, Hf, and perhaps Th and trivalent lanthanides such as Dy, Er, Tm, Lu, and Tb allow the δ-Pu structure to be retained as a metastable phase during rapid cooling [97]. In particular, the incorporation of low concentrations of Ga or Al makes it possible to study metastable δ-Pu solid solution phases at room temperature (e.g., [106, 111, 120, 133-141]), and much of the recent research on properties of "δ-Pu" actually involves these solid solutions. Np extends the stability of the α-Pu structure (reference [97] and Section 3.3.2.1).

Much of the data about phase transformations in Pu was collected before 1970. This data varies in quality, and detailed experimental descriptions and information about sample purity were not provided for some data. Early measurements were summarized in reviews by Oetting et al. [6] and Konings and Beneš [7], and will not be considered here. Data in this section of the Handbook is from more recent measurements using high-purity Pu with total impurities of at most a few hundred parts per million by weight.

Transition onset temperatures and enthalpies measured during DSC experiments that involve a constant rate of temperature increase may differ from those measured in experiments with isothermal holds to allow the samples to anneal between transitions [100-103]. These differences are attributed to incomplete transitions and the effects of internal strains due to the large volume changes associated with some of the transitions. Further research is needed, particularly for cooling transitions, and will require careful experimental design to ensure that measurements for individual transitions are not affected by the previous thermal histories of the samples.

All of the solid-state phase transitions in Pu produce well-defined, approximately symmetrical, peaks during heating in a DSC, suggesting a "normal" phase transition mechanism involving nucleation and growth [142 (Figure 3)]. The ε-δ' and δ'-δ cooling transitions also produce well-defined single peaks, with enthalpies similar to those from the corresponding heating transitions and a "normal" amount of undercooling. These characteristics suggest that the δ-δ' and δ'-ε transitions are reversible [142].

Although the characteristics of the δ-γ cooling transition are strongly dependent on the thermal history of the sample, its onset temperature is apparently about 60-65°C below that of the γ-δ heating transition. DSC data commonly show a series of spikes occurring over a temperature range of ~80°C. Decreasing the cooling rate increases the number of spikes and the temperature range over which the reaction occurs, and a sample that was held at 260°C (where the stable Pu phase is γ-Pu) for 4 hours, heated to 450 C (where δ-Pu is stable) and held at that temperature for 12 hours, then cooled through the δ-γ transition at 5°C/min showed only one significant peak [100]. The combined enthalpy from all of the spikes is significantly below that from the γ-δ heating transformation [100, 140, 142]. These characteristics are generally interpreted as indicating an incomplete martensitic (diffusionless) transformation, in which the reaction rate and number of spikes in DSC data are strongly influenced by local strain caused by the large volume change during this transition [100, 140, 142, 143].

The onset temperature for the γ-β cooling transition is~100°C below that of the β-γ heating transition, and the γ–β transition occurs over a wider temperature range. The enthalpy of the γ–β transition is significantly smaller than that of the β-γ transition, suggesting that the γ–β transition is commonly incomplete in DSC cooling data [140].

The onset temperature of the β-α cooling transformation is significantly below that of the α-β heating transition. The enthalpy of the β-α transition is smaller than that of the α-β transition, suggesting that the cooling transition is incomplete. Ennaceur [101] reported that enthalpy of the β-α transition equaled that of the α-β transition if the DSC measurement was continued for a minimum of three hours after the sample had been cooled to 25°C, but that the onset temperature of the α-β transition was higher in samples that had been held at 25°C for less than 24 hours after being cooled through the β-α transition than in samples that had been held at 25°C for longer periods of time. A detailed investigation of the β-α transformation suggests that it is probably martensitic, but also involves diffusion of a small fraction of the atoms in the β-Pu crystal lattice to form interstitials in α-Pu [140].

Transitions from γ-Pu directly to α-Pu or a phase called α' have been studied in Pu-Ga alloys with low concentrations of Ga. No analogous transitions have been reported in pure Pu at atmospheric pressure, or in Pu alloys with δ-stabilizing elements of interest for FCRD fuels (Zr, Ce, and Am).

Table 5 and Table 6 summarize the available data on the onset temperatures and reactions in high-purity Pu. Data from reference [140] and the PC-DSC data from reference [142] appear to represent the same experimental results. There is generally good agreement between the reported onset temperatures of all transitions (and also with the recommended values in Revision 1 of this Handbook, which followed Konings and Beneš [7]), although differences between the reported onset temperatures are generally larger than indicated by error bars on individual measurements.

Enthalpies for the α-β and β-γ heating transitions from different measurements agree to within about 10%, with wider variations between enthalpies of other heating transitions. Enthalpies of cooling transitions are less well understood, but are commonly smaller than those of the corresponding heating transitions. Although further research is needed, the measurements by Ennaceur are probably the most accurate representations of enthalpies of individual phase transitions because of the care given to ensure that measurements of each phase transition are not affected by previous phase transitions. However, a recent conference paper showing that an as-cast sample of Pu retained a large fraction of β-Pu several months after casting suggests that the 24-hour hold at room temperature that Ennaceur used to remove effects of previous transformations may not be sufficient [144]. Some of Ennaceur's values differ from the recommended values in Revision 1 of this Handbook, which were based on a review by Konings and Beneš [7] that used values from Oetting and Adams (reference [145]) for lower-temperature transitions and data from Zocco et al. (reference [142]) for higher-temperature ones. If consistent data involving phase transitions across a wide range of temperatures is needed, it is probably appropriate to use the values from Konings and Beneš.

Table 5. Onset temperatures of solid-state phase transitions in high-purity Pu, °C.

Transition	**Mitchell et al. [140][a]**	**Zocco et al. [142][b]**		**Ennaceur [100-103][c]**	**Oetting and Adams [145][h]**	**Konings and Beneš [7]**
		HF-DSC	**PC-DSC**			
α→β (heating)	126	127.5 ±0.3	126.25±0.05	131.5 ±0.3 [101][d]	124.45±1.0	126±1
β→α (cooling)	78.278	80.4±0.6	78.3±0.5	—	—	—
β→γ (heating)	214	212.9±0.3	213.9±0.51	216.2±0.5 [103][e]	214.75±1.0	215±1
γ→β (cooling)	113.624	—	113.6±0.7	—	—	—
γ→δ (heating)	323	322.9±1.6	323.42±0.04	323.5±0.4 [102][f]	319.95±1.0	323±2
δ→γ (cooling)	260	260.7±0.8	257.1±0.4	[7]—	—	—

Table 5. (continued).

Transition	Mitchell et al. [140][a]	Zocco et al. [142][b]		Ennaceur [100-103][c]	Oetting and Adams [145][h]	Konings and Beneš [7]
		HF-DSC	PC-DSC			
δ→δ' (heating)	468	468.6±2.3	467.6±0.44	—	—	468±4
δ' →δ (cooling)	461.199	462.6±1.3	461.2±0.005	—	—	—
δ' →ε (heating)	486	485.6±0.3	485.9±0.13	—	—	496±4
ε→δ' (cooling)	483.911	483.5±0.1	483.9±0.02	—		—
Melting	—	—	—	—	—	640±2

a. Zone-refined Pu with total impurities of ~200 ppm by weight. Major impurity element is U. Data was collected with heating and cooling rates of 10°C/minute.
b. Zone-refined Pu, apparently from the same source as that used by [140]. Data was collected with heating and cooling rates of 10°C/minute. Similar experiments were performed using two kinds of DSC: heat flux (HF) and power compensating (PC), with generally excellent agreement.
c. Electrorefined Pu with total impurities of ~420 ppm by weight. The major impurity element is W.
d. "Hightly repeatable" measurement from sample that had been allowed to rest at 25°C for 24 hours. Samples that had shorter rest times after experiencing a β-α transition had lower onset temperatures
e. Measured after isothermal hold of 4-50 hours at 150°C (β-Pu). Samples with shorter isothermal holds had lower onset temperatures
f. Measured after isothermal hold of 50 hours at 360°C (γ-Pu). Onset temperature for samples heated from room temperature without holds was 318.0±0.3°C.
g. Transition occurs between 260 and 180 C in a sample heated to 500°C (ε-Pu) and cooled at 5°C/minute. Samples with other thermal histories had significantly different results
h. Pu with < 100 ppm total impurities by weight. Major impurity element is Am. Data was collected by adiabatic calorimetry [146]. Each sample was heated only once to avoid introducing errors due to lack of reversibility in phase transitions

Table 6. Enthalpies of solid-state transformations in Pu. Samples are the same as in Table 5. Values are assumed to be measured during heating unless indicated in the notes. Units vary between references.

Transition	Mitchell et al. [140] (J/g)	Zocco et al. [142]		Ennaceur [100-103] (J/g)	Oetting and Adams [145] (J/g)	Konings and Beneš [7] (J/mol)
		HF DSC (J/g)	PC DSC (J/g)			
α-β	15.43	13.22±0.9	15.43±0.34	14.4±0.2 [101]	15.5	3706±30
β-α	-10.4685	—	—	—	—	—
β-γ	2.18	2.134±0.05	2.18±0.04	2.1±0.1 [103][a]	2.0	478±20
γ-β	-1.7225	—	—	—	—	—
γ-δ	2.35	3.012±0.18	2.35±0.01	2.4±0.1 [102][b]	2.98	713±50
δ-γ	-2.1405	—	—	—	—	—
δ-δ'	0.27	0.335±0.03	0.273±0.022	—	—	65±20
δ'-δ	-0.222	—	—	—	—	—
δ'-ε	7.16	9.205±0.54	7.16±0.16	—	—	1711±50
ε-δ'	-7.125	—	—	—	—	—
Melting	—	—	—	—	—	2766±100

a. Enthalpy not changed by isothermal hold at 150°C
b. Enthalpy in sample held at room T for at least 50 hours, then heated at 5°C/minute without isothermal hold was 2.2±0.2 J/g

2.3.3 Heat Capacity and Related Properties

2.3.3.1 Standard Thermodynamic Values

The standard enthalpy of solid Pu at 298.15 K, standard entropy of Pu gas, and enthalpy of formation of Pu gas are:

- S^0(298.15 K) = 54.46 ± 0.80 J/mol·K for α-Pu [7, 69]
- S^0(298.15 K) = 177.19 ± 0.10 J/mol·K for Pu gas [7]
- $\Delta_f H^0$(298.15 K) = 348.9 ± 3.0 kJ/mol for Pu gas [7].

2.3.3.2 Heat Capacities of Solid and Liquid Phases

Figure 11 shows the heat capacities for solid and liquid Pu recommended by Lemire et al. [69] and by Konings and Beneš [7]. These reviews have identical heat capacities for β-, γ-, and δ-Pu because both are quoting equations from Oetting and Adams (reference [145]). The heat capacity for α-Pu is also from Oetting and Adams, except that Konings and Beneš adjusted it slightly upward to match their preferred values for lower-temperature measurements. Heat capacities for δ′ and ε-Pu are identical in both reviews because they are originally from a Mound Laboratory report by Wittenberg et al. (reference [147]). The heat capacity for liquid Pu recommended by Konings and Beneš is also from the report by Wittenberg et al., and the source of the heat capacity for liquid Pu recommended by Lemire et al. is not specified. The preferred values (from Konings and Beneš [7]) are expressed by Equation 18 through Equation 24.

Equation 18. Heat capacity of α-Pu ([7] with temperature range from [145])

$C_p = 17.6186 + 45.5523 \times 10^{-3} \times T$

where C_p is constant-pressure heat capacity in J/mol·K, T is temperature in K, and T is between 330 and 390 K

Equation 19. Heat capacity of β-Pu [7, 69, 145]

$C_p = 27.4160 + 13.060 \times 10^{-3} \times T$

where C_p is constant-pressure heat capacity in J/mol·K, T is temperature in K, and T is between 408 and 476 K

Equation 20. Heat capacity of γ-Pu [7, 69, 145]

$C_p = 22.0233 + 22.959 \times 10^{-3} \times T$

where C_p is constant-pressure heat capacity in J/mol·K, T is temperature in K, and T is between 493 and 586 K

Equation 21. Heat capacity of δ-Pu [7, 69, 145]

$C_p = 28.4781 + 10.807 \times 10^{-3} \times T$

where C_p is constant-pressure heat capacity in J/mol·K, T is temperature in K, and T is between 602 and 680 K

Equation 22. Heat capacity of δ′-Pu [7, 69]

$C_p = 35.56$

where C_p is constant-pressure heat capacity in J/mol·K and T is temperature in K

Equation 23. Heat capacity of ε-Pu [7, 69]

C_p (ε-Pu) = 33.72

where C_p is constant-pressure heat capacity in J/mol·K and T is temperature in K

Equation 24. Heat capacity of liquid Pu [7]

C_p (liquid Pu) = 42.80

where C_p is constant-pressure heat capacity in J/mol·K and T is temperature in K

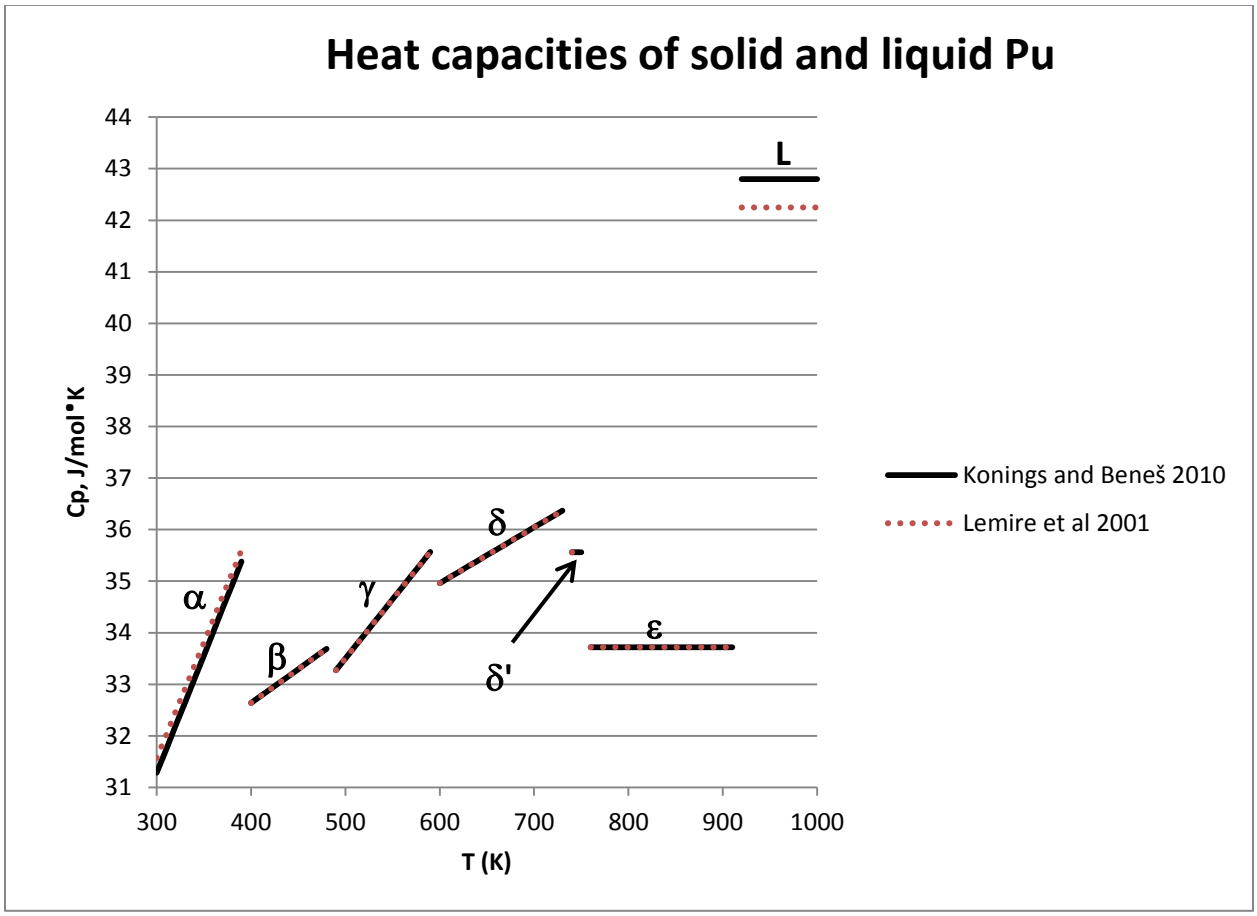

Figure 11. Heat capacities of solid and liquid Pu. Values from Konings and Beneš [7] (solid black lines, Equation 18 through Equation 24) are preferred.

Measurement of heat capacities in Pu at temperatures below ~20 K is complicated by defects from self-irradiation by α-particles produced by radioactive decay of the sample. At room temperature and above, these defects are annealed rapidly enough that they do not significantly affect experimental measurements (e.g., [105-109]).

2.3.3.3 Heat Capacity of the Ideal Gas

Konings and Beneš [7] calculated the heat capacity of ^{239}Pu as an ideal gas and fitted the heat capacity by two polynomials (Figure 12, Equation 25, and Equation 26). These polynomials match those calculated from a similar database at temperatures up to 2000K by Lemire et al. [69] to within a few hundredths of a J/mol K.

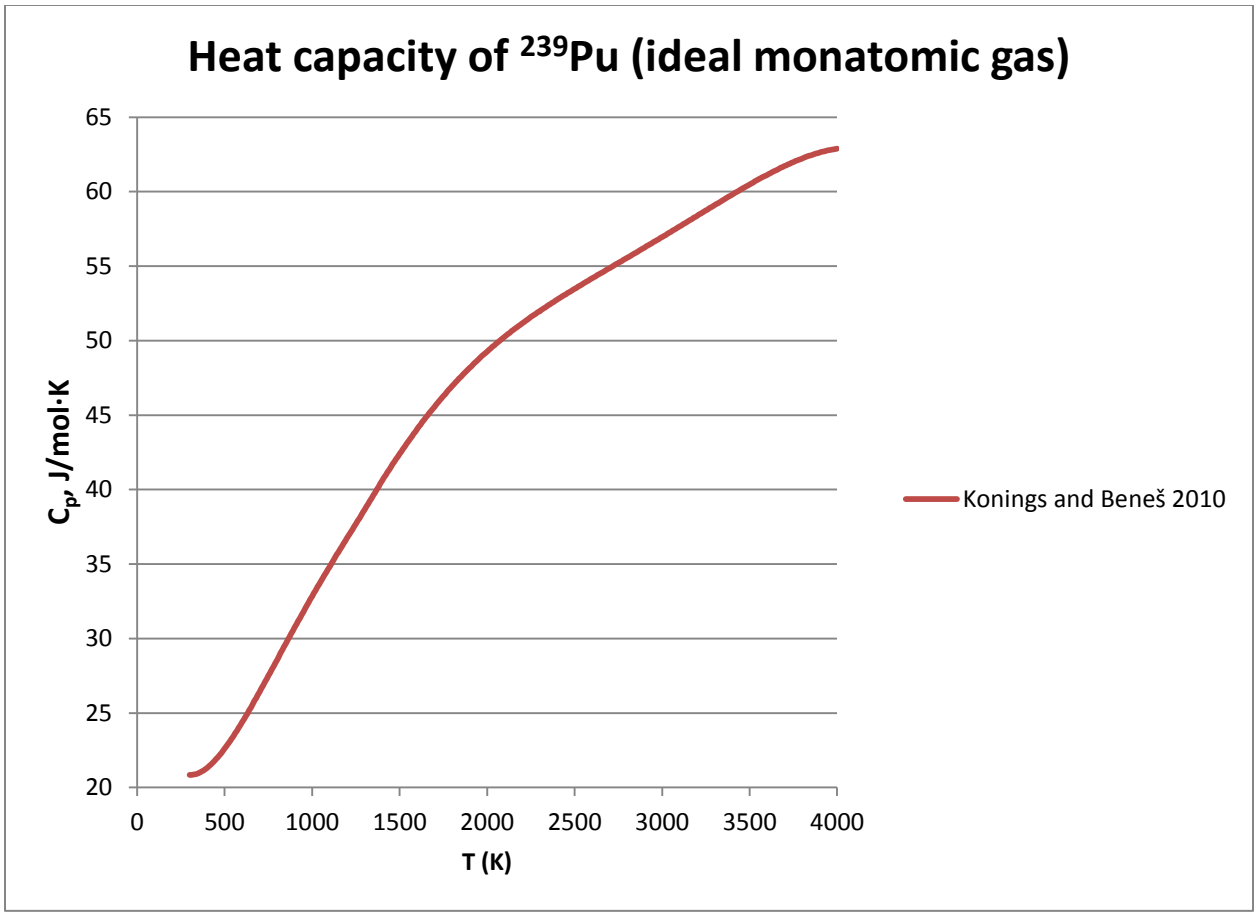

Figure 12. Heat capacity of ^{239}Pu as an ideal gas, calculated using Equation 25 and Equation 26.

Equation 25. Heat capacity of Pu gas from 298.15 to 1400 K [7]

$$C_p = 24.2954 - 37.0413 \times 10^{-3} \times T + 95.1224 \times 10^{-6} \times T2 - 65.8404 \times 10^{-9} \times T^3 + 16.2344 \times 10^{-12} \times T^4 + 6.7865 \times 10^4 \times T^{-2}$$

where C_p is constant-pressure heat capacity in J/mol·K, T is temperature in K, and T is between 298.15 and 1400 K

Equation 26. Heat capacity of Pu gas from 1400 to 4000 K [7]

$$C_p = -112.0172 + 187.5714 \times 10^{-3} \times T - 86.6780 \times 10^{-6} \times T^2 + 18.8245 \times 10^{-9} \times T^3 - 1.5431 \times 10^{-12} \times T^4 + 2.7817 \times 10^{7\ 2}$$

where C_p is constant-pressure heat capacity in J/mol·K, T is temperature in K, and T is between 1400 and 4000 K

Heat capacities at very low temperatures may be affected by defects caused by self-irradiation from α particles produced as a result of radioactive decay. This effect may be significant at temperatures below ~20 K but can be neglected at room temperature and above (e.g., [105-109]).

2.3.4 Thermal Expansion and Density

2.3.4.1 Thermal Expansion

Reviews of experimental measurements of thermal expansion of Pu [55, 97, 98, 148] generally agree about the thermal expansion of individual Pu phases (Figure 13), although there is less good agreement about changes in length associated with phase transformations.

Equations representing the thermal expansion of α-Pu were developed by Schonfeld and Tate [148] and by Touloukian et al. [55] (Equation 27). Values produced by the two equations agree to within ~0.1%.

The thermal expansions of β-, γ-, δ-, δ′-, and ε-Pu are linear functions temperature and can be represented using the thermal expansion coefficients in Table 7.

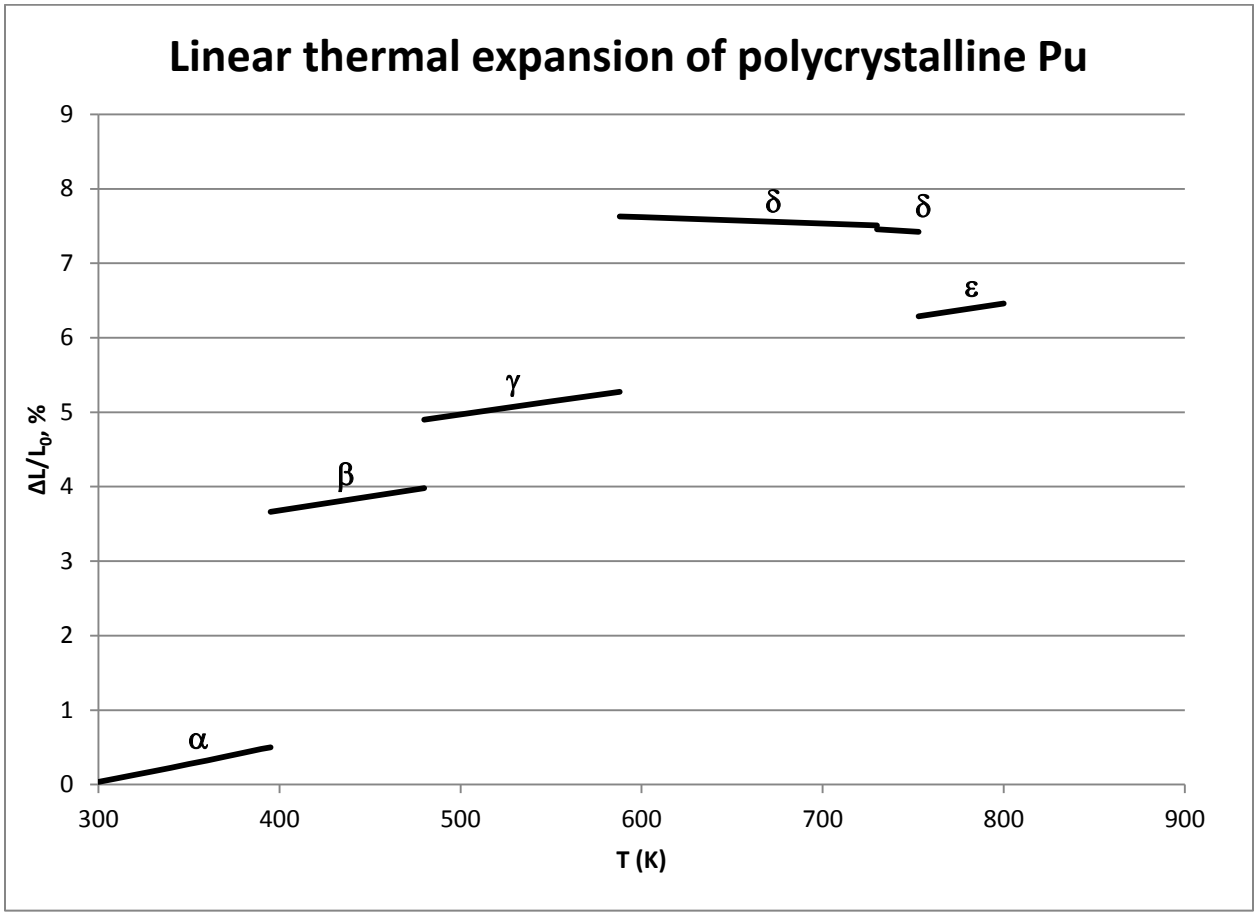

Figure 13. Linear thermal expansion of polycrystalline Pu [148].

Equation 27. Thermal expansion of α-Pu [55]

$$(L-L_0)/L_0 = -0.407 + 4.099 \times 10^{-3} \times (T-200) + 3.552 \times 10^{-6} \times (T-200)^2 - 3.360\times10^{-9} \times (T-200)^3$$

Where $(L-L_0)/L_0$ is thermal expansion in %, T is temperature in K, T is between 200 and 395 K, L is length at temperature T, and L_0 is length at 293 K

2.3.4.2 Thermal Expansion Coefficients

Table 7 summarizes mean coefficients of thermal expansion for β-, γ-, δ-, δ'-, ε- and liquid Pu from several reviews. There is generally good agreement between the reviews for all of the phases in the table. Values for solid

phases are for ideal polycrystalline materials with no preferred orientation. The thermal expansion coefficients in the table are largely independent of temperature, and the mean coefficients can be used throughout the stability fields of the individual phases [149]. The thermal expansion coefficient of α-Pu is not included in the table because the thermal expansion of α-Pu is a non-linear function of temperature, so its thermal expansion is not a constant. Values for liquid Pu are volumetric thermal expansion coefficients, each of which is approximately three times the corresponding linear coefficient, and are independent of temperature.

Table 7. Thermal expansion coefficients (10^{-6}/K) of solid and liquid Pu [55, 98, 148].

Phase	Reference [98]	Reference [55]	Reference [148]
β	42	37.3	42.3
γ	34.6±0.7	34.6	34.7
δ	-8.6±0.3	-8.6	-9.0
δ′	-65.6±10.1	-16.1	-66
ε	36.5	36.6	—
Liquid	93 (volumetric)	90.4 (volumetric)	—

Table 8 shows values of mean coefficients of thermal expansion along single directions for anisotropic Pu phases. δ-Pu, ε-Pu, and liquid are not included in the table because their thermal expansion is isotropic.

Table 8. Mean linear coefficients of thermal expansion along single directions for anisotropic Pu phases [98].

Phase	Coefficient[a]	Crystallographic orientation	Temperature range (°C)	Value ($\times 10^{-6}$/C)
α	$\bar{\alpha}_1$	⊥ c-axis	21-104	60
—	$\bar{\alpha}_2$	∥ b-axis	—	75
—	$\bar{\alpha}_3$	∥ c-axis	—	29
β	$\bar{\alpha}_1$	—	93-190	94
—	$\bar{\alpha}_2$	∥ b-axis[b]	—	14
—	$\bar{\alpha}_3$	$\perp(10\bar{1})$	—	19
γ	$\bar{\alpha}_a$	∥ a-axis	210-310	-19.7±1.0
—	$\bar{\alpha}_b$	∥ b-axis	—	39.5±0.6
—	$\bar{\alpha}_c$	∥ c-axis	—	84.3±1.6
δ′	$\bar{\alpha}_a$	∥ a-axis	452-480	444.8±12.1
—	$\bar{\alpha}_c$	∥ c-axis	—	-1063.5±18.2

a. Overbar indicates that these are mean coefficients; subscripts identify individual coefficients. All coefficients for each phase are mutually orthogonal.
b. In space group *I*2/*m*

2.3.4.3 Density

Table 9 summarizes the lattice parameters, unit-cell volumes, and calculated densities for Pu phases. Lattice parameters are repeated from Section 2.3.2.1. Densities in Table 9 are calculated based on Pu-239; densities for other isotopic compositions can be calculated from information in the table using Equation 5

from reference [5]. Densities in Table 9 agree with densities in references [98 (Table 7.9)] and [21 (Table 2.13)] to within 0.03 g/cm^3 except as noted.

Although measured densities of α-Pu and β-Pu have been reported, they were intended primarily to assist in X-ray structure refinements by suggesting the numbers of atoms per unit cell, and were therefore collected with less care than the X-ray data. As a result, it seems likely that the calculated densities represent the actual sample densities better than the measured densities do.

Table 9. Lattice parameters, unit-cell volumes, and calculated densities for Pu phases.

Phase	T (K)	Lattice parameters				Unit-cell Volume (Å^3)	Atoms per unit cell	Density (g/cm^3)	References
		a (Å)	*b* (Å)	*c* (Å)	β (degrees)				
α-Pu	294	6.183	4.822	10.963	101.79	319.960	16	19.84[a]	[123]
β-Pu	463	9.284	10.463	7.859	92.13[b]	762.273	34	17.69[c,d]	[126, 150]
γ-Pu	508	3.159	5.7682	10.162	—	185.163	8	17.14	[127]
δ-Pu	593	4.637	—	—	—	99.704	4	15.92	[98]
δ'-Pu	738	3.34	—	4.44	—	49.531	2	16.03	[98]
ε-Pu	763	3.6361	—	—	—	48.074	2	16.51	[98]

a. Corresponds to measured density of 19.77 g/cm^3 for Pu of 99.9% purity with atomic weight 239.05 [123]
b. Reference [98 Table 7.9] lists this value as 93.13. As the original source of their data is reference [126], this is apparently an error.
c. Corresponds to reported density of 17.8 g/cm3 at 423 K (reference [150] quoting reference [151]).
d. A relatively recent review by the IAEA lists the density of this phase as 17.77 g/cm^3.The source of density is unknown, as the lattice parameters in the review agree with the values used here [21 (Tables 2.12 and 2.13)].

2.3.4.4 Changes in Volume as a Result of Phase Transitions

Although solid-state phase transitions in Pu are generally considered to result in large volume changes, these changes are rarely quantified. The volume of Pu decreases by 2.4% during melting, with the result that ε-Pu floats on liquid Pu [152].

2.3.5 Thermal Conductivity and Related Properties

2.3.5.1 Lorenz Number

Values of the room-temperature Lorenz number for Pu determined before 1974 vary widely, with a thorough review by Ho et al. [95] concluding that a value of 3.15 x 10^{-8} WΩ/K^2 for polycrystalline α-Pu based on the electrical resistivity and thermal conductivity measurements of Andrew [153] appeared the most plausible. This value appeared in a recent review by Konings [8 (Figure 22)] and may be the best currently available estimate of the Lorenz number for Pu. However, the good agreement between the measured thermal conductivities of Pu phases and values calculated from electrical resistivity data using the theoretical value of the Lorenz number (2.44 x 10^{-8} WΩK/K^2) suggest that more investigation is needed.

2.3.5.2 Thermal Conductivity

Recent attempts to determine the thermal conductivity of Pu have taken different approaches: Alexander and Wood [104] calculated thermal conductivity based on their new measurements of the thermal diffusivity of zone-refined Pu and heat-capacity, density, and thermal-expansion data from previous publications. They determined that the thermal conductivity of each phase except δ′-Pu (which is difficult to study because of its narrow temperature range of stability) increased approximately linearly with temperature, and that the thermal conductivity of δ′-Pu decreased with temperature. They also noted that all of their data could be fitted to within an error of ~5% by a single quadratic equation.

In contrast, Kim et al. [19] relied on older publications with thermal-conductivity values for α-Pu, β-Pu, and γ-Pu and estimated the thermal conductivity of other phases based on their electrical resistivity

and the theoretically determined Lorenz number (2.45×10^{-8} WΩ/K^2) Their results agreed with those of Alexander and Wood [104] to within ~10% for all phases except δ′-Pu (Figure 14). The two studies apparently have no data in common.

Both of these assessments have thermal conductivity values that are significantly higher than those in a recent IAEA data summary [21] for all solid Pu phases except α-Pu. However, the good agreement between the thermal conductivities determined by Alexander and Wood and by Kim et al. suggests that these studies are good approximations of the actual behavior of Pu, with preference given to the results of Alexander and Wood because they are based on direct measurements of well-characterized starting materials. Either of these studies is probably a more accurate representation of the actual behavior of Pu than the values in the IAEA tabulation. Unless phase-specific information is required, the single quadratic equation developed by Alexander and Wood (Equation 33) is a convenient approximation.

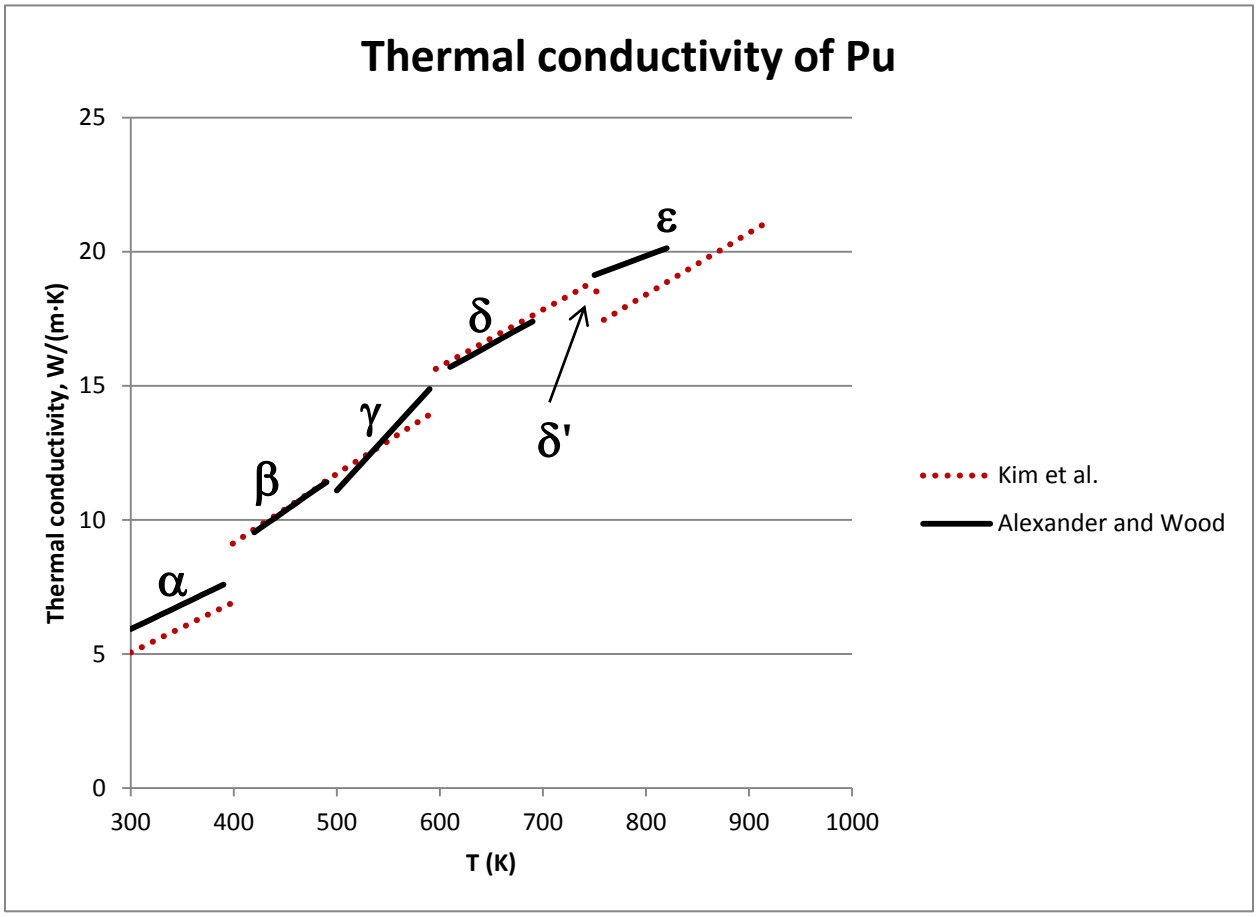

Figure 14. Thermal conductivity of Pu. Data from Alexander and Wood were calculated from Equation 28 through Equation 32.

Alexander and Wood fitted their data for all phases except δ′-Pu to linear equations, each of which matched all of their measured data points to within 5%. These equations are:

Equation 28. Thermal conductivity of α-Pu from 294 to 394 K according to Alexander and Wood [104]

$$k = 0.01844 \times T + 0.390$$

where k is thermal conductivity in W/m·K, T is temperature in K, and T is between 294 and 394 K

Equation 29. Thermal conductivity of β-Pu from 415 to 490 K according to Alexander and Wood [104]

$$k = 0.02679 \times T - 1.716$$

where k is thermal conductivity in W/m·K, T is temperature in K, and T is between 415 and 490 K

Equation 30. Thermal conductivity of γ-Pu from 491 to 595 K according to Alexander and Wood [104]

$$k = 0.04201 \times T - 9.909$$

where k is thermal conductivity in W/m·K, T is temperature in K, and T is between 491 and 595 K

Equation 31. Thermal conductivity of δ-Pu from 602 to 696 K according to Alexander and Wood [104]

$$k = 0.02131 \times T + 2.697$$

where k is thermal conductivity in W/m·K, T is temperature in K, and T is between 602 and 696 K

Equation 32. Thermal conductivity of ε-Pu from 750 to 822 K according to Alexander and Wood [104]

$$k = 0.01428 \times T + 8.423$$

where k is thermal conductivity in W/m·K, T is temperature in K, and T is between 750 and 822 K

Alexander and Wood noted that their data for all phases except δ′ from temperatures between 400 and 820 K could be matched to within ~5.4% by a quadratic equation (Equation 33), which provides a convenient approximation across a wide temperature range. This equation is:

Equation 33. Approximate thermal conductivity of Pu from 400 to 820 K according to Alexander and Wood [104]

$$k = -8.162 + 4.841 \times 10^{-2} \times T - 0.1614 \times 10^{-4} \times T^2$$

where k is thermal conductivity in W/m·K, T is temperature in K, and T is between 400 and 820 K

2.4 Am

2.4.1 Introduction

It is generally believed that there are three solid Am phases that are stable at atmospheric pressure and temperatures above 300 K. The crystal structures and lattice parameters of two of these phases (α-Am and β-Am) have been published, although there is some disagreement about phase-transformation temperatures. Thermal-analysis data shows a third phase (γ-Am), whose structure has not been experimentally determined.

The heat capacities of three samples of Am have been measured at temperatures between 15 and 300 K. Several estimates of higher-temperature heat capacities have been published, but all rely on interpretation of the low-temperature data and reasoning by analogy to rare-earth elements. Povzner et al. [154] calculated the electron contribution to the heat capacity of Am, obtaining good agreement with the low-temperature experimental data of Hall et al. [155].

There are apparently only two papers with original reports of experimental measurements of the thermal expansion of Am. One of these papers is the primary source for data on the crystal structures of α- and β-Am; the other has a single figure showing dilatometry results in a letter reporting the use of thermal expansion measurements to investigate phase-transformation temperatures. Data from these sources is inconsistent.

No experimental measurements of the thermal conductivity or thermal diffusivity of Am are available.

Recent research on Am has focused on understanding its high-pressure behavior, its superconductivity, and the behavior of its 5*f* electrons. Much of this research was reviewed by Johansson and Li [65] and by Moore and van der Laan [66]. More recent research papers include references [67, 156-162].

2.4.2 Phases and Phase Transformations

2.4.2.1 Phases

It is commonly accepted that there are three solid Am phases that are stable at atmospheric pressure. Structure determinations of α-Am and β-Am by McWhan et al. [163] are commonly accepted in more recent reviews (e.g., [8, 164]). There are no published experimental determinations of the structure or lattice parameters of γ-Am, although it is commonly believed to be bcc.

The crystallographic characteristics of the generally recognized solid Am phases are:

- α-Am, dhcp (space group $P6_3/mmc$), a = 3.4681 Å, c = 11.241 Å at 20°C [163]
- β-Am, fcc (space group $Fm\bar{3}m$), a = 4.894 Å [163]
- γ-Am, assumed to be bcc (space group $Im\bar{3}m$) by analogy to the early lanthanides [6], although no crystallographic data is available. This phase is known from dilatometry and differential thermal analysis data (e.g., [165-168]). A recent paper indicating that γ-Am has space group $Fm3m$ and lattice parameter a = 4.894 Å [156 Table 2] is probably mislabeled data from β-Am.

The existence of other Am phases has been suggested as a result of thermophysical analyses [166, 169], but without information on crystal structures. In particular, a phase with a dhcp structure and lattice parameters significantly larger than those of α-Am has been identified by several researchers using X-ray diffraction data [170-172]. Further work is needed to investigate the existence and properties of these phases.

Although a transformation to an orthorhombic phase at a pressure of ~152 kbars has been documented in an Am sample that contained 1000 ppm Yb [173], more recent reviews agree that the lowest-pressure phase transformation in pure Am produces a face-centered cubic structure at a pressure of 5-6 GPa (e.g., [8, 164, 174]). As these pressures are far greater than a nuclear fuel is likely to experience, high-pressure Am phases are not considered in this Handbook.

2.4.2.2 Phase Transformations

Published measurements of phase-transformation temperatures for Am vary widely. Measurement of the α-β transformation has been particularly difficult, possibly because of its small enthalpy, and some authors have not observed any transformations in the relevant temperature range.

Recommended phase-transformation temperatures from a recent re-assessment of the experimental data are [7]:

- α-β, 1042±10 K (769±10°C), based on 4 publications with original measurements that range from 873 to 1066 K

- β-γ, 1350±5 K (1077±10°C) (based on 6 publications with original measurements that range from 1277 to 1352 K)
- γ-liquid, 1449±5 K (1176±10°C) (based on 8 publications with original measurements that range from 1267 to 1466 K).

The corresponding phase-transformation enthalpies (ΔH_t) are [7]:

- α-β, 0.34±0.5 kJ/mol (based on 2 publications with original measurements that range from 0.34 to 0.35 kJ/mol)
- β-γ, 3.8±0.4 kJ/mol (based on 3 publications with original measurements that range from 2.3 to 5.9 kJ/mol)
- γ-liquid, 8.0±2.0 kJ/mol (based on 3 publications with original measurements that range from 4.9 to 14.4 kJ/mol).

2.4.3 Heat Capacity and Related Properties

Hall and colleagues [155, 175] measured the specific heats of two samples of ^{241}Am and one sample of ^{243}Am from 15 to 300K. They originally reported the constant-pressure heat capacity of Am at 298 K as 28 J/mol-K, but later decreased this value to 25.5 J/mol-K based on a more careful analysis of the original measurements [155]. Values accepted by later researchers (e.g., references [6, 54, 164, 176, 177]) differ slightly, but all are between ~25.0 and 25.8 J/mol-K for the heat capacity of α-Am at 298 K.

There are no published experimental measurements of the heat capacity of Am at temperatures above 300 K. Three approaches have been used to estimate it:

- Analogies to heat capacities of phases of lanthanides (primarily La) that have crystal structures similar to those of Am phases. This approach was adopted by Oetting et al. [6] in a review for the IAEA and accepted in a more recent review by Runde and Schulz [164].
- Ward et al. [54, 178] developed a correlation relating entropy to metallic radius, atomic weight, magnetic properties, and atomic structure. They used this correlation with known properties of Pr to estimate the entropy of Am at 298 K as 55.27 J/mol-K, in good agreement with a value of 55.4 J/mol-K determined by Hall et al. [155]. Ward et al. did not explain how they estimated heat capacities at other temperatures, although continuing the analogy to Pr seems likely. Silva et al. [177] generally accepted the values of Ward et al., but with small differences at temperatures below ~600 K to match the low-temperature data better.
- Konings [176] divided the heat capacity of a metal into harmonic, anharmonic, dilatation, electronic, and magnetic contributions. He estimated the heat capacities of α-Am and β-Am by estimating the value of each contribution, combining low-temperature heat-capacity, thermal expansion, compressibility, and energy-level data when available and supplementing by analogy to La when necessary. In the absence of experimental data, Konings estimated heat capacities for γ-Am and Am liquid based on analyses of trends in the lanthanide elements from La to Gd. This estimate is repeated in later reviews by Konings and colleagues [7, 8]

Figure 15 shows estimated heat capacities obtained using these approaches. There is relatively little difference between the results of Oetting et al. and of Ward et al. However, the estimates of Konings are significantly different, particularly for γ-Am and Am liquid. Further measurements are clearly required.

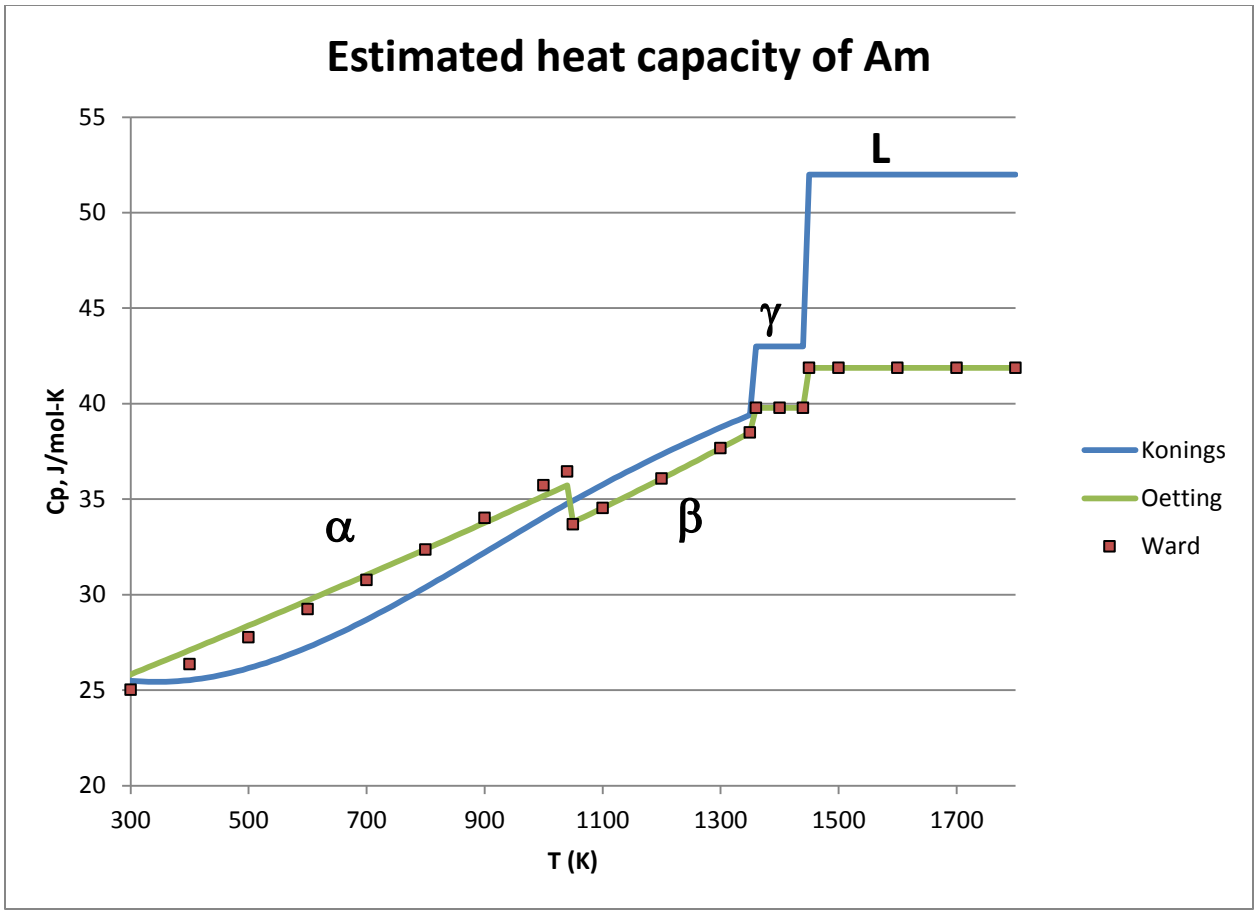

Figure 15. Estimated heat capacity of Am above 300 K, showing values from Oetting et al. [6], Konings [176], and Ward et al. [54 Table A.6]

2.4.4 Thermal Expansion and Density

2.4.4.1 Thermal Expansion

McWhan and colleagues determined the lattice parameters of α-Am at temperatures from −120 to +605°C using high-temperature X-ray diffraction [163]. They fitted their data to two polynomials (Equation 34 and Equation 35) using a least-squares technique.

Equation 34. Lattice parameter of α-Am parallel to the *a* crystallographic direction [163]

$$a = 3.4672+2.60 \times 10^{-5} \times T+0.54\text{x}10^{-8} \times T^2$$

where *a* is a lattice parameter, T is temperature in °C, and T is between −120 and + 605°C

Equation 35. Lattice parameter of α-Am parallel to the *c* crystallographic direction [163]

$$c = 11.237+6.95 \times 10^{-5} \times T+6.8\text{x}10^{-8} \times T^2$$

where *c* is a lattice parameter, T is temperature in °C, and T is between -120 and +605°C

Figure 16 shows the thermal expansion of single crystals of Am parallel to the *a* and *c* lattice parameters, calculated using Equation 34 and Equation 35 with L_0 representing a lattice parameter at 20°C. The corresponding thermal expansion coefficients are ~7.6×10^{-6}/°C parallel to *a* and 5.6×10^{-6}/°C parallel to *c* over the interval between 20 and 30°C. Although differences between the curves for expansion parallel to *a* and *c* suggest that the thermal expansion is anisotropic, it seems likely that the anisotropy is smaller than the errors in the thermal expansion data and it can therefore be neglected.

In a recent review [8], Konings and colleagues present a different equation (Equation 36) that is described as representing the thermal-expansion data of McWhan et al.. This equation does not seem to be an accurate representation of the data of McWhan et al.

Equation 36. Thermal expansion of Am [8]

$$(L-L_0)/L_0 = -2.315 \times 10^{-3} + 6.965 \times 10^{-6} \times T + 3.176 \times 10^{-9} \times T^2 \times 100$$

where $(L-L_0)/L_0$ is thermal expansion in %, T is temperature in K, L is the length at temperature T, and L_0 is the length at 298 K

The thermal expansion measurements of Rose et al. [166 Figure 1] were presented as a single figure in a published letter. The focus of the letter is determination of phase-transition temperatures, and the implications of the data for the thermal expansion of individual phases are not discussed. The data of Rose et al. is qualitatively inconsistent with the data of McWhan et al. in two important respects:

- Rose et al. show that the thermal expansion of α-Am is negative between ~66°C (the minimum temperature for their measurements) and ~300°C, while McWhan et al. observed expansion between 20 and +605°C.
- Rose et al. show a large expansion at the α-β transition, which is inconsistent with the similar densities of α- and β-Am determined from the X-ray data of McWhan et al.

Further experimental data are clearly needed to understand the thermal expansion of Am. In the absence of this data, the results presented by McWhan et al. [163] are probably the best available approximation to the actual thermal expansion of Am.

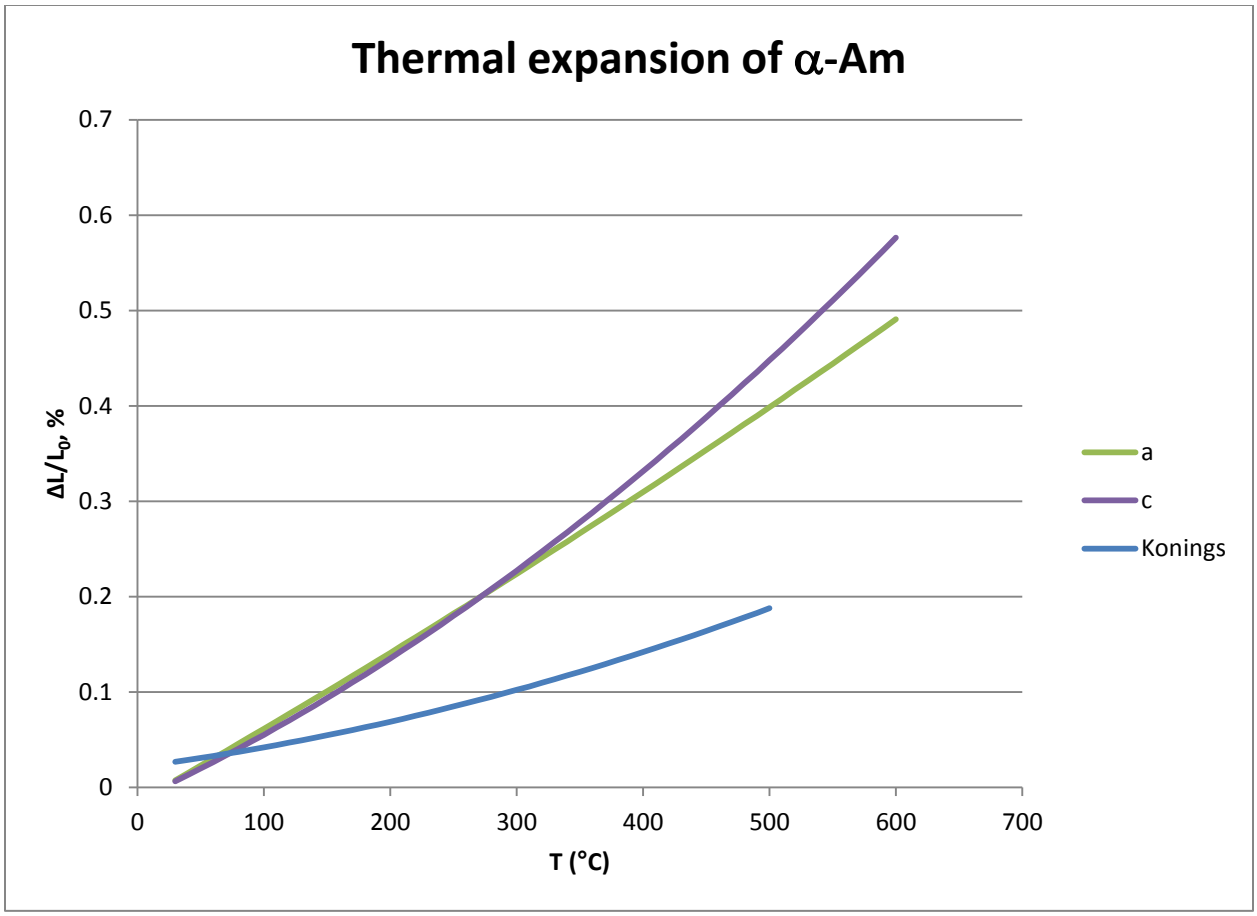

Figure 16. Thermal expansion of α-Am. The *a* and *c* lattice parameters are from McWhan et al. (Equation 34 and Equation 35); "Konings" value is from Equation 36.

2.4.4.2 Coefficients of Thermal Expansion

McWhan and colleagues determined that the coefficients of thermal expansion for α-Am at 20°C are (7.5±0.2) × 10^{-6}/°C in the *a* direction and (6.2±0.4) × 10^{-6}/°C in the *c* direction [163]. These values were repeated in a recent review [164].

McWhan et al. determined that the mean coefficient of thermal expansion for β-Am between 22 and 360°C is 9±3 × 10^{-6}/°C [163].

2.4.4.3 Density

Several researchers have reported that the density of α-Am is ~13.6 g/cm^3 at room temperature [163, 170, 179]. This value is slightly higher than that measured by Rose et al. (13.38 g/cm^3) from a sample that had up to 0.4 wt% of measured impurities [166].

Other researchers [171, 172] report the room-temperature density of Am as ~11.7 g/cm^3. This density probably does not represent α-Am, but instead corresponds to a different phase with the same space group and larger lattice parameters (Section 2.4.2.1).

Although McWhan and colleagues [163] did not quantify the density of β-Am, calculations based on their crystal structure and lattice parameters indicate that the densities of α-Am and β-Am are essentially identical.

2.4.4.4 Changes in Volume as a Result of Phase Transitions

In view of the similar densities of α-Am and β-Am (Section 2.4.4.3), it seems likely that the volume change associated with the α-β transition in Am is negligible relative to the uncertainties in the data.

Stephens et al. applied the Clausius-Clapeyron relation (Section 1.4 of reference [5]) to their compressibility data and previously published values of the latent heats of phase transitions to estimate that the volume increases associated with the β-γ and melting transformations in Am are approximately 1.1 and 2.3%, respectively [165]. The enthalpy values they used (1.40 and 3.44 kcal/mol for the β-γ and melting transformations, respectively) are at the high end of the range reported by Konings and Beneš [7], suggesting that the actual volume increases associated with the phase transformations may be smaller than estimated by Stephens et al.

Melting results in a volume loss (ΔV/V) of 2.3% [90, 91].

2.4.5 Thermal Conductivity and Related Properties

Experimental measurements of the thermal conductivity and thermal diffusivity of Am are not available.

Two publications agreed that the electrical resistivity of Am at 300 K and atmospheric pressure is 68.90 μΩ cm [175, 180]. Given that the first two authors of the papers are the same, values reported in these publications may not have been independently determined.

If the Lorenz number for Am is close to the theoretical value, the Wiedemann-Franz Law (Section 1.6.2 in reference [5]) indicates that the room-temperature thermal conductivity of Am is ~10.64 W/m-K. However, a recent review of properties of the actinide elements suggested (without giving a reason) that the Lorenz number for Am is closer to 3.25×10^{-8} $W\Omega K^{-2}$ [8], which corresponds to a thermal conductivity of ~14.15 W/m K.

Further experimental work on the thermal conductivity and Lorenz number of Am is needed, particularly at temperatures of interest for nuclear fuels.

2.5 La

2.5.1 Introduction

It is generally accepted that lanthanum has three solid phases that are stable at atmospheric pressure. Crystal structures and lattice parameters of all three phases have been known since the early 1960s.

A number of groups have measured the heat capacity of La. The reported heat capacities vary widely for some phases, and heat capacities determined from incremental enthalpy measurements are consistently below those from other sources.

Most of the available quantitative experimental data about thermal expansion of La is from a single reference with measurements of lattice parameters from high-temperature X-ray diffraction data from single crystals of α-La and β-La. Information about the thermal expansion of γ-La is not available. The thermal expansion of liquid La at temperatures within ~100 degrees of the melting point has been measured.

Papers reporting experimental measurements of the thermal diffusivity and conductivity of La at temperatures above ~300 K were commonly first published in Soviet journals, although English translations of many of these papers are available. The majority of the papers present their results graphically rather than numerically.

Most relatively recent research on La involves modeling or attempts to understand low-temperature superconductivity (e.g., [181-190]).

2.5.2 Phases and Phase Transformations

2.5.2.1 Phases

Lanthanum phases that are stable at atmospheric pressure are:

- α-La, dhcp (space group $P6_3/mmc$, a = 3.7740 Å, c = 12.171 Å at 297 K) [191, 192]
- β-La, fcc (space group $Fm\bar{3}m$, a = 5.303 Å at 598 K) [191-193]
- γ-La, bcc (space group $Im\bar{3}m$, a = 4.26 Å at 1160 K) [191-193]

2.5.2.2 Phase Transformations

Recommended phase-transformation temperatures and enthalpies from a recent independent review and assessment of the available data are:

- α-β, 566±10 K (based on 5 publications with original measurements that range from 533 to 583 K) [7]. Gschneidner and Calderwood [194] note a wide variation between phase-transformation temperatures measured during heating (583 K) and cooling (533 K). The phase transformation enthalpy is ~ 0.40 kJ/mol [7, 191].
- β-γ, 1140±5 K (based on 10 publications with original measurements that range from 1108 to 1141 K). The corresponding transformation enthalpy is ~ 3.15 kJ/mol [7, 191].
- γ-liquid, 1192±1 K (based on 8 publications with original measurements that range from 1173 to 1194 K). The corresponding transformation enthalpy is estimated at 6.20 ±0.30 kJ/mol [7, 191].

The temperature of the α-β transformation decreases with increasing pressure, reaching a temperature of ~100°C at a pressure of ~15-20 kbars [83, 195]. The temperature of the β-γ transformation and the solidus both rise with increasing pressure, and γ-La disappears at a pressure of ~20 kbars [195].

2.5.3 Heat Capacity and Related Properties

Three research groups have published measurements of the incremental enthalpy of La at temperatures above 300 K [196-198], although the authors of one of them (reference [197]) indicated that their data was not suitable for determinations of heat capacity. Other research groups have published more direct measurements of heat capacity obtained using a variety of instruments [199-202]. The reported heat capacities vary widely for some phases, and heat capacities determined from incremental enthalpy measurements are consistently below those from other sources.

Konings and Beneš [7] re-assessed the experimental data and developed equations representing the heat-capacity data for La (Equation 37 through Equation 40). These equations are based primarily on incremental enthalpy measurements [196, 198], with adjustments to match lower-temperature measurements for α-La. As a result of these adjustments, the heat capacity for α-La calculated from these equations is somewhat higher than that calculated from the data of Berg et al. [196], but is consistent with the room-temperature heat capacity of La in a recent tabulation (27.1 J/mol-K) [191]. The heat capacities of β-La and γ-La in Equation 38 and Equation 39 are very similar to those published by Berg et al. [196], and the heat capacity of the liquid is identical to that published by Stretz and Bautista [198].

Although further work is desirable to increase confidence that these heat-capacity values are accurate (particularly for γ-La), the values recommended by Konings and Beneš are the best available approximation.

Equation 37. Heat capacity of α-La [7]

$$C_p = 25.8730 + 3.5907 \times 10^{-3} \times T - 0.26059 \times 10^{5} \times T^{-2}$$

where C_p is constant-pressure heat capacity in J/mol·K and T is temperature in K

Equation 38. Heat capacity of β-La (after [7], but with the last coefficient multiplied by T rather than T^2 for consistency with data from Berg et al. [196])

$$C_p = 19.9335 + 12.9990 \times 10^{-3} \times T$$

where C_p is constant-pressure heat capacity in J/mol·K and T is temperature in K

Equation 39. Heat capacity of γ-La [7]

$$C_p = 39.54$$

where C_p is constant-pressure heat capacity in J/mol·K

Equation 40. Heat capacity of La liquid (C_p in J/mol-K) [7]

$$C_p = 32.66$$

where C_p is constant-pressure heat capacity in J/mol·K

Figure 17 shows the experimentally determined heat capacities of lanthanum phases and recommended values from a recent review and assessment [7].

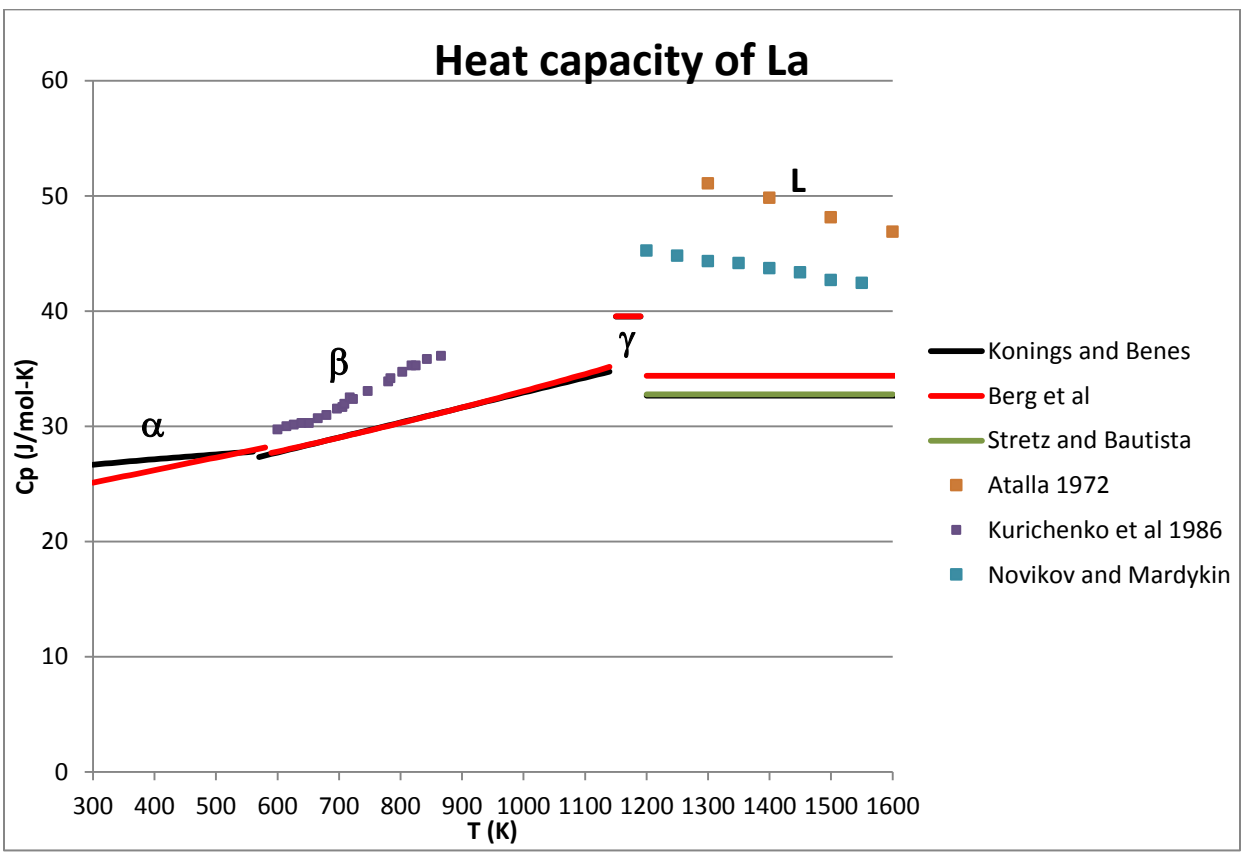

Figure 17. Heat capacity of La (references [196, 198, 199, 201, 202] and Equation **37**, Equation 38, Equation 39, and Equation 40)).

2.5.4 Thermal Expansion and Density

2.5.4.1 Thermal Expansion

Spedding et al. [193] used high-temperature X-ray diffraction to measure the lattice parameters of α- and β-La and developed polynomials that can be used to calculate lattice parameters as functions of temperature (Equation 41 through Equation 43). Figure 18 shows the corresponding thermal expansion of individual lattice parameters of α- and β-La, calculated based on a reference temperature of 300 K (~27°C).

Equation 41. *a* lattice parameter of α-La between 20 and 293°C [193 Table IV]

$$a = 3.77 + 1.7 \times 10^{-5} \times T$$

where *a* is a lattice parameter, T is temperature in °C, and T is between 20 and 293°C

Equation 42. *c* lattice parameter of α-La between 20 and 293°C [193 Table IV]

$$c = 12.13 + 33 \times 10^{-5} \times T$$

where *c* is a lattice parameter, T is temperature in °C, and T is between 20 and 293°C

Equation 43. Lattice parameter of β-La between 20 and 598°C [193 Table IV]

$$a = 5.303 + 3.4 \times 10^{-5} \times T + 1.0 \times 10^{-8} \times T^2$$

where *a* is the lattice parameter, T is temperature in °C, and T is between 20 and 598°C

Barson et al. [203], Spedding et al. [204], and Frizen et al. [205] measured the thermal expansion of polycrystalline La using dilatometry. Although results of these studies were presented graphically, it is clear that measurements from all three studies fall between the single-direction expansions of the *a* and *c* lattice parameters calculated from the high-temperature X-ray data of Spedding et al. [193]. Because the thermal expansion of α-La is anisotropic, the thermal expansion of actual samples may vary between the single-direction expansions as a result of differences in preferred orientation between the samples. Thus, the polycrystalline expansion data of Barson et al., Spedding et al., and Frizen et al. (references [203-205]) is consistent with the single-direction data of reference [193].

The measurements of Barson et al. for polycrystalline β-La [203 (Figure 2)] are significantly higher than the values calculated from the single-direction data of Spedding et al. [193], and the measurements of Frizen et al. [205 (Figure 1)] are significantly lower. It is not clear why these differences occur, although Barson et al. noted difficulties in obtaining accurate measurements because of sample creep or softening at high temperatures. In the absence of further experimental measurements, it seems reasonable to consider the single-crystal data of Spedding et al. to be the best available measurements of the thermal expansion of β-La.

Data from a 1964 paper by Eliseev et al. [206] are inconsistent with those of other researchers and should be disregarded because they were collected from a sample whose DTA curves show several large peaks from transitions involving unidentified phases.

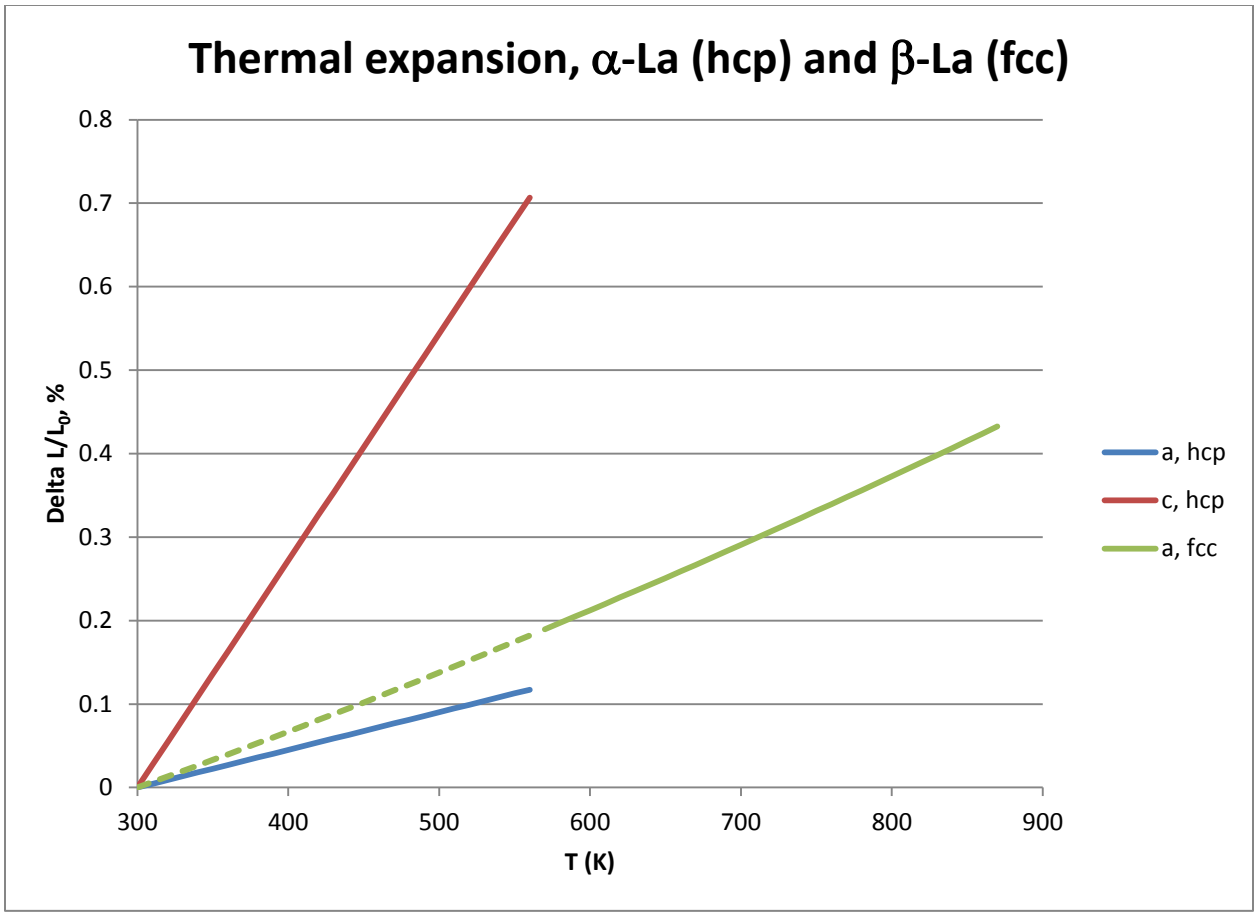

Figure 18. Thermal expansion of single crystals of α- and β-La, based on values calculated from Equation 41 through Equation 43 using a reference temperature of 300 K. Dotted line for β-La indicates that it is likely to be present (particularly during cooling) but is not thermodynamically stable.

2.5.4.2 Coefficients of Thermal Expansion

Published coefficients of thermal expansion for lanthanum are summarized in Table 10. Values from reference [192] are derived from the single-crystal data originally published in reference [193] and repeated in the CRC Handbook of Chemistry and Physics [191]. These values are therefore consistent with each other and with the figures and equations in this section of the handbook. Values from reference [207] are derived from the polycrystalline material measured by Barson et al. [203]. Similarities between the coefficients of thermal expansion for the polycrystalline samples and the single-direction coefficient parallel to the *a* crystallographic axis suggest that the sample used by Barson et al. (reference [207] in Table 10) may have had a high degree of preferred orientation.

Spedding et al. noted that their measurements were generally within ~5% of previous measurements from polycrystalline samples (e.g., reference [203]) for "mid-range" temperatures of approximately 400°C. However, they also noted that average deviations between their measurements and earlier ones were ~20% at the ends of the measurement range. Further measurements are needed.

Wittenberg and colleagues reported that the volumetric coefficient of thermal expansion for liquid La is slightly larger than that for solid lanthanum phases [208, 209].

Table 10. Coefficients of thermal expansion for La. Coefficients with ranges of temperatures are averages across the temperature ranges.

Description	T (°C)	Coefficient ($\times 10^6$/°C)	Reference
α-La, parallel to *a* axis	25	4.5	[191, 192]
α-La, parallel to *c* axis	25	27.2	[191, 192]
α-La, polycrystal	25	12.1	[191, 192]
α-La, polycrystal	25	4.9	[207]
α-La, polycrystal	-173 to +310	5.2	[207]
β-La	400	7.9	[193]
β-La	+325 to +775	9.6	[207]

2.5.4.3 Density

According to information in the CRC Handbook of Chemistry and Physics, the density of α–La is 6.15 g/cm^3 at 297 K, the density of β-La is 6.19 g/cm^3 at 598 K, and the density of γ-La is 5.97 g/cm^3 at 1160 K [191].

Measured densities of liquid La near the melting temperature vary between 5.91 and 5.98 g/cm^3, as summarized by Kononenko et al. [210]. The value of 5.96 g/cm^3 in the CRC Handbook of Chemistry and Physics [191 Table 12] is a defensible approximation to the actual value.

2.5.4.4 Densities and Molar Volumes as Functions of Temperature

Figure 19 shows molar volumes and densities for La as functions of temperature. Data for β-La is extrapolated to the β-γ phase transformation temperature following Spedding et al. [193 (Figure 1)]. Data for γ-La is the average of three widely scattered measurements. Spedding et al. represented their data for the molar volumes of α-La and β-La by Equation 44 and Equation 45.

Equation 44. Molar volume of α-La between 20 and 293°C [193 Table IV]

$$V = 22.5 + 70 \times 10^{-5} \times T$$

where V is the volume of one mole in cm^3, T is temperature in °C, and T is between 20 and 293°C

Equation 45. Molar volume of β-La between 20 and 598°C [193 Table IV]

$$V = 22.46 + 44 \times 10^{-5} \times T + 13 \times 10^{-8} \times T^2$$

where V is the volume of one mole in cm^3, T is temperature in °C, and T is between 20 and 598°C

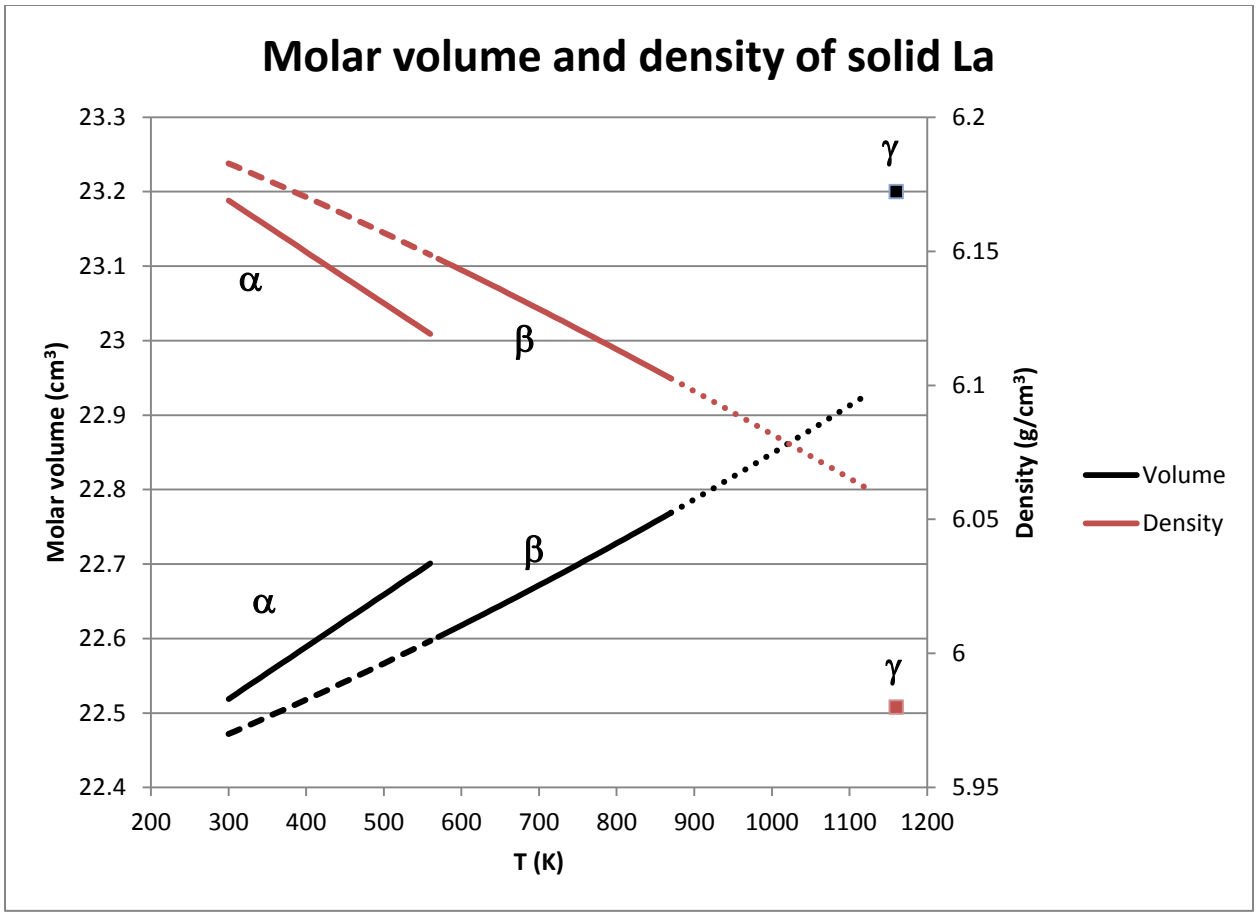

Figure 19. Densities and molar volumes of La phases (reference [193] and Equation 44 and Equation 45). Dashed lines show properties of β-La at temperatures where it is thermodynamically unstable but likely to occur; dotted lines show extrapolation beyond the upper temperatures of the equations following [193 Figure 1].

There is limited data about changes in the density of liquid La as a function of temperature. Wittenberg et al. reported that the density of liquid La decreased by 2.37×10^{-4} g/cm^3·K based on four measurements between 951 and 1004°C (1224 and1277 K) [208, 209], and Kononenko et al. reported that it decreased by 0.61×10^{-4} g/cm^3·K over the temperature range from 1193 to 1873 K [210]. Because of the different temperature ranges involved, these values may be consistent if the change in density is not linear function of temperature.

2.5.4.5 Changes in Volume Due to Phase Transitions

The high-temperature X-ray diffraction data of Spedding et al. [193] indicate a volume decrease of ~0.5% during the α-β transformation and a gain of ~1.3% during the β-γ transformation in lanthanum. These values are consistent with the decrease in volume of ~0.3% during the α-β transformation in polycrystalline La measured by Barson et al. using dilatometry [203]. The volume increase during melting is 0.6% [91].

2.5.5 Thermal Conductivity and Related Properties

2.5.5.1 Lorenz Number

Jolliffe et al. determined the Lorenz number of α-La at 291 K to be 2.9×10^{-8} WΩK^{-2} [211]. This value is somewhat higher than the value of 2.63×10^{-8} WΩK^{-2} reported in an earlier review [207], and also higher than the value of 2.75×10^{-8} WΩK^{-2} calculated from room-temperature thermal conductivity and electrical resistivity data in the CRC Handbook of Chemistry and Physics [191 Table 9]. Although further research is needed to determine the actual Lorenz number and its temperature dependence, it seems likely that the actual Lorenz number of α-La is significantly higher than the theoretical value.

Reported Lorenz numbers for liquid La at temperatures between 1190 and 2000 K are between 2.12 and 2.65×10^{-8} WΩ/K^2, with no obvious relationship between temperature and variations in the Lorenz number [191 Tables 4 and 12, 199].

2.5.5.2 Thermal Conductivity

Figure 20 shows the published numerical values of the thermal conductivity of La.

The thermal conductivity values for α-La recommended by Touloukian, Ho, and colleagues [62, 95] are based on the room-temperature measurements and the data of Golubkov et al. [212], but were increased by ~5% to compensate for the relatively low purity of Golubkov's sample [95]. In the absence of further experimental measurements, all of the thermal conductivity values for α-La in this section are defensible approximations to the actual thermal conductivity of α-La.

The thermal conductivity values for β-La recommended by Touloukian, Ho, and colleagues [62, 95] are based on the Wiedemann-Franz law (Section 1.4 of reference [5]) with the theoretical value of the Lorenz number and a correction for the lattice component of thermal conductivity determined from room-temperature data [95]. Values of the thermal conductivity of La published by Atalla and by Kurichenko et al. [199, 202] were calculated from their measurements of thermal diffusivity and heat capacity (both of which are provided in the original references), combined with previously available information on density. Since the heat capacity values used by Kurichenko et al. [202] are ~15-20% higher than the values recommended in Section 2.5.3, it seems likely that the thermal conductivity values of Kurichenko et al. are correspondingly too high. In the absence of new experimental data, it seems reasonable to assume that the actual thermal conductivity of β-La lies between the values of Kurichenko et al. and Ho et al.

No experimental measurements or experimentally based estimates of the thermal conductivity or diffusivity of materials identified as γ-La are available. Krieg et al. reported the electrical resistivity of La as 126 μΩ-cm at 1157 K and 128 μΩ-cm at 1193 K (the melting temperature for the sample in their study) [213]. Although the phase in this sample was not characterized, the temperatures suggest that these data may be from γ-La. These values are similar to the value of 126 μΩ-cm at 890°C (1163 K) reported in an earlier review by Gschneidner [207].

The Lorenz number for γ-La has not been reported; however, based on a Lorenz number of 2.63×10^{-8} WΩK^{-2} (appropriate for α-La at 25°C, and the best available approximation for other La phases and temperatures) [207], the thermal conductivity of γ-La is approximately 41 W/m-K.

Atalla calculated the thermal conductivity of liquid La using their measurements of thermal diffusivity and heat capacity (both of which are provided in their paper, reference [199]). The heat capacity values in this paper are at least 50% higher than those recommended in Section 2.5.3. If it is assumed that the thermal diffusivity measurements of Atalla are correct, the actual thermal conductivity of liquid La is significantly below that shown in Figure 20.

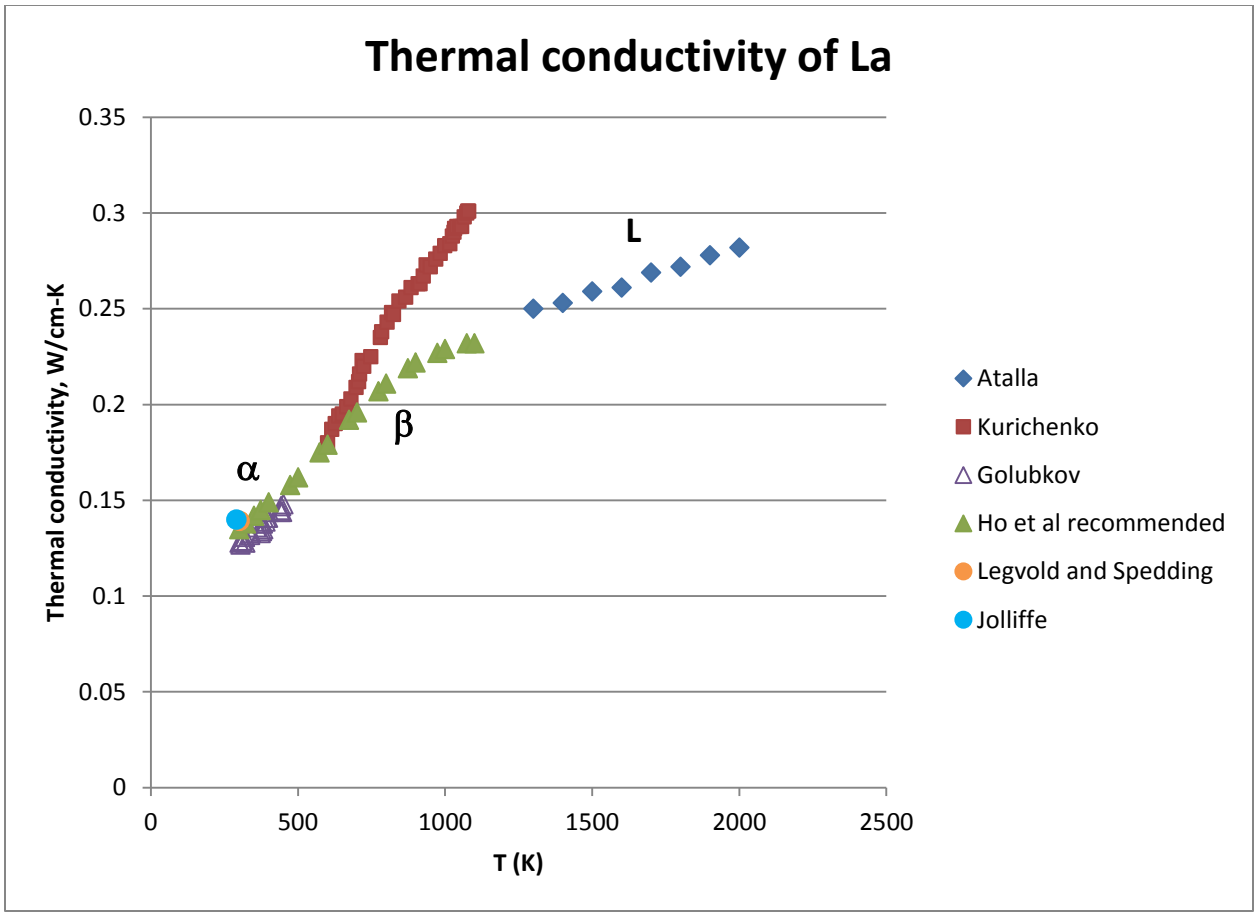

Figure 20. Thermal conductivity of La [95, 199, 202, 211, 212, 214].

2.6 Ce

2.6.1 Introduction

Cerium has four solid phases (α-Ce, β-Ce, γ-Ce, and δ-Ce) that are stable at atmospheric pressure. Two of these phases (α- and β-Ce) are only stable below room temperature. Transformation kinetics are sluggish enough that β-Ce may persist for decades in samples held at room temperature even though γ-Ce is the stable phase at this temperature [215]. α-Ce and γ-Ce both have fcc structures, but with significantly different lattice parameters.

A number of research groups have published values for the heat capacity of Ce above room temperature. There is generally good agreement about the heat capacities of γ-Ce and δ-Ce, but not about the heat capacity of the liquid.

Experimental measurements of the thermal expansion of solid Ce phases are limited to high-temperature X-ray diffraction of single crystals of γ-Ce and a single figure with dilatometer data from a sample of polycrystalline Ce at temperatures between ~0 and 750°C. The thermal expansion shown by the dilatometry data is greater than the thermal expansion from the X-ray diffraction data.

There are very few experimental measurements of the thermal diffusivity or conductivity of Ce at temperatures above ~300 K. Most of the available measurements are from poorly characterized samples, and phases are rarely identified. Reported values for the thermal expansion of liquid Ce vary by an order of magnitude for some temperatures.

Cerium is a subject of active research, with numerous recent publications addressing the nature of the relationship between α-Ce and γ-Ce (e.g., references [216-225] and reviews by Hecker, Moore and van der Laan, and Johansson and Li [65, 66, 226]). Other relatively recent research involves understanding other phase transformations, high-pressure investigations, spectroscopy, and modeling (e.g., [182, 187, 227-237]).

2.6.2 Phases and Phase Transformations

2.6.2.1 Phases

The cerium phases that are stable at atmospheric pressure are [191]:

- α-Ce, fcc (space group $Fm\bar{3}m$, a = 4.85 Å at 77 K)
- β-Ce, dhcp (space group $P6_3/mmc$, a = 3.6810 Å, c = 11.857 Å at 297 K)
- γ-Ce, fcc (space group $Fm\bar{3}m$, a = 5.1610 Å at 297 K)
- δ-Ce, bcc (space group $Im\bar{3}m$, a = 4.12 Å at 1030 K).

α-Ce and γ-Ce both have face-centered cubic crystal structures. Lattice parameters of the two phases are significantly different, and the molar volume of α-Ce is ~17% smaller than that of γ-Ce at atmospheric pressure [238].

2.6.2.2 Phase Transformations

Atmospheric phase-transformation temperatures and enthalpies are:

- α-β, 125 K (-148°C) [7, 191, 239]. This temperature was measured during heating; the β-α transformation temperature measured during cooling is 45 K (-228°C) [191].
- β-γ, 283 K (10°C) [7, 191]. This temperature represents the equilibrium temperature between β-Ce and γ-Ce, as estimated from phase-transformation kinetics [240]; temperatures measured during heating and cooling are 412 K (139°C) and 257 K (−16°C), respectively [191]. The corresponding transformation enthalpy is 0.05 kJ/mol [191]. (The enthalpy of ~3.0 kJ/mol listed by Konings and Beneš [7 (page 043102-7)] for the β-γ transformation seems too large, and may refer to the γ-δ transformation.)
- γ-δ, 998±5 K (724±5°C) (based on 11 publications with original measurements that range from 950 to 1007 K) [7]. The corresponding transformation enthalpy is ~3.10 kJ/mol [7 (Table 40), 191].
- δ-liquid, 1070±3 K (797±3°C) (based on 13 publications with original measurements that range from 1053 to 1080 K) [7]. The corresponding transformation enthalpy is ~5.5 kJ/mol [7 (Table 40), 191].

Although atmospheric-pressure transformations between α-Ce and γ-Ce have been reported at temperatures below 200 K (e.g., [241-243]), these transformations apparently do not represent equilibrium reactions. Pressure-temperature diagrams (e.g., [240, 243]) suggest that equilibrium reactions at atmospheric pressure involve transformations from α-Ce to β-Ce and β-Ce to γ-Ce rather than directly from α-Ce to γ-Ce. Equilibrium transformations between α- and γ-Ce occur at pressures between 0.22 and 1.96 GPa (2.2 and 19.6 kbars) (e.g., [240, 243]), but are not considered here because these pressures are too high to be relevant for metallic fuels.

2.6.3 Heat Capacity and Related Properties

Spedding et al. [244] published measurements of the incremental enthalpy of Ce from room temperature to 1100°C, and Kuntz and Bautista [245] published incremental enthalpy measurements for liquid Ce between ~1400 and 2500 K. Both of these research groups used their enthalpy measurements to calculate heat capacities, which they fitted with equations. Kurichenko et al. [202] published measurements of heat capacity from 600 to 792 K, and Atalla [199] published heat capacity measurements of liquid Ce.

Kuntz and Bautista [245] represented their heat capacity data for liquid Ce with two equations: a linear function of temperature from ~1400 to 1700 K, and a constant from 1700 to 2500 K (Equation 46, Equation 47). Kuntz and Bautista suggested that differences in heat capacities in these two temperature ranges might indicate a change in the clustering of atoms in the liquid as temperature increased. Konings and Beneš suggested alternative equations to fit the same data by a single polynomial for all temperatures between the melting point and 2500 K (Equation 50), then assumed that the heat capacity was constant above that temperature (Equation 51). Further research is needed to determine which of these possibilities best represents the actual behavior of liquid Ce.

All of these heat capacity measurements are shown in Figure 21. The heat capacity measurements of Kurichenko et al. and Spedding et al. are similar, and the measurements of Atalla are similar to those of Kuntz and Bautista for the temperature ranges in which they overlap. Despite the large differences in heat capacity values for liquid Ce in the measurements of Kuntz et al. and Spedding et al., the measured incremental enthalpies published by these researchers are similar.

Konings and Beneš [7] recently assessed the experimental data and developed equations representing heat-capacity values for γ-Ce, δ-Ce, and liquid Ce (Equation 48 through Equation 51). Their recommendations match the available data for γ-Ce and δ-Ce and seem a reasonable approximation to the available measurements of the heat capacity of liquid Ce.

Equation 46. Heat capacity of Ce liquid between 1400 and 1700 K [245]

$C_p = -0.0251xT + 75.305$

where C_p is constant-pressure heat capacity in J/mol·K, T is temperature in K, and T is between 1400 and 1700 K

Equation 47. Heat capacity of Ce liquid between 1700 and 2500 K [245]

$C_p = 31.614$

where C_p is constant-pressure heat capacity in J/mol·K, T is temperature in K, and T is between 1700 and 2500 K

Equation 48. Heat capacity of γ-Ce between 373 and 998 K [7]

$C_p = 20.8689 + 16.8508 \times 10^{-3} \times T + 0.98410 \times 10^{5} \times T^{-2}$

where C_p is constant-pressure heat capacity in J/mol·K, T is temperature in K, and T is between 373 and 998 K

Equation 49. Heat capacity of δ-Ce between 998 and 1070 K [7]

$C_p = 37.85$

where C_p is constant-pressure heat capacity in J/mol·K

Equation 50. Heat capacity of Ce liquid between 1070 and 2500 K [7]

$C_p = 18.7747 + 3.3867 \times 10^{-3} \times T + 2.7240 \times 10^{7} \times T^{-2}$

where C_p is constant-pressure heat capacity in J/mol·K, T is temperature in K, and T is between 1700 and 2500 K

Equation 51. Heat capacity of Ce liquid above 2500 K [7]

$C_p = 31.6$

where C_p is constant-pressure heat capacity in J/mol·K

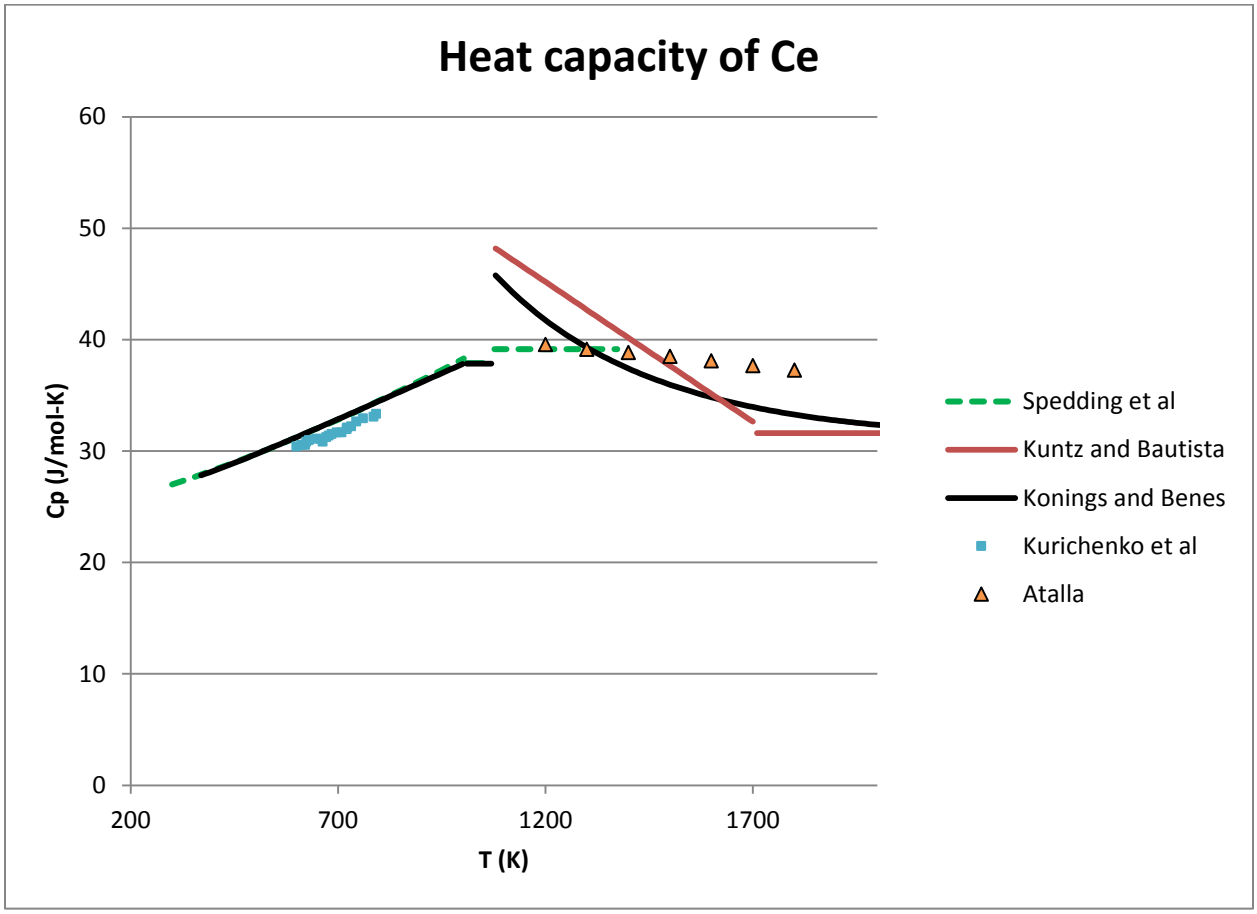

Figure 21. Heat capacity of Ce (references [7, 199, 200, 244, 245] and Equation 48 through Equation 51).

2.6.4 Thermal Expansion and Density

2.6.4.1 Thermal Expansion

Spedding et al. [193] used high-temperature X-ray diffraction of γ-Ce to develop a polynomial that can be used to calculate the lattice parameter as a function of temperature (Equation 52, Figure 22). Their results were quoted in later reviews by Gschneidner and colleagues [191, 192]

Equation 52. Values of the *a* lattice parameter of γ-Ce between 20 and 619 °C [193 Table IV]

$a = 5.1604 + 3.28 \times 10^{-5} \times T - 0.59 \times 10^{-8} \times T^2 + 1.37 \times 10^{-11} \times T^3$

where *a* is the lattice parameter in Å, T is temperature in °C, and T is between 20 and 619°C

Barson et al. measured the thermal expansion of polycrystalline γ-Ce using dilatometry [203 (Figure 3)]. As noted by Spedding et al [193], thermal expansion values based on their X-ray diffraction data are consistent with the dilatometry measurements for "mid-range" temperatures of approximately 400°C. However, the thermal expansion of Barson et al. is significantly higher than that of Spedding et al. at 25°C, and also higher at 600°C than would be expected from the almost linear thermal expansion indicated by the X-ray diffraction data (Figure 22). Barson et al. reported that their sample exhibited plastic flow and permanent deformation at the high-temperature end of their measurement range. It seems likely that the X-ray diffraction data is a better representation of the actual thermal expansion of γ Ce than the dilatometry data.

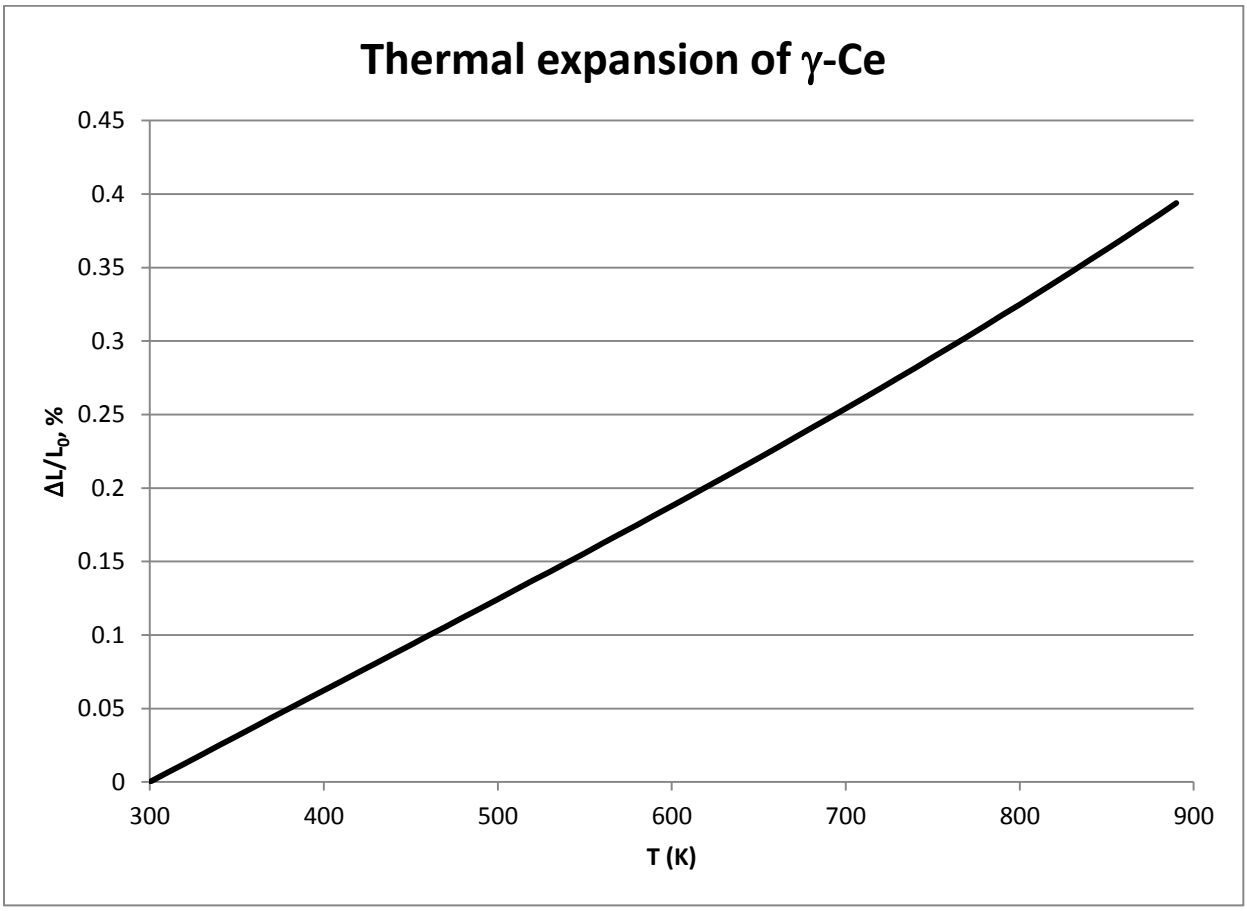

Figure 22. Thermal expansion of γ-Ce, based on values calculated from Equation 52 using a reference temperature of 300 K.

2.6.4.2 Coefficients of Thermal Expansion

Published coefficients of thermal expansion for γ-Ce are summarized in Table 11. Values from references [191] and [192] are derived from the high-temperature X-ray diffraction data of Spedding et al. [193] and are therefore consistent with each other. Values from reference [207] are derived from the dilatometry data of Barson et al. [203], which involved dilatometer measurements.

Table 11. Coefficients of thermal expansion for γ-Ce (single crystals and polycrystals).

T (°C)	Coefficient ($\times 10^6$/°C)	References
25	6.3	[191, 192] following [193]
25	8.5	[207]
400	6.7	[193]
400	~6.5	[203 Figure 2]
600	~8.5	[203 Figure 2]
25 to 725	7.1	[207]

2.6.4.3 Density

According to information in the CRC Handbook of Chemistry and Physics, the density of α-Ce is 8.16 g/cm^3 at 77 K, the density of β-Ce is 6.689 g/cm^3 at 297 K, the density of γ-Ce is 6.770 g/cm^3 at 297 K, and the density of δ-Ce is 6.65 g/cm^3 at 757 K [191].

Measurements of the density of liquid Ce close to the melting point range from 6.41 g/cm^3 [246] to 6.94 g/cm^3 [209]. In the absence of definitive measurements, the average value (~6.68 g/cm^3) may be the best available estimate. This value appears in the CRC Handbook of Chemistry and Physics [191 (Table 12)].

2.6.4.4 Densities and Molar Volumes as Functions of Temperature

Spedding et al. [193] used their high-temperature X-ray diffraction data to develop a polynomial that can be used to express the density of γ-Ce as a function of temperature (Equation 53, Figure 23). This equation indicates a density of ~6.767 g/cm^3 for γ-Ce at 300 K. Spedding et al. reported the density of δ-Ce at 757°C as 6.67 g/cm^3. Both of these values are consistent with recent values in the CRC Handbook of Chemistry and Physics [191 (Tables 2 and 3)]; however, given the scarcity of published data, it seems likely that densities from the CRC Handbook are based on the data of Spedding et al.

Equation 53. Density of γ-Ce between 20 and 619°C [193 (Table IV)]

$$\rho = 6.771 - 12.6 \times 10^{-5} \times T + 1.5 \times 10^{-8} \times T^2 - 4.5 \times 10^{-11} \times T^3$$

where ρ is the density in g/cm^3, T is temperature in °C, and T is between 20 and 619°C

Measurements of the temperature dependence of the density of liquid Ce include decreases of 2.27×10^{-4} g/cm^3-K [247], 2.37×10^{-4} g/cm^3-K [208], 7×10^{-4} g/cm^3·K [210], and 8.31×10^{-4} g/cm^3-K [246], with the larger measurements being the most recent. In the absence of definitive measurements, it seems likely that the density of liquid Ce decreases by ~8×10^{-4} g/cm^3-K.

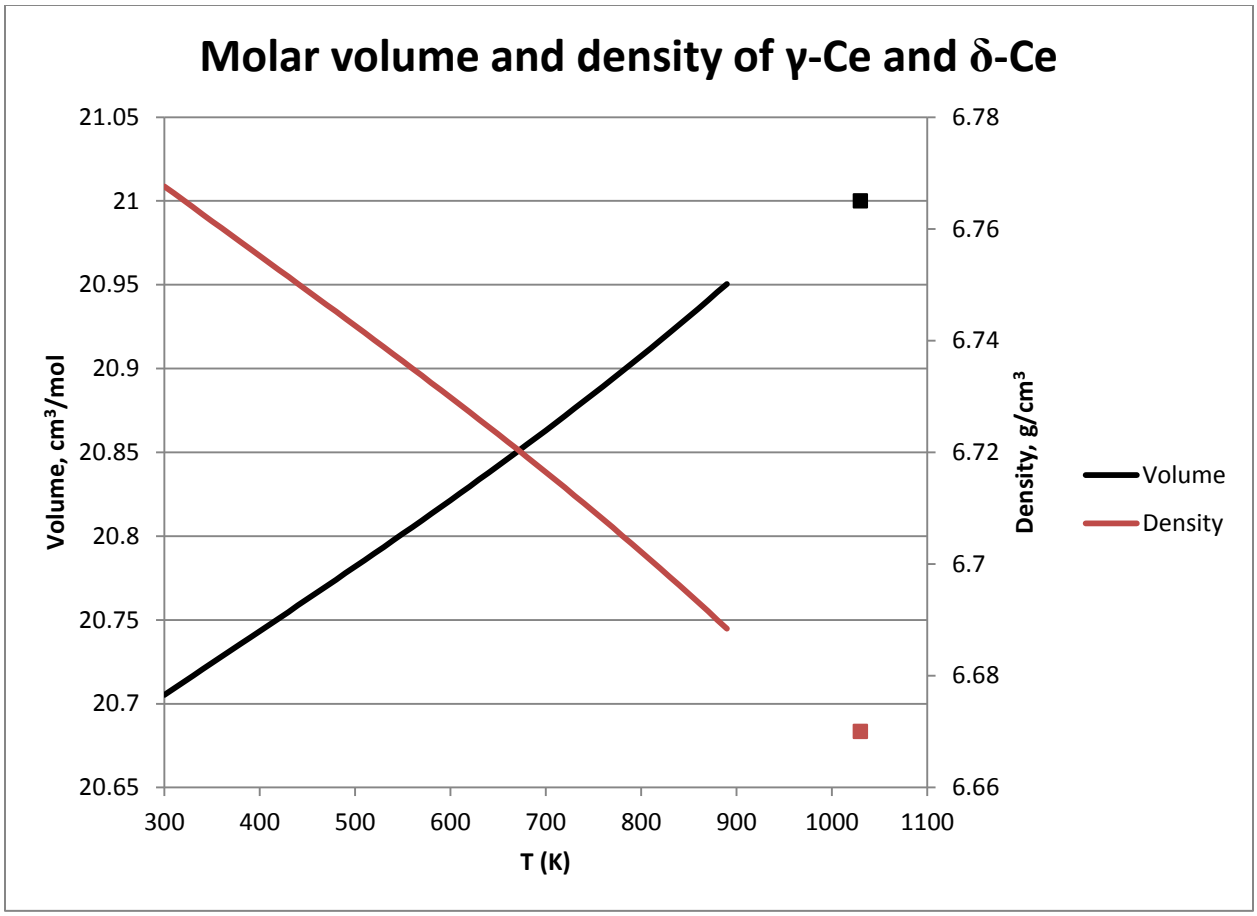

Figure 23. Densities and molar volumes of γ-Ce (lines calculated from Equation 53) and δ-Ce (squares) from reference [193].

2.6.4.5 Changes in Volume as a Result of Phase Transitions

The only available data indicate that the volume of Ce increases by ~0.1±0.7 % as a result of the transformation from γ-Ce to δ-Ce [193 (Table II)] and decreases by ~1% during melting [91].

2.6.5 Thermal Conductivity and Related Properties

2.6.5.1 Lorenz Number

Jolliffe and colleagues calculated the Lorenz number for Ce at 18°C as ~2.8×10^{-8} WΩ/K^2 based on their thermal conductivity and electrical resistivity measurements [211, 248]. This value is consistent with both the value of 2.7×10^{-8} WΩ/K^2 at 25°C in an earlier review by Gschneidner [207] and the value of 2.8×10^{-8} WΩ/K^2 at 300 K calculated from data in the CRC Handbook of Chemistry and Physics [191 Table 9], and indicates that the Lorenz number for Ce is significantly higher than the theoretical value.

Lorenz numbers for liquid Ce are between 2.28×10^{-8} and 2.68×10^{-8} WΩ/K^2 at temperatures between 1200 and 1800 K, and may decrease with increasing temperature [199]. These values are consistent with the value of ~2.55×10^{-8} WΩ/K^2 for the Lorenz number of Ce liquid calculated from thermal expansion and electrical resistivity values "near the melting point" [191 Table 12].

2.6.5.2 Thermal Conductivity

Thermal conductivities published by Atalla [199] and by Kurichenko et al. [202] were calculated from their measurements of thermal diffusivity and heat capacity (both of which are provided in the original references), combined with previously available information on density. The heat capacity values used by Kurichenko et al. are consistent with the values recommended in Section 2.6.3 of this Handbook (Figure 21). Thermal conductivities published by Zinov'ev et al. [249] were derived from earlier studies not otherwise considered in this Handbook. Values from Novikov and Mardykin [250] were calculated from their electrical resistivity values using the Wiedemann-Franz law (Section 1.6.2 of reference [5]) with a Lorenz number of 2.2×10^{-8} WΩ/K^2 (90% of the theoretical value, which Novikov and Mardykin considered appropriate for temperatures between ~1200 and 1300 K).

Figure 24 shows the experimental measurements of the thermal conductivity of Ce at temperatures above 200 K. Phase identifications in the figure are from phase-transformation temperatures in Section 2.6.2, not from experimental identification of the phases actually present.

Figure 24 also shows the provisional thermal conductivity values of Touloukian et al. and Ho et al. [62, 95]. These values were obtained by drawing a smooth curve through data measured at temperatures below ~22 K and the room-temperature data of Powell and Jolliffe [248] and Legvold and Spedding [214]. The provisional values are consistent with the data of Zinov'ev et al. but not those of Kurichenko. Nonetheless, the provisional values of Touloukian and Ho [62, 95] are the most defensible available values for the thermal conductivity solid Ce.

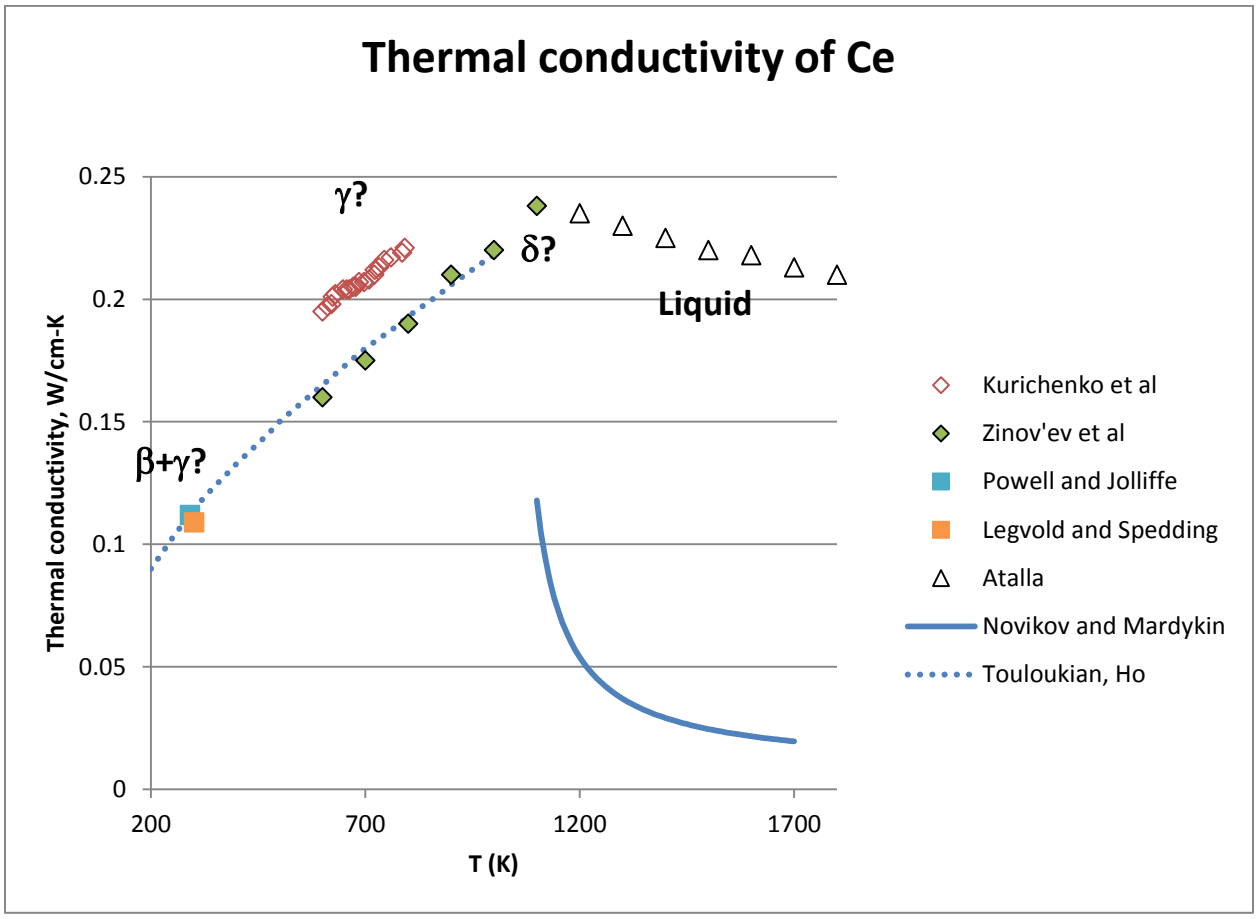

Figure 24. Thermal conductivity of Ce (references [62, 95, 199, 202, 214, 248-250].

2.7 Pr

2.7.1 Introduction

It is generally agreed that praseodymium has two phases that are stable at atmospheric pressure. The crystal structures and lattice parameters of both have been known since the early 1960s. More recent synchrotron data showed a third phase, which has a face-centered cubic structure [251]; however, it is not known whether this phase is stable and it does not appear in recent reviews. It is included in this Handbook because the available data indicates that it may occur in samples of interest to FCRD.

There is generally good agreement about the heat capacity of α-Pr. There is also generally good agreement about the heat capacity of β-Pr, for which only one experimental measurement has been reported. Measured values of the heat capacity of liquid Pr differ by ~10 J/mol-K.

Several research groups have collected data about the thermal expansion of α-Pr, although only one publication that reports quantitative values has been identified for this Handbook. Two publications with average values of the coefficient of thermal expansion of β-Pr were identified. Data on thermal expansion of the fcc phase is found in a single figure.

Although very sparse, the available data on the thermal conductivity of α-Pr show good agreement. No data on the thermal conductivity, thermal diffusivity, or electrical resistivity of β-Pr is available. Only one reference with information about the thermal conductivity of liquid Pr was identified.

Relatively recent research on Pr involves investigations at high pressures (e.g., [252]) and attempts to understand the electronic structure of Pr using spectroscopy and modeling (e.g., [113, 181, 233]).

2.7.2 Phases and Phase Transformations

2.7.2.1 Phases

The generally accepted praseodymium phases that are stable at atmospheric pressure are:

- α-Pr, dhcp (space group $P6_3/mmc$, a = 3.6721 Å, c = 11.8326 Å at 297 K) [191, 192]
- β-Pr, bcc (space group $Im\bar{3}m$, a = 4.13 Å at 1094 K) [191-193]

The existence of a face-centered cubic Pr phase has been known since the 1960s; however, this phase was believed to form only at pressures above ~40 kbars (e.g., [195, 253]). More recently, high-temperature synchrotron diffraction experiments demonstrated formation of a fcc Pr phase at atmospheric pressure [251]. This phase does not appear in recent reviews (e.g., [7, 191]). Little information about it is available, and further research is needed to investigate its thermodynamic stability, relationship to the high-pressure fcc phase, and other properties. It is included in this handbook because the conditions under which it was observed suggest that it may occur in metallic fuels and because it may be useful in understanding possible fcc phases in Pu-Pr and Pu-Nd alloys (Sections 5.11 and 5.12).

The lattice parameter of the atmospheric-pressure fcc Pr phase is 5.134 Å at 575 K [251].

Several other Pr phases have been formed in high-pressure experiments. One of these phases has the same structure as α-U and is therefore sometimes referred to as “alpha-U” or “alpha-uranium” in high-pressure research involving Pr phases. Despite these designations, the high-pressure Pr phase with the α-U structure does not contain any uranium.

2.7.2.2 Phase Transformations

Recommended phase-transformation temperatures and enthalpies from a recent re-assessment of the experimental data are [7]:

- α-β, 1068 ± 3 K (795 ± 3°C) (based on 6 publications with original measurements that range from 1050 to 1073 K). The corresponding transformation enthalpy is estimated at 3.06 ± 0.20 kJ/mol.

- β-liquid, 1208 ± 3 K (935 ± 3°C) (based on 5 publications with original measurements that range from 1190 to 1208 K). The corresponding transformation enthalpy is estimated at 5.58 ± 0.30 kJ/mol.

The face-centered cubic phase forms from α-Pr during heating by a martensitic transformation occurring across the temperature range from 575 to 1035 K [251]. Formation of the fcc phase is slow but occurs more rapidly in samples with thermal gradients.

2.7.3 Heat Capacity and Related Properties

Berg et al. [196] used drop calorimetry to measure the incremental enthalpy of Pr from 25 to 1100°C and developed equations to represent the corresponding heat capacities. Novikov and Mardykin [201], Kurichenko et al. [202], and Banchila and Philippov [254] determined heat capacities over temperature ranges of 1200 to 1550, 746 to 904, and 1210 to 2000 K, respectively. Berezovskii et al. [255] measured the heat capacity of a high-purity sample at temperatures between 5.6 and 314 K. Other lower-temperature measurements were summarized by Konings and Beneš [7].

Konings and Beneš [7] thoroughly re-assessed the experimental data except for that of Banchila and Filippov. They followed the equations of Berg et al. for β-Pr and liquid, but thought that the heat capacities of Berg et al. were probably too low near the lower end of their measurement range based on a comparison with the measurements of Berezovskii et al. [255]. Konings and Beneš therefore suggested an alternative equation for the heat capacity of α-Pr based on the enthalpy data of Berg et al. and the room-temperature heat capacity of 28.15 J/mol-K determined by Berezovskii et al. This value for the room-temperature heat capacity is higher than the value of 27.00 J/mol-K determined by Berg et al., which is consistent with the value of 27.2 J/mol-K in a recent tabulation by Gschneidner [191].

Figure 25 shows the measured and estimated heat capacities of Pr phases. Heat capacities of α-Pr calculated using the equation developed by Konings and Beneš (Equation 54) differ from those of Berg et al. [196] by at most ~4%. The equation for the heat capacity of β-Pr developed by Konings and Beneš (Equation 55) follows Berg et al. All of the available data suggest that the heat capacity of liquid Pr is only slightly dependent on temperature, although there is disagreement about whether it is constant (Equation 55, which follows Berg et al. [196]) or decreases slightly with increasing temperature [201, 254].

Equation 54. Heat capacity of α-Pr [7]

$$C_p = 32.5962 - 18.8071 \times 10^{-3} \times T + 27.6631 \times 10^{-6} \times T^2 - 0.11537 \times 10^6 \times T^{-2}$$

where C_p is constant-pressure heat capacity in J/mol·K, T is temperature in K

Equation 55. Heat capacity of β-Pr [7]

$$C_p = 38.45$$

where C_p is constant-pressure heat capacity in J/mol·K

Equation 56. Heat capacity of Pr liquid [7]

$$C_p = 43.01$$

where C_p is constant-pressure heat capacity in J/mol·K

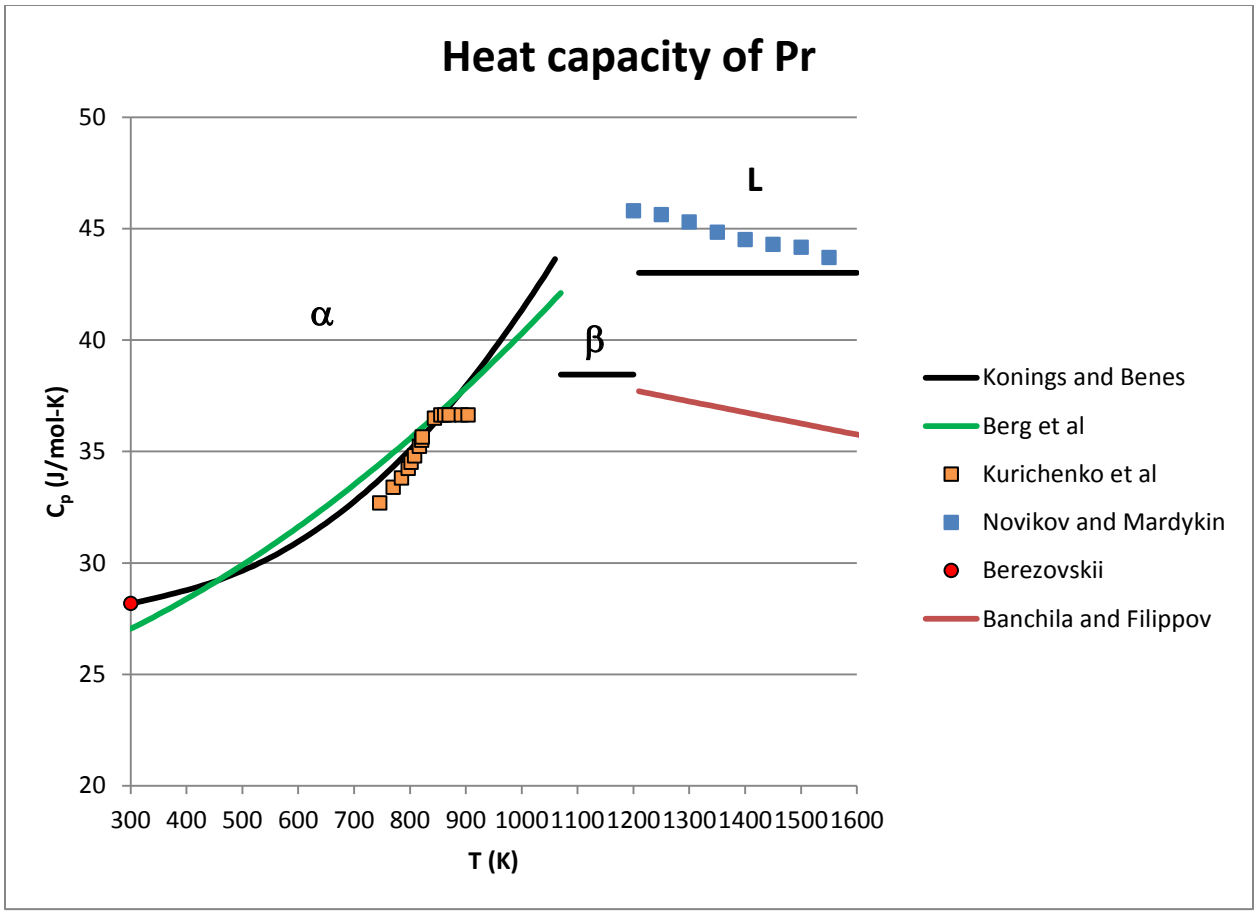

Figure 25. Heat capacity of Pr (references [196, 201, 202, 254, 255] and Equation 54 through Equation 56).

2.7.4 Thermal Expansion and Density

2.7.4.1 Thermal Expansion

Spedding et al. [193] used high-temperature X-ray diffraction to measure the lattice parameters of α-Pr and developed polynomials expressing the lattice parameters as functions of temperature (Equation 57 and Equation 58). Figure 26 shows the corresponding thermal expansion values, calculated based on a reference temperature of 300 K.

Equation 57. *a* lattice parameter of α-Pr between 20 and 449°C [193 Table IV]

$$a = 3.6702 + 1.66 \times 10^{-5} \times T$$

where *a* is a lattice parameter in Å, T is temperature in °C, and T is between 20 and 449°C

Equation 58. *c* lattice parameter of α-Pr between 20 and 449°C [193 Table IV]

$$c = 11.828 + 13.3 \times 10^{-5} \times T$$

where *c* is a lattice parameter in Å, T is temperature in °C, and T is between 20 and 449°C

The thermal expansion of the *c* lattice parameter in Figure 26 is consistent with the "equilibrium" results of Kuznetsov et al. [251 (Figure 5b)], which were obtained using angle-dispersive synchrotron diffraction. (In the context of the Kuznetsov et al. paper, "equilibrium" and "non-equilibrium" refer to whether there was a significant a thermal gradient in the sample during data collection rather than to thermodynamic stability.) The "equilibrium" and "non-equilibrium" results show a similar amount of change between values of *c* at ~300 and 700 K, although the "non-equilibrium" results show a stronger dependence on temperature [251 (Figure 5)].

Barson et al. measured the thermal expansion of polycrystalline Pr using dilatometry. Their results are shown graphically [203 (Figure 2)], and fall between the single-crystal values for the *a* and *c* directions from the high-temperature X-ray diffraction data of Spedding et al. [193] (Figure 26).

In view of the close agreement between the thermal expansion values for the *c* lattice parameter in the data of Spedding et al. and the "equilibrium" data of Kuznetsov et al., it seems likely that both values are fairly accurate representations of the thermal expansion of α-Pr along this crystallographic direction in the absence of a thermal gradient. Differences between the "equilibrium" and "non-equilibrium" values of Kuznetsov et al. may be relevant for nuclear fuels, where thermal gradients are likely during irradiation.

2.7.4.2 Coefficients of Thermal Expansion

Published coefficients of thermal expansion for α-Pr are summarized in Table 12. The table shows values from a review paper by Beaudry and Gschneidner [192], which are derived from the data of Spedding et al. [193] and repeated by Gschneidner in the CRC Handbook of Chemistry and Physics [191]. These values (and the figures and equations in this section of the Handbook) are derived from the same experimental data and are therefore consistent with each other. Values from the 1961 review by Gschneidner [207] are derived from the dilatometry results of Barson et al. [203]. The coefficient of thermal expansion parallel to *c* at 300 K reported by Kuznetsov et al. [251] is an independent measurement, and is ~13% higher than the coefficient derived from the data of Spedding et al.

The coefficient for polycrystalline α-Pr in Table 12 seems to be a weighted average of the coefficients parallel to the *a* and *c* directions rather than an experimental measurement. It is higher than the experimental measurement of Barson et al. [203 Figure 5].

The thermal expansion coefficient of the fcc Pr phase is negative between 550 and 800 K, and close to zero at higher temperatures [251].

Table 12. Coefficients of thermal expansion for α-Pr.

Description	**T (K)**	**Coefficient ($\times 10^6$/K)**	**Reference**
Parallel to *a* axis	298	4.5	[191, 192]
Parallel to *c* axis	298	11.2	[191, 192]
Parallel to *c* axis	300	12.73	[251]
Parallel to *c* axis	900	20.23	[251]
Polycrystal	298	6.7	[191, 192]
Polycrystal	25 C	4.8	[207]
Polycrystal	25-725 C	6.5	[207]

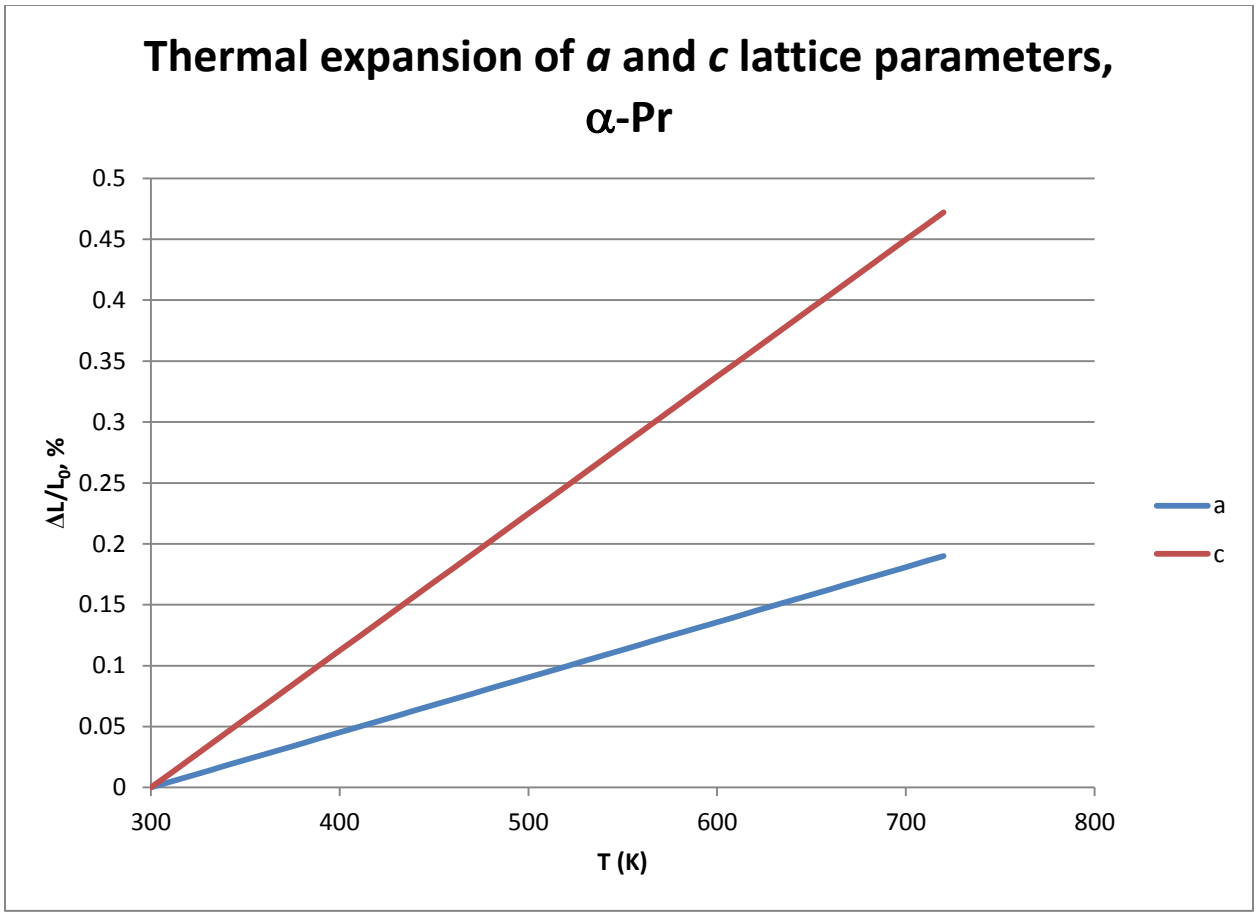

Figure 26. Thermal expansion of a and c lattice parameters of α-Pr, calculated from Equation 57 and Equation 58 with a reference temperature of 300 K.

2.7.4.3 Density

According to information in the CRC Handbook of Chemistry and Physics, the density of α-Pr is 6.15 g/cm^3 at 297 K, the density of β-Pr is 6.19 g/cm^3 at 598 K, and the density of γ-Pr is 5.97 g/cm^3 at 1160 K [191].

Measurements of the density of liquid Pr close to the melting point range from 6.27 g/cm^3 to 6.66 g/cm^3 (as summarized in reference [210]). In the absence of definitive measurements, the value of 6.59 g/cm^3 in the CRC Handbook of Chemistry and Physics [191 (Table 12)] is the most defensible estimate.

2.7.4.4 Densities and Molar Volumes as Functions of Temperature

Figure 27 shows molar volumes of Pr phases as functions of temperature. Approximations for the molar volume of α-Pr are based on the high-temperature X-ray diffraction data of Spedding et al. [193] (Equation 59). Approximations for the molar volume of the fcc phase are shown twice: "equilibrium" measurements from samples without thermal gradients, and "non-equilibrium" measurements from samples with thermal gradients.

Equation 59. Molar volume of α-Pr between 20 and 293 °C [193 (Table IV)]

$$V = 20.778 + 42.4 \times 10^{-5} \times T$$

where V is the molar volume in cm^3, T is temperature in °C, and T is between 20 and 293°C

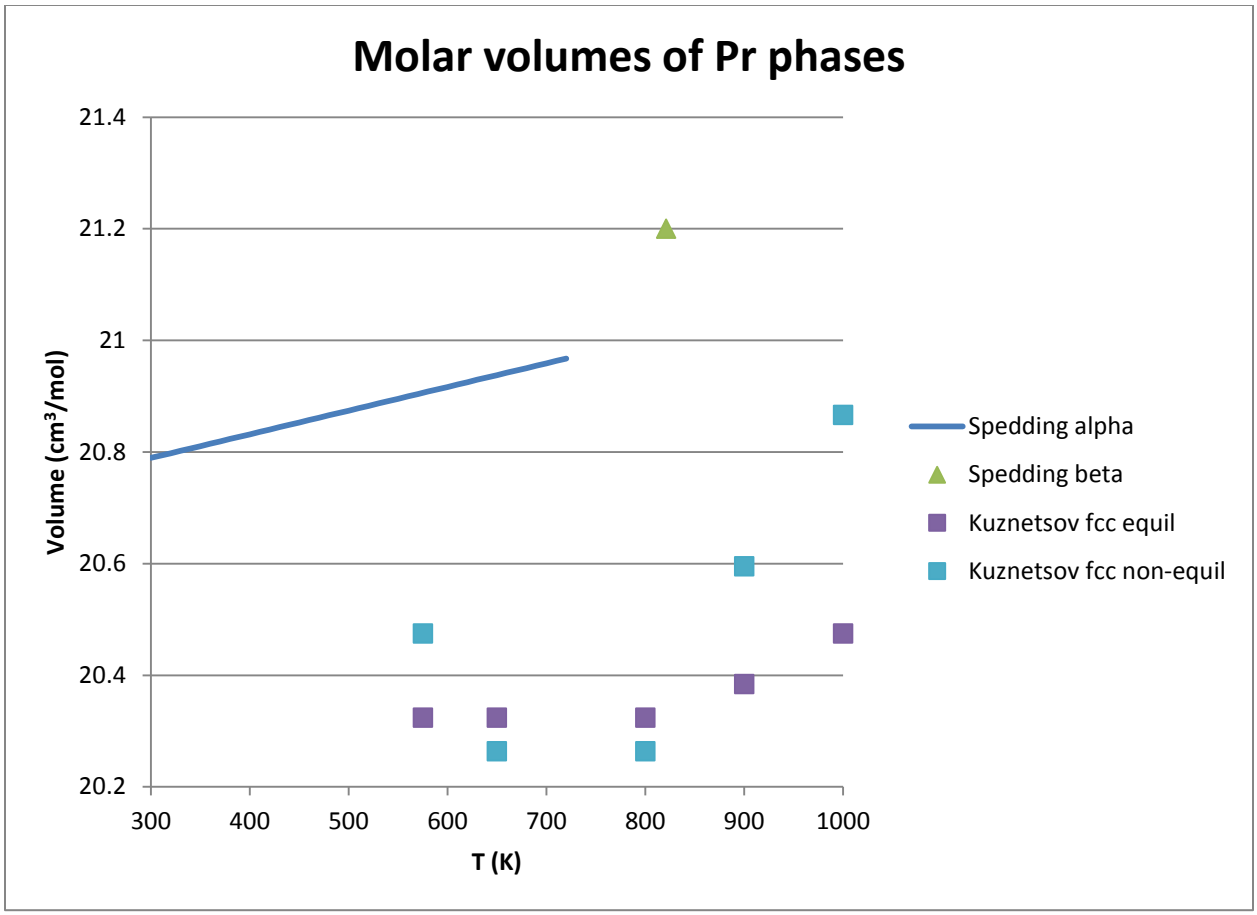

Figure 27. Molar volumes of Pr phases (Equation 59 and references [193 (Table 2)] and [251 (Figure 4)]).

Reported values for the change in the density of liquid Pr as a function of temperature include 2.48×10^{-4} g/cm^3-K [208] and 0.93×10^{-4} g/cm^3-K [210]. Further research is needed to determine the correct value.

2.7.4.5 Changes in Volume as a Result of Phase Transitions

The transformation from β-Pr to liquid causes a volume increase of ~0.02% [91].

2.7.5 Thermal Conductivity and Related Properties

2.7.5.1 Lorenz Number

Jolliffe and colleagues calculated the Lorenz number for Pr at 291 K as ~2.7×10^{-8} WΩ/K^2 based on their thermal conductivity and electrical resistivity measurements [211]. This value is generally consistent with the value of 2.67×10^{-8} WΩ/K^2 at 25°C in an earlier review by Gschneidner [207] and indicates that the room-temperature value of the Lorenz number for Pr is significantly higher than the theoretical value.

2.7.5.2 Thermal Conductivity

Figure 28 shows the available measurements of the thermal conductivity of α-Pr at temperatures between ~290 and 1030 K. These measurements demonstrate reasonably good agreement at temperatures below ~1000 K. The steep rise in the data of Kurichenko et al. between ~1000 and 1100 K is probably related to the α-β phase transformation at ~1068 K.

Thermal conductivity values published by Kurichenko et al. were calculated from new measurements of thermal diffusivity and heat capacity (both of which are provided in the original reference), combined with previously available information on density. The heat capacity values used by Kurichenko et al. are consistent with the values recommended in Section 2.7.3 of this Handbook.

The only available measurements of the thermal conductivity of liquid Pr are from a single paper, in which the heat capacity, thermal diffusivity, and thermal conductivity were measured using an instrument based on the method of radial temperature waves [254]. Equation 60 expresses the thermal diffusivity obtained using this instrument. The heat capacity measurements in this paper are lower than those from other researchers (Figure 25). The thermal conductivity is presented graphically, and shows a linear increase as a function of temperature [254 (Figure 1)].

Equation 60. Thermal diffusivity of liquid Pr [254]

$$\alpha = 0.0188 + 0.0903 \times 10^3 \times T$$

Where α is thermal diffusivity and T is a temperature in K between 1210 and 2000K. Units for thermal diffusivity were not specified; however, dimensional analysis suggests cm^2/s.

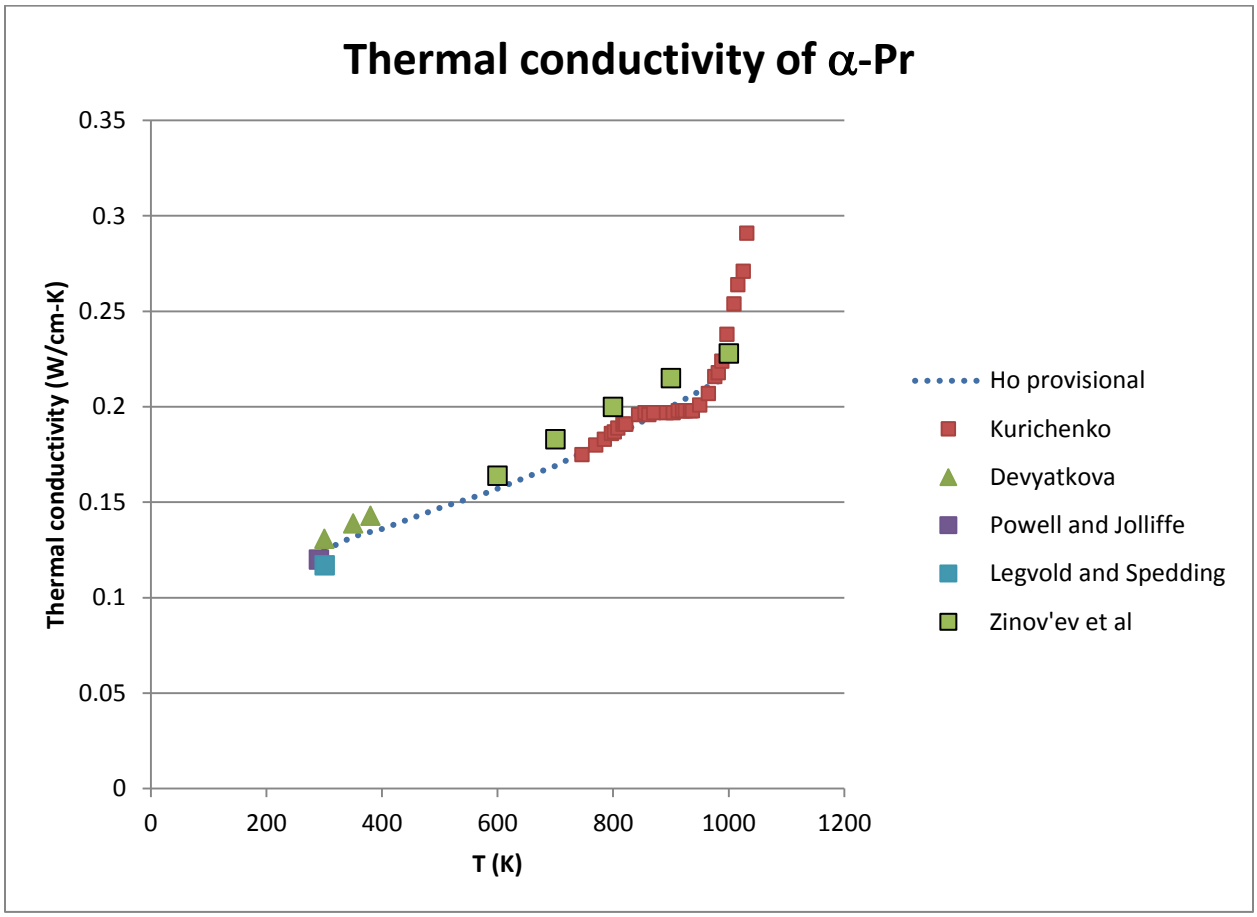

Figure 28. Thermal conductivity of α-Pr from references [202, 214, 248, 249, 256].

2.8 Nd

2.8.1 Introduction

Neodymium has only two solid phases that are stable at atmospheric pressure. Crystal structures and lattice parameters of both phases were determined in the early 1960s (e.g., reference [193]). Phases and phase boundaries at higher pressures have been investigated more recently (e.g., references [257, 258]).

Experimental measurements of incremental enthalpy or heat capacity of Nd at temperatures above 300 K have been published by several of research groups. There is generally good agreement about the heat capacity of α-Nd below ~1000 K. Agreement about the heat capacity of α-Nd at higher temperatures, the heat capacity of β-Nd, and the heat capacity of the liquid is less good.

Most of the available experimental data about thermal expansion of Nd is from a single reference with high-temperature X-ray diffraction data for single crystals of α-Nd. Limited data about the thermal expansion of polycrystalline samples is presented graphically in two other references.

The thermal conductivity of Nd at temperatures above ~300 K has been measured by a number of research groups using a variety of techniques [199, 200, 211, 214, 248, 249, 259, 260]. Room-temperature conductivities agree to within ~0.02 W/cm-K, and higher-temperature thermal conductivities for solid phases agree to within ~0.05 W/cm-K. There is general agreement that thermal conductivities rise with increasing temperature, and that there is little difference between the thermal conductivities of α-Nd and β-Nd.

Relatively recent research involves topics such as understanding the electronic structure of Nd using spectroscopy and modeling (e.g., references [181, 233, 261]).

2.8.2 Phases and Phase Transformations

2.8.2.1 Phases

Neodymium has two solid phases that are stable at atmospheric pressure. They are:

- α-Nd, dhcp (space group $P6_3/mmc$, a = 3.6582 Å, c = 11.7966 Å at 297 K) [191, 192]
- β-Nd, bcc (space group $Im\bar{3}m$, a = 4.13 Å at 1156 K) [191-193]

2.8.2.2 Phase Transformations

Recommended phase-transformation temperatures and enthalpies from a recent re-assessment of the experimental data are [7]:

- α-β, 1133±5 K (860±5°C) (based on 11 publications with original measurements, which range from 1036 to 1168 K). The corresponding transformation enthalpy is estimated at 2.48 ±0.30 kJ/mol.
- β-liquid, 1298±5 K (1025±5°C) (based on 5 publications with original measurements, which range from 1093 to 1298 K). The corresponding transformation enthalpy is estimated at 7.30 ±0.40 kJ/mol.

Although the α-β transformation temperature and solidus temperature both increase with increasing pressure, β-Nd apparently persists to a pressure of at least 50 kbars. The available information indicates that α-Nd transforms to a face-centered cubic phase at ~20-30 kbars [195].

2.8.3 Heat Capacity and Related Properties

Konings and Beneš [7] recently assessed the experimental data and developed equations representing heat-capacity values for Nd (Equation 61 through Equation 63). Although they are not a perfect fit for the data, these equations are probably the most useful approximation of the heat capacity of Nd. Further research is required, particularly at higher temperatures.

Figure 29 shows the heat-capacity values suggested by Konings and Beneš [7] and the experimentally determined heat capacities of Kurichenko et al. [200], Spedding et al. [244], and Atalla [199]. The very old (1938) data from Jaeger et al. [262] is not shown because the incremental enthalpy data seems anomalously high, possibly because of the relatively low purity of the sample. The value suggested by Konings and Benes for β-Nd (44.576 kJ/mol) is close to that of Spedding et al. (44.59 kJ/mol). However, the polynomial suggested by Konings & Beneš for α-Nd (Equation 61) is only close to the experimental data of Spedding et al. and Kurichenko et al. for temperatures between ~300 and 800 K, then increases until it is ~ 4 J/mol-K higher than the experimental data at the α-β phase transformation. The value suggested by Konings and Benes for liquid Nd (44.00 J/mol-K) is ~10% lower than the data of Spedding et al. (48.8 kJ/mol). It is not clear why these differences occur.

Equation 61. Heat capacity of α-Nd [7]

$$C_p = 31.9343 - 20.8734 \times 10^{-3} \times T + 33.3054 \times 10^{-6} \times T^2 - 0.03386 \times 10^6 \times T^{-2}$$

where C_p is constant-pressure heat capacity in J/mol·K and T is temperature in K

Equation 62. Heat capacity of β-Nd (in J/mol-K) [7]

$$C_p = 44.576$$

where C_p is constant-pressure heat capacity in J/mol·K

Equation 63. Heat capacity of Nd liquid (in J/mol-K) [7]

$$C_p = 44.00$$

where C_p is constant-pressure heat capacity in J/mol·K

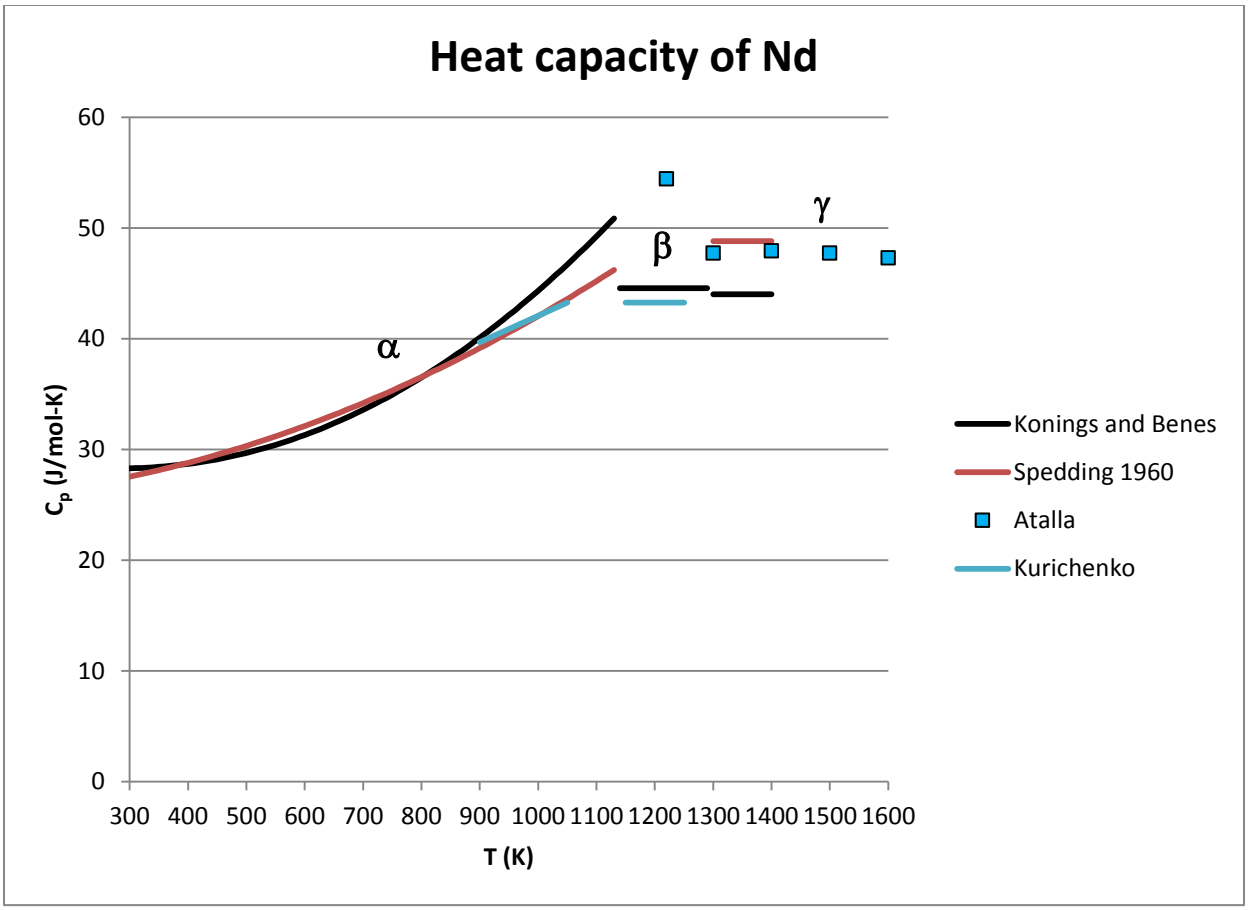

Figure 29. Heat capacity of Nd (references [199, 200, 244] and Equation 61 through Equation 63 from [7]).

2.8.4 Thermal Expansion and Density

2.8.4.1 Thermal Expansion

Spedding et al. [193] used high-temperature X-ray diffraction to measure the lattice parameters of α-Nd and developed polynomial equations expressing the lattice parameters as functions of temperature (Equation 64 and Equation 65). These equations correspond to lattice parameters a = 3.659 Å and c = 11.806 Å at 300 K. Figure 30 shows the corresponding thermal expansions of the individual lattice parameters, calculated based on a reference temperature of 300 K.

Equation 64. a lattice parameter of α-Nd 20 and 969°C [193 Table IV]

$$a = 3.6582 + 3.18 \times 10^{-5} \times T - 3.96 \times 10^{-8} x T^2 + 4.92 \times 10^{-11} \times T^3$$

where a is a lattice parameter in Å, T is temperature in °C, and T is between 20 and 969°C

Equation 65. c lattice parameter of α-Nd between 20 and 969°C [193 Table IV]

$$c = 11.802 + 16.6 \times 10^{-5} \times T - 14.1 x 10^{-8} \times T^2 + 17.8 \times 10^{-11} \times T^3$$

where c is a lattice parameter in Å, T is temperature in °C, and T is between 20 and 969°C

Barson et al. [203] and Frizen et al. [205] measured the thermal expansion of polycrystalline Nd using dilatometry. The measurements of Barson et al. fall between the single-direction expansions of the *a* and *c* lattice parameters in Figure 30. The measurements of Frizen et al. are similar to the single-direction expansion of the *a* parameter from the X-ray diffraction data of Spedding et al. [193].

Because the thermal expansion of α-Nd is anisotropic, the thermal expansion of actual samples may vary as a result of differences in preferred orientation. It therefore seems reasonable to estimate the thermal expansion of an arbitrary sample of polycrystalline Nd by a weighted average of the expansions in the *a* and *c* directions (i.e., expansion in the *a* direction is weighted twice as heavily as expansion in the *c* direction because of crystal symmetry).

No information about the thermal expansion of β-Nd is available.

2.8.4.2 Coefficients of Thermal Expansion

Published coefficients of thermal expansion for Nd are summarized in Table 13. Values from Beaudry and Gschneidner [192] are derived from the data of Spedding et al. [193] and repeated by Gschneidner in a 2015 review [191]. These values are therefore consistent with each other and with the figures and equations in this section of the handbook. The coefficient for polycrystalline α-Nd appears to be a weighted average of the coefficients parallel to the *a* and *c* directions rather than an experimental measurement. Values from a 1961 review by Gschneidner et al. [207] are derived from the work of Barson et al. [203], which involved polycrystalline material.

Spedding et al. noted that their measurements were generally within ~5% of previous measurements (e.g., [203]) for "mid-range" temperatures of approximately 400°C. However, they also noted that average deviations between their measurements and previous ones were ~20% at the ends of the measurement range. Thus, the agreement between the values in Table 13 may indicate that they were all derived from the measurements of Spedding et al. and therefore should not be considered as independent.

Table 13. Coefficients of thermal expansion for α-Nd.

Description	T (°C)	Coefficient ($\times 10^6$/°C)	Reference
α-Nd, parallel to *a* axis	25	7.6	[191, 192]
α-Nd, parallel to *a* axis	400	4.5	[193]
α-Nd, parallel to *c* axis	25	13.5	[191, 192]
α-Nd, parallel to *c* axis	400	11.7	[193]
α-Nd, polycrystal	25	9.6	[191, 192]
α-Nd, polycrystal	25	6.7	[207]
α-Nd, polycrystal	400	6.8	[193]
α-Nd, polycrystal	-173 to 850	8.6	[207]

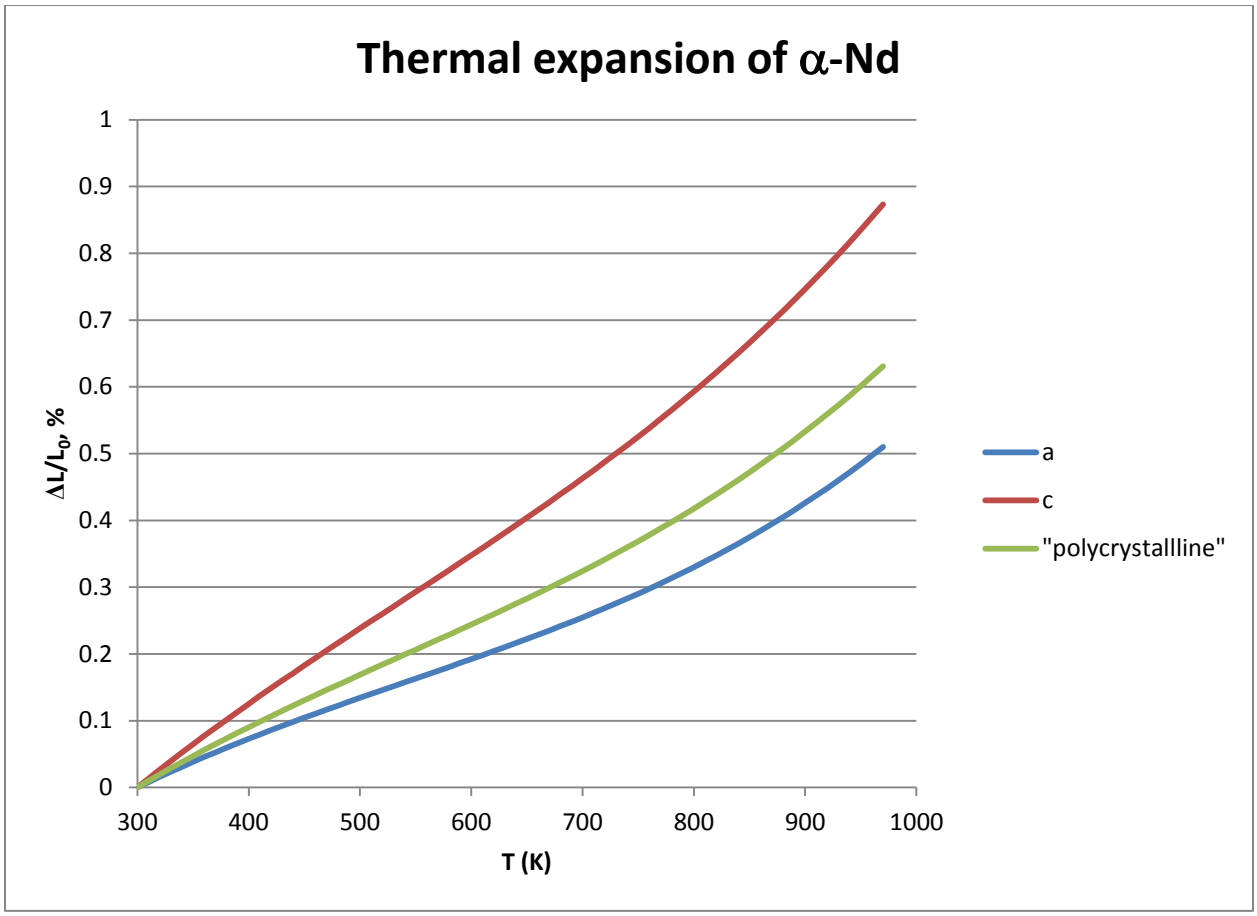

Figure 30. Thermal expansion of α-Nd. "a" and "c" are single-direction expansions in the *a* and *c* directions, based on values calculated from Equation 64 and Equation 65 using a reference temperature of 300 K. The "polycrystalline" value is a weighted average of the single-direction values.

2.8.4.3 Density

According to information in the CRC Handbook of Chemistry and Physics, the density of α-Nd is 7.008 g/cm^3 at 297 K and the density of β-Nd is 6/80 g/cm^3 at 1156 K [191].

Measurements of the density of liquid Nd close to the melting point range from 6.46 g/cm^3 to 6.92 g/cm^3 (as summarized in reference [210]). In the absence of definitive measurements, the value of 6.72 g/cm^3 in the CRC Handbook of Chemistry and Physics [191 Table 12] may be the best available estimate.

2.8.4.4 Densities and Molar Volumes as Functions of Temperature

The molar volume of α-Nd can be calculated as a function of temperature from an equation published by Spedding et al [193] (Equation 66, Figure 31), which indicates that the molar volume of α-Nd is of ~20.6 cm^3 at room temperature. The molar volume of β-Nd is 21.2 cm^3, based on four measurements with an average temperature of 883°C [193]. The corresponding density is 6.80 g/cm^3. These molar volumes are consistent with those in a recent tabulation (20.583 cm^3 for α-Nd at 24°C and 21.2 cm^3 for β-Nd at 883 K) [191], which may be derived from the same experimental data.

The temperature dependence of the density of liquid Nd has been reported twice. Rohr [247] found that the density decreased by ~0.5 mg/cm^3-K between 1310 and 1505 K, while Kononenko et al. [210] reported a decrease of ~0.76 mg/cm^3-K from 1289 to 1630 K.

Equation 66. Molar volume of α-Nd between 20 and 696°C [193 Table IV]

$$V = 20.60 + 65 \times 10^{-5} \times T - 70 \times 10^{-8} \times T^2 + 88 \times 10^{-11} \times T^3$$

where V is molar volume in cm^3, T is temperature in °C, and T is between 20 and 696°C

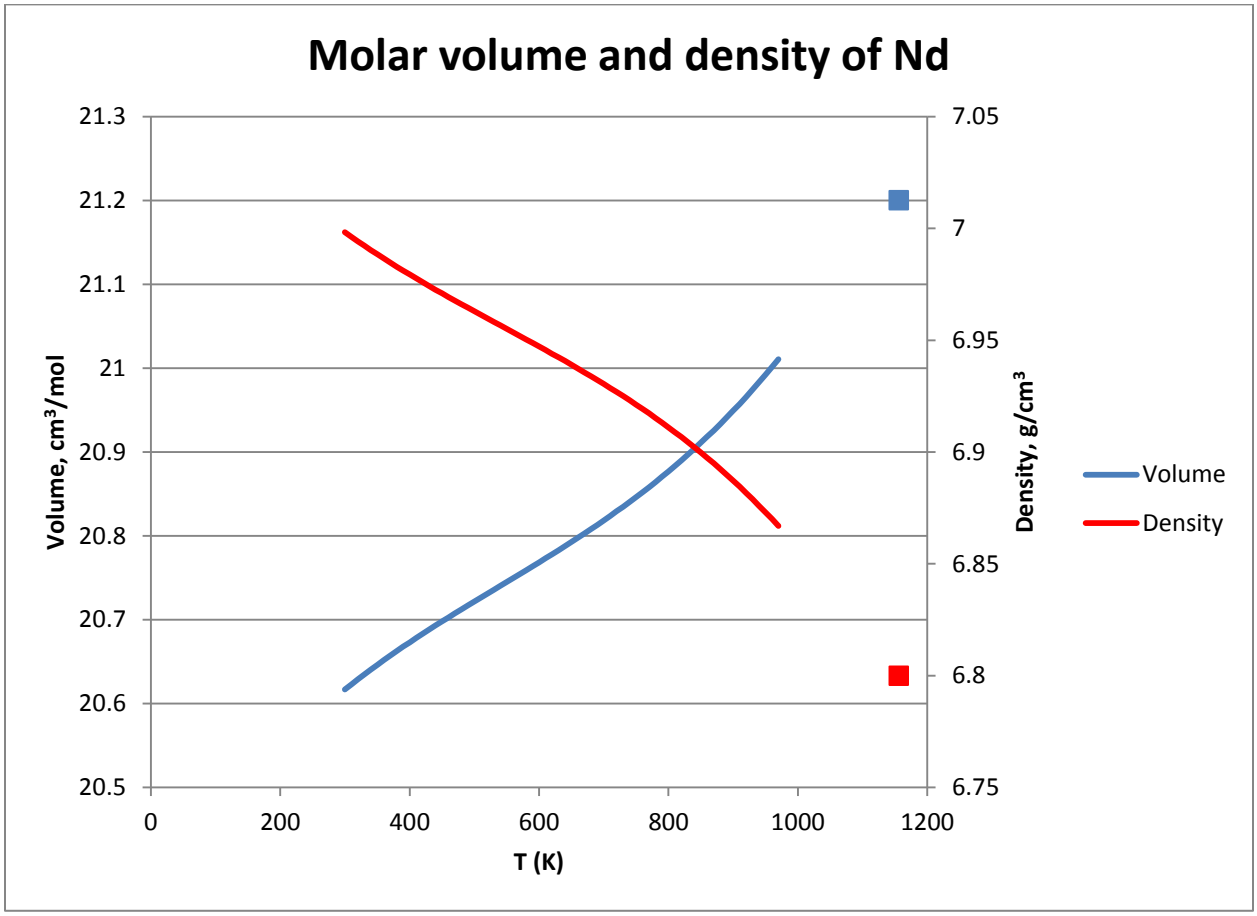

Figure 31. Molar volumes and densities of α-Nd (curves) and β-Nd (squares) (Equation 66 and reference [193]).

2.8.4.5 Changes in Volume as a Result of Phase Transitions

The volume change associated with the transformation from α-Nd to β-Nd is small [193, 203].

The melting of β-Nd causes a volume increase of ~0.9% [91].

2.8.5 Thermal Conductivity and Related Properties

2.8.5.1 Lorenz Number

Jolliffe and colleagues calculated the Lorenz number for Nd at 291 K as ~3.7×10^{-8} $W\Omega/K^2$ based on their measurements of thermal conductivity and electrical resistivity [211]. This value is generally consistent with the value of 3.54×10^{-8} $W\Omega/K^2$ calculated from information in the CRC Handbook of Chemistry and Physics [191 (Table 9)], but is significantly larger than the value of 2.80×10^{-8} $W\Omega/K^2$ at 25°C in an earlier review by Gschneidner [207] and the value of almost 3×10^{-8} $W\Omega/K^2$ reported by Binkele [259 (Figure 5)]. The value of 3.54×10^{-8} $W\Omega/K^2$ from data in the CRC Handbook is probably the most defensible value, as it is the most recent.

According to data from Binkele [259], the Lorenz number of α-Nd decreases with increasing temperature, asymptotically approaching the theoretical value at ~1100-1200 K (Figure 1 in reference [5]), which is close to the temperature of the phase transition between α-Nd and β-Nd (Section 2.8.2.2).

Lorenz numbers for Nd liquids are between 2.2 and 2.40 $W\Omega/K^2$ at temperatures between 1220 and 1600 K, with no obvious relationship between temperatures and variations in values [199]. These values are consistent with the value of ~2.3×10^{-8} $W\Omega/K^2$ for the Lorenz number of Nd liquid calculated from thermal expansion an electrical resistivity values "near the melting point" [191 (Table 12)].

2.8.5.2 Thermal Conductivity

Figure 32 shows the available experimental data on the thermal conductivity of Nd at temperatures above ~300 K. Values published by Kurichenko et al. [200] were calculated from new measurements of thermal diffusivity and heat capacity (both of which are provided in the original reference) obtained using a newly developed instrument, combined with previously available information on density. The heat capacity values used by Kurichenko et al. are consistent with the values recommended in Section 2.8.3 (Figure 29). Values published by Binkele were measured directly using a modification of the Kohlrausch technique, which involves measuring changes in temperature in response to electrical currents [259, 263]. The data from Atalla was obtained using a device developed by Atalla and colleagues for simultaneously measuring thermal conductivity, thermal diffusivity, and heat capacity [199]. Although Atalla indicates that the data is from liquids, it overlaps the temperature range for β-Nd (Section 2.8.2.2).

The provisional values of Ho et al. [62, 95] are provided for comparison, as they are more widely available than much of the other data shown in Figure 32. These values were based on room temperature thermal conductivity and estimated values for electrical resistivity and did not consider higher-temperature thermal conductivity measurements.

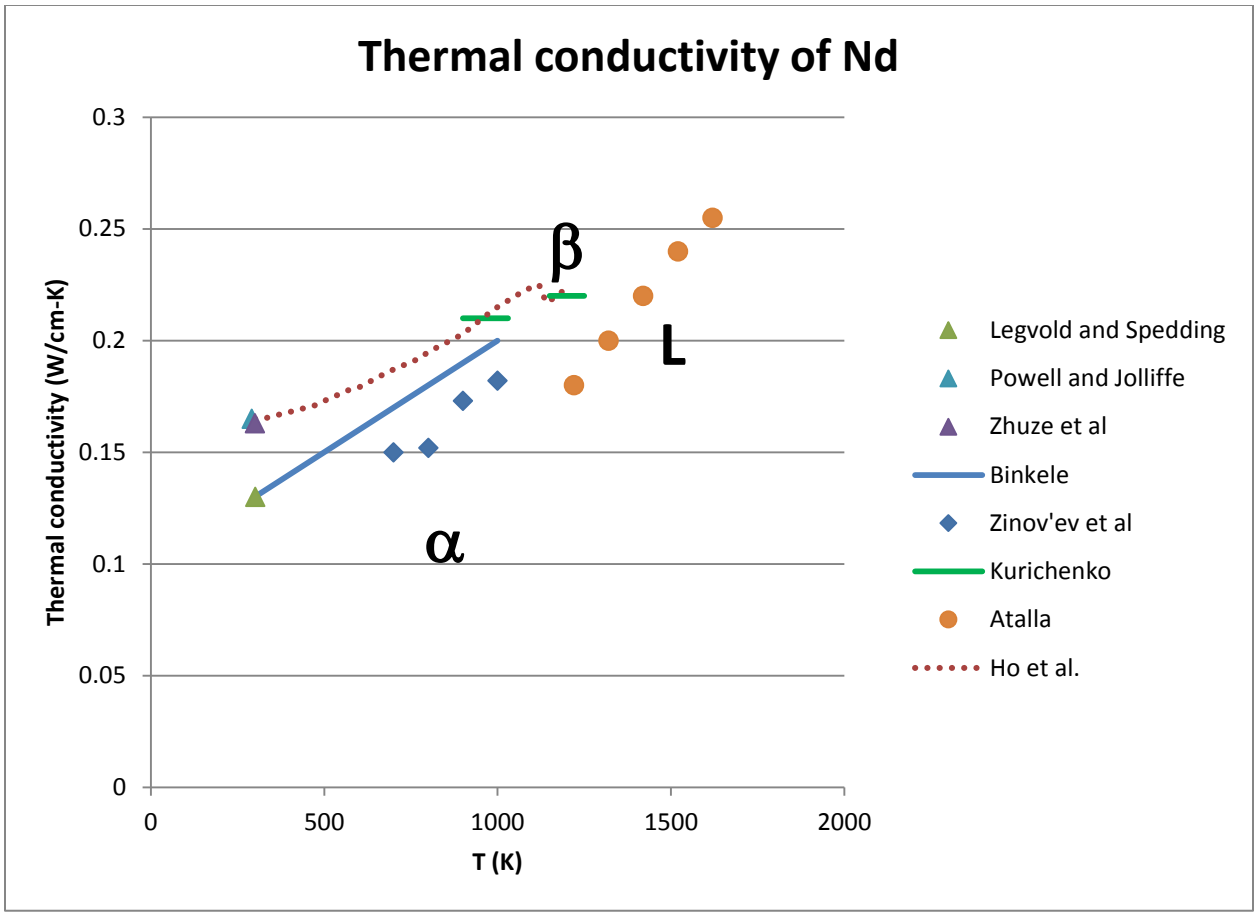

Figure 32. Thermal conductivity of Nd [95, 199, 200, 211, 214, 248, 249, 259, 260].

Experimental data on the electrical resistivity of Nd has been published in a number of papers (e.g., references [249, 264-268] but was not considered in this Handbook because more direct measurements of thermal conductivity are available.

2.9 Zr

2.9.1 Introduction

Zr has two stable crystalline phases (α-Zr and β-Zr) at atmospheric pressure. Crystal structures, lattice parameters, and phase transitions are well known. A third phase (ω-Zr) is stable only at high pressures.

Many measurements of the heat capacities of α- and β- Zr have been made. Recommended values in the NIST-JANAF tables and recent IAEA publications [21, 269] differ by a few J/mol·K for α-Zr, with much smaller differences for β-Zr. The heat capacity of liquid Zr has been measured at temperatures as high as 2200 K, and the heat capacity of the ideal monatomic gas has been calculated [269, 270].

The thermal expansion of α-Zr is anisotropic. There is generally good agreement about thermal expansion for single-crystal and polycrystalline materials [55, 271]. Variations in expansion as a result of thermal cycling have been reported [271]. The thermal expansion of β-Zr is less commonly studied, but there is generally good agreement about values for linear expansion of polycrystalline materials at temperatures up to ~1800 K. Higher-temperature measurements (to 2100 K for β-Zr and 2300 K for liquid) were obtained by Paradis and Rhim [270].

Several hundred measurements of the thermal conductivity and diffusivity of Zr were reviewed in 1995 by Fink and Leibowitz [272], and a polynomial that fit the most of data to within ~10% across a temperature range from 298-2000 K was developed. This polynomial shows a decrease in conductivity from 298 K to an inflection point at ~530 K and an increase from ~530 K to 2000 K, with no changes as a result of the α-β phase transformation. The polynomial of Fink and Leibowitz was adopted by later reviews including those of Kim et al. [19] and the IAEA [21].

Recent research on Zr involves topics such as understanding development of microstructures during deformation of α-Zr [273-276] and investigating relationships between α-Zr and ω-Zr [277-281].

2.9.2 Phases and Phase Transformations

2.9.2.1 Phases

The crystal structures and lattice parameters of Zr phases stable at atmospheric pressure are:

- α-Zr, hcp (space group $P6_3/mmc$), a = 3.2316 Å, c = 5.1475 Å at room temperature [282]
- β-Zr, bcc (space group $Im\bar{3}m$), a = 3.6089 kX (3.616 Å) at 980°C (1252 K) [283, 284]. Summers-Smith reported the room-temperature lattice parameter as 3.59 Å (3.58 kX) [52].

A third phase, ω-Zr, is stable at pressures above 3 GPa in pure Zr [285] and may be present as an unstable phase in shocked zirconium (e.g., [278]). Although ω-Zr itself is unlikely to occur in nuclear fuel, a structurally similar metastable phase is believed to occur in U-Zr alloys during atmospheric-pressure phase transitions (Section 2.1.1.2.1.2.2 of reference [5]). ω-Zr is hexagonal (space group $P6/mmm$), with lattice parameters a = 5.036 Å and c = 3.109 Å [282].

2.9.2.2 Phase Transformations

The generally accepted atmospheric-pressure temperatures and enthalpies for Zr phase transformations are:

- α-β, 863 °C (1136 K) [282], enthalpy 3.98 kJ/mol [286].
- Melting, 1854±8 °C (2127±8 K) [287]. This value is a second-quality point on the International Temperature Scale of 1990 (ITS-90) established by the Consultative Committee on Thermometry (CCT) of the International Committee on Weights and Measures (CIPM). The enthalpy of melting is 21.00 kJ/mol [288].

2.9.3 Heat Capacity and Related Properties

Measurements of the heat capacity of solid Zr were reviewed by Milošević & Maglić [289] and show generally good agreement. Values recommended by the IAEA [21] for α-Zr are slightly higher than those in the NIST-JANAF tables [269] (Figure 33), for reasons that are not clear.

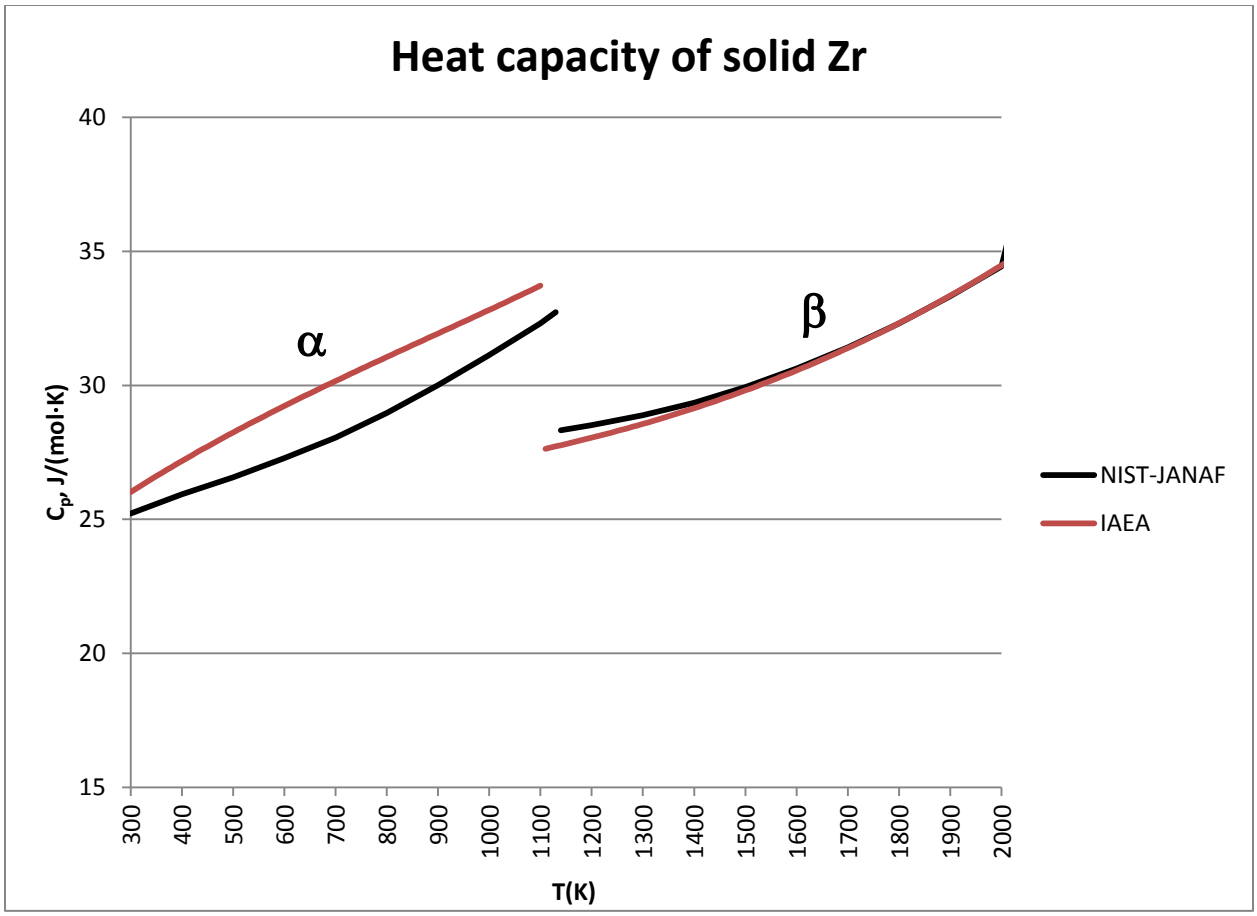

Figure 33. Heat capacities of solid Zr phases (IAEA data calculated using Equation 67 and Equation 68).

The IAEA heat-capacity values can be calculated using Equation 67 and Equation 68. Corresponding equations for the NIST-JANAF heat-capacity values are not available.

Equation 67. Heat capacity of α-Zr from 298 to 1100 K [21]

$$C_p = 238.596 + 0.181 \times T - 96.1 \times 10^{-6} \times T^2 + 36.2 \times 10^{-9} \times T^3$$

where C_p is constant-pressure heat capacity in J/kg·K, T is temperature in K, and T is between 298 and 1100 K

Equation 68. C_p of β-Zr from 1100 to 2128 K [21]

$$C_p = 276.462 + 0.0141 \times T - 3.08 \times 10^{-6} \times T^2 + 10.7 \times 10^{-9} \times T^3$$

where C_p is constant-pressure heat capacity in J/kg·K, T is temperature in K, and T is between 1100 and 2128 K

2.9.4 Thermal Expansion and Density

2.9.4.1 Thermal Expansion

Figure 34 shows recently recommended values for the thermal expansion of polycrystalline Zr [271], which are expressed by Equation 69 and Equation 70. Values for thermal expansion (in %) differ by less than 0.05 from the earlier recommendations of Touloukian et al. [55], with the largest difference occurring immediately above the phase transformation.

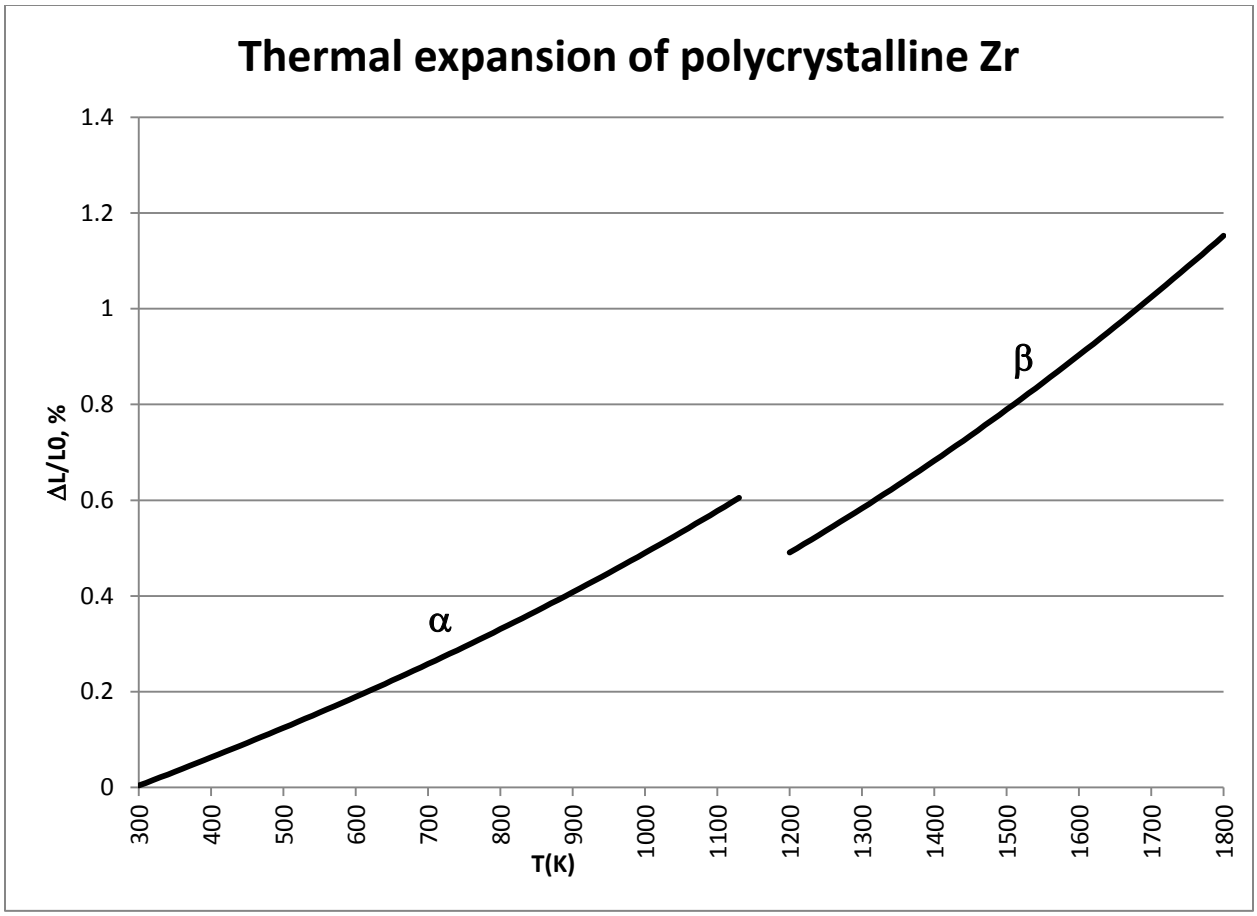

Figure 34. Thermal expansion of polycrystalline Zr, calculated from Equation 69 and Equation 70**.**

Equation 69. Thermal expansion of α-Zr [271]

$$(L-L_0)/L_0 = 5.7406 \times 10^{-4} \times (T-293) + 1.1888\text{x}10^{-7} \times (T-293)^2 + 7.0155 \times 10^{-11} \times (T-293)^3$$

where $(L-L_0)/L_0$ is thermal expansion in %, T is temperature in K, T is between 293 and 1130 K, L is the length at temperature T, and L_0 is the length at 293 K

Equation 70. Thermal expansion of β-Zr [271]

$$(L-L_0)/L_0 = 1.894 \times 10^{-4} \times (T-293) + 3.9735 \times 10^{-7} \times (T-293)^2 - 1.0345 \times 10^{-11} \times (T-293)^3$$

where $(L-L_0)/L_0$ is thermal expansion in %, T is temperature in K, T is between 1200 and 1830 K, L is the length at temperature T, and L_0 is the length at 293 K

2.9.4.2 Coefficients of Thermal Expansion

Equation 71 and Equation 72 express the mean linear thermal expansion coefficients corresponding to the curves in Figure 34.

Equation 71. Mean linear thermal expansion coefficient for polycrystalline α-Zr from 293 to 1130 K [271]

$$\bar{\alpha} \times 10^6 = 5.7406 + 1.1888 \times 10^{-3} \times (T\text{-}293) + 7.0155 \times 10^{-7} \times (T\text{-}293)^2$$

where $\bar{\alpha}$ is thermal expansion in units of 10^{-6}/K, T is temperature in K, and T is between 293 and 1130 K

Equation 72. Mean linear thermal expansion coefficient for polycrystalline β-Zr ($\bar{\alpha}$ in units of 10^{-6}/K, T in K, T from 1200 to 1830 K) [271]

$$\bar{\alpha} \times 10^6\ (\beta\text{-Zr}) = 1.894 + 3.9735 \times 10^{-3} \times (T\text{-}293) - 1.0345 \times 10^{-7} \times (T\text{-}293)^2 \text{ for } 1200 < T < 1830$$

where $\bar{\alpha}$ is thermal expansion in units of 10^{-6}/K, T is temperature in K, and T is between 1200 and 1830 K

Paradis and Rhim [270] determined that the volume expansion coefficients for β-Zr and for liquid Zr at the melting temperature (2128 K) are 2.35×10^{-5} K^{-1} and 4.6×10^{-5} K^{-1}, respectively.

2.9.4.3 Density

Densities of Zr phases are:

- α-Zr, 6.52 g/cm^3 at 298 K [290]
- β-Zr, 6.47 g/cm^3 at 1250 K [270]
- Liquid Zr, 6.24 g/cm^3 at 2128 K [270].

According to a recent review by the IAEA [21], the density of solid Zr at temperatures between 298 and 2128 K can be approximated by Equation 73, which neglects the relatively small density difference due to the α-β phase transformation.

Equation 73. Density of solid Zr from 298 to 2128 K [21]

$$\rho = 6550 - 0.1685 \times T$$

Where ρ is a density in kg/m^3, T is temperature in K, and T is between 298 and 2128 K

2.9.5 Thermal Conductivity and Related Properties

2.9.5.1 Thermal Conductivity

Reviews of the thermal conductivity and diffusivity of Zr include those by Touloukian et al. [62, 291], Fink and Leibowitz [272], Kim et al. [19], and the IAEA [21]. The Fink and Leibowitz review included an assessment of all published data available at the date of publication (1995), including that used by Touloukian et al., and led to development of a widely accepted polynomial expressing the thermal conductivity of Zr at temperatures between 298 and 2000 K (Figure 35, Equation 74). More recent estimates of thermal conductivity based on diffusivity measurements by Milošević & Maglić [289] give somewhat higher values, particularly at higher temperatures. However, because of the large numbers of measurements included in the Fink and Leibowitz review, the values from reference [289] should be considered as outliers unless future measurements indicate otherwise.

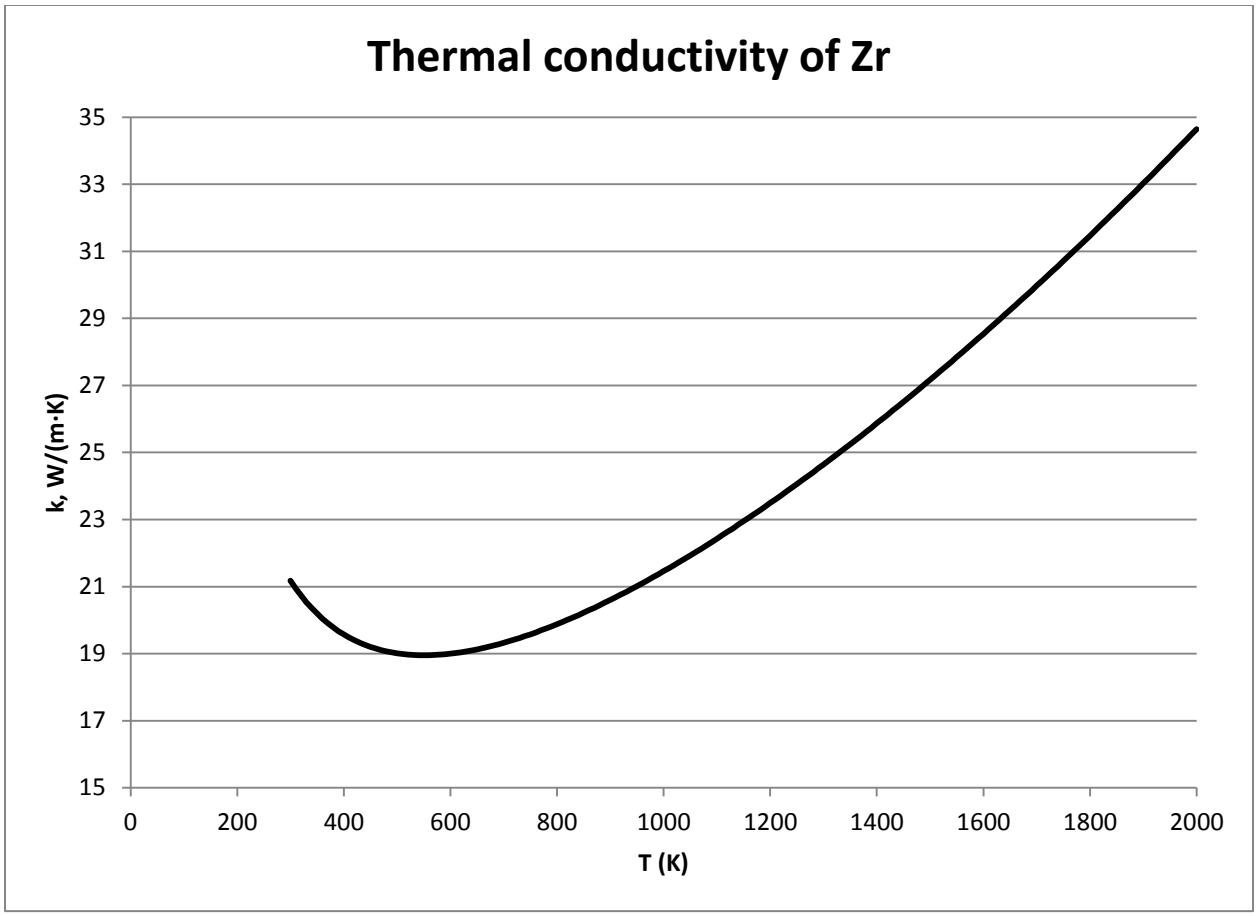

Figure 35. Thermal conductivity of Zr (Equation 74, reference [272]).

Equation 74. Approximate thermal conductivity of Zr according to Fink and Leibowitz [272]

$$k = 8.857 + 7.0820 \times 10^{-3} \times T + 2.5329 \times 10^{-6} \times T^2 + 2.9918 \times 10^3 \times T^{-1}$$

where k is thermal conductivity in W/m·K, T is temperature in K, and T is between 298 and 2000 K

2.9.5.2 Changes in Density as a Result of Phase Transitions

Changes in density as a result of the phase transition between α-Zr and β-Zr are small enough to be neglected for most purposes.

2.9.5.3 Lorenz Number

Milošević & Maglić [289] evaluated the Lorenz number of zirconium at temperatures between 300 and 1450 K by using their new measurements of heat capacity, electrical resistivity, and thermal diffusivity with linear thermal expansion values from Petukhov [271]. Their work, and that of the earlier researchers they cited, establishes that the Lorenz number is not a simple function of temperature and that the Lorenz number of α-Zr is higher than the theoretical value for all of the temperatures considered.

3. ALLOYS CONTAINING ONLY U, Np, Pu, and Am (Except U-Pu and U-Np-Pu, which are in Handbook Volume 1 (reference [5]))

3.1 U-Np

3.1.1 Introduction

Despite possible uncertainties in sample compositions, the 1959 phase diagram of Mardon and Pearce [292] was modified and adopted by Sheldon and Peterson in 1985 [293] and remains the only available experimentally determined phase diagram for the U-Np system. Key features of the phase diagram include a complete solid solution between U and Np in a bcc phase at the solidus, significant mutual solubility of U and Np in other phases, and the existence of the intermediate phase δ-(U,Np).

The U-Np phase diagram has been modeled by several research groups, with generally good agreement with experimental phase-transition temperatures and somewhat less good agreement with phase boundaries from X-ray diffraction [73, 294-296]. Other recent modeling includes an ab-initio study of phase stability by Xie et al. [297].

No systematic studies of thermal expansion or density in U-Np alloys are available, although Mardon and Pearce reported some data as part of their investigation of the U-Np phase diagram [292].

No information about the heat capacity or thermal conductivity of U-Np alloys is available.

3.1.2 Phases and Phase Transformations

3.1.2.1 Phases

Stable phases in the U-Np system are:

- (α-U): Allotropic solid solution of α-U that can dissolve up to ~45 at% Np [293, 302]. Addition of Np causes a slight decrease in all three lattice parameters [292].
- (β-U): Allotropic solid solution of β-U that can dissolve up to ~26 at% Np [293, 302]. This phase transforms to (α-U) and δ-(U,Np) by a eutectoid reaction at ~645°C [293].
- (α-Np): Allotropic solid solution of α-Np. According to Mardon and Pearce, the maximum solubility of U in this phase is ~17 wt% at room temperature, with a maximum of ~20 wt% at ~185°C; according to Okamoto [302], the maximum solubility of U in α-Np is ~4.7 at%. Incorporation of U in α-Np causes increases in all three lattice parameters [292].
- (β-Np): Allotropic solid solution of β-Np that can dissolve up to ~26 at% U at 668°C [293, 302]. This phase transforms to (α-Np) and δ-(U,Np) at 185°C by a eutectoid reaction, and to (γ-Np) and δ-(U,Np) at 612°C by a peritectoid reaction [293]
- γ-(U,Np): Solid solution between γ-U and γ-Np. This phase is believed to be bcc (space group $Im\bar{3}m$) based on the structures of γ-U and γ-Np; however, Mardon and Pearce were unable to confirm the structure by X-ray diffraction because of similarities in d-spacings with the Np oxides in their samples [292]. Some of Mardon and Pearce's data suggested a small miscibility gap in γ-(U,Np) in compositions with high concentrations of U; however, they did not show this gap in their published phase diagram because they were unable to confirm its existence and considered it unlikely based on similarities in sizes of U and Np atoms [292].

- δ-(U, Np): Intermediate phase with ~23-70 at% U [293, 302]. The structure of this phase is unknown, although it was originally believed to be either cubic or tetragonal with a *c*/*a* axis ratio close to unity and a crystal structure like that of ζ-(U,Pu) [292]. It was later established from neutron diffraction that ζ-(U,Pu) is actually rhombohedral with a lattice angle close to 90 degrees [303], and it seems possible that δ-(U, Np) also has a near-cubic rhombohedral unit cell. Based on a cubic structure, the room-temperature lattice parameter of δ-(U, Np) increases from 10.55 Å at 25 wt% U to 10.63 Å at 50 wt% U [292].

3.1.2.2 Phase Transformations

Critical points in the U-Np system are [293]:

- β-Np ↔ α-Np + δ-(U,Np) at 185°C
- β-Np ↔ γ-Np + δ-(U,Np) at 612°C
- β-U ↔ α-U + δ-(U,Np) at 645±5°C
- δ-(U,Np) ↔ β-U + γ-Np at 668±3°C

Mardon and Pearce reported that the enthalpy of melting was smaller than that of the solid-state transformations. However, no quantitative measurements of the enthalpy are available for any transformation in any U-Np alloy.

3.1.2.3 Phase Diagrams

The 1959 phase diagram of Mardon and Pearce was based on experimental data from thermal analysis, dilatometry, X-ray diffraction, and pycnometry (reference [292], with some preliminary results in reference [87]). It was based on measurements from two original 1-gram samples (one sample of Np feedstock and one sample of an alloy with 50% U), which were re-melted with additional U to provide data for other compositions. Major impurities in the Np feedstock were 0.34 wt% Ca and 0.22 wt% U. Masses lost during melting of some compositions were several tens of milligrams (almost half of the mass of the added U), suggesting the possibility of serious errors in sample compositions if the proportions of U and Np that were lost differed significantly from those in the sample. Thermal-expansion data from an alloy with ~50% Np obtained by progressive addition of U to the original Np sample were generally in good agreement with data from the original 50 at% Np sample.

The Mardon and Pearce phase diagram was updated in 1985 by Sheldon and Peterson to reflect more recent phase-transformation temperatures for U and Np [293] (Figure 36), and remains the only available experimentally determined phase diagram for the U-Np system. Key features of these phase diagrams include a bcc phase that forms a complete solid solution between U and Np at the solidus, significant mutual solubility of U and Np in other phases, and the existence of the intermediate phase δ-(U,Np).

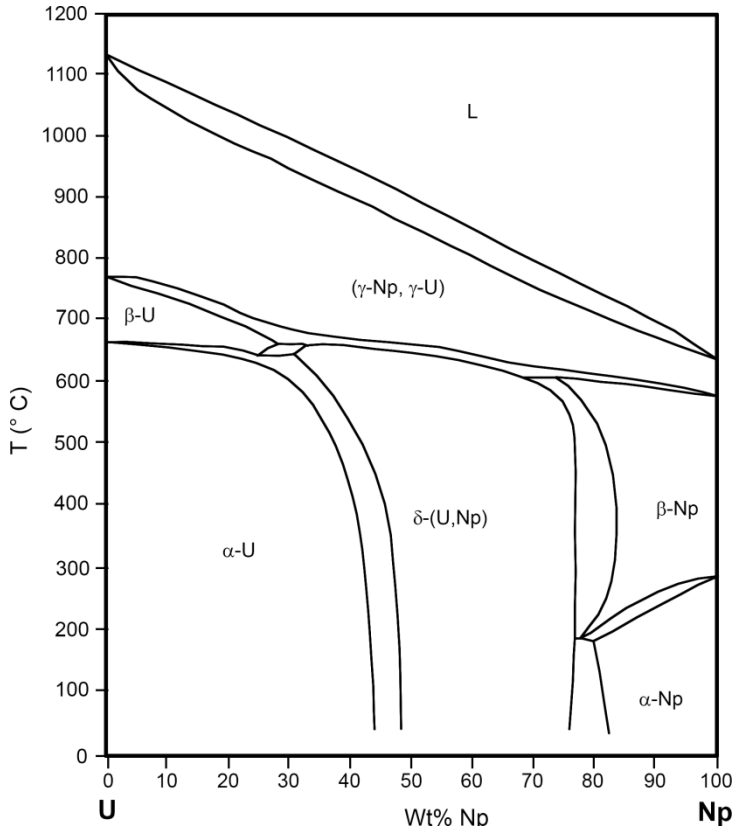

Figure 36. U-Np phase diagram proposed by Mardon and Pearce (re-drawn from [293]).

Two models of the solidus and liquidus as regular solutions [73, 294] produced good agreement with the experimental data. Kurata developed a model of the entire phase diagram based on a thermodynamically consistent database for the U-Np-Pu-Am-Fe-Zr system [295] and produced generally good agreement with the experimentally determined phase diagram. This model was adopted by Okamoto [302]. A new phase diagram based on ab-initio models and CALPHAD was published in 2018 by Xie and Morgan [296 (Figure 3)], with significant differences from the model of Kurata. The largest differences between the phase diagrams involve the maximum solubility of U in α-Np, the temperature dependence of the solubilities of U in β-Np and Np in α-U, the low-temperature stability of δ-(U,Np) (called "ζ" in the phase diagram of Xie and Morgan), and the boundaries of two-phase regions involving δ-(U,Np).

3.1.3 Thermal Expansion and Density

No systematic experimental studies of thermal expansion or density in U-Np alloys are available, although Mardon and Pearce reported some data as part of their investigation of the U-Np phase diagram [292].

3.1.3.1 Thermal Expansion

Quantitative data on the thermal expansion of (α-U) solid solutions is not available. Qualitatively, however, the thermal expansion of (α-U) with 40 wt% Np resembles that of α-U in that both phases expand in the *a* and *c* directions and contract slightly in the *b* direction during heating [292]. In the absence of experimental data, it is probably reasonable to use the thermal expansion of α-U (Section 2.1.4.1) to approximate the thermal expansion of (α-U) solid solutions in U-Np alloys.

3.1.3.2 Coefficients of Thermal Expansion

The *a* lattice parameter of a (β-Np) solid solution with ~15 wt% U varies linearly from ~4.91 Å at 280°C to 5.01 Å at 560°C, and the *c* lattice parameter varies from ~3.39 Å at 280°C to ~3.383 Å at 465°C [292 Fig. 4] (Figure 37). It should be noted, however, that the data for the *c* lattice parameter shows considerable scatter.

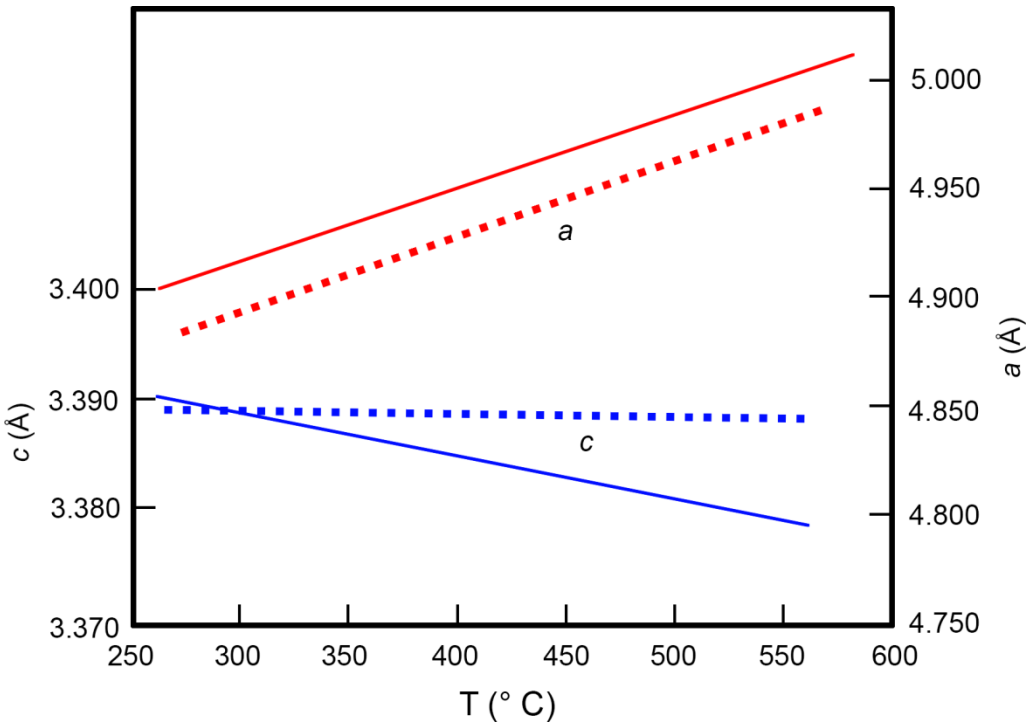

Figure 37. Thermal expansion of individual lattice parameters of Np-14.9 wt% U (solid lines), with β-Np lattice parameters for comparison (dotted lines) (after [292 Fig. 4]).

No information is available about coefficients of thermal expansion for other phases.

3.1.3.3 Density

According to the X-ray data of Mardon and Pearce [292], the room-temperature density of an (α-U) solid solution with the maximum concentration of dissolved Np is ~19.4 g/cm^3. Although it is not possible to calculate the density of δ-(U,Np) from the X-ray data without knowing its structure, pycnometry data suggests that the room-temperature density of δ-(U,Np) with 25% U is ~19.2 g/cm^3 and the room-temperature density of δ-(U,Np) with 50% U is ~18.8 g/cm^3 (Figure 38). Care is needed in interpreting this data, as the pycnometry was intended to assist in identifying phase boundaries rather than to provide quantitative densities. The densities measured by Mardon and Pearce using pycnometry are generally ~0.2-0.3 g/cm^3 lower than the densities calculated from their X-ray diffraction data.

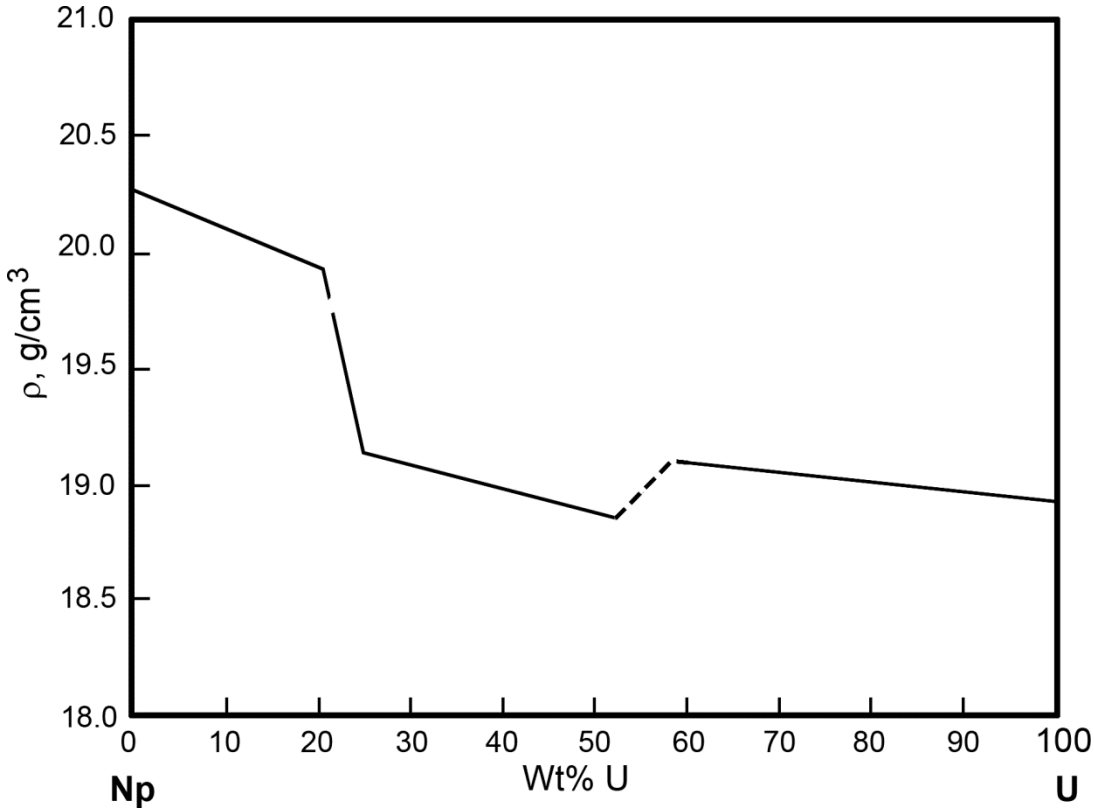

Figure 38. Room-temperature densities of U-Np alloys from pycnometry (re-drawn from [292 Figure 2]). Although Mardon and Pearce did not identify the phases involved, their phase diagram shows that the three room-temperature phases are (β-Np), δ-(U,Np), and (α-U).

3.2 U-Am

3.2.1 Introduction

No experimentally determined U-Am phase diagrams are available. Very limited experimental data has apparently been published in two conference proceedings papers [298, 299], although it was not possible to obtain a copy of reference [299]. The published versions of both of these conference papers apparently involve alloys with 10% Am, although Ogawa [73] reports results from reference [298] involving a composition with ~50% Am.

All of the available data indicates a high degree of immiscibility, and Kurata [300] says that the maximum mutual solubility of Am and U is less than 1 at%. Phase diagrams for the U-Am system were calculated by Ogawa [73], Kurata [295, 300], and Perron et al. [301].

An experimental investigation of this system is needed. In the absence of this investigation, it is probably reasonable to consider the phase diagram of Perron et al. (Figure 39) as the best available representation of the U-Am system.

No information about the heat capacities, thermal expansion, density, or thermal conductivity of U-Am alloys is available.

3.2.2 Phases and Phase Transformations

No experimental information about phases and phase transformations in U-Am alloys is available. Because of the very limited miscibility indicated by both the available data and the phase diagrams, it seems reasonable to assume that properties of solid-solution phases are similar to those of pure elements.

3.2.2.1 Phase Diagrams

U-Am phase diagrams were calculated by Ogawa [73], Kurata [295, 300], and Perron et al. [301]. Although all of the calculated phase diagrams show a high degree of immiscibility in solids and liquids, the extent of solid solution in the Ogawa phase diagram is not consistent with the data of Kurata (which was not available until later), and the Ogawa phase diagram does not address phase transformations occurring below 800 K. The Kurata phase diagram appears in a conference paper and a review, with little discussion in either reference. It is generally similar to the phase diagram of Perron et al., which is presented with far more detail. In the absence of experimental data, it is probably reasonable to consider the calculated phase diagram of Perron et al. (Figure 39) as the best available approximation to the actual U-Am phase diagram.

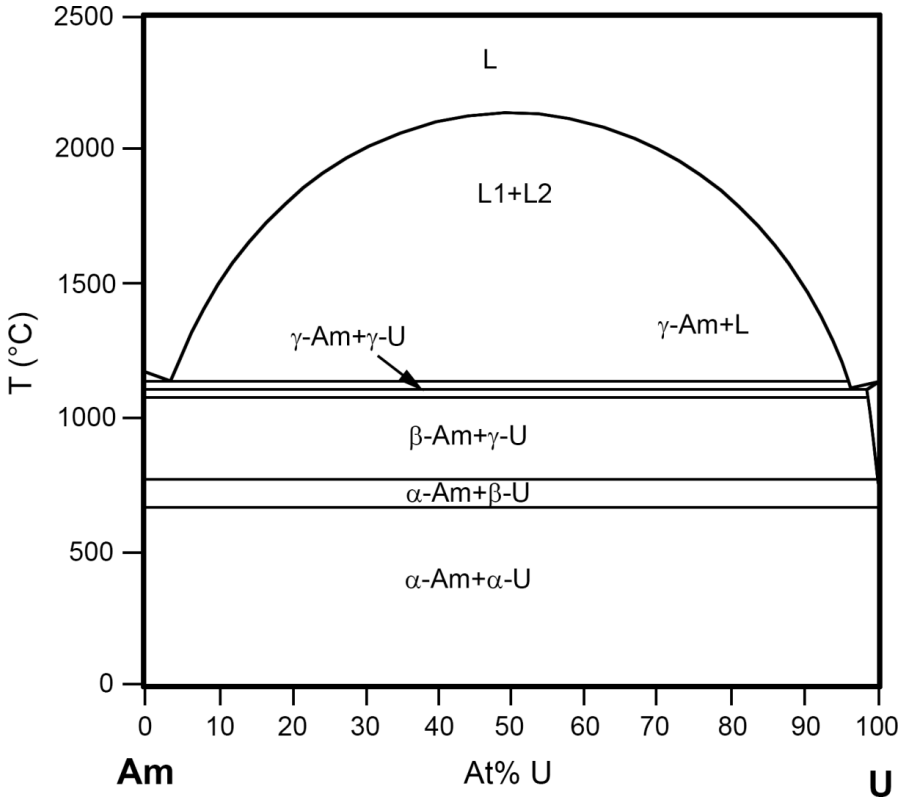

Figure 39. Calculated U-Am phase diagram proposed by Perron et al. (re-drawn from [301])

3.3 Np-Pu

3.3.1 Introduction

Although preliminary data on Np-Pu phases was presented at international conferences in 1958 and 1960 [304-307], the first (and apparently only) thorough experimental investigation of the Np-Pu phase diagram was published by Mardon and colleagues in 1961 [308]. This phase diagram shows far more solubility than is common in binary actinide phase diagrams. Key features include complete miscibility of Np and Pu liquids, a complete solid solution between the bcc phases γ-Np and ε-Pu, very high solubility of Np in α-Pu and β-Pu and low solubility of Np in γ-Pu, δ-Pu, and δ'-Pu, significant solubility of Pu in α-Np and β-Np, and the existence of the intermediate phase η-(Np,Pu). Liquidus and solidus temperatures are lower for alloys than for Np or Pu. Sheldon and Peterson [309] adopted the phase diagram of Mardon and colleagues with small modifications to accommodate improved knowledge of phase-transformation temperatures in Np and Pu.

Models of the liquidus and solidus by Ogawa [73] are in good agreement with the experimental data of Mardon et al. Kurata [295] modeled the entire system, obtaining general agreement with the experimental data of Mardon et al. in compositions with at least 40 wt% Pu despite a lack of thermodynamic data. This phase diagram was presented by Okamoto [310]. Other recent modeling research involves density functional theory calculations by Landa et al. [311].

Further work on the Np-Pu phase diagram is needed to confirm phase boundaries in high-Pu compositions, determine the crystal structure of η-(Np,Pu), and provide information about phase-transformation enthalpies. Experimental work is also needed to understand relationships between (α-Np) and (α-Pu) solid solutions, and between (β-Np) and (β-Pu) solid solutions. These relationships involve compositions with more than 60 at% Np, which are of limited practical interest for FCRD fuels.

No information about the heat capacities of Np-Pu alloys is available.

The thermal expansion and density of Np-Pu alloys have apparently not been systematically studied, although Mardon et al. obtained some information as part of their investigation of the Np-Pu phase diagram [308].

Experimental measurements of the thermal conductivity of Np-Pu alloys are not available, and electrical resistivity values are limited to temperatures below 400 K. All of the measurements are from samples with the α-Pu structure. The electrical resistivity of alloys with 0.5-25 at% Np is within a few percent of the electrical resistivity of pure Pu at temperatures of 300-400 K, suggesting that the thermal conductivity of these alloys can be approximated by the thermal conductivity of Pu (Section 2.3.5.2).

3.3.2 Phases and Phase Transformations

Generally recognized phases in the Np-Pu system are:

- (α-Pu): Allotropic solid solution of α-Pu. According to Mardon et al. [308], the solubility of Np in α-Pu is ~ 75-80 wt% at room temperature, rising to 96 wt% at 275°C. The calculated phase diagram of Kurata shows a much smaller dependence on temperature, with maximum concentrations of Np between ~90 and 95% at temperatures between ~120 and 270°C [310].

  Mardon et al. reported that the *a*, *b*, and *c* lattice parameters of (α-Pu) decrease with increasing Np, while the lattice angle β remains unchanged [308]. The decrease in each lattice parameter is ~0.7% over the entire compositional range of the phase [308, 312]. These observations are generally consistent with lattice parameters $a = 6.12 \pm 0.02$ Å, $b = 4.80 \pm 0.01$ Å, $c = 10.95 \pm 0.04$ Å, $\beta = 101.74 \pm 0.23°$ determined from single-crystal X-ray diffraction of a sample with ~43.4 at% Pu [312].

- (β-Pu): Allotropic solid solution of β -Pu. According to the phase diagram of Mardon et al., the maximum solubility of Np in β -Pu is ~60 wt% at ~300°C, increasing to 86 wt% at 540°C. However, Mardon et al. described the high-Np boundary of the (β-Pu) solid solution field in this temperature range as "extremely uncertain" because of inconsistent data from alloys with similar compositions. The calculated phase diagram of Kurata shows that the maximum concentration of Np in β-Pu is ~20 at%, with little dependence on temperature.

  Mardon et al. reported that the *a*, *b*, and *c* lattice parameters of (β-Pu) decrease with increasing Np.

- (γ-Pu), (δ-Pu), and (δ'-Pu): Allotropic solid solutions of (γ -Pu), (δ -Pu), and (δ'-Pu). Mardon et al. determined that the maximum solubility of Np in each of these phases is less than ~2%, generally consistent with tentative phase boundaries in the preliminary diagram of Cope et al. [306]. Data read from the calculated phase diagram of Kurata [295, 310] suggests a maximum solubility of ~2% in γ -Pu, 6% in δ -Pu, and 7% in δ'-Pu.

- (ε-Pu, γ-Np): A continuous bcc solid solution between γ -Np and ε-Pu. The lattice parameter decreases non-linearly with increasing concentration of Np, and is slightly smaller than would be expected from Vegard's law [308].
- η-(Pu, Np): An intermediate phase with ~3-50 wt% Np, stable between ~288 and 508°C. Mardon et al. determined that this phase is not isostructural with η-(U,Pu) or ζ-(U,Pu) but thought it might be orthorhombic. On this basis, they suggested lattice parameters a = 10.86 Å, b = 10.67 Å, and c = 10.43 Å for an alloy with 19 wt% Np at 375°C. They reported that each lattice parameter increased with increasing Pu, and that ratios between the sizes of the lattice parameters remained constant.

  In his model, Kurata treated η-(Pu,Np) as equivalent to η-(U-Pu) because of similarities between boundaries between these phases and the corresponding body-centered cubic phases in binary phase diagrams. Kurata said this treatment was supported by experimental data in a paper on the U-Np-Pu ternary that is listed in the bibliography of reference [295] as "to be published." Attempts to find this publication were unsuccessful.
- (α-Np): Allotropic solid solution of α-Np. Mardon et al. reported that the solubility of Pu in α-Np increases as the temperature is lowered. Although they had difficulties in determining the maximum solubility of Pu in α-Np because the boundary steepened rapidly at lower temperatures decreased, they believed the maximum solubility to be "somewhat less than 20% plutonium" at room temperature. In contrast, Kurata's calculated phase diagram shows the maximum solubility of Pu in α-Np as ~5 at%, with little dependence on temperature.
- (β-Np): Allotropic solid solution of β -Np. Mardon et al. had difficulties in determining the maximum solubility of Pu in β-Np because of inconsistent results from alloys with similar compositions, but believed the solubility limit was ~ 10% at 540°C and somewhat lower at 300°C. The calculated phase diagram of Kurata suggests that the maximum concentration of Pu in β-Np is slightly more than 20 at%, with very limited dependence on temperature.

The existence of a second intermediate phase, ζ-(Pu,Np), was suggested in an early phase diagram based primarily on variations in the coefficient of thermal expansion [306]; however, attempts to confirm the existence of this phase by X-ray diffraction were not successful [308] and it does not appear in other phase diagrams.

In addition to phase transformations in pure Np and Pu, Sheldon and Peterson [309] listed the following invariant points in the Np-Pu phase diagram. Subscripts indicate compositions in at% Pu.

- $(\gamma\text{-Np},\varepsilon\text{-Pu})_{22} + (\beta\text{-Np})_{10} \leftrightarrow (\beta\text{-Pu})_{15}$: a peritectoid reaction at 540°C
- $(\gamma\text{-Np},\varepsilon\text{-Pu})_{66} + (\beta\text{-Pu})_{47} \leftrightarrow \eta\text{-(Pu,Np)}_{15}$: a peritectoid reaction at 508°C
- $(\varepsilon\text{-Pu})_{95.5} \leftrightarrow \eta\text{-(Pu,Np)}_{94.5} + (\delta'\text{-Pu})_{97.8}$: a eutectoid reaction at 440°C
- $(\delta'\text{-Pu})_{97.6} \leftrightarrow \eta\text{-(Pu,Np)}_{95.0} + (\delta\text{-Pu})_{98.3}$: a eutectoid reaction at 428°C
- $\eta\text{-(Pu,Np)}_{97.1} + (\delta\text{-Pu})_{99.4} \leftrightarrow (\gamma\text{-Pu})_{99.0}$: a peritectoid reaction at 325°C
- $(\beta\text{-Np})_{5.0} + (\beta\text{-Pu})_{38.5} \leftrightarrow (\alpha\text{-Pu})_{25}$: a peritectoid reaction at 300°C
- $\eta\text{-(Pu,Np)}_{96.5} \leftrightarrow (\beta\text{-Pu})_{95.5} + (\gamma\text{-Pu})_{98.3}$: a eutectoid reaction at 288°C
- $(\beta\text{-Np})_{1.6} \leftrightarrow (\alpha\text{-Np})_{1.0} + (\alpha\text{-Pu})_{4.0}$: a eutectoid reaction at 275°C.

3.3.2.1 Phase Diagrams

The first (and apparently the only) thorough experimental investigation of the Np-Pu phase diagram was published by Mardon and colleagues in 1961 [308]. Samples used to determine the phase diagram were made by progressively re-melting alloys that initially had 10, 54, or 97 wt% Np, adding enough Pu to increase the composition of the alloy by 2-3 wt% Pu each time. This approach may have led to increasing accumulation of impurities above the concentrations in the original Np feedstock, which included ~0.34 wt% Ca and 0.22 wt% U.

Preliminary experimental phase diagrams for the Np-Pu system were published by Poole et al. [305] and Cope et al. [306]. The phase diagram of Poole et al. was based in part on unpublished data from Mardon and Pearce, and therefore should probably be considered as a preliminary version of the Mardon et al. phase diagram rather than an independent study. The phase diagram of Cope et al. includes only high-Pu compositions. Its determinations of solubility of Np in α, γ, δ, and δ'-Pu are similar to those in the phase diagram of Mardon et al; however, it differs from other phase diagrams in that it shows far lower solubility of Np in β-Pu and includes the intermediate phase ζ-(Pu,Np).

Sheldon and Peterson [309] made small changes to the phase diagram of Mardon et al. to accommodate more recent measurements of phase-transformations temperatures in Np and Pu. Although some of the phase-transformation temperatures used by Sheldon and Peterson differ by a few degrees from those recommended in other sections of this handbook, the difference is unlikely to cause significant errors. The Sheldon and Peterson phase diagram (Figure 40) is probably the best available representation of the Np-Pu system.

Ogawa [73] modeled the liquidus and solidus using a regular-solution model with interaction parameters determined using Brewer valence bond theory and obtained good agreement with the experimental data. Kurata [295] modeled the Np-Pu system using values from a consistent database of thermodynamic properties for the U-Np-Pu-Zr-Am-Fe system. In the absence of needed thermodynamic measurements for the Np-Pu system, he drew "reasonable" phase boundaries. The resulting phase diagram generally agrees with the phase diagrams of Mardon et al. and Sheldon and Peterson in compositions with at up to 60 wt% Np. The Kurata phase diagram was documented by Okamoto [310].

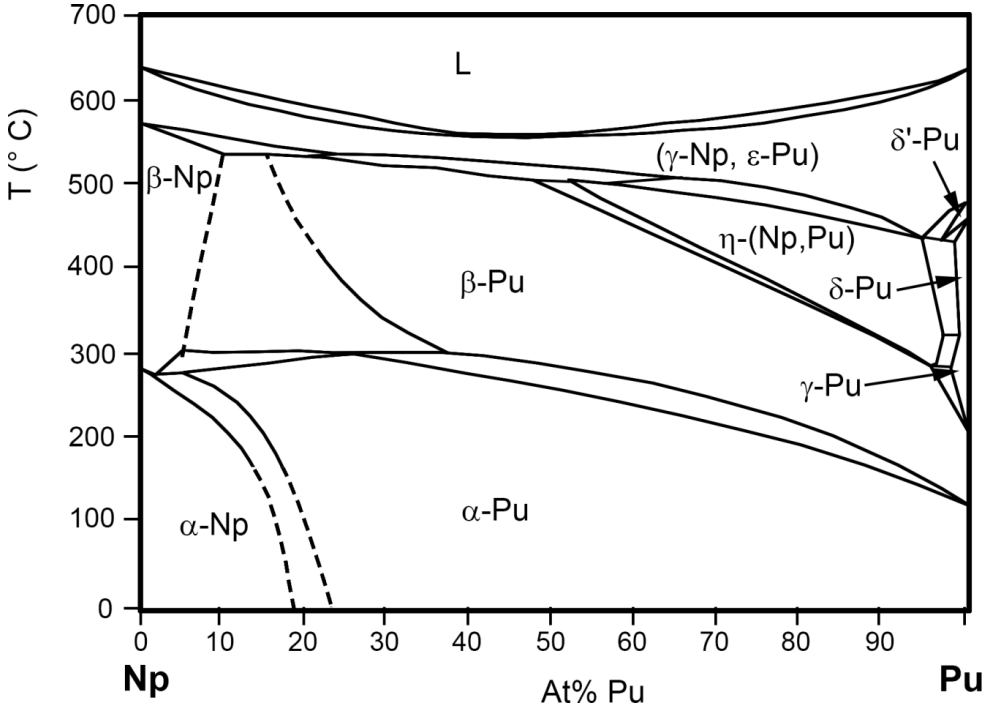

Figure 40. Np-Pu phase diagram of Sheldon and Peterson (re-drawn from [309]).

3.3.3 Thermal Expansion and Density

3.3.3.1 Coefficients of Thermal Expansion

Although Mardon et al. were unable to determine the structure of η-(Np,Pu), they reported its linear thermal expansion coefficients as ~25±5 × 10^{-6}/°C in each of three mutually orthogonal directions based on high-temperature X-ray diffraction data and a postulated orthorhombic structure [308].

Coefficients of thermal expansion for other Np-Pu phases are not available.

3.3.3.2 Densities

Mardon et al. [308] estimated the density of the η-(Np-Pu) structure in an alloy with 19 wt% Np as 17.56 g/cm^3 at 450°C. This estimate was ~5.5% above the actual measured value, matching the adjustment required to bring the measured densities of the α-Pu and β-Pu solid solution phases in the same alloy into agreement with the theoretical densities of these phases. Mardon et al. believed that this adjustment was needed to compensate for voids in the sample.

Mardon et al. reported that the maximum room-temperature density for α-(Pu,Np) solid solution phases is ~20.1 g/cm^3. This value is significantly larger than the value of 19.816 g/cm^3 listed for pure α-Pu in Section 2.3.4.3. Although Mardon et al. reported that the density of α-Pu solid solutions increased slightly with higher concentrations of Np because of a decrease of ~1% in the *a*, *b*, and *c* lattice parameters without a corresponding change in the lattice angle β, it seems likely that most of the difference between Mardon's density and that in Section 2.3.4.3 is due to use of different values for the density of α-Pu. It may be reasonable to approximate the density of α-(Pu,Np) solid solutions by using the change in densities reported by Mardon et al., but starting from the value of the density of α-Pu in Section 2.3.4.3.

Densities of other (Np-Pu) phases are not available.

3.3.4 Thermal Conductivity and Related Properties

3.3.4.1 Thermal Conductivity

Although no measurements of thermal conductivity for Np-Pu alloys are available, two sets of measurements of electrical resistivity have been reported [313, 314].

The earlier set of measurements was apparently in progress at the time of they were presented in a conference paper [314]. These measurements show differences in electrical resistivity of Pu and Np-Pu alloys with 9 and 50 at% Np as a function of temperature, reported relative to resistivities of the same materials at 0°C rather than as measured values (Figure 41). Resistivities of all three materials decrease smoothly with increasing temperatures in the range from ~100-400 K, but resistivities of materials with higher concentrations of Np decrease less rapidly.

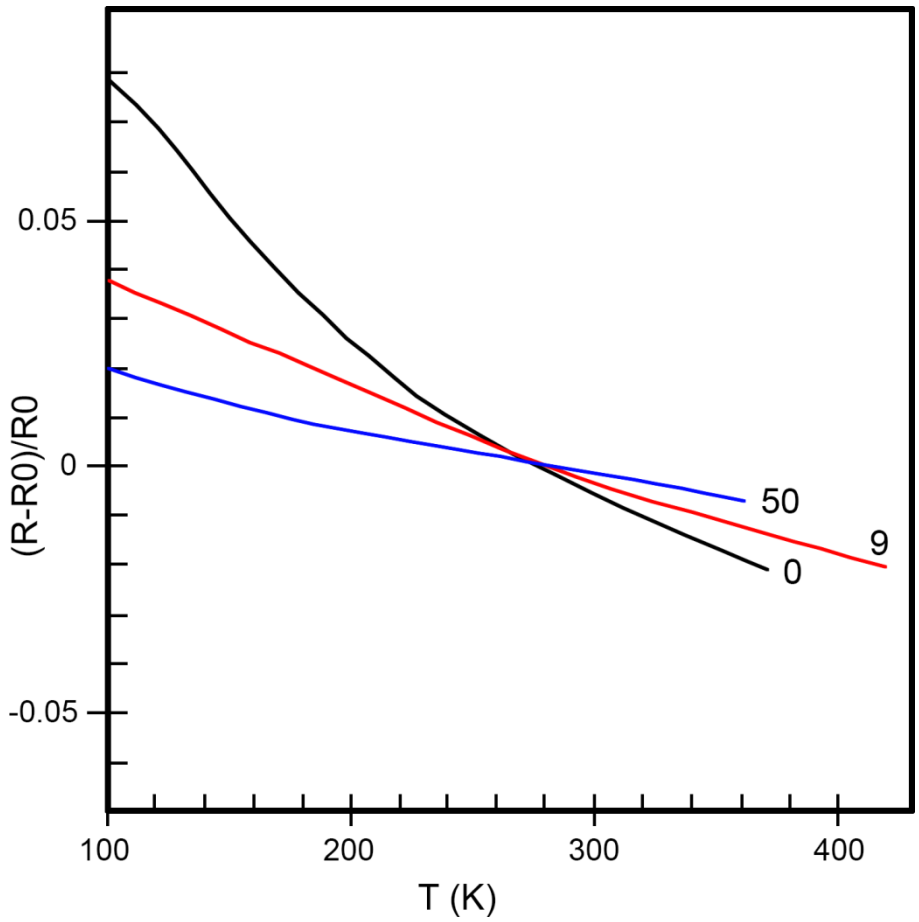

Figure 41. Electrical resistivity of Pu and Np-Pu alloys (after [314 (Figure 2.9)], with lower-temperature data not shown). Data for each material is expressed relative to R0, the resistivity of the material at 273 K. Numbers next to curves indicate compositions in at% Np.

The second set of data includes measurements of electrical resistivity of Np, Pu, and nine Np-Pu alloys at temperatures up to 300 K by Olsen and Elliott [313] (Table 14). The reported electrical resistivity of pure Pu in this study is comparable to that in other studies (e.g., [153, 315]). The reported electrical resistivity of Np is significantly below the resistivity of 116.4 μΩ-cm reported for Np at 310 K in an extensive study by Lee [93]. All of the room-temperature resistivity values for alloys with up to 25 at% Np reported by Olsen and Elliott are within a few percent of the resistivity of Pu, and there is no clear relationship between Np concentration and electrical resistivity.

Table 14 and Figure 42 show thermal conductivity values calculated from the electrical resistivity data of Olsen and Elliott using the Wiedemann-Franz Law (Section 1.6.2 in reference [5]) with the best available estimate of the Lorenz number for Pu (3.15×10^{-8} $W\Omega K^{-2}$, Section 2.3.5.1).

Table 14. Electrical resistivity and thermal conductivity of Np-Pu alloys with the (α-Pu) structure at 300 K. Resistivity data are from Olsen and Elliott [313]; conductivity values were calculated assuming a Lorenz number of 3.15×10^{-8} $W\Omega K^{-2}$

Composition (At% Np)	Resistivity (μΩ-cm)	Conductivity (W/m-K)
0	149.7	6.31
0.5	147.4	6.41
1	146.3	6.46
2	147.0	6.43
4	146.8	6.44
6	150.0	6.30
8	149.8	6.31
15	141.8	6.66
25	146.0	6.47
50	187.6	5.04
100	99.5	9.50

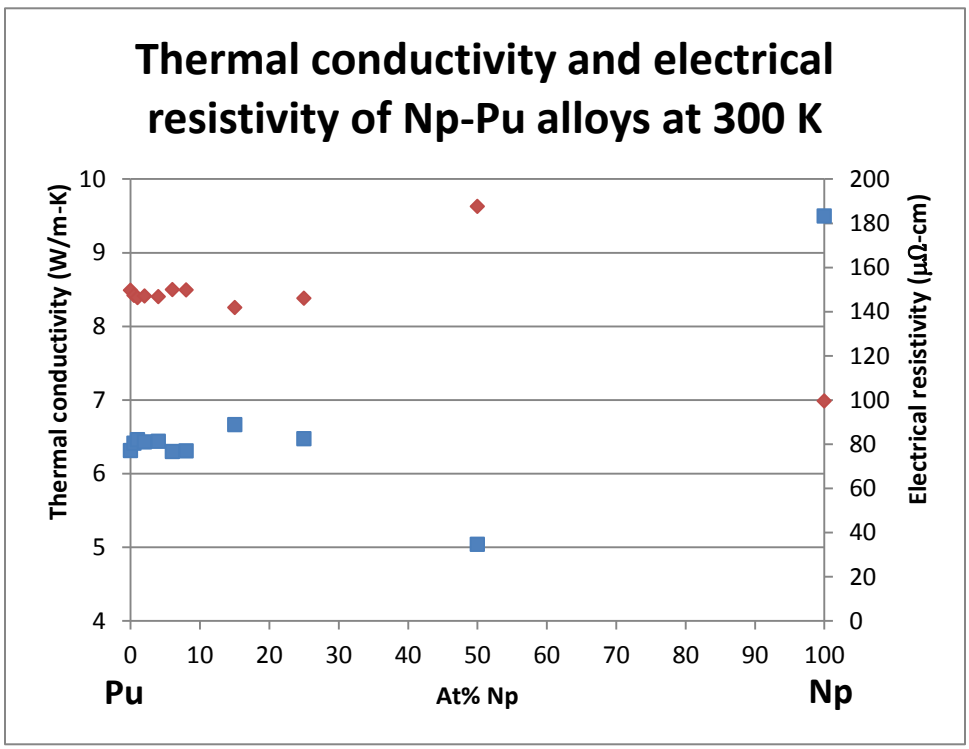

Figure 42. Thermal conductivities (blue squares) and electrical resistivities (red diamonds) from Olsen and Elliott [313].

It seems likely that the differences in electrical resistivity and thermal conductivity as a function of composition are smaller than the uncertainties in the data for Np-Pu alloys with up to ~25 at% Np, and it is therefore reasonable to approximate the thermal conductivity of these alloys by the thermal conductivity of Pu.

3.4 Np-Am

3.4.1 Introduction

Experimental data that can be used to determine the Np-Am phase diagram are limited to a single publication by Gibson and Haire that reports phase-transformation temperatures for alloys with 2.3, 5.6, and 46 at% Am [168]. Data in this publication indicate limited miscibility in the Np-Am system, leading Gibson and Haire to suggest that the Np-Am phase diagram might resemble phase the Pu-Pr (Section 5.11), Pu-Nd (Section 5.12), or Pu-Sm phase diagram more closely than the Pu-Am phase diagram (Section 3.5.1.1).

No information about the heat capacities, thermal expansion, densities, or thermal conductivities of Np-Am alloys is available.

3.4.2 Phases and Phase Transformations

Experimental determinations of the structures of phases in Np-Am alloys are not available. However, Gibson and Haire reported that their measurements showed coexisting high-Np and high-Am phases that "retain the essential features of the phase relations in pure elements" [168 (page 163)].

Transition temperatures in the high-Np phase were ~10-30 °C below those in the Np feedstock. The β-γ and melting transformations in the high-Am phase occurred at similar temperatures, which were ~60°C below the β-γ transformation and ~150°C below the liquidus in the Am feedstock. Enthalpies of transformations in the high-Np phase were slightly smaller than those in the Np feedstock, and those for the high-Am phase were slightly higher than those in the Am feedstock. Gibson and Haire interpreted these differences as indicating a "greater dissolution of Np in Am than vice versa" [168 (page 163)].

Researchers are encouraged to refer to the original paper for details of phase-transformation temperatures and enthalpies, which are presented for a single DTA analysis of an alloy with 46 at% Am [168 (Figure 2)]. Care is needed in interpreting this data because, although phase-transformation temperatures measured from Am and Np feedstocks are similar to those 2.2.2.2 and 2.4.2.2, some phase-transformation enthalpies are significantly higher than the recommended values.

3.4.2.1 Phase Diagrams

Experimental data for the Np-Am system are available in a single publication by Gibson and Haire that reports phase-transformation temperatures for alloys with 2.3, 5.6, and 46 at% Am [168]. This publication suggests that the alloys contain separate Am-rich and Np-rich phases, and that solubility of Np in the Am-rich phases is greater than solubility of Am in the Np-rich phases.

Np-Am phase diagrams were calculated by Ogawa [73, 316] and by Kurata [295, 317]. The calculations used different approaches: the Ogawa phase diagram was calculated using a regular-solution model with interaction parameters derived from Brewer valence bond theory, and the Kurata phase diagram was based on CALPHAD calculations using an internally consistent database of thermodynamic properties for the U-Np-Pu-Am-Fe-Zr system. Both phase diagrams are consistent with the experimental phase-transformation temperatures of Gibson and Haire. Both show complete miscibility of the liquid, although the Ogawa phase diagram has a small liquid miscibility gap that does not appear in the Kurata phase diagram. Both phase diagrams agree that the mutual solubility of Np and Am is limited, and that the solubility of Am in Np is very small.

Despite these similarities, the phase diagrams show significant differences. The primary difference is the extent of solubility of Np in Am (~20 at% according to the phase diagram of Ogawa and a few at% according to the phase diagram of Kurata). A second difference concerns the liquidus temperature, which is higher by up to ~100 degrees for some compositions in the Ogawa phase diagram. The difference between the solubility of Np in Am and the solubility of Am in Np in the Ogawa phase diagram is consistent with Gibson and Haire's interpretation of their data, and the relatively similar solubilities of Np in Am and of Am in Np in the Kurata phase diagram are not. However, all of the differences between the two phase diagrams occur in compositions for which no experimental measurements are available, and further work is clearly needed.

If it is assumed that the relative miscibilities of Np and Am suggested by Gibson and Haire are correct, the phase diagram of Ogawa [73, 316] (Figure 43) is probably the most accurate representation of the available data. Measurements at other compositions are clearly needed.

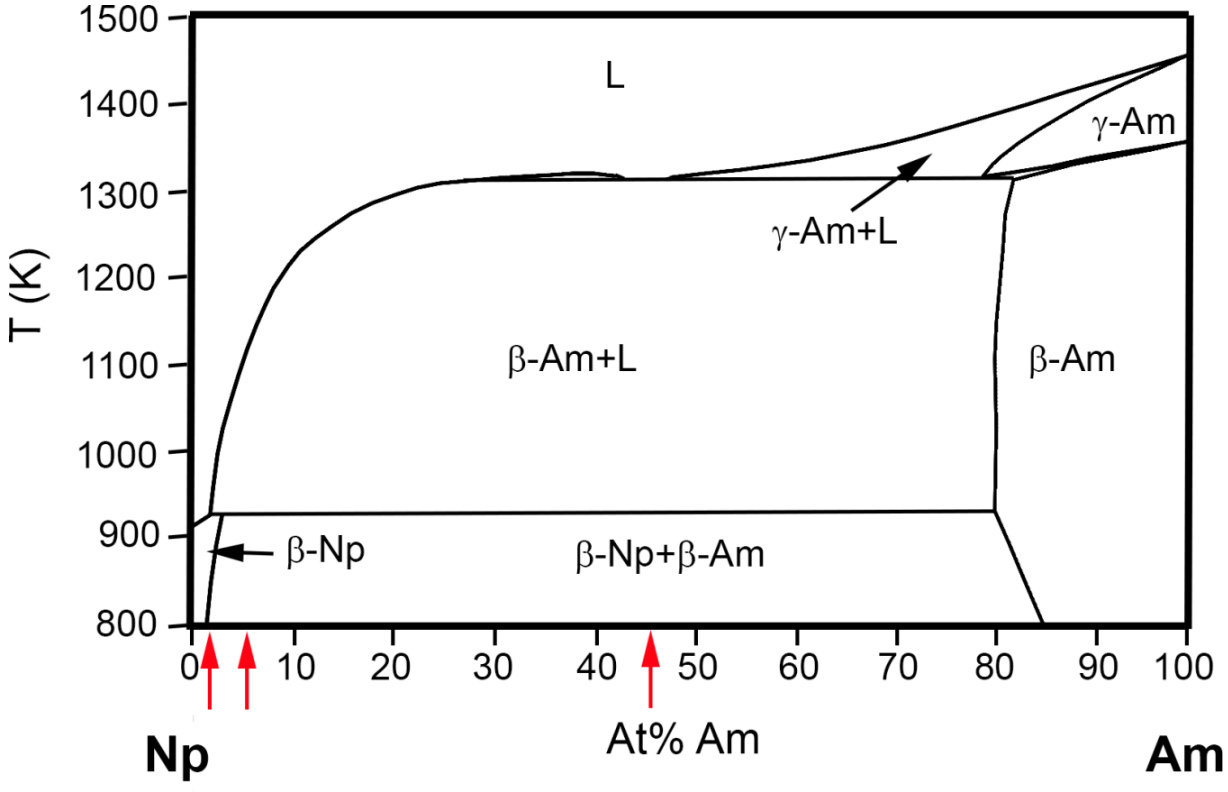

Figure 43. Np-Am phase diagram calculated by Ogawa [73, 316]. Red arrows show compositions corresponding to experimental data.

3.5 Pu-Am

Introduction

Two experimental determinations of the Pu-Am phase diagram have been published. The first was based on X-ray diffraction and micrographic techniques. It was documented by Ellinger et al. in a report and journal paper [318, 319]. The second experimental determination, by Shushakov et al. [320], was documented in a short paper in Russian in 1990 but was apparently not considered in the English-language literature until 2011. Several modeling studies (e.g., [73, 295, 311, 321, 322]) attempted to resolve disagreements between the experimental determinations of Ellinger et al. and Shushakov et al., but without achieving consensus. Recent modeling studies suggest that differences between experimentally determined phase diagrams may be consequences of impurities in the materials [322].

Generally accepted features of the system include the existence of a continuous solid solution between the fcc phases δ-Pu and β-Am, stabilization of the δ-Pu structure down to room temperature in some compositions, limited solubility of Am in α-, β-, γ-, and δ'-Pu, and the absence of intermediate phases. One important area of disagreement is the possible existence of a solid solution between the bcc phases γ-Am and ε-Pu. Relationships between α-Am and (β-Am, δ-Pu) solid solutions and the stability of the δ-Pu structure at temperatures below ~125°C are also areas of disagreement, but may be relatively unimportant for fuels because of the sluggish phase-transformation kinetics of this system.

The only available measurements of heat capacities of Pu-Am alloys are from Am-stabilized δ-Pu alloys (i.e., Pu-Am alloys with the δ-Pu structure at temperatures below the stability limit for pure δ-Pu), measured at temperatures between 4.5 and 300 K [323, 324]. These measurements show that the heat capacities of Am-stabilized δ-Pu alloys with 8, 15, and 20% Am are all ~30 J/mol-K at 300 K.

No experimental measurements of the thermal conductivity of Pu-Am alloys are available. Experimental results show that electrical resistivity is constant at temperatures between ~150 and 300 K, and modeling suggests that the resistivity is constant up to 700 K. According to the Wiedemann-Franz Law (Section 1.6.2 in reference [5]), the thermal conductivity of a material is proportional to the temperature in K when the resistivity and Lorenz numbers are constant, so it seems likely that thermal conductivities of Pu-Am alloys may increase linearly with temperature.

The only information about the thermal expansion of Pu-Am alloys is from Am-stabilized δ-Pu alloys [320]. The thermal expansion of these alloys resembles that of Ce- and Zr-stabilized δ-Pu alloys (Sections 5.10.3 in this part of the Handbook and 2.2.1.4.1 in reference [5], respectively) in that alloys with low concentrations of Am have negative thermal expansion and alloys with higher concentrations of Am have positive thermal expansion.

The focus of much of the relatively recent research on Pu-Am alloys involves understanding the electronic structures of the alloys (e.g., [325-329]).

Experimental designs for further work should consider the likelihood of a high degree of sensitivity to impurities, difficulties in determining equilibrium phases because of sluggish phase-transformation kinetics, and the need to include measurements from Am and Pu to allow comparison with results of other studies.

3.5.1 Phases and Phase Transformations

Pu-Am phases include:

- (α-Pu), (β-Pu), (γ-Pu), (δ'-Pu): Allotropic solid solutions of the corresponding Pu phases. Lattice parameters of the solid-solution phases have not been reported, although they are probably similar to those of the corresponding phases in pure Pu. It is generally accepted that solubility of Am in these phases is very limited, and the experimental data of Ellinger et al. [319] suggest that it is at most ~1.5 at% Am.
- (α-Am): Allotropic solid solution of α-Am. Lattice parameters of this solid-solution phase have not been reported, although they are probably similar to those of α-Am. The solubility of Pu in this phase has not been investigated in detail, although Ellinger et al. thought it was ~5 at% and Shushakov et al. thought it was ~20 at% [319, 320].
- (β-Am, δ-Pu): A solid solution between the fcc phases β-Am and δ-Pu. The experimental data of Ellinger et al. and Shushakov et al. [319, 320] show that alloys with ~6- 80 at% Am retain this phase down to room temperature, although the calculated phase diagrams of Kurata and Gotcu-Freis show significantly lower maximum room-temperature concentrations of Am in this phase [295, 321]. The model of Turchi et al. indicates that this phase decomposes to α-Am and α-Pu below ~100°C [322]. The lattice parameter of (β-Am, δ-Pu) solid solutions increases with increasing concentrations of Am, with a positive deviation from Vegard's law (Figure 44).
- (γ-Am) and (ε-Pu): Structures of these solid-solution phases have not been experimentally determined, although it seems likely that both are bcc. The experimental data of Ellinger et al. showed a maximum concentration of ~8 at% Am in ε-Pu [319], while the experimental data of Shushakov et al. [320] showed a continuous solid solution between γ-Am and ε-Pu. Turchi et al modeled the difference in energy required to change between a solid solution and a miscibility gap and determined that it was small enough to suggest that the difference between the experimental phase diagrams was a possible consequence of impurities in the samples [322].

Temperatures of phase transformations are poorly known, and phase-transformation enthalpies have not been reported.

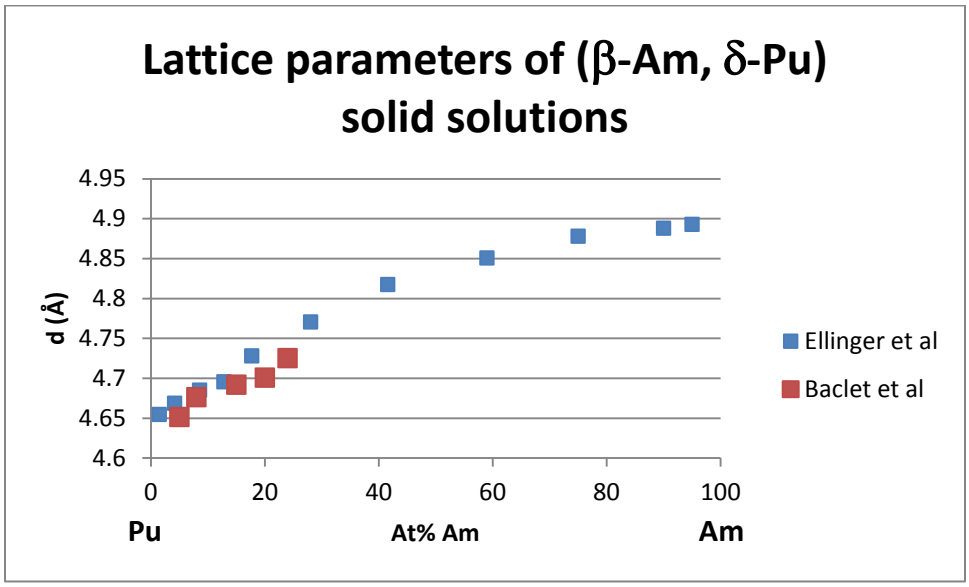

Figure 44. Lattice parameters of (β-Am, δ-Pu) solid solutions [319, 325].

3.5.1.1 Phase Diagrams

Ellinger et al. published the first Pu-Am phase diagram in 1965 based on micrographic and X-ray diffraction data [318, 319] (Figure 45). Key features of this phase diagram include the existence of a continuous fcc solid solution between δ-Pu and β-Am, stabilization of the δ-Pu structure down to room temperature for compositions with ~6-80 at% Am, the possible existence of a two-phase field between δ-Pu and α-Am solid solutions, and limited solubility of Am in α-, β-, γ-, δ'-, and ε-Pu solid solutions. Although the Ellinger et al. study is the most thoroughly documented experimental investigation of the Pu-Am system, the corresponding phase diagram has a number of serious problems. It does not include γ-Am, which was unknown at the time. Its temperatures for the α-β and melting transformations in Am were the only ones available at the time, but are below the currently accepted values in Section 2.4.2.2 by ~170-180 °C. The Am feedstock used by Ellinger et al. initially contained up to 0.52 wt% impurities (primarily La); however, since some samples were obtained by progressively re-casting earlier samples with additional Pu and "appreciable" weight losses occurred during casting, concentrations of impurities in some samples may have been significantly higher.

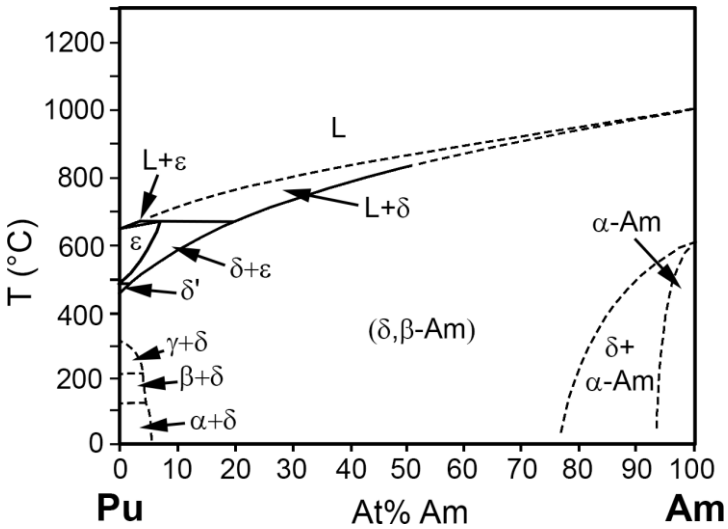

Figure 45. Experimentally determined Pu-Am phase diagram according to Ellinger et al. [318, 319]. α, β, γ, δ, δ' and ε indicate Pu solid solution phases. Although this phase diagram is based on the most thoroughly documented experimental study of the Pu-Am system to date, it is no longer generally accepted.

Shushakov et al. published a second experimentally determined Pu-Am phase diagram using data from high-temperature X-ray diffraction, DTA, microstructural analysis, and densitometry (Figure 46). This phase diagram was documented in a short paper in a Russian-language journal in 1990 [320]. There are no generally available English translations of this paper, and it was apparently not considered in the English-language research literature until 2011. The Shushakov phase diagram remedies two of the problems in the Ellinger phase diagram by incorporating γ-Am and using higher Am phase-transformation temperatures. Other important differences from the Ellinger phase diagram include the existence of a continuous solid solution between γ-Am and ε-Pu and the absence of a two-phase field between α-Am and δ-Pu. No information about the purity of the samples used by Shushakov et al. was provided.

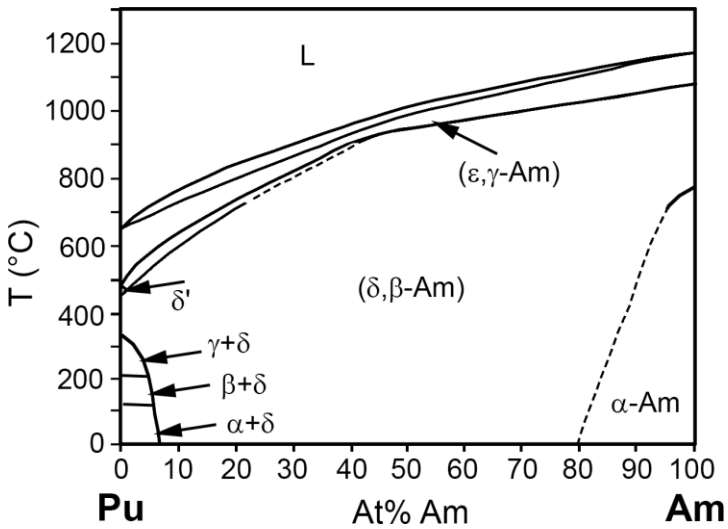

Figure 46. Experimentally determined Pu-Am phase diagram according to Shushakov et al. [320]. α, β, γ, δ, δ' and ε indicate Pu phases.

In 1999, Okamoto suggested a new phase diagram [330] that combines phase boundaries for the fcc, bcc, and liquid phases calculated by Ogawa [73] with other phase transformations based on the phase diagram of Ellinger et al. after adjusting Ellinger's phase-transformation temperatures for Am to the values recommended in Section 2.4.2.2. This phase diagram (Figure 47) is the most recent one that includes some experimentally determined phase boundaries.

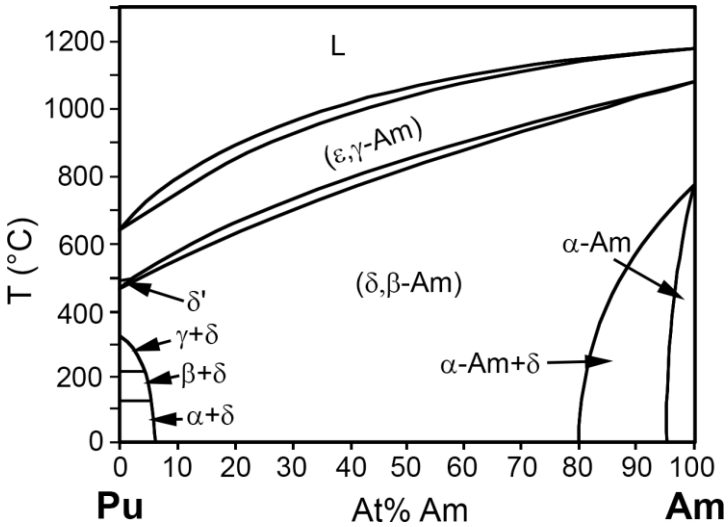

Figure 47. Pu-Am phase diagram of Okamoto [330], which combines the experimental data of Ellinger et al. [319] with modeling by Ogawa [73]. α, β, γ, δ, δ' and ε indicate Pu phases.

More recently, Kurata [295], Gotcu-Freis et al. [321], and Turchi et al. [322] published phase diagrams developed using the CALPHAD method. The phase diagrams of Gotcu-Freis et al. and Turchi et al. considered data from both Ellinger et al. and Shushakov et al., while the Kurata phase diagram considered only data from Ellinger et al. The phase diagrams of Kurata and Gotcu-Freis et al. resemble the phase diagram of Ellinger et al. in that all three phase diagrams show two bcc solid solution phases with significantly different concentrations of Am (Figure 48). In contrast, the phase diagram of Turchi et al. resembles that of Shushakov et al. in that it shows a continuous bcc solid solution (Figure 49).

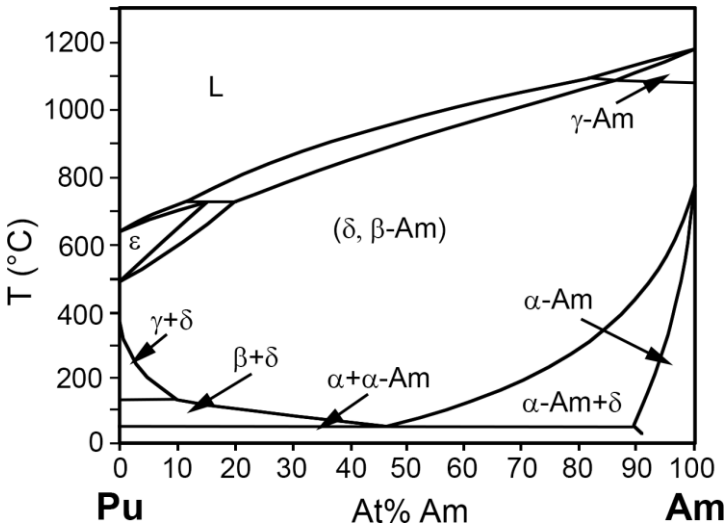

Figure 48. Calculated Pu-Am phase diagram of Gotcu-Freis et al. [321], which shows immiscibility of ε-Pu and γ-Am solid solutions. α, β, γ, δ, δ' and ε indicate Pu solid solution phases.

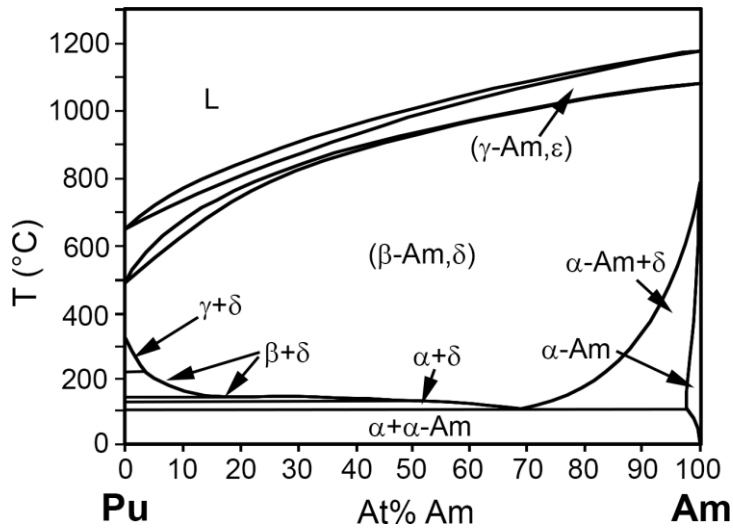

Figure 49. Calculated Pu-Am phase diagram of Turchi et al. [322], which shows a continuous solid solution between ε-Pu and γ-Am. This phase diagram has two "β+δ" fields because of a small miscibility gap in the (δ, β-Am) solid solution. α, β, γ, δ, δ' and ε indicate Pu solid solution phases.

Turchi et al. [322] investigated differences in thermodynamic parameters needed to produce phase diagrams with one or two bcc phases. They concluded that whether a sample was best represented by a phase diagram with or without a continuous (ε-Pu, γ-Am) solid solution might depend on the impurities in the sample. In this context, it is particularly unfortunate that the purity of the samples studied by Shushakov et al. was not reported.

3.5.2 Heat Capacity and Related Properties

The only available heat capacities of Pu-Am alloys are from Am-stabilized δ-Pu alloys (i.e., Pu-Am alloys with the δ-Pu structure at temperatures below the stability limit for pure δ-Pu), measured at temperatures between 4.5 and 300 K [323, 324]. These measurements show that the heat capacities of Am-stabilized δ-Pu alloys with 8, 15, and 20% Am are all ~30 J/mol·K at 300 K.

In the absence of measured heat capacities, it seems reasonable to assume that the heat capacities of (α-Pu), (β-Pu), (γ-Pu), and (δ'-Pu) solid solutions are similar to the heat capacities of the corresponding phases in pure Pu because the maximum concentration of Am in each of these phases is low. Similarly, it seems reasonable to assume that the heat capacity of (α-Am) is similar to that of α-Am. If (ε-Pu) and (γ-Am) are separate phases, it seems reasonable to assume that their heat capacities are similar to those of ε-Pu and γ-Am.

In the absence of experimental data, it may be necessary to approximate the heat capacities of the solid solution phases (δ-Pu, β-Am) and perhaps (ε-Pu, γ-Am) by cautious use of the Kopp-Neumann Law (Section 1.6.1 in reference [5]).

3.5.3 Thermal Expansion and Density

Shushakov et al. [320] studied the thermal expansion of a number of Am-stabilized δ-Pu- alloys (Figure 50). The thermal expansion of Am-stabilized δ-Pu resembles that of Ce-stabilized and Zr-stabilized δ-Pu (Section 5.10.3.2 in this document and Section 2.2.1.4.1 in reference [5]), respectively) in that alloys with low concentrations of δ-stabilizing elements (Am, Ce, and Zr) have negative thermal expansion and alloys with higher concentrations of stabilizing elements have positive thermal expansion.

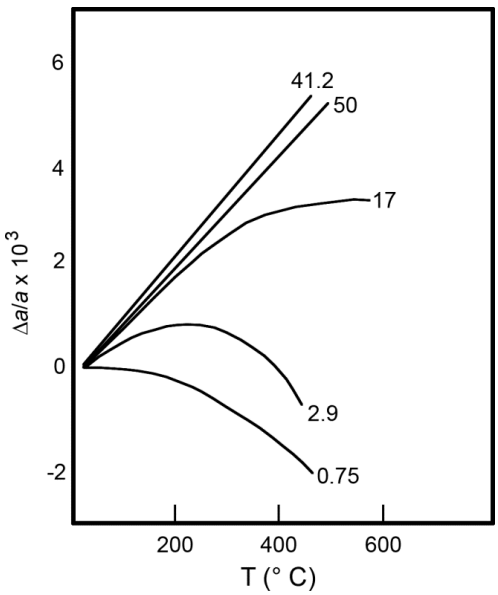

Figure 50. Thermal expansion of Am-stabilized δ-Pu alloys based on changes in the *a* lattice parameter from high-temperature X-ray diffraction (re-drawn from [320 (Figure 2)]). Numbers next to the curves indicate percentages of Am in the alloys.

3.5.4 Thermal Conductivity and Related Properties

Baclet et al. [325] measured the low-temperature electrical resistivities of Am-stabilized δ-Pu solid solutions in four alloys with 8-43 at% Am at temperatures up to 300 K. Their measurements indicate that the electrical resistivity of each alloy is essentially independent of temperature above ~150 K. A model developed by Tsiovkin et al. [331] extends the upper end of the temperature range over which the resistivity of each composition is essentially independent of temperature to 700 K.

Table 15 shows electrical resistivities at 300 K read from reference [325 (Figure 4)] and the corresponding thermal conductivities calculated using the recommended value of the room-temperature Lorenz number for Pu (3.15×10^{-8} WΩK^{-2}, Section 2.3.5.1). The value for the electrical resistivity of Am (which was quoted from a Ph.D. thesis) is ~20 μΩ-cm higher than the values in Section 2.4.5, and the thermal conductivity calculated from this resistivity is correspondingly lower. No other data about the thermal conductivities of Pu-Am alloys is available for comparison.

Despite these problems, the values in Table 15 represent the best currently available approximation to the thermal conductivities of Pu-Am alloys. Further research is needed to confirm both the thermal conductivities in Table 15 and the temperature dependence of the conductivities. It is important that this research should also include measurements of Am and Pu to allow comparison to results from other studies.

Table 15. Electrical resistivities and thermal conductivity of Pu-Am alloys at 300 K. Electrical resistivities were read from reference [325 (Figure 4)]. Thermal conductivities were calculated using the Wiedemann-Franz Law with the recommended value of the Lorenz number for Pu (3.15×10^{-8} WΩK^{-2})

Composition (at% Am)	Electrical Resistivity (μΩ-cm)	Thermal conductivity (W/m-K)
8	335	2.9
23	205	4.6
28	260	3.6
43	290	3.3
100	90	10.5

3.6 Np-Pu-Am

3.6.1 Introduction

No experimental data about ternary Np-Pu-Am phase diagrams is available. Calculated isothermal sections at 792, 1000, and 1300 K have been published based on models developed by Ogawa [73] and Kurata [295, 300]. All of the isothermal sections suggest limited solid-phase miscibility except in alloys with low concentrations of Np.

No information about the heat capacity, thermal expansion, density, or thermal conductivity of Np-Pu-Am alloys is available.

3.6.2 Phases and Phase Transformations

No information about phases and phase transitions is available.

Calculated isothermal sections at 792, 1000, and 1300 K have been published based on models developed by Ogawa [73] and Kurata [295, 300].

The Ogawa model used "a regular solution model with interaction parameters derived from the Brewer valence bond theory" [73] to calculate isotherms at 1000 and 1300 K (Figure 51). Comparison with binary phase diagrams indicates that the fcc phase is the (β-Am, δ-Pu) solid solution. The bcc phase is a solid solution between ε-Pu and γ-Am; however, the existence of a continuous solid solution between these phases has not been conclusively established from experimental evidence (Section 3.5.1.1).

Kurata developed a CALPHAD model for the U-Pu-Am system using thermodynamic properties from a consistent database for the U-Np-Pu-Am-Fe-Zr system [295, 332] and calculated an isothermal section at 792 K for the U-Pu-Am ternary (Figure 52). This model included low-temperature phases not considered in Ogawa's model, as well as experimental data that were not described in detail or available elsewhere. Comparison with binary phase diagrams indicates that the fcc phase is the (β-Am, δ-Pu) solid solution, the bcc phase is (ε-Pu), and the dhcp phase is (α-Am). Although Kurata's binary Pu-Am phase diagram does not show a continuous solid solution between ε-Pu and γ-Am, the existence of a bcc solid solution phase with the composition shown in this isothermal section is consistent with all of the experimental data and models.

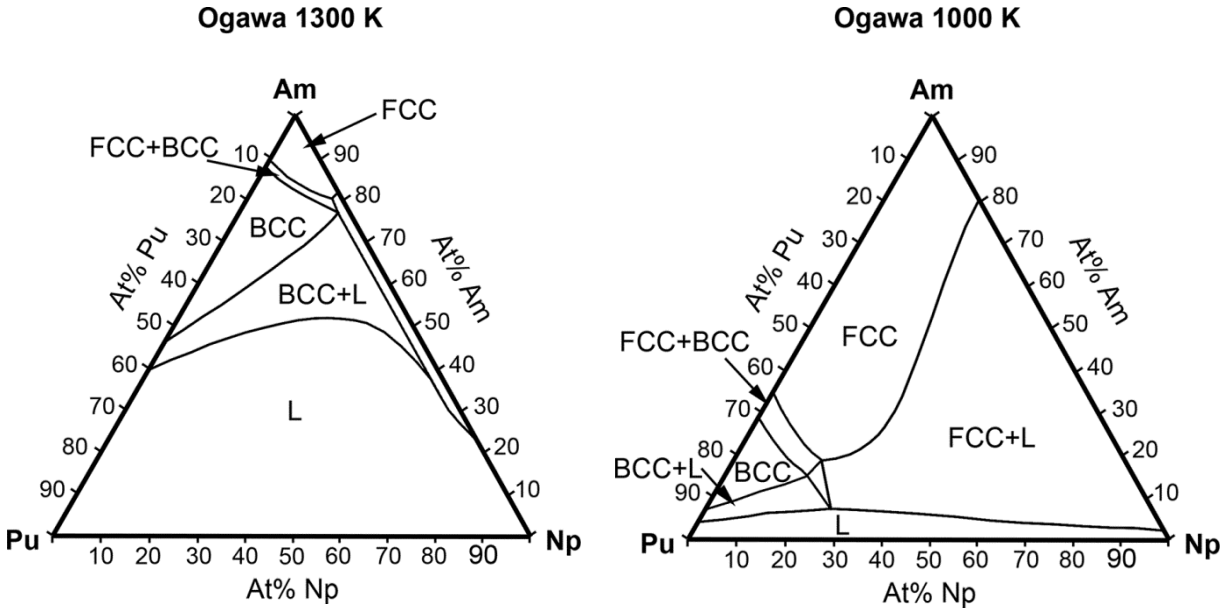

Figure 51. Isothermal sections calculated by Ogawa [73].

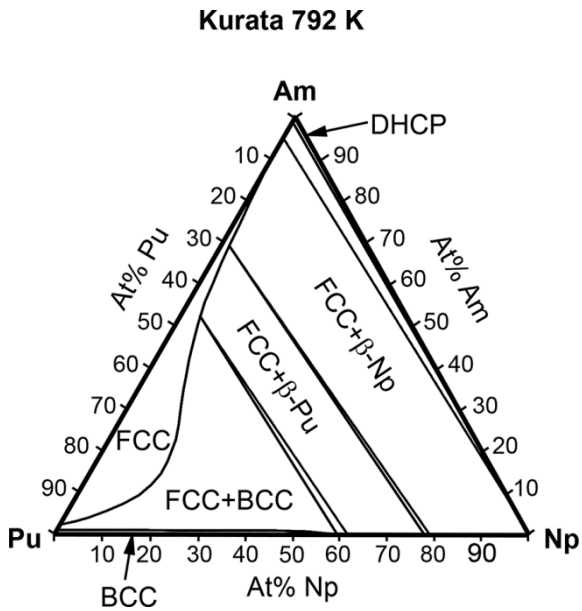

Figure 52. Isothermal section calculated by Kurata [295, 300].

4. ALLOYS CONTAINING ONLY La, Ce, Pr, and Nd

4.1 La-Ce

4.1.1 Introduction

The currently accepted La-Ce phase diagram for temperatures above 0 °C is based on a 1954 publication by Vogel and Klose [333]. More recent revisions have eliminated two-phase regions associated with higher-temperature phase transformations because these were believed to result from impurities in the samples, clarified the structure of the bcc phase, and changed phase-transformation temperatures as a result of new knowledge about La and Ce (e.g., [194, 334]).

Key features of the La-Ce phase diagram include the existence of three continuous solid solutions (a dhcp solid solution between α-La and β-Ce, an fcc solid solution between β-La and γ-Ce, and a bcc solid solution between γ-La and δ-Ce). Boundaries between fcc and bcc solid solutions and between bcc solid solutions and liquid are almost straight lines, and two-phase fields are narrow. As a consequence of sluggish phase-transition kinetics, temperatures associated with the transformation between the dhcp and fcc solid solutions measured during heating and during cooling differ by 50°C for pure La and more than 150°C for pure Ce (Sections 2.5.2.2 and 2.6.2.2), and no reliable experimental measurements of the temperature of this transformation in alloys with intermediate compositions are available.

Relatively recent experimental publications include data on the lattice parameter of a γ-Ce solid solution with 5 wt% La [335] and new measurements of the temperatures of the fcc-dhcp transformation and the liquidus in an alloy with 50 at% La [336]. Other recent research involves first-principles calculations related to high-pressure properties of alloys of α-Ce and β-La [337, 338].

Despite the low purity of the samples used in the original determinations of the phase diagrams and the small discrepancies between the currently accepted phase diagram and the more recent experimental data of Bulanova et al [336] (Figure 54), further investigation with high-purity samples seems unlikely to result in significant changes to higher-temperature phase boundaries. Further research addressing transformations between α-Ce, the (α-La, β-Ce) solid solution, and the (β-La, γ-Ce) solid solution is needed for a complete understanding of the La-Ce phase diagram, but may be of limited relevance for fuels because of the low temperatures and sluggish phase-transformation kinetics involved.

Constant-pressure heat capacities of La-Ce alloys have been measured at temperatures below 300 K [339], and constant-volume heat capacities have been calculated at high pressures [338]. Data on the heat capacities of La-Ce alloys at other temperatures and pressures are not available.

Experimental data on the thermal expansion of La-Ce alloys consists primarily of measurements of the density of liquids with less than ~10 at% Ce [340]. This data shows that the density of these alloys increases with increasing concentration of Ce and decreases linearly with increasing temperature. Reported densities of La-Ce alloys seem anomalously high in comparison to the density of pure La.

No data on thermal conductivity or diffusivity of La-Ce alloys is available, and data on electrical resistivity is limited.

Researchers are encouraged to consult the excellent review of the properties of La-Ce alloys by Gschneidner and Calderwood [194 pp. 9-12].

4.1.2 Phases and Phase Transformations

4.1.2.1 Phases

Atmospheric-pressure phases in the La-Ce system are:

- (α-Ce): Allotropic solid solution of α-Ce. The maximum concentration of La and the influence of La concentration on lattice parameters in this phase have not been experimentally determined, although high-pressure lattice parameters for several alloys were calculated by Zhang et al. [338].
- (β-Ce, α-La): Double hexagonally close packed solid solution between β-Ce and α-La. Lattice parameters of alloys with intermediate compositions have not been published. However, based on the generalization that solid solutions of pure rare-earth elements with similar atomic numbers behave as ideal alloys at high temperatures [194], lattice parameters of dhcp La-Ce alloys can be approximated by linear interpolation between lattice parameters of β-Ce and α-La.
- (γ-Ce, β-La): Face-centered cubic solid solution between γ-Ce and β-La. Gschneidner and Calderwood [194] summarized previously reported lattice parameters from references [341-344] (Figure 53). All of the reported lattice parameters were in good agreement, and were slightly higher than would be expected from linear interpolation between lattice parameters of pure Ce and La (positive deviation from Vegard's Law). It should be noted, however, that the alloys in this summary had different annealing temperatures and cooling histories.

  More recent lattice parameters reported by Scott et al. [335] for Ce and an alloy with 5 wt% (5 at%) La are inconsistent with earlier data, and the 6% change in lattice parameters caused by the introduction of 5% La reported by Scott et al. seems anomalously large. Wheeler and Khan reported variations of ~ 2 at% La within individual grains of an alloy with 5 wt% La and a face-centered cubic structure [345]. Although this chemical variation may imply some variation in lattice parameters, it does not seem likely to be a sufficient explanation for differences between the lattice parameters reported by Scott et al. and those summarized by Gschneidner and Calderwood [194].
- (δ-Ce, γ-La) Body-centered cubic solid solution between δ-Ce and γ-La. Lattice parameters of alloys with intermediate compositions are not available.

4.1.2.2 Phase Transitions

Temperatures of the (α-Ce)↔(γ-Ce) (non-equilibrium) and (β-Ce)↔(γ-Ce) (equilibrium) transformations were investigated for alloys with up to 4 at% La at atmospheric pressure [346]. Addition of La increased the temperature of the γ-β (cooling) transformation. Addition of ~0.5 at% La increased the α-γ phase-transformation temperature but decreased the γ-α transformation temperature. Addition of larger quantities of La caused a decrease in both the α-γ and γ-α transformation temperatures.

Because the boundaries between (β-La, γ-Ce), (γ-La, δ-Ce), and liquid phases are approximately linear, the corresponding phase-transformation temperatures can in principle be obtained by interpolation between the transformation temperatures of La and Ce (Sections 2.5.2.2 and 2.6.2.2). For an alloy with 50 at% La, this interpolation leads to values of 795°C for the (β-La, γ-Ce)↔(γ-La, δ-Ce) transformation and 858°C for melting. Relatively recent experimental measurements by Bulanova et al. [336] of 755°C for the (β-La, γ-Ce)↔(γ-La, δ-Ce) transformation and 845°C for melting are somewhat below the interpolated temperatures.

Phase-transformation enthalpies for La-Ce alloys have not been reported. However, enthalpies for La and Ce are sufficiently similar that it seems reasonable to estimate the transformation enthalpies for specific alloys by interpolation from the enthalpies for La and Ce (Sections 2.5.2.2 and 2.6.2.2). For an alloy with 50 at% La, this interpolation gives the following values:

- (β-Ce, α-La)↔ (γ-Ce, β-La): ~0.23 kJ/mol
- (γ-Ce, β-La)↔ (δ-Ce, γ-La): ~3.1 kJ/mol
- Fusion: ~5.9 kJ/mol

4.1.2.3 Phase Diagrams

An early La-Ce phase diagram by Vogel and Klose [333] showed three solid phases, each forming a continuous solid solution between La and Ce. Each phase transition involved a two-phase field spanning a temperature range up to ~20°C. The La used for the investigation had ~3% impurities (primarily Fe) and the Ce was 99.5% pure.

Somewhat later, Savitskiy and Terekhov [347] developed a second phase diagram for temperatures between ~750 and 850°C using La and Ce that contained 1-1.5% impurities (primarily other rare-earth elements). Savitskiy and Terekhov apparently only recognized two crystal structures (hcp and fcc), and reported a temperature difference of up to 60°C between the liquidus and solidus.

Gschneidner and colleagues modified the phase diagram of Vogel and Klose by depicting phase transitions as straight lines and largely eliminating two-phase fields (e.g., [194, 334]). Both of these changes are consistent with their observation that binary alloys between rare-earth elements with similar atomic numbers behave as ideal solutions at high temperatures. Gschneidner and colleagues also extended the phase diagram to temperatures below 300°C. The phase diagram of Gschneidner and Calderwood [194] (Figure 54) is currently accepted, although it is not consistent with the most recently available information about the temperature of the phase transformation between β-Ce and γ-Ce (Section 2.6.2.2).

A publication by Bulanova et al. [336] about the La-Ce-Si system shows a variant of the Gschneidner and Calderwood phase diagram in which the transformation between the hexagonal (α-La, β-Ce) and face-centered cubic (β-La, γ-Ce) phases is shown by a single line connecting the transformation temperature measured during heating of La with the average of the transformation temperatures measured during heating and cooling of Ce. Bulanova et al. do not explain why they used this phase transformation temperature; however, it involves temperatures well below any of their experimental measurements. The phase diagram of Bulanova et al. does not appear to be an attempt to suggest a modification of an existing La-Ce phase diagram.

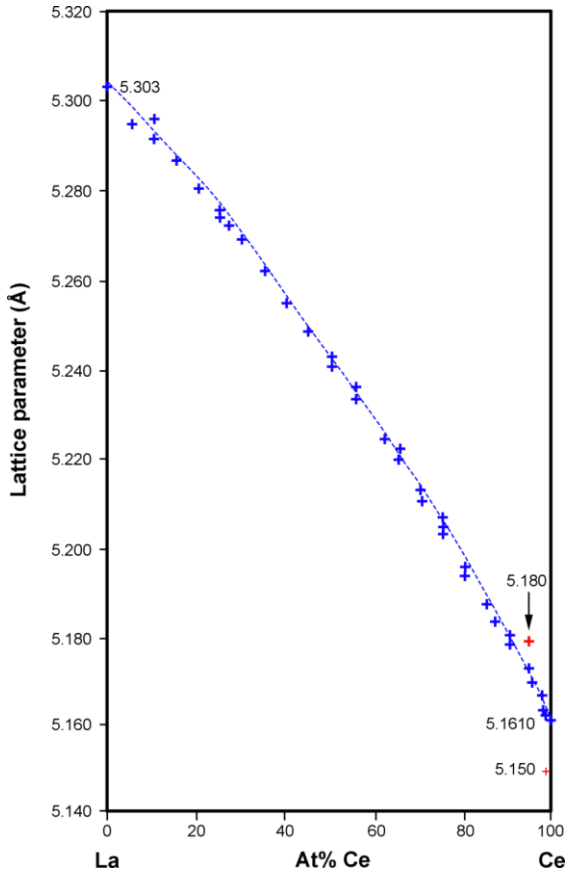

Figure 53. Lattice spacings for (β-La, γ-Ce) solid solutions. Blue symbols indicate values summarized by Gschneidner and Calderwood [194], red symbols indicate values from Scott et al. [335].

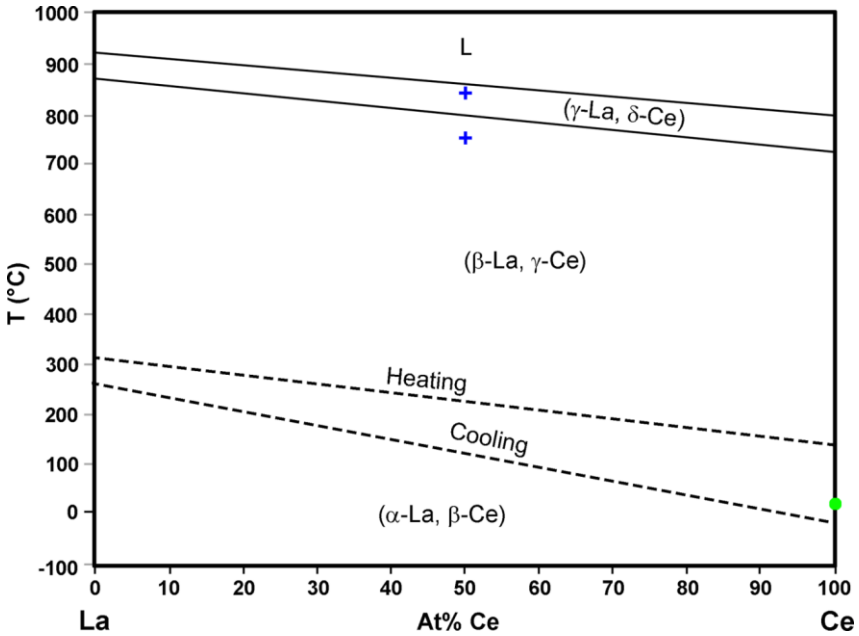

Figure 54. La-Ce phase diagram after Gschneidner and Calderwood [194] with data from Bulanova et al. [336] (blue crosses) and equilibrium β-Ce to γ-Ce transformation temperature from Gschneidner and Pecharsky [240] (green circle).

4.1.3 Heat Capacity and Related Properties

In the absence of experimental data, it may be necessary to approximate the heat capacities of La-Ce alloys using the Kopp-Neumann Law (Section 1.6.1 of reference [5]). Figure 55 shows an example of the use of this law to approximate the heat capacity of a La-Ce alloy with 50 at% La. Because alloys of pure La and Ce behave as ideal alloys at high temperatures, the temperatures of phase transitions in the alloy were determined by interpolation between the transition temperatures of La and Ce. To reduce errors introduced by phase transitions, heat capacities are shown only for temperature ranges in which the binary phase diagram in Section 4.1.2.3 indicates that La, Ce, and the alloy should all have the same crystal structure. As a result, there are no estimated heat capacities for the dhcp and bcc phases.

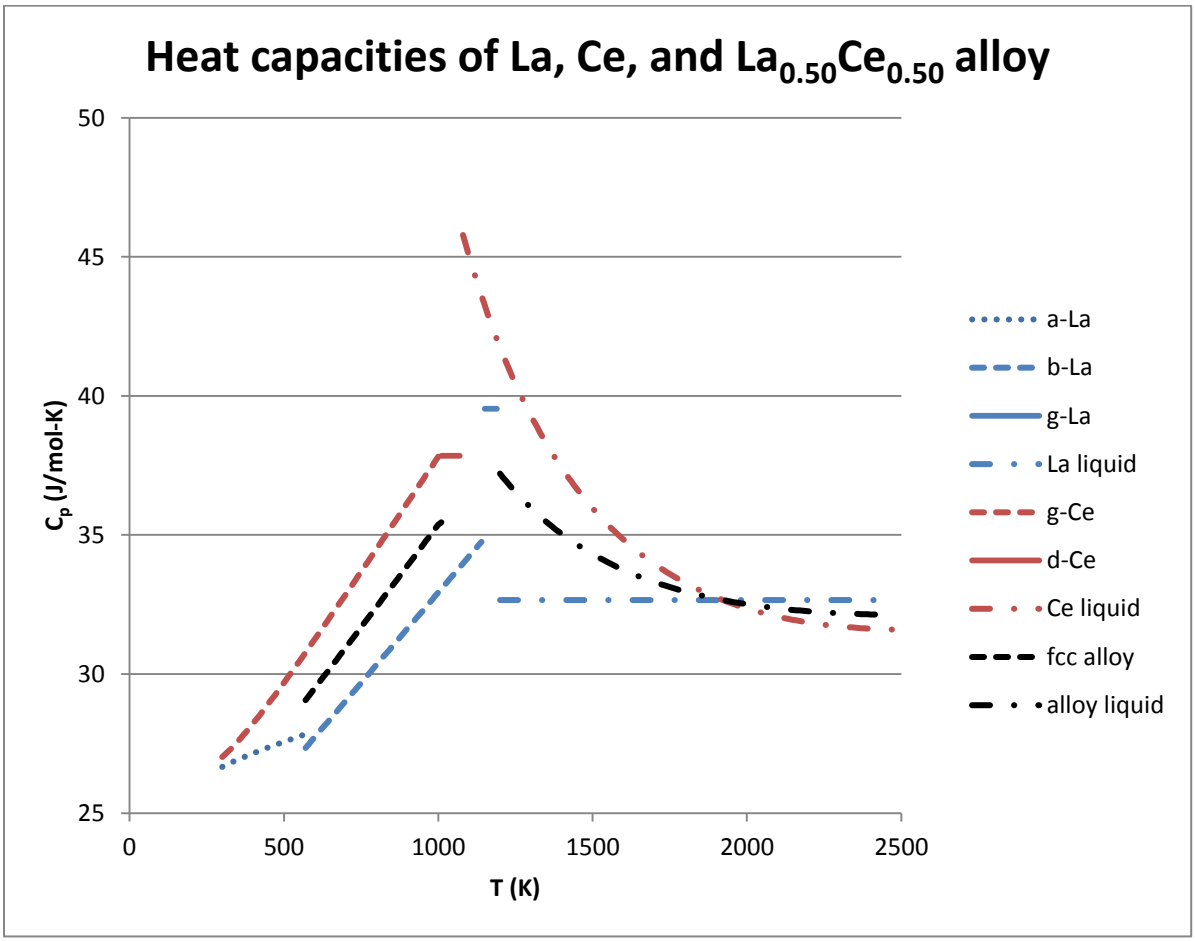

Figure 55. Heat capacity of a La-Ce alloy with 50 at% La, estimated using the Kopp-Neumann Law and elemental heat capacities from the equations in Sections 2.5.3 and 2.6.3 of this handbook. Heat capacities of La and Ce are included for comparison. Colors indicate compositions and line types (dots, etc.) indicate phases. The fcc alloy is a solid solution between β-La and γ-Ce.

4.1.4 Thermal Expansion and Density

4.1.4.1 Densities of Solid Phases

No measurements of the densities of solid La-Ce phases are available. However, densities for (β-La, γ-Ce) (fcc) solid solutions can be calculated from Equation 5 of reference [5] using lattice parameters from the original references cited in Section 4.1.2.1 with 4 atoms per unit cell. Consideration of Figure 53 suggests that densities of (β-La, γ-Ce) solid solutions are lower than would be predicted based on linear interpolation between the densities of La and Ce.

4.1.4.2 Densities of Liquid Alloys

Bezukladnikova et al. measured densities of five La-Ce alloys with ~1.2 to 9.9 at% La using optical microscopy to observe changes in the sizes of drops of liquid in a vacuum [340]. They determined that the density of each alloy decreases linearly with increasing temperature, and developed Equation 75 and Table 16 to express this relationship.

Equation 75. Densities of La-Ce liquids as functions of temperature (after [340])

$$\rho = \rho_0 - b \times 10^{-3} \times T$$

where ρ is the density in g/cm^3, ρ_0 and b are values from Table 16 and T is a temperature in K within the range specified the table.

Table 16. Coefficients for calculating densities of La-Ce liquids (after [340]).

Composition at% Ce	T range (K)	ρ_0	b
1.21	1250-1627	6.86	0.66
2.49	1263-1630	6.82	0.62
5.33	1253-1626	7.01	0.74
7.72	1268-1607	7.07	0.77
9.91	1253-1631	6.87	0.63

Figure 56 shows densities calculated using Equation 75 and Table 16. Densities decrease linearly as a function of increasing temperature. There is a general tendency for the density to increase with increasing concentrations of Ce, consistent with the higher density of Ce in comparison to La (Sections 2.5.4.3 and 2.6.4.3). The density of the alloy with 1.21 at% Ce is ~6.03 g/cm^3 at 980°C, which is slightly higher than the density of 5.96 g/cm^3 for pure La at a temperature "near the melting point" (918°C) [191 (Table 12)].

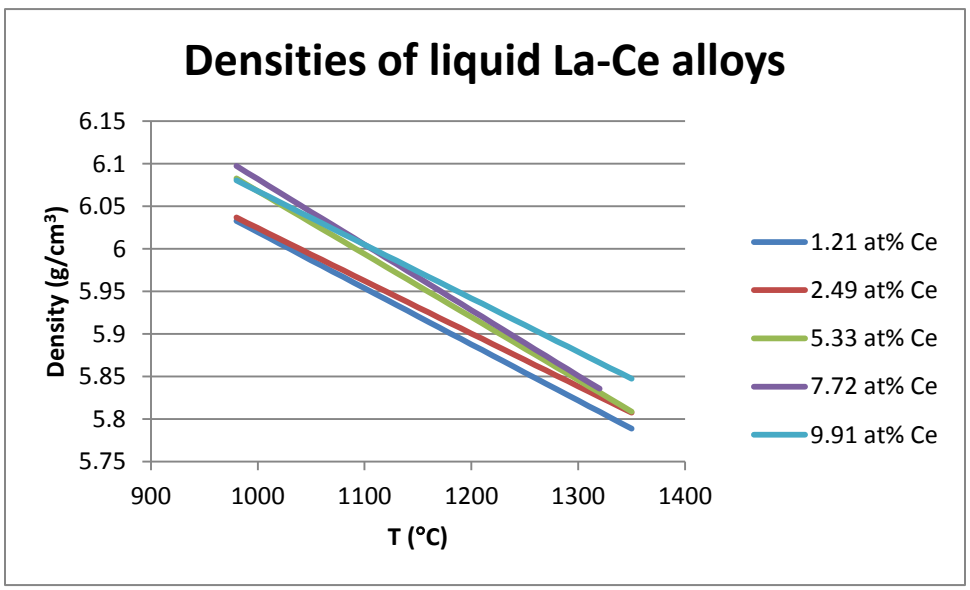

Figure 56. Densities of La-Ce liquids calculated using Equation 75 and Table 16.

4.1.5 Thermal Conductivity and Related Properties

Petersen et al. measured the low-temperature electrical resistivity of two La-Ce alloys and determined that the room-temperature electrical resistivity of an alloy with 70 at% La is ~ 67 μΩ-cm and the room-temperature electrical resistivity of an alloy with 22 at% La is ~74 μΩ-cm [339]. These values are generally consistent with room-temperature electrical resistivities of α-La (61.5 μΩ-cm) and γ-Ce (74.4 μΩ-cm) in the CRC Handbook of Chemistry and Physics [191 (Table 9)].

Vedernikov et al. reported in a very short paper that the room-temperature electrical resistivity of La-Ce alloys is slightly higher than would be expected if the resistivity were a linear function of composition [348]. This paper does not include quantitative resistivity data, information about sample purity, or information about analytical methods.

4.2 La-Pr

4.2.1 Introduction

The La-Pr phase diagram has apparently not been investigated experimentally, although a systematic survey of intra-rare-earth binary phase diagrams suggests that it is similar to the Ce-Pr phase diagram [334]. Based on this suggestion, key features of the La-Pr phase diagram include one end member (La) with three polymorphs, one end member (Pr) with two polymorphs, a continuous high-temperature solid solution between two bcc phases (γ-La and β-Pr), a continuous low-temperature solid solution between two dhcp phases (α-La and α-Pr), and a eutectoid decomposition of the bcc phase into an fcc solid solution (β-La) and the dhcp (α-La,α-Pr) solid solution. Published phase diagrams (e.g. [349, 350]) are qualitatively consistent with the features described above, but have no experimentally determined values except those for pure La and Pr.

No information about the thermal expansion of solid La-Pr alloys is available. Densities of liquid La-Pr alloys increase with increasing concentration of Pr and decrease with increasing temperature [340, 351]. The increase in density as a function of temperature is linear for each alloy. The increase in density as a function of concentration is not precisely linear, possibly because of impurities in the materials used.

No data on the thermal conductivity or diffusivity of La-Pr alloys is available. Information on electrical resistivity is limited to a very short paper that reported that the room-temperature resistivity of these alloys varies linearly with composition [348].

No information about the heat capacity of any La-Pr alloy is available.

4.2.2 Phases and Phase Transformations

4.2.2.1 Phases

Atmospheric-pressure phases in the La-Pr system are:

- (α-La, α-Pr): Double hexagonally close packed solid solution between α-La and α-Pr. Lattice parameters of intermediate compositions are not available.
- (β-La): Allotropic solid solution of β-La. The composition range of this phase has not been investigated, and the only available lattice parameter is for pure β-La (Section 2.5.2.1).
- (γ-La, β-Pr) Body-centered cubic solid solution between γ-La and β-Pr. Lattice parameters of intermediate compositions are not available.

4.2.2.2 Phase Transitions

Phase-transformation temperatures and enthalpies for this system are known only for pure La and Pr (Sections 2.5.2.2 and 2.7.2.2).

4.2.2.3 Phase Diagrams

Published La-Pr phase diagrams (e.g. [349, 350]) are based on the suggestion by Gschneidner et al [334] that the La-Pr phase diagram is similar to the Ce-Pr phase diagram. The phase diagram shown here (Figure 57) follows reference [350], except that dashed lines are used to indicate areas of uncertainty and phase-transformation temperatures have been adjusted slightly to match the recommendations in Sections 2.5.2.2 and 2.7.2.2.

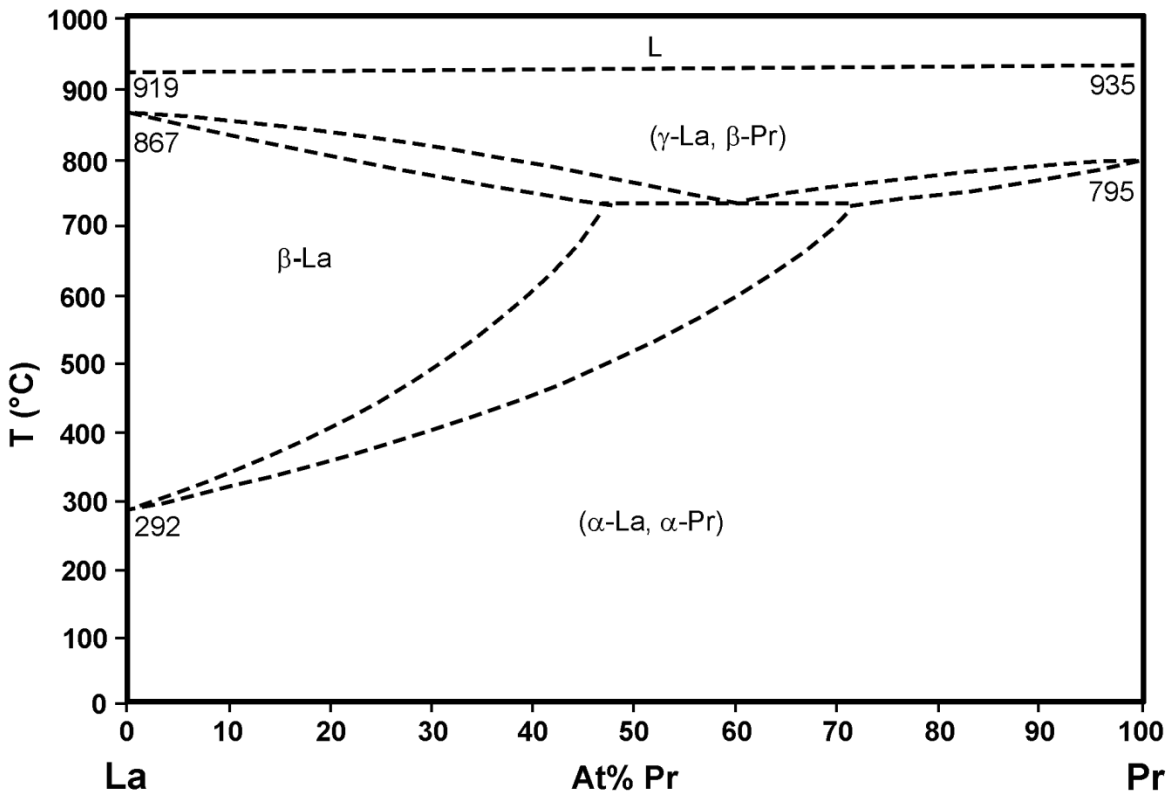

Figure 57. Hypothetical La-Pr phase diagram (based on reference [350] with phase-transformation temperatures adjusted slightly to match the recommendations in Sections 2.5.2.2 and 2.7.2.2).

4.2.3 Thermal Expansion and Density

4.2.3.1 Densities of Liquid Alloys

Bezukladnikova et al. measured densities of liquid La, Pr, and La-Pr alloys by using optical microscopy to observe changes in the sizes of drops of liquid in a vacuum [340, 351]. The La feedstock had ~0.19% impurities and the Pr feedstock had up to ~0.25%. Bezukladnikova et al. determined that the density of each alloy decreases linearly with increasing temperature and developed Equation 76 and Table 17 to express this relationship.

Equation 76. Density of La-Pr alloys (after [340, 351])

$$\rho = \rho_0 - b \times 10^{-3} \times T$$

where ρ is the density in g/cm^3, ρ_0 and b are values from Table 17 and T is a temperature in °C or K within the range specified in the table.

Table 17. Coefficients for calculating densities of La-Pr liquids.

Composition, at% Pr	T range (°C)	T range (K)	ρ_0	b	Reference
0	947-1354	—	6.77	0.73	[351]
1.48	—	1249-1630	7.18	0.87	[340]
3.01	—	1270-1686	7.09	0.80	[340]
5.19	—	1297-1690	7.06	0.77	[340]
7.52	—	1291-1703	7.12	0.81	[340]
11.58	—	1313-1720	7.04	0.75	[340]
11.59	1040-1447	—	6.84	0.75	[351]
19.08	1110-1413	—	7.06	0.89	[351]
29.54	1100-1390	—	6.98	0.8	[351]
39.38	1070-1369	—	7.09	0.87	[351]
49.59	1040-1380	—	7.25	0.95	[351]
59.53	1060-1386	—	7.43	1.01	[351]
69.63	1006-1040	—	7.48	1.00	[351]
80.11	1080-1410	—	7.60	1.04	[351]
89.85	1055-1316	—	7.73	1.11	[351]
100	984-1345	—	7.83	1.14	[351]

Figure 58 shows densities of La, Pr, and nine alloys calculated using Equation 76 and Table 17. The lowest-temperature densities of La and Pr in the figure are both ~0.1 g/cm^3 higher than the values in the CRC Handbook of Chemistry and Physics for densities of liquid rare-earth metals “near the melting point” [191 (Table 12)].

Bezukladnikova et al. noted that the molar volumes of alloys at 1473 K were not linear functions of composition, but considered the deviation as “insignificant” [351].

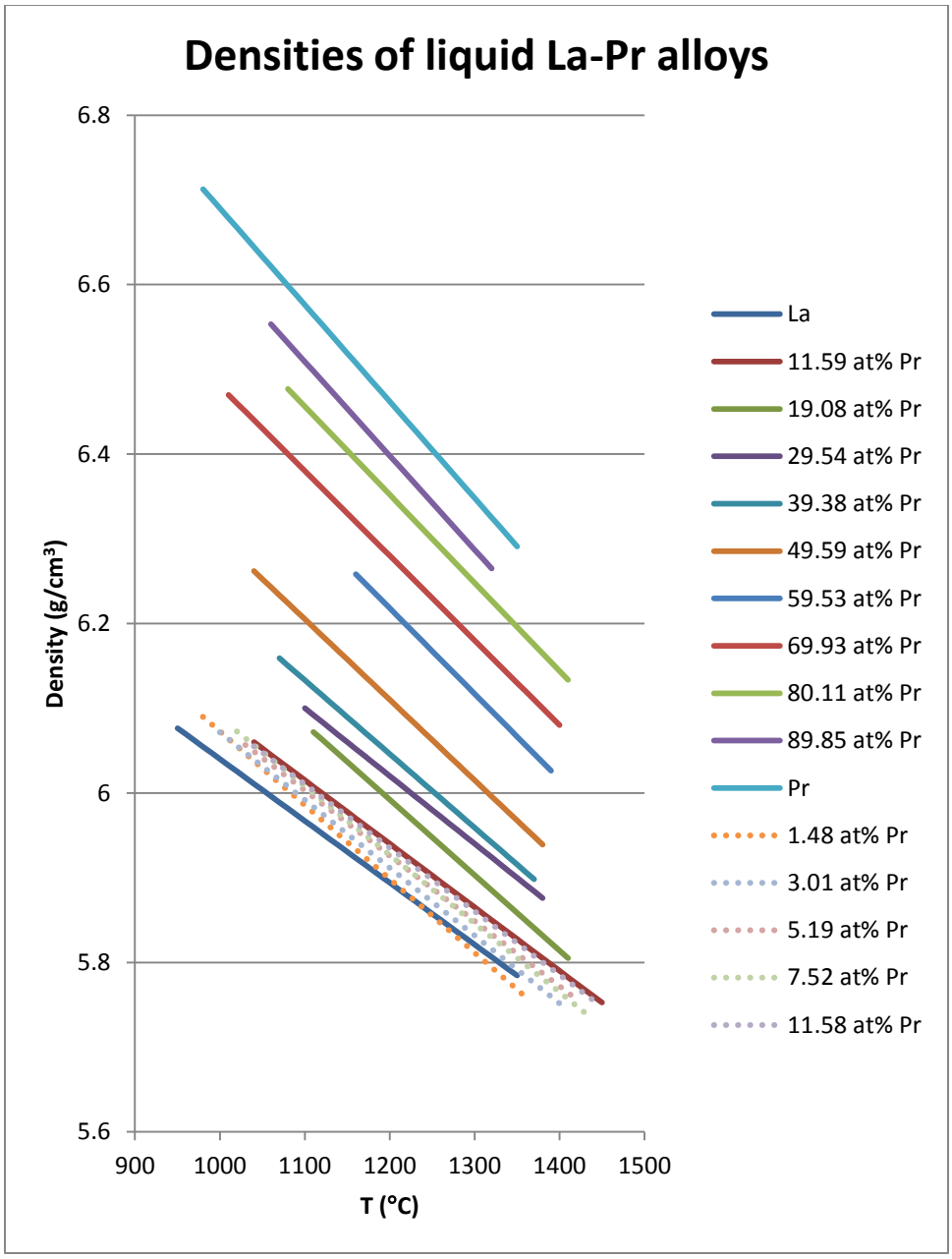

Figure 58. Densities of La-Pr liquids calculated using Equation 76 and Table 17. Solid lines show data from reference [351]; dotted lines show data from reference [340].

4.2.4 Thermal Conductivity and Related Properties

No data about the thermal conductivity or diffusivity of La-Pr alloys is available. Information about electrical resistivity is limited to a very short paper in which Vedernikov et al. reported that the room-temperature resistivity of these alloys varies linearly with composition [348]. This paper does not include quantitative data, information about sample purity, or information about the methods on which the results are based.

4.3 La-Nd

4.3.1 Introduction

Published experimental data for La-Nd phases is limited to phase-transformation temperatures, crystal-structure determinations, and lattice parameters from four alloys in a 1954 quarterly progress report for the Atomic Energy Commission [352] and phase identifications in seven compositions investigated as part of a study of the La-Nd-Fe ternary system [353]. The currently accepted phase diagram was proposed by Gschneidner in 1961 based on a re-interpretation of the 1954 data, which was required because of new knowledge indicating the existence of a third La phase [207]. Minor modifications were made more recently to reflect new measurements of La and Nd [194].

The generally accepted La-Nd phase diagram (black lines in Figure 59) was suggested by Gschneidner and resembles his proposed La-Pr phase diagram (reference [207] and Section 4.2.2.3). Key features of this phase diagram include one end member (La) with three polymorphs, one end member (Nd) with two polymorphs, a continuous high-temperature solid solution between two bcc phases (γ-La and β-Nd), a continuous low-temperature solid solution between two dhcp phases (α-La and α-Nd), and a eutectoid decomposition of the bcc phase into an fcc solid solution (β-La) and the dhcp (α-La, α-Nd) solid solution. A recent CALPHAD model confirms the general topology of the phase diagram suggested by Gschneidner, but suggests that the two-phase field between the bcc and fcc solid solution phases may be considerably narrower than in previously published phase diagrams [354]. Neither of these phase diagrams is consistent with the only available experimental data, which confirm the existence of a two-phase field between fcc and hcp phases but indicate that it involves a much higher Nd content [353]. Further experimental research is needed.

Heat capacities of La-Nd alloys have been measured at temperatures below 300 K [339, 355]. No information about heat capacities of La-Nd alloys at higher temperatures is available.

Experimental data on the density and thermal expansion of La-Nd alloys is limited to measurements of the densities of liquids with less than ~10 at% Nd [340]. This data shows that the density of these alloys increases with increasing concentration of Nd and decreases linearly with increasing temperature.

No information about the thermal conductivity of La-Nd alloys is available.

Researchers are encouraged to consult the excellent review of the properties of La-Nd alloys by Gschneidner and Calderwood [194 pp. 13-14].

4.3.2 Phases and Phase Transformations

4.3.2.1 Phases

Phases in the La-Nd system that are stable at atmospheric pressures are:

- (α-Nd, α-La): Double hexagonally close packed solid solution between α-Nd and α-La. The range of compositions in this phase is unknown. Published lattice parameters for three alloys show considerable scatter and a negative deviation from Vegard's Law [194, 352].
- (β-La): Allotropic solid solution of β-La. The range of compositions in this phase is unknown and lattice parameters are not available.
- (β-Nd, γ-La): Body-centered-cubic solid solution between β-Nd and γ-La.

4.3.2.2 Phase-Transition Temperatures

Phase-transformation temperatures at the upper and lower boundaries of the (β-Nd, γ-La) solid solution were reported by Daane and Spedding [352] and are consistent with the Gschneidner phase diagram.

Phase-transformation enthalpies for La-Nd alloys are not available.

4.3.2.3 Phase Diagrams

The La-Nd phase diagram published in 1954 by Daane and Spedding [352] includes only two La polymorphs and shows continuous solid solutions between hcp and fcc phases of La and Nd. Later research (e.g., [193]) established the existence of a third La phase, and the 1954 Daane and Spedding phase diagram is no longer accepted.

In 1961, Gschneidner re-interpreted the data of Daane and Spedding to include three La phases and suggested that the La-Nd phase diagram is similar to the Ce-Pr system ([207] and black lines in Figure 59). Small changes have been made since then to reflect improved knowledge of phase-transformation temperatures of La and Nd [194]. Despite numerous areas of uncertainty, this phase diagram is commonly accepted.

Although the Gschneidner and Calderwood phase diagram seemed plausible when it was proposed, there was no direct experimental evidence for the eutectoid reaction and two-phase field. Yang et al. recently calculated a new La-Nd phase diagram using CALPHAD [354]. Their results agree with the liquidus, solidus, and general topology of the Gschneidner phase diagram. According to the phase diagram of Yang et al., the two-phase field between β-La and the (α-La, α-Nd) solid solution is narrower than indicated by Gschneidner, and the (γ-La, β-Nd) solid solution is stable at lower temperatures for some compositions (Figure 59).

Neither of these phase diagrams is consistent with experimental data from Wu et al., in which phases in seven La-Ce alloys were identified as part of a study of an isothermal section of the La-Nd-Fe ternary system [353]. The data of Wu et al. confirms the presence of a two-phase field between high-Nd and high-La phases, but suggests that it may occur at significantly higher concentrations of Nd than indicated by either of the suggested phase diagrams.

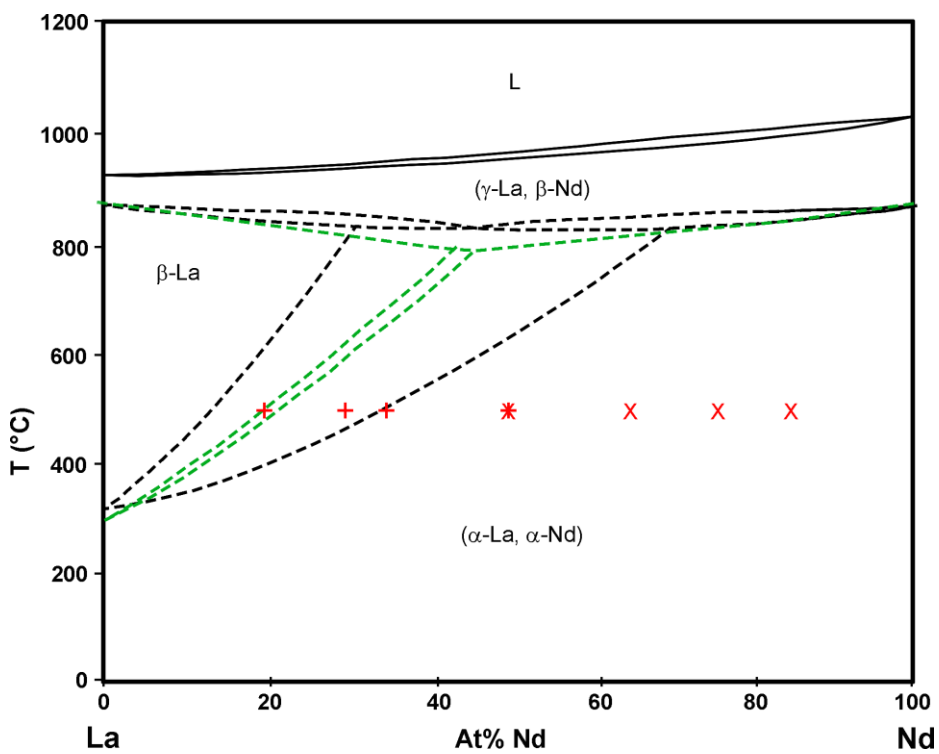

Figure 59. Suggested La-Nd phase diagrams. Red symbols represent data from Wu et al. [353]: plus symbols are (β-La), x symbols are (α-Nd), and superimposed symbols indicate that both phases were identified. Black lines are phase diagram suggested by Gschneidner and Calderwood [194]. Green lines

are from the calculated phase diagram of Yang et al. [354] and show only areas where the phase diagrams differ.

4.3.3 Heat Capacity and Related Properties

Heat capacities of La-Nd alloys have been measured at temperatures below 300 K [339, 355]. No heat capacities of La-Nd alloys at higher temperatures are available.

For some compositions and temperature ranges, it may be appropriate to use approximate heat capacities obtained using the Kopp-Neumann Law (Section 1.6.1 in reference [5]). However, the currently poor understanding of the La-Nd phase diagram makes it difficult to reliably avoid temperatures close to phase transitions. Errors in the heat capacities of La and Nd will propagate into heat capacities of La-Nd alloys estimated using the Kopp-Neumann Law.

4.3.4 Thermal Expansion and Density

4.3.4.1 Densities of Liquid Alloys

Bezukladnikova et al. measured densities of five La-Nd alloys with ~1.1 to 9.9 at% La using optical microscopy to observe changes in the sizes of drops of liquid in a vacuum [340]. Their results showed that the density of each alloy decreases linearly with increasing temperature. Equation 77 and Table 18 express this relationship.

Equation 77. Density of La-Nd alloys (after [340])

$$\rho = \rho_0 - b \times 10^{-3} \times T$$

where ρ is the density in g/cm^3, ρ_0 and b are values from Table 18 and T is a temperature in K within the range specified in the table.

Table 18. Coefficients for calculating densities of La-Nd liquids (after [340]).

Composition, at% Nd	T range (K)	ρ_0	b
1.14	1257-1620	7.13	0.85
2.79	1270-1613	7.12	0.83
5.02	1293-1617	7.07	0.79
7.23	1301-1633	7.19	0.87
9.89	1313-1617	7.22	0.88

Figure 60 shows densities calculated using Equation 77 and Table 18. Densities decrease linearly as a function of increasing temperature. There is a general tendency for the density to increase with increasing concentrations of Nd, consistent with the higher density of Nd in comparison to La (Sections 2.5.4.3 and 2.8.4.3). The density of the alloy with 1.14 at% Nd is ~6.06 g/cm^3 at 980°C, which is slightly higher than the density of 5.96 g/cm^3 for pure La at a temperature “near the melting point” (918°C) in the CRC Handbook of Chemistry and Physics [191 (Table 12)].

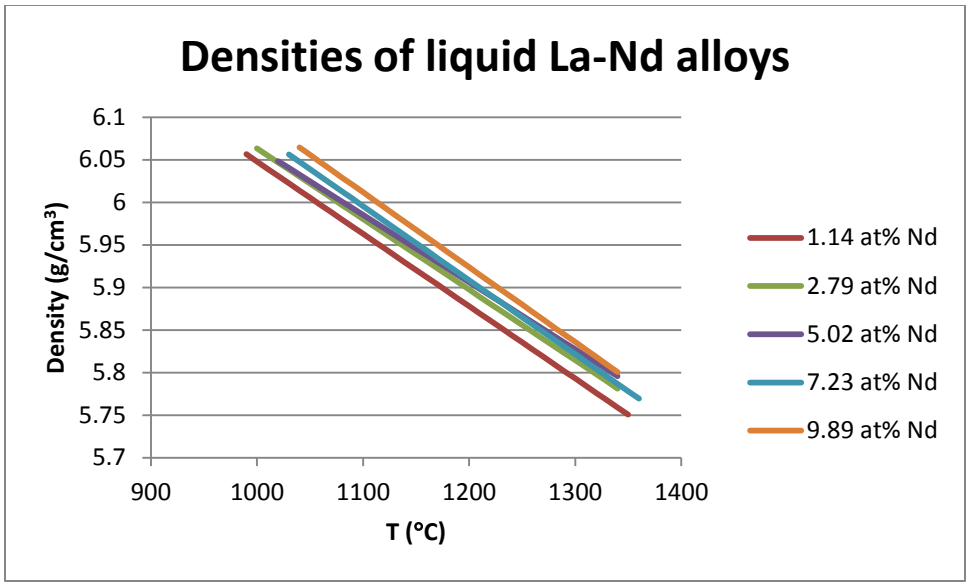

Figure 60. Densities of La-Nd liquids calculated using Equation 77 and Table 18 (after [340]).

4.4 Ce-Pr

4.4.1 Introduction

In 1982, Gschneidner and Calderwood [356] developed a Ce-Pr phase diagram based on the 1980 data of Altunbas and Harris [357]. Key features of this phase diagram include one end member (Ce) with three polymorphs above room temperature, one end member (Pr) with two polymorphs, a bcc (δ-Ce, β-Pr) solid solution, a dhcp (β-Ce, α-Pr) solid solution, and a eutectoid decomposition of the bcc (δ-Ce, β-Pr) solid solution into an fcc solid solution (γ-Ce) and the dhcp (β-Ce, α-Pr) solid solution. Although it was published as "preliminary," the Gschneidner and Calderwood phase diagram has been extensively repeated (e.g., [194, 334, 358, 359]).

Despite the uncertain purity of some of the samples used by Altunbas and Harris, it seems unlikely that further investigation would change the boundaries of higher-temperature phase transitions significantly. Further research addressing transformations involving α-Ce and the boundaries of the (α-Pr, β-Ce) solid solution is needed for a complete understanding of the phase diagram. In the absence of this research, the Gschneidner and Calderwood phase diagram (Figure 61) is the best available approximation of the Ce-Pr phase diagram.

No information about the heat capacities, thermal expansion, or thermal conductivities of Ce-Pr alloys is available. Measurements of electrical resistivity are limited to two temperatures and to compositions with less than 25 at% Ce.

Researchers are encouraged to consult the excellent review of the properties of Ce-Pr alloys by Gschneidner and Calderwood [194 pp. 30-32].

4.4.2 Phases and Phase Transformations

4.4.2.1 Phases

Atmospheric-pressure phases in the Ce-Pr system are:

- (α-Ce): Low-temperature fcc solid solution of α-Ce. The maximum concentration of Pr and influence of Pr concentration on lattice parameters in this phase have apparently not been investigated.

- (β-Ce, α-Pr): Double hexagonally close packed solid solution between β-Ce and α-Pr. Lattice parameters of intermediate compositions have apparently not been published.
- (γ-Ce): Higher-temperature face-centered cubic solid solution of (γ-Ce). The lattice parameter for an alloy with 5 at% Pr is 0.001 Å larger than that for pure Ce, and lattice parameters with lower concentrations of Pr follow Vegard's law [194, 344, 356]. Lattice parameters for alloys with higher concentrations of Pr are not available.
- (δ-Ce, β-Pr): Body-centered cubic solid solutions between δ-Ce and β-Pr. Lattice parameters of intermediate compositions are not available.

4.4.2.2 Phase Transitions

Altunbas and Harris [357] noted differences in onset temperatures measured during heating and cooling in their DTA and resistivity data. They attributed these differences to elastic deformation associated with changes in crystal structures.

Addition of ~1 at% Pr increases the temperature of the (α-Ce)↔(γ-Ce) transformation relative to that in pure Ce. However, addition of larger concentrations of Pr (to a few at%) decrease this transformation temperature [346]. There is no available information about the temperature of the (α-Ce)↔(γ-Ce) transition in alloys with higher concentrations of Pr or the influence of Pr on the (α-Ce)↔(β-Ce) transformation temperature. Nonetheless, it seems likely that (α-Ce) solid solutions occur only at temperatures too low to be experienced by metallic fuels.

Addition of a few percent Pr increased the temperature of the (β-Ce)↔(γ-Ce) transformation by about 15 degrees [346]. Altunbas and Harris published a figure showing that phase-transformation temperatures increase for alloys with higher concentrations of Pr [357]; however, it not possible to reliably quantify the increase because of the scatter in the data.

Altunbas and Harris also published a graphical presentation of temperatures for the liquidus and (γ-Ce)↔ (δ-Ce, β-Pr) transformation [357]. Liquidus temperatures appear to rise linearly with increasing concentration of Pr. The temperature of the (γ-Ce)↔ (δ-Ce, β-Pr) transformation also generally increases with concentration of Pr, but levels off or decreases slightly at high concentrations.

Phase-transformation enthalpies for Ce-Pr alloys are not available.

4.4.2.3 Phase Diagrams

In 1980, Altunbas and Harris [357] used DTA and electrical resistivity to study phase-transformation temperatures in Ce-Pr alloys. They also used X-ray diffraction to determine phases in powdered samples that had been annealed at 600°C and rapidly cooled to room temperature, and reported that samples with 66-74 at% Pr had two phases. They presented their transformation-temperature data graphically as a function of Pr concentration, but did not integrate this data with their X-ray diffraction data or suggest a phase diagram.

In 1982, Gschneidner and Calderwood published a "preliminary" Ce-Pr phase diagram based on the data of Altunbas and Harris [356], which has been modified slightly for this Handbook to reflect current values for phase-transition temperatures in Pr and Ce (Figure 61). The temperature of 61°C for the β-Ce↔γ-Ce transformation in the Gschneidner and Calderwood phase diagram (which is retained in Figure 61) is the average of the transformations measured during heating and cooling, and is higher than the most recent estimate of the equilibrium transformation temperature (10 °C, Section 2.6.2.2). Other phase-transformation temperatures for Ce and Pr are from Sections 2.6.2.2 and 2.7.2.2 and are within a few degrees of the values used by Gschneidner and Calderwood.

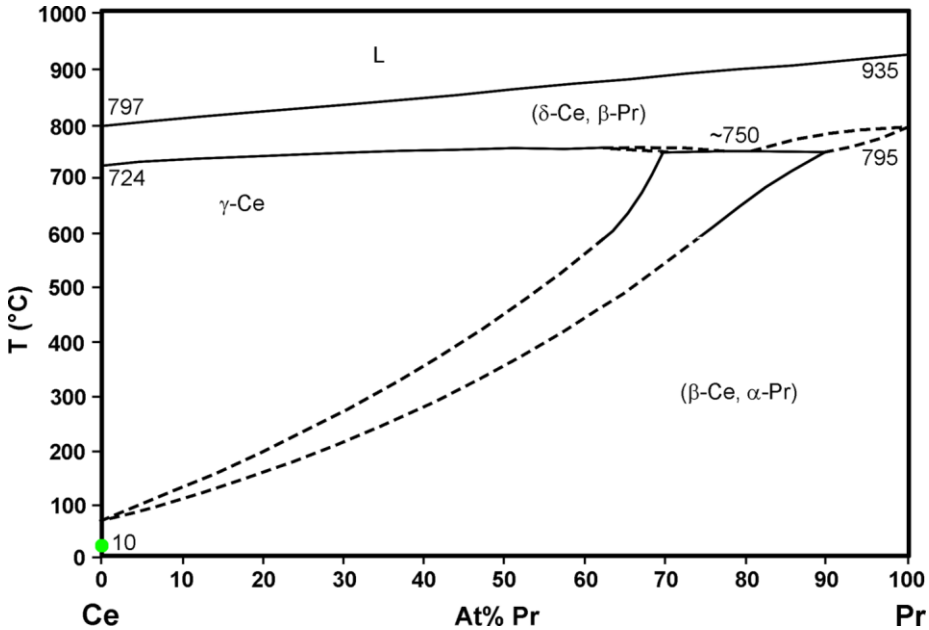

Figure 61. Ce-Pr phase diagram after Gschneidner and Calderwood [194], with phase-transformation temperatures for Ce and Pr from Sections 2.6.2.2 and 2.7.2.2. The green dot is the most recent value of the equilibrium transition temperature between β-Ce and γ–Ce.

4.4.3 Thermal Conductivity and Related Properties

No measurements of the thermal conductivity of Ce-Pr alloys are available. Experimental measurements of resistivity are limited to temperatures of 298 and 368 K and compositions with less than 25 at% Ce [360]. Despite considerable scatter that the authors attributed to inaccuracies in measuring the specimen dimensions (which they apparently used to convert measured resistances to resistivities), it was concluded that there was a linear relationship between composition and electrical resistivity at each temperature. It is not clear how the higher-temperature data in this study was obtained, as the only measurement techniques discussed involved measurements of electrical resistivity at temperatures from 1.5 to 300 K.

4.5 Ce-Nd

4.5.1 Introduction

The Ce-Nd phase diagram has apparently not been investigated systematically, although individual measurements are available in several studies [361-363]. A systematic survey of intra-rare-earth binary phase diagrams suggests that the Ce-Nd and Ce-Pr phase diagrams are similar [334]. If this suggestion is accepted, key features of the Ce-Nd phase diagram include one end member (Ce) with three polymorphs above room temperature, one end member (Nd) with two polymorphs, a continuous bcc (δ-Ce, β-Nd) solid solution, a continuous dhcp (β-Ce, α-Nd) solid solution, and a eutectoid decomposition of the (δ-Ce, β-Nd) solid solution into the (β-Ce, α-Nd) solid solution and an fcc solid solution phase (γ-Ce).

The only available Ce-Nd phase diagram from experimental data was suggested by Moffatt [364] based on X-ray diffraction data from Speight et al. [361]. This phase diagram appears in the ASM Alloy Phase Diagram Database [365]. Phase diagrams from CALPHAD calculations were proposed by Cacciamani and colleagues in 2003 and by Yang and colleagues in 2018. Comparison with the experimental data suggests that the phase diagram of Cacciamani and colleagues is more likely to be an accurate representation of the Ce-Nd system than the phase diagrams of Moffatt et al. and Yang et al., although a thorough experimental investigation is needed.

No experimental information about heat capacities, thermal expansion, or thermal conductivity of Ce-Nd alloys is available. Relatively recent research on these alloys includes investigation of interactions between Ce-Nd alloys and HT9 steel [366] and investigations of grain structure and growth [363].

Researchers are encouraged to consult the excellent review of the properties of Ce-Nd alloys by Gschneidner and Calderwood [194 pp. 33-34].

4.5.2 Phases and Phase Transformations

4.5.2.1 Phases

Atmospheric-pressure phases in the Ce-Nd system are:

- (β-Ce, α-Nd): Double hexagonally close packed solid solution between β-Ce and α-Nd. The *a*-lattice parameters of intermediate compositions vary approximately linearly between ~11.795 Å for Nd and ~11.836 Å for an alloy with 60 at% Ce, and the *c*-lattice parameters vary approximately linearly between 3.656 Å for Nd and 3.673 Å for an alloy with 60 at% Ce [194, 361, 367]. Lattice parameters in the original data of Speight et al. are expressed in units of kX, which can be converted to Å by multiplying by 1.00202 [368].
- (γ-Ce): Face-centered cubic solid solution of γ-Ce. Speight et al. determined that lattice parameters for this phase in alloys with 70-100 at% Ce are essentially independent of composition, with $a \approx 5.161$ Å [194, 361, 367]. This data is consistent with a measurement of 5.1600 Å by Gschneidner et al. [344] in an alloy with 2 at% Nd.
- (δ-Ce, β-Nd) Body-centered cubic solid solution between δ-Ce and β-Nd. Lattice parameters of intermediate compositions have apparently not been published.

4.5.2.2 Phase Transitions

No information about phase-transformation temperatures of Ce-Nd alloys is available; however, because Ce and Nd are trivalent rare-earth metals with similar atomic numbers, it is reasonable to expect that Ce-Nd alloys behave as ideal alloys at high temperatures [194 (page 7)]. As a consequence, the temperatures of the liquidus and solidus are the same to within a few degrees, and the combined liquidus and solidus can be represented by a straight line between the melting temperatures of Ce and Nd [194].

No information about phase-transition enthalpies in Ce-Nd alloys is available.

4.5.2.3 Phase Diagrams

Experimental data about phases in Ce-Nd alloys was published by Speight et al. [361], Keiser et al. [362], and Hachimi et al. [363]. Speight et al. used X-ray diffraction data to identify phases in alloys that had been rapidly cooled from 600°C [361]. Keiser et al. measured coexisting compositions in diffusion couples using SEM-EDX and interpreted these compositions as marking the boundaries of a two-phase region. Hachimi et al. determined that an alloy with 10 wt% Nd that had been heat treated at 610°C for 2 hours was primarily fcc material with some dhcp material and that an alloy with 50 wt% Ce was dhcp [363]. None of these researchers suggested a phase diagram. The only phase diagram based on experimental data was suggested by Moffatt in 1984 [364] and reproduced by Okamoto [350]. Phase diagrams from CALPHAD calculations were proposed by Cacciamani and colleagues in 2003 and by Yang and colleagues in 2018 [354, 369]. The liquidus in all three phase diagrams is identical.

Figure 62 compares the phase diagrams of Moffatt (reference [364]) and of Cacciamani et al. (reference [369]) with the available experimental data. The phase diagram of Yang et al. is generally similar to that of Cacciamani et al. and is not shown because its β-γ transition temperature in pure Ce appears to be at least 50°C higher than the most recent value (Section 2.6.2.2). Comparison with the experimental data suggest that the phase diagram of Cacciamani et al. is probably the most accurate representation of the Ce-Nd phase diagram, although the range of Nd compositions in the two-phase field between γ-Ce and (β-Ce, α-Nd) solid solutions may be the slightly too high. Further experimental work is needed to confirm this understanding.

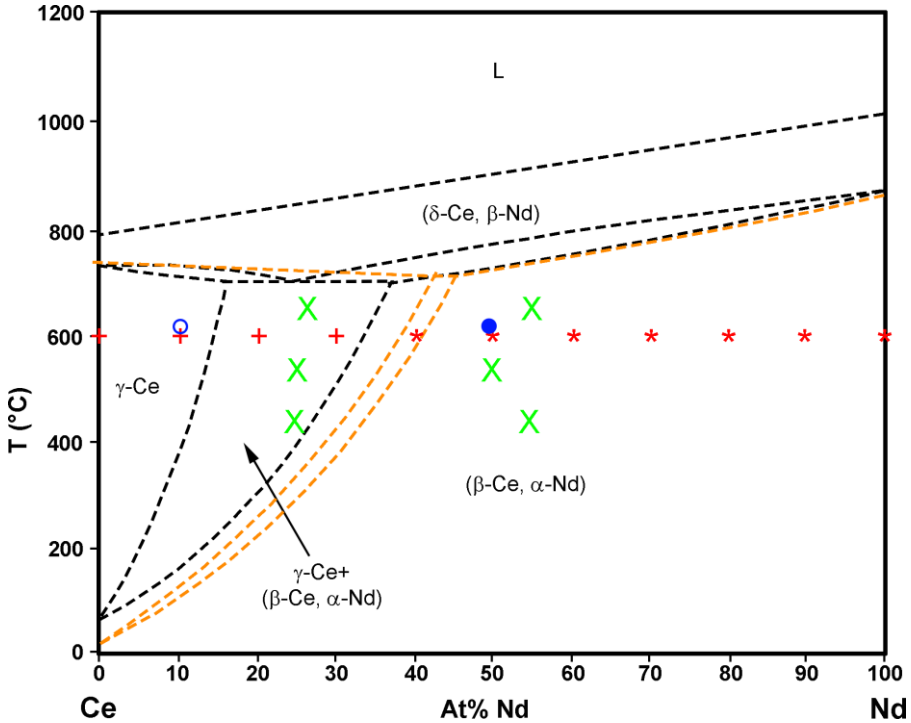

Figure 62. Proposed Ce-Nd phase diagrams. Dashed black lines are a tentative phase diagram suggested by Moffatt [364] and reproduced by Okamoto [350]. Dashed orange lines are sub-solidus phase boundaries calculated by Cacciamani et al. [369]. Symbols are experimental data from Speight et al. [361] (red; + indicates an alloy with reported fcc lattice parameters, * indicates an alloy with reported dhcp lattice parameters), Keiser [362] (green; x symbols indicate boundaries of the two-phase region), and Hachimi et al. [363] (blue; open circle indicates an alloy with predominantly fcc structure, filled circle indicates an alloy with dhcp structure). Liquidus temperatures in all of the proposed phase diagrams are identical.

4.6 Pr-Nd

4.6.1 Introduction

The currently accepted Pr-Nd phase diagram (Figure 63) is based on a 1982 re-interpretation of early experimental data [370-372] by Gschneidner and Calderwood [373]. Key features of this phase diagram include a completely miscible liquid and continuous solid solutions between the dhcp phases α-Pr and α-Nd and between the bcc phases β-Pr and β-Nd. The original experimental data showed two-phase fields associated with phase transformations, which do not appear in the 1982 phase diagram because Gschneidner and Calderwood attributed them to impurities. Although the 1982 phase diagram was published as "provisional," it has been repeated in Massalski's compilation of binary alloy phase diagrams [374] and the ASM Alloy Phase Diagram database [375].

Despite the low purity of some of the samples used in the original determinations of the phase diagrams, it seems unlikely that further investigation would change the boundaries of higher-temperature phase transitions by more than a few degrees. Actual transformation temperatures for specific alloys of interest to fuels programs (including possible two-phase fields) should be experimentally addressed if high-precision values are required.

No information about heat capacities of Pr-Nd alloys is available. However, because Pr and Nd have similar crystal structures and heat capacities, the Kopp-Neumann Law (Section 1.6.1 in reference [5]) may provide accurate estimates.

No information about thermal expansion of Pr-Nd alloys is available, although it appears that densities of solids and liquids can be reliably approximated by those of Pr and Nd as long as there are no differences in crystal structures.

No information about thermal conductivity or thermal diffusivity of Pr-Nd alloys is available. Information about electrical resistivity is limited to a short paper with no quantitative data.

Researchers are encouraged to consult the excellent review of the properties of Pr-Nd alloys by Gschneidner and Calderwood [194 pp 56-59].

4.6.2 Phases and Phase Transformations

4.6.2.1 Phases

Atmospheric-pressure phases in the Pr-Nd system are:

- (α-Pr, α-Nd): Double hexagonally close packed solid solution between α-Pr and α-Nd. Room-temperature lattice parameters decrease linearly as a function of the atomic proportion of Nd [371].
- (β-Pr, β-Nd): Body-centered cubic solid solution between β-Pr and β-Nd. Lattice parameters vary linearly as a function of the atomic proportions of Pr and Nd [371].

4.6.2.2 Phase Transitions

Phase-transformation temperatures have not been reported for Pr-Nd alloys. However, given the ideal behavior of these alloys at high temperatures [371, 376], it seems reasonable to approximate phase-transition temperatures of alloys by linear interpolation between transition temperatures of pure Pr and Nd.

4.6.2.3 Phase Diagrams

The first Pr-Nd phase diagram was published in 1963 by Markova et al. [370] using Pr and Nd with purities of 97 and 98 %, respectively. This phase diagram established the existence of a miscible liquid and two solid-solution phases, each of which included Pr-Nd alloys of all compositions. This phase diagram shows two-phase regions with temperature differences of up to ~100°C between the liquidus and solidus and between the two solid-solution phases.

Slightly later, Lundin and colleagues investigated properties of Pr-Nd alloys, using feedstocks with reported impurities below ~0.3 wt % [371, 372, 376]. They concluded that Pr-Nd alloys behave as ideal solutions. Their investigations included measurements of enthalpies of solution for Pr-Nd alloys, room-temperature lattice parameters and densities for solid and liquid Nd, Pr, and a number of Pr-Nd alloys, and activities of Pr and seven alloys at temperatures of 1475, 1500, and 1525°C. Two-phase regions between the liquidus and solidus and between the dhcp and fcc solid solutions in a phase diagram suggested by Lundin et al. [372 (Figure 1)] are narrower than those in the phase diagram of Markova et al., but are still significantly larger than the estimated errors in the phase-transition temperatures measured by Lundin et al.

In 1982, Gschneidner and Calderwood used the results of Markova et al. and Lundin et al. to develop a new phase diagram (Figure 63). The Gschneidner and Calderwood phase diagram considers Pr-Nd alloys to behave as ideal solutions, and therefore represents phase transformations by straight lines rather than showing two-phase fields. This representation is consistent with the general principle that alloys of trivalent rare-earth elements with atomic numbers that differ by less than ~±4 behave as ideal solutions at high temperatures [194], with the conclusions of Lundin and colleagues [371, 372, 376], and with phase diagrams calculated by Shiflet et al. [377] and by Yang et al. [354]. However, it is not consistent with the phase diagram of Markova et al. and of Lundin et al., both of which show two-phase regions between the liquidus and solidus and between the dhcp and fcc solid solutions. It seems likely that the ranges of temperatures included in possible two-phase fields are highly dependent on the impurity content of the individual samples used to construct the phase diagram [373, 377], and that the two-phase fields may disappear in high-purity alloys.

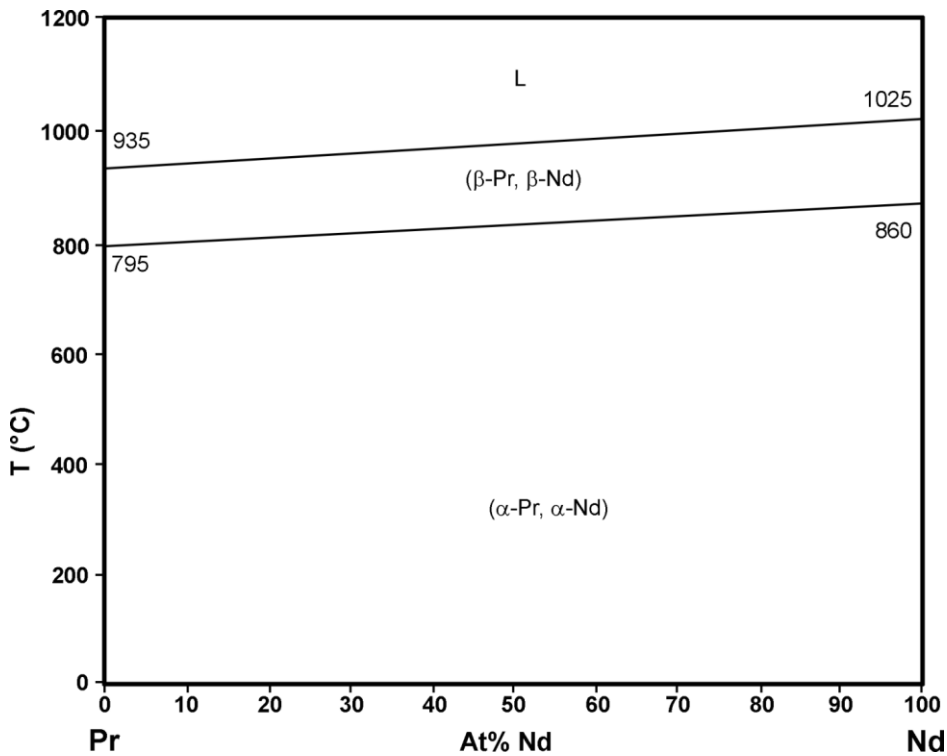

Figure 63. Pr-Nd phase diagram after [373], with phase-transformation temperatures for La and Nd adjusted slightly for consistency with recommendations in Sections 2.7.2.2 and 2.8.2.2.

4.6.3 Heat Capacity and Related Properties

Lundin et al. measured activities of Pr and Nd and determined that the heat of mixing is linearly related to the composition in a variety of Pr-Nd alloys [371, 376].

Currently available measurements indicate that the heat capacities of pure Pr and pure Nd are similar. In the absence of experimental data, the Kopp-Neumann Law (Section 1.6.1 in reference reference [5]) appears to provide a plausible estimate for the heat capacities of Pr-Nd alloys. Figure 64 shows an example of the application of the Kopp-Neumann law to a Pr-Nd alloy with 50 at% Pr. Because alloys of pure Pr and Nd behave as ideal alloys at high temperatures, the temperatures of phase transitions in the alloy were determined by interpolation between the transition temperatures of Pr and Nd. To reduce errors introduced by phase transitions, heat capacities are shown only for temperature ranges in which the binary phase diagram in Section 4.6.2.3 indicates that Pr and Nd have the same crystal structure.

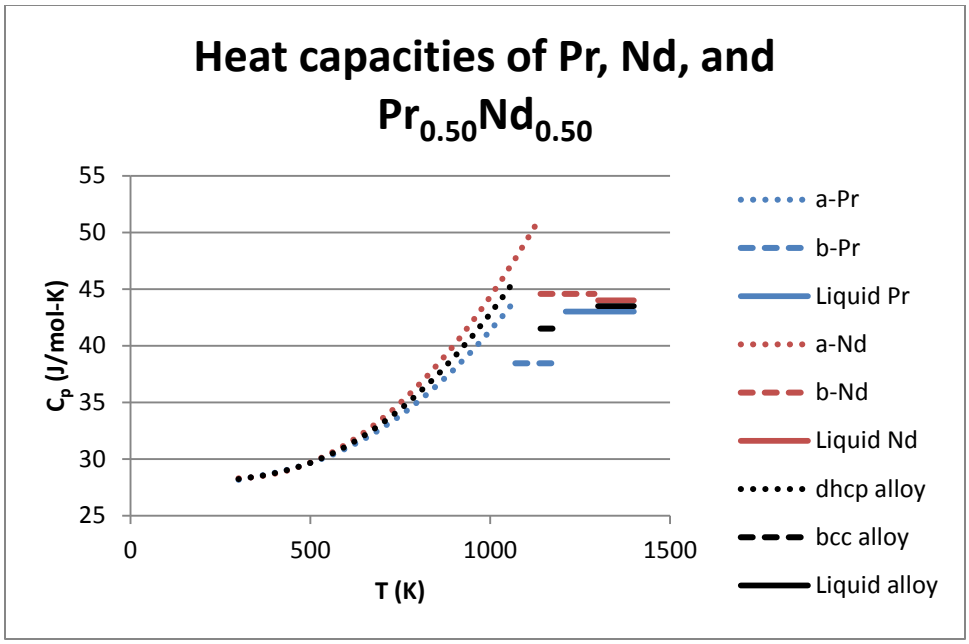

Figure 64. Heat capacity of a Pr-Nd alloy with 50 at% Pr, estimated using the Kopp-Neumann Law with heat capacities of Pr and Nd (Sections 2.7.3 and 2.8.3). Heat capacities of pure Pr and Nd are included for comparison. Colors indicate compositions, and line types (dots, etc.) indicate phases. The dhcp alloy is a solid solution of α-Pr and α-Nd, and the bcc alloy is a solid solution of β-Pr and β-Nd.

Because uncertainties in the heat capacities of elements propagate into the estimated heat capacities of alloys, the most useful information for improving the accuracy of information about heat capacities of Pr-Nd alloys may involve measurements of the heat capacities of pure Pr and pure Nd.

4.6.4 Thermal Expansion and Density

No information about thermal expansion or thermal expansion coefficients is available.

4.6.4.1 Room Temperature Densities of Solids

Lundin et al. measured the room-temperature densities of nine Pr-Nd alloys and observed that the densities of room-temperature solids and of liquids at 1240°C varied linearly between the room-temperature densities of Nd and Pr as a function of composition [371]. The linear variation in densities is consistent with linear variation in lattice parameters observed in the same study and the ideal behavior of Pr-Nd alloys. Given the strong evidence that Pr-Nd alloys behave as ideal alloys [371, 376], it seems reasonable to approximate the densities of Pr-Nd alloys at other temperatures by linear interpolation between the densities of Pr and Nd at those temperatures as long as both phases have the same crystal structure.

4.6.4.2 Densities of Liquids at 1240°C

Lundin et al. measured the densities of three Pr-Nd liquids at 1240°C and observed that the densities varied linearly between those of Pr and Nd as a function of composition [371].

4.6.5 Thermal Conductivity and Related Properties

No data about the thermal conductivity or diffusivity of Pr-Nd alloys is available. Information about electrical resistivity is limited to a very short paper that states that the room-temperature electrical resistivity of Pr-Nd alloys varies linearly with composition [348]. This paper does not include quantitative data or information about the samples and methods on which the results are based.

4.7 Mischmetals (Rare-earth alloys that include La, Ce, Pr, and Nd)

La, Ce, Pr, and Nd are primary constituents of the industrially important rare-earth alloys known as "mischmetals" (also called "misch metals" or "misch-metals"), which are produced from rare-earth minerals by large-scale refining operations. Compositions of commercially available mischmetals vary.

Values for the properties included in this Handbook are rarely published for mischmetals. However, Palmer et al. [378] prepared and characterized eight high-purity mischmetal alloys with ~20-43 at% La, 37-54 at% Ce, 6.2-6.5 at% Pr, 8-20 at% Nd, up to ~2 at% Gd, and up to ~1.6 at% Y. Gschneidner and Calderwood [194] paraphrased the results of these analyses as indicating that the experimentally determined melting and transition temperatures of alloys that had no Y or Gd and less than 50 wt% Ce (a composition range that includes rare-earth alloys of interest for metallic fuels) agreed with temperatures calculated from the properties of the pure elements and the atomic proportions of these elements in each alloy.

A mischmetal alloy with 27.3 at% La, 47.2 at% Ce, 8 at% Pr, and 17.5 at% Nd has a hexagonal structure (space group P63/*mmc* with a = 3.726 Å, c = 11.875 Å, and 4 atoms per unit cell) [379].

5. BINARY ALLOYS OF AN ACTINIDE (U, Np, Pu, Am) AND A RARE-EARTH ELEMENT (La, Ce, Pr, Nd)

5.1 U-La

5.1.1 Introduction

Published experimental measurements for the U-La phase diagram are limited to temperatures between 1000 and 1500°C. These measurements suggest a phase diagram with very limited miscibility and no intermediate phases. Experimental measurements of the limits of solubility [380-382] are generally consistent.

Bayanov calculated a variety of thermodynamic properties for liquids in the U-La system [383]. More recently, McMurray et al. used CALPHAD to perform a thermodynamic assessment of the U-La-O system [384].

No experimental measurements of the heat capacity, thermal expansion, or thermal conductivity of U-La alloys are available.

5.1.2 Phases and Phase Transformations

According to Haefling and Daane [381], the maximum solubility of U in liquid La rises from ~0.422 wt% at 1050°C to ~1.022 wt% at 1250°C. These data are generally consistent with solubilities reported by Rough and Bauer [380] (0.3 wt% at 1000°C and 1.0 wt% at 1250°C). The higher-temperature data of Shoji et al. [382] show a maximum solubility of 6.66 wt% at 1500°C.

Haefling and Daane suggested that binary phase diagrams involving U and rare-earth elements whose melting temperatures are below that of U (including La) have high-U monotectic transformations similar to that in the U-Ce system. There is no experimental evidence to determine whether this transformation actually occurs in the U-La system.

None of the papers with experimental data include phase diagrams; however, Okamoto [385] drew a partial phase diagram from 1000 to 1300°C based on the data of Haefling and Daane [381]. This phase diagram shows a slight depression of the melting temperature of γ-U solid solutions corresponding to the eutectic transformation suggested by Haefling and Daane. Figure 65 (new for this Handbook) follows the topology of the Okamoto phase diagram, but extends the temperature range to 1500°C to accommodate the data of Shoji et al. [382].

No experimental data on crystal structures, lattice parameters, or phase-transformation temperatures or enthalpies in U-La alloys are available. Given the low mutual solubilities of U and La, it seems reasonable to assume that properties of high-U and high-La phases are similar to those of U and La.

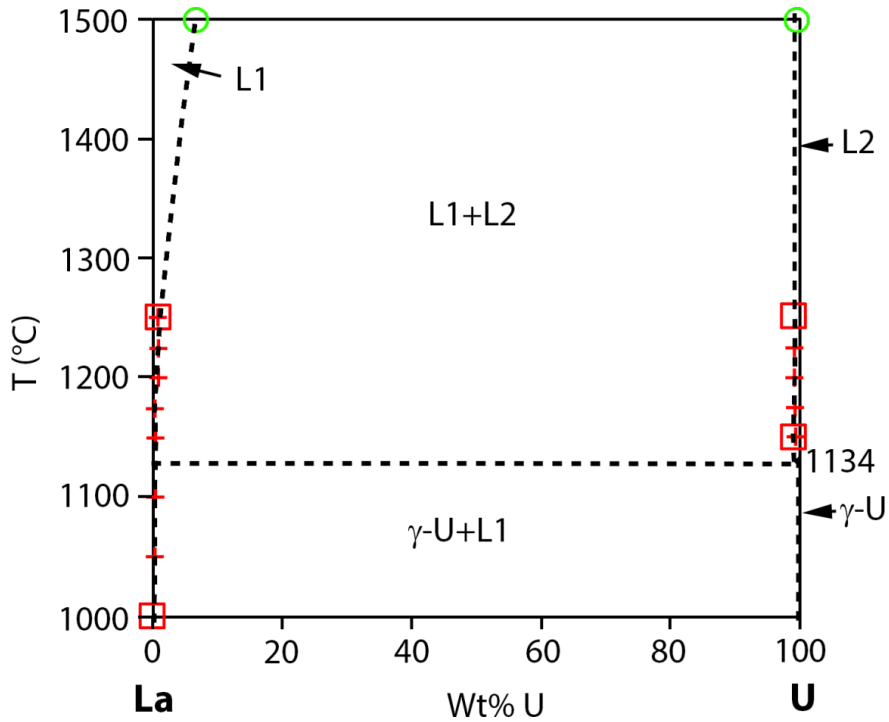

Figure 65. Tentative U-La phase diagram drawn for this Handbook based on the work of Okamoto [385], with experimental data from Haefling and Daane [381] (red "+" symbols), Rough and Bauer [380] (red squares), and Shoji et al. [382] (green circles).

5.2 U-Ce

5.2.1 Introduction

Experimental data on the U-Ce system is limited to temperatures between 1000 and 1500°C. Although the mutual solubility of U and Ce is greater than that of U and Nd, Pr, or La [207, 381], the data suggest a phase diagram with a wide miscibility gap and no intermediate phases.

Bayanov calculated a variety of thermodynamic properties for liquids in the U-Ce system [383].

No information about the heat capacity, thermal expansion, or thermal conductivity of U-Ce alloys is available.

5.2.2 Phases and Phase Transformations

5.2.2.1 Phases

No experimental data about crystal structures, lattice parameters, or phase-transformation enthalpies in U-Ce alloys is available. Given the low mutual solubilities of U and Ce, it seems reasonable to assume that properties of the high-U and high-Ce solid solution phases are similar to those of U and Ce.

Figure 66 summarizes the experimental measurements showing the maximum mutual solubilities of U and Ce.

5.2.2.2 Phase Transitions

Two research groups have found evidence for a eutectic reaction in U-Ce alloys with high concentrations of U at ~1000°C [380, 381]. Detailed investigations established the eutectic temperature as 1106°C and showed that the maximum solubility of Ce in U at this temperature is ~0.18 at% [381].

Haefling and Daane reported that incorporation of 0.7 wt% Ce lowers the temperatures of the α-β and β-γ transformations in U to 636 and 752°C respectively [381].

5.2.2.3 Phase Diagrams

In 1959, Haefling and Daane published experimental data on U-Ce alloys at temperatures between 1000 and 1250°C. Several other reviews of the U-Ce system were published between 1958 and 1961 [207, 380, 386], based on a combination of published and unpublished data. Limits of solubility for similar compositions and temperatures in all of these publications are consistent; however, it is not clear to what extent they should be regarded as independent determinations. Only one of these reviews included a phase diagram (Figure 66).

Shoji et al. [382] determined the mutual solubility of high-purity U and Ce at four temperatures between ~1100 and 1350°C based on vapor-pressure measurements and published a more limited phase diagram based on their data and the data of Haefling and Daane [381]. The phase diagram of Shoji et al. shows the limits of the liquid miscibility gap at temperatures up to ~1525°C.

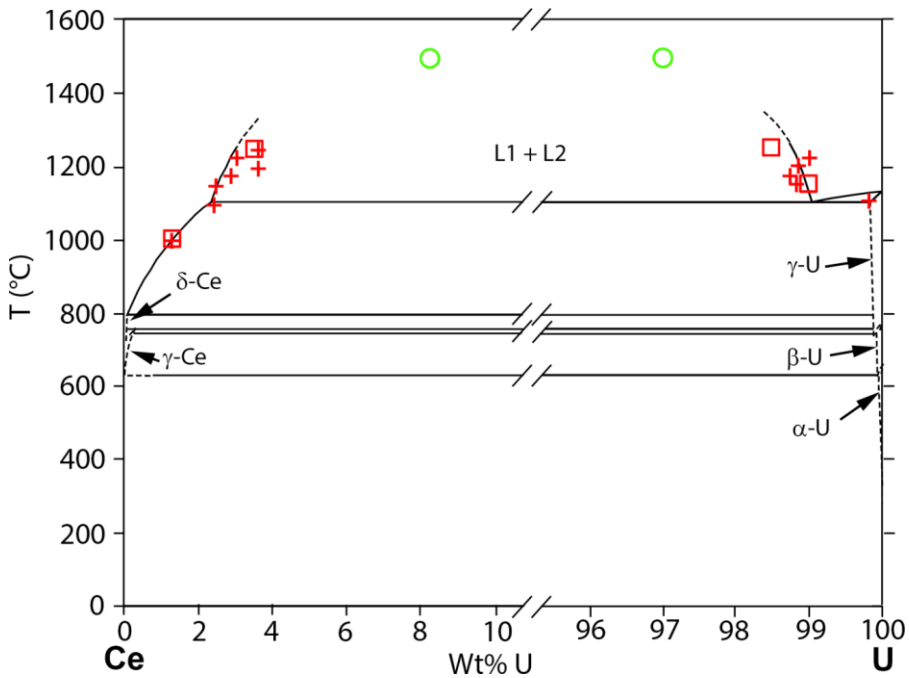

Figure 66. U-Ce phase diagram after Gschneidner [207 Figure 120]. Colored symbols indicate phase boundaries from Haefling and Daane [381] (red "+" symbols), Rough and Bauer [380] (red squares), and Shoji et al. [382] (green circles).

5.3 U-Pr

5.3.1 Introduction

Experimental data about phases in U-Pr alloys is limited to temperatures between 1000 and 1250°C. Most of the data was originally reported by Haefling and Daane in 1959 [381], although a survey by

Rough and Bauer [380] included other unpublished data. All of the available data suggest that U and Pr liquids and solids are almost completely immiscible and that there are no intermediate U-Pr phases.

Bayanov calculated a variety of thermodynamic properties for liquids in the U-Pr system [383], and McMurray and Silva used CALPHAD to perform a thermodynamic assessment of the U-Pr-O system [387].

No information about the heat capacity, thermal expansion, or thermal conductivity of U-Pr alloys is available.

5.3.2 Phases and Phase Transformations

Phase diagrams of the U-Pr system were suggested by Okamoto [388] and Peatfield et al. [389]. Both show very limited miscibility, with numerous phase transformations outside the temperature range of the experimental data. Neither of these phase diagrams provides a detailed representation of the available data.

According to Haefling and Daane, the maximum solubility of U in liquid Pr rises from 1.063 wt% at 1000°C to 2.028 wt% at 1250°C. The maximum solubility of Pr in liquid U rises from 0.22 wt% at 1150°C to 0.39 wt% at 1250°C. Solubilities in solid phases are unknown, but probably very low.

Haefling and Daane suggested that binary phase diagrams involving U and rare-earth elements whose melting temperatures are below that of U (including Pr) have high-U monotectic transformations similar to that in U-Ce. There is no experimental evidence to determine whether this transformation actually occurs in the U-Pr system.

Figure 67 shows the experimental data with tentative phase boundaries drawn for this Handbook based on analogy to the U-Ce system.

No experimental data about crystal structures, lattice parameters, or phase-transformation temperatures or enthalpies in U-Pr alloys are available. Given the low mutual solubility of U and Pr, it seems reasonable to assume that properties of high-U and high-Pr phases are similar to those of U and Pr.

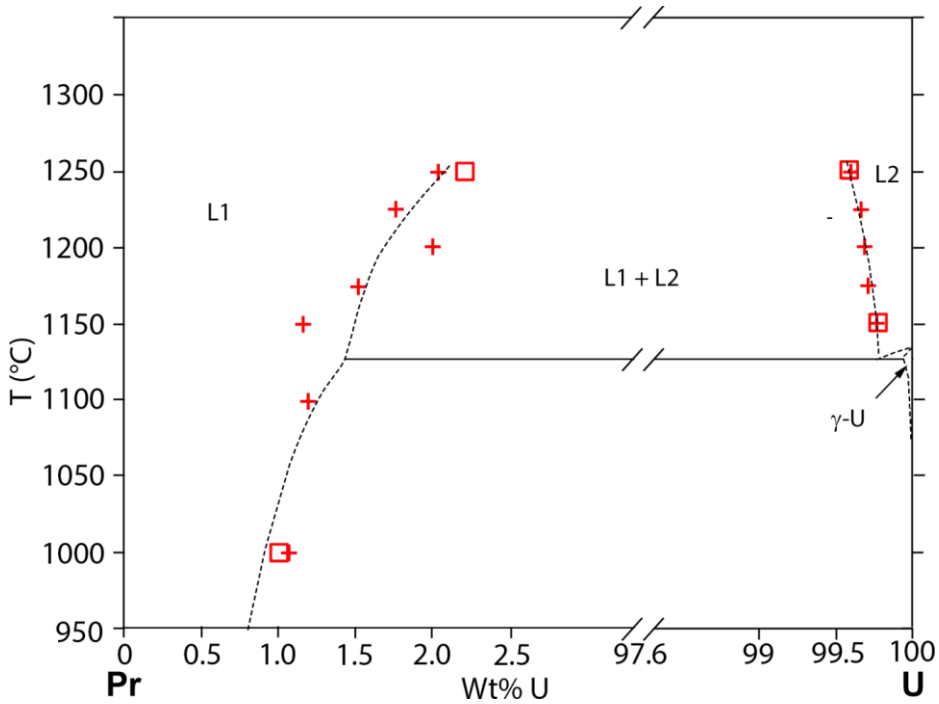

Figure 67. Tentative partial U-Pr phase diagram drawn for this handbook, with experimental data from Haefling and Daane ([381], red "+" symbols) and Rough and Bauer ([380], red squares). Shapes of phase boundaries were assumed to be analogous to those in the U-Ce system.

5.4 U-Nd

5.4.1 Introduction

Experimental data about phases in U-Nd alloys is limited to temperatures between 1000 and 1250°C. Most of the data was originally reported by Haefling and Daane in 1959 [381], although a summary by Rough and Bauer [380] includes earlier unpublished data. The experimental data are consistent and show that U and Nd liquids and solids are almost completely immiscible. Thermodynamic models confirm the immiscibility of U and Nd [390, 391].

No information about heat capacity, thermal expansion, or thermal conductivity of U-Nd alloys is available.

5.4.2 Phases and Phase Transformations

No experimental data about crystal structures, lattice parameters, or phase-transformation temperatures or enthalpies in U-Nd alloys is available. Given the low mutual solubility of U and Nd, it seems reasonable to assume that properties of high-U and high-Nd phases are similar to those of U and Nd.

Haefling and Daane identified a monotectic reaction similar to that in the U-Ce system, but did not report details [381].

5.4.2.1 Phase Diagrams

Parnell et al. [392] published a tentative U-Nd phase diagram as part of an experimental study of U-Nd-Pd ternary alloys (Figure 68,which shows only the temperature range for which there is experimental data). Although the miscibility gap in this phase diagram is narrower than indicated by the experimental data, the difference is small, and this remains the most detailed representation of the U-Nd

phase diagram because of the scale at which it is displayed. Okamoto published a similar diagram for temperatures between 500 and 1300°C [393], but at a scale that makes it impossible to recognize details.

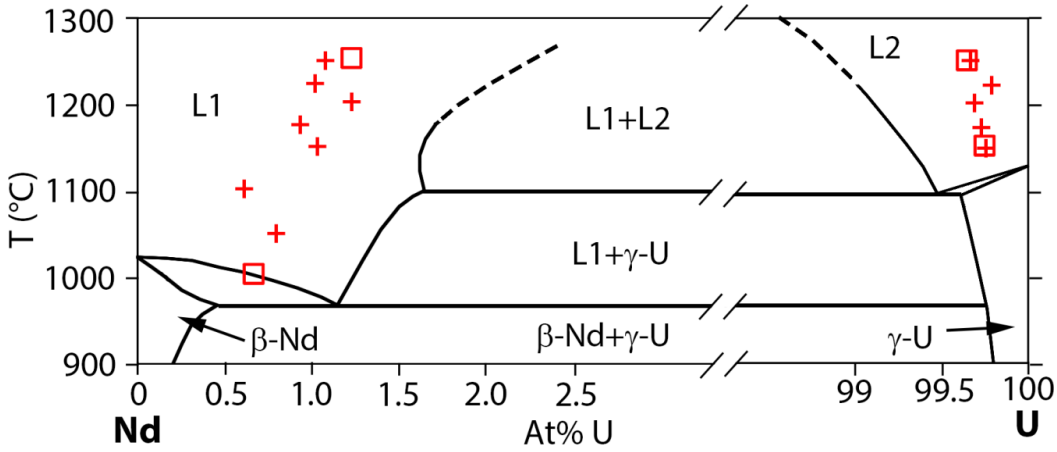

Figure 68. Tentative partial U-Nd phase diagram based on that of Parnell et al. [392], displaying only the temperature range for which there is experimental data. Red "+" symbols indicate data from Haefling and Daane [381]. Red squares indicate data from Rough and Bauer [380].

5.5 Np-La

There are no experimentally determined phase diagrams for the Np-La system, and the only available data is from a DTA study of an alloy with 48 at% La. This data indicated very limited miscibility and suggested that the Np-La phase diagram might be similar to the Pu-La diagram (Section 5.9) [168].

No information about the heat capacity, thermal expansion, or thermal conductivity of Np-La alloys is available.

In view of the apparently limited miscibility of the Np-La system at temperatures up to at least 1200°C, it seems reasonable to assume that phases in this system are similar to those in pure La and Np (Sections 2.5.2.1 and 2.2.2.1, respectively).

The DTA study indicated that the temperatures of all phase transitions in La and Np solid solution phases were lower than those in pure elements. The maximum difference in temperature was less than 15°C [168].

No experimentally determined phase diagrams of the Np-La system are available. Kurata calculated a phase diagram that is consistent with the very limited experimental data [300 Figure 14].

5.6 Np-Ce

There are apparently no Np-Ce phase diagrams. Studies of more complex alloys that include Np and Ce (e.g., [394-399]) show no evidence of phases that contain both Np and Ce, suggesting that these elements have very limited miscibility.

No information about the heat capacity, thermal expansion, or thermal conductivity of Np-Ce alloys is available.

5.7 Np-Pr

There are apparently no published studies of the Np-Pr phase diagram. Studies of more complex alloys that include Np, Ce, and Pr (e.g., [394-399]) show no evidence of phases containing both Np and Pr, suggesting that these elements have very limited miscibility.

No information about the heat capacity, thermal expansion, or thermal conductivity of Np-Pr alloys is available.

5.8 Np-Nd

There are apparently no published studies of the Np-Nd phase diagram, and the only available data is from a DTA study of an alloy with 40 at% Np [168]. This data indicated very limited miscibility and suggested that the Np-Nd phase diagram might be similar to the Pu-Nd diagram (Section 5.12.2.3). Phase-transition temperatures were reported to be unusually difficult to measure because of creeping and volatilization of molten Np-Nd alloys [168].

Studies of more complex alloys that include Np and Nd (e.g., [394-399]) show no evidence of phases containing both Np and Nd, consistent with the suggestion that these elements have very limited miscibility.

No information about the heat capacity, thermal expansion, or thermal conductivity of Np-Nd alloys is available.

5.9 Pu-La

5.9.1 Introduction

A preliminary experimental investigation of the Pu-La phase diagram was carried out by Poole et al. [305], followed by a more thorough investigation by Ellinger et al. [400]. The two investigations agreed about key features of the phase diagram including a liquid miscibility gap, very low solubility of La in all Pu allotropes, maximum solubility of ~20 at% Pu in β-La and γ-La, and no intermediate phases at temperatures above ~250°C. The Ellinger et al. phase diagram (Figure 69) is generally accepted.

Liu et al. [401] modeled the phase diagram using CALPHAD, obtaining good agreement with the experimental data.

No information about the heat capacity, thermal expansion, or thermal conductivity of Pu-La alloys is available.

5.9.2 Phases and Phase Transformations

5.9.2.1 Phases

Phases in the Pu-La system are [400]:

- (α-Pu), (β-Pu), (γ-Pu), (δ-Pu), (δ'-Pu), (ε-Pu): Allotropic solid solutions of Pu phases with very small solubility for La. La does not stabilize δ- or ε-Pu.
- (β-La): Allotropic solid solution of β-La with up to 19 at% Pu. The lattice parameters reported by Ellinger et al. [400] increase linearly from 5.240 Å for a sample with 80 at% La to 5.306 Å for pure β-La (consistent with the lattice parameter for β-La in Section 2.5.2.1).
- (γ-La): Allotropic solid solution of γ-La with up to 19 at% Pu.
- L1 (high-Pu liquid) and L2 (high-La liquid): Immiscible liquids. The limits of solubility and maximum temperature of the miscibility gap have not been experimentally determined.

A sample of (β-La) with 2.5 at% Pu that was annealed for 7 months at 250°C showed no evidence of transformation to (α-La) [400]. However, the β-α transformation is very sluggish in pure La (Section 2.5.2.2). Thus, although there is no experimental data about properties of α-La solid solutions that include Pu, it is nonetheless possible that these solid solutions exist.

5.9.2.2 Phase Transitions

Ellinger et al. report that the incorporation of small amounts of La in ε-Pu lowers the melting temperature by ~8°C. Melting temperatures of other Pu solid-solution phases are similar to those in pure Pu, possibly because of the low solubility of La in Pu.

Invariant points in the phase diagram of Ellinger et al. include [400]:

- L2 → L1 + (γ-La), a monotectic transformation at 846°C and 77 at% La
- γ-La → L1 + (β-La), an inverse peritectic (retrograde melting) transformation at 833°C and 82 at% La
- L2 → (ε-Pu) + (β-La), a eutectic transformation at 632°C. Ellinger et al. did not specify the composition at the eutectic, but their phase diagram suggests 1-2 at% Pu.

The phase diagram also shows a reaction, (β-La) → (α-La) + (α-Pu). Although this reaction seems plausible, it has not been experimentally observed and occurs below the minimum temperature of the experimental data.

5.9.2.3 Phase Diagrams

Figure 69 shows the Pu-La phase diagram proposed by Ellinger et al. [400]. This phase diagram appears in Massalski's compilation of phase diagrams [402] and in the ASM Alloy Phase Diagram Database [403].

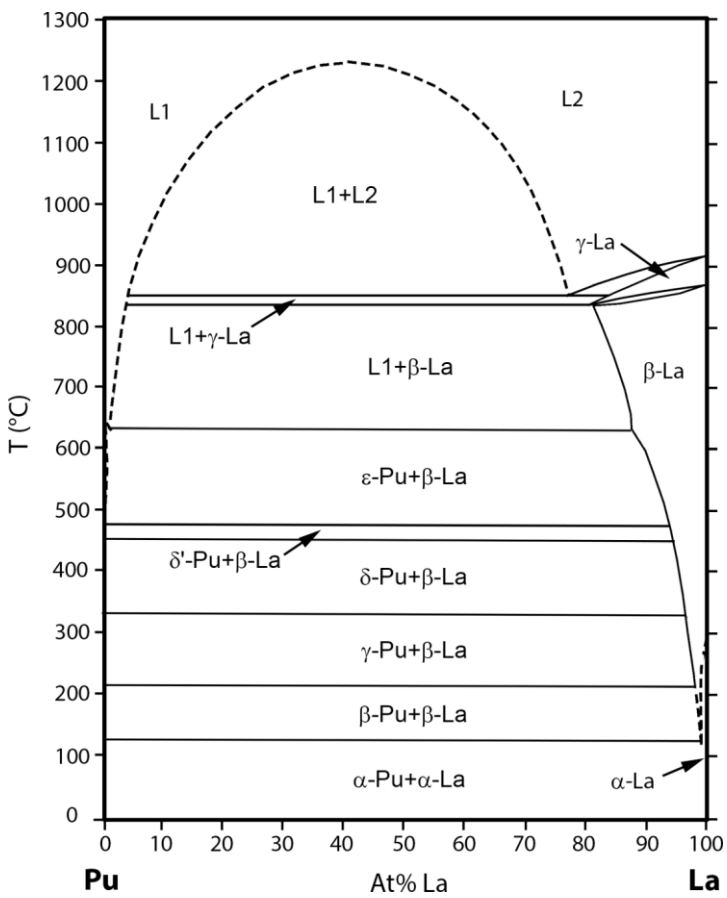

Figure 69. Pu-La phase diagram of Ellinger et al. (re-drawn from [400]).

Despite the generally good agreement between the experimental and modeling studies, further work is needed to determine the limits of the liquid miscibility gap. It may also be worthwhile to analyze the

entire phase diagram again because the La feedstock in the original experimental work was only ~99 wt% La and included ~2000 ppm Fe [400]; however, it seems unlikely that this investigation would cause changes in the key features of the phase diagram listed in the introduction to this section.

5.10 Pu-Ce

5.10.1 Introduction

Pu-Ce phase diagrams based on original investigations were published by Ellinger et al. in 1960 [404] and by Selle and Etter in 1964 [405], but have now been largely replaced by composite phase diagrams that combine selected features of the experimental phase diagrams with phase boundaries from other sources.

Key features of the all of the Pu-Ce phase diagrams include:

- Stability of δ-Pu solid solutions at room temperature.
- Extremely limited solubility of Ce in α-Pu, β-Pu, and γ-Pu.
- Significant solubility of Ce in ε-Pu.
- Significant solubility of Pu in γ-Ce and δ-Ce.
- Absence of intermediate phases.

Further experimental work on the Pu-Ce system is required. Careful consideration of sample purity, phase-transformation kinetics, possible existence of metastable phases, and fine-scale microstructures is crucial.

No information about the heat capacity of Pu-Ce alloys is available.

The thermal expansion of Ce-stabilized δ-Pu is qualitatiely similar to other δ-Pu alloys in that it is negative for alloys with low concentrations of Ce and positive for alloys with higher concentrations. Very little data about other crystal structures is available. The only information about the thermal expansion of Pu-Ce alloys with the β–Pu structure indicates that their average coefficient of thermal expansion is smaller than that of pure β-Pu, and that they expand more in the *b* crystallographic direction and less in the *a* and *c* directions than pure Pu. The only available data about the thermal expansion for Pu-Ce alloys with the ε-Pu structure indicates that the coefficient of thermal expansion is largely independent of temperature for alloys with up to ~6 at% Ce and increases slightly for alloys with higher Ce contents; however, the coefficient of thermal expansion for pure ε-Pu in this study is inconsistent with the values in Section 2.3.4.2.

No measurements of the thermal conductivity, thermal diffusivity, or electrical resistivity of Pu-Ce alloys at temperatures above room temperature are available. Two research groups reported room-temperature electrical resistivities, with inconsistent results. The only reported value of the Lorenz number requires verification, as it seems unexpectedly high relative to that of Pu.

5.10.2 Phases and Phase Transformations

5.10.2.1 Phases

Stable phases in the Pu-Ce system above room temperature are:

- (α-Pu): Allotropic solid solution of α-Pu with extremely limited solubility of Ce [404, 405]. Lattice parameters have not been reported but are probably similar to those of α-Pu.
- (β-Pu): Allotropic solid solution of β-Pu with extremely limited solubility of Ce [404, 405]. Lattice parameters have not been reported but are probably similar to those of β-Pu.

- (γ-Pu): Allotropic solid solution of γ-Pu. Both of the experimental phase diagrams indicate that solubility of Ce in this phase is limited [404, 405]; however, Elliott et al. [406] report that γ-Ce alloys with 15 at% Pu are metastable at room temperature. Lattice parameters of (γ-Pu) solid solutions have not been reported.
- (δ-Pu): Allotropic solid solution of δ-Pu with ~3-18 at% Ce at room temperature and up to 23-25 at% Ce at 613°C [404, 405]. Ellinger et al. notes that δ-Pu may be present in quenched samples with concentrations of Ce that are slightly lower than the minimum concentration required for room-temperature stability. The lattice parameter increases linearly from 4.6485 Å in alloys with 4.68 at% Ce to 4.6804 Å in alloys with 20.03 at% Ce [404].
- (δ'-Pu): Allotropic solid solution of δ'-Pu with less than 0.5 at% Ce [404]. This phase does not appear in the phase diagram of Selle and Etter [405]. Lattice parameters have not been reported but are probably similar to those of δ'-Pu.
- (ε-Pu): Allotropic solid solution of ε-Pu with up to 16 at% Ce [404, 405]
- (γ-Ce): Allotropic solid solution of γ-Ce with up to -35-37 at% Pu [404, 405]. Ellinger et al. refer to this phase as "β-Ce." The lattice parameter decreases linearly from 5.1534±0.0005 Å in alloys with 2 at% Pu to 5.009±0.006 Å in alloys with 30 at% Pu [404].
- (δ-Ce): Allotropic solid solution of δ-Ce with up to ~19.5 at% Pu [405]. Ellinger et al. refer to this phase as "γ-Ce" and say that it can have up to ~10 at% Pu [404].

Gschneidner et al. [238], Elliott et al. [406], and Giessen et al. [407] observed what they believed to be a metastable fcc phase in rapidly cooled Ce alloys with relatively low concentrations of Pu. Gschneidner et al. reported that this phase did not decompose during thermal or pressure cycling, while Elliott et al. thought that it might be an intermediate phase in the decomposition of metastable γ-Pu alloys to form δ-Pu as a result of thermal cycling or abrasion. Elliott et al. indicated that the lattice parameter of this phase was similar to that of δ-Pu. In the absence of research showing the conditions under which this phase forms and decomposes and its relationship to the other fcc phases in the Pu-Ce system (α-Ce, γ-Ce, and δ-Pu) , the significance of this phase for nuclear fuels is unclear.

Incorporation of Pu into (α-Ce) inhibits the formation of (β-Ce) and raises the temperature of the direct transformation from α-Ce to γ-Ce relative to that in pure Ce (Section 2.6.2.2). The maximum temperature for this transition is ~250 K in alloys with ~20 at% Pu [238].

5.10.2.2 Phase Diagrams

Two research groups have published Pu-Ce phase diagrams based on their own experimental studies. The first was published in 1960 by Ellinger et al. [404], and was based on a combination of thermal analysis, dilatometry, metallography, and room- and high-temperature X-ray diffraction data (Figure 70). This phase diagram indicates that δ-Ce transforms to γ-Ce by an "inverse peritectic" (retrograde melting) reaction.

Selle and Etter published the second phase diagram in 1964 [405], using data from thermal analysis, X-ray diffraction, and microprobe analysis (Figure 71). Despite many areas of general agreement, the two phase diagrams differ significantly in their depictions of the nature of the reaction between γ-Ce and δ-Ce. Selle and Etter resolved the disagreement by re-interpreting Ellinger's observations as consequences of non-equilibrium states. A later review by Ellinger et al. follows Selle and Etter's interpretation transformation [408].

According to both of these phase diagrams, invariant reactions in the Pu-Ce system are:

- L ↔ (ε-Pu) + (γ-Ce), a eutectic reaction. Ellinger et al. [404] reported that this reaction involves a liquid with 17.5 at% Ce, (ε-Pu) with 16 at% Ce, and (γ-Ce) with 77 at% Ce. Selle and Etter [405]

indicate that it involves a liquid with 16.5 at% Ce, (ε-Pu) with 16 at% Ce, and (γ-Ce) with 65.5 at% Ce. Both phase diagrams agree that this reaction occurs at at 625°C.

- (ε-Pu) + (γ-Ce) ↔ (δ-Pu), a peritectoid reaction. Ellinger et al. [404] reported that this reaction occurs at 592°C and involves (ε-Pu) with 12 at% Ce, γ-Ce with 63 at% Ce, and δ-Pu with 25 at% Ce. Selle and Etter [405] indicate that it occurs at 613°C and involves (ε-Pu) with 13.5 at% Ce, γ-Ce with 66.5 at% Ce, and δ-Pu with 23 at% Ce.

Both of the experimentally based phase diagrams have been largely replaced by phase diagrams combining selected aspects of the experimental phase diagrams with a liquidus that does not follow either. The maximum difference between liquidus temperatures in all of the phase diagrams is ~75°C, and occurs in compositions with ~20 at% Ce.

A composite phase diagram proposed by Rand et al. [409] (Figure 72) incorporated many of the solid-state reactions and invariant points from the phase diagram of Selle and Etter. This phase diagram is the basis for later phase diagrams published by Massalski et al. [410] and Okamoto [411]. A second composite phase diagram suggested by Ellinger et al. [408] is based on the original phase diagram of Ellinger et al. This phase diagram was reproduced by Giessen et al. [407]. The primary differences between these composite phase diagrams are the temperatures and compositions of invariant points (see above). It seems plausible that these differences are consequences of variations in sample purity or other experiment-specific conditions.

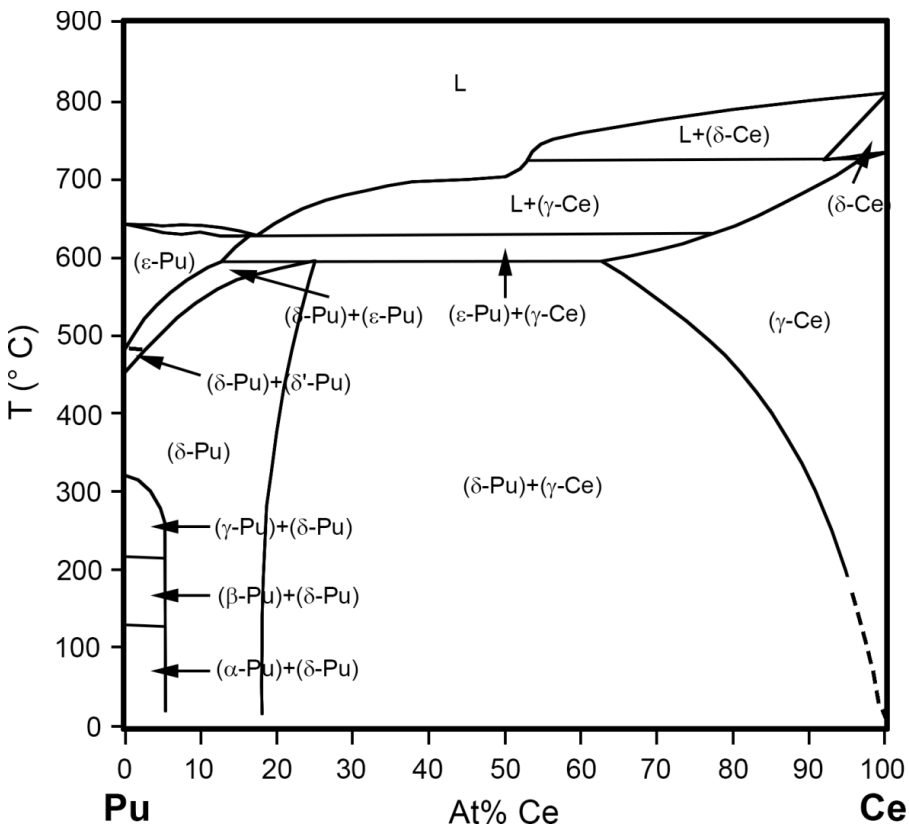

Figure 70. Pu-Ce phase diagram of Ellinger et al. (re-drawn from [404]).

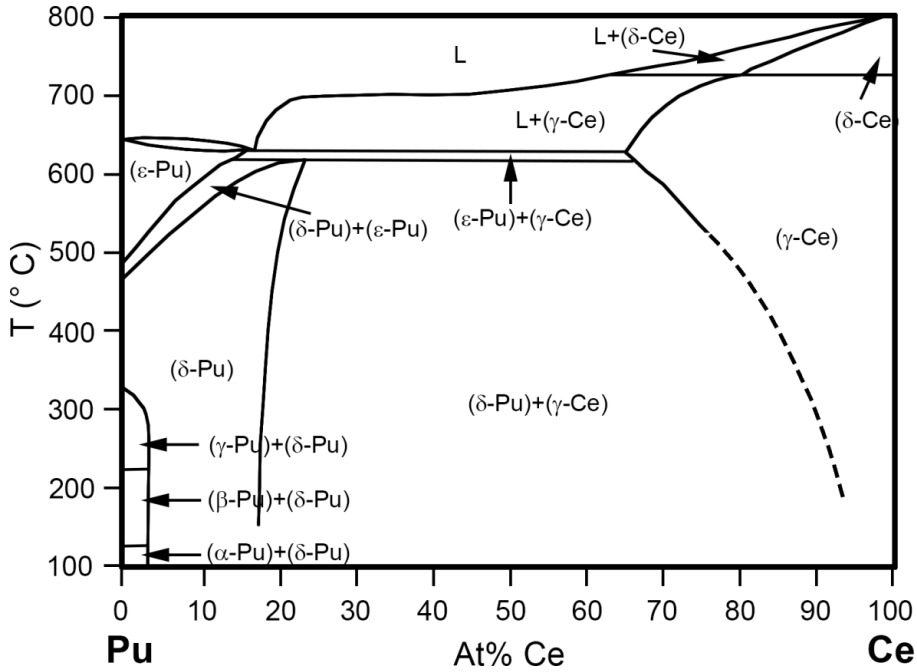

Figure 71. Pu-Ce phase diagram of Selle et al. (re-drawn from [405]).

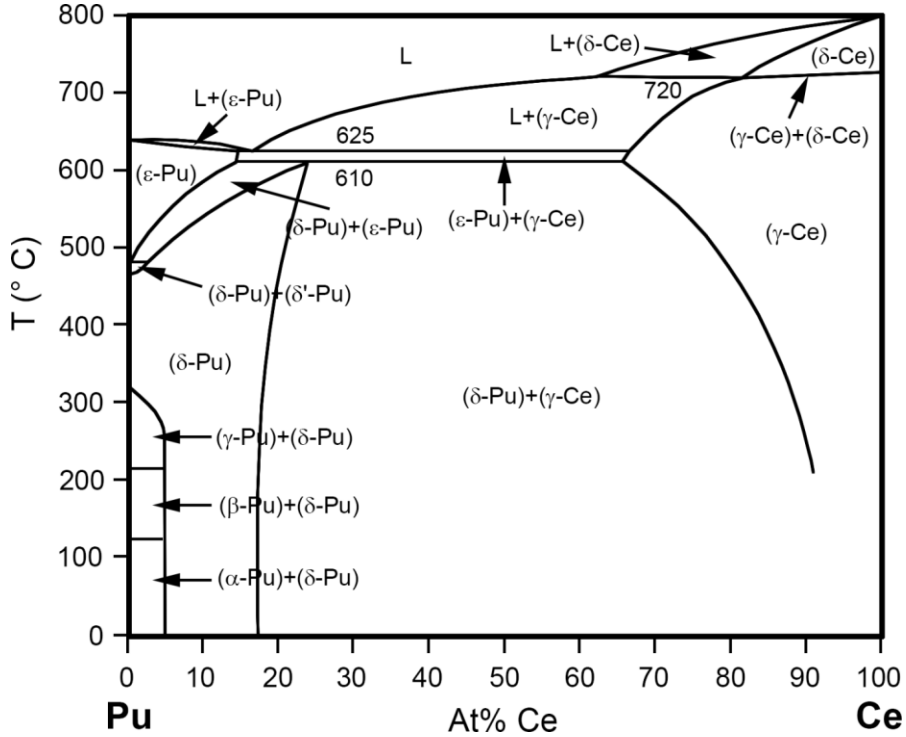

Figure 72. Composite Pu-Ce phase diagram (re-drawn from Okamoto [411]).

5.10.3 Thermal Expansion and Density

5.10.3.1 Thermal expansion of Pu-1Ce (at%) with the β-Pu structure

The only available measurements of the thermal expansion of Pu-Ce alloys with the β-Pu structure is from an alloy with 1 at% Ce [126, 150]. The principal coefficients of thermal expansion for this alloy are in Table 19. They are mutually orthogonal.

Expansion coefficients parallel to the crystallographic axes can be found in reference [150]. Because the crystal structure is monoclinic, these coefficients are not mutually orthogonal.

Comparison with the thermal expansion coefficients for pure β-Pu (Section 2.3.4.2) indicates that the orientation relationships between the crystallographic axes and the principal coefficients are similar in Pu and Pu-1Ce, and that Pu-1Ce expands more parallel to *b* and less parallel to *a* and *c* than pure β-Pu does.

Table 19. Principal linear thermal expansion coefficients for Pu-1Ce (at%) from 133 to 202°C [126, 150]. α_1, α_2, and α_3 are mutually orthogonal, with α_1 parallel to the direction of maximum thermal expansion, α_2 parallel to the *b* crystallographic axis, and α_3 approximately perpendicular to the $(10\bar{1})$ crystallographic plane. $\bar{\alpha}$ is the average of α_1, α_2, and α_3. φ is the angle between α_1 and the *b* crystallographic axis measured in the obtuse angle β and has a value of 38°.

Principal coefficient	Coefficient of linear thermal expansion ($\times 10^6$)
α_1	84
α_2	21
α_3	7
$\bar{\alpha}$	37

5.10.3.2 Thermal Expansion of Ce-stabilized δ-Pu

Experimental X-ray diffraction and dilatometry measurements of the thermal expansion of Ce-stabilized δ-Pu were published by Elliott et al. [412], Gschneidner et al. [413], Goldberg et al. [414], and Dormeval et al. [415]. The papers by Elliott et al. and by Gschneidner et al. were based on the same original experiments and many results are repeated in both papers. Unless indicated otherwise, the results presented here from Gschneidner and colleagues (including Elliott) are from reference [413] rather than [412], as it is the more recent of the two papers.

Gschneidner et al. [413] used least-squares fitting to develop equations to represent lattice parameters from X-ray diffraction data and sample lengths from dilatometry. They expressed their results in a quadratic equation and table of coefficients (Equation 78 and Table 20). Gschneidner et al. emphasized that these values should not be applied for temperatures outside the ranges specified in the table.

Equation 78. Lattice parameter (for X-ray diffraction data) or sample length (for dilatometer data) for Pu-Ce alloys, to be used with coefficients from Table 20 [413]

$$a = A + Bx10^{-5} \times T + C \times 10^{-8} \times T^2$$

where *a* is the lattice parameter (in Å) from X-ray diffraction data or the specimen length for dilatometer data, T is the temperature in °C, and A, B, and C are constants listed in Table 20.

Table 20. Coefficients for calculating thermal expansion of Pu-Ce alloys using Equation 78 [413].

At% Ce	T range (°C)	A	B	C	Measurement type[a]
1.0	294-446	4.6571	-8.881	6.48	XRD
1.4	295-437	4.6556	-9.033	7.79	XRD
2.0	313-392	4.6506	-3.782	—	XRD
2.4	288-445	4.6474	-3.907	—	XRD
3.0	289-457	4.6240	10.824	-19.63	XRD
3.4	276-448	4.6544	-3.778	—	XRD
4.0	297-452	4.6734	-13.258	14.53	XRD
5.0	356-441	0.98697	-1.145	—	DG Dil
8.0	19-473	4.6544	1.202	-0.38	XRD

a. XRD is X-ray diffraction, DG Dil is dial-gauge dilatometer.

Figure 73 shows lattice parameters calculated using Equation 78 and Table 20. The room-temperature lattice parameter of the alloy with 8% Ce and increase in lattice parameters with increasing concentration of Ce are consistent with the room-temperature data reported by Ellinger et al. [404] (Section 5.10.2.1).

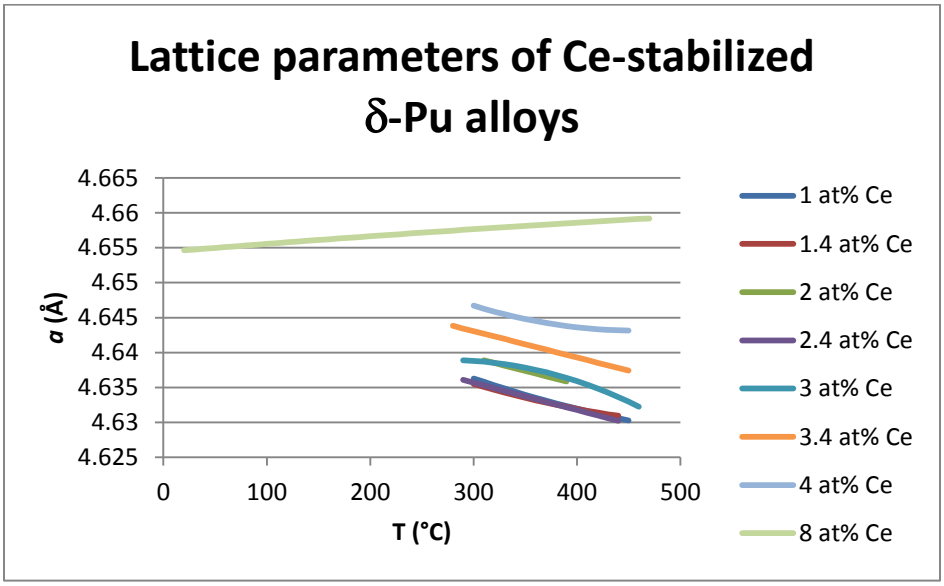

Figure 73. Lattice parameters of δ-Pu alloys from X-ray diffraction data (Equation 78 and Table 20).

Figure 74 shows the linear thermal expansion of Pu-Ce alloys reported by Gschneidner et al. [413]. Thermal expansion is negative for the alloys with Ce concentrations of 5 at% or less and positive for the alloy with 8% Ce, consistent with Figure 73 and the suggestion of Gschneidner et al. that the thermal expansion of δ-Pu alloys with ~6 at% Ce is zero. Although there is some scatter in the data, the thermal expansion for alloys with up to 5 at% Ce generally becomes less negative as the concentration of Ce increases.

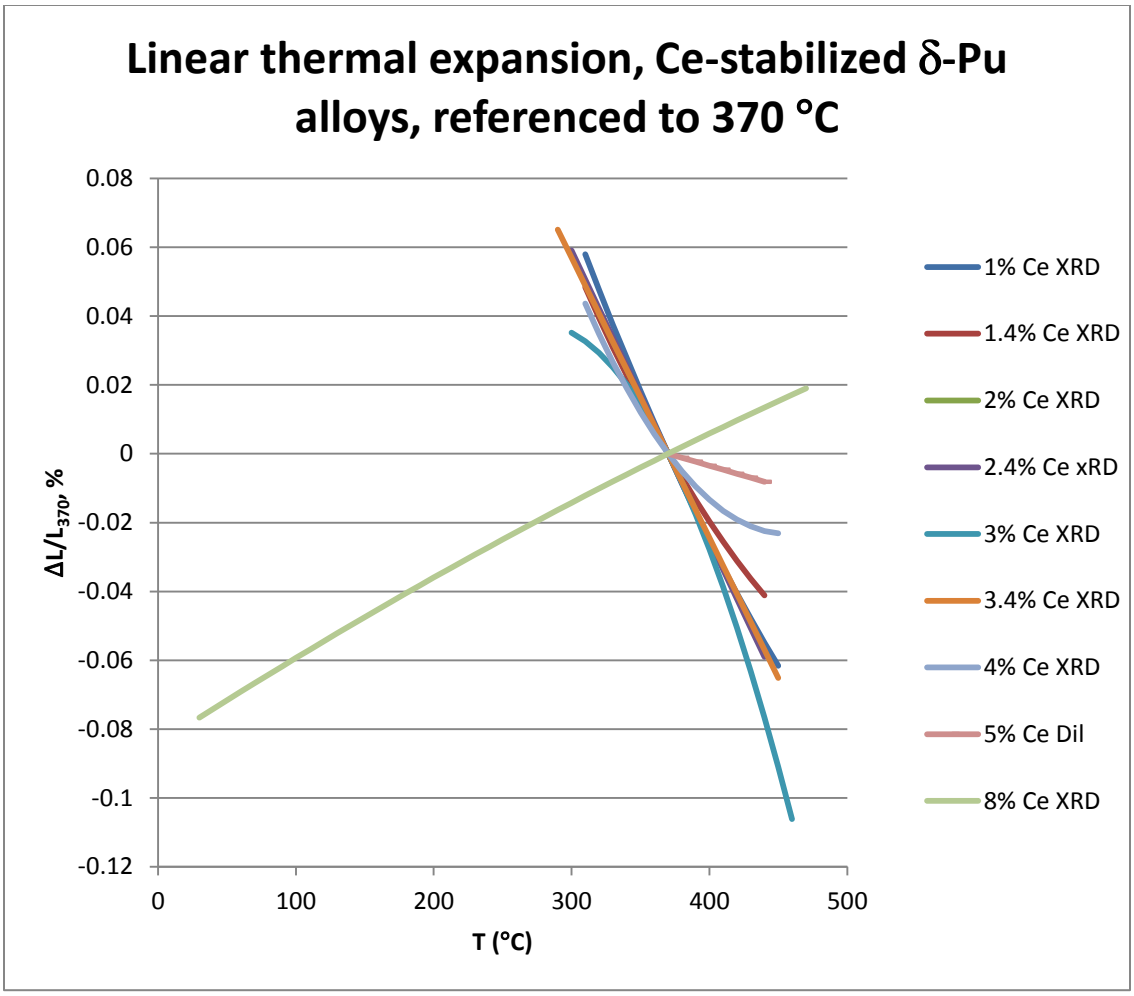

Figure 74. Linear thermal expansion from Equation 78, Equation 79, and Table 20, normalized to length at 370°C.

Equation 79. Linear thermal expansion of Ce-stabilized δ-Pu, referenced to 370°C

$$\frac{\Delta L}{L_{370}} = \frac{L - L_{370}}{L_{370}} \times 100$$

where $\Delta L/L_{370}$ is the linear thermal expansion in percent referenced to the lattice parameter (for X-ray diffraction data) or sample length (for dilatometer data) at 370°C, L is the lattice parameter or sample length at an arbitrary temperature, and L_{370} is the lattice parameter or sample length at 370°C.

5.10.3.3 Coefficients of Thermal Expansion of Ce-stabilized δ-Pu

Gschneidner et al. calculated the average values of the coefficients of linear thermal expansion using data from X-ray diffraction and two kinds of dilatometer (dial-gauge and strain-gauge). Their results, which should be used only within the temperature ranges specified, are in Table 21.

Table 21. Average coefficients of linear thermal expansion for Ce-stablized δ-Pu alloys [413].

At% Ce	T range (°C)	$\bar{\alpha}$ (× 10^6), °C^{-a}	Measurement type
1.0	300-440	-8.81	XRD
1.4	300-437	-7.10	XRD
2.0	313-392	-8.15	XRD
2.4	300-440	-8.43	XRD
3.0	300-440	-7.98	XRD
3.4	300-440	-8.14	XRD
3.4	280-438	-7.8	SG Dil
4.0	300-440	-5.39	XRD
5.0	356-440	-1.16	DG Dil
5.0	280-438	-5.1	SG Dil
5.9	280-438	+0.5	SG Dil
8.0	300-440	+1.98	XRD
8.0	280-438	+1.8	SG Dil
10.0	280-438	+3.1	SG Dil

a. XRD is X-ray diffraction, DG Dil is dial-gauge dilatometer, SG Dil is strain-gauge dilatometer.

Goldberg et al. [414] used a vertical dilatometer to measure thermal expansion of annealed Pu-Ce alloys with ~3-12 at% Ce and determined average coefficients of thermal expansion for temperature ranges of 300-450°C. They indicated that the thermal expansion became positive for compositions with more than ~7 at% Ce but did not report their data numerically.

Dormeval et al. [415] used a horizontal dilatometer to obtain coefficients of thermal expansion for δ-Pu solid solutions with 3.5-8.1 at% Ce. Their results were not reported numerically, but are generally consistent with values reported by other researchers (Figure 75).

Figure 75 shows the coefficients of thermal expansion from the experimental results of Goldberg et al. [414] and Dormeval et al. [415], and a curve that Goldberg et al. believed represented the thermal expansion of Pu-Ce alloys based on their data. Despite considerable scatter and an unusually low coefficient of thermal expansion for pure δ-Pu used by Goldberg et al. (-12.15 × 10^{-6}/°C, which is outside the range of values reported in Section 2.3.4.2), the curve appears to be a reasonably good representation of the data. It is not clear why different researchers obtain different values, although it has been suggested that both sample purity and measurement technique may be important [414] and that samples with low concentrations of Ce may contain both α-Pu and δ-Pu solid solution phases [415].

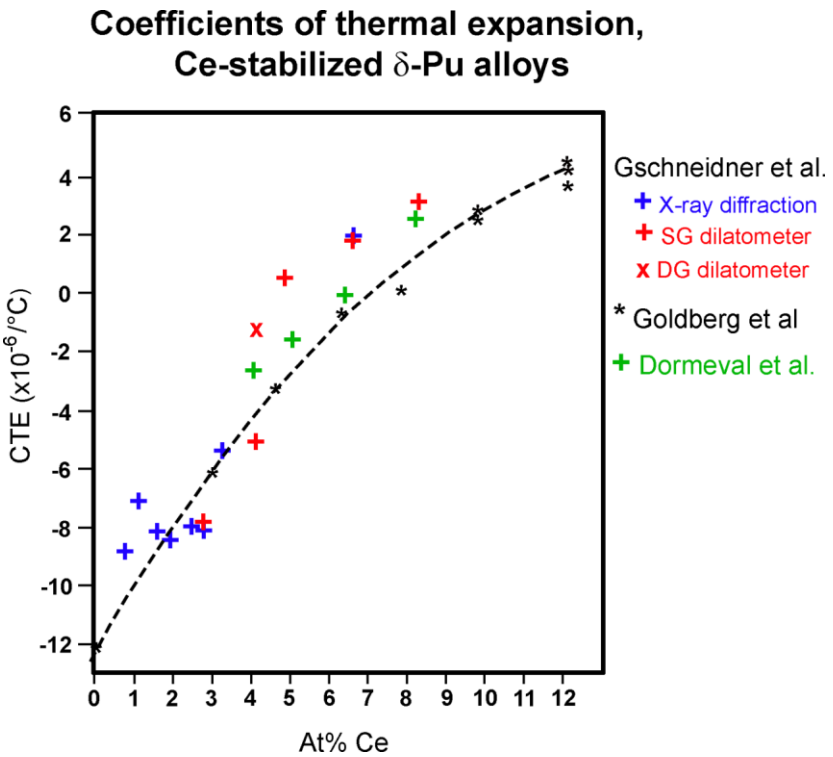

Figure 75. Coefficients of thermal expansion, Ce-stabilized δ-Pu alloys [413, 414]. The dashed line represents the "best fit" estimate of Goldberg et al. [414].

5.10.3.4 Coefficients of Thermal Expansion of ε-Pu Solid Solutions

The only available data on the thermal expansion of ε-Pu solid solutions in Pu-Ce alloys is from Goldberg et al. [414], who measured coefficients of thermal expansion for alloys with up to ~12 at% Ce. Their data shows that the coefficient of thermal expansion has only a limited dependence on composition for alloys with up to ~7 at% Ce, then increases with higher concentrations of Ce (Figure 76).

The coefficient of thermal expansion for ε-Pu in this data is only about 2/3 of the value listed in Section 2.3.4.2. Although the reasons for this difference are not known, Pu has been investigated more thoroughly than Pu-Ce alloys and the values in Section 2.3.4.2 are likely to be more accurate representations of the thermal expansion of Pu and Pu-Ce alloys than the data presented here. Further investigation is required.

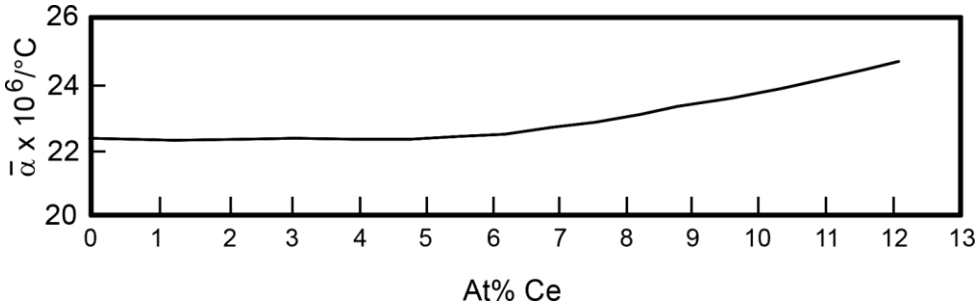

Figure 76. Coefficient of thermal expansion of ε-Pu solid solutions in Pu-Ce alloys as a function of composition (re-drawn from [414 (Figure 7)]).

5.10.3.5 Room Temperature Densities of Ce-stabilized δ-Pu Solid Solutions

Two values for the room-temperature density of Ce-stabilized δ-Pu solid solutions are available. One of these values (~15.3 g/cm^3) is obtained by calculating the density of an alloy with 8 at% Ce using Equation 5 from reference [5] with the lattice parameter calculated from Equation 78 and Table 20. The other value is the room-temperature density of 14.97 g/cm^3, which Andrew [416] reported without specifying how the value was obtained.

In combination, these values suggest that the room-temperature density of a Ce-stabilized δ-Pu alloy with ~8-10 at% Ce is approximately 15 g/cm^3. New measurements are needed if greater precision is required.

5.10.3.6 Densities of Pu-Ce Liquids as a Functions of Temperature

Researchers at Mound Laboratory measured the densities of Pu-Ce alloys with 4.8 and 75 at% Ce from the liquidus to 870°C using vacuum pycnometry [417]. They represented their results by Equation 80 and Equation 81, which indicate that densities of liquids at the liquidus are ~ 16.1 g/cm^3 for the alloy with 4.8 at% Ce and 8.6 g/cm^3 for the alloy with 75 at% Ce. Densities calculated using Equation 80 and Equation 81 are shown in Figure 77.

Equation 80. Density of a liquid Pu-Ce alloy with 4.8 at% Ce [417]

$$\rho = 17.319 - 19.22 \times 10^{-4} \times T$$

Where ρ is density in g/cm^3, T is temperature in °C, and T is between the liquidus (~639°C) and ~800°C

Equation 81. Density of a liquid Pu-Ce alloy with 75 at% Ce [417]

$$\rho = 9.094 - 7.93 \times 10^{-4} \times T$$

Where ρ is density in g/cm^3, T is temperature in °C, and T is between the liquidus (~745°C) and ~900°C

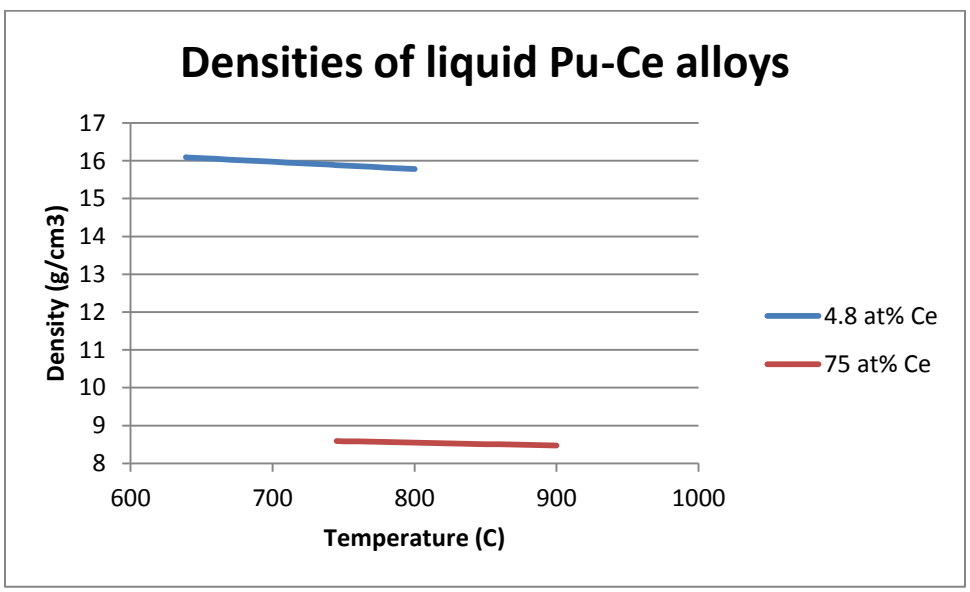

Figure 77. Densities of liquid Pu-Ce alloys in g/cm^3 (Equation 80 and Equation 81).

5.10.3.7 Volume Changes Due to Phase Transitions

Goldberg et al. [414] measured the δ-ε contraction (loss in volume associated with the transition from δ-Pu to ε-Pu solid solutions) in Pu-Ce alloys with up to ~12 at% Pu. The volume loss was always smaller than that in pure Pu (Section 2.3.4.4), and reached a minimum value at ~7 at% Ce (Figure 78).

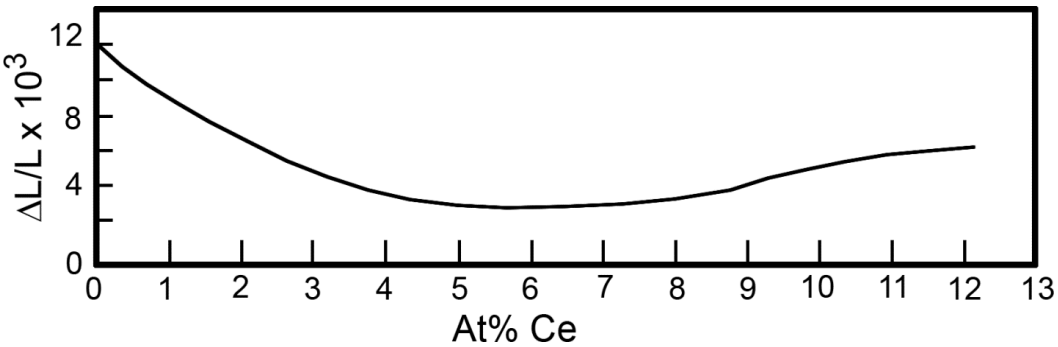

Figure 78. Change in length of Pu-Ce alloys associated with the transition from δ-Pu to ε-Pu structures as a function of composition [414 (Figure 6)].

Researchers at Mound Laboratory reported that volumes of Pu-Ce alloys with 4.8 or 75 at% Ce increased during the transformation from the liquid to the solid phase [417].

5.10.4 Thermal Conductivity and Related Properties

5.10.4.1 Thermal Conductivity

No measurements of the thermal conductivity, thermal diffusivity, or electrical resistivity of Pu-Ce alloys above room temperature are available. Andrew reported that the thermal conductivity of a Ce-stabilized δ-Pu solid solution with 10 at% Ce increases monotonically between 75 K and room temperature, with a room-temperature electrical resistivity of 98.1 μΩ-cm and thermal conductivity of ~10.75 W/m-K [416].

More recently, Dormeval et al measured the low-temperature electrical resistivities of Pu-Ce alloys with 4.6, 6.1, and 8.1 at% Ce, and reported room-temperature electrical resistivities between ~180 and 220 μΩ-cm. They found that the resistivities increased with the concentration of Ce and was essentially independent of temperature between ~150 and 300 K [415].

Electrical resistivity values in the two references are inconsistent, and further research is needed to determine accurate thermal conductivity values for Pu-Ce alloys.

5.10.4.2 Lorenz Number

Andrew used a modified Kohlrausch apparatus to determine that the the room-temperature electrical resistivity and thermal conductivity of Ce-stabilized δ-Pu alloy with 10 at% Ce are 98.1 μΩ-cm and 10.75 W/m-K respectively [416]. The corresponding Lorenz number (~3.86×10^{-8} WΩ/K^2) seems anomalously large in comparison to the recommended value of the room-temperature value of the Lorenz number for α-Pu (3.15×10^{-8} WΩ/K^2, Section 2.3.5.1).

5.11 Pu-Pr

5.11.1 Introduction

Two research groups published experimentally determined Pu-Pr phase diagrams in the 1960s. Kutaitsev et al. [418, 419] published a preliminary Pu-Pr phase diagram for temperatures up to 800°C. Ellinger et al. published a second phase diagram and brief discussion in 1968, followed by a more extensive

publication in 1969 [408, 420]. More recent references (including this handbook) follow the 1969 phase diagram of Ellinger et al. [420], which is more thoroughly investigated and documented than the phase diagram of Kutaitsev et al.

Key features of the Ellinger et al. phase diagram include complete miscibility of the liquid phase, limited solubility of Pr in any Pu phase, Pu contents up to 29-30 at% in α-Pr and β-Pr, coexistence of α-Pr and β-Pr in a limited temperature range, and an absence of intermediate phases. The Ellinger et al. Pu-Pr phase diagram shows an inverse peritectic (retrograde melting) reaction similar to that in their Pu-Ce phase diagram, which was re-interpreted after careful consideration of non-equilibrium microstructures (Section 5.10.2.2).

No information about the heat capacities, thermal expansion, or thermal conductivities of Pu-Pr alloys is available.

5.11.2 Phases and Phase Transformations

5.11.2.1 Phases

Solid phases in the Pu-Pr system at atmospheric pressure are [420]:

- (α-Pu): Allotropic solid solution of α-Pu with a monoclinic structure and no significant solubility of Pr. Lattice parameters have not been reported but are probably similar to those of α-Pu.
- (β-Pu): Allotropic solid solution of β-Pu with a monoclinic structure and no significant solubility of Pr. Lattice parameters have not been reported but are probably similar to those of β-Pu.
- (γ-Pu): Allotropic solid solution of γ-Pu with an orthorhombic structure and no significant solubility of Pr. Lattice parameters have not been reported but are probably similar to those of γ-Pu.
- (δ-Pu): Allotropic solid solution of δ-Pu with a face-centered cubic structure that can contain up to 2 at% Pr. (δ-Pu) solid solutions could be retained to room temperature in quenched alloys that contained 15 at% Pr, but not in samples made from filings with 5 at% Pr. Ellinger et al. believed this was because the (δ-Pu) alloys were stabilized by finely dispersed particles of (α-Pr). Lattice parameters have not been reported but are probably similar to those of δ-Pu.
- (δ'-Pu): Allotropic solid solution of δ'-Pu with body-centered tetragonal structure and no significant solubility of Pr. Lattice parameters have not been reported but are probably similar to those of δ'-Pu.
- (ε-Pu): Allotropic solid solution of ε-Pu with body-centered cubic structure that can contain up to 2 at% Pr.
- (α-Pr): Allotropic solid solution of α-Pr with a hexagonal structure that can contain up to ~27-29 at% Pu. Ellinger et al. noted that the *a* and *c* lattice parameters of this phase both increase linearly with the concentration of praseodymium.
- (β-Pr): Allotropic solid solution of β-Pr with body-centered cubic structure and up to ~30 at% Pu.

Ellinger et al. [420] observed that a face-centered cubic material which they called "α'-Pr" coexisted with α-Pr in alloys with 5 at% Pu, and noted that the fraction of α'-Pr generally increased with increasing temperature and concentration of plutonium. They thought that the transformation from α-Pr to α'-Pr might be a second-order reaction involving a change in stacking order and did not believe that α-Pr and α'-Pr were "separate phases in the usual sense." They were unable to distinguish α-Pr and α'-Pr in micrographic analyses. In a slightly earlier review with different authors, Ellinger et al. suggested that α'-Pr might be an impurity-stabilized phase [408].

5.11.2.2 Phase Transitions

According to Ellinger et al., addition of Pr decreases the melting temperature of Pu by ~15 degrees, forming a eutectic with 2-3 at% Pr. There is a second invariant point (an inverse peritectic reaction in which β-Pr decomposes to α-Pr and liquid upon cooling) at 794°C and 30 at% Pu. The transformation from α-Pr to β-Pr is congruent, and occurs over a narrow temperature range between 792°C for pure Pr and 801°C for alloys with 10 at% Pu.

5.11.2.3 Phase Diagrams

Kutaitsev et al. [418, 419] published a preliminary Pu-Pr phase diagram for temperatures up to 800°C (Figure 79). Little information about experimental methods is provided, and the results are presented in one figure and one paragraph. The Kutaitsev phase diagram shows that incorporation of ~15-20 at% Pu causes a decrease of several hundred degrees in the melting temperature of (α-Pr), leading to a broad range of temperatures over which (α-Pr) and (β-Pr) coexist. A statement that, "In alloys containing more than 5% plutonium, the face-centered cubic lattice of the β-phase of praseodymium can be retained down to room temperature by quenching" [419 (page 1280)] suggests that Kutaitsev et al. may have observed a face-centered cubic phase; however, its identity and relationship to other Pu-Pr phases are unclear because the structure of β-Pr is bcc rather than fcc.

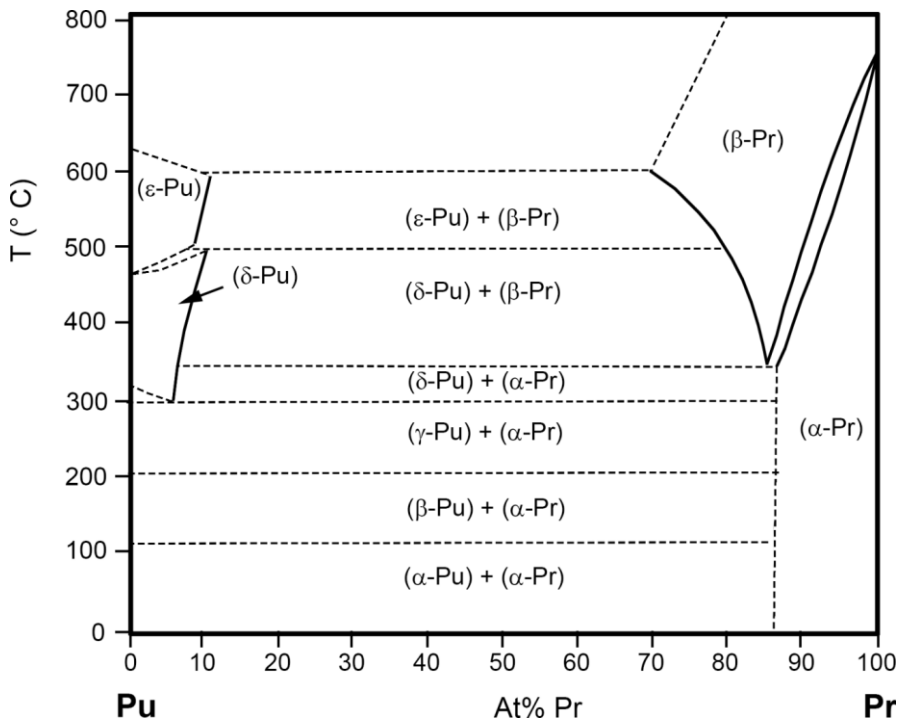

Figure 79. Pu-Pr phase diagram of Kutaitsev et al. (re-drawn from [419]).

Ellinger and colleagues developed a second Pu-Pr phase diagram using data from thermal analysis, X-ray diffraction, and metallography [408, 420] (Figure 80). Although this is the most commonly accepted Pu-Pr phase diagram, several features suggest areas where further research is needed:

- The liquidus. Ellinger et al. suggested that the liquidus for compositions with 10-40 at% Pr may be less flat than is shown in the figure because of experimental difficulties caused by the segregation of rare-earth phases near the top of the sample during slow heating.
- The nature, occurrence, stability, and formation mechanism of the fcc material α'-Pr and its relationship to other Pu-Pr phases

- The transformation between (β-Pr) and (α-Pr) during cooling. Ellinger et al. indicated that this transformation involves an inverse peritectic (retrograde melting) reaction in which β-Pr decomposes into α-Pr and a Pu-rich liquid. A similar transformation in Pu-Ce was later re-interpreted as a consequence of disequilibrium in the sample (Section 5.10.2.2).

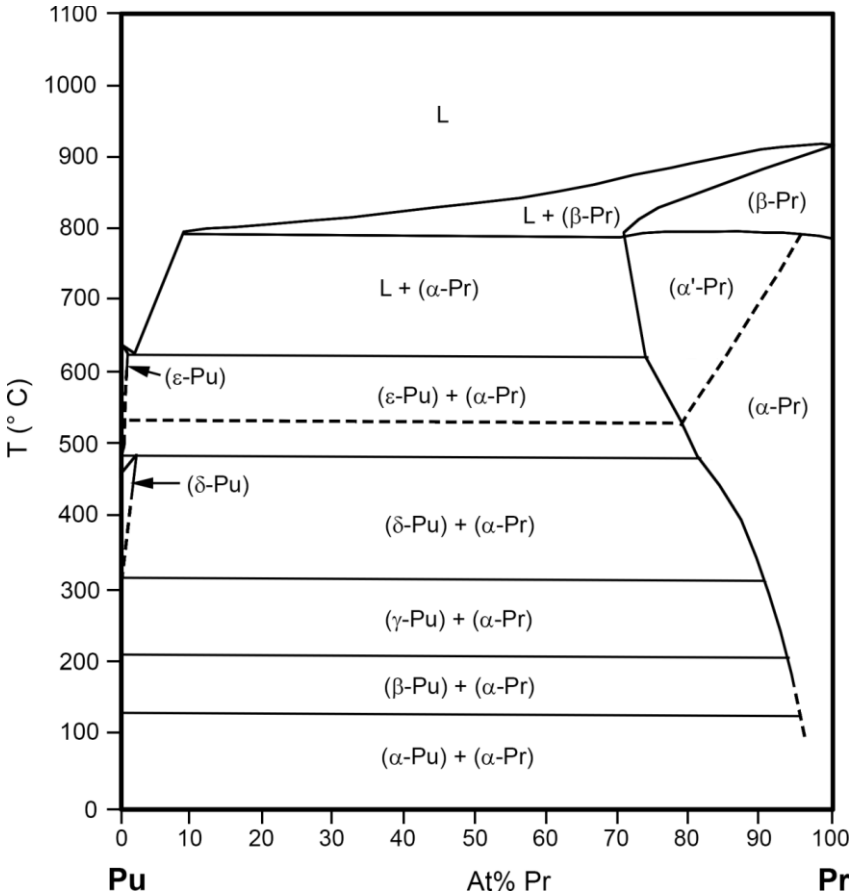

Figure 80. Pu-Pr phase diagram of Ellinger et al. (re-drawn from [420]).

Further investigation of phases in Pu-Pr alloys is required. Careful consideration of sample purity, phase-transformation kinetics, and fine-scale microstructures is crucial. In addition to providing information about the Pu-Pr system, this investigation may increase our understanding of the enigmatic face-centered cubic structures that have been reported in pure Pr and in Pu-Ce and perhaps Pu-Nd alloys (Sections 2.7.2.1, 5.10.2.1, and 5.12.2.1, respectively) in addition to Pu-Pr alloys.

5.12 Pu-Nd

5.12.1 Introduction

Two research groups published experimentally determined Pu-Nd phase diagrams in the 1960s. Although the phase diagrams differ significantly, each closely resembles the Pu-Pr phase diagram proposed by the same research group (Section 5.11.2.3). Kutaitsev et al. [418, 419] published a preliminary Pu-Nd phase diagram for temperatures up to 800°C. Ellinger et al. published a second phase diagram and brief discussion in 1968, followed by a more extensive publication in 1969 [408, 420]. The phase diagrams show numerous areas of disagreement. More recent references (including this handbook) follow the 1969 phase diagram of Ellinger et al. [420], which is more thoroughly researched and documented than the phase diagram of Kutaitsev et al.

Key features of the Ellinger et al. phase diagram include complete miscibility of the liquid phase, limited solubility of Nd in any Pu phase, Pu concentrations up to 29-30 at% in α- and β-Nd, coexistence of α-Nd and β-Nd over a limited temperature range, and an absence of intermediate phases. The Ellinger et al. Pu-Nd phase diagram shows an inverse peritectic (retrograde melting) reaction similar to that in their Pu-Ce phase diagram, in which the reaction was re-interpreted after careful consideration of non-equilibrium microstructures (Section 5.10.2.2).

No information about the heat capacity, thermal expansion, or thermal conductivity of Pu-Nd alloys is available.

5.12.2 Phases and Phase Transformations

5.12.2.1 Phases

Stable phases in the Pu-Nd system are [420]:

- (α-Pu): Allotropic solid solution of α-Pu with no significant solubility of Nd. Lattice parameters have not been reported but are probably similar to those of α-Pu.
- (β-Pu): Allotropic solid solution of β-Pu with no significant solubility of Nd. Lattice parameters have not been reported but are probably similar to those of β-Pu.
- (γ-Pu): Allotropic solid solution of γ-Pu with no significant solubility of Nd. Lattice parameters have not been reported but are probably similar to those of γ-Pu.
- (δ-Pu): Allotropic solid solution of δ-Pu that can contain up to 2 at% Nd. The (δ-Pu) solid solution could be retained to room temperature in quenched alloys that contained 15 at% Nd, but not in samples made from filings with 5 at% Nd. Ellinger et al. believed this was because the (δ-Pu) alloys were stabilized by finely dispersed particles of (α-Nd) [420]. Lattice parameters have not been reported but are probably similar to those of δ-Pu.
- (δ'-Pu): Allotropic solid solution of δ'-Pu with no significant solubility of Nd. Lattice parameters have not been reported but are probably similar to those of δ'-Pu.
- (ε-Pu): Allotropic solid solution of ε-Pu that can contain up to 2 at% Nd.
- (α-Nd): Allotropic solid solution of α-Nd that can contain up to ~27-29 at% Pu. The *a* lattice parameter of this phase increases linearly from 3.597 Å for an alloy with 75 at% Nd to 3.6646 Å for an alloy with 95% Nd. The *c* lattice parameter increases linearly from 11.614 Å for an alloy with 75 at% Nd to 11.760 Å for an alloy with 95% Nd.
- (β-Nd Allotropic solid solution of β-Nd with up to ~30 at% Pu.

Ellinger et al. specifically stated that they did not observe a high-Nd fcc phase. The 1965 paper by Kutaitsev et al. [418 (page 422)] referred to a "f.c.c. solid solution of β-Nb" (probably a typographical error that should have read β-Nd) in alloys with more than 5 at% Pu; however, this phase is not mentioned in a 1967 paper by Kutaitsev et al. [419] that otherwise generally repeats the results from the 1965 paper.

5.12.2.2 Phase Transitions

According to Ellinger et al., the melting temperature of Pu decreases by ~15 degrees to a eutectic with 2-3 at% Nd. A second invariant point (an inverse peritectic reaction in which β-Nd decomposes to α-Nd and liquid upon cooling) occurs at 820°C and 33 at% Pu.

5.12.2.3 Phase Diagrams

Kutaitsev et al. [418, 419] published a preliminary Pu-Nd phase diagram for temperatures up to 800°C. Little information about experimental methods is provided, and the results are presented in one figure and one paragraph. Their phase diagram (Figure 81) shows that incorporation of ~15-20 at% Pu causes a decrease of several hundred degrees in the melting temperature of (α-Nd), leading to a broad range of temperatures over which (α-Nd) and (β-Nd) coexist.

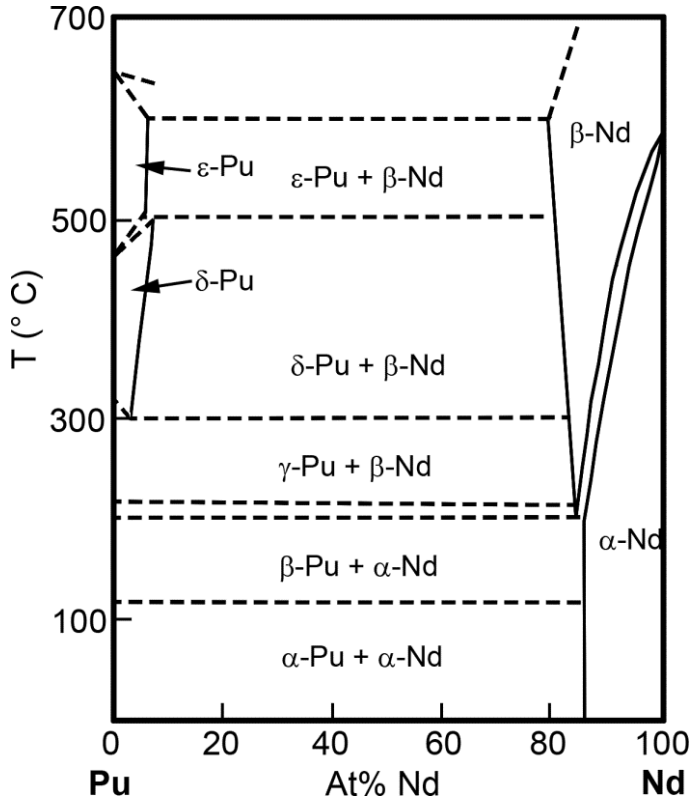

Figure 81. Pu-Nd phase diagram of Kutaitsev et al. [419].

Ellinger and colleagues developed a second Pu-Nd phase diagram using data from thermal analysis, X-ray diffraction, and metallography [408, 420] (Figure 82). Although this is the most commonly accepted Pu-Nd phase diagram, further research is needed in at least two areas:

- The liquidus. Ellinger et al. suggested that the liquidus for compositions with 10-40 at% Nd may be less flat than is shown in their phase diagram because of experimental difficulties caused by the segregation of rare-earth phases near the top of the sample during slow heating.
- The transformation from (β-Nd) to (α-Nd) during cooling. Ellinger et al. indicated that this transformation involves an inverse peritectic (retrograde melting) reaction in which (β-Nd) decomposes into (α-Nd) and a Pu-rich liquid. A similar transformation in the Pu-Ce phase diagram which was later re-interpreted as a consequence of disequilibrium in the sample (Section 5.10.2.2).

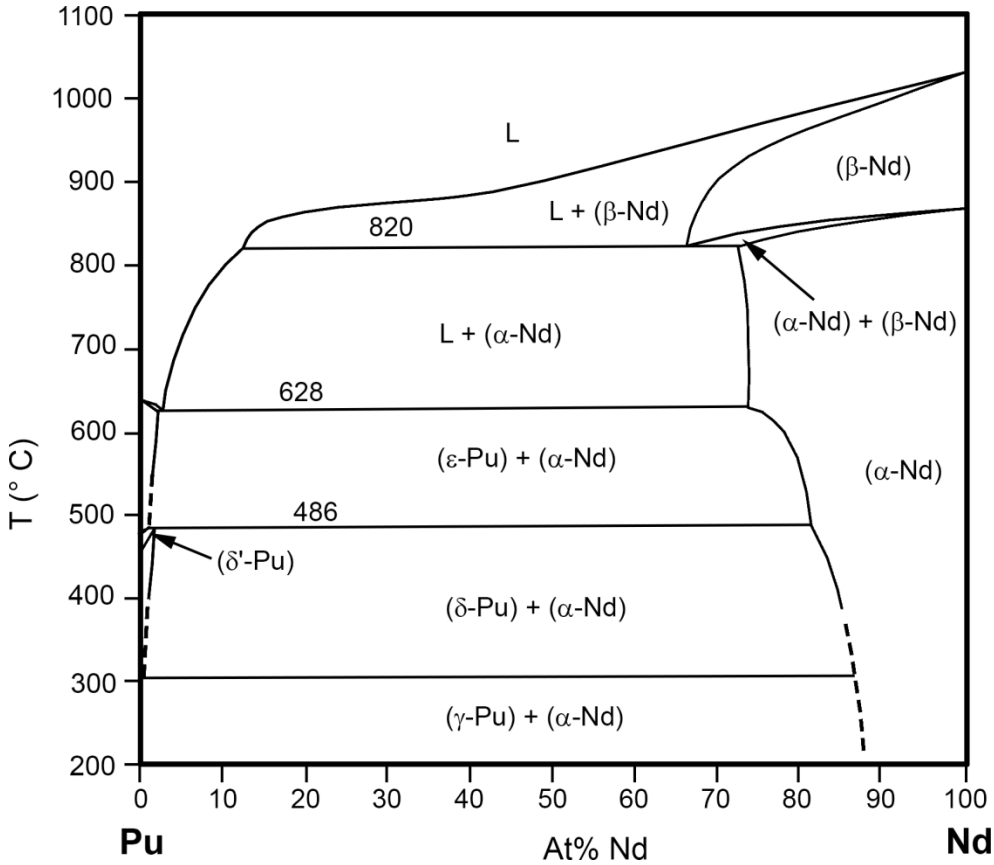

Figure 82. Pu-Nd phase diagram after Ellinger et al. [408, 420].

5.13 Am-La

5.13.1 Introduction

There are apparently no systematic investigations or published phase diagrams of the Am-La binary system, and experimental data at room temperature and above are limited to a single study involving alloys with at most ~3 at% Am [421].

No information about the heat capacity, thermal expansion, or thermal conductivity of Am-La alloys is available. Room-temperature densities of fcc phases can be calculated from lattice parameters in Table 22 using Equation 5 from reference [5].

5.13.2 Phases

Table 22 shows relationships between lattice parameters and as-cast compositions of La and three La-Am alloys determined using X-ray diffraction [421]. Samples were produced by arc-melting. Significant weight losses during casting were assumed to result from volatilization of Am, leading to differences between starting and as-cast compositions. All four materials had fcc structures.

Lattice parameters of the Am-La alloys decrease linearly as a function of Am content. If it is assumed that the measurements represent equilibrium phases, the X-ray diffraction data suggest that the maximum solubility of Am in β-La is at least 3 at%.

The lattice parameter of the La sample in Table 22 is consistent with the lattice parameter of 5.303 Å at 598 K for β-La in Section 2.5.2.1.

Table 22. Lattice parameters of arc-melted La and Am-La alloys [421].

Starting Am (at%)	As-cast Am (at%)	Lattice parameter (Å)
0	0	5.3058
1.25	0.92	5.3017
2.20	1.39	5.2998
3.70	2.73	5.2932

5.14 Am-Ce

There are no systematic investigations or published phase diagrams of the Am-Ce binary system. Small amounts of information have been published in a report and patent award addressing possible uses of Am-Ce alloys as radiation sources or materials for radiation detectors [422, 423]. The purity of the starting materials was not reported because it is not important for the intended uses of the alloys.

Conner [423] reported the room-temperature densities of Ce and of alloys with 10.5 and 21 wt% Am as 6.771, 7.183 and 7.649 g/cm^3 respectively. If it is assumed that the Ce is β-Ce, the Ce density reported by Conner is in reasonably good agreement with the value of 6.689 g/cm^3 in the CRC Handbook of Chemistry and Physics [191].

No other information about the heat capacity, thermal expansion, or thermal conductivity of Am-Ce alloys is available.

6. BINARY ALLOYS OF A MINOR ACTINIDE (Np, Am) WITH Zr

6.1 Np-Zr

6.1.1 Introduction

Two groups of researchers have attempted to determine the Np-Zr phase diagram experimentally, leading to contradictory phase diagrams. Both phase diagrams were considered “tentative” or “preliminary” by the authors of the papers describing them. One important difference between the phase diagrams is that the phase diagram of Rodríguez et al. shows a continuous solid solution between the bcc phases γ-Np and β-Zr [424] and the phase diagram of Gibson et al. does not [425-428]. Another difference involves the number of intermediate phases (one in the phase diagram of Rodríguez et al. and two in the phase diagram of Gibson et al.).

The available phase-transition temperatures are generally consistent with either of the proposed phase diagrams. Attempts to use models to determine which phase diagram is correct have consistently led to the conclusion that further experimental data is required [300, 429-432]. Although the 2018 phase diagram of Xie and Morgan [296] showed a miscibility gap between bcc Np and Zr phases, it cannot be used to assess whether the gap exists because the existence of the gap was assumed during model development.

Further experimental investigations of this phase diagram are clearly needed. It is particularly important to understand the miscibility between γ-Np and β-Zr because of its implications for predicting possible high-Np phases in fuels containing minor actinides. In the absence of this research, the phase diagram of Rodríguez et al. [424], which shows a continuous solid solution between γ-Np and β–Zr, seems less plausible than that of Gibson et al. [425-428], which does not. The reasons for this assessment are discussed below. It should be noted, however, that the existence of a miscibility gap between the bcc phases in the Np-Zr phase diagram implies significant differences between the Np-Zr system and the U-Zr and Pu-Zr systems, both of which have complete bcc solid solutions between actinides and Zr

(Sections 2.1.1.3 and 2.2.1.2.3 of reference [5]). Ogawa et al. proposed a possible explanation for these differences in terms of the behavior of the 5*f* electrons [429].

No information about heat capacities, thermal expansion, or thermal conductivity of Np-Zr alloys is available.

6.1.2 Phases and Phase Transformations

6.1.2.1 Phases

No systematic survey of phases in the Np-Zr system is available, although some observations have been published. In the absence of experimental data, it may be necessary to assume that Np-Zr phases are similar to those in Np and Zr. Based on this assumption, phases in the Np-Zr system are:

- (α-Np): Allotropic solid solution of α-Np with negligible solubility of Zr [433]
- (β-Np): Allotropic solid solution of β-Np. No other information is available.
- (γ-Np) Allotropic solid solution of γ-Np. The phase diagram of Rodríguez et al. shows a continuous solid solution between γ-Np and β-Zr [424]; that of Gibson and colleagues does not [425-428]. Gibson and Haire suggested that incorporation of Zr might stabilize γ-Np at the expense of β-Np and possibly of α-Np [426].
- (α-Zr): Allotropic solid solution of α-Zr with a maximum of ~10% Np, decreasing to zero as the temperature increases to 600°C [433]. Incorporation of Np into α-Zr increased the *c* lattice parameter by 4.0 pm and did not change the *a* parameter [433].
- (β-Zr) Allotropic solid solution of β-Zr. The phase diagram of Rodríguez et al. shows a continuous solid solution with γ-Np; that of Gibson and colleagues does not.
- δ-$NpZr_2$: Hexagonal solid-solution phase (space group *P*6/*mmm*, *a* = 5.024 Å, *c* = 3.075 Å) [433], with a structure similar to those of δ-UZr_2 and κ-$PuZr_2$ (Sections 2.1.1.2.1.1.5 and 2.2.1.2.1 of reference [5]). High-temperature powder diffraction data indicates that δ-$NpZr_2$ decomposes at ~550 C [434]. The range of compositions in this phase is unknown.
- θ-(Np,Zr) Intermediate phase analogous to θ-(Pu,Zr). Similarities between powder patterns of this phase and those of Pu_4Zr (Section 2.2.1.2.1 of reference [5]) suggest that θ-(Np,Zr) is a tetragonal phase with composition Np_4Zr; however, a composition of Np_6Zr has also been suggested [433]. This phase appears in the phase diagram of Gibson et al. [425] and in some modeled phase diagrams [300, 430-432], but not in the phase diagram of Rodríguez et al. [424]. No analyses of the composition of this phase are available.

6.1.2.2 Phase Transitions

Although both Gibson et al. and Rodríguez et al. published phase-transformation temperatures, it is not clear which transitions are associated with each temperature. It seems likely that some temperatures represent more than one transition. Many of the measurements were described as "preliminary."

Table 23 summarizes the available experimental data on phase transition temperatures. Values for DSC data include ranges of onset temperatures observed during heating of similar samples. Ranges of values for dilatometry data are those given by Rodríguez et al. [424].

Table 23. Phase-transformation temperatures in Np-Zr alloys.

Composition (at% Np)	T (°C)	Experiment type	References
9	545-577, 780, 1630	Dilatometer	[424]
25	540, 630?	DSC	[426, 427]

Table 23. (continued).

Composition (at% Np)	T (°C)	Experiment type	References
28	530-543, 1325	Dilatometer	[424]
50	511-540, 638-640	DSC	[426, 427]
52	540-550, 640	DSC	[426, 427]
60	533-542, 615-642, 894	Dilatometer	[424]
73	270, 550, 640	DSC	[426, 427]
78	280, 550-553, 640	DSC	[426, 427]

Table 24 includes the only available experimental data on enthalpies of phase transitions.

Table 24. Phase-transformation enthalpies in Np-Zr alloys [426].

Wt% Np	T (°C)	ΔH (J/g)
90	553	13.514
74	540	4.444
—	640	37.7787
72	511	6.156
—	638	24.406
46	540	8.333

6.1.2.3 Phase Diagrams

The phase diagram of Gibson et al. [425-428] (Figure 83) was developed using DSC data. Much of the data was collected using an "in-situ alloying" technique in which starting materials were melted during the first heating and data on properties of alloys was collected during later heating cycles [426]. Later work including both in-situ alloying and arc-melted samples found that results of these techniques were comparable [427].

The DSC data showed that Np-Zr alloys with up to ~20 at% Zr have the same melting temperature as pure Np. Because the melting temperature of β-Zr is much higher than that of γ-Np, and because other actinide-Zr phase diagrams with complete miscibility between bcc actinides and Zr show sharp increases in melting temperature with increasing concentrations of Zr, Gibson et al. interpreted their data as indicating a miscibility gap between β-Zr and γ-Np. Later measurements using high-temperature X-ray diffraction data showing that the maximum concentration of Zr in γ-Np is only ~4% at 600°C support the conclusion that there is no continuous high-temperature Np-Zr solid solution [434].

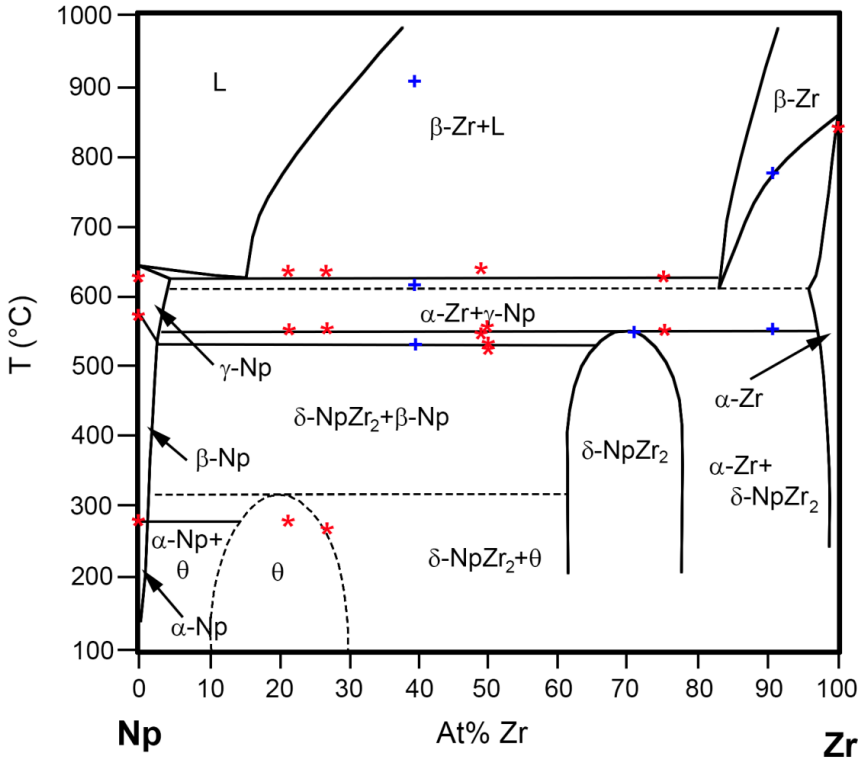

Figure 83. Tentative Np-Zr phase diagram proposed by Gibson and Haire [425]. Colored symbols show data from Table 23. Red symbols are data from Gibson and Haire [426, 427]; blue symbols are data from Rodríguez et al. [424]. Note that this phase diagram expresses compositions in atomic % Zr.

In contrast, the phase diagram of Rodríguez et al. [424] (Figure 84) assumes that the Np-Zr phase diagram is similar to those for U-Zr and Pu-Zr, and therefore has a continuous solid solution between the bcc phases γ-Np and β-Zr. This phase diagram is supported by microscopic observations and microprobe data showing that Np-Zr alloys with 50 wt% Zr that had been annealed for a week have only one phase, while those with 20 or 80% Zr have two phases. Although this phase diagram is consistent with the available phase-transformation temperatures, reasons to regard it with caution include:

- It is inconsistent with the high-temperature X-ray diffraction results of Y. Okamoto et al. [434]
- H. Okamoto [435] suggested that what appears to be the melting curve for the (γ-Np, β-Zr) solid solution has not been correctly identified.
- Given the sluggish kinetics of phase separations in other actinide-Zr alloys, it is not clear that it would be possible to recognize early stages of phase separation using optical microscopy or microprobe techniques without longer annealing times.

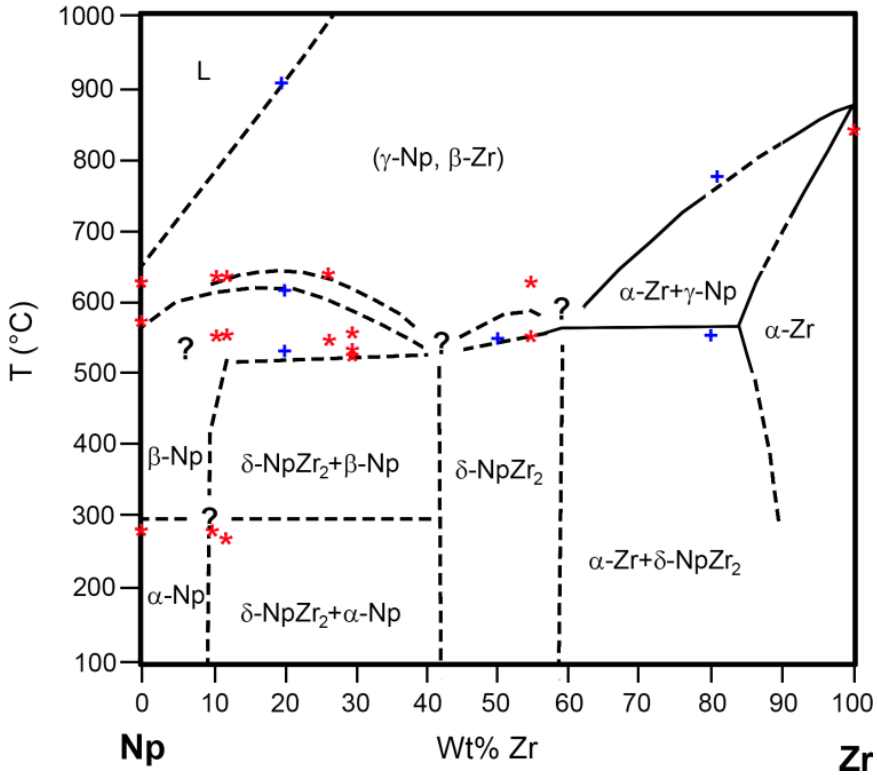

Figure 84. Tentative Np-Zr phase diagram proposed by Rodríguez et al. [424], showing only temperatures from 100 to 1000°C. Colored symbols are as in Figure 83. Note that this phase diagram expresses compositions in weight percent Zr.

6.2 Am-Zr

No experimental data about phases, heat capacity, thermal expansion, or thermal conductivity of any Am-Zr alloy is available.

Kurata [295] calculated a phase diagram using an internally consistent database of thermodynamic properties for the U-Np-Pu-Am-Fe-Zr alloy system (Figure 85). This phase diagram was repeated by Okamoto [436]. It shows essentially complete immiscibility between Am and Zr solids and liquids at temperatures up to 1500 K, with mutual solubilities increasing to ~25 at% at 2500 K.

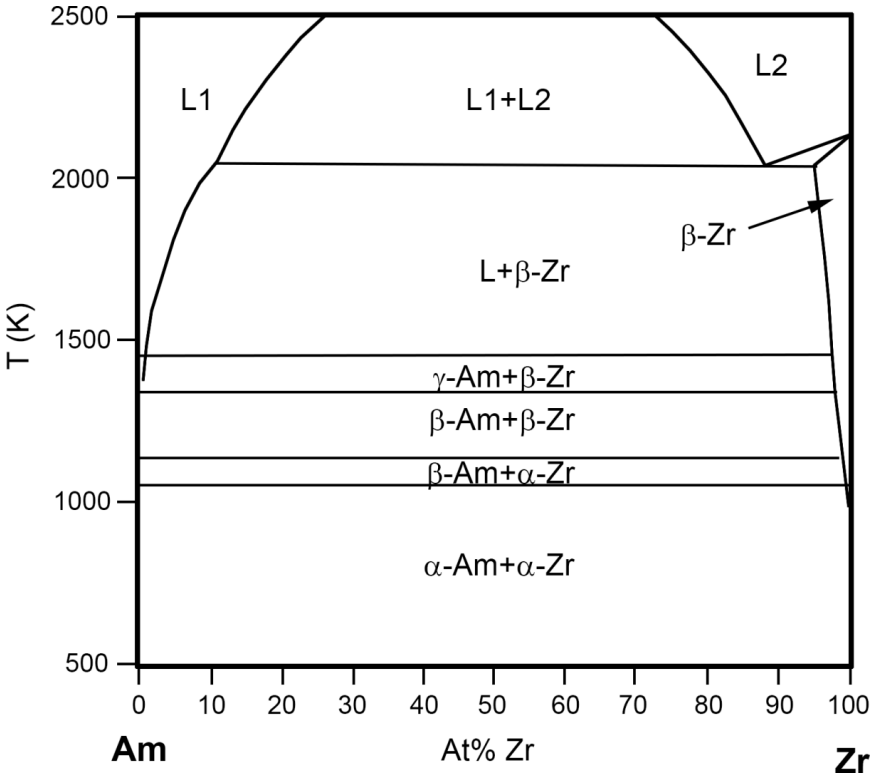

Figure 85. Calculated Am-Zr phase diagram (after [295]).

7. BINARY ALLOYS OF A RARE-EARTH ELEMENT (La, Ce, Pr, Nd) With Zr

7.1 La-Zr

7.1.1 Introduction

The first systematic investigation of the La-Zr phase diagram was published by Mattern et al. in 2016 [437], based on a combination of thermodynamic modeling with new experimental data from high-temperature conventional and synchrotron X-ray diffraction and DSC. This phase diagram was summarized by Okamoto [438]. As a result of this work, the La-Zr phase diagram is better known than many of the other phase diagrams in this Handbook.

Key features of the phase diagram of Mattern et al. include limited miscibility between solid phases, a miscible liquid phase, liquidus temperatures that increase with Zr content, and an absence of intermediate phases. This phase diagram is consistent with the very limited previously reported experimental data, which indicated that there was no detectable solid solution between La and Zr in an arc-melted alloy [352], and that there were no intermediate La-Zr phases in isothermal sections of the La-Zr-Si and Al-La-Zr ternary systems at 500°C [439, 440].

No experimental measurements of phase-transition enthalpies, heat capacities, thermal expansion, or thermal conductivities of La-Zr alloys are available.

7.1.2 Phases and Phase Transformations

7.1.2.1 Phases

Stable solid phases in the La-Zr system at atmospheric pressure are [437, 438]:

- (α-La): Allotropic solid solution of α-La with negligible concentrations of Zr. At room temperature, the *a* lattice parameter increases slightly and the *c* lattice parameter decreases slightly with increasing concentration of Zr in the alloy for alloys with 10-50 at% La [437 Table 2].
- (β-La): Allotropic solid solution of β-La with up to 0.08 at% Zr. The lattice parameter is identical to that of pure β-La to within experimental error.
- (γ-La): Allotropic solid solution of γ-La with up to 0.8 at% Zr
- (α-Zr): Allotropic solid solution of α-Zr with up to 0.29 at% La. Room-temperature lattice parameters are identical to within experimental error for alloys with 50-90 at% Zr. The *a* lattice parameter is smaller than that of pure Zr by ~0.005 Å, and the *c* lattice parameter is larger by ~0.01 Å [437 Table 2].
- (β-Zr): Allotropic solid solution of β-Zr with up to 4 at% La. The lattice parameter is slightly larger than that of pure β-Zr [437 Figure 17].

The liquid phase is completely miscible [437].

Comparisons between high-temperature X-ray diffraction data collected during heating and microstructures in as-cast arc-melted alloys indicate that significant undercooling may occur before crystallization begins. The degree of undercooling is composition-dependent, with a maximum value of about 300°C. Although Mattern et al. provided data for only one cooling rate, which they did not specify, it seems likely that the amount of undercooling is also strongly dependent on the cooling rate. Researchers interested in details of the undercooling should refer to the original paper.

7.1.2.2 Phase Transitions

Invariant reactions identified by Mattern et al are:

- $L_{2.15} \leftrightarrow (\gamma\text{-La})_{0.8} + (\beta\text{-Zr})_{99.20}$, a eutectic reaction with a calculated temperature of 1169K and an experimental temperature of 1175±20 K
- $(\beta\text{-Zr})_{99.33} \leftrightarrow (\gamma\text{-La})_{0.67} + (\alpha\text{-Zr})_{99.71}$, a eutectoid reaction with a calculated temperature of 1130 K and an experimental temperature of 1130±5 K
- $(\gamma\text{-La})_{0.62} \leftrightarrow (\beta\text{-La})_{0.08} + (\alpha\text{-Zr})_{99.73}$, a eutectoid reaction with a calculated temperature of 1116 K and an experimental temperature of 1110±6 K
- (β-La) ↔ (α-La), a polymorphous reaction with a calculated temperature of 550 K and an experimental temperature of ~583 K

Where subscripts represent calculated compositions (at% Zr)

These temperatures are similar to phase transitions observed by high-temperature XRD in an alloy with 80 at% Zr, which had a liquidus temperature of 1950 K [437 (Table 3)].

The eutectoid reaction involving α-Zr, β-Zr, and γ-La is consistent with the α↔β transition temperature in pure Zr (Section 2.9.2.2). The eutectoid reaction involving β-La, γ-La, and α-Zr is within the range of previous measurements of the β↔γ transition temperature in pure La, but is approximately 30 K below the value recommended in Section 2.5.2.2.

7.1.2.3 Phase Diagrams

Figure 86 shows the recently determined phase diagram of Mattern et al. [437]. There are no earlier phase diagrams of this system for comparison.

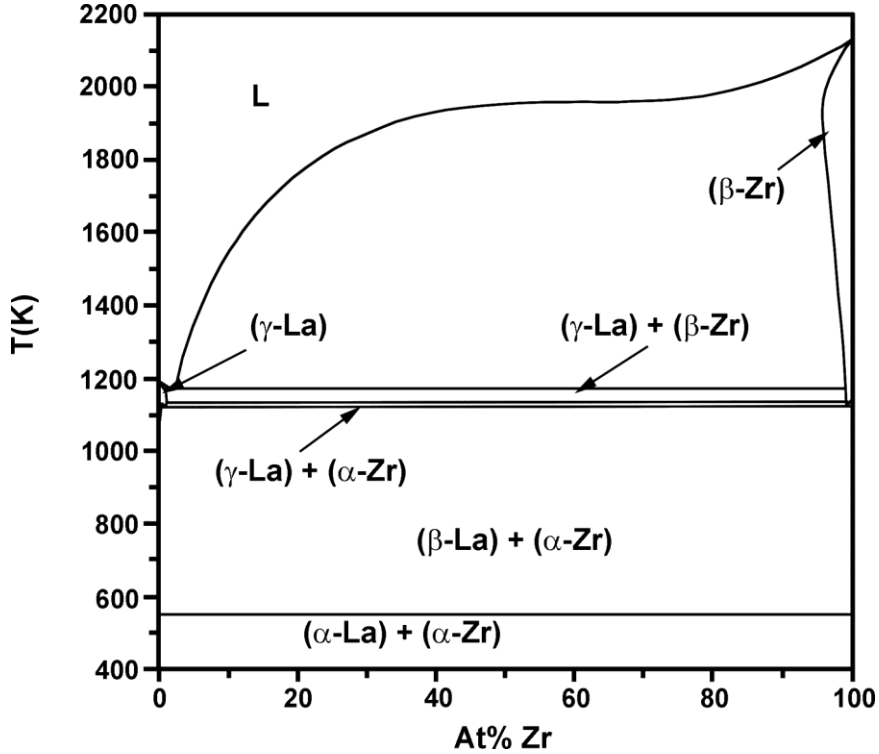

Figure 86. La-Zr phase diagram of Mattern et al. [437]

7.2 Ce-Zr

7.2.1 Introduction

The first systematic investigation of the Ce-Zr phase diagram was published by Mattern et al. in 2014 [441], using a combination of new experimental data from temperatures between ~600 and 1600 K and thermodynamic modeling. This phase diagram was reviewed by Okamoto [442]. As a result of this work, the Ce-Zr phase diagram is far better known than many of the other phase diagrams in this Handbook.

Key features of this phase diagram include limited miscibility between solid phases, a miscible liquid phase, liquidus temperatures that increase with Zr content, and an absence of intermediate phases. The low miscibility of the solid phases, absence of intermediate phases, and phase transformation temperatures in this phase diagram are consistent with older experimental data (e.g., [352, 443]).

No information about the heat capacities, thermal expansion, or thermal conductivities of Ce-Zr alloys is available.

7.2.2 Phases and Phase Transformations

7.2.2.1 Phases

Stable solid phases in the Ce-Zr system at atmospheric pressure and above room temperature are:

- (α-Zr): Allotropic solid solution of α-Zr. The maximum solubility of Ce is ~3-6 at% [441, 443]. The *a* and *c* lattice parameters both increase with increasing concentration of Zr; however, quantifying the rate of increase is complicated by differences in annealing temperatures in the available data [443 (Table 1, Figure 1, and Figure 2)].
- (β-Zr): Allotropic solid solution of β-Zr. The maximum solubility of Ce is ~8 at% [441]
- (γ-Ce): Allotropic solid solution of γ-Ce. The maximum solubility of Zr is < 2 at% [441]. The lattice parameter is similar to that of pure γ-Ce [443].
- (δ-Ce): Allotropic solid solution of δ-Ce. The maximum solubility of Zr is < 1 at% [441]

The liquid phase is completely miscible [441].

7.2.2.2 Phase Transitions

Phase-transformation temperatures were measured by a number of early researchers, with conflicting results. The values quoted here are from new DSC measurements by Mattern et al. [441]. They are generally consistent with the X-ray diffraction data from annealed samples reported by Harris and Raynor [443].

Except for the liquidus, phase-transformation temperatures show little variation with composition. They are [441]:

- (α-Zr) to (β-Zr): ~1110 K
- (γ-Ce) to (δ-Ce): ~990 K
- Melting of (δ-Ce): ~1060 K.

No information on phase-transformation enthalpies is available.

7.2.2.3 Phase Diagrams

Until recently, there were no systematic investigations of the Ce-Zr phase diagram. Moffatt [444] suggested a phase diagram based on the X-ray diffraction data of Harris and Raynor [443] and the assumption that the Ce-Zr and Ce-Ti systems are similar. This phase diagram is shown here (Figure 87) because it has been widely reproduced (e.g., [445-447]), although it is almost certainly less accurate than the recent phase diagram of Mattern et al. [441] (Figure 88).

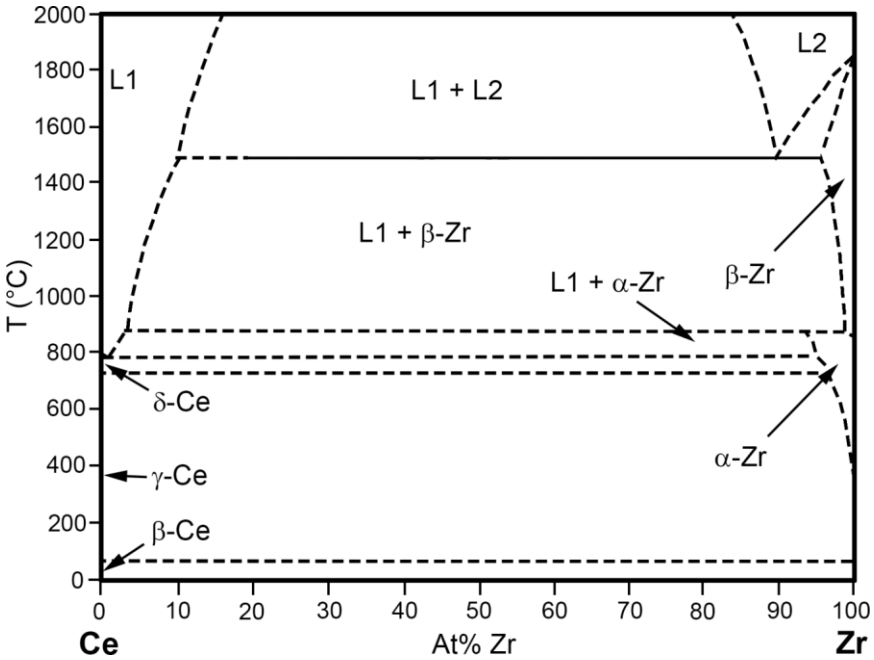

Figure 87. Commonly reproduced Ce-Zr phase diagram suggested by Moffatt [444], based on the assumption that the Ce-Zr and Ce-Ti phase diagrams are similar (redrawn from [447]). This diagram has been recently superseded by the new phase diagram of Mattern et al. (Figure 88).

Mattern et al. [441] suggested a new Ce-Zr phase diagram in 2014, based on their experimental data and thermodynamic modeling (Figure 88). The new data included extensive measurements of the liquidus at temperatures up to 1600 K using in-situ high-temperature synchrotron diffraction to observe structure changes in small droplets of liquid. Other new measurements included DSC and high-temperature X-ray data to confirm temperatures of solid-state phase changes and SEM observations of microstructures and phase compositions. A thermodynamic model produced good agreement with the experimental observations and was used to supplement the experimental data.

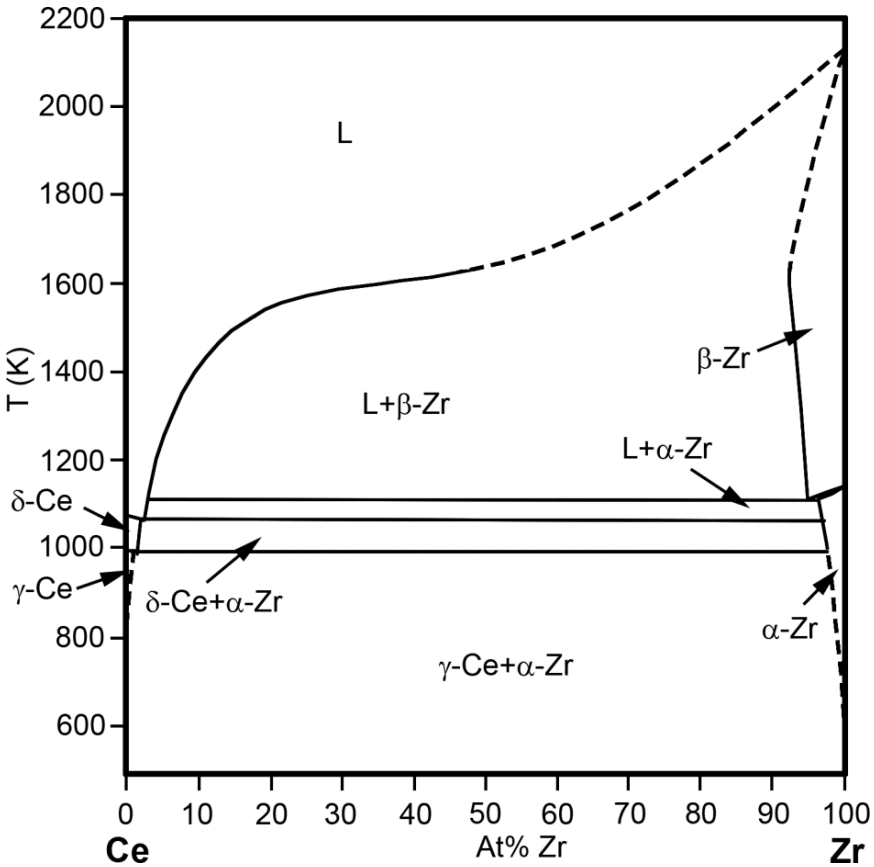

Figure 88. Newer Ce-Zr phase diagram based on new experimental data and thermodynamic modeling (after Mattern et al. [441]). Solid lines indicate areas with new data.

7.3 Pr-Zr

There are no published phase diagrams for the Pr-Zr binary system. An investigation of the Pr-Zr-Al ternary system at 500°C (773 K) concluded that the Pr-Zr binary system has little solid solution and no intermediate phases [448, 449].

No information about heat capacities, thermal expansion, or thermal conductivity of Pr-Zr alloys is available.

7.4 Nd-Zr

7.4.1 Introduction

Although research on ternary alloys indicated that miscibility of Nd and Zr was limited (e.g., [450]), there were apparently no published binary Nd-Zr phase diagrams until 2014. Recent interest in improving the properties of Mg alloys by addition of Nd and Zr led to publication of three binary Nd-Zr phase diagrams in 2014 and 2015 [451-453]. Each of these phase diagrams was based on a combination of new experimental research and thermodynamic modeling. The phase diagram of Mattern et al. was reviewed by Okamoto [442].

All three phase diagrams agree about the existence of a reaction involving Nd, Zr, and a high-Nd liquid, and all three agree that there is a phase transformation at ~830-845°C. Two of the phase diagrams agree that there is a second transformation at ~995-1000°C. Despite these areas of agreement, the phase diagrams disagree about the identities of the phases involved in each reaction, the liquidus temperature,

and the possible existence of immiscible liquids. Careful consideration of the data involved shows that the phase diagram of Mattern et al. [452] is the only one to include high-temperature X-ray diffraction data or measurements at temperatures above ~1000°C, and that none of the phase diagrams used diffraction data to identify the phases involved in lower-temperature reactions.

Further detailed research involving samples with only a few at% of Nd or Zr is needed to understand phase-transformation reactions. Unless this information is of specific interest for fuels, it seems reasonable to consider the phase diagram of Mattern et al. [452] to be an adequate representation of the Nd-Zr system. Researchers interested in details of solid-state phase-transformation reactions should also consider the phase diagram of Cheng et al. [451].

No information about heat capacities, thermal expansion, or thermal conductivity of Nd-Zr alloys is available.

7.4.2 Phases and Phase Transformations

7.4.2.1 Phases

Phases in the Nd-Zr phase diagram are:

- (α-Nd): Allotropic solid solution of α-Nd that can contain up to ~2 at% Zr (Table 25). Because of the low concentration of Zr, it seems likely that lattice parameters of (α-Nd) solid solutions are similar to those of α-Nd.
- (β-Nd): Allotropic solid solution of β-Nd that can contain up to ~3-4 at% Zr (references [451, 452] and Table 25). Mattern et al. assume that the lattice parameters of solid solutions of β-Nd and β-Zr follow Vegard's Law (i.e., they vary linearly between the lattice parameters of Nd and Zr as a function of composition), which means that lattice parameters of (β-Nd) solid solutions are slightly smaller than those of pure β-Nd. However, because the maximum concentration of Zr is small, differences in lattice parameters of β-Nd and (β-Nd) solid solutions are probably unimportant for most purposes.
- (α-Zr): solid solution of α-Zr (hcp structure, space group $P6_3/mmc$) that can contain ~3-4 at% Nd (reference [452] and Table 25). Because of the low concentration of Nd, it seems likely that lattice parameters of (α-Zr) solid solutions are similar to those of pure α-Zr.
- (β-Zr): solid solution of β-Zr (bcc structure, space group $Im\bar{3}m$) that can contain up to ~5 at% Nd at 1700 K [452]. The phase diagram of Cheng et al. [451] shows a calculated maximum concentration of ~10 at% Zr but has no experimental data at this temperature. Mattern et al. assume that the lattice parameters of solid solutions of β-Nd and β-Zr follow Vegard's Law, which means that lattice parameters of (β-Zr) solid solutions are slightly larger than those of pure β-Zr [452].

7.4.2.2 Phase Transitions

Table 25 shows the experimentally measured phase-transformation temperatures from all three phase diagrams, with associated reactions indicated by the references. Differences between phase transitions associated with each temperature may be due to the very similar temperatures of the α-β transformations in Nd and Zr (Sections 2.8.2.2 and 2.9.2.2). Because of the limited miscibility of Nd and Zr, the temperature of each reaction is essentially independent of the alloy composition.

Table 25. Phase transformations in the Nd-Zr system [451 (Table III), 452 (Table 3), 453 (Figure 4)]. Subscripts in the data from Mattern et al. indicate the calculated composition (at% Zr) in each phase.

T (K)	T (°C)	Mattern et al. [452]	Cheng et al. [451]	Peng et al. [453]
1274±10	1001±10	$L_{4.0} \leftrightarrow \beta\text{-}Nd_{2.0} + \beta\text{-}Zr_{97.0}$	—	—
—	990-997	—	L+β-Zr↔α-Nd	—
—	962-964	—	—	(Not identified)[a]
—	983[b]	—	L+α-Nd↔α-Nd	—
1167±10	894±10	$\beta\text{-}Nd_{2.2} + \beta\text{-}Zr_{97.8} \leftrightarrow \alpha\text{-}Zr_{96.6}$	—	—
1118±10	845±10	$\beta\text{-}Nd_{1.9} \leftrightarrow \alpha\text{-}Zr_{97.1} + \alpha\text{-}Nd_{1.5}$	—	—
—	833-842	—	β-Zr↔α-Zr+α-Nd	—
—	831-834	—	—	(Not identified)

a. Assumed to correspond to the highest-temperature reaction reported by other authors despite the difference in temperature because it produces the second of two large peaks in DSC heating curves
b. Only observed in alloy with 5 at% Zr

7.4.2.3 Phase Diagrams

The phase diagram of Mattern et al. [441, available on-line on March 13, 2014] was apparently the first binary Nd-Zr phase diagram to be published. Temperatures between ~1160 and 1270 K were investigated using DSC and SEM data (including EDX analyses) from four alloys with 40 to 95 at% Zr. Coexisting compositions at temperatures between ~1200 and 1800 K were determined using *in situ* high-temperature synchrotron X-ray diffraction and pyrometry applied to gas-levitated droplets of an alloy with 40 at% Nd. This data made it possible to determine temperatures of solid-state transformations, as well as compositions of liquids and (β-Zr) solid solutions at a large number of temperatures. Thermodynamic modeling was used at temperatures above 1800 K and to determine the limits of solid solution in α-Zr, α-Nd, and β-Nd.

The phase diagram of Cheng et al. [451, available on-line on April 1, 2014] used a combination of DSC, SEM, room-temperature XRD, and microprobe data to determine phase-transformation temperatures and compositions in nine annealed and quenched alloys with 5 to 97 at% Zr. All of the data represents temperatures between 500 and 1000 °C. Thermodynamic modeling was used to determine the liquidus and details of phase transformations and to determine the limits of solid solution at temperatures outside the range of the experimental data. The Cheng et al. phase diagram does not have a (β-Nd+α-Zr) field, and details of phase transformations in high-Nd and high-Zr solids differ from those in the phase diagram of Mattern et al. Although the shape of the liquidus generally resembles the liquidus in the Mattern phase diagram, liquidus temperatures for most compositions in the Cheng phase diagram are lower.

The phase diagram of Peng et al. [453, available in print in 2015] was based on EDS and DSC of three alloys with 5 to 30 at% Zr. At temperatures below the liquidus (at ~1600°C for most compositions), this phase diagram generally resembles that of Cheng et al. However, the Peng et al. phase diagram shows a broad liquid-phase miscibility gap. The maximum temperature of this miscibility gap is not indicated, but is above the melting temperature of Zr.

Figure 89 shows the phase diagram of Mattern et al. [452]. As it is the only one of the three phase diagrams with experimental data at temperatures above 1000°C (1273 K), it is probably the best representation of the liquidus and maximum concentration of Nd in β-Zr. None of the phase diagrams used diffraction data to identify the Nd and Zr solid-solution phases in lower-temperature reactions, and researchers interested in these transformations should also consult the publication by Cheng et al. [451].

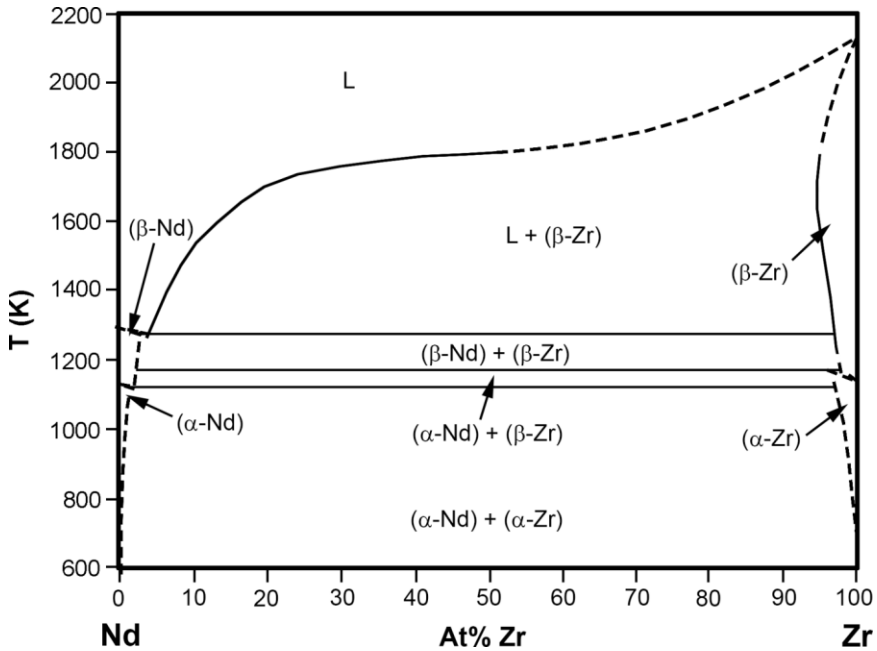

Figure 89. Nd-Zr phase diagram after Mattern et al. [452]. Solid lines indicate areas with new data.

8. REFERENCES

[1] D.E. Janney, C.A. Papesch, FCRD Transmutation Fuels Handbook 2015 (Idaho National Laboratory Report INL/EXT-15-36520 revision 0), Idaho Falls, ID, 2015.

[2] D.E. Janney, C.A. Papesch, S.C. Middlemas, FCRD Advanced Reactor (Transmutation) Fuels Handbook (Idaho National Laboratory Report INL/EXT-15-36520 revision 1), Idaho Falls, ID, 2016.

[3] D.E. Janney, Metallic Fuels Handbook, Part 1: Alloys based on U-Zr, Pu-Zr, U-Pu, or U-Pu-Zr, including those with minor actinides (Np, Am, Cm), rare-earth elements (La, Ce, Pr, Nd, Gd), and Y (Idaho National Laboratory Report INL/EXT-15-36520 rev 2 part 1), Idaho Falls, ID, 2017.

[4] D.E. Janney, Metallic Fuels Handbook, Part 2: Elements and Alloys not Based on U-Zr, Pu-Zr, U-Pu, or U-Pu-Zr (Idaho National Laboratory Report INL/EXT-15-36520 Revision 2 Part 2), Idaho Falls, ID, 2017.

[5] D.E. Janney, Metallic Fuels Handbook, Part 1: Alloys based on U-Zr, Pu-Zr, U-Pu, or U-Pu-Zr, including those with minor actinides (Np, Am, Cm), rare-earth elements (La, Ce, Pr, Nd, Gd), and Y (Idaho National Laboratory Report INL/EXT-15-36520 rev 3 part 1), Idaho Falls, ID, 2018.

[6] F.L. Oetting, M.H. Rand, R.J. Ackermann, The chemical thermodynamics of actinide elements and compounds, part 1: The actinide elements, International Atomic Energy Agency, Vienna, Austria, 1976.

[7] R.J.M. Konings, O. Beneš, The Thermodynamic Properties of the *f*-Elements and Their Compounds. I. The Lanthanide and Actinide Metals, Journal of Physical and Chemical Reference Data, 39 (2010) 043102.

[8] R.J.M. Konings, O. Beneš, J.-C. Griveau, The actinides elements: properties and characteristics, in: R.J.M. Konings (Ed.) Comprehensive Nuclear Materials, volume 2, Elsevier, 2012, pp. 1-20.

[9] I. Grenthe, J. Drożdżyński, T. Fujino, E.C. Buck, T.E. Albrecht-Schmitt, S.F. Wolf, Uranium, in: L.R. Morss, N.M. Edelstein, J. Fuger (Eds.) The Chemistry of the Actinide and Transactinide Elements, Springer, Dordrecht, The Netherlands, 2010, pp. 253-698.

[10] I. Grenthe, J. Fuger, R.J.M. Konings, R.J. Lemire, A.B. Muller, C. Nguyen-Trung, H. Wanner, Chemical Thermodynamics of Uranium, Elsevier North-Holland, Amsterdam, 1992.

[11] M. Krupska, N.-T.H. Kim-Ngan, S. Sowa, M. Paukov, I. Tkach, D. Drozdenko, L. Havela, Z. Tarnawski, Structure, Electrical Resistivity and Superconductivity of Low-alloyed γ-U phase retained to low temperatures by means of rapid cooling, Acta Metallurgica Sinica (English Letters), 29 (2016) 388-398.

[12] N.T.H. Kim-Ngan, L. Havela, Superconductivity in U-T alloys (T=Mo, Pt, Pd, Nb, Zr) stabilized in the cubic gamma-U structure by splat-cooling technique, Journal of Science - Advanced Materials and Devices, 1 (2016) SI 121-127.

[13] Z. Ren, J. Wu, R. Ma, G. Hu, C. Luo, Thermodynamic properties of α-uranium, Journal of Nuclear Materials, 480 (2016) 80-87.

[14] J. Korn, Investigation of cones of zero expansion and thermal coefficients for single-crystal of alpha-uranium, Journal of Nuclear Materials, 71 (1978) 320-326.

[15] Mu Yeh Wu, J. Wadsworth, O.D. Sherby, Internal stress superplasticity in anisotropic polycrystalline zinc and uranium, Metallurgical Transactions A (Physical Metallurgy and Materials Science), 18A (1987) 451-462.

[16] C.A. Calhoun, J.A. Wollmershauser, D.W. Brown, R.P. Mulay, E. Garlea, S.R. Agnew, Thermal residual strains in depleted α-U, Scripta Materialia, 69 (2013) 566-569.

[17] D.W. Brown, M.A.M. Bourke, B. Clausen, D.R. Korzekwa, R.C. Korzekwa, R.J. McCabe, T.A. Sisneros, D.F. Teter, Temperature and direction dependence of internal strain and texture evolution during deformation of uranium, Materials Science and Engineering A-Structural Materials Properties Microstructure and Processing, 512 (2009) 67-75.

[18] H.H. Klepfer, P. Chiotti, Characteristics of the solid state transformations in uranium (Ames Laboratory, report ISC-893 to the United States Atomic Energy Commission), Ames Laboratory, Ames, IA, 1957.

[19] Y.S. Kim, T.W. Cho, D.-S. Sohn, Thermal conductivities of actinides (U, Pu, Np, Cm, Am) and uranium-alloys (U-Zr, U-Pu-Zr, and U-Pu-TRU-Zr), Journal of Nuclear Materials, 445 (2014) 272-280.

[20] S. Kaity, J. Banerjee, M.R. Nair, K. Ravi, S. Dash, T.R.G. Kutty, A. Kumar, R.P. Singh, Microstructural and thermophysical properties of U-6 wt.%Zr alloy for fast reactor application, Journal of Nuclear Materials, 427 (2012) 1-11.

[21] International Atomic Energy Agency (IAEA), Thermophysical Properties of Materials for Nuclear Engineering: A Tutorial and Collection of Data, International Atomic Energy Agency (IAEA), Vienna, Austria, 2008.

[22] R.T. Murzaev, R.I. Babicheva, K. Zhou, E.A. Korznikova, S.Y. Fomin, V.I. Dubinko, S.V. Dmitriev, Discrete breathers in alpha-uranium, European Physical Journal B, 89 (2016) 168.

[23] O.A. Dubovsky, V.A. Semenov, A.V. Orlov, Soliton and multiphonon microdynamics of thermal conductivity of plutonium and uranium in the temperature range of martensitic phase transitions, Physics of the Solid State, 56 (2014) 24-28.

[24] L.N. Kolotova, A.Y. Kuksin, D.E. Smirnova, S.V. Starikov, V.I. Tseplyaev, Features of structure and phase transitions in pure uranium and U-Mo alloys: atomistic simulation, Condensed Matter and Materials Physics Conference, CMMP10, 774 (2016) 012036.

[25] D.E. Smirnova, A.Y. Kuksin, S.V. Starikov, V.V. Stegailov, Atomistic modeling of the self-diffusion in γ-U and γ-Mo, Physics of Metals and Metallography, 116 (2015) 445-455.

[26] D.E. Smirnova, A.Y. Kuksin, S.V. Starikov, Investigation of point defects diffusion in bcc uranium and U-Mo alloys, Journal of Nuclear Materials, 458 (2015) 296-303.

[27] J.R. Fernández, M.I. Pascuet, On the accurate description of uranium metallic phases: a MEAM interatomic potential approach, Modelling and Simulation in Materials Science and Engineering, 22 (2014) 055019.

[28] R. Zhiyong, J. Wu, R. Ma, G. Hu, C. Luo, Thermodynamic properties of α-uranium, Journal of Nuclear Materials, 480 (2016) 80-87.

[29] M. Knezevic, R.J. McCabe, R.A. Lebensohn, C.N. Tomé, C. Liu, M. Lovato, B. Mihaila, Integration of self-consistent polycrystal plasticity with dislocation density based hardening laws within an implicit finite element framework: application to low-symmetry metals, Journal of the Mechanics and Physics of Solids, 61 (2013) 2034-2046.

[30] M. Knezevic, R.J. McCabe, C.N. Tomé, R.A. Lebensohn, S.R. Chen, C.M. Cady, G.T. Gray III, B. Mihaila, Modeling mechanical response and texture evolution of α-uranium as a function of strain rate and temperature using polycrystal plasticity, International Journal of Plasticity, 43 (2013) 70-84.

[31] R. Kapoor, A.N. Behera, J.K. Chakravartty, M.M. Hussain, Hot deformation of uranium in the α, β, and γ phases, Metallurgical and Materials Transactions A, 46 (2015) 251-259.

[32] R.J. McCabe, A.W. Richards, D.R. Coughlin, K.D. Clarke, I.J. Beyerlein, M. Knezevic, Microstructure effects on the recrystallization of low-symmetry alpha-uranium, Journal of Nuclear Materials, 465 (2015) 189-195.

[33] M. Zecevic, M. Knezevic, I.J. Beyerlein, R.J. McCabe, Texture formation in orthorhombic alpha-uranium under simple compression and rolling to high strains, Journal of Nuclear Materials, 473 (2016) 143-156.

[34] M.A. Steiner, R.J. McCabe, E. Garlea, S.R. Agnew, Monte Carlo modeling of recrystallization processes in α-uranium, Journal of Nuclear Materials, 492 (2017) 74-87.

[35] R.D. Field, R.J. McCabe, D.J. Alexander, D.F. Teter, Deformation twinning and twinning related fracture in coarse-grained α-uranium, Journal of Nuclear Materials, 392 (2009) 105-113.

[36] M. Knezevic, L. Capolungo, C.N. Tomé, R.A. Lebensohn, D.J. Alexander, B. Mihaila, R.J. McCabe, Anisotropic stress-strain response and microstructure evolution of textured α-uranium, Acta Materialia, 60 (2012) 702-715.

[37] M.K. Jacobsen, Velisavljevic, High pressure elasticiety and thermal properties of depleted uranium, Journal of Applied Physics, 119 (2016) 165904.

[38] B.W. Chung, R.G. Erler, N.E. Teslich, Three-dimensional microstructural characterization of bulk plutonium and uranium metals using focused ion beam technique, Journal of Nuclear Materials, 473 (2016) 264-271.

[39] V.N. Serezhkin, A.V. Savchenkov, D.V. Pushkin, L.B. Serezhkina, Crystal-chemical features of thermal polymorphism of actinides, Radiochemistry, 58 (2016) 561-570.

[40] R.C. Lobb, V.D. Scott, Microstructural changes in adjusted uranium during thermal cycling, Journal of Nuclear Materials, 60 (1976) 291-298.

[41] J.J. Stobo, C.C. Robinson, G.H. May, Preferred orientations in alpha uranium, Acta Metallurgica, 13 (1965) 629-634.

[42] A.C. Lawson, C.E. Olsen, J.W. Richardson Jr., M.H. Mueller, G.H. Lander, Structure of β-uranium, Acta Crystallographica, B44 (1988) 89-96.

[43] C.S. Barrett, M.H. Mueller, R.L. Hitterman, Crystal structure variations in alpha uranium at low temperatures, Physical Review, 129 (1963) 625-629.

[44] G.H. Lander, M.H. Mueller, Neutron diffraction study of α-uranium at low temperature, Acta Crystallographica B: Structural Science, 26 (1970) 129-136.

[45] M.H. Mueller, R.L. Hitterman, H.W. Knott, The atomic position parameter in alpha uranium -- room temperature and above, Acta Crystallographica, 15 (1962) 421-422.

[46] H.L. Yakel, Review of x-ray diffraction studies in uranium alloys, in: J.J. Burke, D.A. Colling, A.E. Gorum, J. Greenspan (Eds.) Physical Metallurgy of Uranium Alloys (Proceedings of the third Army

Materials Technology Conference held at Vail, Colorado, February 12-14, 1974, Brook Hill Publishing Company, Chestnut Hill, Massachusetts, 1976, pp. 259-308.

[47] A.F. Berndt, Room temperature lattice constants of alloys of plutonium in alpha-uranium, Journal of Nuclear Materials, 9 (1963) 53-58.

[48] A.C. Lawson, J.A. Goldstone, B. Cort, R.I. Sheldon, E.M. Foltyn, Atomic thermal vibrations of the light actinide elements, Journal of Alloys and Compounds, 213/214 (1994) 426-428.

[49] E.J. Nelson, P.G. Allen, K.J.M. Blobaum, M.A. Wall, C.H. Booth, Local structure and vibrational properties of α-Pu, α-U, and the α-U charge-density wave, Physical Review B, 71 (2005) 184113.

[50] J. Donohue, H. Einspahr, The structure of β-uranium, Acta Crystallographica, B27 (1971) 1740-1743.

[51] J.G. Huber, P.H. Ansari, The superconductivity of BCC U-Zr alloys, Physica, 135B (1985) 441-444.

[52] D. Summers-Smith, The constitution of uranium-zirconium alloys, Journal of the Institute of Metals, 83 (1954-1955) 277-282.

[53] A.S. Wilson, R.E. Rundle, The structures of uranium metal, Acta Crystallographica, 2 (1949) 126-127.

[54] J.W. Ward, P.D. Kleinschmidt, D.E. Peterson, Thermochemical properties of the actinide elements and selected actinide-noble metal intermetallics, in: A.J. Freeman, C. Keller (Eds.) Handbook on the Physics and Chemistry of the Actinides, Elsevier, 1986, pp. 309-412.

[55] Y.S. Touloukian, R.K. Kirby, R.E. Taylor, P.D. Desai, Thermal Expansion: Metallic elements and alloys (Thermophysical Properties of Matter vol. 12), IFI/Plenum, New York, 1975.

[56] C. Basak, G.J. Prasad, H.S. Kamath, N. Prabhu, An evaluation of the properties of as-cast U-rich U-Zr alloys, Journal of Alloys and Compounds, 480 (2009) 857-962.

[57] J. Thewlis, An X-ray powder study of β-uranium, Acta Crystallographica, 5 (1952) 790-794.

[58] P. Chiotti, H. Klepfer, R. White, Lattice parameters of uranium from 25 to 1132 C, Trans Am Soc Met, 51 (1959) 772-782.

[59] R.W. Logan, D.H. Wood, Thermal expansion of rolled and extruded uranium, Journal of the Less-Common Metals, 90 (1983) 233-241.

[60] N.M. Edelstein, J. Fuger, J.J. Katz, L.R. Morss, Summary and comparison of the properties of the actinide and transactinide elements, in: L.R. Morss, N.M. Edelstein, J. Fuger (Eds.) The Chemistry of the Actinide and Transactinide Elements, Springer, Dordrecht, The Netherlands, 2010, pp. 1753-1832.

[61] W.G. Rohr, L.J. Wittenberg, Density of liquid uranium, Journal of Physical Chemistry, 74 (1970) 1151.

[62] Y.S. Touloukian, R.W. Powell, C.Y. Ho, P.G. Klemens, Thermal Conductivity (Thermophysical Properties of Matter vol. 1), IFI/Plenum, New York, 1970.

[63] International Atomic Energy Agency (IAEA), Thermophysical properties of materials for water-cooled reactors (IAEA-TECDOC-949), 1997.

[64] Y. Takahashi, M. Yamawaki, K. Yamamoto, Thermophysical properties of uranium-zirconium alloys, Journal of Nuclear Materials, 154 (1988) 141-144.

[65] B. Johansson, S. Li, Itinerant *f*-electron elements, Philosophical Magazine, 89 (2009) 1793-1799.

[66] K.T. Moore, G. van der Laan, Nature of the 5*f* states in actinide metals, Reviews of Modern Physics, 81 (2009) 235-298.

[67] A.V. Lukoyanov, A.O. Shorikov, V.B. Bystrushkin, A.A. Dyachenko, L.R. Kabirova, Y.Y. Tsiovkin, A.A. Povzner, V.V. Dremov, M.A. Korotin, V.I. Anisimov, Electronic structure and magnetic state of transuranium metals under pressure, Journal of Physics: Condensed Matter, 22 (2010) 495501.

[68] S. Bajaj, C. Sevik, T. Cagin, A. Garay, P.E.A. Turchi, R. Arróyave, On the limitations of the DFT+U approach to energetics of actinides, Computational Materials Science, 59 (2012) 48-56.

[69] R.J. Lemire, J. Fuger, H. Nitsche, P. Potter, M.H. Rand, J. Rydberg, K. Spahiu, J.C. Sullivan, W.J. Ullman, P. Vitorge, H. Warner, Chemical Thermodynamics of Neptunium and Plutonium, Elsevier North Holland, Amsterdam, The Netherlands, 2001.

[70] J.A. Lee, P.G. Mardon, J.H. Pearce, R.O.A. Hall, Some physical properties of neptunium metal II: A study of the allotropic transformations in neptunium, Journal of Physics and Chemistry of Solids, 11 (1959) 177-181.

[71] E.M. Foltyn, Allotropic transitions of neptunium and plutonium determined using differential thermal analysis, Journal of Nuclear Materials, 172 (1990) 180-183.

[72] S. Dabos, C. Dufour, U. Benedict, M. Pagès, Bulk modulus and *P-V* relationship up to 52 GPa of neptunium metal at room temperature, Journal of Magnetism and Magnetic Materials, 63-64 (1987) 661-663.

[73] T. Ogawa, Alloying behaviour among U, Np, Pu and Am predicted with the Brewer valence bond model, Journal of Alloys and Compounds, 194 (1993) 1-7.

[74] P. Söderlind, B. Johansson, L. Yongming, L. Nordström, Calculated thermal-expansion of the actinide elements, International Journal of Thermophysics, 12 (1991) 611-615.

[75] B. Amadon, First-principles DFT plus DMFT calculations of structural properties of actinides: role of Hund's exchange, spin-orbit coupling, and crystal structure, Physical Review B, 94 (2016) 115148.

[76] W.H. Zachariasen, Crystal chemical studies of the 5*f*-series of elements. XVIII. Crystal structure studies of neptunium metal at elevated temperatures, Acta Crystallographica, 5 (1952) 664-667.

[77] W.H. Zachariasen, Crystal chemical studies of the 5*f*-series of elements. XVII. The crystal structure of neptunium metal, Acta Crystallographica, 5 (1952) 660-664.

[78] Z. Yoshida, S.G. Johnson, T. Kimura, J.R. Krsul, Neptunium, in: L.R. Morss, N.M. Edelstein, J. Fuger (Eds.) The Chemistry of the Actinide and Transactinide Elements, Springer, Dordrecht, The Netherlands, 2010, pp. 699-812.

[79] M.F. Stevens, An examination of twinning in alpha-neptunium, Journal of Nuclear Materials, 148 (1987) 99-106.

[80] J.J. Rechtien, A.G. Crocker, R.D. Nelson, Twinning in alpha-neptunium, Journal of Nuclear Materials, 40 (1971) 134-140.

[81] B. Cort, Thermal expansion of neptunium, Journal of the Less-Common Metals, 135 (1987) L13-L17.

[82] J.E. Selle, J.J. Rechtien, Internal friction of neptunium, Journal of Nuclear Materials, 31 (1969) 203-210.

[83] D. McWhan, P.W. Montgomery, H.D. Stromberg, G. Jura, Pressure-temperature-resistance properties of lanthanum, bismuth, neptunium, plutonium, and americium to 450 degrees and 30 kb, Journal of Physical Chemistry, 67 (1963) 2308-2311.

[84] V.W. Eldred, G.C. Curtis, Some properties of neptunium metal, Nature (London), 179 (1957) 910.

[85] J.P. Evans, P.G. Mardon, Some physical properties of neptunium metal I: A determination of the specific heat of α-neptunium, Journal of Physics and Chemistry of Solids, 10 (1959) 311-313.

[86] A. Filanovich, A. Povzner, The influence of photon anharmonicity on thermal and elastic properties of neptunium, Journal of Nuclear Materials, 437 (2013) 102-106.

[87] J.A. Lee, A review of the physical metallurgy of neptunium, in: H.M. Finniston, J.P. Howe (Eds.) Progress in Nuclear Energy Series V: Metallurgy and Fuels, Pergamon, Oxford, 1961, pp. 453-467.

[88] E.F. Westrum, L. Eyring, The melting point and the density of neptunium metal -- a micro melting point apparatus for metals, Journal of the American Chemical Society, 73 (1951) 3399-3400.

[89] D.R. Stephens, Phase diagram and compressibility of neptunium, Journal of Physics and Chemistry of Solids, 27 (1966) 1201-1204.

[90] L.J. Wittenberg, D.A. Vaughn, R. DeWitt, Phase relationships in uranium, neptunium, and plutonium, in: W.N. Miner (Ed.) Plutonium 1970 and Other Actinides, The Metallurgical Society of AIME, 1970, pp. 659-668.

[91] L.J. Wittenberg, R. DeWitt, Volume contraction during melting; emphasis on lanthanide and actinide metals, Journal of Chemical Physics, 56 (1972) 4256.

[92] P. Wagner, Thermal conductivity of neptunium at 300 degrees K, Journal of the Less-Common Metals, 24 (1971) 106.

[93] J.A. Lee, J.P. Evans, R.O.A. Hall, E. King, Some physical properties of neptunium metal III: The electrical resistivity and thermoelectric power of neptunium metal in the range 300-900 degrees K, Journal of Physics and Chemistry of Solids, 11 (1959) 278-283.

[94] W.G. Kannuluik, On the thermal conductivity of some metal wires, Proceedings of the Royal Society of London Series A--Mathematical and Physical Sciences, 131 (1931) 320-335.

[95] C.Y. Ho, R.W. Powell, P.E. Liley, Thermal conductivity of the elements: a comprehensive review, Journal of Physical and Chemical Reference Data, 3 (1974) 1-1 to 1-796.

[96] W.M. Haynes, ed., Thermal and physical properties of pure metals, in: CRC Handbook of Chemistry and Physics, 96th Edition (Internet Version 2016), CRC Press/Taylor and Francis, Boca Raton, FL, 2016.

[97] S.S. Hecker, M. Stan, Properties of plutonium and its alloys for use as fast reactor fuels, Journal of Nuclear Materials, 383 (2008) 112-118.

[98] D.L. Clark, S.S. Hecker, G.D. Jarvinen, M.P. Neu, Plutonium, in: L.R. Morss, N.M. Edelstein, J. Fuger (Eds.) The Chemistry of the Actinide and Transactinide Elements, Springer, Dordrecht, The Netherlands, 2010, pp. 813-1264.

[99] S.M. Ennaceur, Phase stability of α'-phase in a Pu-1at% Ga alloy following low temperature treatment, Thermochimica Acta, 593 (2014) 22-29.

[100] S.M. Ennaceur, The effects of thermal conditioning and recovery processes on the δ→γ phase transformation mechanisms in plutonium, Thermochimica Acta, 565 (2013) 151-158.

[101] S.M. Ennaceur, Methodology for describing the α→β phase transformation in plutonium, Thermochimica Acta, 539 (2012) 84-91.

[102] S.M. Ennaceur, Study of the γ→δ phase transformation kinetics and reaction mechanism in plutonium, Thermochimica Acta, 566 (2013) 181-185.

[103] S.M. Ennaceur, A differential scanning calorimetry study of the kinetics of the β→γ phase transformation in plutonium, Thermochimica Acta, 547 (2012) 99-105.

[104] C.A. Alexander, V.E. Wood, Thermal conductivity of plutonium above room temperature, Journal of Applied Physics, 103 (2008) 063704.

[105] J.A. Lee, K. Mendelssohn, D.A. Wigley, Effect of self-irradiation on the resistivity of plutonium, Physics Letters, 1 (1962) 325-327.

[106] C.H. Booth, D.T. Olive, Effect of temperature and radiation damage on the local atomic structure of metallic plutonium and related compounds, Advances in Physics X, 2 (2017) 1-21.

[107] S.K. McCall, M.J. Fluss, B.W. Chung, M.W. McElfresh, D.D. Jackson, G.F. Chapline, Emergent magnetic moments produced by self-damage in plutonium, Proceedings of the National Academy of Sciences of the United States of America, 103 (2006) 17179-17183.

[108] S.K. McCall, M.J. Fluss, B.W. Chung, M.W. McElfresh, G.F. Chapline, D.D. Jackson, R.J. Haire, Isochronal annealing studies in Pu and Pu alloys using magnetic susceptibility, Journal of Alloys and Compounds, 444-445 (2007) 168-173.

[109] R. Lallement, D.A. Wigley, Étude de la variation de longueur du plutonium α par autoirradiation à 4° K, Physica Status Solidi, 21 (1967) 145-150 (in French).

[110] M. Janoschek, P. Das, B. Chakrabarti, D.L. Abernathy, M.D. Lumsden, J.M. Lawrence, J.D. Thompson, G.H. Lander, J.N. Mitchell, S. Richmond, M. Ramos, F. Trouw, J.-X. Zhu, K. Haule, G. Kotliar, E.D. Bauer, The valence-fluctuating ground state of plutonium, Science Advances, 1 (2015) e1500188.

[111] B. Maiorov, J.B. Betts, P. Söderlind, A. Landa, S.C. Hernandez, T.A. Saleh, F.J. Freibert, A. Migliori, Elastic moduli of δ-Pu^{239} reveal aging in real time, Journal of Applied Physics, 121 (2017) 125107.

[112] A.V. Karavaev, V.V. Dremov, MD study of the finite temperature effects on the phase ordering, stacking fault energy, and edge dislocation core structure in elemental Pu and Pu–Ga alloys, Journal of Nuclear Materials, 457 (2015) 94-99.

[113] N. Lanatà, Y. Yao, C.-Z. Wang, K.-M. Ho, G. Kotliar, Phase diagram and electronic structure of praseodymium and plutonium, Physical Review X, 5 (2015) 011008.

[114] J.J. Ríos-Ramírez, J.F. Rivas-Silva, A. Flores-Riveros, Ground state stability of δPu by way of introducing exact exchange within a DFT potential for correlated electrons, Computational Materials Science, 126 (2017) 12-21.

[115] S.C. Hernandez, F.J. Freibert, J.M. Willis, Density functional theory study of defects in unalloyed δ-Pu, Scripta Materialia, 134 (2017) 57-60.

[116] Y.-J. Zhu, Y.-L. Gao, Density function theory calculation of crystal properties and electronic structure of δ-Pu, Key Engineering Materials, 727 (2017) 712-717.

[117] P. Söderlind, Lattice dynamics and elasticity for epsilon-plutonium, Scientific Reports, 7 (2017) 1116.

[118] B. Dorado, F. Bottin, J. Bouchet, Phonon spectra of plutonium at high temperatures, Physical Review B, 95 (2017) 104303.

[119] A.N. Filanovich, Phonon anhormonicity and Gruneisen parameters of alpha-plutonium, Journal of Nuclear Materials, 467 (2015) 894-898.

[120] C.-M. Li, R. Yang, B. Johansson, e. al., Anomalous thermodynamic properties and phase stability of delta-$Pu_{1-x}M_x$ (M = Ga and Al) alloys from first-principles calculations, Physical Review B, 94 (2017) 214108.

[121] A. Migliori, P. Söderlind, A. Landa, F.J. Freibert, B. Maiorov, B.J. Ramshaw, J.B. Betts, Origin of the multiple configurations that drive the response of δ-plutonium's elastic moduli to temperature, Proceedings of the National Academy of Sciences of the United States of America, 113 (2016) 11158-11161.

[122] A. Perron, P.E.A. Turchi, A. Landa, B. Oudot, B. Ravat, F. Delaunay, Thernodynamic assessments and inter-relationships between systems involving Al, Am, Ga, Pu, and U, Journal of Nuclear Materials, 482 (2016) 187-200.

[123] W.H. Zachariasen, F.H. Ellinger, The crystal structure of alpha plutonium metal, Acta Crystallographica, 16 (1963) 777-783.

[124] W.H. Zachariasen, F. Ellinger, The crystal structure of alpha-plutonium metal, Journal of Chemical Physics, 27 (1957) 811-812.

[125] T. Hahn, ed., International Tables for Crystallography, Volume A: Space-Group Symmetry, Springer, Dordrecht, The Netherlands, 2005.

[126] W.H. Zachariasen, F.H. Ellinger, The crystal structure of beta plutonium metal, Acta Crystallographica, 16 (1963) 369-375.

[127] W.H. Zachariasen, F.H. Ellinger, Crystal chemical studies of the 5*f*-series of elements. XXIV. The crystal structure and thermal expansion of γ-plutonium, Acta Crystallographica, 8 (1955) 431-433.

[128] F.H. Ellinger, Crystal structure of δ'-plutonium and the thermal expansion characteristics of δ, δ', and ε plutonium, Journal of Metals (Transactions AIME), 8 (1956) 1526-1529.

[129] E.R. Jette, Some physical properties of plutonium metal, Journal of Chemical Physics, 23 (1955) 365.

[130] D.R. Stephens, The phase diagram of plutonium, Journal of Physics and Chemistry of Solids, 24 (1963) 1197-1202.

[131] R.G. Liptai, R.J. Friddle, The phase diagram of plutonium at pressures up to 75 kbar, Journal of the Less-Common Metals, 10 (1966) 292-294.

[132] J.R. Morgan, New pressure-temperature diagram of plutonium, in: W.N. Miner (Ed.) Plutonium 1970 and other actinides, Metallurgical Society of AIME, Santa Fe, NM, 1970, pp. 669-678.

[133] F. Lalire, B. Ravat, B. Outot, B. Appolaire, A. Perron, E. Aeby-Gautier, F. Delaunay, Phase transformation in PuGa 1 at.% alloy: New valuable information into the isothermal martensitic δ-α' transformation, Acta Materialia, 123 (2017) 125-136.

[134] M.B. Matthews, D.W. Wheeler, Quantitative method for describing heterogeneity in plutonium-gallium alloys, Philosophical Magazine, 97 (2017) 989-1011.

[135] M. Ling, Thermal cycling as a novel method to determine the "equilibrium" Pu-Ga phase diagram, Journal of Thermal Analysis and Calorimetry, 127 (2017) 345-353.

[136] D.W. Wheeler, S.M. Ennaceur, M.B. Matthews, P. Roussel, P.D. Bayer, Structure and phase stability of a Pu-0.32 wt% Ga alloy, Journal of Nuclear Materials, 476 (2016) 205-212.

[137] A.V. Karavaev, V.V. Dremov, G.V. Ionov, Equilibrium thermodynamics of radiation defect clusters in delta-phase Pu-Ga alloys, Journal of Nuclear Materials, 468 (2016) 46-55.

[138] D.W. Wheeler, S.M. Ennaceur, M.B. Matthews, Phase stability of an aged Pu–0.27 wt.% Ga alloy, Journal of Nuclear Materials, 456 (2015) 68-73.

[139] A.V. Karavaev, V.V. Dremov, G.V. Ionov, B.W. Chung, Equilibrium thermodynamics of helium in d-phase Pu-Ga alloys, Acta Materialia, 79 (2014) 248-257.

[140] J.N. Mitchell, M. Stan, D.S. Schwartz, C.J. Boehlert, Phase stability and phase transformations in plutonium and plutonium-gallium alloys, Metallurgical and Materials Transactions A, 35 (2004) 2267-2278.

[141] A.J. Schwartz, H. Cuynn, K.J.M. Blobaum, M.A. Wall, K.T. Moore, W.J. Evans, D.L. Farber, J.R. Jeffries, T.B. Massalski, Atomic structure and phase transformations in Pu alloys, Progress in Materials Science, 54 (2009) 909-943.

[142] T.G. Zocco, D.S. Schwartz, J. Park, Investigation of plutonium allotropic phase transformations through differential scanning calorimetry, Journal of Nuclear Materials, 353 (2006) 119-126.

[143] D. Schwartz, J. Mitchell, Heating-cooling asymmetry in the g-d transformation in plutonium: Clausius-Clapeyron considerations (LA-UR-25832), 2015, pp. 529-530.

[144] A. Farrow, J. Mitchell, T. Mitchell, T. Saleh, C. Knapp, D. Korzekwa, Solid-solid phase transformations during casting of plutonium, in: PTM 2015 - Proceedings of the International Conference on solid-solid phase transformations in inorganic materials 2015, 2015, pp. 1075-1080.

[145] F.L. Oetting, R.O. Adams, The chemical thermodynamics of nuclear materials VII. The high-temperature heat capacity of unalloyed plutonium metal, Journal of Chemical Thermodynamics, 15 (1983) 537-554.

[146] F.L. Oetting, E.D. West, An adiabatic calorimeter for the range 300 to 700 K, Journal of Chemical Thermodynamics, 14 (1982) 107-114.

[147] L.J. Wittenberg, C.R. Hudgens, T.K. Engel, D.L. Roesch, D.B. Sullenger, P.A. Tucker, D.E. Etter, K.D. Phipps, W.G. Rohr, J.E. Selle, G.A. Vaughn, Reactor fuels and materials development, Plutonium research: April-September, 1966 (Mound Laboratory Report MLM-1347), Mound Laboratory, Miamisburg, OH, 1967.

[148] F.W. Schonfeld, R.E. Tate, The thermal expansion behavior of unalloyed plutonium (Los Alamos National Laboratory Report LA-13034-MS), Los Alamos, NM, 1996.

[149] O.J. Wick, ed., Plutonium Handbook, Gordon and Branch, New York, 1967.

[150] W.H. Zachariasen, F.H. Ellinger, Unit cell and thermal expansion of β-plutonium metal, Acta Crystallographica, 12 (1959) 175-176.

[151] A.S. Coffinberry, M.B. Waldron, A review of the physical metallurgy of plutonium, in: H.M. Finniston, J.P. Howe (Eds.) Progress in Nuclear Energy, Series V (Metallurgy and Fuels), Pergamon Press, New York, 1956, pp. 354-410.

[152] C.Z.J. Serpan, L.J. Wittenberg, Trans AIME, 221 (1961) 1017.

[153] J.F. Andrew, Thermal conductivity of plutonium metal, Journal of Physics and Chemistry of Solids, 28 (1967) 577-580.

[154] A.A. Povzner, A.N. Filanovich, V.A. Os'kina, A.G. Volkov, Electron heat capacity and lattice properties of americium, Technical Physics, 58 (2013) 1844-1847 (translated from Zhurnal Tekhnicheskoi Fiziki, vol. 1883, no. 1812, pp. 1141-1143, 2013).

[155] R.O.A. Hall, J.A. Lee, M.J. Mortimer, D.L. McElroy, W. Müller, J.-C. Spirlet, Thermodynamic functions of americium metal, Journal of Low Temperature Physics, 41 (1980) 397-404.

[156] J.-C. Griveau, É. Colineau, Superconductivity in transuranium elements and compounds, Comptes Rendus Physique, 15 (2014) 599-615.

[157] A.G. Volkov, A. Povzner, A. Filanovich, The peculiarities of americium electronic structure and magnetic susceptibility, Journal of Superconductivity and Novel Magnetism, 26 (2013) 1765-1769.

[158] P. Söderlind, K.T. Moore, A. Landa, B. Sadigh, J.A. Bradley, Pressure-induced changes in the electronic structure of americium metal, Physical Review B, 84 (2011) 075138.

[159] A.B. Shick, J. Kolorenc, A.I. Lichtenstein, L. Havela, Electronic structure and spectral properties of Am, Cm, and Bk: Charge-density self-consistent LDA plus HIA calculations in the FP-LAPW basis, Physical Review B, 80 (2009) 085106.

[160] Y.Y. Tsiovkin, A.V. Lukoyanov, A.O. Shorikov, L.Y. Tsiovkina, A.A. Dyachenko, V.B. Bystrushkin, M.A. Korotin, V.I. Anisimov, V.V. Dremov, Electrical resistivity of pure transuranium metals under pressure, Journal of Nuclear Materials, 413 (2011) 41-46.

[161] A. Kutepov, K. Haule, S.Y. Savrasov, G. Kotliar, Electronic structure of Pu and Am metals by self-consistent relativistic GW method, Physics Review B: Condensed Matter, 85 (2012) 155129.

[162] A.K. Verma, P. Modak, S.M. Sharma, S.K. Sikka, Investigation of equation of states and electronic properties of Am and Cm metals in their gamma plutonium phase using GGA+SO+U method, Solid State Communications, 164 (2013) 22-26.

[163] D.B. McWhan, B.B. Cunningham, J.C. Wallman, Crystal structure, thermal expansion, and melting point of americium metal, Journal of Inorganic and Nuclear Chemistry, 24 (1962) 1025-1038.

[164] W.H. Runde, W.W. Schulz, Americium, in: L.R. Morss, N.M. Edelstein, J. Fuger (Eds.) The Chemistry of the Actinide and Transactinide Elements, Springer, Dordrecht, The Netherlands, 2010, pp. 1265-1395.

[165] D.R. Stephens, H.D. Stromberg, E.M. Lilley, Phase diagram. Compressibility and resistance of americium as a function of pressure, Journal of Physics and Chemistry of Solids, 29 (1968) 815-821.

[166] R.L. Rose, R.E. Kelley, D.R. Lesuer, Dilatometry and differential thermal analysis of americium metal, Journal of Nuclear Materials, 79 (1979) 414-416.

[167] C. Sari, W. Müller, U. Benedict, Phase transition of americium metal, Journal of Nuclear Materials, 45 (1972/73) 73-74.

[168] J.K. Gibson, R.G. Haire, Phase relations in neptunium, americium, and the binary alloy systems Np-Am and Np-Ln (Ln = La, Nd, Lu), Journal of Nuclear Materials, 195 (1992) 156-165.

[169] R.O.A. Hall, M.J. Mortimer, D.L. McElroy, W. Müller, J.C. Spirlet, The specific heat of americium-241 metal from 15 to 300K, in: W. Müller, R. Lindner (Eds.) Transplutonium Elements, North-Holland Publishing Company, Amsterdam, 1976.

[170] D.B. McWhan, J.C. Wallman, B.B. Cunningham, L.B. Asprey, F.H. Ellinger, W.H. Zachariasen, Preparation and crystal structure of americium metal, Journal of Inorganic and Nuclear Chemistry, 15 (1960) 185-187.

[171] P. Graf, B.B. Cunningham, C.H. Dauben, J.C. Wallman, D.H. Templeton, H. Ruben, Crystal structure and magnetic susceptibility of americium metal, Journal of the American Chemical Society, 78 (1956) 2340.

[172] E.F. Westrum Jr., L. Eyring, The preparation and some properties of americium metal, Journal of the American Chemical Society, 73 (1951) 3396-3398.

[173] R.B. Roof, R.G. Haire, D. Schiferl, L. Schwalbe, E.A. Kmetko, J.L. Smith, High-pressure phase in americium metal, Science, 207 (1980) 1353-1355.

[174] A. Lindbaum, S. Heathman, T. Le Bihan, R.G. Haire, M. Idiri, G.H. Lander, High-pressure crystal structures of actinide elements to 100 GPa, Journal of Physics: Condensed Matter, 15 (2003) S2297-S2303.

[175] W. Müller, R. Schenkel, H.E. Schmidt, J.C. Spirlet, D.W. McElroy, R.O.A. Hall, M.J. Mortimer, The electrical resistivity and specific heat of americium metal, Journal of Low Temperature Physics, 30 (1978) 561.

[176] R.J.M. Konings, The high-temperature heat capacity of americium, Journal of Alloys and Compounds, 348 (2003) 38-42.

[177] R.J. Silva, G. Bidoglio, M.H. Rand, P.B. Robouch, H. Wanner, I. Puigdomenech, Chemical Thermodynamics of Americium, Elsevier North-Holland, Amsterdam, 1995.

[178] J.W. Ward, Systematic properties of actinide metals, Journal of the Less-Common Metals, 121 (1986) 1-13.

[179] W.Z. Wade, T. Wolf, Preparation and some properties of americium metal, Journal of Inorganic and Nuclear Chemistry, 29 (1967) 2577-2587.

[180] R. Schenkel, W. Müller, The electrical resistivity of ^{241}Am metal, Journal of Physics and Chemistry of Solids, 38 (1977) 1301-1305.

[181] Z. Felfli, A.Z. Msezane, D. Sokolovski, Resonances in low-energy electron elastic cross sections for lanthanide atoms, Physical Review A - Atomic, Molecular, and Optical Physics, 79 (2009) 012714.

[182] J.K. Baria, A.R. Jani, Lattice dynamics of La, Yb, Ce and Th, Physica B: Condensed Matter, 405 (2010) 2065-2071.

[183] H.M. Tütüncü, G.P. Srivastava, Ab initio investigations of the phonon anomaly and superconductivity in fcc La, Journal of Applied Physics, 104 (2008) 063916.

[184] L.W. Nixon, D.A. Papaconstantopoulos, M.J. Mehl, Electronic structure and superconducting properties of lanthanum, Physical Review B, 78 (2008) 214510.

[185] P. Souvatzis, T. Björkman, O. Eriksson, P. Andersson, M.I. Katsnelson, S.P. Rudin, Dynamical stabilization of the body centered cubic phase in lanthanum and thorium by phonon-phonon interaction, Journal of Physics Condensed Matter, 21 (2009) 175402.

[186] P. Loptien, L. Zhou, A.A. Khajetoorians, J. Wiebe, R. Wiesendanger, Superconductivity of lanthanum revisited: enhanced critical temperature in the clean limit, Journal of Physics Condensed Matter, 26 (2014) 425703.

[187] F. Jie, J. Zhao, Gupta potential for rare earth elements of the fcc phase: lanthanum and cerium, Modelling and Simulation in Materials Science and Engineering, 21 (2013) 065003.

[188] C. Wei, J.L. Fan, H.R. Gong, Structural, thermodynamic, and mechanical properties of bulk La and a-La2O3, Journal of Alloys and Compounds, 618 (2015) 615-622.

[189] P.H. Pan, D.K. Finnemore, A.J. Bevolo, H.R. Shanks, B.J. Beaudry, F.A. Schmidt, G.C. Danielson, Heat-capacity of high-purity lanthanum, Physical Review B: Condensed Matter, 21 (1980) 2809-2814.

[190] F. Mozaffari, Improved equation of state for metals from surface tension, Physics and Chemistry of Liquids, 53 (2015) 481-489.

[191] K.A. Gschneidner Jr., Physical Properties of the Rare Earth Metals, in: W.M. Haynes (Ed.) CRC Handbook of Chemistry and Physics, 96th Edition (Internet Version 2016), CRC Press/Taylor and Francis, Boca Raton, FL, 2015.

[192] B.J. Beaudry, K.A. Gschneidner Jr., Preparation and basic properties of the rare earth metals, in: K.A. Gschneidner Jr., L. Eyring (Eds.) Handbook on the Physics and Chemistry of Rare Earths, North Holland Publishing Company, 1978, pp. 173-232.

[193] F.H. Spedding, J.J. Hanak, A.H. Daane, High temperature allotropy and thermal expansion of the rare-earth metals, Journal of the Less-Common Metals, 3 (1961) 110-124.

[194] K.A. Gschneidner Jr., F.W. Calderwood, Intra rare earth binary alloys: phase relationships, lattice parameters and systematics, in: K.A. Gschneidner Jr., L. Eyring (Eds.) Handbook on the Physics and Chemistry of Rare Earths, Elsevier Science Publishers B.V., Amsterdam, 1986, pp. 1-161.

[195] J.F. Cannon, Behavior of the elements at high pressures, Journal of Physical and Chemical Reference Data, 3 (1974) 781-824.

[196] J.R. Berg, F.H. Spedding, A.H. Daane, The high temperature heat contents and related thermodynamic properties of lanthanum, praseodymium, europium, ytterbium, and yttrium (US-AEC Technical Report IS-327), 1961.

[197] F.M. Jaeger, J.A. Bottema, E. Rosenbohm, The exact measurement of the specific heats of metals at high temperatures. XXVII. The specific heats and the electrical resistance of lanthanum, Proceedings of the KNAW (Koninklijke Nederlandse Akademie van Wetenschappen), 38 (1936) 921-927.

[198] L.A. Stretz, R.G. Bautista, The high-temperature enthalpy of liquid lanthanum by levitation calorimetry, Journal of Chemical Thermodynamics, 7 (1975) 83-88.

[199] S.R. Atalla, Experimental investigation of thermophysical properties of liquid metals at elevated temperatures, High Temperatures-High Pressures, 4 (1972) 447-451.

[200] A.A. Kurichenko, A.D. Ivliev, V.E. Zinoviev, Thermal and kinetic properties of light rare earth metals near high temperature structural transition points, Solid State Communications, 56 (1985) 1065-1068.

[201] I.I. Novikov, I.P. Mardykin, Specific heat of yttrium, lanthanum, and praseodymium at high temperatures, High Temperature 13 (1975) 293-297 (translated from Teplofizika Vysokikh Temperatur, vol 213, no. 292, pp. 318-323, 1975).

[202] A.A. Kurichenko, A.D. Ivliev, V.E. Zinoviev, The study of the thermophysical properties of rare-earth metals with the use of molecular laser radiation, High Temperature, 24 (1986) 369-375 (translated from Teplofizika Vysokikh Temperatur, vol. 324, no. 363, pp. 493-499, 1986).

[203] F. Barson, S. Legvold, F.H. Spedding, Thermal expansion of rare earth metals, Physical Review, 105 (1957) 418-424.

[204] F.H. Spedding, K.A. Gschneidner Jr., A.H. Daane, The lanthanum-carbon system, Transactions of the Metallurgical Society of AIME, 215 (1959) 192-199.

[205] S.A. Frizen, A.D. Ivliyev, L.K. Katanova, N.I. Moreva, Peculiarities of the thermal expansion of polycrystalline lanthanum, praseodymium and neodymium in the temperature range 290-970 K, Physics of Metals and Metallography, 60 (1985) 176-178 (translated from Fizika metallov i metallovedenie, vol. 160, no. 172, pp. 398-400, 1985).

[206] A.A. Eliseev, E.I. Yarembash, E.S. Vigileva, L.I. Antonova, V.A. Zachatskaya, Polymorphism of lanthanum, Russian Journal of Inorganic Chemistry, 9 (1964) 565-567.

[207] K.A. Gschneidner Jr., Rare earth alloys: a critical review of the alloy systems of the rare earth, scandium, and yttrium metals, D. Van Nostrand Company, Inc. (on-line copy at http://hdl.handle.net/2027/mdp.39015078670422), Princeton, New Jersey, 1961.

[208] L.J. Wittenberg, D. Ofte, W.G. Rohr, The viscosity and density of molten lanthanum, cerium, and praseodymium metals, in: K.S. Vorres (Ed.) Rare Earth Research, Gordon and Breach, New York, 1964, pp. 257-275.

[209] L.J. Wittenberg, D. Ofte, W.G. Rohr, The viscosity and density of molten lanthanum, cerium, and praseodymium metals, in: Third International Rare Earth Conference, Clearwater, FL, 1963.

[210] V.I. Kononenko, A.L. Sukhman, S.L. Gruverman, V.V. Torokin, Density and surface tension of liquid rare earth metals, scandium, and yttrium, Physica Status Solidi A, 84 (1984) 423.

[211] B.W. Jolliffe, R.P. Tye, R.W. Powell, The thermal and electrical conductivities of scandium, yttrium and manganese and twelve rare-earth metals, at normal temperature, Journal of the Less-Common Metals, 11 (1966) 388-394.

[212] A.V. Golubkov, E.D. Devyatkova, V.P. Zhuze, V.M. Sergeeva, I.A. Smirnov, Thermal conductivity of lanthanum and its monochalcogenides, Soviet Physics--Solid State (Translated from Fizika Tverdogo Tela), 8 (1966) 1403-1410.

[213] G. Krieg, R.B. Genter, A.V. Grosse, Electrical conductivity of liquid lanthanum, Inorganic and Nuclear Chemistry Letters, 5 (1969) 819-823.

[214] S. Legvold, F.H. Spedding, Quarterly summary research report in physics for April, May, and June 1954 (USAEC report ISC-508), Ames Laboratory, Ames, Iowa, 1954.

[215] K.A. Gschneidner Jr., V.K. Pecharsky, J. Cho, S.W. Martin, β to γ transformation in cerium -- a twenty year study, Scripta Materialia, 34 (1996) 1717-1722.

[216] B. Amadon, A. Gerossier, Comparative analysis of models for the alpha-gamma phase transition in cerium: A DFT plus DMFT study using Wannier orbitals, Physical Review B, 91 (2015) 161103.

[217] M.-F. Tian, H.-F. Song, H.-F. Liu, C. Wang, Z. Fang, X. Dai, Thermodynamics of the α-γ transition in cerium studied by an LDA + Gutzwiller method, Physical Review B, 91 (2015) 125148.

[218] N. Devaux, M. Casula, F. Decremps, S. Sorella, Electronic origin of the volume collapse in cerium, Physical Review B, 91 (2015) 081101(R).

[219] B. Johansson, W. Luo, S. Li, R. Ahuja, Cerium; Crystal Structure and Position in The Periodic Table, Scientific Reports, 4 (2014) 6398.

[220] T. Jarlborg, Role of thermal disorder for magnetism and the alpha-gamma transition in cerium: Results from density-functional theory, Physical Review B, 89 (2014) 184426.

[221] J. Bieder, B. Amadon, Thermodynamics of the alpha-gamma transition in cerium from first principles, Physical Review B, 89 (2014) 195132.

[222] B. Chakrabarti, M.E. Pezzoli, G. Sordi, K. Haule, G. Kotliar, Alpha-gamma transition in cerium: Magnetic form factor and dynamic magnetic susceptibility in dynamical mean-field theory, Physical Review B, 89 (2014) 125113.

[223] A.O. Shorikov, S.V. Streltsov, M.A. Korotin, V.I. Anisimov, Phase stability of α-, γ-, and ε-Ce: DFT+DMFT Study, JETP Letters, 102 (2015) 616-619.

[224] L. Zhang, Y.-H. Li, X.-M. Li, Z.-G. Zhang, X.-P. Ye, L.-C. Cai, γ- and α-Ce phase diagram: first-principle calculation, Chinese Physics B, 25 (2016) 033102.

[225] M. Casadei, X. Ren, P. Rinke, A. Rubio, M. Scheffler, Density functional theory study of the α-γ phase transition in cerium: role of electron correlation and *f*-orbital localization, Physical Review B, 93 (2016) 075153.

[226] S.S. Hecker, The magic of plutonium: 5*f* electrons and phase instability, Metallurgical and Materials Transactions A, 35A (2004) 2207-2221.

[227] C.-E. Hu, Z.-Y. Zeng, L. Zhang, L.-C. Cai, Lattice stability and thermal equation of state of β-La from first-principles calculations, Solid State Communications, 151 (2011) 1802-1805.

[228] B. Siberchicot, J. Clérouin, Properties of hot liquid cerium by LDA+U molecular dynamics, Journal of Physics Condensed Matter, 24 (2012) 455603.

[229] S.S. Agafonov, M.S. Blanter, V.P. Glazkov, V.A. Somenkov, M.N. Shushunov, Thermal vibrations and polymorphic β→γ transition in cerium, Physics of Metals and Metallography, 110 (2010) 338-345.

[230] V.V. Hung, D.T. Hai, H.K. Hieu, Thermodynamic properties and structural phase transition of cerium under high pressure, Vacuum, 114 (2015) 119-123.

[231] I. Loa, E.I. Isaev, M.I. McMahon, D.Y. Kim, B. Johansson, A. Bosak, M. Krisch, Lattice dynamics and superconductivity in cerium at high pressure, Physical Review Letters, 108 (2012) 045502.

[232] A. Cadien, Q.Y. Hu, Y. Meng, Y.Q. Cheng, M.W. Chen, J.F. Shu, H.K. Mao, H.W. Sheng, First-order liquid-liquid phase transition in cerium, Physical Review Letters, 110 (2013) 125503.

[233] J.A. Bradley, K.T. Moore, G. van der Laan, J.P. Bradley, R.A. Gordon, Core and shallow-core *d*- to *f*-shell excitations in rare-earth metals, Physical Review B, 84 (2011) 205105.

[234] Z.-K. Liu, S.-L. Shang, Y. Wang, Fundamentals of thermal expansion and thermal contraction, Materials, 10 (2017) UNSP 410.

[235] C. Ma, Z.-Y. Dou, H.-Y. Zhu, G.-Y. Fu, X. Tan, B. Bai, P.-C. Zhang, Q.-L. Cui, Structure phase transformation and equation of state of cerium metal under pressures up to 51 GPa, Chinese Physics B, 25 (2016).

[236] A. Östlin, I. Di Marco, I.L.M. Locht, J.C. Lashley, L. Vitos, Stacking fault energetics of α- and γ-cerium investigated with *ab initio* calculations, (2016).

[237] B.J. Jensen, F.J. Cherne, M.B. Prime, K. Fezzaa, A.J. Iverson, C.A. Carlson, J.D. Yeager, K.J. Ramos, D.E. Hooks, J.C. Cooley, G. Dimonte, Jet formation in cerium metal to examine material strength, Journal of Applied Physics, 118 (2015) 195903.

[238] K.A. Gschneidner Jr., R.O. Elliott, R.R. McDonald, Effects of alloying additions on the α ↔ γ transformation of cerium--part II. Effects of scandium, thorium, and plutonium additions, Journal of Physics and Chemistry of Solids, 23 (1962) 1191-1199.

[239] K.A. Gschneidner Jr., Systematics in lanthanide and actinide solids, Journal of Alloys and Compounds, 223 (1995) 165-169.

[240] K.A. Gschneidner Jr., V.K. Pecharsky, The standard state of cerium, Journal of Phase Equilibria, 20 (1999) 612-614.

[241] C.J. McHargue, H.L.J. Yakel, L.K. Jetter, Allotropic modifications of metallic cerium, Acta Crystallographica, 10 (1957) 832-833.

[242] A.F. Schuch, J.H. Sturdivant, The structure of cerium at the temperature of liquid air, Journal of Chemical Physics, 18 (1950) 145.

[243] K.A. Gschneidner Jr., R.O. Elliott, R.R. McDonald, Effects of alloying additions on the $\gamma \leftrightarrow \alpha$ transformation of cerium--part I. Pure cerium, Journal of Physics and Chemistry of Solids, 23 (1962) 555-566.

[244] F.H. Spedding, J.J. McKeown, A.H. Daane, The high temperature thermodynamic functions of cerium, neodymium and samarium, Journal of Physical Chemistry, 64 (1960) 289-294.

[245] L.K. Kuntz, R.G. Bautista, The heat capacities and heat content of molten cerium by levitation calorimetry, Metallurgical Transactions B, 7 (1976) 107-113.

[246] J. Li, T. Ishikawa, J. Okada, Y. Watanabe, J. Yu, S. Yoda, Z. Yuan, Noncontact thermophysical property measurement of liquid cerium by electrostatic levitation, Journal of Materials Research, 24 (2009) 2449-2452.

[247] W.G. Rohr, The liquid densities of cerium and neodymium metals, Journal of the Less-Common Metals, 10 (1966) 389-391.

[248] R.W. Powell, B.W. Jolliffe, The thermal conductivities of scandium and some rare earth metals, Physics Letters, 14 (1965) 171-172.

[249] V.E. Zinov'ev, P.V. Gel'd, A.L. Sokolov, High-temperature transport properties of cerium, praseodymium, neodymium, and europium, Soviet Physics--Solid State 18 (1976) 764-766 (Translated from Fizika Tverdogo Tela vol 718 pp. 1329-1332, May 1976).

[250] I.I. Novikov, I.P. Mardykin, Thermal properties of lanthanides at high temperatures, High Temperature, 11 (1974) 472-476 (Translated from Teplofizika Vysokikh Temperatur vol. 411, no 473, pp. 527-532, 1973).

[251] A.Y. Kuznetsov, V.P. Dmitriev, O.I. Bandilet, H.P. Weber, High-temperature fcc phase of Pr: Negative thermal expansion and intermediate valence state, Physical Review B, 68 (2003) 064109.

[252] S.R. Evans, I. Loa, L.F. Lundegaard, M.I. McMahon, Phase transitions in praseodymium up to 23 GPa: An x-ray powder diffraction study, Physical Review B, 80 (2009) 134105.

[253] G.J. Piermarini, C.E. Weir, Allotropy in some rare-earth metals at high pressures, Science, 144 (1964) 69-71.

[254] S.N. Banchila, L.P. Filippov, Experimental study of the set of thermal properties of certain rare-earth metals at high temperatures, Journal of Engineering Physics, 27 (1974) 839-841 (Translated from Inzhenerno-Fizicheskii Zhurnal, vol. 827, no. 831, pp. 868-871, 1974).

[255] G.A. Berezovskii, G.S. Burkhanov, N.B. Kal'chugina, I.E. Paukov, A.B. Tagaev, O.D. Chistyakov, Specific heat of praseodymium in the range from 5.6 to 314 K, Russian Journal of Physical Chemistry, 64 (1990) 1419-1422 (translated from Zhurnal Fizicheskoi Khimii vol 1464 pp 2636-2640, 1990).

[256] E.D. Devyatkova, V.P. Zhuze, A.V. Golubkov, V.M. Sergeeva, I.A. Smirnov, Thermal conductivity of Sm, Pr, and their monochalcogenides, Soviet Physics--Solid State, 6 (1964) 343-346 (Translated from Fizika Tverdogo Tela, vol. 346 no. 342 pp 430-435, 1964).

[257] N. Velisavljevic, Y.K. Vohra, S.T. Weir, Simultaneous electrical and X-ray diffraction studies on neodymium metal to 152 GPa, High Pressure Research, 25 (2005) 137-144.

[258] A. Nakaue, Studies on the pressure-temperature phase diagram of Nd, Sm, Gd, and Dy, Journal of the Less-Common Metals, 60 (1978) 47-58.

[259] L. Binkele, Transport properties of yttrium and six rare-earth metals in the temperature range 300-1000 K, High Temperatures-High Pressures, 21 (1989) 131-137.

[260] V.P. Zhuze, A.V. Golubkov, E.V. Goncharova, V.M. Sergeeva, Electrical properties of rare-earth monochalcogenides (cerium subgroup), Soviet Physics--Solid State, 6 (1964) 205-212 (Translated from Fizika Tverdogo Tela, vol. 206, no. 201, pp. 257-267, January 1964).

[261] Z. Felfli, A.Z. Msezane, D. Sokolovski, Low-energy electron elastic scattering from complex atoms: Nd, Eu, and Tm, Canadian Journal of Physics, 87 (2009) 321-327.

[262] F.M. Jaeger, J.A. Bottema, E. Rosenbohm, The exact measurement of the specific heats of metals at high temperatures. XXIX. Specific heats, electrical resistance, thermoelectrical behaviour and thermal expansion of neodynium in connection with its allotropic changes, Proceedings of the KNAW (Koninklijke Nederlandse Akademie van Wetenschappen), 41 (1938) 120-138.

[263] H.G. Jensen, Kohlrausch heat conductivity apparatus for intermediate or advanced laboratory, American Journal of Physics, 38 (1970) 870-874.

[264] C. Hiemstra, P. Keegstra, W.T. Masselink, Electrical resistitivities of solid and liquid Pr, Nd, and Sm, Journal of Physics F--Metal Physics, 14 (1984) 1867-1875.

[265] A.T. Burkov, M.V. Vedemikov, Temperature dependences of the thermoelectric power and electrical resistivity of praseodymium and neodymium in solid and liquid states, Soviet Physics--Solid State, 26 (1984) 2211-2212 (Translated from Fizika Tverdogo Tela, vol 2216, no 2211, pp 3673-3676, December 1984).

[266] I.P. Mardykin, Electrical resistivity of lanthanum, neodymium, and erbium at high temperatures, High Temperature, 13 (1975) 191-193 (Translated from Teplofizika Vysokikh Temperatur, vol 113, no 191, pp 211-213, January-February 1975).

[267] J.K. Alstad, R.V. Colvin, S. Legvold, F.H. Spedding, Electrical resistivity of lanthanum, praseodymium, neodymium, and samarium, Physical Review, 121 (1961) 1637-1639.

[268] F.H. Spedding, A.H. Daane, K.W. Herrmann, Electrical resistivities and phase transformations of lanthanum, cerium, praseodymium, and neodymium, Journal of Metals, 9 (1957) 895-897.

[269] M.W. Chase Jr., NIST-JANAF Thermochemical Tables, Fourth Edition, Part II (Cr-Zr), Journal of Physical and Chemical Reference Data, Monograph No. 9 (1998).

[270] P.F. Paradis, W.K. Rhim, Thermophysical properties of zirconium at high temperature, Journal of Materials Research, 14 (1999) 3713-3719.

[271] V. Petukhov, Thermal expansion of zirconium in the solid phase, High Temperatures-High Pressures, 35/36 (2003/2004) 15-23.

[272] J.K. Fink, L. Leibowitz, Thermal conductivity of zirconium, Journal of Nuclear Materials, 226 (1995) 44.

[273] H. Zhao, X. Hu, M. Song, S. Ni, Mechanisms for deformation induced hexagonal close-packed structure to face-centered cutic structure transformation in zirconium, Scripta Materialia, 132 (2017) 63-67.

[274] O. MacKain, M. Cottura, D. Rodney, E. Clouet, Atomic-scale modeling of twinning disconnections in zirconium, Physical Review B, 95 (2017) 134102.

[275] J. Singh, S. Matesh, S. Roy, G. Kumar, D. Srivastava, G.K. Dey, N. Saibaba, I. Samajdar, Temperature dependence of work hardening in sparsely twinning zirconium, Acta Materialia, 123 (2017) 337-349.

[276] V.N. Chuvil'deev, A.V. Semenchaya, Model of grain-boundary self-diffusion in alpha- and beta-phases of titanium and zirconium, Physics of the Solid State, 59 (2017) 1-8.

[277] T.D. Swinburne, M.G. Glavicic, K.M. Rahman, N.G. Jones, J. Coakley, D.E. Eakins, T.G. White, V. Tong, D. Milathianaki, G.J. Williams, D. Rugg, A.P. Sutton, D. Dye, Picosecond dynamics of a shock-driven displacive phase transformation in Zr, Physical Review B, 93 (2016) 144119.

[278] C. Nisoli, H. Zong, S.R. Niezgoda, D.W. Brown, T. Lookman, Long-time behavior of the ω-->α transition in shocked zirconium: interplay of nucleation and plastic deformation, Acta Materialia, 108 (2016) 138-142.

[279] M.K. Jacobsen, N. Velisavljevic, S.V. Sinogeikin, Pressure-induced kinetics of the α to ω transition in zirconium, Journal of Applied Physics, 118 (2015) 025902.

[280] H.-R. Wenk, P. Kaercher, W. Kanitpanyacharoen, E. Zepeda-Alarcon, Y. Wang, Orientation relations during the alpha-omega phase transition of zirconium: in situ texture observations at high pressure and temperature, Physical Review Letters, 111 (2013) 195701.

[281] H.K. Yeddu, H. Zong, T. Lookman, Alpha-omega and omega-alpha phase transformations in zirconium under hydrostatic pressure: a 3D mesoscale study, Acta Materialia, 102 (2016) 97-107.

[282] H.W. King, ed., Crystal structures and lattice parameters of allotropes of the elements, in: CRC Handbook of Chemistry and Physics, 96th Edition (Internet Version 2016), CRC Press/Taylor and Francis, Boca Raton, FL, 2016.

[283] A. Heiming, W. Petry, J. Trampenau, W. Miekeley, J. Cockcroft, The temperature dependence of the lattice parameters of pure BCC Zr and BCC Zr-2 at% Co, Journal of Physics and Condensed Matter, 4 (1992) 727-733.

[284] G.B. Skinner, H.L. Johnston, Thermal expansion of zirconium between 298°K and 1600°K, The Journal of Chemical Physics, 21 (1953) 1383-1384.

[285] J. Zhang, Y. Zhao, C. Pantea, J. Qian, L.L. Daemen, P.A. Rigg, R.S. Hixson, C.W. Greeff, G.T. Gray III, Y. Yang, L. Wang, Y. Wang, T. Uchida, Experimental constraints on the phase diagram of elemental zirconium, Journal of Physics and Chemistry of Solids, 66 (2005) 1213-1219.

[286] A. Cezairliyan, F. Righini, Thermodynamic studies of the $\alpha \rightarrow \beta$ phase transformation in zirconium using a subsecond pulse heating technique, Journal of Research of the National Bureau of Standards, 79A (1974) 81-84.

[287] Reference points on the ITS-90 temperature scale, in: W.M. Haynes (Ed.) CRC Handbook of Chemistry and Physics, 97th Edition (Internet Version 2017), CRC Press/Taylor and Francis, Boca Raton, FL, 2017.

[288] W.M. Haynes, ed., Enthalpy of fusion, in: CRC Handbook of Chemistry and Physics, 96th Edition (Internet Version 2016), CRC Press/Taylor and Francis, Boca Raton, FL, 2016.

[289] N.D. Milošević, K.D. Maglić, Thermophysical properties of solid phase zirconium at high temperatures, International Journal of Thermophysics, 27 (2006) 1140-1159.

[290] W.M. Haynes, ed., Physical constants of inorganic compounds, in: CRC Handbook of Chemistry and Physics, 96th Edition (Internet Version 2016), CRC Press/Taylor and Francis, Boca Raton, FL, 2016.

[291] Y.S. Touloukian, P.W. Powell, C.Y. Ho, M.C. Nicolaou, Thermal Diffusivity (Thermophysical Properties of Matter vol. 10), IFI/Plenum, 1973.

[292] P.G. Mardon, J.H. Pearce, An investigation of the neptunium-uranium equilibrium diagram, Journal of the Less-Common Metals, 1 (1959) 467-475.

[293] R.I. Sheldon, D.E. Peterson, The Np-U (Neptunium-Uranium) System, Bulletin of Alloy Phase Diagrams, 6 (1985) 217-219.

[294] K.S. Chan, J.K. Lee, H.I. Aaronson, Kaufman approach calculations of partial phase diagrams amongst Th, U, Np and Pu, Journal of Nuclear Materials, 92 (1980) 237-242.

[295] M. Kurata, Thermodynamic database on U-Pu-Zr-Np-Am-Fe alloy system II - Evaluation of Np, Am, and Fe containing systems, IOP Conference Series: Materials Science and Engineering, 9 (Actinides 2009) (2010).

[296] W. Xie, D. Morgan, CALPHAD modeling and ab initio calculations of the Np-U-Zr system, Computational Materials Science, 143 (2018) 505-514.

[297] W. Xie, Y.A. Chang, D. Morgan, *Ab initio* energetics for modeling phase stability of the Np-U system, Journal of Nuclear Materials, 479 (2016) 260-270.

[298] T. Inoue, T. Matsumura, A. Sasahara, L. Koch, J.C. Spirlet, Transmutation of transuranium elements by a metallic fuel FBR, in: Information Exchange Meeting on Actinide and Fission Product Separataion and Transmutation, OECD Nuclear Energy Agency, 1990, pp. 397-423.

[299] M. Kurata, in: Materials Models and Simulations for Nuclear Fuels, Tokyo University, Japan, December 13-14 2007, 2007.

[300] M. Kurata, Phase diagrams of actinide alloys, in: R.J.M. Konings (Ed.) Comprehensive Nuclear Materials, volume 2, Elsevier, 2012, pp. 139-195.

[301] A. Perron, P.E.A. Turchi, A. Landa, P. Söderlind, B. Ravat, B. Oudot, F. Delaunay, The Pu–U–Am system: An *ab initio* informed CALPHAD thermodynamic study, Journal of Nuclear Materials, 458 (2015) 425-441.

[302] H. Okamoto, Np-U (Neptunium-Uranium), Journal of Phase Equilibria and Diffusion, 34 (2013) 70-71.

[303] A.C. Lawson, J.A. Goldstone, B. Cort, R.J. Martinez, F.A. Vigil, T.G. Zocco, J.W. Richardson Jr., M.H. Mueller, Structure of ζ-phase plutonium-uranium, Acta Crystallographica B: Structural Science, 52 (1996) 32-37.

[304] H.A.C. McKay, J.S. Nairn, M.B. Waldron, The chemistry and metallurgy of neptunium, in: Proceedings of the Second United Nations International Conference on the Peaceful Uses of Atomic Energy (held in Geneva, 1 September - 13 September 1958), 1958, pp. 299-306.

[305] D.M. Poole, M.G. Bale, P.G. Mardon, J.A.C. Marples, J.L. Nichols, Phase diagrams of some plutonium binary alloy systems, in: E. Grison, W.B.H. Lord, R.D. Fowler (Eds.) Plutonium 1960 (Proceedings of the second international conference on plutonium metallurgy, Grenoble, France, 19-22 April 1960), Cleaver-Hume Press Limited for Commissariat à l'énergie atomique, London, 1961, pp. 267-281.

[306] R.G. Cope, D.G. Hughes, R.G. Loasby, D.C. Miller, The plutonium-ruthenium and plutonium-neptunium binary phase diagrams, in: E. Grison, W.B.H. Lord, R.D. Fowler (Eds.) Plutonium 1960 (Proceedings of the second international conference on plutonium metallurgy, Grenoble, France, 19-22 April 1960), Cleaver-Hume Press Limited for Commissariat à l'énergie atomique, London, 1961, pp. 280-289.

[307] M.B. Waldron, J. Garstone, J.A. Lee, P.G. Mardon, J.A.C. Marples, D.M. Poole, G.K. Williamson, The physical metallurgy of plutonium, in: Proceedings of the Second United Nations International Conference on the Peaceful Uses of Atomic Energy (Geneva, 1 September - 13 September 1958), United Nations, Geneva, 1958, pp. 162-169.

[308] P.G. Mardon, J.H. Pearce, J.A.C. Marples, Constitution studies on the neptunium-plutonium alloy system, Journal of the Less-Common Metals, 3 (1961) 281-292.

[309] R.I. Sheldon, D.E. Peterson, The Np-Pu (Neptunium-Plutonium) System, Bulletin of Alloy Phase Diagrams, 6 (1985) 215-217.

[310] H. Okamoto, Np-Pu (Neptunium-Plutonium), Journal of Phase Equilibria and Diffusion, 34 (2013) 154-155.

[311] A. Landa, P. Söderlind, P.E.A. Turchi, L. Vitos, O.E. Peil, A.V. Ruban, Density-functional study of bcc Pu-U, Pu-Np, Pu-Am, and Pu-Cm alloys, Journal of Nuclear Materials, 408 (2011) 61-66.

[312] A.F. Berndt, Single crystal study of an alpha-plutonium-neptunium alloy, Journal of Nuclear Materials, 11 (1964) 352.

[313] C.E. Olsen, R.O. Elliott, Electrical behavior of plutonium-neptunium alloys, Physical Review, 139 (1965) A437.

[314] J.A. Lee, R.O.A. Hall, E. King, G.T. Meaden, Some properties of plutonium and plutonium-rich alloys, in: E. Grison, W.B.H. Lord, R.D. Fowler (Eds.) Plutonium 1960 (The proceedings of the second international conference on plutonium metallurgy, Grenoble, France, 19-22 April 1960), Cleaver-Hume Press Ltd., London, 1961, pp. 39-50.

[315] T.A. Sandenaw, R.B. Gibney, The electrical resistivity and thermal conductivity of plutonium metal, Journal of Physics and Chemistry of Solids, 6 (1958) 81-88.

[316] H. Okamoto, Am-Np (Americium-Neptunium), Journal of Phase Equilibria, 20 (1999) 450.

[317] H. Okamoto, Am-Np (Americium-Neptunium), Journal of Phase Equilibria and Diffusion, 33 (2012) 502.

[318] F.H. Ellinger, K.A. Johnson, V.O. Struebing, The plutonium-americium system (Los Alamos Scientific Laboratory Report LA-DC-7095), Los Alamos, New Mexico, 1965.

[319] F.H. Ellinger, K.A. Johnson, V.O. Struebing, The plutonium-americium system, Journal of Nuclear Materials, 20 (1966) 83-86.

[320] V.D. Shushakov, N.S. Kosulin, N.T. Chebotarev, Pu-Am phase diagram, Voprosy Atom. Nauki Tekh. Ser. Materialoved. Novye Mater., 3 (1990) 14-15 (in Russian).

[321] P. Gotcu-Freis, J.-Y. Colle, C. Guéneau, N. Dupin, B. Sundman, R.J.M. Konings, A thermodynamic study of the Pu-Am-O system, Journal of Nuclear Materials, 414 (2011) 408-421.

[322] P.E.A. Turchi, A.I. Landa, P.A. Söderlind, Thermodynamic assessment of the Am-Pu system with input from *ab initio*, Journal of Nuclear Materials, 418 (2011) 165-173.

[323] P. Javorský, L. Havela, F. Wastin, E. Colineau, D. Bouëxière, Specific heat of delta-Pu stabilized by Am, Physical Review Letters, 96 (2006) 156404.

[324] L. Havela, P. Javorský, A. Shick, F. Wastin, E. Colineau, Specific heat in the Pu-Am system, in: Materials Research Society Symposium Proceedings vol. 986 (Actinides 2006--Basic Science, Applications, and Technology), 2007, pp. 129-134.

[325] N. Baclet, M. Dormeval, L. Havela, J.M. Fournier, C. Valot, F. Wastin, T. Gouder, E. Colineau, C.T. Walker, S. Bremier, C. Apostolidis, G.H. Lander, Character of 5*f* states in the Pu-Am system from magnetic susceptibility, electrical resistivity, and photoelectron spectroscopy measurements, Physical Review B, 75 (2007) 035101.

[326] A. Shick, L. Havela, J. Kolorenč, V. Drchal, T. Gouder, P.M. Oppeneer, Electronic structure and nonmagnetic character of δ-Pu-Am alloys, Physical Review B, 73 (2006) 104415.

[327] J. Kolorenč, A.B. Shick, L. Havela, A.I. Lichtenstein, Electronic structure theory of Pu-Am and Pu-Ce alloys, and thin δ-Pu films, in: Basic Actinide Science and Materials for Nuclear Applications, 2010, pp. 111-115.

[328] B. Ravat, L. Jolly, C. Valot, N. Baclet, Local structure in plutonium alloys stabilized in delta-phase, Plutonium Futures--The Science, 673 (2003) 7-8.

[329] P. Söderlind, A. Landa, W.G. Wolfer, Atomic-volume variations of α-Pu alloyed with Al, Ga, and Am from first-principles theory, Journal of Computer-Aided Materials Design, 14 (2007) 349-355.

[330] H. Okamoto, Am-Pu (americium-plutonium), Journal of Phase Equilibria, 20 (1999) 451.

[331] Y.Y. Tsiovkin, A.A. Povzner, L.Y. Tsiovkina, V.V. Dremov, L.R. Kabirova, A.A. Dyachenko, V.B. Býstrushkin, M.V. Ryabukhina, A.V. Lukoyanov, A.O. Shorikov, Temperature and concentration dependences of the electrical resistivity for alloys of plutonium with americium under normal conditions, Journal of Experimental and Theoretical Physics, 111 (2010) 1019-1027 (translated from Zhurnal Ëksperimental'noï i Teoterischeskoï Fiziki, Vol. 1138, No. 1015, pp. 1153-1162, 2010).

[332] M. Kurata, Thermodynamic database on U-Pu-Zr-Np-Am-Fe alloy system I - Re-evaluation of U-Pu-Zr alloy, IOP Conference Series: Materials Science and Engineering, 9 (Actinides 2009) (2010) 1-8.

[333] R. Vogel, H. Klose, Über die Zustandsbilder Cer-Lanthan, Lanthan-Antimon und Cer-Indium, Zeitschrift für Metallkunde, 45 (1954) 633-638.

[334] K.A. Gschneidner Jr., Systematics of the intra-rare-earth binary alloy systems, Journal of the Less-Common Metals, 114 (1985) 29-42.

[335] T.B. Scott, C.M. Younes, M. Ling, C.P. Jones, J.A. Nicholson, P.J. Heard, R. Jenkins, Initial microstructural study of a Ce-La alloy using electron backscattered diffraction, Journal of Alloys and Compounds, 509 (2011) 4284-4289.

[336] M.V. Bulanova, P.N. Zheltov, K.A. Meleshevich, Lanthanum-cerium-silicon system, Journal of Alloys and Compounds, 347 (2002) 149-155.

[337] Z.-Y. Zeng, C.-E. Hu, Z.-G. Li, W. Zhang, L.-C. Cai, High pressure phase transition of Ce-La alloy from first-principles calculations, Journal of Alloys and Compounds, 640 (2015) 201-204.

[338] L.-Q. Zhang, Y. Cheng, Z.-W. Niu, G.-F. Ji, First-principles investigations on structural, elastic, and thermodyamic properties of Ce-La alloys under high pressure, Zeitschrift für Naturforschung Section A, 69 (2014) 52-60.

[339] T.S. Petersen, S. Legvold, K.A. Gschneidner, T.-W.E. Tsang, J.O. Moorman, Magnetic ordering in Ce-La and Nd-La alloys, Journal of Applied Physics, 49 (1978) 2115-2117.

[340] L. Bezukladnikova, V. Kononenko, Influence of small amounts of rare-earth metals on the surface and volume properties of lanthanum, Russian Metallurgy (Metally), (1997) 22-27 (Translated from Izvestiya Rossiiskoi Akademii Nauk. Metally no. 25, pp. 22-27, 1997).

[341] E. King, I.R. Harris, High pressure resistance measurements of some lanthanum-cerium alloys, Journal of the Less-Common Metals, 27 (1972) 51-63.

[342] M. Norman, I.R. Harris, G.V. Raynor, Lattice spacings and effective atomic diameters in the ternary systems formed by Th and Ce with Y, La, Gd and Er, and by Th, Pr, and Y, Journal of the Less-Common Metals, 13 (1967) 24-44.

[343] D.S. Evans, G.V. Raynor, Lattice spacing relationships in system thorium-cerium-lanthanum, Journal of Nuclear Materials, 5 (1962) 308-316.

[344] K.A. Gschneidner Jr., R.O. Elliott, R.Y. Prince, The lattice spacings of some cerium-rich, cerium-rare-earth alloys, in: J.F. Nachman, C.E. Lundin (Eds.) Rare Earth Research (Proceedings of the 2nd conference on rare-earth research, 1961), Gordon and Breach, New York, 1962, pp. 71.

[345] D.W. Wheeler, I. Khan, A Raman spectroscopy study of cerium oxide in a cerium-5 wt% lanthanum alloy, Vibrational Spectroscopy, 70 (2014) 200-206.

[346] K.A. Gschneidner Jr., R.O. Elliott, R.R. McDonald, Effects of alloying additions on the $\alpha \leftrightarrow \gamma$ transformation of cerium--part III. Effects of yttrium and rare earth additions, Journal of Physics and Chemistry of Solids, 23 (1962) 1201-1208.

[347] Y.M. Savitskiy, V.F. Terekhov, Phase diagrams of alloys of lanthanum with cerium, and lanthanum with calcium, Journal of Inorganic Chemistry, USSR, 3 (1958) 298-309 (translated from Zhurnal Neorganicheskoi Khimii vol III no 293 pp 758-762, 1958).

[348] M.V. Vedernikov, I.A. Markova, G.N. Meshkova, Electrical resistivity and thermal EMF of La-Ce, La-Pr, and Pr-Nd alloys, Fiz. Tverd. Tela, 7 (1965).

[349] H. Okamoto, La-Pr phase diagram, in: P. Villars, H. Okamoto, K. Cenzual (Eds.) ASM Alloy Phase Diagrams Center, ASM International, Materials Park, OH, 1990.

[350] H. Okamoto, La-Pr (Lanthanum-Praseodymium), in: T.B. Massalski, H. Okamoto, P.R. Subramanian, L. Kacprzak (Eds.) Binary Alloy Phase Diagrams, Second Edition, ASM, Materials Park, OH, 1990, pp. 2411, 2413.

[351] L.L. Bezukladnikova, V.I. Kononenko, M.M. Mit'ko, Density and surface tension of La-Pr melts, Russian Metallurgy (Metally), 5 (1989) 25-29 (Translated from Izvestiya Akademii Nauk SSSR, Metally, No. 25 pp. 31-35).

[352] A.H. Daane, F.H. Spedding, Quarterly Summary Research Report in Physics for July, August, and September, 1954 (USAEC report ISC-530), Ames Laboratory, Ames, IA, 1954.

[353] S. Wu, L. Zhang, L. Zeng, Y. Zhuang, Phase relationship of the La-Nd-Fe system at 770 K, Journal of Alloys and Compounds, 291 (1999) 220-221.

[354] K. Yang, L. Xu, M. Rong, Q. Yao, J. Wang, Thermodynamic calculation of phase diagrams for the rare-earth binary alloys: RE-Nd (RE = La, Ce, Pr, Y) systems, in: Y. Han (Ed.) Advances in Materials

Processing, Lecture Notes in Mechanical Engineering (Proceedings of Chinese Materials Conference 2017), 2018, pp. 1305-1313.

[355] E.M. Forgan, S.L. Lee, W.G. Marshall, S. Zochowski, Magnetism in the Nd-La system, Journal of Magnetism and Magnetic Materials, 104-7 (1992) 1519-1520.

[356] K.A. Gschneidner Jr., F.W. Calderwood, The Ce-Pr (cerium-praseodymium) system, Bulletin of Alloy Phase Diagrams, 3 (1982) 187-188.

[357] M. Altunbas, I.R. Harris, Structural and constitutional studies of some cerium-praseodymium alloys, Journal of Materials Science, 15 (1980) 693-701.

[358] K.A. Gschneidner Jr., Cerium-praseodymium binary phase diagram, in: P. Villars, H. Okamoto, K. Cenzual (Eds.) ASM Alloy Phase Diagrams Center, ASM International, Materials Park, OH, 1990.

[359] K.A. Gschneidner Jr., F.W. Calderwood, Ce-Pr (cerium-praseodymium), in: T.B. Massalski, H. Okamoto, P.R. Subramanian, L. Kacprzak (Eds.) Binary Alloy Phase Diagrams, Second Edition, ASM, Materials Park, OH, 1990, pp. 1095, 1097.

[360] M. Altunbas, K.N.R. Taylor, G.A. Wilkinson, Kondo resistivity of Pr-Ce alloys, Philosophical Magazine, 29 (1974) 349-371.

[361] J.D. Speight, I.R. Harris, G.V. Raynor, Alloys of cerium with neodymium, samarium and terbium, and of praseodymium with terbium, Journal of the Less-Common Metals, 15 (1968) 317-330.

[362] D.D. Keiser Jr., Diffusion in the Ce-Nd system, Scripta Metallurgical et Materialia, 33 (1995) 959-965.

[363] O. Hachimi, S. Hayun, A. Venkert, M.P. Dariel, Microstructural study of Ce-Nd alloys, Journal of Alloys and Compounds, 427 (2007) 104-109.

[364] W.G. Moffatt, ed., Handbook of Binary Phase Diagrams, Genium Publishing Corp., Schenectady, NY, 1984.

[365] H. Okamoto, Ce-Nd phase diagram, in: P. Villars, H. Okamoto, K. Cenzual (Eds.) ASM Alloy Phase Diagrams Center, ASM International, Materials Park, OH, 1990.

[366] J.H. Kim, J.S. Cheon, B.O. Lee, J.H. Kim, Interaction behavior between binary xCe-yNd alloy and HT9, Journal of Nuclear Materials, 479 (2016) 394-401.

[367] K.A. Gschneidner Jr., F.W. Calderwood, The Ce-Nd (cerium-neodymium) system, Bulletin of Alloy Phase Diagrams, 3 (1982) 90.

[368] W.L. Bragg, E.A. Wood, The conversion factor for kX units to Ångstrom units, Journal of the American Chemical Society, 69 (1947) 2919.

[369] G. Cacciamani, A.M. Cardinale, G. Borzone, R. Ferro, Thermodynamic modelling and optimization of the Al-Ce-Nd system, Computer Coupling of Phase Diagrams and Thermochemistry, 27 (2003) 227-233.

[370] I.A. Markova, V.F. Terekhova, E.M. Savitskii, Equilibrium diagram of the alloys of the neodymium-praseodymium system, Russian Journal of Inorganic Chemistry, 8 (1963) 1041-1042.

[371] C.E. Lundin, A.S. Yamamoto, J.F. Nachman, Studies of solution ideality in the praseodymium-neodymium system, Acta Metallurgica, 13 (1965) 149-154.

[372] C.E. Lundin, J.F. Nachman, A.S. Yamamoto, Investigations of the praseodymium-neodymium system, in: K.S. Vorres (Ed.) Proceedings of the 3rd conference on rare-earth research, Clearwater, 1964, pp. 315-328.

[373] K.A. Gschneidner Jr., F.W. Calderwood, The Nd-Pr (neodymium-praseodymium) system, Bulletin of Alloy Phase Diagrams, 3 (1982) 196-198.

[374] K.A. Gschneidner Jr., F.W. Calderwood, Nd-Pr (Neodymium-Praseodymium), in: T.B. Massalski, H. Okamoto, P.R. Subramanian, L. Kacprzak (Eds.) Binary Alloy Phase Diagrams, Second Edition, ASM, Materials Park, OH, 1990, pp. 2794, 2796.

[375] K.A. Gschneidner Jr., Neodymium-praseodymium binary phase diagram, in: P. Villars, H. Okamoto, K. Cenzual (Eds.) ASM Alloy Phase Diagrams Center, ASM International, Materials Park, OH, 1990.

[376] C.E. Lundin, M.J. Pool, Heats of mixing in praseodymium-neodymium solid solutions, Journal of the Less-Common Metals, 9 (1965) 48-53.

[377] G.J. Shiflet, J.K. Lee, H.I. Aaronson, Application of the Kaufman approach to the calculation of intra-rare earth phase diagrams, CALPHAD, 3 (1979) 129-137.

[378] P.E. Palmer, H.R. Burkholder, B.J. Beaudry, K.A. Gschneidner Jr., The preparation and some properties of pure misch metal, Journal of the Less-Common Metals, 87 (1982) 135-148.

[379] P. Villars, PAULING FILE in: Inorganic Solid Phases, SpringerMaterials (online database), in: P. Villars (Ed.), SpringerMaterials, Heidelberg, La-rich misch metal (La0.273C30.472Pr0.08Nd0.175) Crystal Structure.

[380] F.A. Rough, A.A. Bauer, Constitution of uranium and thorium alloys (Battelle Memorial Institute Report BMI-1300), Battelle Memorial Institute, Columbus, OH, 1958.

[381] J.F. Haefling, A.H. Daane, The immiscibility limits of uranium with the rare-earth metals, Transactions of the Metallurgical Society of AIME, 215 (1959) 336-338.

[382] Y. Shoji, T. Matsui, K. Nakamura, T. Inoue, Vaporization study on lanthanum-uranium and cerium-uranium alloys, Journal of Nuclear Materials, 265 (1999) 134-138.

[383] A.P. Bayanov, Thermodynamic properties of liquid alloys of uranium with certain rare earth metals, Soviet Radiochemistry, 12 (1970) 735-737 (Translated from Radiokhimiya, vol. 712, no. 735, pp. 768-771, 1970).

[384] J.W. McMurray, D. Shin, T.M. Besmann, Thermodynamic assessment of the U–La–O system, Journal of Nuclear Materials, 456 (2015) 142-150.

[385] H. Okamoto, La-U (lanthanum-uranium), Journal of Phase Equilibria, 20 (1999) 639.

[386] C.E. Lundin, Rare-earth metal phase diagrams, in: F.H. Spedding, A.H. Daane (Eds.) The Rare Earths, John Wiley & Sons, Inc., for the American Society for Metals in Cooperation with the Office of Technical Information, United States Atomic Energy Commission, New York, 1961, pp. 224-385.

[387] J.W. McMurray, C.M. Silva, Experimental oxygen potentials for U1-xPryO2 +/-x and thermodynamic assessment of the U-Pr-O system, Journal of Nuclear Materials, 470 (2016) 111-118.

[388] H. Okamoto, Pr-U phase diagram, in: P. Villars, H. Okamoto, K. Cenzual (Eds.) ASM Alloy Phase Diagrams Center, ASM International, Materials Park, OH, 1990.

[389] M. Peatfield, N.H. Brett, P.E. Potter, Constitutional studies on carbide nuclear fuels for fast breeder reactors II. The uranium-praseodymium-carbon ternary system, Journal of Nuclear Materials, 89 (1980) 27-34.

[390] S.M. Lee, T.W. Knight, J.W. McMurray, T.M. Besmann, Measurement of the oxygen partial pressure and thermodynamic modeling of the U-Nd-O system, Journal of Nuclear Materials, 473 (2016) 272-282.

[391] G. Dottavio, Y. Pontillon, L. Desgranges, C. Guéneau, R.C. Belin, Characterizing the U-Nd-O miscibility gap by an experimental and a theoretical approach, Journal of Nuclear Materials, 458 (2015) 394-405.

[392] D.G. Parnell, N.H. Brett, H.R. Haines, P.E. Potter, Phase relationships in the ternary system U-Nd-Pd, Journal of the Less-Common Metals, 118 (1986) 141-152.

[393] H. Okamoto, Nd-U phase diagram, in: P. Villars, H. Okamoto, K. Cenzual (Eds.) ASM Alloy Phase Diagrams Center, ASM International, Materials Park, OH, 1990.

[394] T. Inoue, M. Kurata, L. Koch, J.C. Spirlet, C.T. Walker, C. Sari, Characterization of fuel alloys with minor actinides, Transactions of the American Nuclear Society, 64 (1991) 552-553.

[395] M. Kurata, T. Inoue, C. Sari, Redistribution behavior of various constituents in U-Pu-Zr alloy and U-Pu-Zr alloy containing minor actinides and rare-earths in a temperature-gradient, Journal of Nuclear Materials, 208 (1994) 144-158.

[396] C. Sari, C.T. Walker, M. Kurata, T. Inoue, Interaction of U-Pu-Zr alloys containing minor actinides and rare-earths with stainless-steel, Journal of Nuclear Materials, 208 (1994) 201-210.

[397] D.E. Janney, J.R. Kennedy, As-cast microstructures in U-Pu-Zr alloy fuel pins with 5-8 wt% minor actinides and 0-1.5 wt% rare-earth elements, Materials Characterization, 61 (2010) 1194-1202.

[398] D.E. Janney, J.R. Kennedy, J.W. Madden, T.P. O'Holleran, Am phases in the matrix of a U-Pu-Zr alloy with Np, Am, and rare-earth elements, Journal of Nuclear Materials, 456 (2015) 46-53.

[399] D.E. Janney, J.W. Madden, T.P. O'Holleran, High- and low-Am RE inclusion phases in a U-Np-Pu-Am-Zr alloy, Journal of Nuclear Materials, 458 (2015) 106-114.

[400] F.H. Ellinger, C.C. Land, K.A. Johnson, The plutonium-lanthanum system, Transactions of the Metallurgical Society of AIME, 239 (1967) 895-898.

[401] X.J. Liu, Q. He, D. Wang, Y. Lu, M.H. Chen, J.P. Jia, C.P. Wang, Thermodynamic assessments of the Pu–Zn and La–Pu systems, Journal of Nuclear Materials, 453 (2014) 169-175.

[402] T.B. Massalski, H. Okamoto, P.R. Subramanian, L. Kacprzak, ed., Binary Alloy Phase Diagrams, Second Edition, ASM International, 1990.

[403] P. Villars, H. Okamoto, K. Cenzual, ASM Alloy Phase Diagrams Database, in, ASM International, Materials Park, OH, 2016.

[404] F.H. Ellinger, C.C. Land, E.M. Cramer, Plutonium-Cerium Phase Diagram, in: Extractive and Physical Metallurgy of Plutonium and its Alloys (Proceedings of a symposium sponsored by the Metallurgical Society of AIME, San Francisco, February 16-17, 1959), Interscience, 1960, pp. 149-166.

[405] J.E. Selle, D.E. Etter, The plutonium-cerium system, Transactions of the Metallurgical Society of AIME, 230 (1964) 1000-1005.

[406] R.O. Elliott, W.N. Miner, R.B. Roof Jr., C.C. Land, Transformation-induced precipitation of δ-plutonium in metastable cerium-plutonium alloys, Journal of the Less-Common Metals, 15 (1968) 106-108.

[407] B.C. Giessen, V.O. Struebing, R.O. Elliott, Metastable fcc Pu-Ce solid solutions, Materials Science and Engineering, 18 (1975) 239-243.

[408] F.H. Ellinger, W.N. Miner, D.R. O'Boyle, F.W. Schonfeld, Constitution of Plutonium Alloys (Los Alamos National Laboratory Report LA-3870), Los Alamos National Laboratory, Los Alamos, NM, 1968.

[409] M.H. Rand, D.T. Livey, P. Feschotte, H. Nowotny, K. Seifert, R. Ferro, ed., Plutonium: Physico-chemical properties of its compounds and alloys, International Atomic Energy Agency, Vienna, 1966.

[410] T.B. Massalski, Ce-Pu (cerium-plutonium), in: T.B. Massalski, H. Okamoto, P.R. Subramanian, L. Kacprzak (Eds.) Binary Alloy Phase Diagrams, Second Edition, ASM, Materials Park, OH, 1990, pp. 1132, 1134.

[411] H. Okamoto, Ce-Pu phase diagram, in: P. Villars, H. Okamoto, K. Cenzual (Eds.) ASM Alloy Phase Diagrams Center, ASM International, Materials Park, OH, 1990.

[412] R.O. Elliott, K.A. Gschneidner Jr., C.A. Kempter, Thermal expansion of some delta plutonium solid solution alloys, in: E. Grison, W.B.H. Lord, R.D. Fowler (Eds.) Plutonium 1960, Cleaver-Hume Press, London, 1961, pp. 142-155 (Paper no. 134).

[413] K.A. Gschneidner Jr., R.O. Elliott, J.T. Waber, Influence of alloying on the negative thermal expansion of delta plutonium, Acta Metallurgica, 11 (1963) 947-955.

[414] A. Goldberg, R.L. Rose, D.K. Matlock, The delta and epsilon thermal expansion coefficients and the delta-to-epsilon contraction for some plutonium-rich alloys, in: W.N. Miner (Ed.) Proceedings of the

4th International Conference on Plutonium and Other Actinides, The Metallurgical Society of AIME, 1970, pp. 1056.

[415] M. Dormeval, N. Baclet, C. Valot, P. Rofidal, J.M. Fournier, Crystalline and electronic structure of Pu-Ce and Pu-Ce-Ga alloys stabilized in the δ phase, Journal of Alloys and Compounds, 350 (2003) 86-94.

[416] J.F. Andrew, Thermal conductivity of some delta-plutonium alloys, Journal of Nuclear Materials, 30 (1969) 343-345.

[417] Monsanto Research Corporation, Reactor Fuels and Materials Development Plutonium Research: 1966 Annual Report (Mound Laboratory Report MLM-1402), Miamisburg, OH, 1967.

[418] V.I. Kutaitsev, N.T. Chebotarev, I.G. Lebedev, M.A. Andrianov, V.N. Konev, T.S. Menshikova, Phase diagrams of plutonium with the metals of groups IIA, IVA, VIIIA and IB, in: A.E. Kay, M.B. Waldron (Eds.) Plutonium 1965, Chapman and Hall for The Institute of Metals, 1965, pp. 420-449.

[419] V.I. Kutaitsev, N.T. Chebotarev, M.A. Andrianov, V.N. Konev, I.G. Lebedev, V.I. Bagrova, A.V. Beznosikova, A.A. Kruglov, P.N. Petrov, E.S. Smotritskaya, Phase diagrams of plutonium with metals of groups IIA, IVA, VIII, and IB, Soviet Atomic Energy, 23 (1967) 1279-1287 (Translated from Atomnaya Énergiya, vol 1223, no. 1276, pp. 1511-1519, 1967).

[420] F.H. Ellinger, C.C. Land, K.A. Johnson, Binary systems of plutonium with praseodymium, neodymium, and samarium, Journal of Nuclear Materials, 29 (1969) 178-183.

[421] H.H. Hill, F.H. Ellinger, The effective size of americium dissolved in lanthanum, Journal of the Less-Common Metals, 23 (1971) 92-94.

[422] W.V. Conner, Investigation of americium-241 metal alloys (Rocky Flats Plant Report RFP-3106), 1981.

[423] W.V. Conner, Ductile transplutonium alloys (United States Patent 4380470), (1983).

[424] R.J. Rodríguez, C. Sari, A.J.C. Portal, Investigation of the Np-Zr and U-Np-Zr systems, Journal of Alloys and Compounds, 209 (1994) 263-268.

[425] J.K. Gibson, R.G. Haire, M.M. Gensini, T. Ogawa, Alloying behavior in selected neptunium binary systems: the role of 5f bonding, Journal of Alloys and Compounds, 213/214 (1994) 106-110.

[426] J.K. Gibson, R.G. Haire, High-temperature DTA of transuranium metals with application to the Np-Zr phase diagram, Thermochimica Acta, 207 (1992) 65-78.

[427] J.K. Gibson, R.G. Haire, Investigation of the neptunium-zirconium phase diagram by differential thermal analysis, Journal of Nuclear Materials, 201 (1993) 225-230.

[428] J.K. Gibson, R.G. Haire, T. Ogawa, Semi-empirical models of actinide alloying, Journal of Nuclear Materials, 273 (1999) 139-145.

[429] T. Ogawa, J.K. Gibson, R.G. Haire, M.M. Gensini, M. Akabori, Thermodynamic analysis of Zr-U and Zr-Np alloys in view of f-d interaction, Journal of Nuclear Materials, 223 (1995) 67-71.

[430] S. Bajaj, A. Garay, A. Landa, P. Söderlind, P. Turchi, R. Arróyave, Thermodynamic study of the Np-Zr system, Journal of Nuclear Materials, 409 (2011) 1-8.

[431] W. Xiong, W. Xie, D. Morgan, Thermodynamic evaluation of the Np–Zr system using CALPHAD and ab initio methods, Journal of Nuclear Materials, 452 (2014) 569-577.

[432] H. Okamoto, Np-Zr (Neptunium-Zirconium), Journal of Phase Equilibria and Diffusion, 34 (2013) 59-60.

[433] M.M. Gensini, R.G. Haire, J.K. Gibson, Investigation of the neptunium-zirconium system by X-ray diffraction, Journal of Alloys and Compounds, 213/214 (1994) 402-405.

[434] Y. Okamoto, R.G. Haire, J.K. Gibson, T. Ogawa, The investigation of selected Np-Zr alloys by X-ray diffraction up to 700 °C, Journal of Alloys and Compounds, 232 (1996) 302-306.

[435] H. Okamoto, Np-Zr (Neptunium-Zirconium), Journal of Phase Equilibria, 17 (1996) 166-167.

[436] H. Okamoto, Am-Zr (Americium-Zirconium), Journal of Phase Equilibria and Diffusion, 33 (2012) 504.

[437] N. Mattern, Y. Yokoyama, A. Mizuno, J.H. Han, O. Fabrichnaya, M. Richter, S. Kohara, Experimental and thermodynamic assessment of the La-Ti and La-Zr systems, CALPHAD, 52 (2016) 8-20.

[438] H. Okamoto, Supplemental literature review of binary phase diagrams: B-Fe, Cr-Zr, Fe-Np, Fe-W, Fe-Zn, Ge-Ni, La-Sn, La-Ti, La-Zr, Li-Sn, Mn-S, and Nb-Re, Journal of Phase Equilibria and Diffusion, 37 (2016) 621-634.

[439] D. Peng, Y. Zhang, J. She, M. Pang, Y. Du, Phase equilibria in the ternary Al-Zr-La system, Journal of Alloys and Compounds, 507 (2010) 62-66.

[440] C. Li, Y. Zhan, J. She, Q. Huang, M. Pang, W. Yang, Phase diagrams of the Zr-Si-Re (RE = La and Er) ternary systems at 773 K (500 °C), Metallurgical and Materials Transactions A, 43 (2012) 20-28.

[441] N. Mattern, Y. Yokoyama, A. Mizuno, J.H. Han, O. Fabrichnaya, H. Wendrock, T. Harada, S. Kohara, J. Eckert, Experimental and thermodynamic assessment of the Ce-Zr system, CALPHAD: Computer Coupling of Phase Diagrams and Thermochemistry, 46 (2014) 213-219.

[442] H. Okamoto, Supplemental literature review of binary phase diagrams: Ag-Cl, Br-PPb, Br-Zn, C-Cu, Ce-Zr, Cl-Zn, Fe-Lu, Fe-Tm, Ga,V, Nd-Ti, Nd-Zr, and Si-Ta, Journal of Phase Equilibria and Diffusion, 37 (2016) 246-257.

[443] I.R. Harris, G.V. Raynor, The electronic state of cerium in zirconium-cerium alloys, Journal of the Less-Common Metals, 6 (1964) 70-80.

[444] W.G. Moffatt, ed., Handbook of Binary Phase Diagrams, Genium Publishing Corporation, Schenectady, NY, 1978.

[445] T.B. Massalski, Ce-Zr (cerium-zirconium), in: T.B. Massalski, H. Okamoto, P.R. Subramanian, L. Kacprzak (Eds.) Binary Alloy Phase Diagrams, Second Edition, ASM, Materials Park, OH, 1990, pp. 1132, 1134.

[446] H. Okamoto, Ce-Zr phase diagram, in: P. Villars, H. Okamoto, K. Cenzual (Eds.) ASM Alloy Phase Diagrams Center, ASM International, Materials Park, OH, 1990.

[447] A. Palenzona, S. Cirafici, The Ce-Zr (cerium-zirconium) system, Journal of Phase Equilibria, 12 (1991) 49-52.

[448] V. Raghavan, Al-Pr-Zr (Aluminum-Praseodymium-Zirconium), Journal of Phase Equilibria and Diffusion, 32 (2010) 67.

[449] J. She, Y. Zhan, C. Li, Y. Du, H. Xu, Y. He, Phase equilibria of the Al-Pr-Zr ternary system at 773 K, Journal of Alloys and Compounds, 503 (2010) 57-60.

[450] V. Raghavan, Al-Nd-Zr (Aluminum-Neodymium-Zirconium), Journal of Phase Equilibria and Diffusion, 32 (2011) 468.

[451] K. Cheng, H. Zhou, B. Hu, Y. Du, L. Zhang, S. Liu, H. Xu, L. Liu, Experimental investigation and thermodynamic modeling of the Nd-Zr and the Mg-Nd-Zr systems, Metallurgical and Materials Transactions A, 45A (2014) 2708-2718.

[452] N. Mattern, Y. Yokoyama, A. Mizuno, J.H. Han, O. Fabrichnaya, T. Harada, S. Kohara, J. Eckert, Experimental and thermodynamic assessment of the Nd-Zr system, CALPHAD: Computer Coupling of Phase Diagrams and Thermochemistry, 46 (2014) 103-107.

[453] K. Peng, Z. Jieyu, L. Qian, Z. Zhang, Phase equilibria in the Mg-Nd-Zr ternary system, Shanghai Metals, 37 (2015) 60-65 (in Chinese with English abstract and captions).